Proceedings of the 11th Brazilian Congress of Thermal Sciences and Engineering – ENCIT 2006
Braz. Soc. of Mechanical Sciences and Engineering – ABCM, Curitiba, Brazil, Dec. 5-8, 2006

Paper CIT06-1074

ON THE VORTEX PAIRING AEROACOUSTICS OF A 2D MIXING LAYER UNDER TEMPORAL DEVELOPMENT

Alysson Kennerly Colaciti
USP - Universidade de São Paulo, NPA - SMM - EESC. Av. Trabalhador Sãocarlense, 400, Centro, cep:13560-970, São Carlos - SP Brasil
alyssonkennerly@gmail.com

Ricardo A. Coppola Germanos
University of Arizona / USP - Universidade de São Paulo, NPA - SMM - EESC. Av. Trabalhador Sãocarlense, 400, Centro, cep:13560-970, São Carlos - SP Brasil
gercop@sc.usp.br

Marcello Augusto Faraco de Medeiros
USP - Universidade de São Paulo, NPA - SMM - EESC. Av. Trabalhador Sãocarlense, 400, Centro, cep:13560-970, São Carlos - SP Brasil
marcello@sc.usp.br

Abstract. *The aim of the present work is to investigate numerically the aeroacoustics of a vortex pairing in the temporal development of a free shear layer. Direct numerical simulation with high accuracy finite difference scheme was employed in this research. A characteristic-type formulation of the compressible 2D Navier Stokes equations was used. One of the main challenges found on the development of this research was to produce a single vortex pairing in the middle of a wide computational domain. Time development of mixing layers adopts the periodic boundary condition in x-direction, what makes it more difficult to reproduce a single vortex pairing inside a wide domain. The domain must be large enough to provide a clear observation of the acoustic field produced by the pairing. The simulation produced a double spiral structure, corresponding to the rotating quadrupole associated to two co-rotative vortices, which agreed with the literature on the vortex pairing aeroacoustics. Some different behaviors of the acoustic field can also be observed for this pairing geometry.*

keywords: *Aeroacoustics, Vortex pairing, Hydrodynamic instability, Mixing layer, DNS*

1. Introduction

Flow generated sound is a serious problem in many engineering applications. It can cause human discomfort; it affects the stealth operation of military vehicles; etc. Due to the current aircraft traffic, community noise concerns at busy airports constraint the operation of noisy aircraft. In response to this fact, FAA also included stringent regulations to the aircraft noise level operation and certification [Wang *et al.*, 2006; Colonious and Lele, 2004]. Airframe noise is the major responsible for the sound level of landing aircraft, since the propulsion system is near to the lowest power level. The impact of those mentioned facts on the worldwide aircraft industry is the greater attention paid to noise in the design stage, leading to the need of an efficient noise level prediction method.

Hydrodynamic instability phenomena are determinant to a wide family of aerodynamically generated sound. This strong link is due to the transient and periodic nature of both the Hydrodynamic instability and the aerodynamic sound generation phenomena. Two classical cases of aerodynamic sound generation are the vortex-shedding and vortex pairing [Wang *et al.*, 2006; Colonious and Lele, 2004]. The vortex pairing phenomenon follows a chain of events starting with the primary disturbance amplification leading to the production of vortex structures, which is the classical Kelvin Helmholz instability mechanism. Those small primary disturbances exponentially grow in time or space and reach the saturation point, when the vortex structures are formed. Thus, when the vortex distribution geometry is already established, the secondary instability takes place leading to the pairing of the primary vortices. Those steps are better explained in the following sections.

Vortex pairing is a remarkable phenomenon that generates noise in the jet flow case [Colonious *et al.*, 1997; Colonious and Lele, 2004; Wang *et al.*, 2006]. In Colonious *et al.*, 1997 an investigation of the sound radiation in a mixing layer under spatial development was performed. Their work used one fundamental frequency disturbance and its three subharmonic frequencies ($f/2$,$f/4$ and $f/8$) which would lead to three pairings. Once

a shorter streamwise domain was adopted, only two pairings were observed. Direct Numerical Simulation (DNS) results filtered with the pairing frequency and subsequent comparison with the results obtained with the Lilley's acoustic analogy (using DNS data to compute the source terms) were shown. Colonius, et. al. concluded, for the free shear layer problem, that acoustic sources are better modeled by modulated wave packets in the streamwise direction than by the Lighthill's compact quadrupole acoustic sources.

A double spiral structure, corresponding to the rotation of a quadrupole source type was obtained by Large Eddy Simulations (LES) of a free shear layer under spatial development in Bogey *et al.*, 2000. Bogey, et. al. attributed this rotation of the quadrupoles sources to the rollup of the two co-rotative vortices, i.e., the rotation of the vortex structures during the pairing. By comparing the wave pattern generated by the rotation of two close rigid objects on a deep-water surface, one can find analogous to those structures reported in Bogey *et al.*, 2000. This analogy can be done due to the vortex structure momentum, since during the pairing begining there is no much mixture between the two vortices.

In numerical simulations of sound generation, Colonious and Lele, 2004; Colonious *et al.*, 1997 showed typical discrepancies between the disturbances near the vortical region and the acoustic disturbances at the far field region of 4 or even 5 orders of magnitude lower. This shows that, the code accuracy is strongly relevant for aeroacoustic study purposes. A code developed by Germanos and Medeiros, 2005 was used to investigate the flow instability of a compressible shear layer. The code accuracy was an important concern in their work. They used a high order compact finite difference scheme for computing the spatial derivatives and a 4^{th} order Runge-Kutta scheme for the time integration. Germanos and Medeiros, 2005 verified the code against the Linear Stability Theory (LST).

The current work presents the tests performed to validate and verify the code used to investigate the vortex pairing aeroacoustics. The strategy adopted in this code was the DNS with a 6^{th} order compact finite difference scheme, proposed by Lele, 1992. A 4^{th} order Runge Kutta integration scheme was also used in this code. The same code developed by Germanos and Medeiros, 2005 was used with a different formulation. The formulation adopted was proposed by Sesterhenn, 2001.

In the present work, the pairing simulations were performed under temporal development. The domain used for the simulations was large enough to capture the acoustic far field. Qualitative acoustic source characterization, such as the directivity and the acoustic structures caused by a single pairing, could be done with the simulation results. The aim of this analysis is to investigate the sound source features found by Colonious *et al.*, 1997 and Bogey *et al.*, 2000. Apparently, the time development of a single pairing in a wide domain has not been reported previously in the literature. Once we characterize the acoustic source of sound of a single pairing it can become easier to understand more complex cases, such as a shear layer under spatial development with more than one pairing.

2. Linear stability theory

The aim of this section is to show the results of a verification test with comparisons with the LST prediction. The case study is the Kelvin-Helmholz instability in a temporal development of a 2D free shear layer problem. The LST predicts the time amplification of eigenfunctions for a time constant base-flow. To keep a constant base-flow in time, a source term was used for the x-direction momentum equation in such a way that no viscous enlargement occurred in time. A $0 < x < 7; -14 < y < 14$ domain was adopted with 32 points along the x-direction and 128 points along the y-direction. Periodic boundary conditions for the x-direction and the free-slip boundary condition for the y-direction were used. A similar validation methodology was employed by Fortuné, 2000. The base-flow can be viewed in Fig. 1.

The problem set-up is:

$$\delta_w = 1; \qquad c_{ref} = 340.21 \qquad Ma = 0.05; \qquad U_{max} = Mac_{ref};$$

$$u(x, y, t = 0) = U_{max} \tanh\left(\frac{2y}{\delta_w}\right) + u_p(x, y); \qquad v(x, y, t = 0) = v_p(x, y);$$

$$Re = \frac{\rho U_{max} \delta_w}{\mu} = 80;$$

where: δ_w is the mixing layer vorticity thickness; c_{ref} is the reference speed of sound; Ma is the local Mach number on the upper free stream; $u_p(x, y)$ and $v_p(x, y)$ are disturbances of the velocity components in x and y directions, respectively. For the nondimensionalization, the reference scale is δ_w, the reference velocity is U_{max}, time is non-dimensionalized by $\frac{\delta_w}{U_{max}}$, entropy by c_p, density by the reference density (ρ_{ref}), temperature by $T_{ref} = \frac{c_{ref}^2}{\gamma R}$ and the pressure by the reference dynamic pressure ($\rho_{ref} U_{max}^2$). The disturbance v_p used was:

$$v_p(x, y) = e^{-\sigma\left(\frac{y}{\delta_w}\right)} \left[A_0 \cos\left(\frac{2\pi x}{L_x}\right)\right].$$

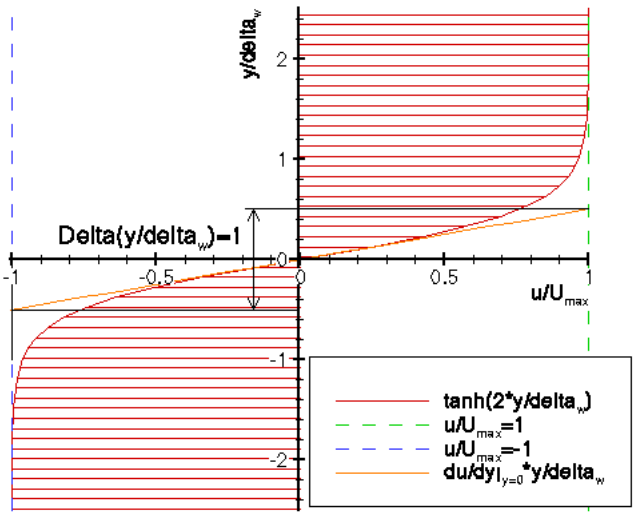

Figure 1: Base-flow sketch of the velocity profile and the δ_w definition.

By assuming the disturbance field as incompressible, i.e., $\frac{\partial u_p}{\partial x} + \frac{\partial v_p}{\partial y} = 0$, an appropriate u_p disturbance field could be obtained.

For this set of parameters defined above, the linear stability theory predicts a amplification rate of 0.31, i.e., any disturbance variable should grow in time as: $e^{0.31t}$. The exponential growth region and the saturation point of the disturbance can be seen in Fig. 2. This figure shows the LST prediction and the simulation result. The CFL number employed in this simulation was 0.55 and the viscous criterion stand beneath 0.002. The time development of the vorticity field obtained from this simulation is showed in the frame sequence of Fig. 3. The saturation point starts near the frame 3(f), i.e., when the vortex takes its recognizable shape.

3. Formulation

The aim of this section is to provide a clear understanding on the fundamentals of the characteristic-type variables proposed by Sesterhenn, 2001. The formulation will adopt the classical notation: ρ, c, p, u, s as the density, speed of sound, pressure, velocity and entropy, respectively.

3.1. Thermodynamic state equation and properties

In the present work we shall assume the thermally ideal gas equation:

$$p = \rho R T. \tag{1}$$

Differentiating equation (1):

$$dp = d\rho RT + \rho R dT. \tag{2}$$

Using the fundamental equation of enthalpy and the thermally ideal gas hypothesis ($dh = c_p dT$) we can write:

$$dh = c_p dT = Tds + \frac{dp}{\rho}. \tag{3}$$

Replacing (dT) and (T) in (3) from the equations (2) and (1), respectively, we obtain:

$$c_p\left(\frac{dp}{\rho R} - \frac{pd\rho}{\rho^2 R}\right) = \frac{p}{\rho R} ds + \frac{dp}{\rho}.$$

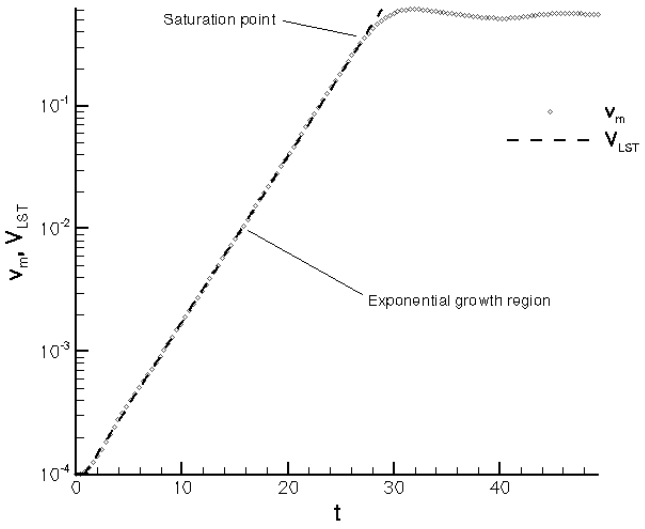

Figure 2: Time development predicted by the simulation and predicted by the LST.

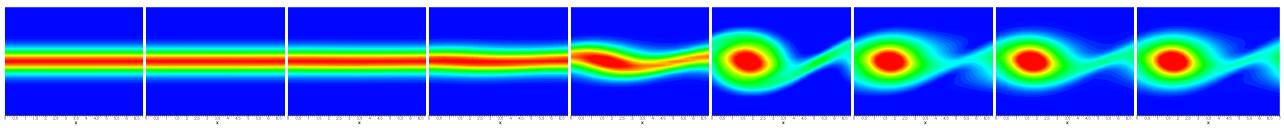

(a) (b) (c) (d) (e) (f) (g) (h) (i)

Figure 3: Time sequence of the vorticity field, the first frame is at $t = 0.0551\frac{\delta_w}{U_{max}}$ the time step between each frame is $\Delta t = 0.174\frac{\delta_w}{U_{max}}$.

Now, using $(R = c_p - c_v)$ and $\left(\gamma = \frac{c_p}{c_v}\right)$ we can write:

$$dp\frac{1}{\gamma - 1} = \frac{p}{R}ds + \frac{\gamma RT}{\gamma - 1}d\rho.$$

Thus, using $\left(c^2 = \gamma RT\right)$ we obtain equation:

$$d\rho = \frac{dp}{c^2} - \frac{p}{c^2 c_v}ds. \tag{4}$$

3.2. 1D Equations of motion

The one dimensional Euler equations of motion for a plane wave, for the reversible case, are:

$$\frac{\partial \rho}{\partial t} + \rho\frac{\partial u}{\partial x} + u\frac{\partial \rho}{\partial x} = 0 \tag{5}$$

$$\rho\left(\frac{\partial u}{\partial t} + u\frac{\partial u}{\partial x}\right) + \frac{\partial p}{\partial x} = 0 \tag{6}$$

$$\frac{\partial s}{\partial t} + u\frac{\partial s}{\partial x} = 0. \tag{7}$$

Again, using the hypothesis of thermally ideal gas, we can now plug Eq. (4) into the term $\partial\rho$ for the continuity equation (5):

$$\frac{\partial p}{\partial t} + u\frac{\partial p}{\partial x} + \rho c^2 \frac{\partial u}{\partial x} - \frac{p}{c_v}\left(\frac{\partial s}{\partial t} + u\frac{\partial p}{\partial x}\right) = 0 \tag{8}$$

$$\rho\left(\frac{\partial u}{\partial t} + u\frac{\partial u}{\partial x}\right) + \frac{\partial p}{\partial x} = 0 \tag{9}$$

$$\frac{\partial s}{\partial t} + u\frac{\partial s}{\partial x} = 0. \tag{10}$$

The entropy equations (7) and (10) assumes that the flow is under a reversible process, i.e., the entropy rate of change for a given point is only caused by the convection of entropy. Likewise, it assumes that there is no viscous dissipation mechanisms and that there is no entropy generation. In fact, the entropy term in the continuity equation (10) could be simplified. However, to provide a wider valid solution we shall keep this term and generic flows, such as irreversible flows, could be simulated by the continuity equation as it stands.

Multiplying the Eq. (8) by $\left(\frac{1}{\rho c}\right)$, adding $\left(\frac{1}{\rho}\right)$ times the Eq. (9), using $\left(c_v = \frac{c_p}{\gamma}\right)$ and $\left(c^2 = \gamma RT\right)$, one can write Eq. (11). Now with analogous operations but instead of adding, subtracting $\left(\frac{1}{\rho}\right)$ times the Eq. (9) we can write Eq. (12):

$$\left(\frac{1}{\rho c}\frac{\partial p}{\partial t} + \frac{\partial u}{\partial t}\right) + (u+c)\left(\frac{1}{\rho c}\frac{\partial p}{\partial x} + \frac{\partial u}{\partial x}\right) - \frac{c}{c_p}\left(\frac{\partial s}{\partial t} + u\frac{\partial s}{\partial x}\right) = 0 \tag{11}$$

$$\left(\frac{1}{\rho c}\frac{\partial p}{\partial t} - \frac{\partial u}{\partial t}\right) + (u-c)\left(\frac{1}{\rho c}\frac{\partial p}{\partial x} - \frac{\partial u}{\partial x}\right) - \frac{c}{c_p}\left(\frac{\partial s}{\partial t} + u\frac{\partial s}{\partial x}\right) = 0 \tag{12}$$

$$\frac{\partial s}{\partial t} + u\frac{\partial s}{\partial x} = 0. \tag{13}$$

Using the fundamental enthalpy equation (3), the differential form of speed of sound $\left(\delta T = \frac{2c}{\gamma R}\delta c\right)$ and the speed of sound definition, the value $\left(\frac{\delta p}{\rho c} \pm \delta u\right)$ can be written in the following form:

$$\frac{\delta p}{\rho c} \pm \delta u = \frac{2}{(\gamma-1)}\delta c \pm \delta u - \frac{c}{\gamma R}\delta s.$$

Using the definition of Riemann variables $\left(\mathfrak{R}^{\pm} = \frac{2}{(\gamma-1)}c \pm u\right)$ we can write Eq. (14):

$$\frac{\delta p}{\rho c} \pm \delta u = \delta\mathfrak{R}^{\pm} - \frac{c}{\gamma R}\delta s. \tag{14}$$

For the case of homentropic flow ($\delta s \equiv 0$), using (14), both the Eq. (11) and Eq. (12) can be written as functions of the Riemann variables:

$$\frac{\partial \mathfrak{R}^{\pm}}{\partial t} + (u \pm c)\frac{\partial \mathfrak{R}^{\pm}}{\partial x} = 0. \tag{15}$$

Eqs. (15) state that the Riemann variables ($\mathfrak{R}^{\pm}$) are conserved along the characteristic paths $\left(\frac{\partial x}{\partial t} = (u \pm c)\right)$ in space and time. Due to this conservation, for homentropic flow, Riemann variables are named Riemann invariants.

Now, defining $X^{\pm}$:

$$X^{\pm} = (u \pm c)\frac{\partial \mathfrak{R}^{\pm}}{\partial x}$$
$$X^{\pm} = (u \pm c)\left(\frac{1}{\rho c}\frac{\partial p}{\partial x} \pm \frac{\partial u}{\partial x}\right); \tag{16}$$

$X^{\pm}$ represents the ($\mathfrak{R}^{\pm}$) rate of change in time. Observe that Eq. (15) traduces the conservation of the quantity ($\mathfrak{R}^{\pm}$) traveling with the relative speed of sound ($u \pm c$). Thus, $X^{\pm}$ represents the acoustic wave in the linear analysis. Through this variable one may explicitly handle the acoustic wave propagation phenomena.

Analogous interpretation of the correlations between the $X^{\pm}$ terms and $\mathfrak{R}^{\pm}$ terms for ($\delta s = 0$) along the path $\left(\frac{\partial x}{\partial t} = u\right)$, i.e. $\left(\frac{\partial s}{\partial t} + u\frac{\partial s}{\partial x} = 0\right)$, and for irreversible flow cases $\left(\frac{\partial s}{\partial t} + u\frac{\partial s}{\partial x} = \sigma\right)$ can be seen in Sesterhenn, 2001.

Now, one shall diagonalize the set of Eqs. (8), (9) and (10) by adding and subtracting to the Eq. (8), $\frac{c}{2}$ times the Eq. (9). This operation basically added zero to the continuity equation, but it will enable us to explicitly write the acoustics terms in the continuity equation:

$$\frac{\partial p}{\partial t} + \frac{\rho c}{2}\left[(u+c)\left(\frac{1}{\rho c}\frac{\partial p}{\partial x} + \frac{\partial u}{\partial x}\right) + (u-c)\left(\frac{1}{\rho c}\frac{\partial p}{\partial x} - \frac{\partial u}{\partial x}\right)\right] - \frac{p}{c_v}\left(\frac{\partial s}{\partial t} + u\frac{\partial p}{\partial x}\right) = 0.$$

By performing analogous operation, i.e. adding and subtracting to the Eq. (9) $\frac{1}{\rho c}$ times the Eq. (8), one can write:

$$\frac{\partial u}{\partial t} + \frac{1}{2}\left[(u+c)\left(\frac{1}{\rho c}\frac{\partial p}{\partial x} + \frac{\partial u}{\partial x}\right) - (u-c)\left(\frac{1}{\rho c}\frac{\partial p}{\partial x} - \frac{\partial u}{\partial x}\right)\right] = 0.$$

With the two above equations and defining the entropy wave term as: $X^s = u\frac{\partial s}{\partial x}$, we can write the 1D Euler equations in the wave like form:

$$\frac{\partial p}{\partial t} + \frac{\rho c}{2}\left[X^+ + X^-\right] - \frac{p}{c_v}\left(\frac{\partial s}{\partial t} + X^s\right) = 0 \tag{17}$$

$$\frac{\partial u}{\partial t} + \frac{1}{2}\left[X^+ - X^-\right] = 0 \tag{18}$$

$$\frac{\partial s}{\partial t} + X^s = 0. \tag{19}$$

Algebraically, there is no difference between the set of Eqs. (17), (18) and (19) and the set of Eqs. (5), (6) and (7). But in practice the first set of Eqs., 17, 18 and 19, enable to explicitly handle the wave terms. It makes it easier to introduce the non-reflecting boundary condition.

Now, for illustration and definition purposes, suppose a coordinate system in which the x-axis grows from left to right. For a subsonic flow case: X^+ plane wave will travel towards x-direction, X^- plane wave will travel towards the opposite direction, X^s waves will travel with the same direction as the local velocity (u). This is sketched in the Fig. 4 as a sound wave which travels from left to right (X^+), another sound wave which travels from right to left (X^-) and, for a positive velocity u, an entropy wave which travels from left to right.

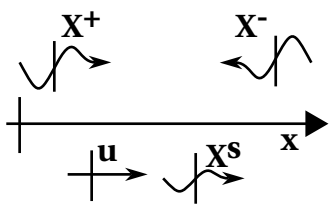

Figure 4: Characteristic-type variables scheme for a subsonic flow.

With this background of the characteristic-type variables for the 1D flow case provided by the present section, we shall present the 3D flow case equations.

3.3. 3D Equations of motion

Three-dimensional formulation can be derived by decomposing the Navier Stokes equations and performing analogous steps given for the 1D formulation for each direction, i.e., diagonalizing the Navier Stokes equations. For brevity, we shall not give details of the necessary steps to obtain the full 3D equations. A detailed characteristic-type formulation of the 3D Navier Stokes equations can be found in Sesterhenn, 2001. The 3D set of equations written in the wave-like form are:

$$\begin{aligned}
\frac{\partial p}{\partial t} &= -\frac{\rho c}{2}\left[\left(X^+ + X^-\right) + \left(Y^+ + Y^-\right) + \left(Z^+ + Z^-\right)\right] + \frac{p}{c_v}\left(\frac{\partial s}{\partial t} + X^s + Y^s + Z^s\right) \\
\frac{\partial u}{\partial t} &= -\left[\frac{1}{2}\left(X^+ - X^-\right) + Y^u + Z^u\right] + \frac{1}{\rho}\frac{\partial \tau_{1j}}{\partial x_j} \\
\frac{\partial v}{\partial t} &= -\left[X^v + \frac{1}{2}\left(Y^+ - Y^-\right) + Z^v\right] + \frac{1}{\rho}\frac{\partial \tau_{2j}}{\partial x_j} \\
\frac{\partial w}{\partial t} &= -\left[X^w + Y^w + \frac{1}{2}\left(Z^+ - Z^-\right)\right] + \frac{1}{\rho}\frac{\partial \tau_{3j}}{\partial x_j} \\
\frac{\partial s}{\partial t} &= -\left(X^s + Y^s + Z^s\right) + \frac{R}{p}\left(-\frac{\partial q_i}{\partial x_i} + \phi\right).
\end{aligned} \tag{20}$$

With the wave terms, heat transfer term, viscous term and viscous dissipation term defined as follows:

$$\begin{aligned}
X^+ = (u+c)\left(\frac{1}{\rho c}\frac{\partial p}{\partial x} + \frac{\partial u}{\partial x}\right); \qquad X^- &= (u-c)\left(\frac{1}{\rho c}\frac{\partial p}{\partial x} - \frac{\partial u}{\partial x}\right); \\
X^v = u\frac{\partial v}{\partial x}; \qquad X^w = u\frac{\partial w}{\partial x}; \qquad X^s &= u\frac{\partial s}{\partial x}; \\
Y^+ = (v+c)\left(\frac{1}{\rho c}\frac{\partial p}{\partial y} + \frac{\partial v}{\partial y}\right); \qquad Y^- &= (v-c)\left(\frac{1}{\rho c}\frac{\partial p}{\partial y} - \frac{\partial v}{\partial y}\right); \\
Y^u = v\frac{\partial u}{\partial y}; \qquad Y^w = v\frac{\partial w}{\partial y}; \qquad Y^s &= v\frac{\partial s}{\partial y}; \\
Z^+ = (w+c)\left(\frac{1}{\rho c}\frac{\partial p}{\partial z} + \frac{\partial w}{\partial z}\right); \qquad Z^- &= (w-c)\left(\frac{1}{\rho c}\frac{\partial p}{\partial z} - \frac{\partial w}{\partial z}\right); \\
Z^u = w\frac{\partial u}{\partial z}; \qquad Z^v = w\frac{\partial v}{\partial z}; \qquad Z^s &= w\frac{\partial s}{\partial z}; \\
\tau_{ij} = \mu\left[\frac{\partial u_j}{\partial x_i} + \frac{\partial u_i}{\partial x_j} - \frac{2}{3}\left(\nabla\vec{V}\right)\delta_{ij}\right]; \\
q_i = -\lambda\frac{\partial T}{\partial x_i}; \\
\phi = \tau i j E_{ij}; \\
E_{ij} = \frac{1}{2}\left(\frac{\partial u_i}{\partial x_j} + \frac{\partial u_j}{\partial x_i}\right).
\end{aligned}$$

Observe that new terms which were not present in the previous formulation (1D flow case) have appeared in the 3D flow case. Those terms are called momentum waves, ${X_i}^{u_j}\left(1-\delta_{ij}\right)$, and represent the injection of x_j-direction momentum due to its gradient in x_i-direction.

A sketch of the acoustic wave terms belonging to the characteristic formulation of the 2D Navier Stokes is showed in Fig. 5.

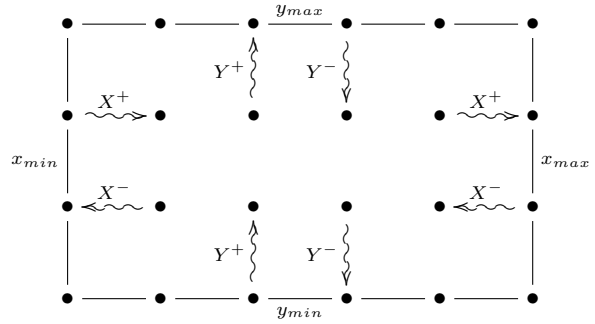

Figure 5: Acoustic wave terms in a two-dimensional domain

4. Anechoic boundary condition test

Non reflecting boundary condition is a challenge for the development of numerical studies in fluid mechanics. Due to the wave like form of the Navier-Stokes equations, the acoustic waves are decomposed into terms with different traveling directions. For the 2D case, the anechoic boundary condition can be implemented in an explicitly way by imposing null incoming waves into the domain. For example, to apply the anechoic boundary condition at the boundary $y = y_{max}$ showed in Fig. 5, it is necessary to impose $Y^- = 0$ along $y = y_{max}$.

The test presented in this section used a Gaussian pressure distribution as the initial condition. The pressure variation amplitude was 10% of that at the far field. The initial entropy field was uniform and the velocities were null. This initial condition could represent a time instant in which two acoustic waves with the same amplitude cross each other. At $y = -0.5$ the anechoic boundary condition was applied, at $y = 0.5$ the rigid boundary condition was applied. Fig. 6 shows the time development of the pressure field. The color scale employed presents from the overall maximum to the minimum pressure.

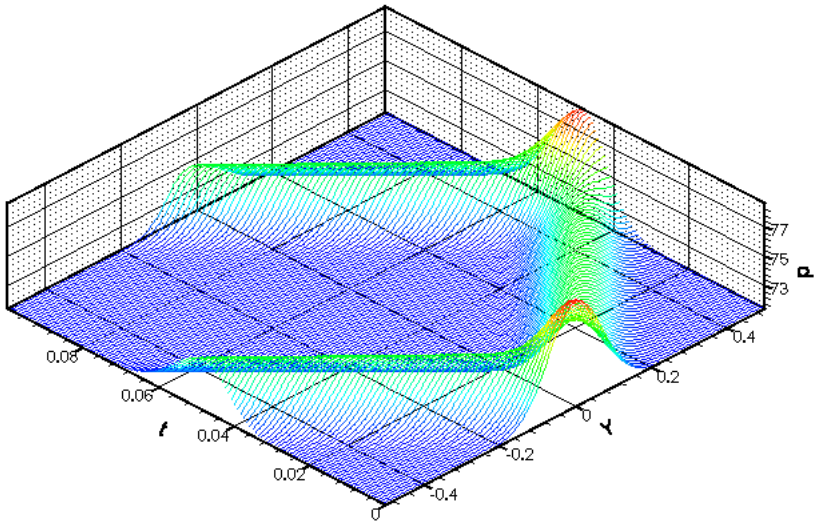

Figure 6: Contour plot of the pressure field development in t and y.

Two tests were performed:

(a) First test case: For a first test, a reflection of 4.5% was obtained in the anechoic boundary. It means that the spurious reflected acoustic wave had an amplitude below 5% of the acoustic wave amplitude outgoing the domain. For this first test, the Neumman boundary condition was used for the pressure ($\frac{\partial p}{\partial y} = 0$), no specified boundary condition was adopted for $\frac{\partial v}{\partial y}$ and it was subsequently computed Y^- and $Y^+ \rightarrow 0$ along $y = -0.5$.

(b) Second test case: For a second test changing the advection scheme, i.e., using none specified boundary condition for both $\frac{\partial v}{\partial y}$ and $\frac{\partial p}{\partial y}$ and subsequently computing Y^- and $Y^+ \rightarrow 0$ along the path $y = -0.5$, it was possible to obtain a reflection rate below 0.08%.

Fig. 7 shows the development of the pressure field $P(y)$ in time t. In Fig. 7(a) the color scale shows the pressure level of the spurious reflection obtained by the technique used in test (a). In Fig. 7(b) the same is

done for test (b) but the color scale is different to indicate the reflected wave. Through those two Figs. it is possible to observe the different reflection amplitude obtained by tests (a) and (b).

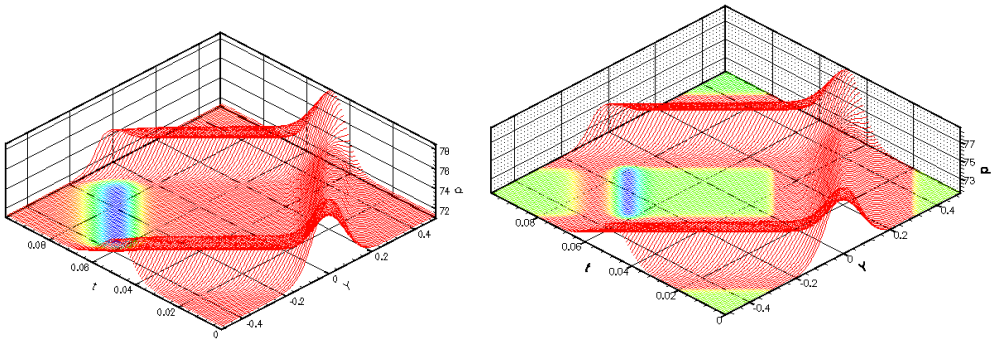

(a) First test case (b) Second test case

Figure 7: Color scale ranging the pressure field caused by spurious reflection for cases (a) and (b). The scales ranges from blue color (lowest reflected pressure level) to red color (highest reflected pressure level).

4.1. Anechoic boundary condition conclusion

By changing the advection scheme, a reflection factor reduction of more than 50 was observed. Test (a) was possibly overconstrained. The imposition of $Y^+ = 0$ along $y = -0.5$ is one constraint which implicitly states a relationship between $\frac{\partial v}{\partial y}$ and $\frac{\partial p}{\partial y}$ during the simulation. Likewise, for a pure sound wave propagation case, it is better to assume neither $\frac{\partial v}{\partial y} = 0$ nor $\frac{\partial p}{\partial y} = 0$.

It is important to emphasize that the only technique used to mimic the anechoic boundary condition employed for both simulations was the imposition $Y^+ = 0$ along $y = -0.5$. By using other techniques, such as *buffer zones* and gradual acceleration of the sound speed near the boundary with the technique employed for both simulations an even lower spurious reflection can be obtained.

5. Free Shear Layer

Different initial conditions were tested aimed at reproduce the acoustic field caused by a single pairing. By the first technique used to generate the disturbance field presented in section 5.1, spurious acoustic waves were created at the initial condition. Due to the periodic boundary conditions adopted for the x-direction, those waves were present during all the simulation time. It eventually presented sound waves with amplitudes equal or higher than those produced by the vortex pairing. With initial disturbances compounded by wave packets no spurious acoustic waves were created at the initial conditions.

5.1. Initial conditions

For the present and following sections, the same non-dimensional scheme of section 2 is used. For the free shear layer problem the initial condition adopts a parallel base-flow with a temperature profile proposed by Crocco-Busemman, Fortuné, 2000. The initial velocity field takes the form: $u(x,y) = \tanh\left(\frac{2y}{\delta_w}\right) + u_p(x,y)$ and $v(x,y) = 0 + v_p(x,y)$. In which $u_p(x,y)$ and $v_p(x,y)$ are small disturbances of the flow. The performed simulations had a disturbance level of:

$$max\left[\frac{max\left[u_p(x,y)\right]}{U_{max}}; \frac{max\left[v_p(x,y)\right]}{U_{max}}\right] < 10^{-5}$$

.

A number of tests were done aiming at the production of a single vortex pairing in a wide domain. In one of them, the disturbance field:

$$u_p(x,y) = 2\frac{\sigma y}{\delta_w}e^{-\sigma\left(\frac{y^2}{\delta_w}\right)}\frac{L_x}{2\pi}\left[A_0\sin\left(\frac{2\pi x}{L_x}\right)+\frac{A_1}{2}\sin\left(\frac{4\pi x}{L_x}\right)\right]; \quad (21)$$

$$v_p(x,y) = e^{-\sigma\left(\frac{y^2}{\delta_w}\right)}\left[A_0\cos\left(\frac{2\pi x}{L_x}\right)+A_1\cos\left(\frac{4\pi x}{L_x}\right)\right]; \quad (22)$$

was multiplied by a windowing function obtained from the combination of two hyperbolic tangent functions:

$$f_w(x,y) = \frac{\tanh\left[k\left(x-x_0\right)\right]+\tanh\left[k\left(x_1-x\right)\right]}{2}.$$

Once the disturbance field was multiplied by the windowing function, $\frac{\partial\rho}{\partial t}$ assumed non-zero values for the whole domain at the initial condition and spurious acoustic waves created at the initial condition disallowed the clear observation of the pairing acoustic field.

5.1.1. Complex wave packets

This technique was used by Medeiros, 1996 to study the nonlinear behavior of modulated Tollmien-Schlichting waves. This technique is capable of almost-punctually disturb the flow near a given point. The disturbance contains a wide range of frequencies. Aiming at investigate the growth of Tollmien-Schlichting waves created by a wider range of frequencies, Medeiros, 1996 used this technique. To understand this methodology, a disturbance field generated by a single complex wave packet is described below:

$$u_p(x,y) = 2\frac{\sigma y}{\delta_w}e^{-\sigma\left(\frac{y^2}{\delta_w}\right)}A\Re\left[e^{\imath\phi}\left(\sum_{n=1}^{n_{max}}\frac{e^{\imath\frac{2n\pi(x-x_p)}{L_x}}}{\imath\frac{2\pi n}{L_x}}\right)\right]; \quad (23)$$

$$v_p(x,y) = e^{-\sigma\left(\frac{y^2}{\delta_w}\right)}A\Re\left[e^{\imath\phi}\left(\sum_{n=1}^{n_{max}}e^{\imath\frac{2n\pi(x-x_p)}{L_x}}\right)\right]. \quad (24)$$

where x_p is the x coordinate where the disturbances are concentrated. A Gaussian y-profile multiply the wave packet making the disturbances active only in the free shear layer vortical region. Depending on the phase angle ϕ, different disturbance shapes, but with an identical amplitude envelope, are formed at the point x_p.

It is possible to verify that this disturbance field satisfy the mass conservation law for an incompressible flow. By substituting Eqs. (23) and (24) into the mass conservation equation:

$$\frac{\partial u_p}{\partial x}+\frac{\partial v_p}{\partial y} = 2\frac{\sigma y}{\delta_w}e^{-\sigma\left(\frac{y^2}{\delta_w}\right)}A\Re\left[e^{\imath\phi}\left(\sum_{n=1}^{n_{max}}\frac{\imath\frac{2n\pi}{L_x}e^{\imath\frac{2n\pi(x-x_p)}{L_x}}}{\imath\frac{2n\pi}{L_x}}\right)\right]-2\frac{\sigma y}{\delta_w}e^{-\sigma\left(\frac{y^2}{\delta_w}\right)}A\Re\left[e^{\imath\phi}\left(\sum_{n=1}^{n_{max}}e^{\imath\frac{2n\pi(x-x_p)}{L_x}}\right)\right];$$

$$\Rightarrow \frac{\partial u_p}{\partial x}+\frac{\partial v_p}{\partial y} = 2\frac{\sigma y}{\delta_w}e^{-\sigma\left(\frac{y^2}{\delta_w}\right)}A\Re\left[e^{\imath\phi}\left(\sum_{n=1}^{n_{max}}e^{\imath\frac{2n\pi(x-x_p)}{L_x}}\right)\right]-2\frac{\sigma y}{\delta_w}e^{-\sigma\left(\frac{y^2}{\delta_w}\right)}A\Re\left[e^{\imath\phi}\left(\sum_{n=1}^{n_{max}}e^{\imath\frac{2n\pi(x-x_p)}{L_x}}\right)\right];$$

$$\Rightarrow \frac{\partial u_p}{\partial x}+\frac{\partial v_p}{\partial y} = 0.$$

It means that the incompressible disturbance field hypothesis is satisfied and no spurious acoustic waves are created at the initial condition.

For illustration purposes, we define a domain $0 \leq x \leq L_x = 150$ and $-200 \leq y \leq 200$ and one point $x_p = 75$. Figs. 8 shows the contour plots of the vorticity field with a vector plot of the local velocity disturbance compounded by Eqs. 23 and 23 for different ϕ values inside the previously defined domain. These figures uses a strong zoom near the point $x = x_p = 75; y = 0$. It is possible to observe that:

(a) For $\phi = \frac{-\pi}{2}$ an anti-clockwise rotating vortex is found at $(x_p, 0)$ (Fig. **??**);

(b) For $\phi = 0$ two counter-rotating vortices are found at $(x_p, 0)$ (Fig. **??**);

(c) For $\phi = \frac{\pi}{2}$ an clockwise rotating vortex is found at $(x_p, 0)$(Fig. **??**);

(d) For $\phi = \pi$ two counter-rotating vortices are found at $(x_p, 0)$(Fig. **??**).

Some of those wave-packets shown in Fig.8 will be used to compound the final disturbance necessary to reproduce a single vortex pairing inside a wide domain.

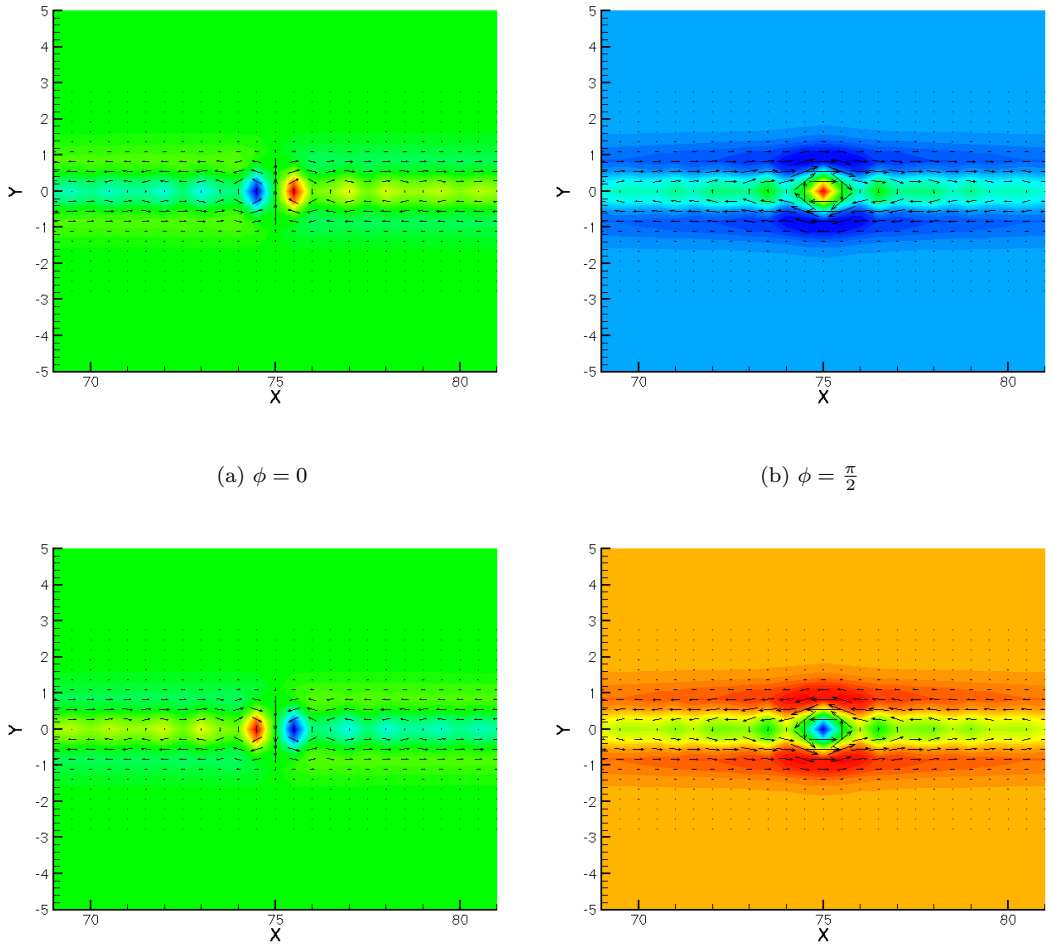

(a) $\phi = 0$ (b) $\phi = \frac{\pi}{2}$

(c) $\phi = \pi$ (d) $\phi = \frac{3\pi}{2}$

Figure 8: Contourplot of vorticity disturbance and vector plot of local velocity disturbance produced by wave packets with $x_p = 75$ and with different phase angle ϕ. Some of those disturbances will be united to compound the final disturbance field used to generate a single vortex pairing inside a wide domain.

5.2. Results

The domain adopted for the present formulation is $0 \leq x \leq L_x = 300$ and $-150 \leq y \leq 150$. The mesh used for this case was uniformely distributed along x-direction with $\delta x = 0.6$ and the y distribution was slightly stretched with a expansion factor of 1.1 and 600 points. For non-aliasing the disturbances, a cut off wavenumber of $n_{max} = 80$ was adopted. 4 different wave packets were used to generate the initial disturbance field. Each one of these 4 wave packet was composed by 80 different wavelengths. The 4 employed wave packets are shown below:

(a) Eqs. 23 and 24 with $\phi = \frac{\pi}{2}$ and $x_p = 145.75$;

(b) Eqs. 23 and 24 with $\phi = 0$ and $x_p = 145$;

(c) Eqs. 23 and 24 with $\phi = \frac{\pi}{2}$ and $x_p = 154.25$;

(d) Eqs. 23 and 24 with $\phi = \pi$ and $x_p = 155$;

(a) and (b) wave packets were concentrated in $x \approx 146$; $y = 0$;(c) and (d) wave packets were concentrated in $x \approx 154$; $y = 0$.

The disturbances nuclei $x \approx 146$ and $x \approx 154$ had equal magnitude, i.e., a constant value of A was used for each one of the wave packets presented in 5.2. The disturbances did not reached $max[u_p(x,y)/U_{max}; v_p(x,y)/U_{max}] > 10^{-2}$. During the simulation an odd symmetry around the axis defined by $x = L_x/2$ and $y = 0$ was found. The frame sequence of Fig. 9 shows the contour plot of vorticity field along the temporal development of the vortex pairing. It is possible to observe that the vortex pairing occurs near the point $x \approx L_x/2 = 150$; $y = 0$, i.e., at the center of the domain.

Fig. 10 shows the contour plots of the dilatation ($\frac{\partial \rho}{\partial t}$). 40 uniformly varying levels are shown between $-3 \cdot 10^{-5}$ and $3 \cdot 10^{-5}$. The white region of each frame has a vorticity level above 0.1. Through this region it is possible to observe the vortex shape dynamics. With the long x-domain, the effect of the x-direction periodic boundary condition is not clearly observed on the acoustic field presented in Fig. 10. Through the Fig. 10, it is possible to observe the double spiral found by Bogey *et al.*, 2000.

6. Conclusion

In the present work, a brief overview of the verification of a code used to simulate a vortex pairing aeroacoustics is done against the LST results. Tests of the anechoic boundary condition were done aimed at reducing the spurious reflection at the boundaries.

The usage of a disturbance field compounded by modulated wave packets was shown as a efficient way to generate a single vortex pairing inside a wide x-domain of a shear layer flow under temporal development. The results of a single vortex pairing aeroacoustics in a shear layer under temporal development with a large x-domain are presented in section 5.2. For this case it was possible to observe and interpret the acoustic structure patterns generated by the pairing as a double spiral, according to the previous results reported by Bogey *et al.*, 2000. Due to the usage of a low wavenumber cut off, secondary vortices stabilize in a short time period. Only the begining of the pairing could be isolated.

The acoustic field generated by the pairing was found to be some scales larger than the vortices structures on the pairing. A typical size of the vortices reproduced in the presented simulations is about $\frac{L_E}{\delta_w} = 4$ and a $\frac{L_x}{\delta_w} = 300$ x-domain was enough to capture the acoustic structures generated by the vortex pairing.

7. Acknowledgments

We greatly acknowledge the financial support of CAPES and FAPESP. We thanks Prof. Dr. Marcio T. Mendonça and Prof. Dr. Jörn Sesterhenn for the fruitful discussions.

8. Author rights

Authors are the sole responsible for the contents of their papers.

9. References

Bogey, C., Bailly, C., and Juvé, D., 2000, Numerical simulation of sound generated by vortex pairing in a mixing layer, "AIAA Journal", Vol. 12, pp. 2210–2218.

Colonious, T. and Lele, S. . K., 2004, Computacional aeroacoustics: progress on nonlinear problems of sound genereation, "Progress in Aerospace Sciences", Vol. 40, pp. 345–416.

Colonious, T., Lele, S. S. K., and Moin, P., 1997, Sound generation in a mixing layer, "J. Fluid Mech.", Vol. 330, pp. 375–409.

Fortuné, V., 2000, "Étude par Simulation Numérique Directe du rayonnement acoustique de couches de mélabge isothermes et anisothermes", PhD thesis, Université de Poitier.

Germanos, R. A. C. and Medeiros, M. A. F., 2005, Development of a code for a direct numerical simulation of compressible shear flow instabilities, "Congresso Brasileiro de Engenharia Mecânica - COBEM 2005". ABCM, In CD-ROM.

Lele, S. K., 1992, Compact finite difference schemes with spectral-like resolution, "J. Comp. Phys.", Vol. 103, pp. 16–42.

Medeiros, M. A. F., 1996, "The nonlinear behaviour of modulated Tollmien-Schlichting waves", PhD thesis, Cambridge University - UK.

Sesterhenn, J., 2001, A Chracteristic-type formulation of the Navier-Stokes equations for high order upwind schemes, "Computers and Fluids", Vol. **30**, pp. 37–67.

Wang, M., Freund, J. B., and Lele, S. K., 2006, Computational Prediction of Flow-Generated Sound, "Annu. Rev. Fluid Mech.", Vol. 38, pp. 483–512.

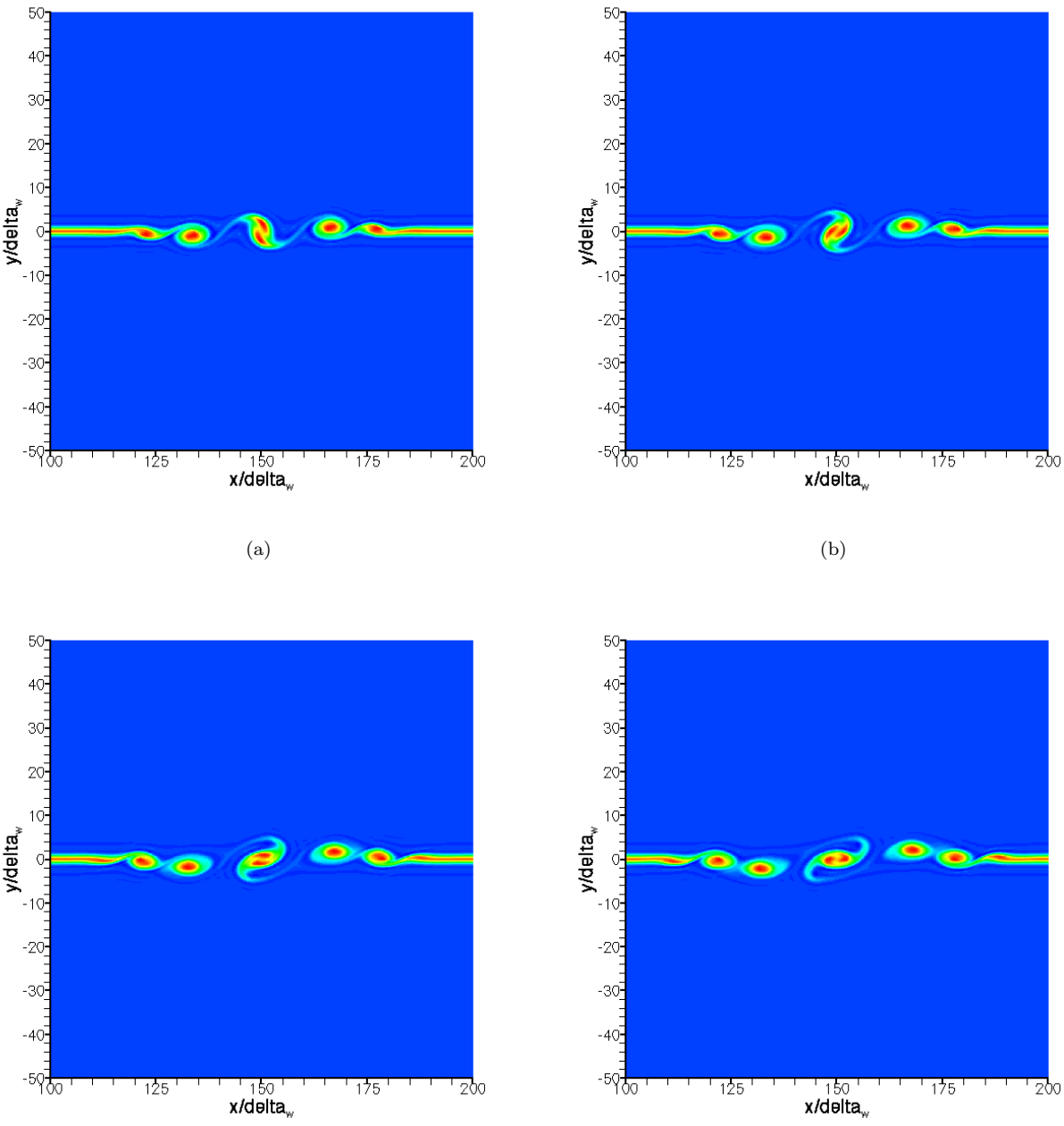

(a) (b)

(c) (d)

Figure 9: Time development of the vorticity field during the pairing.

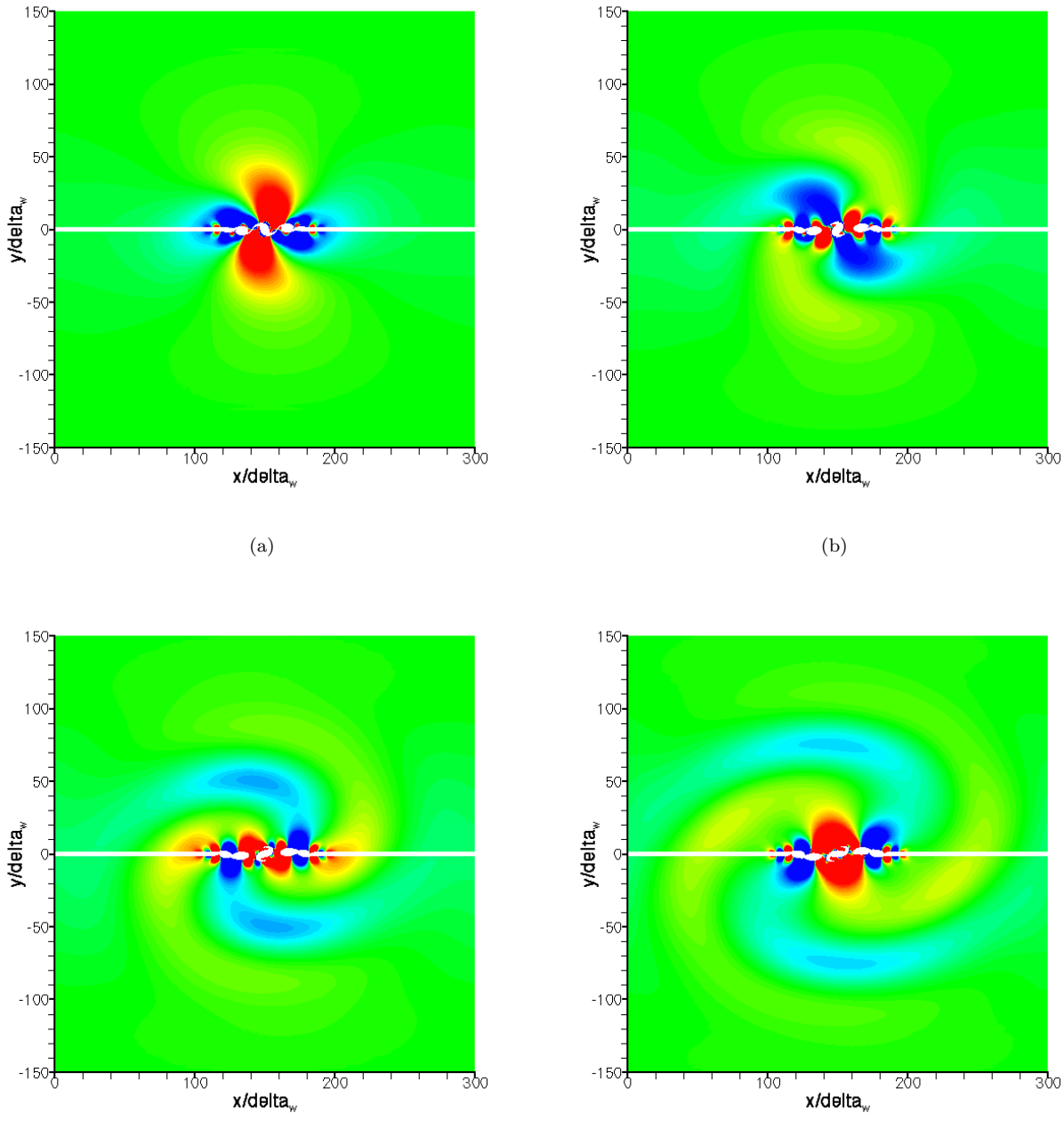

(a) (b)

(c) (d)

Figure 10: Temporal development of the dilatation field ($\frac{\partial \rho}{\partial t}$) during the pairing.

Proceedings of the 11th Brazilian Congress of Thermal Sciences and Engineering -- ENCIT 2006
Braz. Soc. of Mechanical Sciences and Engineering -- ABCM, Curitiba, Brazil, Dec. 5-8, 2006

Paper CIT06-0238

INVESTIGAÇÕES EXPERIMENTAIS NUMA ASA CURTA COM *FLAPS* DE SUPERFÍCIE

Roger Paul Dorweiler
Instituto de Tecnologia para o Desenvolvimento - LACTEC
Centro Politécnico da UFPR
Cx. Postal 19067 - Curitiba – PR.
CEP: 81513-980
roger.dorweiler@lactec.org.br

Resumo. *Observações em aves mostram que as penas de cobertura podem se levantar formando pequenas bolsas, no caso de voar em escoamentos turbulentos, ou em situações críticas de vôo. Nesses casos surgem separações locais na asa, conhecidas como efeito estol. O objetivo desse trabalho foi investigar em um túnel de vento os efeitos aerodinâmicos desse mecanismo.*
De acordo com as características da permeabilidade e da rigidez das penas foram construídos eddy flaps, como também uma asa, cujo aerofólio utilizado é o NACA 2412, que mostra o efeito de estol para medir sustentação, arrasto e distribuição de pressão com e sem o uso dos flaps.
Através das medições, mostrou-se que as bolsas formadas trabalham como eddy breaks para o escoamento invertido que se propaga do bordo de fuga em direção ao bordo de ataque, em situações de estol na camada limite.
Entre o bordo de ataque e a bolsa houve a formação de um vórtice que se adaptou ao ângulo de ataque. Foi descoberto que isto funciona como uma adaptação automática da espessura da asa, aumentando significativamente a sustentação nessa área.
Como conclusão, o uso dos eddy flaps disponibiliza para o construtor de asas uma ferramenta adicional para a realização de um vôo mais seguro.

Palavras chave: Aerodinâmica, Estol, Túnel de Vento, Eddy flaps

1. Introdução

Observações em aves mostram que as penas de cobertura das asas se levantam em situações críticas de vôo como, por exemplo, em pousos ou quando voando em correntes com alta turbulência. Como aves conseguem administrar sem dificuldade essas situações de vôos perigosos, conclui-se que as penas levantadas freiam o escoamento invertido que aparece na camada limite em efeito estol, evitando assim a queda total da sustentação na asa (Rechenberg e Bannasch, 1995).

Figura 1. Skua com bolsa formada na asa (Rechenberg, 1995)

Este fato originou o projeto de pesquisa "*Flaps* de superfície aeroflexíveis como freios da contra corrente: exemplo de penas de aves", financiado pelo BMBF (Bundesministerium für Bildung und Forschung).

O gradiente adverso de pressão na asa em caso de ocorrência do estol é alto, gerando uma região de baixa pressão no extradorso que cria uma contra corrente dentro da camada limite, começando no bordo de fuga e indo em direção ao bordo de ataque. Isto causa uma separação súbita de linhas de corrente, também na área dianteira da asa (Leder, 1992). O perigo para o piloto de um avião se encontra não somente no fato que essa separação se propaga muito rápido, mas também porque o mencionado efeito acontece na maioria dos casos primeiro em uma asa só, quando a outra ainda mantém sustentação. Isto causa um torque de rolamento que deixa o avião girar ou até entrar numa caída espiral (Dubs, 1990). Especialmente nos pousos isto é um dos principais perigos, porque correções na proximidade do solo são limitadas. Através de medições em túnel de vento, esta pesquisa tentou explicar os efeitos aerodinâmicos da aplicação de *eddy flaps* artificiais e verificar as conclusões postuladas.

Assim o objetivo do projeto foi claramente definido (Patone e Müller, 1996) como uma tentativa de modificar o coeficiente de sustentação usando *flaps* na superfície, como mostra a figura 2:

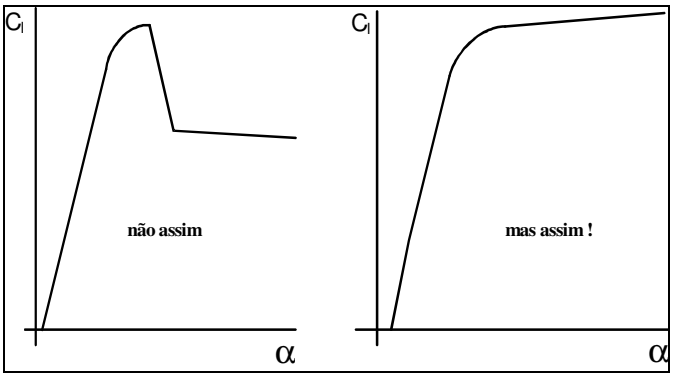

Figura 2. Objetivo do projeto.

2. Exames preliminares

O conhecimento sobre a biomecânica das penas das aves obtido nas investigações da primeira parte do projeto foi usado para copiar da melhor forma possível suas características. Especificamente, essas investigações observaram os seguintes fatores importantes (Patone e Müller, 1996):

1. Os bordos de fuga dos *flaps* precisam ser muito macios para que possam imediatamente detectar a contra corrente (recirculação) e servir assim como um atuador.
2. Os *flaps* precisam possuir uma certa rigidez na haste da pena, mas ainda com uma possibilidade de deformação na envergadura. Isto garante a possibilidade de formar bolsas somente nas áreas com linhas de corrente separadas, ou seja, não perturbam áreas sem estol.
3. Os *flaps* precisam possuir uma certa permeabilidade para prevenir um levantamento prematuro, causado pelo gradiente de pressão da asa (figura 3).
4. As hastes não têm nenhuma ligação com músculos ou tendões garantindo que o levantamento é causado somente pelas forças aerodinâmicas.

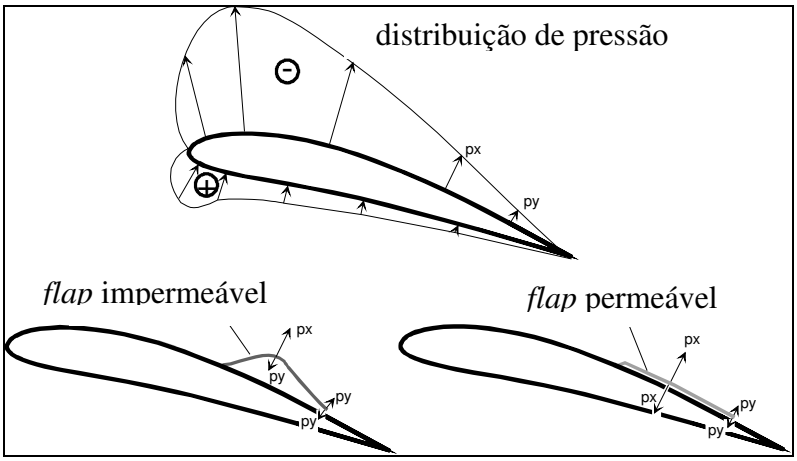

Figura 3. Levantamento do *flap* impermeável causado pela distribuição de pressão (Patone,1996)

3. Construção da asa e do *eddy flap*

Para encontrar a melhor adaptação das características descritas no capitulo 2, foram testados vários materiais diferentes como, por exemplo, transparência furada, tecido para bordar e outros tipos de tecidos. Os melhores resultados foram obtidos com seda. Ela é macia suficiente para servir como atuador e a permeabilidade foi suficiente para a seda não se levantar prematuramente pelo gradiente de pressão. Para evitar que a contra corrente enrole a seda, foram colados alguns arames de aço na sua superfície. O importante aqui é que os arames não alcançaram a fita, ou seja, apenas a fita funcionou como dobradiça da seda. Os arames não reproduziram a distribuição da rigidez das penas. Assim este ponto não segue as recomendações das investigações anteriores. O objetivo do projeto não era otimizar a "pena artificial", mas sim entender o funcionamento e a aerodinâmica dela.

O tamanho do *flap* foi 100 mm versus 600 mm e os arames tinham um diâmetro de 0,2 mm.

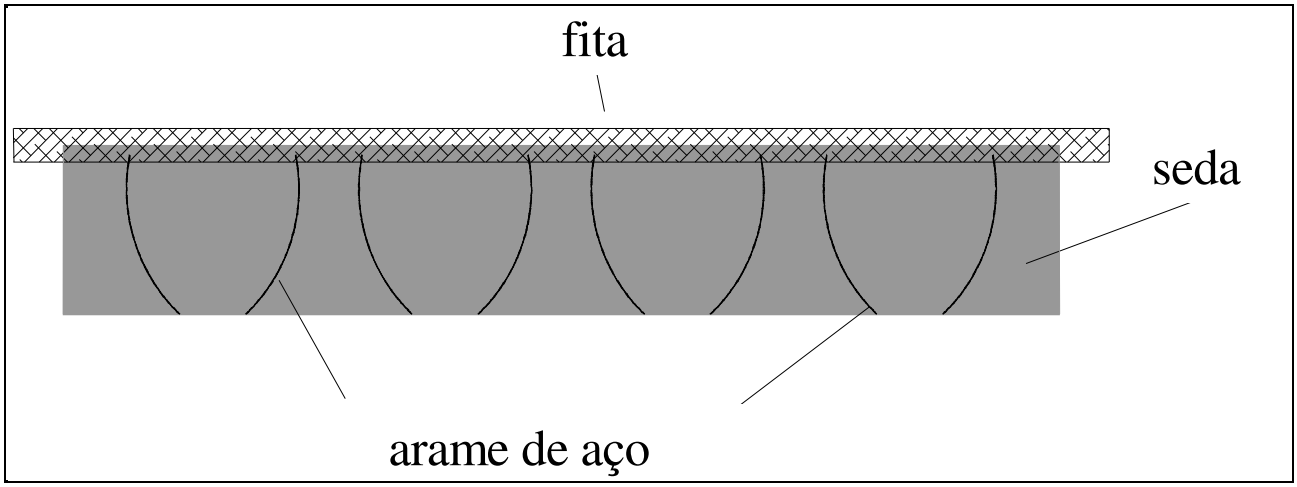

Figura 4. *eddy flap* em seda com arames de aço

Devido às distintas características de estol foi escolhido o perfil NACA 2412 (Althaus, 1980) com 700 mm de envergadura e 200 mm ao longo da corda, que resulta num alongamento de 3,5. Para realizar as medições de pressão, a asa foi perfurada em 7 linhas, cada uma com 40 furos distribuídos ao redor do perfil. Por simetria, somente um lado da asa precisou ser perfurado. O *flap* foi colado a 37,5% em relação ao bordo de ataque. A Figura 5 mostra esquematicamente a asa utilizada.

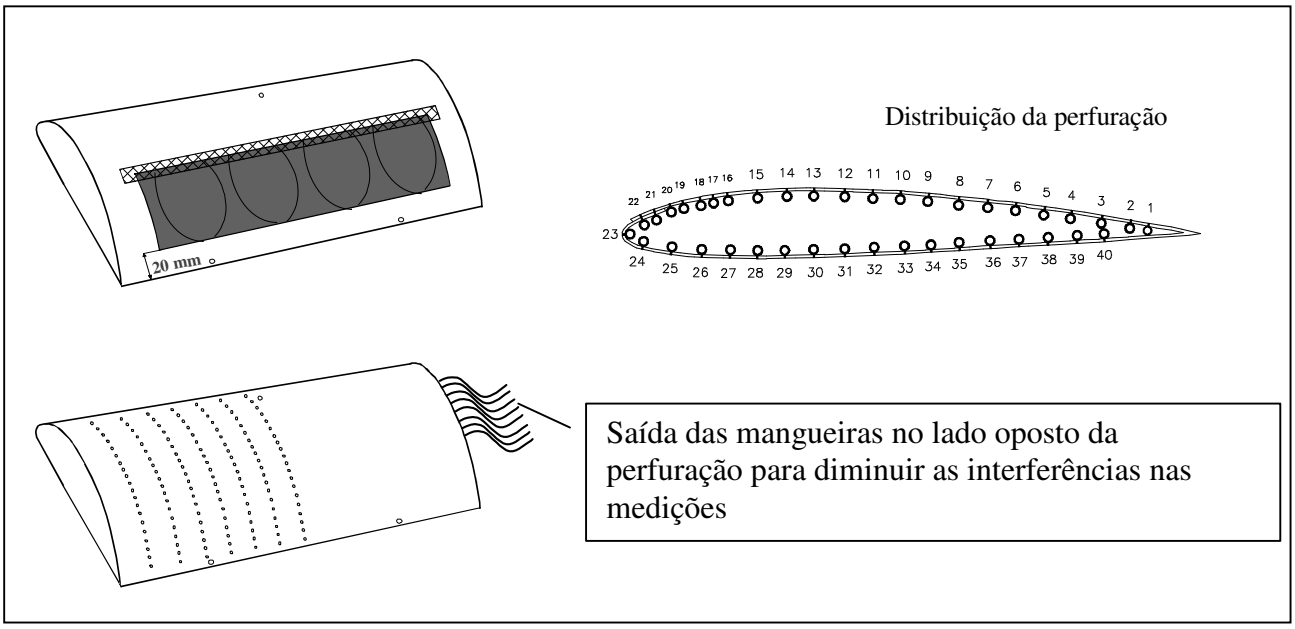

Figura 5. Perfil com *flap* aplicado e distribuição da perfuração.

4. Considerações sobre a estrutura do experimento

O experimento foi realizado num túnel de vento aberto com diâmetro de abertura de 1,2 m. Foi escolhida uma velocidade de vento de 9,5 m/s que corresponde a um número de Reynolds de 130.000, para simular as condições físicas de vôo de uma ave de tamanho médio como, por exemplo, um pombo.

A asa foi pendurada por três fios em uma balança eletrônica para medir a sustentação. Isto significa que um aumento da sustentação é proporcional a uma diminuição no peso na balança. Uma segunda balança eletrônica para medir o arrasto foi conectada via roldanas e fios no bordo de fuga da asa, ou seja, também neste caso um aumento da força - o arrasto - é proporcional a uma diminuição no peso da balança. Mais um fio fixado no meio do bordo de ataque conectou a asa, atravessando um potenciômetro, com um servomotor para mudar os ângulos de ataque. A variação da resistência elétrica do potenciômetro vai de 0 até 40º.

A medição de distribuição de pressão foi realizada através de mangueiras de silicone com um diâmetro interno de 1mm, as quais foram ligadas aos furos dentro do corpo da asa. Para diminuir a perturbação na medição causada pelas mangueiras, elas foram guiadas para fora da asa pelo lado oposto das perfurações, ligando-as a um sistema de válvulas comutadoras de pressão da Scanivalve e um medidor de pressão diferencial do tipo Baratron® da MKS com uma faixa de leitura de 0,1 a 10 Torr.

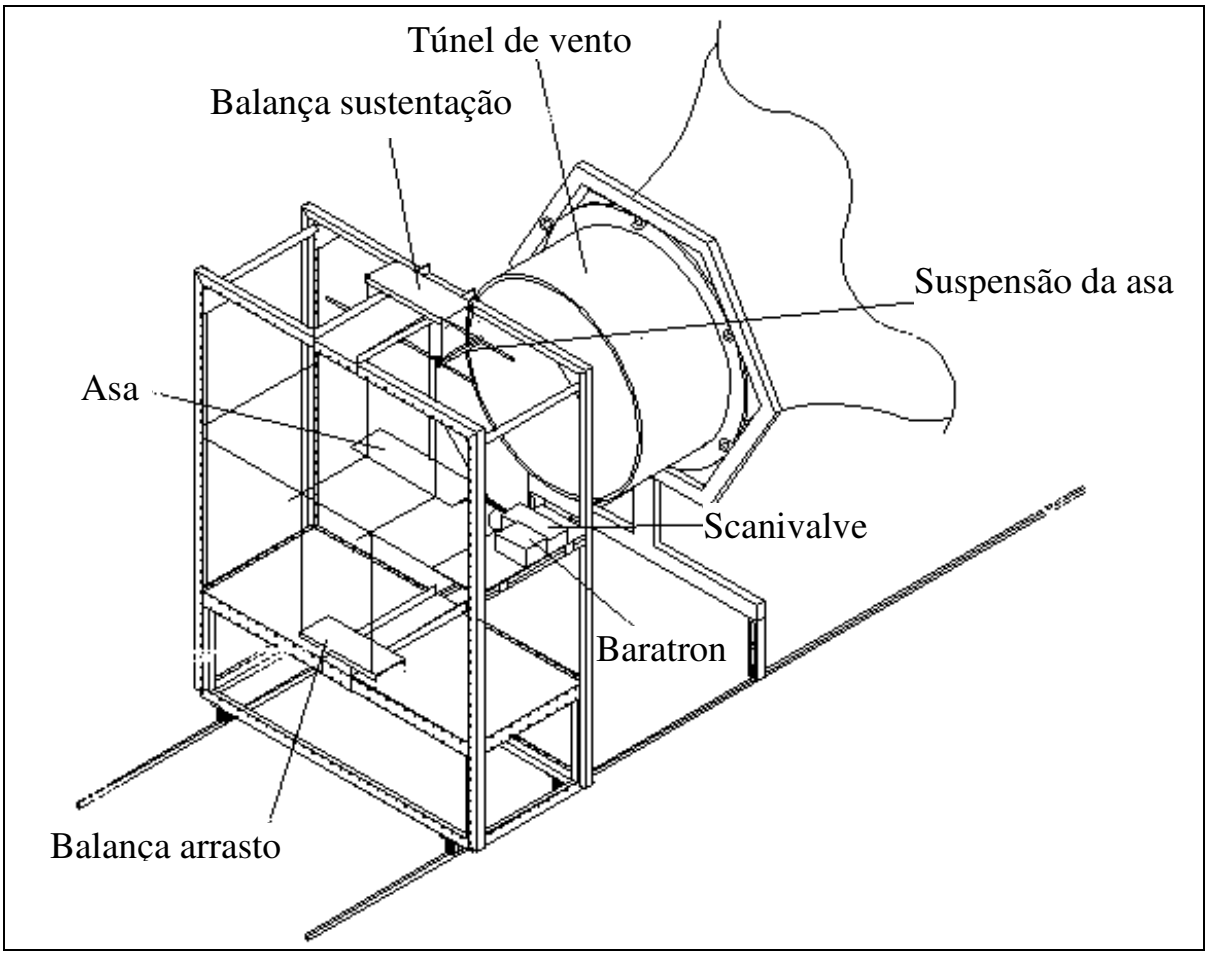

Figura 6. Imagem esquemática de túnel de vento

5. Resultados das medições de forças

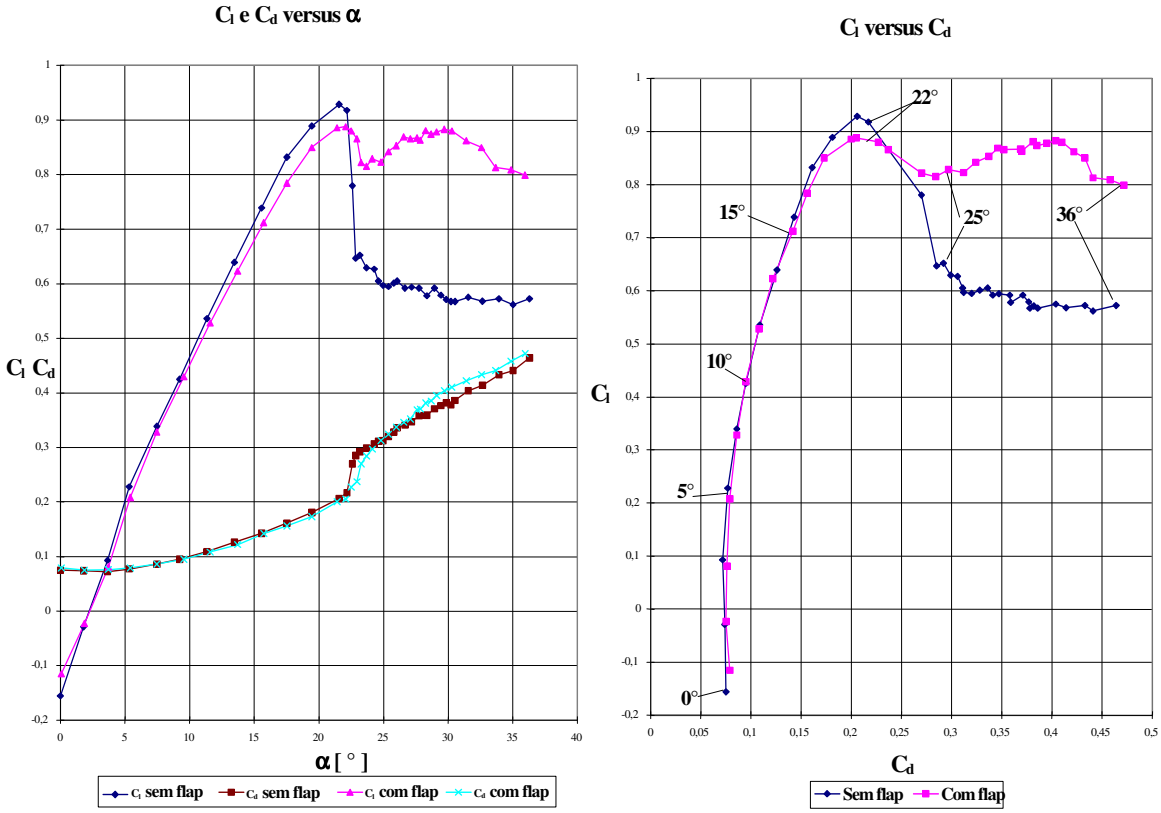

Figura 7. Diagrama polar e diagrama de Lilienthal

O diagrama polar mostra o coeficiente da sustentação C_l e o coeficiente do arrasto C_d representado graficamente, versus o ângulo de ataque, com e sem *flaps*. Como esperado, sem *flap* a sustentação cai de forma significante de C_l = 0,92 até C_l = 0,64, que pode-se explicar através do conhecido efeito estol. Aumentando o ângulo de ataque até 36º a curva suaviza-se continuamente até C_l = 0,58.

Aplicando a *flap*, o gradiente da curva se torna um pouco menor e não alcança o máximo valor C_l = 0,92 devido ao fato de que no *flap* apareceram pequenos inchaços a partir de um ângulo de ataque de 8º. Isto provavelmente pode ser evitado usando *flaps* mais porosos e que têm assim uma melhor possibilidade de ajustar o gradiente de pressão acima da asa. Próximo ao ângulo de ataque de estol a sustentação cai também um pouco, de C_l = 0,89 até C_l = 0,81 $\Rightarrow$ ΔC_l = 0,09 (em comparação de $\Rightarrow$ ΔC_l = 0,32 sem *flap*, ou seja uma diminuição de aproximadamente 35% da sustentação), mostra depois um aumento para C_l = 0,89 até α = 30° e diminui de novo para C_l = 0,79 até α = 36°.

Comparando o arrasto não se nota diferencas significativas até o estol. Depois, a curva mostra um aumento mais suave com o *flap*, mas fica com valores mais altos em α = 36°.

O diagrama polar de Lilienthal (figura 7) mostra a sustentação versus o arrasto. No início ocorre um rápido aumento na sustentação e o arrasto se mantém praticamente constante. Usando o *flap* no início, a razão se tornou um pouco pior e começou a se igualar em α = 10°. A melhor razão de planeio ε_{opt} foi igual em ambos os casos, mas se moveu em direção a um ângulo menor com o *flap* aplicado:

$$\varepsilon_{opt} = \left(\frac{c_l}{c_d}\right)_{opt} = 5{,}17 \qquad \text{Sem } \textit{flap} \text{ em } \alpha = 15{,}87° \tag{1}$$

$$\varepsilon_{opt} = \left(\frac{c_l}{c_d}\right)_{opt} = 5{,}11 \qquad \text{Com } \textit{flap} \text{ em } \alpha = 13{,}71° \tag{2}$$

5.1 Resumo das medições de forças

As medições confirmaram basicamente o efeito positivo dos *eddy flaps*. O mais modesto aumento de C_l em $\alpha = 10°$ pode ser explicado através dos já mencionados inchaços. Isto significa que a seda não foi suficientemente permeável para ajustar o gradiente da pressão acima da asa. Antes de atingir a máxima sustentação, a seda começou a ondular e perturbou assim as linhas de corrente. Isto explica porque a sustentação não chegou ao mesmo nível enquanto se usa o *flap*. Não obstante, este corte do máximo valor de C_l pode ser também uma vantagem devido ao fato de que os valores antes e depois do estol se mantêm quase iguais, ou seja, o *flap* pode tornar uma asa com estol abrupto em uma asa com comportamento aerodinâmico mais suave, apresentando menor gradiente de forças aerodinâmicas.

Entre $\alpha = 24°$ e $\alpha = 30°$ o coeficiente de sustentação aumenta até $C_l = 0{,}89$ e depois diminui de novo. Pode-se observar que o aumento do ângulo de ataque levantou o *flap* até que as forças entre a escoamento invertido e as linhas de corrente se balancearam. A diminuição de C_l com ângulos maiores pode ser evitada usando-se *flaps* mais compridos. Contudo, as forças de arrasto numa situação de vôo como essa são enormes, exigindo um empuxo muito grande para manter a velocidade.

Deve-se mencionar aqui que um escoamento ao redor de uma asa com um alongamento de 3,5 é quase completamente tridimensional. Devido às diferenças de pressão entre extradorso e intradorso surgem nas pontas da asa vórtices de equalização de pressão. Por isso o ângulo de ataque efetivo da asa tem um forte gradiente indo do meio às pontas. Ou seja, no meio da asa pode ocorrer o estol, enquanto nas pontas ainda existem linhas de corrente do escoamento coladas ao extradorso.

Para esclarecer onde exatamente o *flap* causa o aumento da sustentação, é necessário se fazer ainda as medições de pressão.

6. Resultados das medições de pressão

6.1 A distribuição do coeficiente de pressão

Os diagramas abaixo mostram, em ângulos de ataque diferentes, as curvas de nível da parte superior da asa. O primeiro com o *flap* aplicado, o segundo sem *flap* e o terceiro com a diferença entre as duas, ou seja, o valor do c_p com flap menos o valor do c_p sem flap. Estão mostradas ainda as situações com linhas de corrente num ângulo de 20° e pouco depois do estol num ângulo de 24°. Estes diagramas indicam perfeitamente as áreas onde são os ganhos e as perdas de sustentação. As imagens mostram a distribuição da asa como um todo. Como as medições foram feitas somente em um lado da asa, os resultados foram interpolados e refletidos com o programa Axum 4.0 para o outro lado. Não obstante, a interpolação para calcular as curvas de nível não resultou em imagens exatamente iguais em ambos os lados, o que não impediu que fosse feita uma interpretação adequada dos resultados. Todas as imagens foram colocadas de maneira que o bordo de ataque é direcionado para baixo.

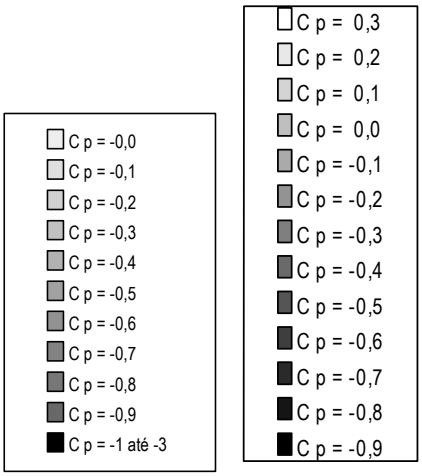

Figura 8. Legendas da distribuição das curvas de nível de pressão.

A Figura 8 mostra as legendas para as curvas de nível. A legenda no lado esquerdo se refere aos resultados das medições. Embora, os valores do C_p tenham variado muito entre os diferentes ângulos e com uma resolução ainda adequada de 0,1, a legenda precisaria de pelo menos 40 cores diferentes. Como esta resolução não é possível de ser diferenciada pelo olho humano, os ganhos acima de $C_p = -1$ foram enegrecidos.

A legenda no lado direito se refere as imagens de ganhos e perdas. Por questões da resolução foi escolhida uma distribuição de cores diferente, ou seja, a distribuição das cores com os valores não combinam com as da primeira legenda.

$\alpha = 20°$:

Sem *flap*

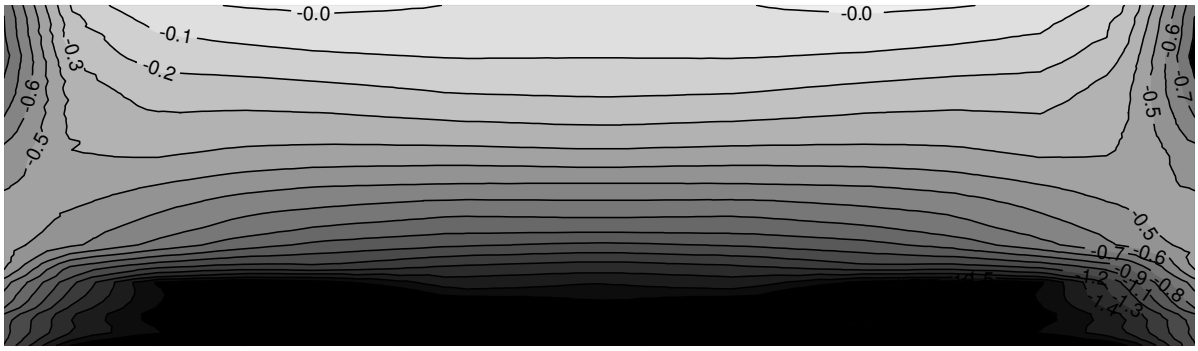

Com *flap*

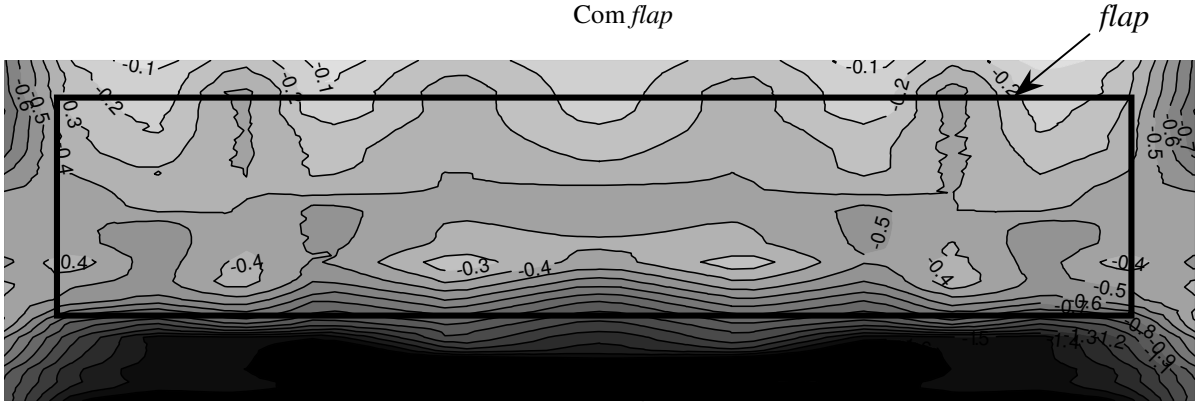

Ganhos e perdas locais

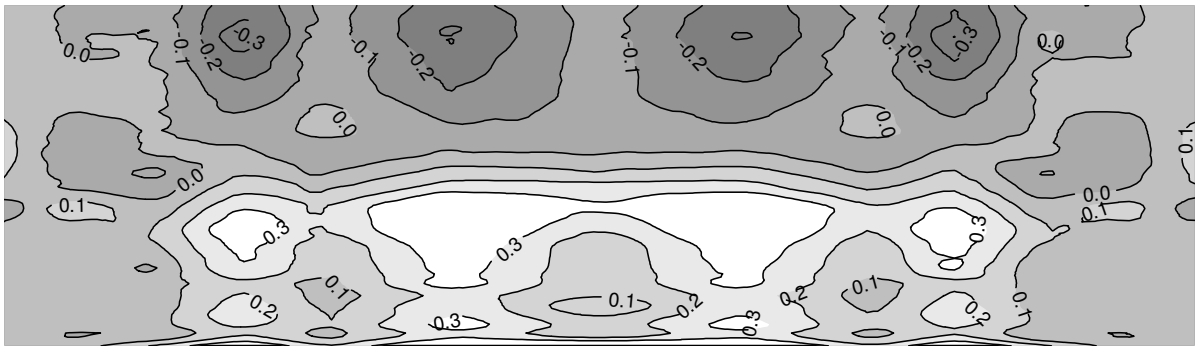

Direção de escoamento

Figura 9. Diagrama de nível de pressão em $\alpha = 20°$

Já em condições com linhas de corrente que é o caso em $\alpha = 20º$, o *flap* influencia a distribuição de pressão. Isto confirma os resultados das medições das forças com a conclusão que a seda apresentou uma porosidade insuficiente. No diagrama este efeito é visível através das linhas de C_p onduladas perto do bordo de fuga. Os pequenos ganhos nessas áreas podem ser explicados através da aceleração do escoamento causado pelo *flap*. Como o *flap* não foi plenamente integrado no perfil, ele perturbou as linhas de corrente e causou assim perdas na área da frente da asa de 7%.

α = 24°:

Sem *flap*

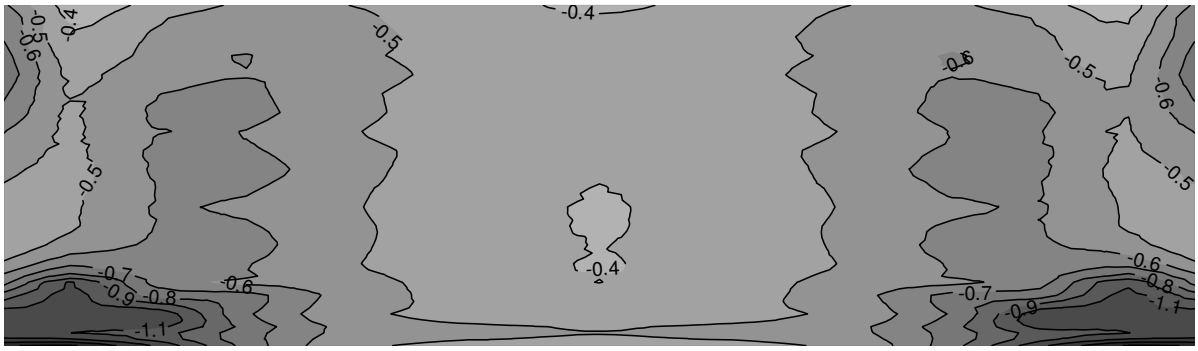

Com *flap*

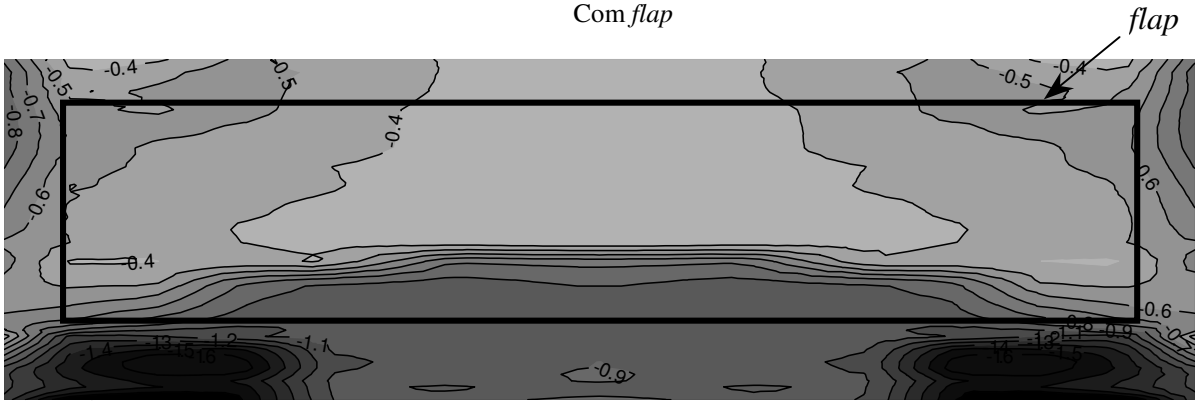

Ganhos e perdas locais

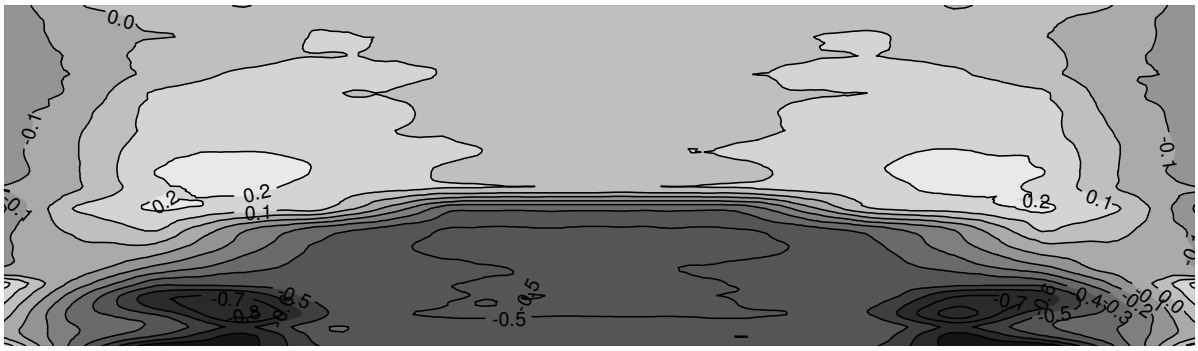

Direção de escoamento

Figura 10. Diagrama de nível de pressão em α = 24°

Nesse ângulo de ataque o escoamento está quase completamente em estol. Os vórtices da equalização de pressão nas pontas da asa são responsáveis para que nesta área as linhas de corrente do escoamento estejam ainda coladas ao extradorso. Agora o *flap* é completamente levantado e mostra vibrações aeroelásticas. O ganho de 26% em comparação com o ângulo anterior é significativo. As pequenas perdas abaixo do *flap* são mais do que compensadas com os ganhos na área da frente.

O diagrama na figura 11 mostra para um melhor entendimento a distribuição do C_p numa outra forma.

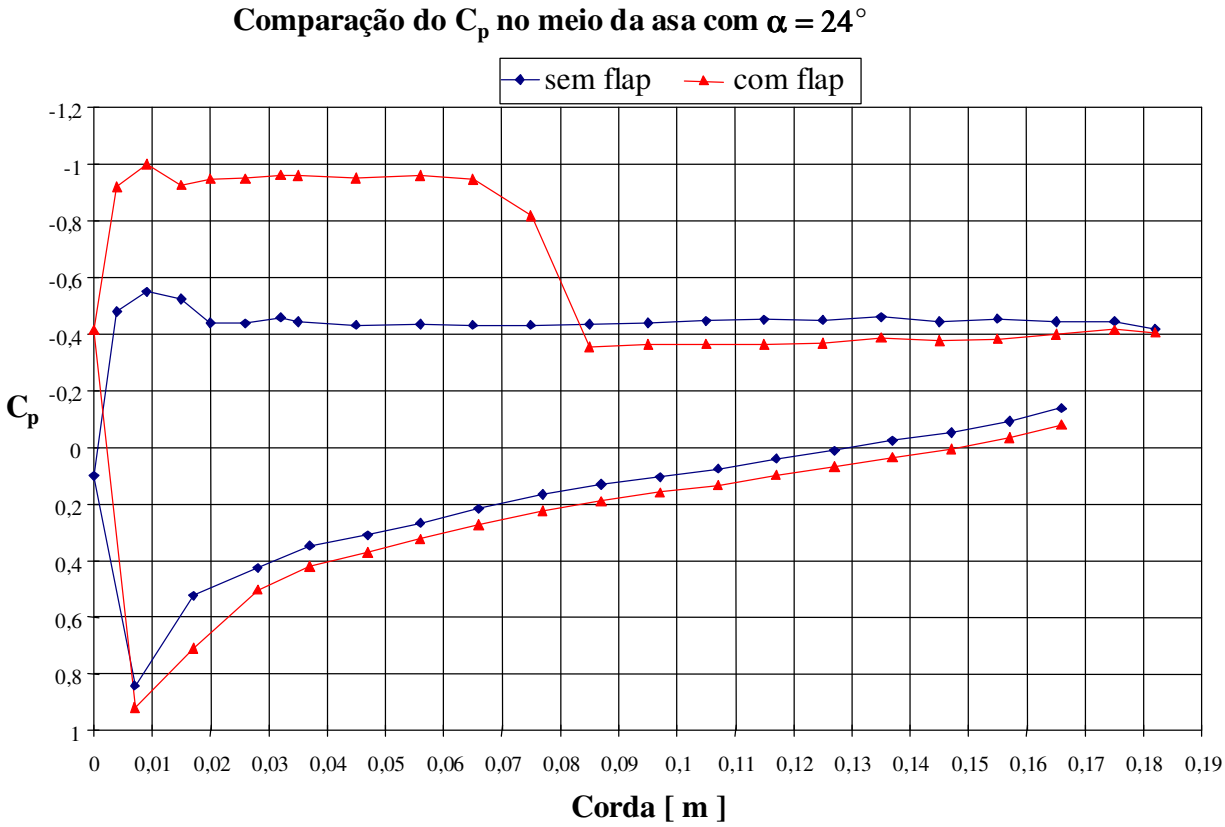

Figura 11. Diagrama de distribuição de pressão num corte de perfil em $\alpha = 24°$

A distribuição é claramente dividida em duas secções da pressão praticamente constantes – uma em frente e uma atrás do *flap*. Isto mostra que emergiram duas áreas da separação divididas pelo *flap*.

A constância da pressão na parte dianteira somente é explicável se o escoamento for restringido por um vórtice, formando uma zona de recirculação. Ademais, um aumento do ângulo de ataque deixa também o *flap* levantar mais e reprime o vórtice até as resultantes das forças aerodinâmicas estarem em balanço. O significado disso será investigado mais profundamente na seção 7 "Visualização do escoamento e configuração de vórtices".

6.2 Resumo das medições de pressão em comparação com os da força

Ambas as medições mostraram perfeitamente o efeito positivo dos *eddy flaps*. As diferenças do C_l com ângulos de ataque antes do estol podem diminuir usando-se um material mais permeável. Também uma melhor integração do *flap* na asa, ou seja, um *flap* que não perturbe a camada limite, como um fio da turbulência, pode melhorar o ângulo de planeio. As pequenas perdas com ângulos grandes podem ser evitadas usando *flaps* mais prolongados.

De qualquer maneira, voar nesses grandes ângulos de ataque é praticamente impossível devido às grandes forças de arrasto. Ainda assim, podem ser realizadas aterrissagens com velocidades menores e com pistas mais curtas.

Através das medições realizadas pode-se concluir que o maior ganho de sustentação se encontrou na frente do *flap*. O que não podia ser esclarecido foi o verdadeiro transcurso do escoamento. Isto é, em que condições tomam as partículas do escoamento determinados caminhos? Para tentar esclarecer essa questão foram ainda feitas algumas visualizações do escoamento com fumaça.

7. Visualização do escoamento e configuração de vórtices

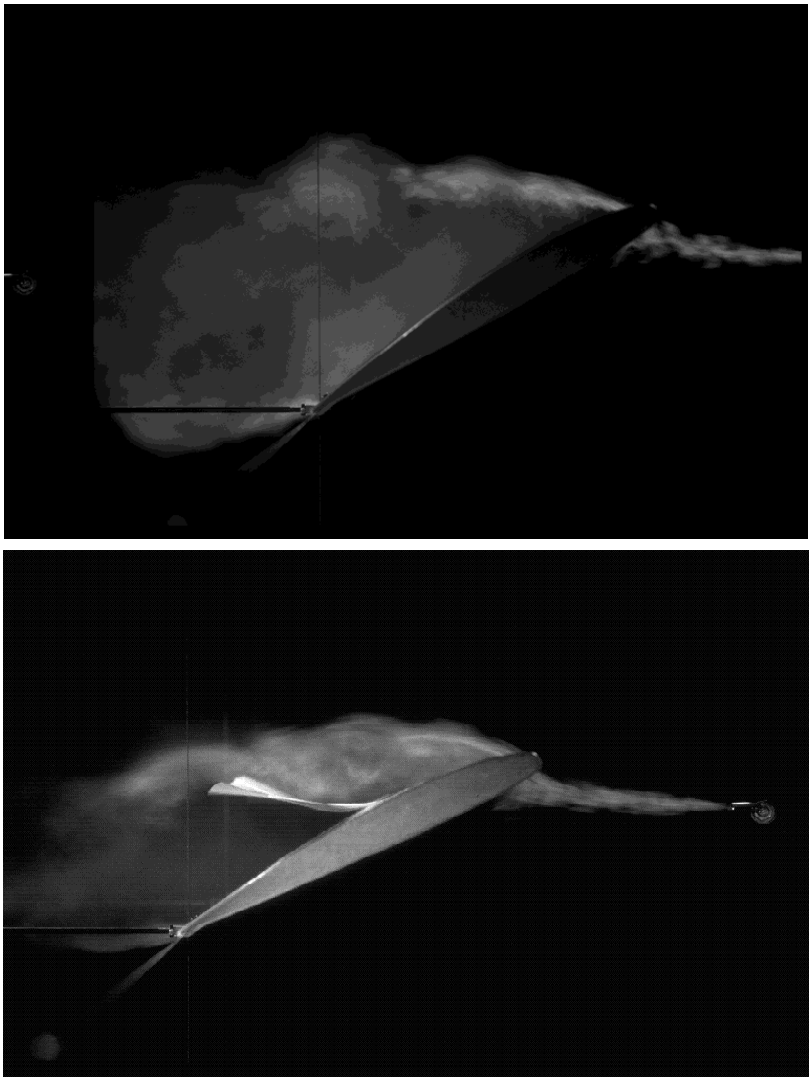

Figura 12. Visualização do escoamento com uma sonda de fumo

A figura 12 mostra os resultados da visualização das condições do escoamento em $\alpha = 25°$, realizado com uma sonda de fumaça. Na primeira imagem se pode examinar que o escoamento não é mais capaz de seguir na superfície do perfil. O escoamento é separado e completamente turbulento. Na imagem com o *eddy flap* aplicado se pode reconhecer um vórtice estacionário em frente do *flap* que possui a mesma direção da rotação que o vórtice ligado. Abaixo do *flap*, por outro lado, não foi possível descobrir qualquer ordem na estrutura do escoamento.

A figura 13 mostra mais esquematicamente estas condições dos vórtices.

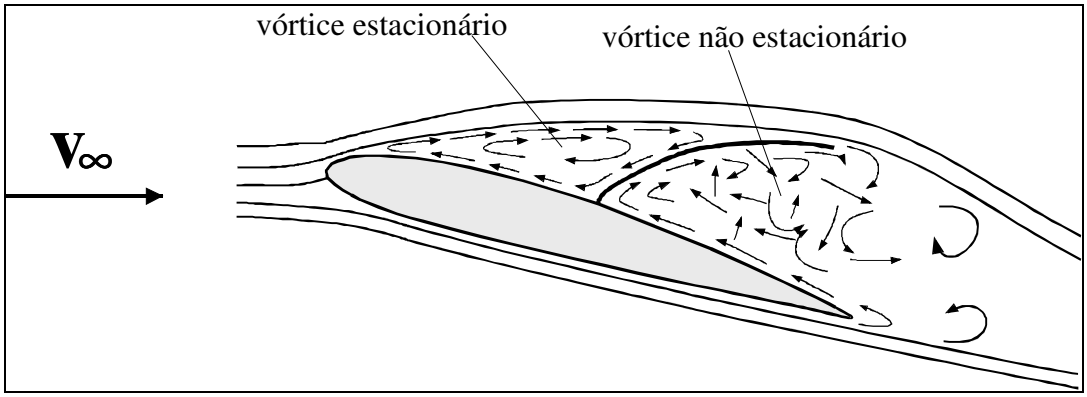

Figura 13. Imagem esquemática da distribuição de vórtices

Com o aumento do ângulo de ataque o *flap* se levanta sem parar, o vórtice estacionário se prende cada vez mais e muda assim também a sua superfície. Isto pode ser comparado com uma adaptação automática do perfil que aumenta o raio no bordo de ataque com o aumento do ângulo de ataque. Se for possível encher o vórtice com material criando assim um novo perfil, poder-se-ia, muito provavelmente, aumentar ainda mais a sustentação. Neste caso não se trata mais de uma separação com uma distribuição de pressão constante, mas sim de uma aceleração do escoamento que causaria uma sustentação maior.

8. Analise de incertezas

A metodologia utilizada precisa ser consistente para poder comparar os resultados obtidos. Por isso, os exames preliminares para conhecer melhor a biomecânica das penas das aves foram muito importantes. Medições com *flaps* que não aplicaram os resultados obtidos nestes exames não mostraram resultados esperados. Por exemplo, *flaps* sem porosidade se levantaram prematuramente e perturbaram o escoamento resultando em um ângulo de planeio pior e *flaps* sem arames de aço se enrolaram, mostrando assim mais nenhuma similaridade com as bolsas formadas pelas penas.
Muito importante foi também a informação que as penas não possuem ligações para levantar-se de forma ativa, sendo assim a prova que se trata realmente de um efeito aerodinâmico. No *flap* usado a própria fita funcionou como dobradiça. Este mecanismo é menos resistente do que a ligação haste / pele das aves, mas as considerações já feitas no caput sobre a rigidez dos arames de aço valem também aqui.
Como o objetivo deste trabalho concentrou-se em explicar apenas o efeito aerodinâmico do levantamento das penas das aves, as exatidões dos valores medidos são de menor importância.
A maior influência na exatidão nos valores de c_l e c_d foi causada pela suspensão da asa. Os fios 1, 2 e 3 ligaram a asa com a balança de sustentação. Através de duas hastes 5 e 6, e os fios 8 e 9, a asa foi ligada com a balança de arrasto. Os cabos 4 e 7 estabilizaram a asa nas direções laterais. Para dividir as forças de forma exata nos seus dois componentes sustentação e arrasto, todas as ligações da suspensão precisam ser alinhadas na vertical e na horizontal. Caso contrário, forças de sustentação podem entrar na medição do arrasto ou através do cabo 4 na estrutura e vice versa. Todos os alinhamentos foram realizados visualmente com um nível. Ademais as roldanas não representaram uma ligação completamente imóvel e as forças medidas sofreram influências do atrito atravessando elas.

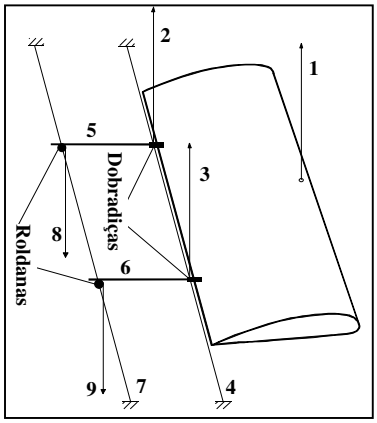

Figura 14. Suspensão da asa

Comparações com pesos calibrados mostram influências menores que 1 % na medição da sustentação e até 7 % na medição de arrasto.
O ângulo do potenciômetro foi calibrado através da luz de um laser que foi fixado numa distância conhecida. Através da definição do tangente foram calculados vários ângulos para definir a curva de calibração para o potenciômetro. Medições repetitivas mostraram uma boa conformidade. A discrepância na reprodutividade do ângulo pelo servomotor variou até 0,3°.

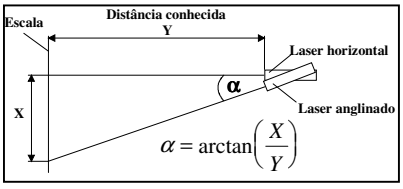

Figura 15. Calibração do potenciômetro

Nas medições de pressão precisa-se mencionar que os valores obtidos variaram bastante no estol e diretamente após da mudança para um novo ângulo. Para diminuir estas variações foram feitas medições contínuas, até 20 valores seguidos ficaram abaixo de um valor predefinido (< 7 Pa). Depois foi gravada a média das próximas 20 medições.

As incertezas na medição de pressão podem ser avaliadas comparando os resultados com os obtidos pelas balanças. Para isso foram definidas áreas dx·dy e dy·dz para cada furo que representaram a pressão medido e para qual se pode, considerando ainda o ângulo de ataque, calcular as forças desejadas. As somas de todas as forças sobre a asa foram comparadas com as forças medidas nas balanças, encontrando-se um desvio máximo de 8 %.

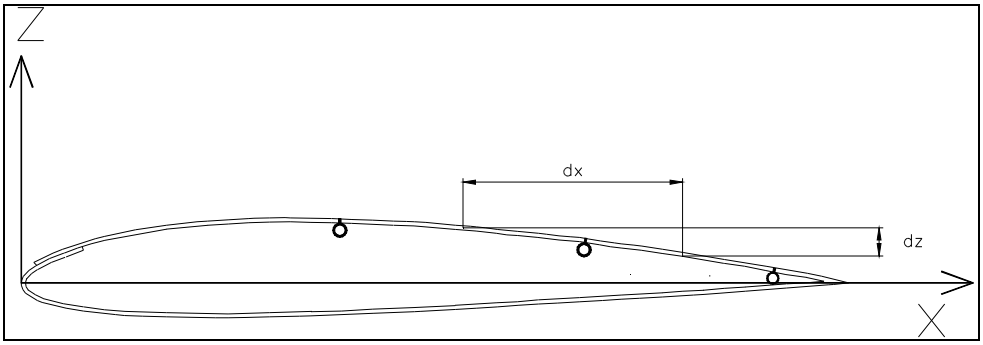

Figura 16. Divisão da asa em áreas

9. Referências

Althaus D., 1980, „Profilpolaren für den Modellflug“, Neckar Verlag VS-Villingen.

Dubs F.,1990, „Aerodynamik der reinen Unterschallströmung“ - 6. Auflage, Birkhäuser Verlag Basel Boston Berlin.

Leder A., 1992, „Abgelöste Strömungen - physikalische Grundlagen“, Braunschweig, Vieweg.

Patone G., Müller, W, 1996, „Aeroflexible Oberflächenklappen als "Rückstrombremsen" nach dem Vorbild der Deckfedern des Vogelflügels“, Teilprojekt: “Biomechanik der Vogelfedern und deren bionische Umsetzung" Technical Report TR-96-05

Rechenberg I, Bannasch R, Patone G, Müller W, 1995, „Statusbericht für das Jahr 1995 zum Forschungsvorhaben 13N6536 des BmBF“.

EXPERIMENTAL INVESTIGATIONS ON A SHORT WING WITH SURFACE FLAPS

Roger Paul Dorweiler
Instituto de Tecnologia para o Desenvolvimento - LACTEC
Laboratório De Emissões Veiculares - LEME
Av. Prefeito Lothario Meissner, 01
Jardim Botânico, Curitiba - PR
CEP: 80210-170
Roger.dorweiler@lactec.org.br

Abstract

Observations in birds show, that their covert feathers can lift of the surface in turbulent flow or in critical flight situations. In those flight situations appears a local separation of the aerodynamic lines, known as effect stall. Due to the fact that the feathers of birds do not possess connections that allow an active movement, only aerodynamics forces can explain that rising effect.

The object of this work was to investigate in wind tunnel experiments the operation of the feathers as well as to explain the aerodynamic effect in case of an application on a wing with a significant stall. In accordance of the porosity and stiffness characteristics of the feathers from several birds, artificial feathers were constructed. It was also built a wing NACA 2412 with defined holes to measure the pressure distribution over the profile in comparison with and without the applied feathers. The results were also compared with the datas obtained through the measurements of lift and drag realized by two electronic balances.

Through the measurements it was demonstrated that the pockets, formed by the feathers, work as eddy brakes for the cross-current that propagate from the trailing edge towards the leading edge in the boundary layer in stall situations, avoiding like this the total drop of lift until an angle of attack of 40°. Between the board of attack of the wing and the pocket a vortex appears, that changes their form relative to the angle of attack. It was found that this deformation works like an automatic adaptation, which increase the thickness of the profile and cause for that an increase of lift in that area. Behind the pocket the conditions are not stationary and with a reduced lift. Nevertheless in the sum it results in a larger lift.

Like this, the use of "*aeroflexíbel surface flaps*" makes in the area of aerodynamics one more tool available to aid in practice a safer flying.

Keywords: Aerodynamic, Stall, Wind Tunnel, Eddy Flaps

Proceedings of the 11th Brazilian Congress of Thermal Sciences and Engineering -- ENCIT 2006
Braz. Soc. of Mechanical Sciences and Engineering -- ABCM, Curitiba, Brazil, Dec. 5-8, 2006

Paper CIT06-0259

CÁLCULO DA PRESSÃO EM SUPERFÍCIES SUJEITAS À AQUECIMENTO AERODINÂMICO

Humberto Araujo Machado
Instituto de Aeronáutica e Espaço – IAE
Comando-Geral de Tecnologia Aeroespacial - CTA
Pr. Mal. Eduardo Gomes, 50, Vila das Acácias, 12228-904
São José dos Campos, SP
humbertoam@iae.cta.br

Danton José Fortes Villas Boas
Instituto de Aeronáutica e Espaço – IAE
Comando-Geral de Tecnologia Aeroespacial - CTA
Pr. Mal. Eduardo Gomes, 50, Vila das Acácias, 12228-904
São José dos Campos, SP
danton@iae.cta.br

Resumo. *Veículos espaciais submetidos a um escoamento hipersônico sofrem um forte processo de aquecimento aerodinâmico, o que produz a elevação da temperatura do ar ao redor da parede externa do veículo em várias centenas de graus. Em geral, este aquecimento é estimado através de métodos aproximados, fundamentados em observações empíricas. Um dos aspectos mais importantes na aplicação desses cálculos é a variação da pressão ao longo da superfície externa, que exerce grande influência nos resultados da temperatura, o que, por sua vez, é de extrema importância no dimensionamento do escudo térmico do veículo. Neste trabalho são comparados os resultados obtidos com a aplicação de duas metodologias, o método de Newton modificado e o emprego do software Missile Datcom, baseado em métodos de cálculo semi-empíricos, para a determinação das temperaturas atingidas pela superfícies externa da plataforma suborbital SARA durante a trajetória prevista.*

Palavras chave: aquecimento aerodinâmico, veículo espacial, cálculo de pressão.

1. Introdução

Veículos espaciais e sub-orbitais atingem grandes velocidades dentro da atmosfera, que se estende até aproximadamente 100 km acima da superfície terrestre, o que acarreta o aquecimento aerodinâmico desses veículos. Este ocorre pela formação de uma onda de choque próxima ao veículo em velocidades supersônicas e devido ao atrito com as moléculas de ar, e envolve troca de calor por convecção e radiação entre o ar aquecido e a superfície do veículo.

Esses veículos transportam uma carga útil, que deve ser protegida contra as altas temperaturas através de um escudo térmico. O dimensionamento desse escudo é um dos aspectos críticos do projeto de sistemas espaciais, pois proteções térmicas subdimensionadas podem levar à perda da carga útil, e o superdimensionamento acarreta aumento de peso e custo (Da Costa, 1996). Esse dimensionamento é feito a partir dos dados de fluxo de calor ao longo da trajetória e carga térmica e temperaturas alcançadas pela superfície ao longo da trajetória (Machado, 2006).

Em geral, é empregado um modelo de engenharia para a determinação do coeficiente de transferência de calor por convecção ao longo da superfície do veículo. Os modelos usualmente empregados se baseiam extensivamente na aproximação pela entalpia de referência de Eckert (Hurwicz e Rogan, 1973). Nesse modelo, a transferência de calor em uma camada limite compressível pode ser calculada através das relações disponíveis para escoamento incompressível, sendo todas a propriedades avaliadas na condição de referência. O cálculo, descrito em detalhe mais adiante, depende fundamentalmente da pressão sobre ponto da parede em que a troca de calor é avaliada.

A avaliação da pressão dentro da camada limite compressível pode ser feita através da solução das equações de camada limite, via simulação computacional por método discreto, por exemplo. No entanto, essa via de solução demanda um grande esforço computacional, e nas fases iniciais do projeto seria inviável sua aplicação. Nesse caso, são aplicados métodos aproximados, que possibilitem obter resultados com uma acuidade suficiente para o desenvolvimento do projeto.

O mais utilizado tem sido o método de Newton (Anderson, 1989), que envolve basicamente a descrição da geometria do veículo em relação ao campo de escoamento. Esse método apresenta excelente precisão quando aplicado próximo do ponto de estagnação do veículo, a velocidades próximas ou superiores a Mach 5. Embora essas sejam as condições em que em geral ocorre o maior aquecimento da superfície do veículo, existe a necessidade de se determinar a troca de calor em outras regiões e faixas de velocidade, para o melhor dimensionamento do escudo de proteção térmica do veículo.

Neste trabalho, é calculado o aquecimento superficial da plataforma recuperável SARA, que vem sendo desenvolvida pelo IAE/CTA, na fração mais crítica de sua trajetória ascendente (em que incide a maior carga térmica). O cálculo da pressão na superfície do veículo ao longo da trajetória é feito empregando-se o método de Newton, e

comparada com aquele obtido a partir da distribuição de pressão calculada pelo software Missile Datcom, que emprega um método semi-empírico para determinação da pressão na parede do veículo. O objetivo é detectar discrepâncias entre o método de Newton e outros métodos, especialmente em regiões fora do intervalo de aplicação apropriado do método.

O SARA é concebido como uma plataforma recuperável para a realização de experimentos em ambiente de microgravidade, e vem sendo desenvolvido pelo IAE/CTA. Sua massa total é da ordem de 250 kg e a carga útil prevista por volta de 25 kg. A versão atualmente em desenvolvimento prevê emprego em vôos sub-orbitais. A versão definitiva deverá ser capaz de manter-se em órbita de 300 km ao longo da Terra por 10 dias (Moraes, 1998).

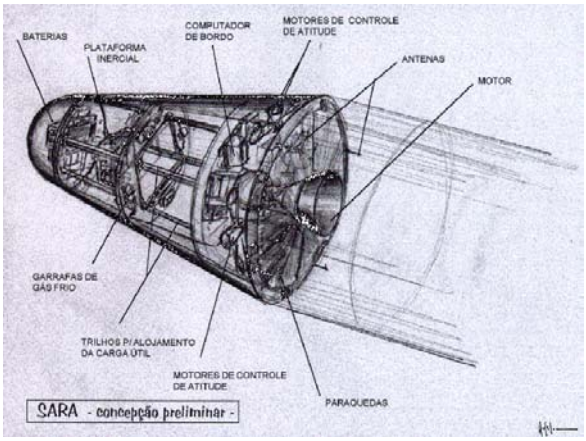

Figura 1. O SARA e seus subsistemas.

As características da trajetória ascendente inicialmente prevista para o SARA sub-orbital são mostradas na Fig. (2). É possível observar, a partir da evolução dos valores da velocidade e número de Mach, e considerando que a massa específica da atmosfera só se torna significativa abaixo de 90 km, que a maior parcela do aquecimento deve ocorrer 10 e 60 segundos, quando o escoamento é hipersônico, ainda dentro do limite da atmosfera. Essa fração da trajetória é destacada em vermelho nos gráficos, e será o intervalo considerado para o cálculo.

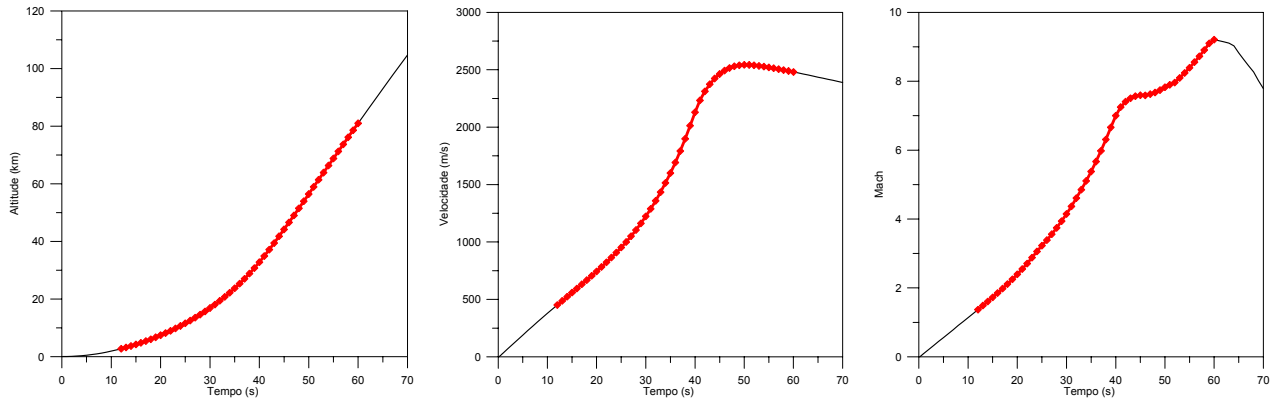

Figura 2. Características da trajetória ascendente prevista do SARA sub-orbital.

2. Modelo matemático para cálculo do aquecimento aerodinâmico

O processo de aquecimento aerodinâmico envolve a combinação de diversos fenômenos físicos simultâneos, de difícil modelagem, Fig. (3). Para o cálculo do aquecimento aerodinâmico do SARA, é necessário conhecer os campos de pressão, velocidade e temperatura ao redor da superfície externa da parede. Esses campos podem ser determinados numericamente através da solução das equações de camada limite, porém a um custo relativamente alto para essa fase do projeto. No presente trabalho, um método de engenharia é empregado para estimar o fluxo de calor convectivo na parede da plataforma SARA, a partir das seguintes hipóteses:

- Ângulo de ataque zero e ausência de rotação.
- As propriedades físicas são consideradas constantes com a temperatura.
- O ar atmosférico é considerado um gás calórica e termicamente perfeito, e o processo ocorre na ausência de reações químicas (tal hipótese é considerada adequada, uma vez que apresenta resultados conservadores em relação ao modelo de gás com propriedades variáveis, segundo Miranda e Mayall, 2001).
- Camada limite fina

- Escoamento não-viscoso na região da camada de choque externa à camada limite
- Escoamento isentrópico numa mesma linha de corrente
- As linhas de corrente próximas à superfície do corpo passam através da parte normal da onda de choque.

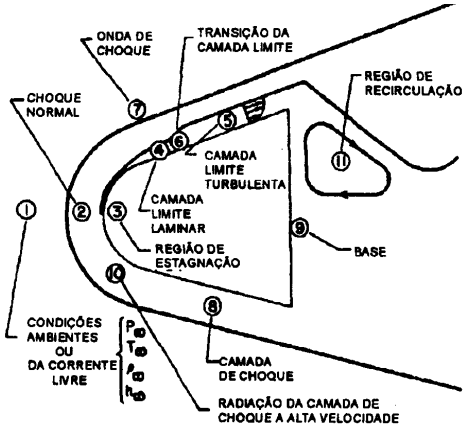

Figura 3. Fenômenos físicos envolvidos na reentrada atmosférica de um veículo espacial.

Assume-se que as condições da corrente livre são dadas por v_∞, T_∞, p_∞, respectivamente a velocidade, temperatura e pressão. As condições atmosféricas (propriedades do ar com a altitude) são obtidas a partir da U. S Standart Atmosfere (1976), de onde se extraem a pressão e temperatura ambientes, velocidade do som e demais propriedades físicas do ar.

Ao atingir escoamento supersônico ($M_\infty > 1$), forma-se uma onda de choque ao redor do corpo. As propriedades do ar após a onda de choque, v_1, T_1 e p_1, são obtidas a partir das relações para choque normal disponíveis na literatura (Anderson, 1982). As propriedades de estagnação do gás são calculadas através das relações para gás perfeito (Anderson, 1982).

Para o cálculo do fluxo de calor incidente na superfície externa da parede, foi empregado o método de Zoby (Miranda e Mayal, 2001), que relaciona o coeficiente de película da troca convectiva com o coeficiente de atrito na parede, através de uma forma modificada da analogia de Reynolds. A partir da equação de troca de calor por convecção, tem-se:

$$q = H(T_{aw} - T_w) \tag{1}$$

onde q é o fluxo de calor, T_w é a temperatura da parede e T_{aw} é a temperatura da parede adiabática, também chamada temperatura de recuperação, dada por:

$$T_{aw} = T_e + F_R \frac{V_e^2}{2C_p} \tag{2}$$

onde C_p é o calor específico do ar, T_e e V_e são respectivamente a temperatura e velocidade na fronteira da camada limite e F_R é o fator de recuperação, igual a $\sqrt{Pr_w}$ no regime laminar e $\sqrt[3]{Pr_w}$ para regime turbulento, sendo Pr_w o número de Prandtl à temperatura da parede.

O coeficiente de película H é dado por:

$$H = 0.5\rho_e C_p V_e \, Pr_w^{-a} \, C_F \tag{3}$$

onde a é igual a 0.6 e 0.4 nos regimes laminar e turbulento, respectivamente. C_F é o coeficiente de atrito modificado para computar os efeitos da compressibilidade:

$$C_F = K_1 (Re_\theta)^{K_2} \left(\frac{\rho_e^*}{\rho_e} \right) \left(\frac{\mu_e^*}{\mu_e} \right)^{K_3} \tag{4}$$

onde Re_θ é o número de Reynolds baseado na espessura da camada limite (θ):

$$Re_\theta = \frac{\rho_e V_e \theta}{\mu_e} \tag{5}$$

O sobrescrito "*" refere-se à propriedades avaliadas à temperatura de referência de Eckert (T_e*).

A variação da viscosidade com a temperatura é obtida a partir da formula de Sutherland (Miranda e Mayal, 2001). As constantes presentes na eq. (4) são avaliadas de acordo com o regime de escoamento: em regime laminar, K_1= 0.44, K_2 = -1 e K_3 = 1. Em regime turbulento, $K_2 = K_3 = -m$, sendo:

$$K_1 = 2\left(\frac{1}{C_5}\right)^{\frac{2N}{N+1}}\left[\frac{N}{(N+1)(N+2)}\right]^m \tag{6.a}$$

$$m = \frac{2}{N+1} \tag{6.b}$$

$$C_5 = 2.2433 + 0.93N \tag{6.c}$$

$$N = 12.76 - 6.5\log_{10}(Re_\theta) + 1.21[\log_{10}(Re_\theta)]^2 \tag{6.d}$$

A espessura da camada limite laminar é estimada por:

$$\theta_L = \frac{0.664\left(\int_0^S \rho_e^* \mu_e^* V_e R^2 dy\right)^{\frac{1}{2}}}{\rho_e V_e R} \tag{7}$$

onde a integral é calculada numericamente. No ponto de estagnação R=0 e a eq. (7) se torna indeterminada. Nesse caso, quando y < 0.1 R_N (raio da região esférica), foi empregado o limite da eq. (7) quando $R \to 0$:

$$\theta_L = \frac{0.332\left(\rho_e^* \mu_e^*\right)^{\frac{1}{2}}}{\rho_e \sqrt{\frac{1}{R_N}\left[\frac{2(p_s - p_\infty)}{\rho_s}\right]^{\frac{1}{2}}}} \tag{8}$$

A espessura da camada limite turbulenta é avaliada numericamente através da equação:

$$\frac{D(\rho_e V_e R_e \rho_e)}{Dy} = 0.5 C_F \rho_e V_e R \tag{9}$$

No caso de transição, o fluxo de calor é avaliado como uma combinação linear dos fluxos laminar e turbulento:

$$q_{Tr} = q_L + F(y)(q_T - q_L) \tag{10}$$

onde o fator de transição F(y) é dado por:

$$F(y) = 1 - exp\left\{-0.412\left[\frac{4.74(y - y_L)}{(y_T - y_L)}\right]\right\} \tag{11}$$

onde y_L é o limite do escoamento laminar (quando se inicia a transição) e y_T é o início do escoamento turbulento. Admite-se que a transição se inicia quando Re_θ = 163 e termina quando Re_θ = 275 (Miranda e Mayal, 2001).

As propriedades do ar na fronteira da camada limite, sobre um ponto i qualquer da superfície, são dadas por:

$$\rho_{e,i} = \rho_s \left(\frac{p_{e,i}}{p_s}\right)^{\frac{1}{\gamma}} \tag{12.a}$$

$$h_{e,i} = h_s \left(\frac{p_{e,i}}{p_s} \right)^{\frac{\gamma-1}{\gamma}} \tag{12.b}$$

$$V_{e,i} = \sqrt{2\left(h_s - h_{e,i}\right)} \tag{12.c}$$

$$T_{e,i} = \frac{h_{e,i}}{C_p} \tag{12.d}$$

Para a correção dos efeitos da compressibilidade no escoamento, é empregada a temperatura de referência de Eckert (Anderson, 1989):

$$\frac{T^*_{e,i}}{T_{e,i}} = 1 + 0.032 M^2_{e,i} + 0.58 \left(\frac{T_W}{T_{e,i}} - 1 \right) \tag{13}$$

3. Cálculo da pressão na superfície do veículo

3.1. Método de Newton Modificado

O Método de Newton Modificado é um método de inclinação local da superfície (Anderson, 1989). A premissa básica para sua aplicação é que, em escoamentos a altas velocidades, a camada limite viscosa é fina, e as linhas de corrente se tornam paralelas à superfície do corpo. Esse método obtém os melhores resultados para escoamento hipersônico (Mach > 5), próximo ao ponto de estagnação (região em que a espessura da camada limite é mínima). A pressão é calculada por:

$$\frac{p_i}{p_s} = \left(1 - \frac{p_\infty}{p_s} \right) cos^2 \varphi_i + \frac{p_\infty}{p_s} \tag{14}$$

onde p_s é a pressão no ponto de estagnação, p_i é a pressão em um ponto qualquer na superfície e φ_i é o ângulo formado pela normal à superfície no ponto i e o eixo de simetria do SARA, Fig. (4). Apesar de ser um método aproximado, o Método de Newton Modificado apresenta boa precisão para o regime de vôo hipersônico, onde se dá o aquecimento mais intenso (Anderson, 1989). A simplicidade e acuidade deste método justificam sua ampla utilização neste tipo de aplicação.

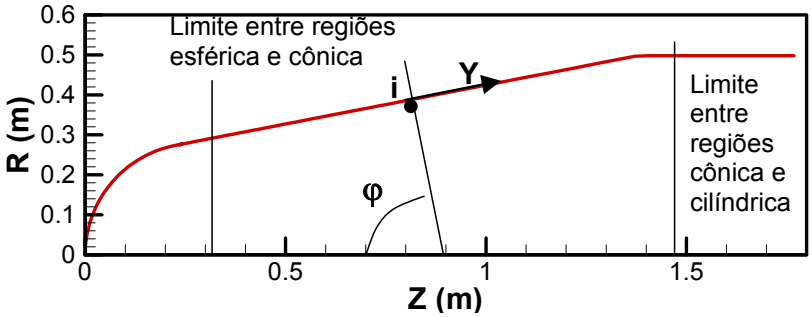

Figura 4. Geometria e dimensões do SARA, e sistemas de coordenadas usado.

3.2. Missile DatCom

Uma das formas mais eficazes para a determinação de características aerodinâmicas de veículos espaciais nas fases iniciais do desenvolvimento e para geometrias simples é a utilização de programas de cálculo semi-empíricos. Um desse programas é o Missile Datcom.O programa Missile Datcom foi desenvolvido inicialmente entre 1981 e 1985 pela McDonnell Douglas Astronautics Company. Ele utiliza um método descrito como "método de decomposição" onde o veículo é decomposto em módulos ou partes e a cada parte é aplicado um procedimento de cálculo (Vukelich et. al., 1988; Blake, 1998). Para números de Mach iguais ou superiores a 1.2 o Missile Datcom possibilita o cálculo da distribuição de pressão na superfície do corpo e das empenas do veículo, quando existentes. São disponíveis três metodologias: Van Dyke Híbrido, *Second-Order Shock Expansion* - SOSE (Mason et. al.,1981; Syverton and Dennis, 1956) e escoamento Newtoniano, que são selecionadas pelo usuário. Para o presente trabalho foi utilizado o método SOSE para ao cálculo da distribuição de pressão no Missile Datcom.

4. Resultados

Os dois métodos foram utilizados no cálculo da pressão sobre a superfície externa do SARA, durante o trecho em vermelho, mostrado nos gráficos da Fig. (2). Foram usados como inputs para o programa o trecho de trajetória e a geometria do SARA, descrita por 50 pontos, conforme mostrado na Fig. (5). O maior número de pontos está concentrado próximo ao ponto de estagnação, onde as mudanças são mais sensíveis, para obter a precisão desejada na integral da Eq. (7).

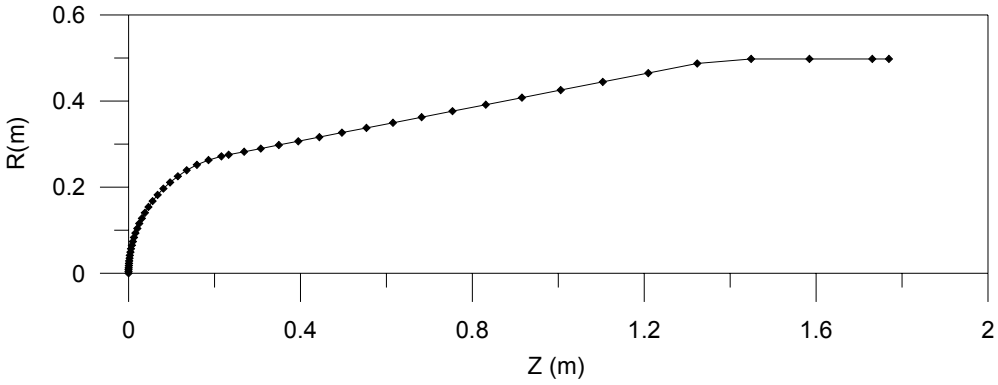

Figura 5. Pontos usados para a descrição geométrica da superfície externa do SARA.

Os coeficientes de pressão (Cp) são dados por:

$$Cp = \frac{P - P\infty}{\left(\frac{\rho V^2}{2}\right)} \tag{15}$$

onde P_{oo} é a pressão da corrente livre, e o denominador é a pressão dinâmica exercida pelo escoamento externo. Cp foi calculado pelos dois métodos. O resultado é mostrado na Fig. (6), onde é possível observar que, apesar da diferença em torno 10 % no coeficiente de pressão sobre o ponto de estagnação, no resto da curva essa diferença se reduz gradativamente. O comportamento é absolutamente similar, e as diferenças são mais acentuadas na passagem da seção cônica para cilíndrica.

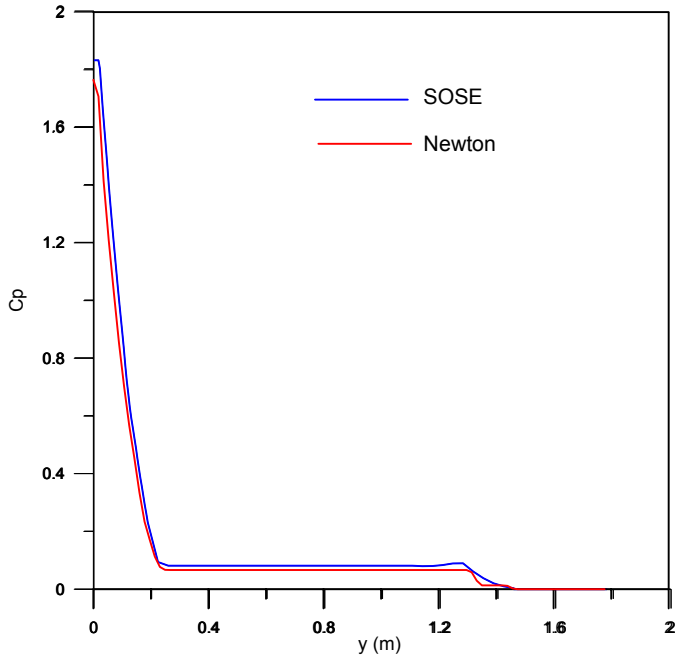

Figura 6. Coeficiente de pressão ao longo da superfície externa do SARA, durante a trajetória, obtido pelos dois métodos de cálculo.

Na fig. (7) é mostrada a variação do número de Reynolds local ao longo da superfície, durante a trajetória. O número de Reynolds tende a aumentar com a distância do ponto de estagnação. A redução ao longo do tempo se deve à diminuição da massa específica da atmosfera á medida que maiores altitudes são alcançadas. Mais uma vez, é possível observar a excelente concordância entre os dois métodos, com pequenas discrepâncias na região cilíndrica. Nota-se que o regime turbulento (Re > 275) é rapidamente atingido, e que as discrepâncias na região laminar são desprezíveis.

Na Fig. (8), observam-se os reflexos dos comportamentos de Cp e Re. O coeficiente de troca térmica por convecção se reduz ao longo do tempo, devido à redução da densidade da atmosfera, e aumenta bruscamente após a passagem do regime laminar para o turbulento. A descontinuidade observada, maior no método SOSE, deve-se à mudança da geometria esférica da calota para a geometria cilíndrica. O método SOSE é mais sensível à essa mudança que o método de Newton (uma vez que existe uma concordância entre as inclinações das duas superfícies naquele ponto). No entanto, o SOSE se mostra mais suave na passagem da geometria cônica para cilíndrica, onde a descontinuidade da inclinação e ausência de concordância provoca um salto na curva relativa o ao método de Newton.

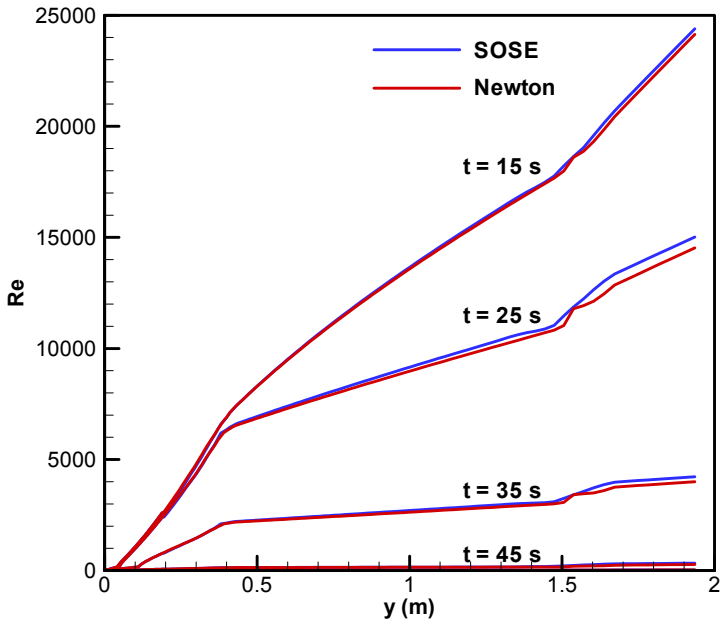

Figura 7. Variação do número de Reynolds local ao longo da superfície externa do SARA, durante a trajetória, obtido pelos dois métodos de cálculo.

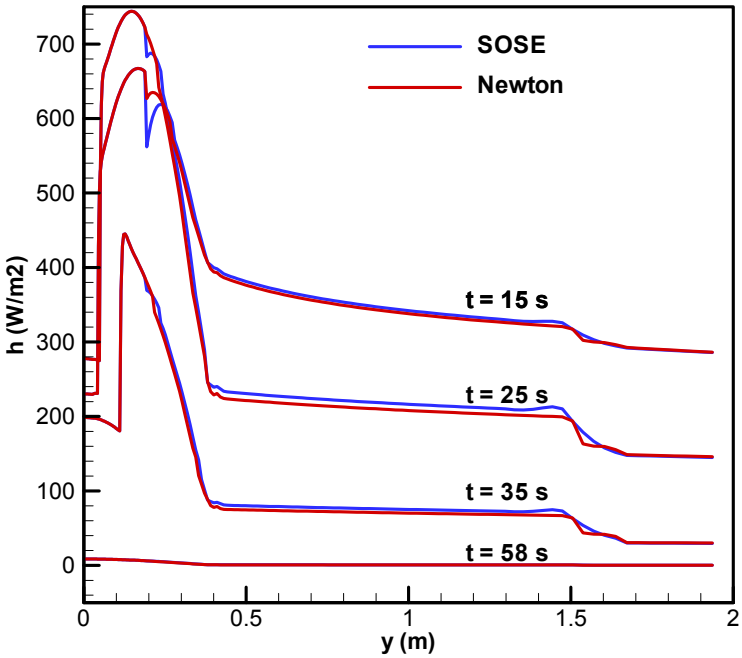

Figura 8. Variação do coeficiente de transferência de calor por convecção ao longo da superfície externa do SARA, durante a trajetória, obtido pelos dois métodos de cálculo.

Na Fig. (9), são mostrados os perfis de temperatura da superfície externa em vários momentos da trajetória, até o ponto final considerado (58 s). Mais uma vez, observa-se a excelente concordância entre os dois métodos, com valores ligeiramente maiores obtidos pelo método SOSE na seção cônica, e pequenas discrepâncias nas regiões de mudança de geometria, onde são observadas descontinuidades nos perfis geométricos.

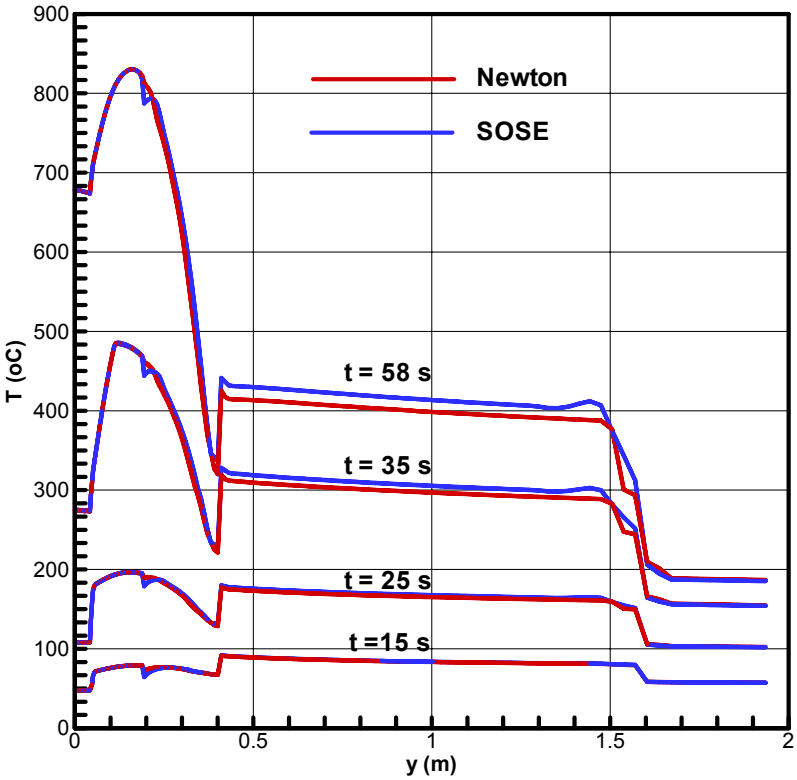

Figura 9. Variação da temperatura ao longo da superfície externa do SARA, durante a trajetória, obtido pelos dois métodos de cálculo.

A carga térmica total absorvida pela superfície externa do SARA por convecção pode ser obtida por:

$$Q_{Total} = \int_{ti}^{tf} \int_{0}^{zf} h(T_w - T_\infty) dz.dt \tag{16}$$

O resultado para cada método é mostrado na Tab. (1). Em vista da semelhança entre os resultados, a discrepância observada é de aproximadamente 2 %.

Tabela 1. Carga térmica total acumulada durante a trajetória, obtido pelos dois métodos de cálculo.

	Carga térmica (MW)
SOSE	17.99
Método de Newton	17.61
Variação	2.16 %

5. Conclusões

Neste trabalho, foi calculado o aquecimento aerodinâmico da superfície externa da plataforma sub-orbital recuperável SARA, durante um trecho da trajetória ascendente, através do método de Zoby. Foram empregados dois métodos de cálculo da pressão na superfície do veículo: o método de Newton modificado, de vasta utilização neste tipo de problema, e o método SOSE, de base empírica, através do software Missile Datcom.

A comparação dos resultados obtidos ao longo do trecho de trajetória analisado mostrou que os resultados apresentaram excelente concordância, com uma discrepância de apenas 2 % quanto ao valor total da carga térmica imposta à superfície do veículo. Dessa forma, considera-se que o método de Newton modificado, pela facilidade de implementação, se mostra confiável e suficiente para aplicação no cálculo do aquecimento aerodinâmico de veículos espaciais em vôo hipersônico.

6. Referências

Anderson Jr., J. D., 1982, "Modern Compressible Flow", McGraw-Hill.

Anderson Jr., J. D., 1989, "Hyphersonic and High Temperature Gas Dynamics", McGraw-Hill.

Blake, W.B., "Missile Datcom – User´s Manual – 1997 Fortran 90 Revison", Air Force Research Laboratory, Ohio, Fev 1998, AFRL-VA-WP-TR-1998-3009

Da Costa, L. E. V. L., De Mello, F. C. and Pardini, L. C., 1996, "Estudo da Viabilidade da Proteção Térmica do Sistema SARA", Nota Técnica NT-130-ASE-N/96 (interna), IAE/CTA, São José dos Campos.

Hurwicz, H. e Rogan, 1973, J. E., "High Temperature Thermal Protection Systems", Handbook of Heat Transfer, edited by Rohsenow, W. M. and Hartnett, J. P., McGraw-Hill, NY.

Machado, H. A., 2006, "Proteção Térmica para Aquecimento Aerodinâmico da Plataforma Sub-Orbital SARA", Anais do Congresso Nacional de Engenharia Mecânica – CONEM, Recife.

Mason, A., L., Devan, L., Moore, F., G., McMillan, D., "Aerodynamic Design Manual for Tactical Weapons," Naval Surface Weapons Center, NSWC/TR 81-156, Dahlgren, Virginia, July 1981.

Miranda, I. F. and Mayall, M. C de M., 2001, "Fluxo de Calor Convectivo em Micro-Satélites em Reentrada atmosférica", Graduate Dissertation, ITA, Brazil.

Moraes Jr., P., 1998, "Design Aspects of the Recoverable Orbital Platform SARA", Proceedings of 8th Chilean Congress of Mechanical Engineering, Concepcíon, Chile.

Syverton, C.A., Dennis, D.H., "A second-order shock expansion method applicable to bodies of revolution near zero lift" , National Advisory Committee for Aeronautics, NACA TN 3527, Washington, Jan 1956

U.S. Standard Atmosphere, 1976.

Vukelich, S.R., Stoy, S.L., Burns, K.A., Castillo, J.A., Moore, M.E., "Missile Datcom – Volume 1 – Final Report", McDonnel Douglas Missile Systems Company, St. Louis, Missouri, Dec 1988

PRESSURE CALCULATION IN SURFACES SUBMITTED TO AERODYNAMIC HEATING

Humberto Araujo Machado
Instituto de Aeronáutica e Espaço – IAE
Comando-Geral de Tecnologia Aeroespacial - CTA
Pr. Mal. Eduardo Gomes, 50, Vila das Acácias, 12228-904
São José dos Campos, SP
humbertoam@iae.cta.br

Danton José Fortes Villas Boas
Instituto de Aeronáutica e Espaço – IAE
Comando-Geral de Tecnologia Aeroespacial - CTA
Pr. Mal. Eduardo Gomes, 50, Vila das Acácias, 12228-904
São José dos Campos, SP
danton@iae.cta.br

Abstract
Space vehicles in hypersonic flight are submitted to a strong aerodynamic heating, which yields a temperature rising of hundreds of degrees in the air around its external wall. This heating is commonly estimated through approximate methods, which are based on empirical observation. One of the most important aspects of such calculation is the variation of the pressure along the external surface, which strongly influences the results of temperature, what is fundamental for the thermal shield dimensioning. In this work the results for pressure calculation of two methodologies, the Newton Method and the Missile Datcom software, are compared, in order to determine the temperatures reached by the external surface of the sub-orbital SARA capsule during its flight trajectory.

Keywords: Aerodynamic heating, Space vehicle, Pressure calculation

Proceedings of the 11th Brazilian Congress of Thermal Sciences and Engineering – ENCIT 2006
Braz. Soc. of Mechanical Sciences and Engineering – ABCM, Curitiba, Brazil, Dec. 5-8, 2006

Paper CIT06-0269

COMPUTATIONAL SIMULATIONS OF HIGH-LIFT CONFIGURATIONS USING UNSTRUCTURED GRIDS

João Alves de Oliveira Neto
Instituto Tecnológico de Aeronáutica, CTA/ITA/IEE, 12228-903 - São José dos Campos - SP - Brazil
alves@ita.br

Darci Cavali
Universidade do Vale do Paraíba, UNIVAP, São José dos Campos - SP - Brazil
darcicavali@gmail.com

Carlos Breviglieri Júnior
Universidade do Vale do Paraíba, UNIVAP, São José dos Campos - SP - Brazil
carbrevi@gmail.com

João Luiz F. Azevedo
Instituto de Aeronáutica e Espaço, CTA/IAE/ASA-L, 12228-900 - São José dos Campos - SP - Brazil
azevedo@iae.cta.br

Ana Lúcia Fernandes de Lima e Silva
Universidade Federal de Itajubá, UNIFEI, Itajubá - MG - Brazil
alfsilva@unifei.edu.br

Abstract. *The purpose of the present work is to perform a study of high-lift devices using CFD simulations in order to attempt to establish guidelines for the analysis of such systems through computational aerodynamic techniques. Flowfields over high-lift systems are characterized by highly complex flow physics, which pose significant challenges for CFD codes. For this purpose, results for several high-lift devices will be obtained using a CFD code currently under development by the group and these results will be compared with data available in the literature and/or with computational results obtained using well-established commercial codes. The study will look into 2-D and 3-D configurations, under high-lift conditions, and assess the capability of predicting lift, drag and pressure coefficients for such configurations. As usual with RANS simulations for such high Reynolds number flows, the addition of turbulence models is required in order to capture the correct turbulent transport. In the present case, the use of both the Spalart-Allmaras (SA) one-equation and the Menter SST (SST) two-equation models is envisioned. These calculations will be compared to the available data in order to assess the accuracy of the capability implemented as well as to validate the computational tool under development.*

keywords: *high-lift configurations, aerodynamic coefficients, CFD, maximum lift.*

1. Introduction

The design of an optimized high-lift system is an important part of the development of a modern transport aircraft. The manufacturers must make simple yet efficient high-lift designs, and in particular they must avoid having to make large and expensive changes in a late project stage. The cost and Reynolds number scaling problems involved in the optimization of slat and flap positions by wind tunnel tests is a strong driver in the effort to develop CFD tools which can be used in the design process. This paper describes one step on the road to establish CFD analysis tools for high-lift aerodynamics, by development methods and validation of two-dimensional high-lift CFD analysis.

High-lift flows are inherently three-dimensional and a complete study should include the modeling and analysis of such effects. However, several aspects of high-lift flows may be understood by simplified two-dimensional analysis. Figure (1) points to a number of important flow phenomena which govern the behavior of the flow over a two-dimensional high-lift configuration. Viscous interaction effects are responsible for the most important limiting aspects of the flow. The confluence of the wake of one element with the suction side boundary layer of the following elements plays an important role in determining maximum lift. Massive flow separation on one or more of the elements may, depending on operational condition, set the maximum lift which can be obtained. The fact that many parts of the flow develop in strong adverse pressure gradients increases the modeling difficulties. The knowledge of turbulence development in adverse pressure gradients is much less developed than it is for zero pressure gradient flows. Most turbulence models used in Reynolds

averaged computational methods are calibrated in zero pressure gradient flows, with more or less *ad hoc* modifications to account for the development of turbulence in adverse pressure gradient regions. Many effects in high-lift flows are

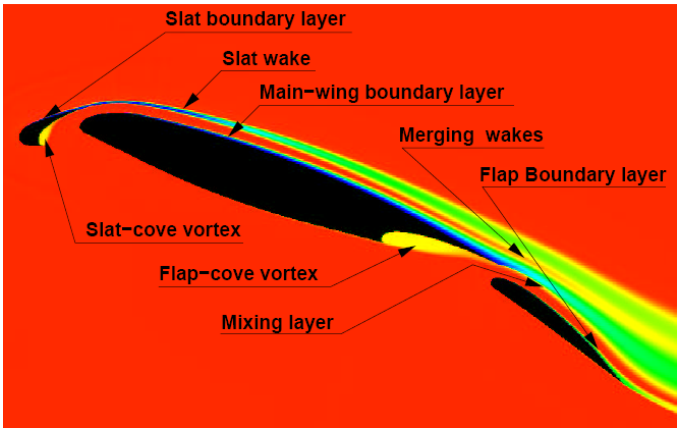

Figure 1: Important flow phenomena in two-dimensional high-lift aerodynamics.

governed by the detailed transition process. This can be quite different in wind tunnel tests taken at lower Reynolds number compared to the flight situation. Several mechanisms may cause the transition from laminar to turbulent flow. Transition may occur by a laminar separation bubble which reattaches as a turbulent boundary layer. Even though the typical take-off or approach speeds are quite low, there may be transonic effects on a slat, so that the flow may be strongly affected by shock-wave boundary layer interaction. With the known limitations of two-dimensional analysis in mind, the results are still quite useful in project design phases and to increase the understanding of the governing flow phenomena.

The computational tools available range from the more efficient and simpler inviscid/viscous coupled methods, to a Reynolds-averaged Navier-Stokes (RANS) analysis. An example of the former method is given by the MSES code (Drela, 1996). It is based on the solution of the Euler equations coupled with the boundary layer equations. These methods have been found to be successful in accurately computing the pressure distribution for multi-element airfoils, including cases up to maximum lift, some of which involve separation. The coupled method has been proven to be useful as an effective engineering design tool. Unfortunately, this method is limited by its inability to compute beyond maximum lift conditions, and it may have problems with certain features of some airfoil systems such as flap wells, thick trailing edges, or unsteady effects. The performance of high-lift configurations, especially close to stall, can be difficult to predict and requires the solution of, at least, the Reynolds-averaged Navier-Stokes equations with an appropriate turbulence model. This is an expensive computational task which is made even more time consuming by the need of generating a field grid. High-lift configurations are usually complex geometries, at which complex flow physics are present. The work here described uses the MSES and CFD++ (CFD++, 2005) codes, as well as an in-house developed code, to simulate flows around high-lift aerodynamic configurations aiming at the prediction of lift and pressure coefficient distributions. In order to understand the flow physics over high-lift devices, three configurations are chosen for the studies to be performed in the present context. The multi-element airfoils selected were the NLR 7301 (den Berg and Gooden, 1994) and NHLP-2D (Moir, 1994) airfoils. Moreover, a 3-D configuration based on the RAE 1372 (Lovell, 1977) profile was also selected. Such configurations were chosen based on availability of geometry and experimental data for the flight conditions of interest for the present simulations.

2. High-Lift Configurations: Geometry, Grid Generation and Boundary Conditions

Geometry of the 2D profiles was obtained in coordinate files and the trailing edges were not collapsed in either airfoil. Mesh generation was performed with ANSYS ICEM CFD (ICEM, 2005). The work has analyzed several geometric parameter variations in order to verify their influences on the final CFD result. For instance, such studies considered the effects of farfield distance, boundary layer grid resolution and general mesh refinement, as well as the overall mesh topology.

Three geometries and flow conditions are considered in the present effort. These include subsonic flows over an NLR 7301 airfoil, an NHLP-2D airfoil and an RAE 1372 configuration. The following specific test cases are considered:

- Simulations of subsonic flows about the NLR 7301 airfoil. The simulations for this case are performed for Reynolds number Re = 2.51 x 10^6 and freestream Mach number $M_\infty = 0.185$. Numerical results are compared to available experimental results in order to assess the correctness of the present simulations. A representative mesh over the NLR 7301 profile is shown in Fig. (2). In the particular case of this figure, a triangular grid is shown. However, both triangular and quadrilateral meshes were generated for this configuration.

- Simulations of subsonic flows about the NHLP-2D airfoil. The simulations for this case are performed for Reynolds number Re = 3.52 x 10^6 and freestream Mach number $M_\infty = 0.197$. Numerical results are also compared to available experimental results. A representative grid over the NHLP-2D profile is also shown in Fig. (2). In this case, a quadrilateral mesh is shown in Fig. (2), but as before both triangular and quadrilateral meshes were generated for this configuration.

- Simulations of subsonic flows about an RAE 1372 configuration (Lovell, 1977). The simulations for this case are performed for Reynolds number Re = 1.35 x 10^6 and freestream Mach number $M_\infty = 0.223$. The geometry of the wing profile was obtained from (Lovell, 1977), along with the parameters to construct the 3-D wing in a CAD environment. The wing features a slat and double flap configuration, with 31 deg. of leading edge sweepback and high-lift devices along the complete semi-span. However, it should be emphasized that the present study only analyzed this wing in the cruise configuration. Such approach was chosen in order to address the 3-D high-lift configuration in an incremental manner, and the results here reported represent the current status of such development in the group. In this context, the discussion of the present 3-D results should be seen as a work-in-progress report of such development. Nevertheless, a tetrahedral mesh with a total of 3,375,912 control volumes was generated for this configuration, including both the wing, in cruise condition, and the fuselage. Such a fairly fine grid was required in order to appropriately discretize the wing trailing edge. A view of the mesh over the RAE 1372 configuration is also shown in Fig. (2). It should further emphasized that, although the current simulations for this configuration are considering a tetrahedral grid, it is possible that further studies in the future will also include hexahedral meshes for this configuration, in order to improve mesh quality and robustness. The surface and volumetric meshes for the configuration were also generated using the ICEM CFD software.

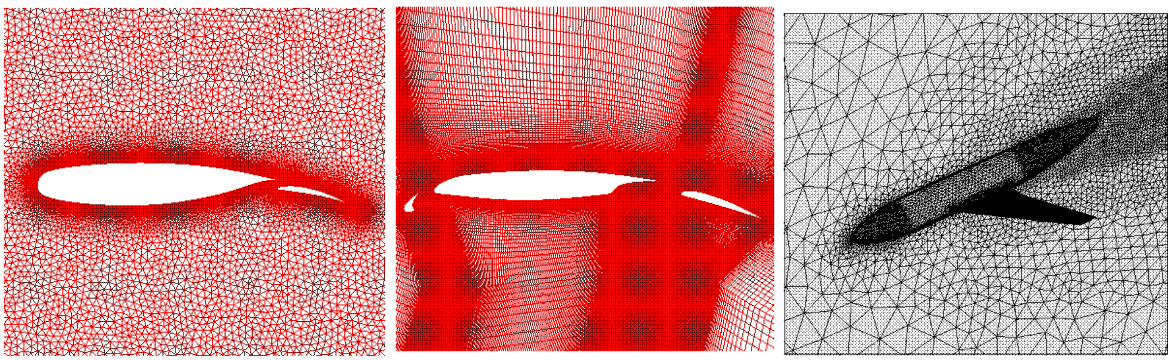

Figure 2: Grids on the studied configurations.

Due to the space limitations in the present paper, the authors will not be able to include all the results concerning grid refinement and grid topology influence. Hence, a brief summary of such results is included in the remainder of this section, in order to allow the discussion of the aerodynamic results in the forthcoming sections. For instance, the current simulations have indicated that the farfield boundary should be placed, at least, at approximately 100 chord lengths from the configuration in order to avoid any influence of farfield position on the aerodynamic results. Moreover, it was also found, as one should expect, that boundary layer resolution has a crucial effect in the final result. Therefore, adequate grid refinement inside the boundary layer, as well as an appropriate, *i.e.*, sufficiently mild, grid stretching as one moves away from the wall are necessary for resolving the flow over high-lift airfoils. The results obtained so far seem to indicate that quadrilateral meshes, in 2-D, and hexahedral meshes, in 3-D, are better suited for high-lift CFD analyses, since such grid topologies lend themselves, in an easier fashion, for ensuring mesh orthogonally or, at least, a lower level of grid skewness. Hence, in this context, such topologies clearly contribute to overall grid quality.

Moreover, another aspect that deserves attention concerns a consistent method for studying convergence of the computed solutions with increasing grid density. Consistency of the grid system is difficult to achieve in analyzing high-lift flows. The difficulty arises out of the need to ensure sufficient grid density in regions of interesting flow phenomena while preventing deterioration of grid density and smoothness in other areas of the flow. The problem is further compounded by a lack of guidelines regarding grid resolution requirements for the complex flow physics involving disparate length scales that arise in flowfields of multi-element, high-lift configurations. In particular, the grid requirements for adequate capture of the wakes of upstream elements and/or the merging of wakes of different elements are quite stringent.

3. Flow Solution Method

3.1. Simulation Conditions

Usually, the solving step in the simulation process consumes most of the time. In order to know the number of simulations and flow conditions in this phase to dimension the time to dispend, it is indicated to have an estimation of expected results. In the early stages of the preliminary design of an airplane, some of the aerodynamic coefficients are already know due to a certain airplane performance that has to be achieved. In particular, the high-lift devices are intrinsically connected with the landing and the take-off performance. This two phases of the airplane mission are very important due to the operational implications that they have. An overestimated take-off lift coefficient maximum implicates in limitations in the maximum weight to take-off, or the need for an longer track. In the same way, an overestimated landing lift coefficient maximum implicates in the necessity for a longer track. The aerodynamic coefficients are directly influenced by the flow conditions (speed, altitude, temperature, etc), angle of attack and elements individual displacement parameters (gaps and overlaps). The designer must opt for the configuration where maximum lift coefficient is achieved, and to do so the number of simulations, combining all the cited parameters and conditions can grow out of limit on design time and costs to compute all the possible combinations. A solution must be addressed to reduce simulation time mainly. The codes to simulate flows around aeronautic configurations aiming prediction of drag, lift and pressure coefficients to evaluate how codes is inserted in the main objective of this collaboration, and which consists in getting the aerodynamic coefficients as real as possible.

3.2. MSES Code

The MSES code is a two dimensional analysis, design and optimization framework for multi-element airfoil sections. It is based on the steady state conservative Euler equations. The Euler equations are used to describe the inviscid part of the flow. The assumption that the viscous part is restricted to a thin boundary layer and wake is made, and the viscous part is described with the boundary layer theory given by the integrated Prandtl boundary layer equations (White, 1991). The equations are discretized in an intrinsic grid, where one set of coordinate lines correspond to the streamlines around the body. With this procedure the number of unknowns per grid node is reduced from four to two because the continuity equation and the energy equation can be replaced by the simple condition of constant mass flux and constant stagnation enthalpy along each streamtube. The Newton method is used for solving the system of nonlinear equations. Simulations are performed quickly and the aerodynamic coefficients are obtained. A comparison of experimental data and the MSES code results are presented in the present paper.

3.3. CFD++ Code

The CFD++ code (CFD++, 2005) allows easy treatment meshes of complex geometries mainly due to its integration of structured, unstructured and multi-blocks grids. Its flexibility allows the use of various elements within the same mesh such as hexahedral, triangular prism and tetrahedral elements in 3-D. However, as usual with RANS simulations for such high Reynolds number flows, the addition of turbulence models is required in order to capture the correct turbulent transport. In the present report, the use of both the Spalart-Allmaras (SA) one-equation and Menter SST (SST) two-equation models is foreseen.

4. Results and Discussion

NLR 7301 Airfoil

The NLR 7301 is supercritical airfoil/flap configuration with 32% chord flap and considering a $\delta_f = 20^o$ flap deflection. In this present study, two different configurations are evaluated. The first analysis is performed for the configuration with a flap gap of 1.3% and the second one with the flap gap of 2.6%. In the present simulation, a triangular and quadrilaterals grid was used with 200,229 elements. The gap is defined as the radius of the circumference centered in the trailing edge of the main element and tangent to the flap profile in a certain point. This point of tangency is defined by the overhang, which is held at a constant at a value of 5.3% for both test cases here considered. It worth to mention that the gap and the overhang are defined as a percentage of the nominal profile cruise chord. The flap lower surface exhibited laminar flow at all times. The main element and flap boundary layers were found to be confluent for the flap gap of 1.3%. Simulations of subsonic flow over NLR 7301 profile were computed with freestream Mach number $M_\infty = 0.185$ and Re = 2.51 x 10^6, using inviscid and viscous flow. In these simulations both Spalart-Allmaras (SA) and Menter SST (SST) turbulence models are exercised, as a form of comparing their results. In Fig. (3), one can observe the pressure contours over NLR 7301 airfoil obtained in the present calculations for the SA turbulence model. The lift coefficient as a function of angle of attack can be observed in detail in Fig. (4). This figure compares SA and SST turbulence models and the MSES code with the experimental data. Comparison of experimental and calculated lift coefficients also show good agreement

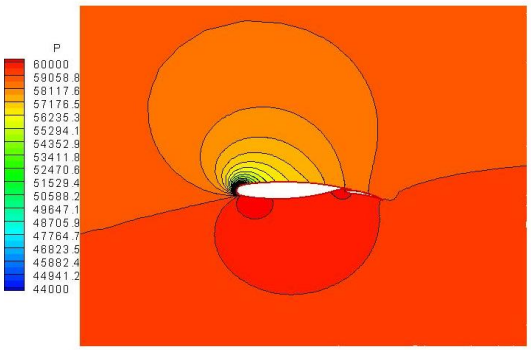

Figure 3: Pressure contours using SA turbulence model for α = 13.1^o and Re = 2.51 x 10^6 for the NLR 7301 airfoil.

which is a clear indication of the good quality of the results that can be obtained with the CFD++ numerical tool. One can observe in this figure that the numerical distributions compare very well with experimental data, less the MSES code. The relative worse agreement of predicted and experimental lift coefficient values for the configuration with 1.3% gap may be attributed to a greater sensitivity of this case to the boundary layer development. In the actual experiment, the literature (den Berg and Gooden, 1994) indicates that there is laminar flow on the flap upper surface and, also, that the boundary layer relaminarizes in the flap cove region. However, none of these effects is correctly simulated with the current RANS solutions since both turbulence models used, i.e., SA and SST models, assume fully turbulent flow. The lift coefficient

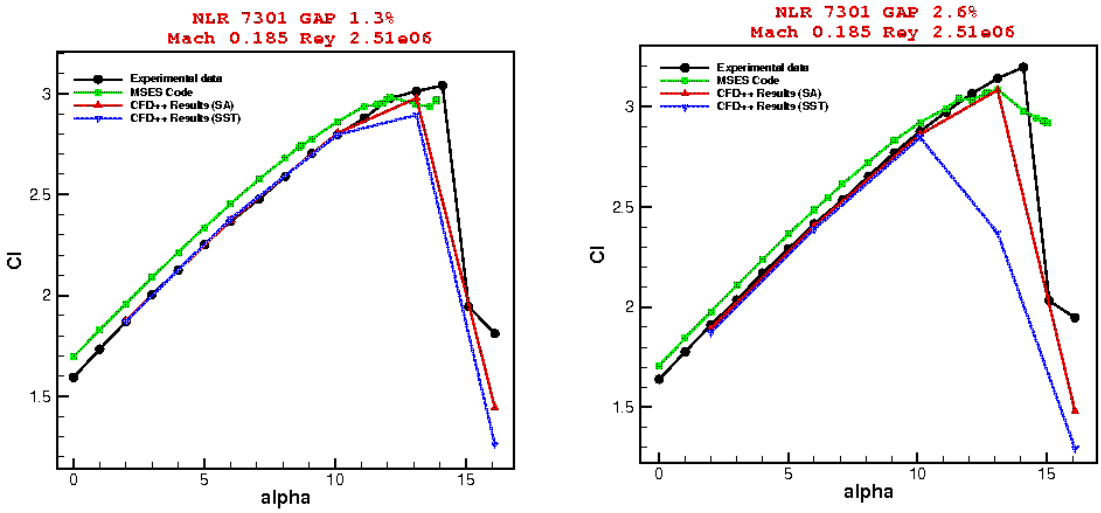

Figure 4: The lift coefficient as a function of the angle of attack with Mach number 0.185 for NLR 7301 gap 1.3% and 2.6%.

as a function of angle of attack can be observed in detail in Fig. (4) for NLR 7301 (2.6% gap). This figure compares SA and SST turbulence models and the MSES code with the experimental data. In Fig. (4), as in the NLR 7301 airfoil (1.3% and 2.6% gap) study the MSES results also present an overprediction of lift coefficient for this geometry. Due to the complexity of this simulated geometry, the differences in the lift coefficient as a function of angle of attack curve seem to have been more accentuated. For an perfect match with the experimental results, all the complex physics has to be perfectly capture. This includes the flow features at the cove of the main element, as well as the interactions between the free shear layer of the main element and the boundary layer of the flap.

MSES code show a good capability to effectively reproduce the experimental data at the linear range. The limitations presented in the non-linear region are intrinsic to the MSES formulation (Lima-Silva *et al.*, 2005), as well the lack of a better control in relation to the mesh generation. This verification does not take the merits of the code since even other numerical codes with a formulation more adequate, Navier-Stokes an turbulence model, presents the same difficulty to present the aerodynamic coefficients with accuracy. The experimental results are available (den Berg and Gooden, 1994).

The numerical pressure coefficient distribution shows an excellent agreement with the experimental data for the evaluated angles of attack. Figure (5) for flap gap 1.3% at an angle of attack of $\alpha = 6^o$, the comparison between the numerical and the experimental pressure coefficient distribution.

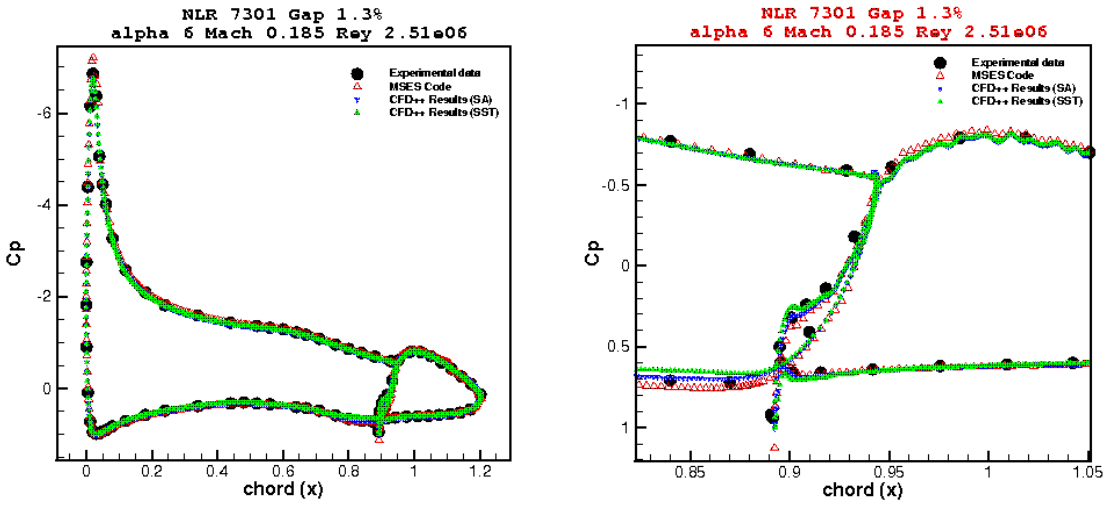

Figure 5: The pressure coefficient as a function of the chord with $\alpha = 6^o$ for NLR 7301 gap 1.3%.

In Fig. (5), one can observe the difference in the C_p distributions in the region of the cove. In Fig. (6), one can observe the comparison for an angle of attack of $\alpha = 13.1^o$. In Fig.(6), one can observe the difference in the C_p distributions in the region of the cove for $\alpha = 13.1^o$

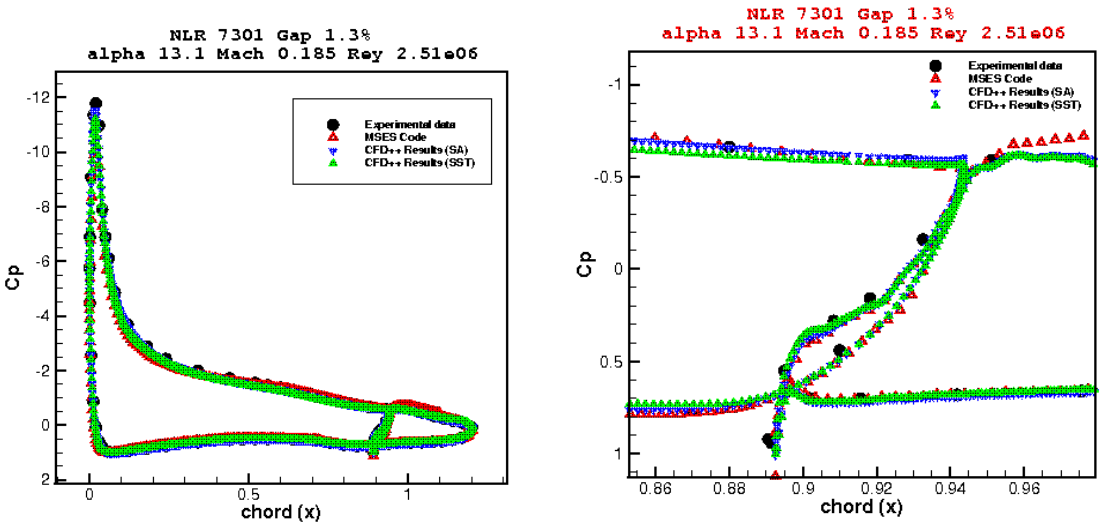

Figure 6: The pressure coefficient as a function of the chord with $\alpha = 13.1^o$ for NLR 7301 gap 1.3%.

NHLP-2D Airfoil

The NHLP-2D airfoil is again a supercritical airfoil with a high-lift devices, including a 12.5% leading-edge slat and a 33% single-slotted flap (Moir, 1994). For the results showed here, the slat and flap are deflected 25 and 20 deg., respectively, which is typical of take-off configurations with leading-edge stall. In the present simulation, a triangular and quadrilaterals mesh was used with 148,014 elements. Simulations of subsonic flow over NHLP-2D profile were computed with freestream Mach number $M_\infty = 0.197$ and Re = 3.52 x 10^6, using inviscid and viscous flow. Comparison of experimental and calculated lift coefficients also show good agreement, which is a clear indication of the good quality of the results that can be obtained with the CFD++ numerical tool. The NHLP-2D airfoil illustrated in Fig. (7) shows

the flow over a typical high-lift airfoil with a leading edge slat and a single-slotted flap. The total pressure profiles as a

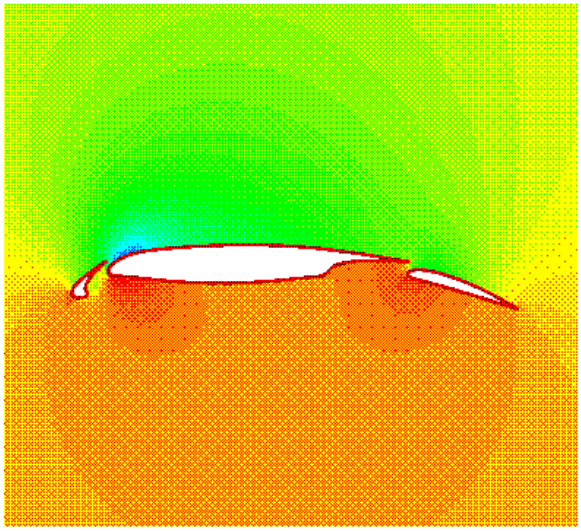

Figure 7: Pressure contours using SA turbulence model for α = 4^o and Re = 3.52 x 10^6 for the NHLP-2D airfoil.

function of chord is shown in Fig. (8). The numerical results obtained by Morrison (Morrison, 1998) using the Wilcox k - ω turbulence model are also presented together with experimental data (Moir, 1994). The plot at x/c = 0.35 shows the

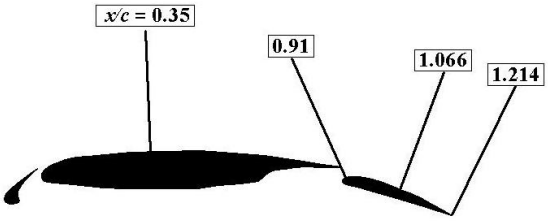

Figure 8: Location of total pressure profiles for NHLP-2D airfoil.

slat wake and the boundary layer on the main element in the Fig. (9). The experimental data is more sparse in the region of the slat wake and shows a narrow and weak wake compared with the numerical results. The results of Morrison predict a the slat wake too large. The plot at x/c = 0.91 and other downstream positions show the merging of the slat and main element wakes as described in Fig. (9). A distinct slat wake is predicted in the outer edge of the main element boundary layer all the way to the flap trailing edge in Fig. (10).

The pressure coefficient results are shown for the three elements for $\alpha = 4^o$ in Fig. (11). The numerical results better compared with the experimental results at the main element and at the flap. It will be seen that the trailing-edge of the slats sits in the high-velocity region of the flow around the leading edge of the main wing. Because of this, the pressure coefficient at the trailing edge is significantly negative and thus the pressure rise on the slat is reduced. The same happens at the trailing-edge of the main wing due to the high velocities around the leading-edge of the highly deflected flap.

In addition, the circulation around the slat induces a downwash on the main wing. This downwash clearly reduces with distance from the slat, so that it modifies the local velocities most strongly near the leading-edge of the wing, reducing it is peak suction markedly. The same mechanism operates near the leading-edge of the flap. As a result of this, the pressure rise to the trailing-edge of the overall wing split up into a number of smaller pressure rises, when each of these is sufficient to just cause separation of the boundary layer, the overall pressure rise can clearly be very large.

RAE 1372 Configuration

Simulations of subsonic flows about a RAE 1372 configuration (Lovell, 1977). The simulation for this case is performed for Reynolds number Re = 1.35 x 10^6 and freestream Mach number $M_\infty = 0.233$. Numerical results are considered in order to evaluate the correctness of the validation. A detail extremely important that verified it is that the results with wing-fuselage are merely qualitative. In fact, the configuration of the fuselage it is not given in details in the

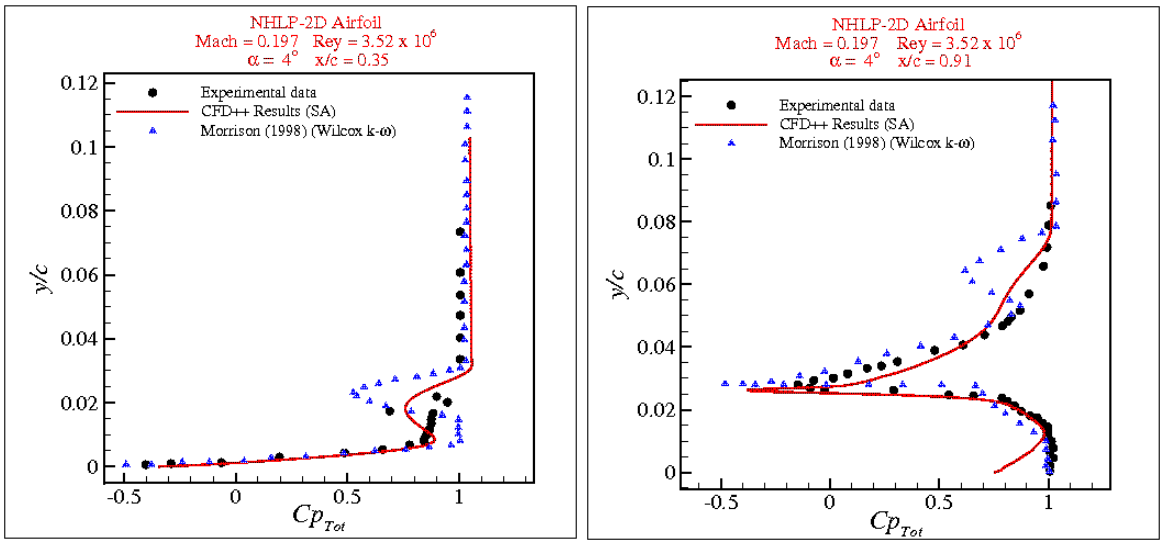

Figure 9: Total pressure profile at x/c = 0.35 (left) and x/c = 0.91 (right).

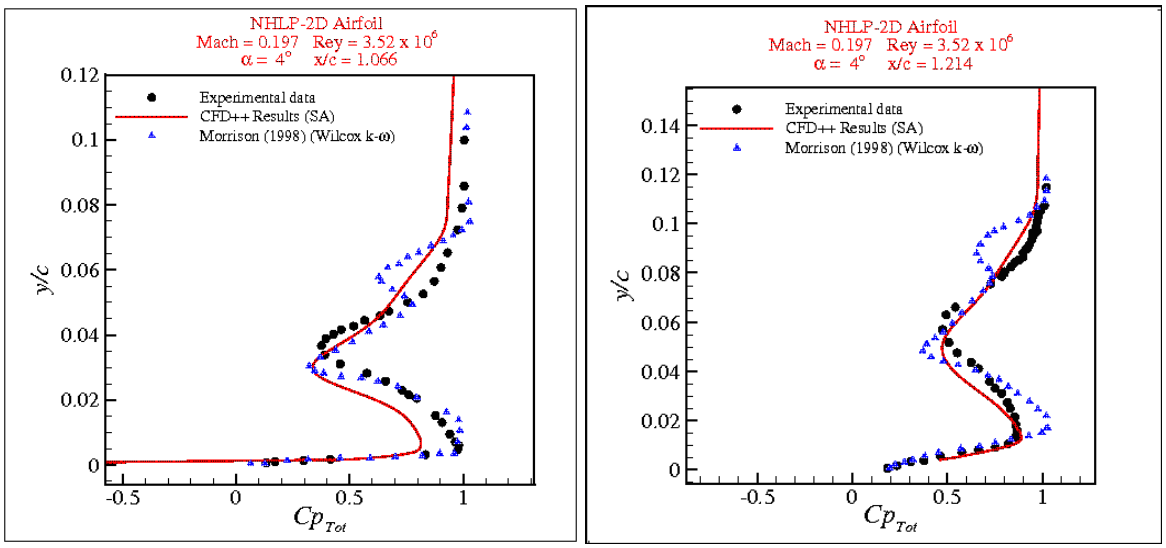

Figure 10: Total pressure profile at x/c = 1.066 (left) and x/c 1.214 (right).

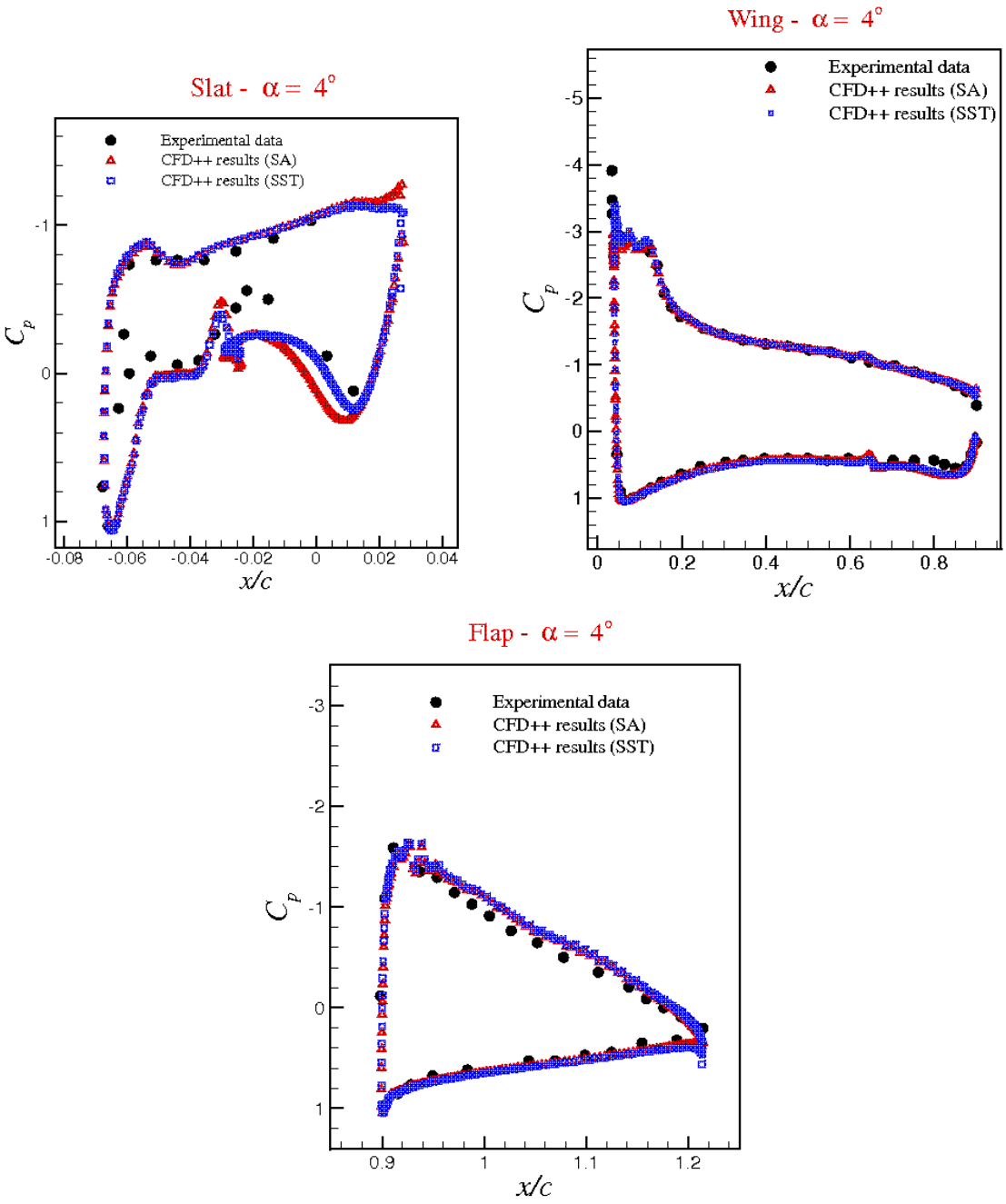

Figure 11: Pressure coefficient at the three elements for $\alpha = 4^o$ and Re = 3.52 x 10^6 for the NHLP-2D airfoil.

reference base, but the group did an approach judging to be interesting to analyze that case. Later, we will have quantitative results, because they will be just made simulations with the wing, disrespecting the fuselage. The Fig. (12) it shows pressure and mach contours for $\alpha = 0.05^o$, $M_\infty = 0.223$ and Re = 1.35 x 10^6 such for the Spalart-Allmaras turbulence model. Comparison of experimental and calculated lift, drag and moment coefficients also show good agreement which is a clear indication of the good quality of the result that can be obtained with the CFD++ numerical tool.

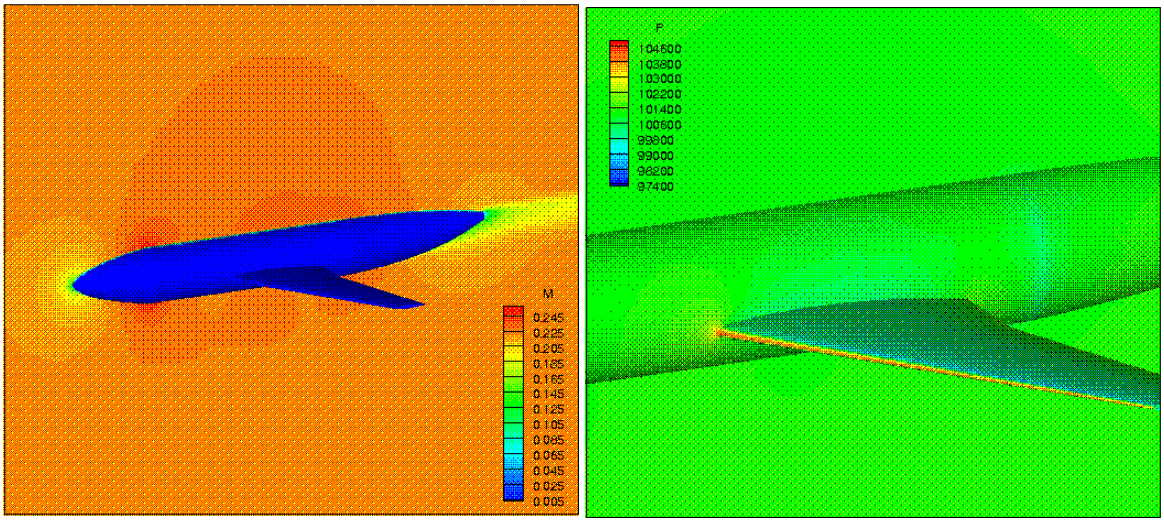

Figure 12: Mach contours using SA turbulence model for α = 0.05^o and Re = 1.35 x 10^6 for the RAE 1372 configuration.

Table 1: Aerodynamic coefficients.

Aerodynamic Coefficients	C_L	C_D	C_M
Experimental Data	0.118	0.0092	-0.0528
Numerical Data	0.1123	0.007324	-0.05716

In Tab. (1), the results for the aerodynamic coefficients at $\alpha = 0.05$ deg. are presented. Although the results are rather preliminary, one can observe a fairly good agreement with the experimental data (Lovell, 1977). One should observe, however, that only qualitative comparisons are actually reasonable at this point due to the following reasons:

- The 3-D configuration, including fuselage and wing, is only an approximation of the real configuration and, therefore, the final result is affected;
- A large portion of the area of the fuselage is a cylinder, because the original reference (Lovell, 1977) does not give the exact configuration. Hence, the authors have used the reported fuselage diameter in order to define a cylindrical fuselage. It is hoped that the use of the correct fuselage diameter at the wing-fuselage junction will minimize the errors so incurred.

5. General Remarks

In the present paper, simulation results obtained with the SA and SST turbulence models are presented. Three geometries are considered in the present effort. These include a NLR 7301 airfoil, a NHLP-2D airfoil and an RAE 1372 airfoil-based wing configuration. The following test cases are considered:

- Simulations of subsonic flows about the NLR 7301 airfoil. The simulations for this case are performed for Reynolds number Re = 2.51 x 10^6 and freestream Mach number $M_\infty = 0.185$. Numerical results are compared to available experimental data in order to assess the agreement obtained in this case.
- Simulations of subsonic flows about the NHLP-2D airfoil. The simulations for this case are performed for Reynolds number Re = 3.52 x 10^6 and freestream Mach number $M_\infty = 0.197$. Numerical results are again compared to available experimental data.

- Simulations of subsonic flows about an RAE 1372 configuration, considering Re = 1.35 x 10^6 and $M_\infty = 0.223$.

The paper provides a detailed comparison of the Spalart-Allmaras and Menter SST turbulence models in the context of two-dimensional high-lift aerodynamic flows. The results show that the Menter model is more accurate in separated flow regions. The SA model is more accurate in attached flows and wakes, including merging boundary layers and wakes. The SA model is somewhat more robust, though for several cases the computational costs are about equal. Considering the uncertainties associated with the experimental data and the use of the RANS approximation, as well as the limitations on the grid resolution that can be used, the performance of these two turbulence models is excellent. They represent the state-of-the-art for this application. The SA model is preferred for general computations of aerodynamic flows, whereas the Menter model is the better choice if separated flows are of primary interest. A summary of the major conclusions of the study could be stated as follows:

- SA and SST models yielded generally similar results.
- Not surprisingly, grid sizes tended to increase in density from less than $50,000$ points to about triple such size as the decade advanced. Many independent grid studies seemed to suggest that 50,000 points may be sufficient to resolve surface pressures, but flow field quantities such as velocity profiles require significantly more grid points. Some estimates indicate that, at least, 100,000 to 200,000 elements are required, unless a scheme with higher order spatial accuracy is employed. Grid issues tend to still remain very important in general. Those references that exercise the greatest care in ensuring high-quality, sufficiently refined grids with an accurate representation of the wind tunnel geometry tended to produce the best correlations with experiment. Underresolution in key areas, such as wakes, can lead to overdissipation and incorrect conclusions. Moreover, for 2-D computations, it is important to have a farfield grid extent of, at least, 50 to 60 chords or, otherwise, special farfield boundary condition treatment is required in order to accurately predict drag (Basso *et al.*, 2006). The inclusion of tunnel walls in the computations appears to be increasingly important at higher angles of attack.
- Grid distribution is also an important factor: sufficient grid resolution is required in key areas of the flowfield, *e.g.*, wakes and vortices.
- The configuration should be modeled as accurately as possible, *e.g.*, with the inclusion of support brackets, aeroelastic deformations, tunnel walls, chines), or otherwise these effects should be known. Geometry fidelity appears to be more crucial as the angle of attack approaches maximum lift.
- The fine grid was probably sufficiently fine for use at the lower angles of attack. However, its adequacy at higher angles of attack was dubious, particularly because of underresolution of the wall vortex.

Aside from the points listed above, some general conclusions from this work were: (a) 2-D CFD should not be expected to agree with the nominally 2-D wind tunnel experiment at high-lift conditions because the experiment looses its 2-D characteristics at high angles of attack, and (b) 3-D CFD using the current grids and methodology compared well with experiment at low angles of attack, but did not adequately model the character of the wind tunnel flow field near maximum lift. To improve this deficiency, based on the present experience, it is recommended that future 3-D CFD efforts include (in order of importance):

- Finer grid resolution in the region of the wall vortex, and overall finer resolution for unstructured grids;
- Top and bottom walls, and mounting brackets;
- Better characterization of the incoming side-wall boundary layer.

6. Acknowledgments

The authors are indebted to Fundação de Amparo à Pesquisa do Estado de São Paulo, FAPESP, which provided support for the work through the Research Grant No. 2000/13768-4. The authors also acknowledge the partial support of Conselho Nacional de Desenvolvimento Científico e Tecnológico, CNPq, through the Integrated Project Research Grants No. 501200/2003-7 and 502053/2004-6.

7. References

Basso, E., Azevedo, J. L. F., Bitencourt, L. O., and Andrade, T. J., São José dos Campos, SP, Brazil, 2006, Cálculo do Escoamento Bidimensional sobre o Perfil RAE 2822 Utilizando o Software CFD++, Relatório do IAE para o Núcleo de CFD, Instituto de Aeronáutica e Espaço.

CFD++, 2005, The CFD++ Computational Fluid Dynamics Software.

den Berg, B. V. and Gooden, J. H. M., 1994, Low-Speed Surface Pressure and Boundary Layer Measurement Data for the NLR 7301 Airfoil Section With Trailing Edge Flap, "A Selection of Experimental Test Cases for the Validation of CFD Codes - AGARD AR-303", Vol. 2, pp. A9–1–A9–12.

Drela, M., 1996, A User's Guide to MSES 2.92.

ICEM, 2005, ANSYS ICEM CFD.

Lima-Silva, A. L. F., Neto, J. A. O., Antunes, A. P., Mendonça, M. T., Azevedo, J. L. F., and Neto, A. S., 2005, Numerical Study of Two-Dimensional High-Lift Configurations Using the MSES Code, "Proceedings of the 18th International Congress of Mechanical Engineering", Ouro Preto, Brazil.

Lovell, D. A., 1977, A Wind-Tunnel Investigation of the Effects of Flap Span and Deflection Angle, Wing Planform and a Body on the High-Lift Performance of a 28° Swept Wing, "Aeronautical Research Council, ARC C.P. 1372", Vol. .

Moir, I. R. M., 1994, Measurements on a Two-Dimensional Aerofoil With High-Lift Devices, "A Selection of Experimental Test Cases for the Validation of CFD Codes - AGARD AR-303", Vol. 2, pp. A9–1–A9–12.

Morrison, J. H., 1998, Numerical Study of Turbulence Model Predictions for the MD 30P/30N and NHLP-2D Three-Element High-lift Configurations, Vol. NASA/CR-1998-208967.

White, F. M., Second edition, 1991, "Viscous Fluid Flow", McGraw-Hill International Editions.

8. Author rights

The authors are the sole responsible for the contents in this paper.

Proceedings of the 11th Brazilian Congress of Thermal Sciences and Engineering – ENCIT 2006
Braz. Soc. of Mechanical Sciences and Engineering – ABCM, Curitiba, Brazil, Dec. 5-8, 2006

Paper CIT06-0271

ADVANCED EDDY-VISCOSITY AND REYNOLDS-STRESS TURBULENCE MODELS FOR AEROSPACE FLOWS

Enda Dimitri V. Bigarella
Instituto Tecnológico de Aeronáutica, CTA/ITA, São José dos Campos, BRAZIL
enda.bigarella@gmail.com

João Luiz F. Azevedo
Instituto de Aeronáutica e Espaço, CTA/IAE, São José dos Campos, BRAZIL
azevedo@iae.cta.br

Abstract. *Recent improvements on a 3-D unstructured-mesh finite-volume method for complex aerospace applications are presented. The correct modelling of turbulence effects in aerospace flows is paramount for their successful computation. One-equation and two-equation models based on the linear approximation of the Boussinesq hypothesis are used. The linear approximation is also extended to include a nonlinear formulation resulting from an explicit algebraic Reynolds-stress model. Finally, two Reynolds-stress closures are also available. Both nonlinear eddy-viscosity and Reynolds-stress model formulations naturally offer the potential for more reliable predictions than linear approximations since anisotropy of the Reynolds stresses can be accounted for. Experimental and DNS results are used for verification and validation of the turbulence model implementation. Focus is directed towards the effect of anisotropy for the resolution of the interaction between shock wave and boundary layers. In general, good agreement with theoretical or experimental results is obtained.*

keywords: *CFD, Turbulence model, Aerospace flows.*

1. Introduction

The present paper reports on recent improvements on a 3-D unstructured-mesh finite-volume method for complex aerospace applications developed by the CFD group at Instituto de Aeronáutica e Espaço (IAE). The objective of the CFD group at IAE is to develop the capability of simulating 3-D, viscous turbulent flows over general launch vehicle configurations. Viscous simulations at high Reynolds numbers are typical for aerospace applications, such as the ones of interest to IAE, and turbulence is certainly important for these flow regimes. The correct modelling of turbulence effects in aerospace flows is decisive for consistent computation of complex phenomena such as boundary layers subjected to adverse-pressure gradients, boundary-layer/shock-wave interactions, wing wakes, mixing layers, and others.

The current code has already been used to simulate turbulent viscous flows over typical aerospace configurations with linear eddy-viscosity turbulence models (EVMs), with successful results so far (Bigarella *et al.*, 2004). For such effort, the Spalart and Allmaras, 1994, one-equation and the Menter, 1994, SST two-equation turbulence models have been chosen. Further extension of the code included the realisable k-ϵ (Shih *et al.*, 1994) and the low-Reynolds-number k-ω (Fluent, 1998) models. The linear approximation resulting from the Boussinesq hypothesis, used by the previous models, is currently extended to include a nonlinear formulation resulting from the explicit algebraic Reynolds-stress model (EARSM) of Wallin and Johansson, 2000. The nonlinear formulation allows for better capture of normal stress and streamline curvature effects, which are important for the already mentioned flow phenomena.

For completeness of the modelling effort, two Reynolds-stress models (RSMs) are also included. Their formulation naturally offers the potential for more reliable prediction of the aforementioned turbulence effects, since important terms are exactly treated. The high-Reynolds number Menter StressBSL uses a linear approximation for the pressure correlation term and an isotropic approximation to the turbulent dissipation. The more advanced Craft-Launder RSM (Batten *et al.*, 1999) is a low-Reynolds number closure, with an anisotropic representation of the turbulent dissipation, and a cubic model for the pressure correlation term.

Extensive validation of this code had already been initiated (Scalabrin, 2002; Bigarella *et al.*, 2004; Bigarella and Azevedo, 2005). Currently, turbulence models are validated for a parallel-wall channel flow case. Numerical results are compared to DNS results. Further results are presented for transonic flows over a supercritical aerofoil. Simulation results are compared to available wind-tunnel experimental data. In general, acceptable numerical results are obtained.

2. Theoretical Formulation

2.1. RANS Equations

The flows of interest in the present context are modelled by the 3-D compressible Reynolds-averaged Navier-Stokes (RANS) equations (Scalabrin, 2002), written in dimensionless form and assuming a perfect gas, as

$$\frac{\partial \mathbf{Q}}{\partial t} + \nabla \cdot (\mathbf{P}_e - \mathbf{P}_v) = 0 \ , \qquad \mathbf{Q} = \left[\ \rho \quad \rho\, u \quad \rho\, v \quad \rho\, w \quad e \ \right]^{\mathrm{T}} \ , \tag{1}$$

where $\mathbf{Q}$ is the dimensionless vector of conserved variables, ρ is the fluid density, $\mathbf{v} = \{u, v, w\}$ is the Cartesian velocity vector and e is the fluid total energy per unit of volume. The inviscid flux vector, $\mathbf{P}_e$, and the viscous flux vector, $\mathbf{P}_v$, are given as

$$\mathbf{P}_e = \left\{ \begin{array}{c} \rho\,\mathbf{v} \\ \rho\, u\mathbf{v} + p\,\hat{\imath}_x \\ \rho\, v\mathbf{v} + p\,\hat{\imath}_y \\ \rho\, w\mathbf{v} + p\,\hat{\imath}_z \\ (e+p)\,\mathbf{v} \end{array} \right\} \ , \quad \mathbf{P}_v = \frac{1}{Re} \left\{ \begin{array}{c} 0 \\ \left(\tau^{\ell}_{xi} + \tau^{t}_{xi}\right)\,\hat{\imath}_i \\ \left(\tau^{\ell}_{yi} + \tau^{t}_{yi}\right)\,\hat{\imath}_i \\ \left(\tau^{\ell}_{zi} + \tau^{t}_{zi}\right)\,\hat{\imath}_i \\ \beta_i\,\hat{\imath}_i \end{array} \right\} \ , \tag{2}$$

where $i = x$, y or z are the indices used within the Einstein indexing notation; and $\hat{\imath} = \{\hat{\imath}_x, \hat{\imath}_y, \hat{\imath}_z\}$ is the Cartesian coordinate unit vector. Furthermore, τ^{ℓ}_{ij} is the shear-stress tensor, u_i is the Cartesian velocity component, x_i is the Cartesian coordinate, δ_{ij} is the Kronecker delta, and $\beta_i = \tau^{\ell}_{ij} u_j + q_i$, where q_i is the heat transfer vector Cartesian component. The dimensionless pressure, p, can be calculated from the perfect gas equation of state.

This set of equations is solved according to a finite volume formulation (Scalabrin, 2002). For convective-flux calculations on the volume faces, the Roe, 1981, flux-difference splitting scheme is currently used. In order to achieve 2nd-order of accuracy in space, properties are linearly reconstructed in the faces based on the van Leer, 1979, MUSCL algorithm. The implementation follows a modified and generalised Barth and Jespersen, 1989, multidimensional limiter formulation from Bigarella and Azevedo, 2005. Diffusive-flux terms are discretized based on a usual centred scheme, with properties in the faces obtained as an arithmetical average of the properties in the neighbouring cells. Flow equations are integrated in time by a fully explicit, 2nd-order accurate, 5-stage, Runge-Kutta time stepping scheme. An agglomeration full-multigrid scheme (FMG) is included in order to achieve better convergence rates for the simulations. More details on the theoretical and numerical formulations can be found in Bigarella *et al.*, 2004, and Bigarella and Azevedo, 2005.

2.2. Turbulence Modelling

High-Reynolds number simulations of flows over complex aerodynamic configurations require adequate turbulence closures in order to correctly account for the large transport effects of the turbulence at such flight conditions. The turbulence effects are included into the RANS equations by the Reynolds-stress tensor, defined by $\tau^{t}_{ij} = -Re\rho\overline{u_i'' u_j''}$. The model transport equations are also solved according to the finite volume approach. The time march is performed using the implicit Euler scheme as in Scalabrin, 2002. For the discretization of the advection term a 1st-order upwind scheme is used, in order to avoid oscillations near discontinuities. For the discretization of the diffusion term an alternative method to compute non-oscillatory derivatives in the face is used as an approximate finite difference scheme. This approximation uses the adjacent cell centroid property and relative distance to build the derivative in the face. More details can be found in Bigarella and Azevedo, 2006.

3. Eddy-Viscosity Turbulence Models

Eddy viscosity models compute the Reynolds stresses through the Boussinesq hypothesis, which states that the turbulence stresses are a linear function of the mean flow straining rate times a modifying constant such as

$$\tau^{t}_{ij} = \mu_t \left[\left(\frac{\partial u_i}{\partial x_j} + \frac{\partial u_j}{\partial x_i} \right) - \frac{2}{3} \frac{\partial u_m}{\partial x_m} \delta_{ij} \right] - \frac{2}{3} \rho k\, \delta_{ij} \ , \tag{3}$$

where μ_t is the eddy viscosity coefficient, computed by the chosen turbulence model.

3.1. Spalart-Allmaras (SA) Model

The Spalart and Allmaras, 1994, single equation model solves a transport equation for the modified eddy viscosity coefficient $\tilde{\mu}$. This models is derived along intuitive and empirical lines, relying heavily on calibration

by reference to a wide range of experimental data (Spalart and Allmaras, 1994). It can be easily integrated to the wall for meshes that guarantee $y+ \approx 1$ close to the wall. This same model has been applied without any further modification by the CFD community for 3-D compressible flows with good results so far (Spalart, 2000; Leschziner and Drikakis, 2002) in shock-induced separations and adverse pressure gradient boundary layers.

3.2. Low-Reynolds-Number Wilcox k-ω (WKOM) Model

The k-ω model is an empirical closure based on transport equations for k and ω (Wilcox, 1998). This model is constantly evolving over the years, including corrections and improvements to a wide range of different flow cases. A low-Reynolds number version of the k-ω model, also enhanced for improved accuracy in free shear flows, from Fluent, 1998, is currently used. The model is closed with constants (Fluent, 1998) obtained from calibration against key test cases for turbulent flows (Wilcox, 1998). This model can also be integrated to the wall.

3.3. Realisable k-ϵ (RKE) Model

The realisable k-ϵ model from Shih *et al.*, 1994, solves transport equations for k and ϵ. Differently from a standard k-ϵ model (Jones and Launder, 1972), this model employs in the dissipation-rate equation a realisable estimate of the turbulent time scale, and an additional term developed to improve the model response to adverse-pressure gradient regions, to guarantee acceptable model behaviour. Furthermore, the eddy viscosity coefficient is defined for this model as a function of the local flow straining in order to also increase the model realisability and response to adverse pressure gradients. A low-Reynolds number damping function, designed to account for the damping of turbulent fluctuations near solid walls, is also considered in the eddy viscosity definition. These enhancements render this model robust and consistent behaviour near solid walls, and better response to pressure gradients.

3.4. Shear-Stress Transport (SST) Model

The Menter, 1994, SST model is derived from a blend of the original k-ω (Wilcox, 1998) and the standard k-ϵ (Jones and Launder, 1972) models. It solves reported problems of the k-ω closure regarding freestream value dependency (Menter, 1994) while keeping the better numerical behaviour of this model close to the wall. Model constants are generally calculated as $\phi = F_1\phi_1 + (1 - F_1)\phi_2$, where ϕ_1 represents the set of constants for the k-ω model and ϕ_2, the set for the standard k-ϵ model (Menter, 1994). The F_1 variable is a blending function that turns on the k-ω closure near solid walls and the standard k-ϵ model outside boundary layers. This function is computed based on checks over turbulence properties through the boundary layer.

Standard two-equation models are acknowledged for not being capable of accurately computing adverse pressure gradient or separated flows (Menter, 1994). It is demonstrated that this is a result of the missing effect of turbulent shear-stress transport in this type of flow (Johnson and King, 1985). In order to take this shear-stress into account, at least in an ad-hoc fashion, the eddy viscosity coefficient is here constrained by the magnitude of the shear-stress tensor. This limiting comes from the knowledge that the shear stress inside the boundary layer is proportional to k as $\tau_{ij}^t = a_1\rho k$ for $i \neq j$, and that, in adverse pressure gradient regions, the Boussinesq assumption $\tau_{ij}^t = 2\mu_t S$ is known to overproduce that term (Menter, 1994). Thus, in such an adverse pressure gradient region, production of k, which is proportional to S, would incorrectly be larger than its dissipation, ω, or $S > a_1\omega$. The SST eddy viscosity coefficient is defined so as to avoid this undesired behaviour. In the simpler BSL model (Menter, 1994), the SST constraint in the eddy viscosity is ignored.

4. Reynolds-Stress Turbulence Models

4.1. General Considerations

Reynolds stress models use the exact equations for the transport of Reynolds stresses obtained by taking velocity-weighted moments of the Navier-Stokes equations and neglecting density fluctuations. The general form of a RSM is given by

$$\frac{D\rho\overline{u_i^{''}u_j^{''}}}{Dt} = P_{ij} + D_{ij}^{\nu} + D_{ij}^{t} + D_{ij}^{p} + \Phi_{ij}^{*} - \epsilon_{ij} \ , \tag{4}$$

with the individual terms representing specific turbulence mechanisms, where P_{ij} is the turbulent production; D_{ij}^{ν} is the molecular diffusion; D_{ij}^{t} is the turbulent diffusion; D_{ij}^{p} is the pressure diffusion; Φ_{ij}^{*} is the pressure-strain correlation; and ϵ_{ij} is the turbulent dissipation. The turbulent production and the molecular diffusion

terms do not require modelling. The representation of the remaining terms is model dependent and they are discussed separately in the respective following subsections.

RSMs also require the solution of another transport equation for a measure of the turbulent length scale, usually represented by a turbulent kinetic energy dissipation quantity. The estimation of this quantity is perhaps the weakest point in Reynolds-stress modelling. An exact equation for the dissipation rate can be derived from the Navier-Stokes equations, but this results in a very complicated form. The usual solution is to use an empirically built equation, calibrated against typical turbulence test cases.

4.2. Modified Craft-Launder RSM (CLMRSM)

This RSM is a variation of the nonlinear RSM of Craft and Launder, 1996, which does not require wall-topology parameters such as normal-to-wall vectors and distance from the wall. Modifications of some wall-proximity corrections have been applied to correct the latter model incorrect response to shock waves, which were falsely interpreted as regions of strong inhomogeneity (Batten *et al.*, 1999).

The generalised gradient diffusion hypothesis (GGDH) of Daly and Harlow, 1970, is used for modelling the turbulent diffusion. The pressure diffusion term is also modelled by an empirical approach. Inhomogeneity-indicator vectors are used to indicate regions close to the wall, where turbulence is highly anisotropic. These vectors are based on the Lumley's stress-flatness parameter (Lumley, 1978), which varies between unity in isotropic turbulence regions and zero as the turbulence approaches a two-component limit.

The pressure-strain correlation is considered a critical element for RSMs since it can be of the order of the production and dissipation terms, hence playing a crucial role in most flow cases. Moreover, since it involves correlations which essentially cannot be measured, its modelling requires substantial effort. A cubic pressure-strain model is here used in conjunction with additional coefficients and inhomogeneity corrections. The proposed (Batten *et al.*, 1999) cubic invariant aims at integration through the viscous sublayer and at consistently acting through shock waves, which is an important feature for the flows of interest to IAE.

The dissipation tensor blends isotropic and wall-limiting terms, with an additional term to account for the dip in the shear-stress dissipation rate in the buffer layer. An equation for the homogeneous dissipation rate, ϵ^*, is proposed to determine ϵ. The equation of ϵ^* incorporates a few modifications to better match low-Reynolds number effects near solid walls (Batten *et al.*, 1999). The advantage of using the equation for the homogeneous dissipation rate, ϵ^*, is the simple wall boundary condition $\epsilon^*_{wall} = 0$. Details of this model are given by Batten *et al.*, 1999, and Bigarella and Azevedo, 2006.

4.3. StressBSL RSM

A numerically more robust isotropic turbulence diffusion formulation is chosen for this model. The pressure diffusion, as usual in RSMs, is here neglected. This option uses a linear pressure-correlation model derived from Rotta, 1951 and Launder *et al.*, 1975, along with an isotropic turbulence assumption for the turbulent dissipation tensor. The turbulence-length-scale determining equation is based on the Menter BSL ω equation (Menter, 1994). This set of equations composes a high-Reynolds number turbulence closure. The interested reader is referred to Bigarella and Azevedo, 2006, for thorough details on this model.

4.4. Wallin-Johansson EARSM (NLBSL)

The main motivation in the development of EARSMs is the general need for improvements in the prediction of complicated turbulent flow phenomena using the platform of existing CFD codes based on two-equation eddy-viscosity turbulence modelling capability. This idea represents an interesting way of cheaply incorporating advanced turbulence effects, such as streamline curvature and normal stress separation, into an already existing two-equation turbulence model framework, avoiding thus the large amount of computational resources required by the solution of RSMs.

The classical *algebraic* RSM (ARSM) starts by assuming equilibrium turbulence, which is equivalent to neglecting advection and diffusion in the RSM transport equations. In the formulation of Wallin and Johansson, 2000, the isotropic assumption for the dissipation tensor along with a slight modification of the linear pressure-strain correlations of the StressBSL model are employed. As a result, one gets an implicit algebraic equation for the compressible Reynolds-stress tensor. In the formulation of Wallin and Johansson, 2000, the anisotropy tensor (Bigarella and Azevedo, 2006) is taken instead of the Reynolds-stress tensor, in order to ease the mathematical notation.

The solution of this implicit equation is known to be numerically cumbersome and, thus, a general form for the anisotropy tensor in terms of the shear-stress and rotation tensors is proposed by Wallin and Johansson, 2000. This is the most general form for this tensor rank, composed of ten tensorial independent groups to which all higher-order tensor combinations can be reduced with the aid of the Caley-Hamilton theorem. Each n-th

expansion term is multiplied by a controlling coefficient, β_n, which may be function of independent invariants derived from the shear-stress and rotation tensors. The explicit solution for the anisotropy tensor now relies on the determination of the β_n coefficients. Some researches adopt the approach of calibrating those terms to a set of representative turbulence problems, as Craft *et al.*, 1996. This approach, however, may decrease the generality of the expanded nonlinear terms.

The proposed anisotropy tensor expansion is inserted into the implicit ARSM equation. An explicit algebraic equation for the nonlinear Reynolds stress terms can now be fully determined, as detailed by Wallin and Johansson, 2000. The EARSM is implemented as a plugin to the BSL model. However, the BSL equation was designed in conjunction with a linear constitutive Boussinesq hypothesis. This fact can compromise the performance of the model if rather combined with a nonlinear closure, such as an EARSM (Hellsten, 2005). In order to circumvent these limitations, Hellsten, 2005, proposed a recalibration of the BSL model to make it consistent when augmented with the EARSM nonlinear terms.

5. Results and Discussion

5.1. Initial Remarks

Linear turbulence models are developed considering effects that are essentially linked to the shear stress in the local streamwise direction. Such effects are, for instance, the skin friction or the effect of the boundary layer displacement into the outer irrotational flow. Isotropy of normal stresses is assumed along a streamline because, in a simple shear flow, which usually serves as a calibration milestone for linear EVMs, the normal stresses are dynamically inactive, not contributing to the momentum balance.

The response of the boundary layer to adverse pressure gradient or streamline curvature is, however, dictated by the shear stress as well as the normal stresses. In that case, normal stresses are dynamically active, and they also work towards sensitising the shear stress to the normal straining (as through a shock wave) and curvature. In other words, the shear stress is generated by an interaction between the crossflow normal stress and the local flow straining in such cases. Near the wall, strong anisotropy is found, where the streamwise normal stress is generated by local flow shear straining, and other normal stresses are fed by the redistributive pressure-strain correlation, which tends to steer turbulence towards isotropy. Those aspects emphasise the need for all turbulence models to return realistic levels of anisotropy. These effects are addressed in the test cases to come.

5.2. Fully-Developed Channel Flow

A fully-developed plane-symmetric channel flow DNS experiment as studied by Kim *et al.*, 1987, at friction Reynolds number $Re_\tau = 180$ based on the channel half height, is reproduced with the current numerical code. A grid configuration which supports mesh-independent results, with 90 points along the wall-normal direction and the wall-nearest node located at $y^+ \approx 1$, is used. Reynolds stress tensor components obtained with the present computation and DNS data are plotted in Fig. 1. It is interesting to observe in this figure the already commented fact that the linear EVMs, namely the SA, SST, RKE and WKOM models, predict isotropic normal stress components. In the SA case, the normal stresses are actually zero. The nonlinear augmentation of the NLBSL formulation allows for separation of the normal stresses. Since NLBSL is a high-Reynolds-number closure, the normal stresses close to the wall do not match the actual stress distribution. The same behaviour is found for the StressBSL RSM. Both closures are high-Reynolds-number models and they predict similar Reynolds stresses. The more advanced low-Reynolds-number CLMRSM presents much stronger anisotropy and a very good match with DNS data. Although the streamwise normal stress is underpredicted by this model, this is of no impact in this particular flow because the shear stress is sensitive to the crossflow normal stress, as already discussed. Careful validation of the boundary layer results and additional details can be found in Bigarella and Azevedo, 2006. Although the current Reynolds number may be considered somewhat low, no differences in the models have been found for larger Reynolds number. This is an indication that the models act consistently even for lower Reynolds number flows.

5.3. OAT15A Supercritical Aerofoil

The interaction between shock waves and boundary layers is of considerable practical importance in transonic and supersonic aerospace vehicle design. Strong shock waves may cause massive flow separation leading to early wing stall or other adverse effects. The mechanics of such interactions are complex and poorly understood. However, it is well known that the interaction is highly sensitive to the boundary layer turbulence state, and its response to the deceleration caused by the shock wave. The turbulence field is highly anisotropic in that region and it responds differently under shear, normal or curvature straining. Therefore, there lies the importance

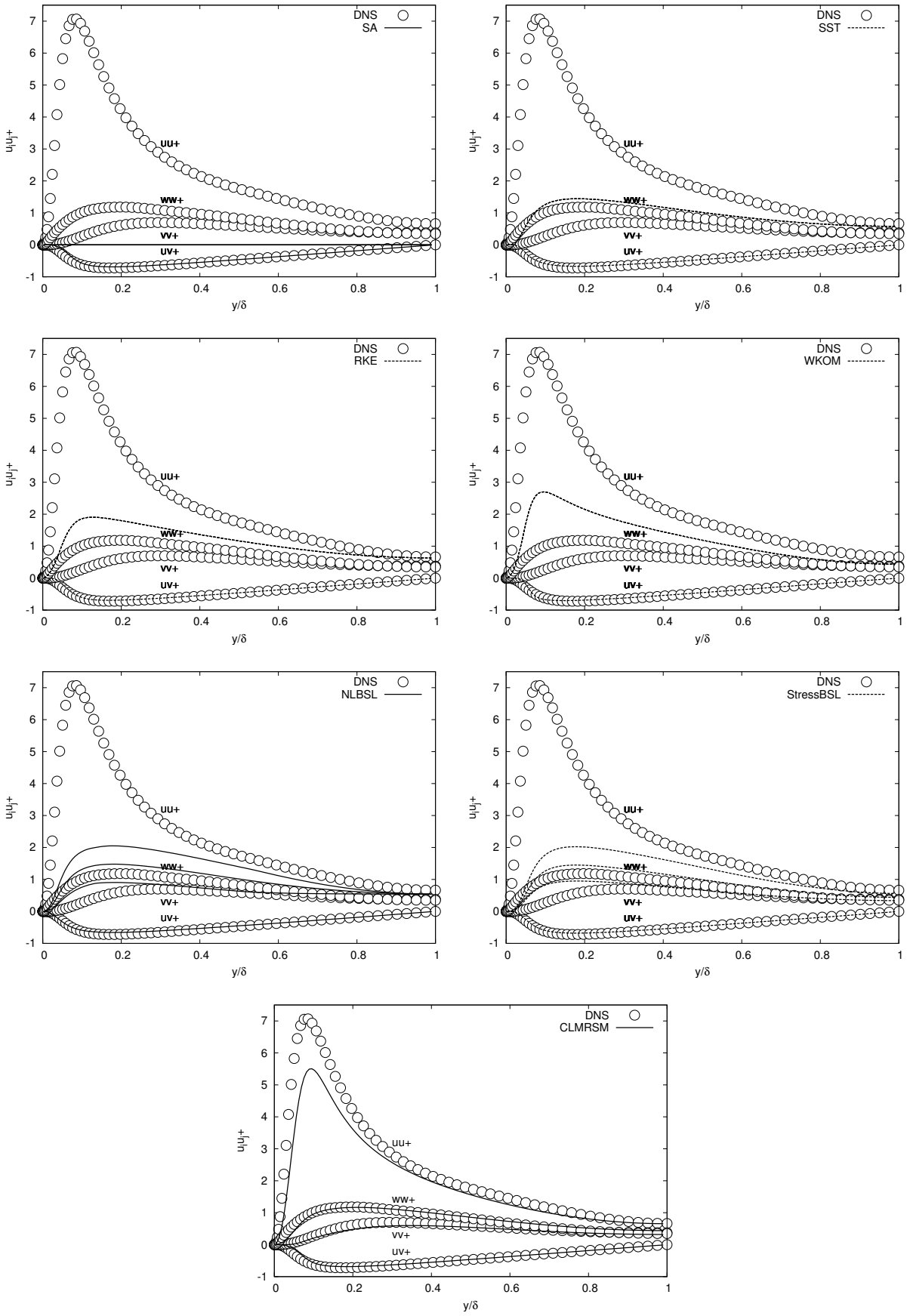

Figure 1: Channel flow at $Re_\tau = 180$. Present computation and DNS Reynolds stresses.

of consistently modelling the turbulence anisotropy and its sensitivity to those types of straining, as earlier discussed.

In order to demonstrate the importance of these remarks, a transonic flow condition over the OAT15A supercritical aerofoil (Rodde and Archambaud, 1994) is addressed. Flight conditions are $M_\infty = 0.724$, $Re = 3$ million, and angle of attack $\alpha = 1.15$ deg. This regime is chosen because the resulting thick boundary layer may more largely interact with the shock wave, being a highly demanding test case for the turbulence models. A grid configuration that is known to support mesh independent results (Bigarella and Azevedo, 2006), with 410 cells along the chord, 34 cells within the boundary layer, and the farfield located 240 chords away, is used. Convergence is considered when the maximum residue of the density field drops 7 orders of magnitude. However, lift and drag coefficients are also monitored to verify force convergence in case density residue would stall.

Numerical pressure coefficient distributions obtained with all turbulence models are compared to the respective experimental data, case 14 in AGARD 303 data (Rodde and Archambaud, 1994), in Fig. 2. It can be clearly seen in this figure the beneficial effects of anisotropy-capable formulation in the turbulence model. All anisotropy-resolving closures, namely NLBSL, StressBSL, and CLMRSM, present good correlation with the experimental result in capturing the shock wave position and the overall pressure distribution. As usual with Boussinesq-based eddy-viscosity models, however, all other linear models indicate a further downstream shock wave location. In the SST case, nevertheless, the eddy viscosity coefficient, limited by the Bradshaw-type constraint, returns a more consistent result among other linear models.

External-probe boundary layer plots at $x/c = 95\%$ for this case are also available. Numerical results are compared to the respective experimental data in Fig. 3. Determining differences are observed in the boundary layer plots in Fig. 3. It is initially seen a strikingly match of the boundary layer obtained with NLBSL and the experimental result. No other model achieves such high accuracy level, in this case. SST, CLMRSM and StressBSL adequately compare to the experimental data, whereas other models present larger differences.

6. Concluding Remarks

The paper presents results obtained with a finite volume code developed to solve the compressible RANS equations. The code uses a Runge-Kutta type scheme to perform time marching. The code is designed to use unstructured meshes composed by any combination of tetrahedra, hexahedra, prisms and pyramids. An agglomeration multigrid scheme provides large convergence acceleration for the numerical simulations. In general, numerical solutions of complicated flows such as transonic turbulent flows about typical aerospace configurations can be obtained in half the previous time used by the single-grid simulation. The convective fluxes are computed by the Roe upwind scheme with MUSCL-type property reconstruction at the faces to achieve 2nd-order of accuracy in space.

Turbulence effects are added to the RANS equations by several advanced turbulence models. The chosen models are specifically designed for aerospace-type flows. The closures range from linear eddy-viscosity, such as the Spallart-Allmaras, SST, realisable k-ϵ, and low-Reynolds-number k-ω models, to nonlinear eddy-viscosity and Reynolds-stress closures. The linear BSL eddy-viscosity formulation is augmented with nonlinear terms coming from an explicit algebraic expansion of a simplified Reynolds-stress equation to compose the NLBSL model. Furthermore, two Reynolds-stress models are also considered. The high-Reynolds-number, linear, and isotropic-dissipation StressBSL model, and the low-Reynolds-number, nonlinear, and anisotropic-dissipation CLMRSM closure are the available Reynolds-stress model options.

Comparison against DNS data for a parallel-wall channel flow case shows the levels of turbulence representativeness that is obtained with each modelling approach. Differences are observed when anisotropy is considered. In these cases, separation of normal stresses can be observed. The code is also able to correctly solve for complex flows, such as the transonic turbulent flow about a supercritical aerofoil. In this case, it is observed that the correct modelling of the turbulence effects inside the boundary layer, mainly regarding the anisotropy of the normal stresses, is of paramount importance for the successful computation of shock wave/boundary layer flows. The NLBSL model presents a large advantage over the other currently considered options since it returns much higher accurate results than other models at computational costs similar to those of a standard two-equation model. The results presented here are a good indication of the capability of simulating turbulent flows about relevant aerospace geometries that can be achieved with the present numerical tool.

7. Acknowledgements

The authors would like to acknowledge Conselho Nacional de Desenvolvimento Científico e Tecnológico, CNPq, which partially supported the project under the Integrated Project Research Grant No. 501200/2003-7. The authors also acknowledge Dr. P. Batten of Metacomp Technologies, USA, and Dr. S. Wallin at Linköping University, Sweden, for their insights on specifics of the respective turbulence model implementations.

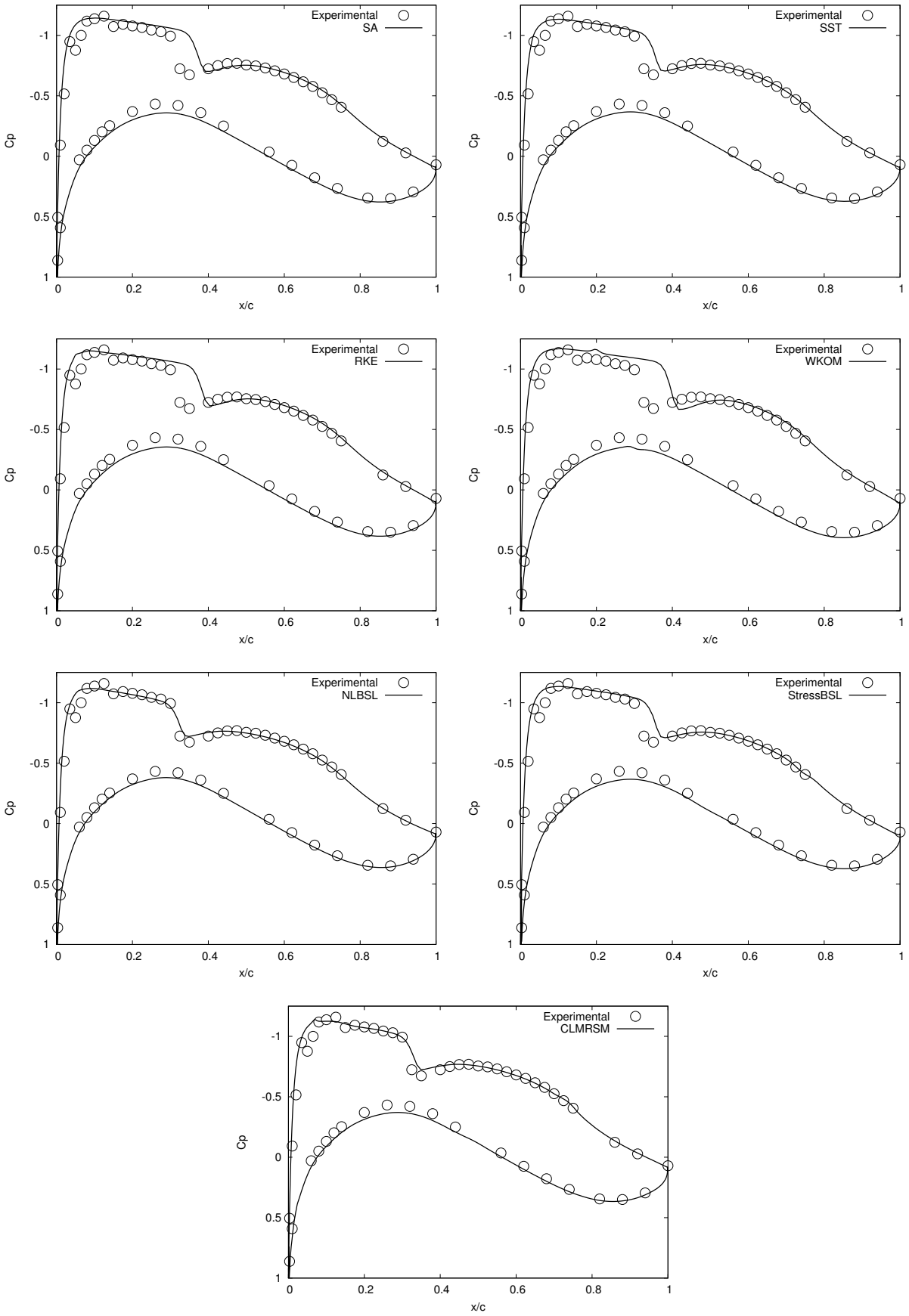

Figure 2: Numerical and experimental Cp distributions for flow conditions $M_\infty = 0.724$, $Re = 3$ million and $\alpha = 1.15$ deg.

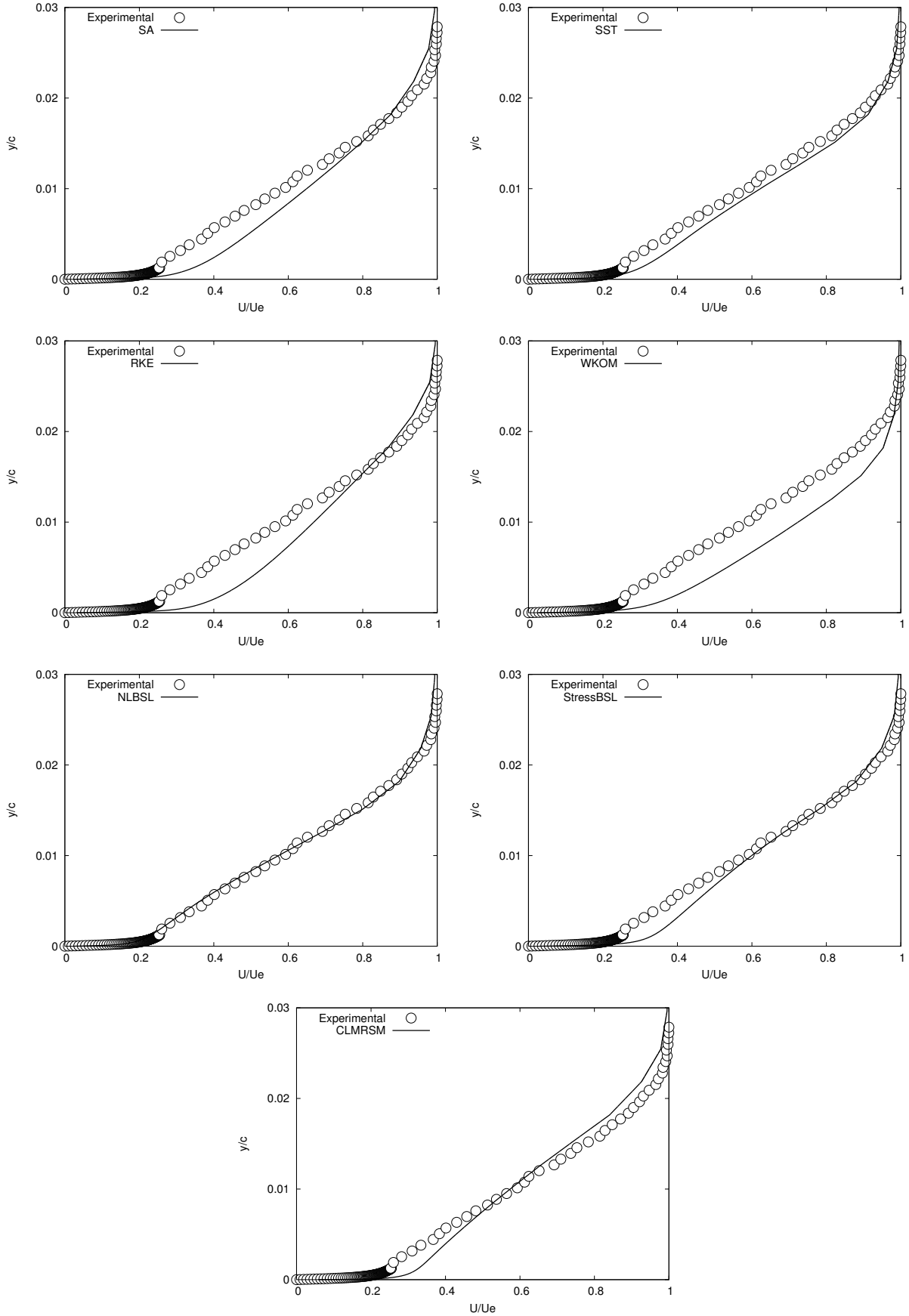

Figure 3: Numerical and experimental boundary layers at $x/c = 95\%$ for flow conditions $M_\infty = 0.724$, $Re = 3$ million and $\alpha = 1.15$ deg.

8. References

Barth, T. J. and Jespersen, D. C., 1989, The Design and Application of Upwind Schemes on Unstructured Meshes, "27th AIAA Aerospace Sciences Meeting", AIAA Paper No. 89-0366, Reno, NV.

Batten, P., Craft, T. J., Leschziner, M. A., and Loyau, H., 1999, Reynolds-Stress-Transport Modeling for Compressible Aerodynamics Applications, "AIAA Journal", Vol. 37, No. 7, pp. 785–796.

Bigarella, E. D. V. and Azevedo, J. L. F., 2005, A Study of Convective Flux Computation Schemes for Aerodynamic Flows, "43rd AIAA Aerospace Sciences Meeting and Exhibit", AIAA Paper No. 2005-0633, Reno, NV.

Bigarella, E. D. V. and Azevedo, J. L. F., 2006, Advanced Eddy-Viscosity and Reynolds-Stress Turbulence Model Simulations of Aerospace Applications, "24th AIAA Applied Aerodynamics Conference", AIAA Paper No. 2006-2826, San Francisco, CA.

Bigarella, E. D. V., Basso, E., and Azevedo, J. L. F., 2004, Centered and Upwind Multigrid Turbulent Flow Simulations with Applications to Launch Vehicles, "22nd AIAA Applied Aerodynamics Conference and Exhibit", AIAA Paper No. 2004-5384, Providence, RI.

Craft, T. J. and Launder, B. E., 1996, A Reynolds Stress Closure for Complex Geometries, "International Journal of Heat and Fluid Flow", Vol. 17, No. 3, pp. 245–254.

Craft, T. J., Launder, B. E., and Suga, K., 1996, Development and Application of a Cubic Eddy-Viscosity Model of Turbulence, "International Journal of Heat and Fluid Flow", Vol. 17, No. 2, pp. 108–115.

Daly, B. and Harlow, F., 1970, Transport Equation in Turbulence, "Physics of Fluids", Vol. 13, pp. 2634–2649.

Fluent, 1998, FIDAP 8 – Tutorial Manual.

Hellsten, A., 2005, New Advanced k-ω Turbulence Model for High-Lift Aerodynamics, "AIAA Journal", Vol. 43, No. 9, pp. 1857–1869.

Johnson, D. A. and King, L. S., 1985, A Mathematically Simple Turbulence Closure Model for Attached and Separated Turbulent Boundary Layers, "AIAA Journal", Vol. 23, No. 11, pp. 1684–1692.

Jones, W. P. and Launder, B. E., 1972, The Prediction of Laminarization with a Two-Equation Model of Turbulence, "International Journal of Heat and Mass Transfer", Vol. 15, No. 2, pp. 301–314.

Kim, J., Moin, P., and Moser, R., 1987, Turbulence Statistics in Fully Developed Channel Flow at Low Reynolds Number, "Journal of Fluid Mechanics", Vol. 177, pp. 133–166.

Launder, B. E., Reece, G. J., and Rodi, W., 1975, Progress in the Development of a Reynolds-Stress Turbulence Closure, "Journal of Fluid Mechanics", Vol. 68, No. 3, pp. 537–566.

Leschziner, M. A. and Drikakis, D., 2002, Turbulence Modelling and Turbulent-Flow Computation in Aeronautics, "The Aeronautical Journal", Vol. 106, No. 1061, pp. 349–383.

Lumley, J. L., 1978, Computational Modeling of Turbulent Flows, Yih, C. -S., editor, "Advances in Applied Mechanics", Vol. 18, pp. 123–176. Academic Press, New York.

Menter, F. R., 1994, Two-Equation Eddy-Viscosity Turbulence Models for Engineering Applications, "AIAA Journal", Vol. 32, No. 8, pp. 1598–1605.

Rodde, A. M. and Archambaud, J. P., 1994, OAT15A Airfoil Data, "A Selection of Experimental Test Cases for the Validation of CFD Codes", number AGARD-AR-303. NATO Advisory Group for Aerospace Research & Development, Case A11.

Roe, P. L., 1981, Approximate Riemann Solvers, Parameter Vectors, and Difference Schemes, "Journal of Computational Physics", Vol. 43, No. 2, pp. 357–372.

Rotta, J., 1951, Statistischer Theorie nichthomogener Turbulenz 1, "Zeitschrift für Physik", Vol. 129, pp. 547–572.

Scalabrin, L. C., 2002, Numerical Simulation of Three-Dimensional Flows over Aerospace Configurations, Master's thesis, Instituto Tecnológico de Aeronáutica, São José dos Campos, SP, Brazil.

Shih, T., Liou, W. W., Shabbir, A., Yang, Z., and Zhu, J., 1994, A New Eddy Viscosity Model for High Reynolds Number Turbulent Flows – Development and Validation, NASA TM 106721, National Aeronautics and Space Administration, Lewis Research Center, Cleveland, Ohio 44135-3191.

Spalart, P. R., 2000, Strategies for Turbulence Modelling and Simulations, "International Journal of Heat and Fluid Flow", Vol. 21, pp. 252–263.

Spalart, P. R. and Allmaras, S. R., 1994, A One-Equation Turbulence Model for Aerodynamic Flow, "La Recherche Aeropastiale", Vol. 1, pp. 5–21.

van Leer, B., 1979, Towards the Ultimate Conservative Difference Scheme. V. A Second-Order Sequel to Godunov's Method, "Journal of Computational Physics", Vol. 32, No. 1, pp. 101–136.

Wallin, S. and Johansson, A. V., 2000, An Explicit Algebraic Reynolds Stress Model for Incompressible and Compressible Turbulent Flows, "Journal of Fluid Mechanics", Vol. 403, pp. 89–132.

Wilcox, D. C., 1998, "Turbulence Modeling for CFD", DCW Industries, La Cañada, CA, second edition.

Proceedings of the 11th Brazilian Congress of Thermal Sciences and Engineering – ENCIT 2006
Braz. Soc. of Mechanical Sciences and Engineering – ABCM, Curitiba, Brazil, Dec. 5-8, 2006

Paper CIT06-0298

HIGH-ORDER NON-UNIFORM GRID SCHEMES FOR NUMERICAL INVESTIGATION OF COMPRESSIBLE SHEAR LAYERS

Ricardo A. C. Germanos
USP - Universidade de São Paulo
Escola de Engenharia de São Carlos - Departamento de Engenharia Aeronáutica
Av. Trabalhador São Carlense, 400 - SP - 13566-590, Brazil
gercop@sc.usp.br

Stefan Wernz
The University of Arizona
Department of Aerospace and Mechanical Engineering
1130 North Mountain Ave., Tucson, Arizona, USA
wernzs@email.arizona.edu

Hermann F. Fasel
The University of Arizona
Department of Aerospace and Mechanical Engineering
1130 North Mountain Ave., Tucson, Arizona, USA
faselh@email.arizona.edu

Marcello A. Faraco de Medeiros
USP - Universidade de São Paulo
Escola de Engenharia de São Carlos - Departamento de Engenharia Aeronáutica
Av. Trabalhador São Carlense, 400 - SP - 13566-590, Brazil
marcello@sc.usp.br

Abstract. *The engineering research and design requirements of today pose great challenges in computer simulation to engineers and scientists who are called on to analyze phenomena in continuum mechanics. The study of hydrodynamic instability is a subject well researched, and comes in numerous practical situations such as aerodynamics, combustions and environmental engineering. In the current work, the instability of a compressible free shear layer at relatively low Reynolds numbers was investigated. In the aerospace context, important applications involve compressible flows at relatively low Reynolds numbers. Among them, the flow on gas turbine blades and the flow on high lift devices such as slats and flaps at high angle of attack are particularly important. In aerodynamic applications at low Reynolds numbers, often a substantial portion of the flow is in the transition regime, or in the initial turbulent stages. Despite the extensive research carried out in the field, there are various aspects of the transition process that require further studies. The transition in compressible flows is an example. Here, simulations of compressible Navier-Stokes equations have been performed. Spatial derivatives in these equations were discretized using of a sixth-order finite-difference method. In order to solve the time derivatives a fourth-order Runge-Kutta method was adopted. As the last step of the integration scheme, a compact filter was applied to remove short length scales in the streamwise and normal directions. Moreover, the compact schemes were modified to work with non-uniform grids. In this case, a stretching in y-direction was implemented with the objective to reduce the sound waves generated by shear region and to improve the resolution in the interior of the domain. The numerical investigation starts with an analysis of the amplification rate in linear regime. Tests were also performed in the non-linear regime and it was possible to reproduce the vortex roll-up and pairing. Through these results, the effect of the Mach number on the evolution of shear instabilities was analyzed.*

keywords: *hydrodynamic instability, transition, compressible shear layer, compact schemes, grid stretching*

1. Introduction

The study of transition in mixing layers has constituted one of the main research themes in turbulence over the last thirty years. This flow types is found in many situations in nature like in atmospheric flows, volcanic eruptions, stellar jets and in industrial applications such as gas turbine combustors, airfoil wakes and rocket

exhausts. A detailed understanding of the physics of free shear layers is essential for the development of new turbulence and mixing models. Improved models of mixing in free shear layers will lead to a better capability of predicting chemical reactions and controlling pollutant emissions, for example from oil and gas burners in power generation plants. Also progress in space research is dependent on developing more efficient propulsion systems, and vehicles capable of carrying a higher payload into orbit.

A mixing layer develops at the interface of two-stream of different speeds. The velocity profile formed possesses an inflection point that is unstable to infinitesimal disturbances. This phenomenon called Kelvin-Helmholtz instability is inviscid and is responsible for the formation of vorticity structures aligned in the lateral direction. This behavior was observed laboratory experiments carried out by Birch and Eggers, 1973 and Brown and Roshko, 1974. According to Lesieur, 1997 due to the vorticity concentration, the recognizable form, and the unpredictability in relation to the location in the time and space, these vortical structures exhibit all the characteristics of coherent structures.

In addition to Kelvin-Helmholtz instability vortex, experimental works presented by Bernal and Roshko, 1986 and numerical works published by Metcalfe *et al.*, 1987 put in evidence the existence of one secondary instability that causes, in the stagnation area between the Kelvin-Helmholtz vortices, intense longitudinal counter-rotative vortices. These longitudinal vortices, denominated hairpins are easily identifiable in a transverse cut in the form of a mushroom and responsible for the largest portion of the transfer of mass, momentum and energy conservation in transitional and turbulent flows.

Studies of the linear stability of compressible mixing layers presented by Lessen *et al.*, 1966, Blumen *et al.*, 1975 show a strong reduction in the amplification rate of two-dimensional disturbances in the flow as Mach number is increased. In compressible mixing layers there are two flows with different speeds, and consequently, with different characteristic Mach numbers. Therefore the representative parameter is the convective Mach number (Papamoschou and Roshko, 1988). Experiments show that this parameter characterizes the flow correctly for Mach number below 0.6. Simulations carried out by Sandham and Reynolds, 1989 show that for convective Mach number lower than 0.6 the two-dimensional disturbances is the most strongly amplified whilst for convective Mach number above to 0.6, the oblique waves are dominant in the flow and the mixing layer will have a highly three-dimensional structure.

These kinds of flows possess wide range of space and time scales and therefore require high accuracy in the numerical solution. This accuracy requirement can be achieve by the use of spectral methods (Canuto *et al.*, 1987). These methods can be used to assure that all relevant scales are captured, but high-order finite-difference are also able to represent short length scales with good accuracy. Lele, 1992, emphasizes the importance of using high-order schemes for first and second derivatives. Mahesh, 1998, presents high-order finite-difference schemes, introducing a method that, using the same stencil is more accurate than the standard Padé schemes. A disadvantage of his method is that it requires the solution of first and second derivatives simultaneously. Souza *et al.*, 2002a; Souza *et al.*, 2002b, used high-order compact methods for transition phenomenon problems. In these studies it was investigated the propagation of the Tollmien-Schlichting waves in incompressible flows.

In the present work, a high-order compact scheme was adopted to solve the spatial derivatives (Lele, 1992). The computational domain is periodic in x-direction. In the y-direction, the free-slip condition was adopted according to Medeiros *et al.*, 2000 and Souza, 2003. Emphasizing that this boundary condition produces accurate results for a sufficiently large distance from the mixing layer. Another possibility would be to use an exponential decay condition, except that this method is only rigorously correct in the linear regime. Thompson, 1987 presents non-reflecting boundary conditions whereas the idea of these boundary conditions is to consider the characteristic form of the Euler equation at the boundary. Finally, to solve the temporal derivatives, the time-advancement is obtained by using a high-order Runge-Kutta scheme in agreement with Williamson, 1980. This scheme is conditionally stable and therefore small time increments are required to assure that the stability criterion is satisfied. A similar scheme was used by Kloker *et al.*, 1993.

The linear and non-linear temporal evolution of two-dimensional instability waves in the unconfined mixing layer was simulated. Tests based on the linear stability theory were used to validate the code. In these tests, the growth rates obtained in the present simulations was compared with results from other numerical works. Simulations in the non-linear regime were also performed. The long term objective of this work is the simulation of compressible boundary layer phenomena, such as the present studied, the authors of this work consider essential to verify the code first with as the case of mixing layer and acoustic wave problems. Previous works present other verification tests with the simulation of the linear acoustic wave problem (Germanos *et al.*, 2004).

The organization of the paper is as follows. Section 2 presents the formulation of the governing equations adopted in the current work. Details of the numerical method are described in the section 3. Section 4 shows a numerical simulation of the mixing layer instability. The last section presents the conclusion of this work.

2. Formulation

In this study, the governing equations are the compressible, Navier-Stokes equations according to Sandham and Reynolds, 1991 and Eibler and Bestek, 1996. They consist of the momentum equations for the velocity components (u,v) in the streamwise direction (x) and normal direction (y)

$$\frac{\partial \rho u_i}{\partial t} + \frac{\partial \rho u_i u_j}{\partial x_j} = -\frac{\partial p}{\partial x_i} + \frac{\partial \tau_{ij}}{\partial x_j}, \tag{1}$$

and the continuity and energy equation

$$\frac{\partial \rho}{\partial t} + \frac{\partial \rho u_j}{\partial x_j} = 0, \tag{2}$$

$$\frac{\partial E}{\partial t} + \frac{\partial u_j (E+p)}{\partial x_j} = -\frac{\partial q_j}{\partial x_j} + \frac{\partial u_j \tau_{ij}}{\partial x_j}, \tag{3}$$

where x_i are the Cartesian coordinates (x,y), t is the time, u_i are the velocity components (u,v), ρ is the density and p is the pressure. The non-dimensional constitutive relations for a Newtonian fluid with Fourier heat conduction are

$$\tau_{ij} = \frac{1}{Re}\left(\frac{\partial u_i}{\partial x_j} + \frac{\partial u_j}{\partial x_i} - \frac{2}{3}\frac{\partial u_k}{\partial x_k}\delta_{ij}\right), \tag{4}$$

$$q_i = -\frac{1}{(\gamma-1)M^2 PrRe}\frac{\partial T}{\partial x_j}. \tag{5}$$

The total energy E_t is given by $E_t = \rho\left(e + \frac{u^2+v^2}{2}\right)$, where e is the internal energy. The Reynolds number of the flow is defined as

$$Re = \frac{\rho_1 \, U_1 \, \delta^*_{\omega_0}}{\mu}, \tag{6}$$

where U is the velocity, ρ is the density and μ is the dynamic viscosity of the flow. The variable $\delta^*_{\omega_0}$ is the vorticity thickness of the initial velocity given by

$$\delta^*_{\omega_0} = \frac{U_1^* - U_2^*}{|d\bar{u_0}^*/dy^*|_{max}}, \tag{7}$$

where the subscript 1 and 2 refers to the upper ($y > 0$) and lower ($y < 0$) free stream, respectively. The perfect-gas law for pressure and temperature in this non-dimensional scheme is

$$p = (\gamma - 1)\rho e, \tag{8}$$

$$T = \frac{\gamma M^2 p}{\rho}, \tag{9}$$

where γ is the relation of the specific heat. The Prandtl number $Pr = \frac{c_p \, \mu}{k}$ was assumed constant $Pr = 1$, where k is the thermal conductivity.

These equations were defined with the following non-dimensionalization scheme

$$u_i = \frac{u_i^*}{U_1}, \quad \rho = \frac{\rho^*}{\rho_1}, \quad p = \frac{p^*}{\rho_1 \, U_1^2}, \quad t = \frac{t^* U_1}{\delta^*_{\omega_0}}, \quad x_i = \frac{x_i^*}{\delta^*_{\omega_0}}, \quad \alpha = \alpha^* \delta^*_{\omega_0}, \quad \omega = \frac{\omega^* \delta^*_{\omega_0}}{U_1}, \tag{10}$$

where α^* is the dimensional wavenumber of the disturbed flow, ω^* is the dimensional frequency of the flow.

3. Methodology

3.1. Initial Condition

The first step for simulating instabilities in a shear layer is to implement a initial velocity profile. In the velocity profile adopted in this work, the upper part of the stream travels faster than the lower part. The choice of transition between these two different speeds is crucial in order not to generate waves in the first time steps, which could then be reflected on edges. In this work, the two-dimensional problem was considered because it has been shown that for low Mach numbers (typically under 0.4), the dominant instability mode for the shear layer is two-dimensional and that three-dimensional instabilities only become important for high Mach numbers.

Many different velocity profiles have been proposed in the literature for modelizing a shear layer. Rayleigh, 1880 has demonstrated that the profile has to have an inflexion point to be unstable. This means that disturbances will be amplified and lead to the formation of vortice structures, which will also be in an unstable equilibrium and therefore will create some pairing until the energy has dispersed through viscous dissipation. The profile used in this numerical work corresponds in an hyperbolic tangent function that uses a velocity means at upper and lower of the free stream flow to calculate the velocity in coordinate y.

Along with the velocity profile the disturbance flow has to be defined. Numerical errors engender perturbations, which are sufficient to suscitate such instabilities in the shear layer flow but only after a very long time. The formation of vortice structures can be largely accelerated by using some disturbance functions, which correspond to the eigenfunctions of stream. This idea of exciting a stream adding to the mean flow a little disturbance to accelerated the process is widely spread in the scientific community. This technique was often used by Colonius *et al.*, 1997 for spatial development, Michalke, 1964 for temporal development in incompressible flows and Sandham and Reynolds, 1991 for compressible case.

Thus the variables were decomposed into two parts: the temporary mean and a small disturbance. This way the primitive variables can be rewritten in the following way

$$\begin{aligned} u(x,y,z,t) &= u_0(y) \quad + u', \\ v(x,y,z,t) &= v', \\ \rho(x,y,z,t) &= 1 \\ T(x,y,z,t) &= T_0(y) \\ p(x,y,z,t) &= \tfrac{1}{\gamma M^2}. \end{aligned} \tag{11}$$

where the subscript $(_0)$ refers to a temporary mean flow and $(')$ refers to a small disturbance. The mean flow is invariant in the streamwise direction and the component (v) of the mean velocity is null. In other words, the mean flow is locally parallel.

In this work the velocity profile is defined as

$$\bar{u}_0(y) = \frac{U_1 + U_2}{2} + \frac{U_1 - U_2}{2} \tanh(\frac{2y}{\delta_{\omega_0}}). \tag{12}$$

The vorticity thickness is given by equation 7. This profile has often been used because it has the great advantages of being analytical. Consequently, speed can be calculated exactly for each value of y. The derivatives of this function are known as well. The tangent profile was used by Michalke, 1964 and by Fortuné, 2000 in their papers about shear layer developing in time and by Colonius *et al.*, 1997 for shear layers developing in space. A disadvantage of using the tangent profile is that it neither satisfies the momentum equation nor the energy equation and, therefore, it can cause an impact in first time steps in the numerical integration of the temporal primitives variables of Navier-Stokes equation.

The initial mean temperature profile can be specified as a solution to the compressible boundary layer energy equation (White, 1974), assuming unity Prandtl number. For the antisymmetric mean velocity profile considered here, and with equal free stream temperatures the general relation of Crocco-Busemann is given by

$$\bar{T}_0(y) = 1 + M_c^2 \frac{\gamma - 1}{2}(1 - \bar{u}_0^2(y)), \tag{13}$$

This relation assumes parallel flow. It is noted that for all simulations here the convective Mach number M_c is equal to the free stream Mach number M. Uniform pressure is assumed for the initial mean flow ($p_0 = \frac{1}{\gamma M^2}$), so the mean density profile is calculated with equation 8.

The disturbances can be generalized by

$$u'(x,y,t) = \phi_1(y) e^{i(\alpha x - \omega t)} + \phi_2(y) e^{i\frac{1}{2}(\alpha x - \omega t)} \tag{14}$$

where α refers to the spatial wavenumber and ω to the frequency of the disturbance flow. The variable ϕ_1 correspond to an eigenfunction of the stream and ϕ_2 refers to the first subharmonic mode. The eigenfunction u' is a function of the y-coordinate only. For the time-developing shear layer problem, disturbances grow in time. Thus, the wavenumber α is real. The streamwise wavelength of a disturbance is given by $L_x = 2\pi/\alpha$, the phase speed by $c_r = \omega_r/\alpha$ and the amplification rate by ω_i.

In this work the eigenfunctions were approximated by exponential functions (Michalke, 1964). Exponential functions are convenient because they decrease really quick and respect the boundary conditions $u'(\bar{+}\infty) = 0$. Furthermore, those functions can easily be analytically differentiated. For find the disturbance flow some assumptions were made. First the flow is considered inviscid because mechanism of instability is inviscid and the only effect of viscosity is to damp the growing disturbances. Second the flow is considered incompressible, which is only true for very small Mach numbers. Based on these hypotheses the disturbance flow can be defined as

$$u' = \frac{2\sigma y}{(\alpha_1\alpha_2)}\left[A_1\sin(\alpha_1 x)\alpha_2 + A_2\sin(\alpha_2 x)\alpha_1\right]\exp(-\sigma y^2), \tag{15}$$

$$v' = \left[A_1\sin(\alpha_1 x) + A_2\sin(\alpha_2 x)\right]\exp(-\sigma y^2), \tag{16}$$

where A is the amplitude, α is the wavenumber and σ is the spread of the disturbance in the y-direction. The subscript 1 refers to the dominant mode fundamental and subscript 2 refers to the subharmonic mode.

3.2. Boundary Conditions

In these simulations we are considering the problem of an unbounded compressible mixing layer. The infinite extent could be obtained by using a mapping function, but this would lead to poor resolution of the flow far away from the mixing layer. In particular, sound waves would propagate into regions of the computational domain where these waves would be poorly resolved, and might be reflected back and contaminate the main flow. Thus, we require boundary conditions which simulate an infinite domain, even though the computational domain is finite. In order to reproduce this mechanism, the appropriate specification of boundary conditions represents an important task for the development of computational simulations. At the free stream boundary the flow was assumed to be irrotational. This assumption is usually satisfied to machine precision in numerical calculations. Thus, the normal component of velocity in the free stream is set to zero. This condition satisfies the impermeability conditions. For other primitive variables the first derivatives are set to zero to satisfies the condition of free-slip. These schemes can be seen below

$$\begin{aligned} v &= 0, \\ \frac{\partial}{\partial y}(u, w, \rho, p) &= 0. \end{aligned} \tag{17}$$

Ideally, one would like enforcing a vanishing perturbation velocity at a very large distance from the shear layer, but these requires a very large computational domain. For a sufficient large distance form shear layer, this boundary condition should produce accurate results.

Another assumption used in this work is to considered a boundary condition of Roubin that specified the disturbance velocity for normal component as

$$\frac{\partial v}{\partial y} = -\alpha v \tag{18}$$

This condition imposes exponential decay of disturbances at the free-stream. In the case of shear layer, this exponential decay follows from linear stability theory. For sufficiently large distance from the shear zone the solution is quite insensitive to the value of α.

Finally, in x-direction a periodic boundary conditions was used as proceed below.

$$\begin{aligned} f(0) &= f(L), \\ \frac{\partial^\eta f(0)}{\partial x_i^\eta} &= \frac{\partial^\eta f(L)}{\partial x_i^\eta}. \end{aligned} \tag{19}$$

This method was verified through linear acoustic waves problems. Details about these tests can be found in the technical report by Germanos and Medeiros, 2004.

3.3. Numerical Methods

This section presents the numerical method adopted for a time-developing free shear layer problem. These types of flows possess wide range of space and time scales and therefore require high accuracy at the numerical

solution. This requirement of accuracy can be achieve by the use of spectral methods (Canuto *et al.*, 1987). The use of this scheme is restricted to flows in simple domains and with simple boundary conditions. In order to overcome these difficulties an alternative numerical representations can be used as the finite-differences schemes and the finite volume schemes. The advantage of finite volume schemes has advantages in working with complex domains and also with complex boundary conditions. On the other hand the finite-differences schemes is justified by the possibility of the use of more general boundary conditions, although the schemes with high-order of accuracy is also restricted to the problem with simple domains. The advantage of these schemes in relation to finite volume schemes is that high-order approximations can be obtained. These schemes can be classified as explicit or implicit. Although the cost of inverting a banded matrix to obtain the nodal derivatives, the implicit schemes are significantly more accurate for the small scales than explicit schemes with the same stencil width (Collatz, 1966 and Kopal, 1961). Since tridiagonal matrices can be inverted quite efficiently (Strang, 1988), the implicit schemes are extremely attractive when explicit time advancement schemes are used. The most popular of the implicit schemes also called compact schemes is the symmetric sixth order version. These schemes is non-dissipative due to the symmetry.

Here the finite-difference approximation to the derivative of the function is expressed as a linear combination of the given function values on a set of nodes. First a uniformly spaced mesh was considered where the nodes are indexed by i. The independent variable at the nodes is $x_i = ih$ for $0 \leq i \leq N$. In these schemes the value of f'_i possess a dependence with all the nodal values. In general implicit or compact schemes are significantly more accurate for short length scales than explicit schemes (Collatz, 1966 and Kopal, 1961). This increase of accuracy can be reached with the inversion of a tridiagonal matrix to obtain the derivative values. Strang, 1988 presents quite efficient methods to solve linear system like this. Lele, 1992 emphasizes the importance of using methods of high-order and proposes schemes with 6^{th} order approximation in the interior of the mesh whereas at the boundaries and near the boundaries the 3^{rd} and 4^{th} order approximation was used, respectively.

Below, the discretization used in the streamwise and the normal direction are present. The letters i, j represent the grid position in the x and y directions, which varies from 0 to M, N respectively. In the x-direction, the 6^{th} order implicit (compact) derivatives for $0 < i < M$ as follows

$$\begin{bmatrix} 3 & 1 & & & & & 1 \\ 1 & 3 & 1 & & & & \\ & \ddots & \ddots & \ddots & & & \\ & & 1 & 3 & 1 & & \\ & & & \ddots & \ddots & \ddots & \\ & & & & 1 & 3 & 1 \\ 1 & & & & & 1 & 3 \end{bmatrix} \begin{bmatrix} f'_0 \\ f'_1 \\ \vdots \\ f'_i \\ \vdots \\ f'_{M-1} \\ f'_M \end{bmatrix} = \begin{bmatrix} \frac{1}{12dx}(f_{M-1} + 28f_M - 28f_1 - f_2) \\ \frac{1}{12dx}(f_M + 28f_0 - 28f_2 - f_3) \\ \vdots \\ \frac{1}{12dx}(f_{i+2} + 28f_{i+1} - 28f_{i-1} - f_{i-2}) \\ \vdots \\ \frac{1}{12dx}(f_{M-3} + 28f_{M-2} - 28f_M - f_0) \\ \frac{1}{12dx}(f_{M-2} + 28f_{M-1} - 28f_0 - f_1) \end{bmatrix}, \tag{20}$$

The viscous terms in the governing equations require evaluation of successive derivatives, for instance $\frac{\partial}{\partial y}(\frac{\partial u}{\partial y})$. When a spectral method is used there is no loss of accuracy if these derivatives are computed by two applications of a first derivatives. However, with finite-difference methods we find that two applications of a first derivative gives a significantly worse representation of the high wavenumbers than a single second derivative computation. This is because the modified wavenumber (Lele, 1992) goes to zero for the first derivative at high wavenumbers. The solution for this problem is to expand all terms in the y direction and calculate the primitives variables in the non-conservative formulation. Therefore the schemes of second derivatives adopted in this work are

$$\begin{bmatrix} 2 & 11 & & & & & 2 \\ 2 & 11 & 2 & & & & \\ & \ddots & \ddots & \ddots & & & \\ & & 2 & 11 & 2 & & \\ & & & \ddots & \ddots & \ddots & \\ & & & & 2 & 11 & 2 \\ 2 & & & & & 2 & 11 \end{bmatrix} \begin{bmatrix} f''_0 \\ f''_1 \\ \vdots \\ f''_i \\ \vdots \\ f''_{N-1} \\ f''_N \end{bmatrix} = \begin{bmatrix} \frac{1}{4h^2}(3f_{N-1} + 48f_N - 102f_0 + 48f_1 + 3f_2) \\ \frac{1}{4h^2}(3f_N + 48f_0 - 102f_1 + 48f_2 + 3f_3) \\ \vdots \\ \frac{1}{4h^2}(3f_{i-2} + 48f_{i-1} - 102f_i + 48f_{i+1} + 3f_{i+2}) \\ \vdots \\ \frac{1}{12h}(3f_{N-3} + 48f_{N-2} - 102f_{N-1} + 48f_N + 3f_0) \\ \frac{1}{12h}(3f_{N-2} + 48f_{N-1} - 102f_N + 48f_0 + 3f_1) \end{bmatrix}. \tag{21}$$

In the normal direction, a non-periodic scheme was studied. This scheme was used by Souza *et al.*, 2002c. At the boundaries a 5^{th} order asymmetric approximation was proposed, whilst for points near the boundaries the 6^{th} order asymmetric approximation was used. For the interior points, the 6^{th} order symmetric approximation was adopted whereas this scheme satisfies free-slip conditions. In this work an alternative scheme was used. This alternative scheme consist in using a 2^{nd} order approximation at the boundaries and for the points near the boundaries. Tests were performed with both schemes and the results confirm that the numerical scheme is more

stable over time. Details about these tests can be found in the technical report by Germanos and Medeiros, 2006. Emphasizes that these schemes will be used only at the free-stream for a sufficiently distance from the shear zone. This compact scheme for first and second derivatives can be seen below

$$\begin{bmatrix} 1 & & & & & & \\ & 1 & & & & & \\ & \ddots & \ddots & \ddots & & & \\ & & 1 & 3 & 1 & & \\ & & & \ddots & \ddots & \ddots & \\ & & & & & 1 & \\ & & & & & & 1 \end{bmatrix} \begin{bmatrix} f'_0 \\ f'_1 \\ \vdots \\ f'_j \\ \vdots \\ f'_{N-1} \\ f'_N \end{bmatrix} = \begin{bmatrix} \frac{1}{2dy}(-3f_0 + 4f_1 - f_2) \\ \frac{1}{2dy}(-f_0 + f_2) \\ \vdots \\ \frac{1}{12dy}(f_{j+2} + 28f_{j+1} - 28f_{j-1} - f_{j-2}) \\ \vdots \\ \frac{1}{2dy}(-f_{N-2} + f_N) \\ \frac{1}{2dy}(f_{N-2} - 4f_{N-1} + 3f_N) \end{bmatrix}, \quad (22)$$

$$\begin{bmatrix} 1 & & & & & & \\ & 1 & & & & & \\ & \ddots & \ddots & \ddots & & & \\ & & 2 & 11 & 2 & & \\ & & & \ddots & \ddots & \ddots & \\ & & & & & 1 & \\ & & & & & & 1 \end{bmatrix} \begin{bmatrix} f''_0 \\ f''_1 \\ \vdots \\ f''_i \\ \vdots \\ f''_{N-1} \\ f''_N \end{bmatrix} = \begin{bmatrix} \frac{1}{h^2}(f_0 - 2f_1 + f_2) \\ \frac{1}{h^2}(f_0 - 2f_1 + f_2) \\ \vdots \\ \frac{1}{4h^2}(3f_{i-2} + 48f_{i-1} - 102f_i + 48f_{i+1} + 3f_{i+2}) \\ \vdots \\ \frac{1}{h^2}(f_{N-2} - 2f_{N-1} + f_N) \\ \frac{1}{h^2}(f_{N-2} - 2f_{N-1} + f_N) \end{bmatrix}. \quad (23)$$

The schemes above were modified to work with free-slip condition as proceeds below

$$\begin{bmatrix} 1 & & & & & & \\ & 1 & & & & & \\ & \ddots & \ddots & \ddots & & & \\ & & 1 & 3 & 1 & & \\ & & & \ddots & \ddots & \ddots & \\ & & & & & 1 & \\ & & & & & & 1 \end{bmatrix} \begin{bmatrix} f'_0 \\ f'_1 \\ \vdots \\ f'_j \\ \vdots \\ f'_{N-1} \\ f'_N \end{bmatrix} = \begin{bmatrix} 0.0 \\ \frac{1}{2dy}(-f_0 + f_2) \\ \vdots \\ \frac{1}{12dy}(f_{j+2} + 28f_{j+1} - 28f_{j-1} - f_{j-2}) \\ \vdots \\ \frac{1}{2dy}(-f_{N-2} + f_N) \\ 0.0 \end{bmatrix}, \quad (24)$$

$$\begin{bmatrix} 1 & & & & & & \\ & 1 & & & & & \\ & \ddots & \ddots & \ddots & & & \\ & & 1 & 3 & 1 & & \\ & & & \ddots & \ddots & \ddots & \\ & & & & & 1 & \\ & & & & & & 1 \end{bmatrix} \begin{bmatrix} f'_0 \\ f'_1 \\ \vdots \\ f'_j \\ \vdots \\ f'_{N-1} \\ f'_N \end{bmatrix} = \begin{bmatrix} \frac{1}{2dy^2}(-7f_0 + 8f_1 - f_2) \\ \frac{1}{2dy^2}(f_0 - 2f_1 + f_2) \\ \vdots \\ \frac{1}{4dy^2}(3f_{j-2} + 48f_{j-1} - 102f_j + 48f_{j+1} + 3f_{j+2}) \\ \vdots \\ \frac{1}{2dy^2}(f_{N-2} - 2f_{N-1} + f_N) \\ \frac{1}{2dy^2}(-7f_{N-2} + 8f_{N-1} - f_N) \end{bmatrix}. \quad (25)$$

Table 1 shows the round-off error for the first derivatives schemes and the stencil size of 2^{nd} order explicit and 6^{th} order compact methods:

Schemes	Max L.H.S. Stencil Size	Max R.H.S. Stencil Size	Truncation Error
2^{nd} order - 1st derivatives	1	3	$-\frac{1}{6}h^2f^4$
2^{nd} order - 2nd derivatives	1	3	$-\frac{1}{12}h^2f^4$
6^{th} order compact - 1st derivatives	3	5	$\frac{1}{28}h^6f^7$
6^{th} order compact - 2nd derivatives	3	5	$-\frac{1}{2414}h^6f^8$

Table 1: Stencil size and round-off error.

The non-linear terms in Navier-Stokes equation can produce an numerical instability adding disturbances non physical of high frequency in the variables during the simulation. In order to remove a short length scales

a high-order compact filter was implemented in agreement with Lele, 1992. The numerical filter was applied in the last step of Runge-Kutta scheme. This filter consist in to recalculate the distribution of primitive variables through one 4^{th} compact scheme. These schemes can be solved through one pentadiagonal system as follow below

$$\begin{bmatrix} 1 & \alpha & \beta & & & & & \alpha & \beta \\ \beta & 1 & \alpha & \beta & & & & & \alpha \\ \alpha & \beta & 1 & \alpha & \beta & & & & \\ & \ddots & \ddots & \ddots & \ddots & \ddots & & & \\ & & \alpha & \beta & 1 & \alpha & \beta & & \\ & & & \ddots & \ddots & \ddots & \ddots & \ddots & \\ & & & & \alpha & \beta & 1 & \beta & \alpha \\ \alpha & & & & & \alpha & \beta & 1 & \beta \\ \beta & \alpha & & & & & \alpha & \beta & 1 \end{bmatrix} \begin{bmatrix} \widehat{f}_0 \\ \widehat{f}_1 \\ \widehat{f}_2 \\ \vdots \\ \widehat{f}_i \\ \vdots \\ \widehat{f}_{N-2} \\ \widehat{f}_{N-1} \\ \widehat{f}_N \end{bmatrix} = \tag{26}$$

$$\begin{bmatrix} \frac{d}{2}f_{N-3} + \frac{c}{2}f_{N-2} + \frac{b}{2}f_{N-1} + af_0 + \frac{b}{2}f_1 + \frac{c}{2}f_2 + \frac{d}{2}f_3 \\ \frac{d}{2}f_{N-2} + \frac{c}{2}f_{N-1} + \frac{b}{2}f_0 + af_1 + \frac{b}{2}f_2 + \frac{c}{2}f_3 + \frac{d}{2}f_4 \\ \frac{d}{2}f_{N-1} + \frac{c}{2}f_0 + \frac{b}{2}f_1 + af_2 + \frac{b}{2}f_3 + \frac{c}{2}f_4 + \frac{d}{2}f_5 \\ \vdots \\ \frac{d}{2}f_{i-3} + \frac{c}{2}f_{i-2} + \frac{b}{2}f_{i-1} + af_i + \frac{b}{2}f_{i+1} + \frac{c}{2}f_{i+2} + \frac{d}{2}f_{i+3} \\ \vdots \\ \frac{d}{2}f_{N-5} + \frac{c}{2}f_{N-4} + \frac{b}{2}f_{N-3} + af_{N-2} + \frac{b}{2}f_{N-1} + \frac{c}{2}f_0 + \frac{d}{2}f_1 \\ \frac{d}{2}f_{N-4} + \frac{c}{2}f_{N-3} + \frac{b}{2}f_{N-2} + af_{N-1} + \frac{b}{2}f_0 + \frac{c}{2}f_1 + \frac{d}{2}f_2 \\ \frac{d}{2}f_{N-3} + \frac{c}{2}f_{N-2} + \frac{b}{2}f_{N-1} + af_0 + \frac{b}{2}f_1 + \frac{c}{2}f_2 + \frac{d}{2}f_3 \end{bmatrix}, \tag{27}$$

where the coefficients of the system are given by

$$\alpha = 0.6522474,\ \beta = 0.1702929,\ a = 0.9891856,\ b = 1.3211800,\ c = 0.3333548,\ d = 0.001359850.$$

Implementation of the filtering schemes on domains with non-periodic boundaries requires the near boundary nodes to be treated separately. Therefore explicit near boundary formulas are

$$\widehat{f}_1 = \frac{15}{16}f_1 + \frac{1}{16}(4f_2 - 6f_3 + 4f_4 - f_5) \tag{28}$$

$$\widehat{f}_2 = \frac{3}{4}f_2 + \frac{1}{16}(f_1 + 6f_3 - 4f_4 + f_5) \tag{29}$$

$$\widehat{f}_3 = \frac{5}{8}f_3 + \frac{1}{16}(-f_1 + 4f_2 + 4f_4 - f_5) \tag{30}$$

The truncation error for these methods is shown in table below

Schemes	Max L.H.S. Stencil Size	Max R.H.S. Stencil Size	Truncation Error
27	5	7	$-\frac{1}{228}h^4f^4$
28	1	5	$\frac{3}{48}h^4f^4$
29	1	5	$\frac{11}{192}h^4f^4$
30	1	5	$-\frac{3}{48}h^4f^4$

Table 2: Stencil size and round-off error for numerical filter.

Time-advance of the computational variables (ρ,ρu_i,E_t) is obtained by the 4^{th} order Runge-Kutta method. The discretized transport equations are used to determine the values of the variables at each point of the computational domain at time $t_{n+1} = t_n + dt$. The schemes here described works in 4 steps (Ferziger and Peric, 1997). The first two steps use a formulation of Euler "predictor" explicit and a formulation of Euler "corrector" implicit for the same time $t + dt/2$. The following step is a "predictor" based on the rule of the medium point for the whole step $(t + dt)$ and the last, "corrector" is based on Simpson's rule. The combination of these steps results in a 4^{th} order accuracy algorithm.

3.4. Grid Stretching

The classical governing equations of fluid dynamics have been presented in section 3. These equations have been written in either vector or tensor form. These equations can be expressed in terms of any generalized orthogonal coordinate system. For many applications, a orthogonal coordinate system is desirable such as a shear layer problem. In this section, we will show how the governing equations can be transformed from a Cartesian coordinate system to any general orthogonal coordinate system. In this process, we will demonstrate how simple transformations can be used to cluster grid points in regions of large gradients and how to transform a non-rectangular computational region in the physical plane into a rectangular uniformly-spaced grid in the computational plane.

Flow-field has to precisely gridded because important variations of velocity and temperature are observed in this field. Therefore we would like to simulate some fields with axes y between $-Ly/2.0$ and $Ly/2.0$. In the points near free stream the field requires a resolution with less accuracy, while in the interior of the domain we need greater resolution. It is possible to realize a stretching of the grid to decrease number of points required.

In this work we use a formula coming from Anderson *et al.*, 1984 giving a constant stretching, with β, which is a stretching parameter and y_c, the locations, where this stretching is centered.

$$y = D\left\{1 + \frac{\sinh[\beta(\eta - A)]}{\sinh(\beta A)}\right\} \tag{31}$$

where

$$A = \frac{1}{2\beta}\ln\left[\frac{1 + (e^{\beta} - 1)(y_c/H)}{1 + (e^{-\beta} - 1)(y_c/H)}\right] \tag{32}$$

In order to apply this transformation to the governing equations, the following partial derivatives are formed. For the first derivatives we have the following simple relation

$$\frac{\partial f}{\partial y} = \frac{\partial f}{\partial \eta}\frac{\partial \eta}{\partial y} \tag{33}$$

where

$$\frac{\partial \eta}{\partial y} = \frac{\sinh(\beta A)}{\beta D\sqrt{1 + [(y/D) - 1]^2\sinh(\beta A)^2}} \tag{34}$$

This relation should be used with high-order compact schemes. Applying the relation 33 for derivatives approximations, we are obtained the following tridiagonal compact schemes for first derivatives

$$\alpha\psi'_{j-1}\left.\frac{\partial f}{\partial y}\right|_{j-1} + \psi'_j\left.\frac{\partial f}{\partial y}\right|_{j} + \alpha\psi'_{j+1}\left.\frac{\partial f}{\partial y}\right|_{j+1} = a\frac{f_{i+1} - f_{i-1}}{\delta\eta} + b\frac{f_{i+2} - f_{i-2}}{\delta\eta} \tag{35}$$

where $\psi'_j = \frac{1}{\partial\eta/\partial y}$.
The same procedure can be applied for the second derivatives

$$\frac{\partial^2 f}{\partial y^2} = \frac{\partial^2 \eta}{\partial y^2}\frac{\partial f}{\partial \eta} + \left(\frac{\partial \eta}{\partial y}\right)^2\frac{\partial^2 f}{\partial \eta^2} \tag{36}$$

where

$$\frac{\partial^2 \eta}{\partial y^2} = -\frac{\sinh(\beta A)^3(y/D - 1)}{[\beta D^2\sqrt{1 + [(y/D) - 1]^2\sinh(\beta A)^2}]^{\frac{3}{2}}} \tag{37}$$

Equation 36 can be rewritten as

$$\frac{\partial^2 f}{\partial \eta^2} = \frac{1}{\psi'^2}\frac{\partial^2 f}{\partial y^2} - \left[\frac{\psi''}{\psi'^2}\frac{\partial f}{\partial \eta}\right] \tag{38}$$

Using the relation $\frac{\psi''}{\psi'^2}\frac{\partial f}{\partial \eta} = \frac{\psi''}{\psi'^3}\frac{\partial f}{\partial y}$ and replacing the term in square brackets between hook in equation 38 we have

$$\frac{\partial^2 f}{\partial \eta^2} = \frac{1}{\psi'^2}\frac{\partial^2 f}{\partial y^2} - \frac{\psi''}{\psi'^3}\frac{\partial f}{\partial y} \tag{39}$$

Therefore, applying the relation 39 to the second derivative approximation we have the tridiagonal system as follow below

$$\alpha \frac{1}{\psi'^2_{j-1}} \frac{\partial^2 f}{\partial y^2}\bigg|_{j-1} + \frac{1}{\psi'^2_j} \frac{\partial^2 f}{\partial y^2}\bigg|_j + \alpha \frac{1}{\psi'^2_{j+1}} \frac{\partial^2 f}{\partial y^2}\bigg|_{j+1} = a\frac{f_{i+1} - f_{i-1}}{\delta\eta} + b\frac{f_{i+2} - f_{i-2}}{\delta\eta} + \frac{\psi''}{\psi'^3}\frac{\partial f}{\partial y} \tag{40}$$

Bogey *et al.*, 2000 recommend that the grid stretching should not exceed 1.8% in order to avoid problems with space derivatives. Another assumption of these methods is that the mesh must be sufficiently smooth so that $\partial y/\partial\eta$ and $\partial^2 y/\partial\eta^2$ can be defined, and, in practice, calculated without appreciable loss in the overall accuracy. For this simulation $\beta = 12$ was assumed. Other tests was performed with this parameter and this value showed the best results. With $\beta = 15$ the code presents a numerical instabilities in the time integration. These results will be discussed in the next sections.

4. Numerical Results

In this section, results from direct numerical simulations of the compressible Navier-Stokes equations are used to show the physics of the vorticity transport phenomenon in the linear and non-linear regime of the time-developing mixing layer problem. Firstly, an analysis of the amplification rate in the linear regime was performed to compared the growth rate obtained numerically with other theoretical results. These validation tests were extended to a regime governed by non-linear. First, it was simulated a flow using a small disturbance of a stipulated mode. In this case, it was possible to reproduce the vorticity phenomenon in streamwise direction. After, a subharmonic mode was introduced in the disturbance flow to develop the pairing that corresponding to the secondary instability. According to these studies was possible to confirm the strong reduction in shear layer growth rate as Mach number is increased. In all simulations here a non-uniform grid was used to reproduce the phenomenon, and consequently, an analysis of the efficacy of grid stretching was performed in these studies.

In these numerical investigations a relatively high Reynolds number was chosen to ensure that the viscous effects were small. The high Mach number was select to analyze the effects of compressibility in the evolution of two-dimensional disturbances. Moreover, a high-order compact finite-difference scheme was used to solve spatial derivatives. Time-advance of the computational primitives variables were obtained by a 4^{th} order explicit Runge-Kutta scheme. In x-direction, periodic boundary conditions were utilized, while in y-direction a free-slip condition was used. In order to remove short length scales, a 4^{th} order compact numerical filter was applied in x- and y-directions. The analysis of the filter implementation is show in the technical report given by Germanos and Medeiros, 2005.

4.1. Linear Stability

This section presents the evolution of two-dimensional sinusoidal disturbances in a free shear layer problem for the tangent hyperbolic profile in the regime governed by linear theory. The objective of this simulation was to compare the growth rate of the two-dimensional disturbances with other works. Theoretical results used in this paper were obtained through the temporal linear stability analysis carried out by Sandham and Reynolds, 1991. Here, simulations were performed to verify the effect of Mach number in the evolution of instabilities. These results confirm the prediction of linear stability theory that at low Mach numbers the two-dimensional instability waves are the most unstable.

An important aspect to be considered in these simulations is the treatment of the vertical diffusion. This diffusion increases the width of the free shear layer during the simulation, which implies a variation of the mean flow over time. Thus, there should be a variation of the amplification rate, even in the linear regime. The strategy adopted here to avoid this diffusion was to cancel the vertical diffusions terms for the base flow.

First the problem was simulated with Euler equations. In this case, the convective Mach number selected were 0.4 and 0.8. The mesh for these problems has a dimension of 40×80, that corresponds to the number of points in $x-$ and $y-$ directions. The grid spacing used in the simulation with a uniform mesh was $dx = 0.41$ and $dy = 0.30$, respectively, grid spacing in longitudinal and normal direction. In the non-uniform mesh in y-direction the minimum and maximum mesh spacing was $dy_{min} = 0.0089$ and $dy_{max} = 1.67$. The mesh spacing is constant in x-direction. Moreover, the initial amplitude of the disturbance was approximately 10^{-6}. This amplitude ensure that the phenomenon will start in regime governed by linear theory. The time step dt of this simulation was 10^{-3}. These tests were performed using a disturbance with only one mode. The wavenumber α of this disturbance was $\alpha_1 = 0.75$. This is close to the wavenumber of maximum amplification.

Figure 1 shows the growth rate of unstable waves at convective Mach number equals to 0.4 as a function of non-dimensional time. In this figure the vertical coordinate is in logarithm scale. The dashed-dotted line is the numerical result for a uniform grid. The amplification rate obtained from this line is about 0.27. The disagreement could be attributed to the numerical order generate by constant spacing grid used in these simulations.

The solid line shows the result for a non-uniform grid with a stretching parameter of $\beta = 12$. The growth rate in this line corresponds to an amplification rate of 0.30 which is in agreement with theoretical results.

Figure 2 presents the amplification rate at convective Mach number $M_c = 0.8$. Similar to the previous results, the dashed-dotted line gives an amplification rate of about 0.17 for uniform grid. The theoretical results for this convective Mach number shows a amplification rate about of 0.14. The solid line represents the same results with the use of a grid stretching. The growth rate obtained in this simulation was 0.15. This result is very close to the prediction. Based on these results we can observe that the amplification rate obtained in these simulations was significantly reduced with increasing of convective Mach number. These results confirm the reduction in the amplification rate for high Mach numbers. Therefore the agreement of these results is remarkable.

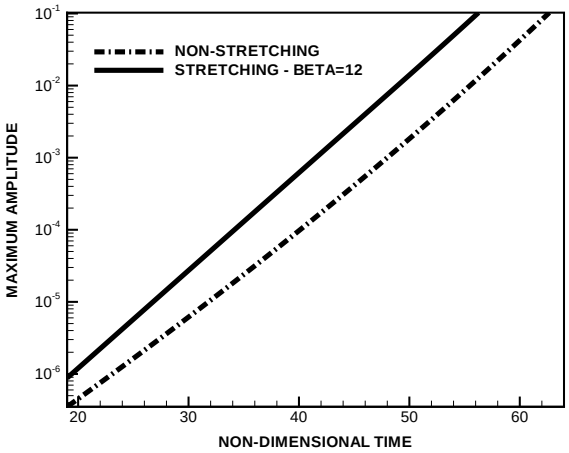

Figure 1: Amplitude evolution from inviscid flow at Mach number equals to 0.4 and wavenumber approximately to 0.75.

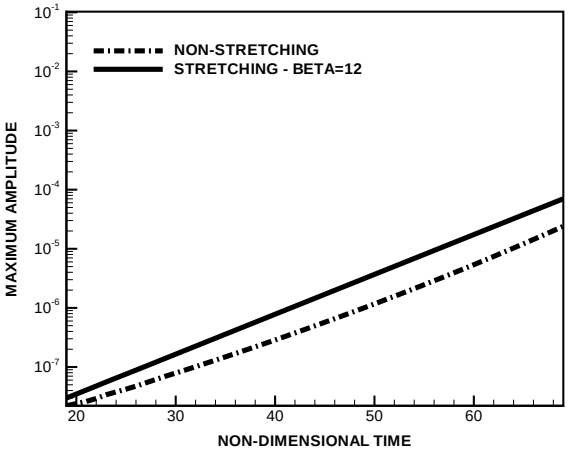

Figure 2: Amplitude evolution from inviscid flow at convective Mach number equals to 0.8 and wavenumber approximately to 0.75.

In the following, simulations for the compressible Navier-Stokes equations were performed. The initial amplitude of the disturbance of the dominant mode was the same as in previous simulations. The wavenumber of the disturbance selected for the simulations was $\alpha = 0.82$. This growth rate was chosen to compare the results with theoretical results. In figure 3 the dashed-dotted line show the time evolution of two-dimensional disturbance at convective Mach number equals 0.4 for a grid with constant spacing. The amplification rate obtained in these results is about 0.26. This is a underestimate rate compared to theoretical results that gives a amplification rate about 0.28. The solid line show a growth rate approximately of 0.29 with the use of grid stretching. Although these results be overestimate in relation to the theory, it is closed to the linear analysis. These results confirm that the simulations with grid stretching lead to improved amplification rate obtained numerically.

Figure 4 shows the time evolution for convective Mach number equals to 0.8 and Reynolds number equals to 500. The same analysis was made. The amplification rate generate for a uniform mesh was 0.14, while for a mesh with stretching the rate was approximately 0.13. Both results are close to the analytical results where gives a grow rate about 0.11. Furthermore, we can realize that using of grid stretching improved the agreement in the analysis of amplification rate. Emphasizes that the same number of points in y-direction was used to simulate the phenomenon with an uniform and non-uniform mesh. Therefore, the grid stretching significantly improves the accuracy for a number of grid points. Alternatively, the same numerical accuracy can be achieved with fewer grid points by clustering the points in the region of interest thus reducing computational cost.

4.2. Non-linear Stability

For the a numerical investigations discussed here, the full compressible Navier-Stokes equations were considered to analyze the problem in the non-linear regime. The evolution of a small two-dimensional disturbance in shear layer was performed in a non-uniform grid. This grid allows fro greater resolution in the interior of the computational domain where the instability phenomenon occurs. Consequently, the numerical error in this zone is reduced due to the refinement of the grid. Another aspect considered here is that the grid is stretched in zones close to the boundaries where the instabilities waves have decayed. In order to verify the code, simu-

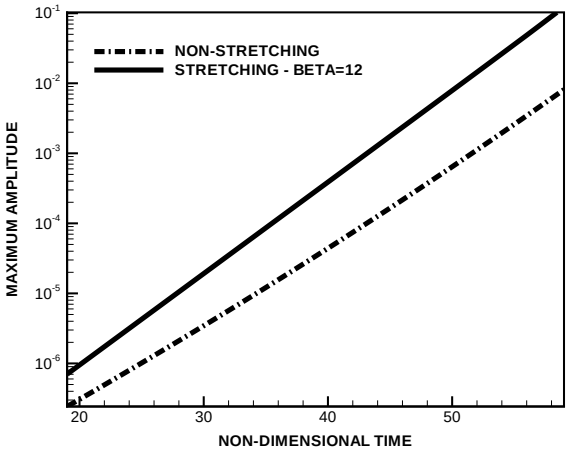

Figure 3: Amplitude evolution from inviscid flow at convective Mach number equals to 0.4 and wavenumber approximately to 0.75.

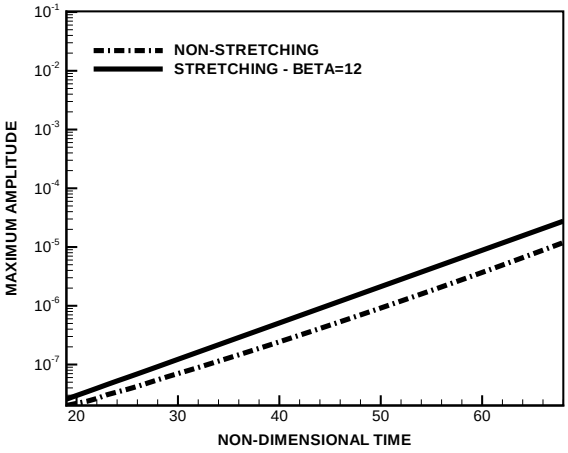

Figure 4: Amplitude evolution from inviscid flow at convective Mach number equals to 0.8 and wavenumber approximately to 0.75.

lations were carried out to reproduce the secondary instability mechanism. According to the theory a pairing phenomenon produces waves that propagate towards the boundaries. These waves can be reflected from the boundaries resulting in a non-physical distortion of the numerical results. The grid stretching can prevent that these waves reaches the boundaries, rendering the code more stable in time-advancement.

As a first step, the simulation of the compressible Euler equations for a two-dimensional flow was performed. The objective here is to determine the maximum allowable grid stretching for which the computational remains stable. For this problem a mesh with a dimension of 40×80, number of points in x- and y-direction was chosen. The grid spacing used in this simulation for a uniform mesh was $dx = 0.50$ and $dy = 0.30$, respectively, grid spacing in longitudinal and normal direction. For non-uniform grid the minimum and maximum spacing in y-direction was $dy_{min} = 0.0089$ and $dy_{max} = 1.67$. Mesh spacing is constant in the x-direction. The initial amplitude of the disturbance was approximately 10^{-6}. This value satisfies the CFL condition. The wavenumber of the disturbance selected for the simulation was $\alpha_1 = 0.75$ for dominant mode and $\alpha_2 = \alpha_1/2$ for the subharmonic mode. This is close to the wavenumber of maximum amplification. Figure 5 show the non-linear evolution of the disturbances in time for a uniform mesh. In this figure, the coordinate z presents the vorticity component in the x-direction. It can be observed that the shear region produces waves that propagate towards the free stream boundaries. This production of sound waves is undesirable and has to be minimized.

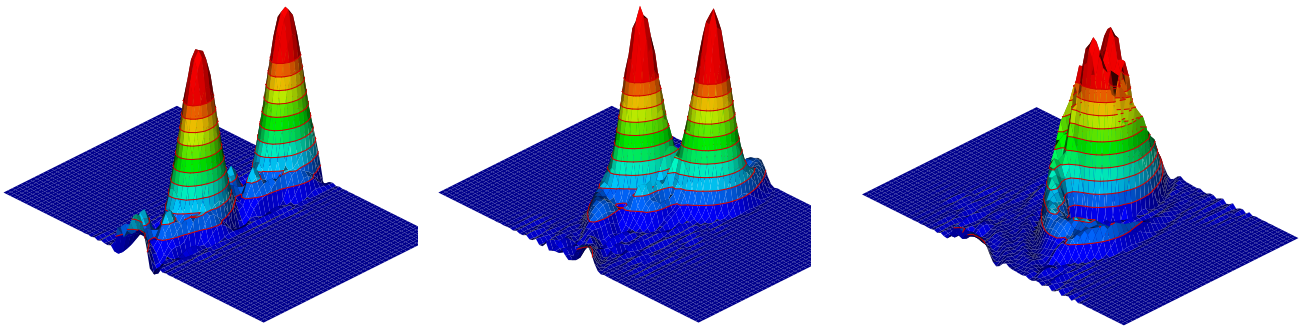

Figure 5: Amplitude evolution from inviscid flow at convective Mach number equals to 0.4 and wavenumber approximately to 0.89. The subharmonic mode was introduced here to reproduce the secondary instability. A uniform grid in the y-direction was used in these simulations. The frames presented correspond to the non-dimensional times 60, 68 and 78.

Figure 6 shows the evolution of the same problem on a non-uniform grid. Different from the stretching parameter used for the linear regime, the stretching parameter chosen for the non-linear regime was $\beta = 10$. Many values for this parameter have been tested and this value presents the best results in relation computational efficiency, without causing numerical problems with the spatial derivatives. It can be seen in this figure that the formation of sound waves in the shear zone was strongly reduced with the application of stretching. In figure 7 we can seen a simulation with the application of $\beta = 15$. In this case, the numerical scheme becomes unstable in time. These results confirm that the grid stretching cannot exceed 1.8% of the maximum grid lengths.

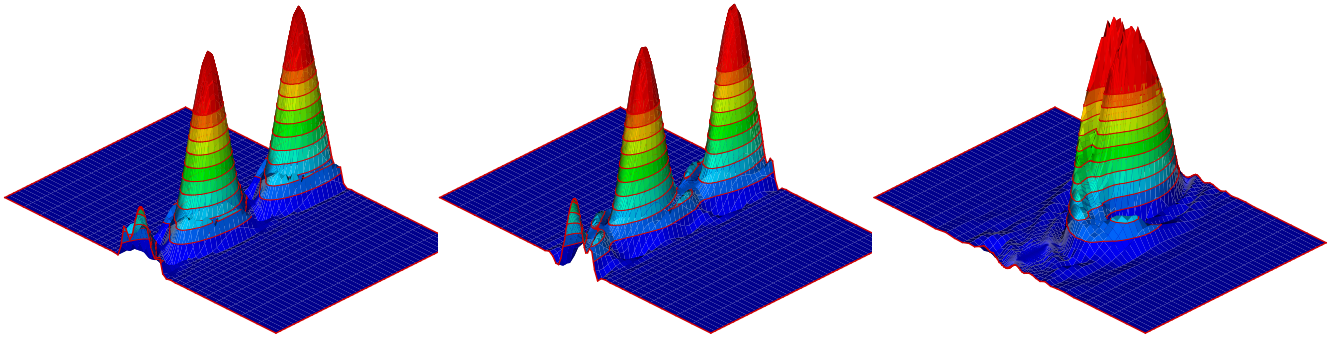

Figure 6: Amplitude evolution from inviscid flow at convective Mach number equals to 0.4 and wavenumber approximately to 0.89 for a non-uniform grid. The disturbance here was composed of a fundamental and subharmonic mode. A non-uniform grid in y-direction was used in these simulations and the stretching parameter was selected by $\beta = 12$. The frames presented correspond to the non-dimensional times 60, 68 and 96.

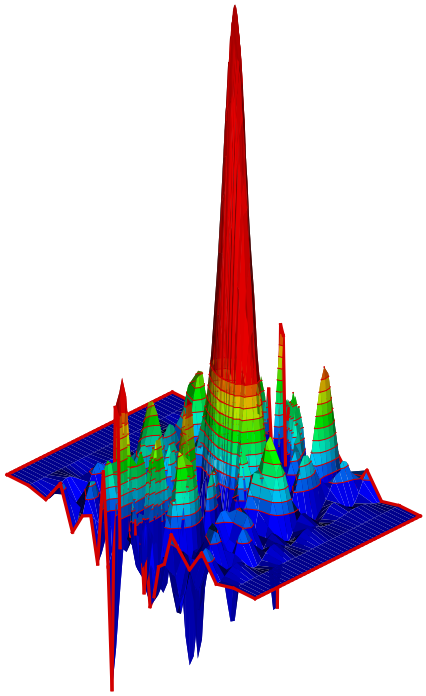

Figure 7: Amplitude evolution from inviscid flow at convective Mach number equals to 0.4 and wavenumber approximately to 0.89 for a non-uniform grid. The disturbance here was composed of a fundamental and subharmonic mode. A non-uniform grid in y-direction was used in this simulations and the stretching parameter was selected as $\beta = 15$. The frame presented corresponds to the non-dimensional time of 96.

More tests were performed for the evolution of non-linear instabilities. Here the non-linear tests were carried out to verify the code when the disturbances have reached large amplitudes. In this case, the non-linear effects

need to be considered. The theory associated with these effects is more complex than for small-amplitude, linear disturbances and will not be present here. Previews of the subject can be found in Herbert, 1988 and Medeiros, 2000. The summary of the main results, given below, is enough for carrying out the tests proposed. Both theory and experiment show that in a shear layer the disturbance does not grow to infinity. Instead this disturbance satures in a limit cycle pattern of co-rotating vortices. In turn, the vortices are themselves unstable to a subharmonic disturbance. It means that if a subharmonic oscillation exists in the flow this oscillation will grow. The result is a pairing of vortices. It is important to emphasize that in the system there is no mechanism for the production of subharmonic disturbances, but only for amplification. In the numerical solution of the equations of motion, this seeding of subharmonic waves may come from round-off error. The growth of subharmonic provides a good indication of the numerical error of CFD codes.

The simulations performed for this analysis employ the full compressible Navier-Stokes equations, including the viscous terms. The initial disturbance amplitude of the dominant and subharmonic mode was the same that in the previous studies. First, the disturbance was composed of only one mode with wavenumber $\alpha = \pi/4$. Figure 8 shows a sequence of the evolution of two-dimensional disturbances over time. Initially in the linear regime, the disturbance is very small and display a sinusoidal pattern. The fundamental mode grows and two satures vortices are formed, which corresponds to the limit cycle oscillation. The vortices dissipate due to viscous effects. Under these circumstances the non-linear theory predicts no pairing. Although there are no tendency of pairing, but at very late times a pairing occurs. Figure 9 shows, that indeed, the vortices take a rather long time to pair. It occurred only when the vortices were almost entirely dissipated by viscous effects. Since the subharmonic excitation was not excited, the explanation for this behavior is that the subharmonic seed for the pairing must have arisen from numerical error.

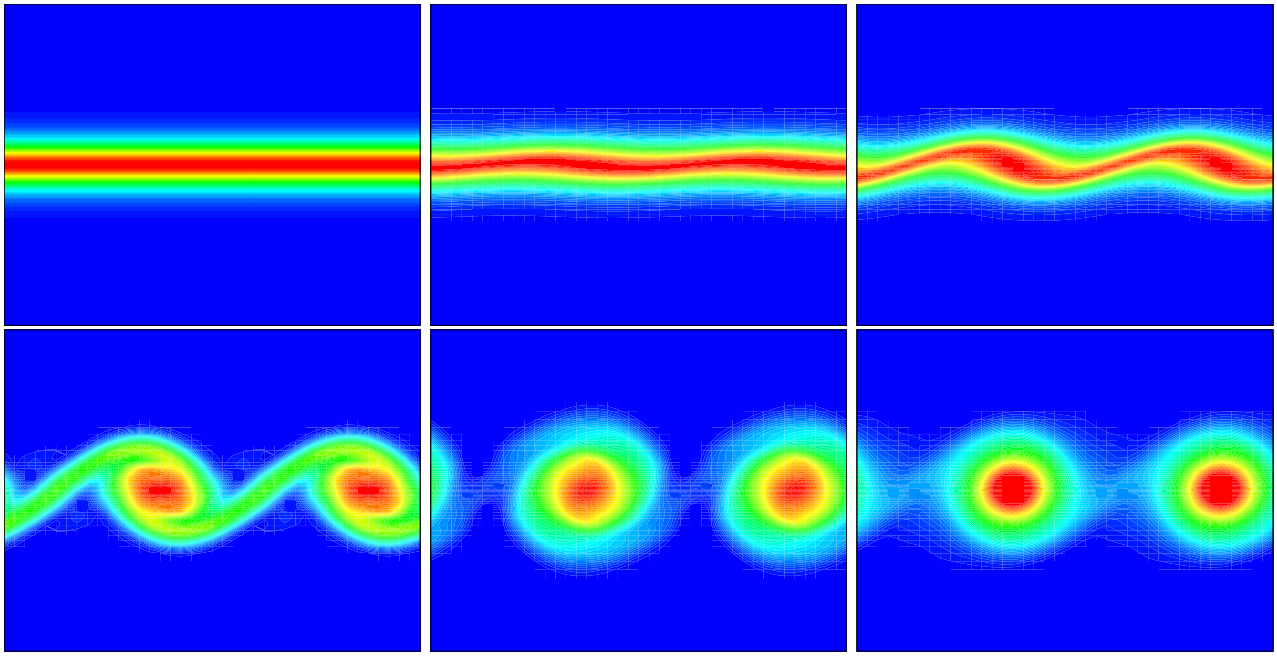

Figure 8: The linear and nonlinear two-dimensional evolution of disturbance composed of a dominant mode. A non-uniform grid in y-direction was used in these simulations. The frames presented correspond to the non-dimensional times 10, 55, 60, 65, 75 and 100

The following simulations were performed with the deliberate introduction of a subharmonic perturbations. The wavenumber of the disturbance selected for the simulation was $\alpha_1 = 0.82$ for fundamental mode, and $\alpha_2 = \alpha_1/2$ for the subharmonic mode. The characteristics of the flow in first stages were identical to the previous test. In this case the same behavior can be seen in figure 10. In the initially stage a sinusoidal growth was displayed. After the fundamental mode arises and saturates, the subharmonic mode grows and two of the primary structures begin to rotate around each other. After, the pairing occurs between these two vortices and one large vortex results. In this case, the pairing occurs due a excited subharmonic disturbance rather than numerical error. As result that the pairing occurs in earlier non-dimensional time of approximately 105. In the previous simulation the same phenomenon occurs for non-dimensional time approximately 200. These results indicate that the secondary instability was trigged by growing of the numerical error, which was very small compared to the amplitude of the perturbations introduced.

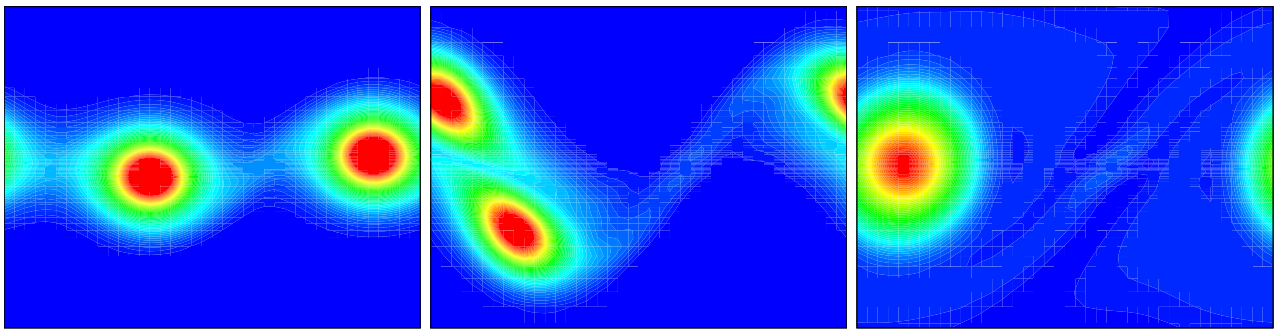

Figure 9: The linear and nonlinear two-dimensional evolution of disturbance composed of a dominant mode. A non-uniform grid in y-direction was used in these simulations. The frames presented correspond to the non-dimensional times 140, 150 and 200

Results for convective Mach number equals to 0.6 are shown in sequence 11. The first frame shows the flow at non-dimensional time equals to 55. Here the two-dimensional disturbances excited by the fundamental mode is not evident. At the same time, it can be observed in the sequence of $M_c = 0.4$ that the flow presents a sinusoidal pattern. In order words, at this stage the disturbance at $M_c = 0.4$ grows faster than the disturbance at $M_c = 0.6$. Proceeding with this analysis at $M_c = 0.6$, it can be observed in the second frame that the fundamental mode grows becoming more clear for non-dimensional time equals to 73. The next frame presents the structures of co-rotating vortices before a merger at time about 85. The previous results at $M_c = 0.4$ show the same phenomenon at an earlier time of 65. Later the disturbance excited by the subharmonic perturbation become evident leading to the pairing which occurs at time of 117. At $M_c = 0.4$ the same phenomenon occurred at a time of about 100. According to these studies we can conclude that the amplification rate is strongly reduced as the convective Mach number is increased.

This analysis was extended to the case of a convective Mach number of 0.8 where compressibility effects become important, as shown in figure 12. An interesting behavior can be observed in this sequence. First we can seen that the growth rate of two-dimensional waves is strongly reduced with the convective Mach number is increased. According to this sequence we can realize that the fundamental mode grows and are displayed with more clear at non-dimensional time of 115. This delay correspond a 52% of time that occurs the same behavior at convective Mach number of 0.4. Once again the amplification rate was reduced at high convective Mach numbers in accordance with theory. Another aspect can be analyzed for this simulation. The plots of vorticity show a clear change in structure as the convective Mach number is raised. The vortices become very elongated in the streamwise direction at convective Mach number of 0.8. A physical explanation of the shape change will now be suggested. A fluid element approaching the structure from the upper left-hand-side experiences an expanding flow, and a reduction in vorticity, until it is alongside the vortex. Then the element is subject to a compression, with an associated increase in vorticity as it approaches the trailing edge of the vortex, and the stagnation region behind. A similar process affects fluid elements approaching from the lower right-hand-side. The overall effect is that vorticity above and below the vortex is reduced, and vorticity in front and behind the vortex is increased, leading to a structure elongated in the streamwise direction. The elongated vortex does not wrap any new fluid around the structure, and it cannot then be engulfed and mixed, and there is only growth by viscous diffusion. The circular vortex wraps fluid from the free streams around itself, and grows strongly. If we assume a monotonic trend we see that the effect of an elongated vortex is to reduce the growth rate of the shear layer.

5. Conclusions

In this work the numerical simulation of a compressible free shear layer was performed. The governing equations were the compressible Navier-Stokes equations. A 6^{th} order compact finite-difference scheme was used for discretizing the spatial derivatives. In order to remove a short length scales, a $4th$ order compact filter was implemented. The method adopted was time accurate, using a 4^{th} order Runge-Kutta scheme. A free-slip boundary condition was used in y-direction. As well as a exponential decay condition in y-direction. Periodic boundary condition was implemented in x-direction. Lastly, these simulations were carried out on a

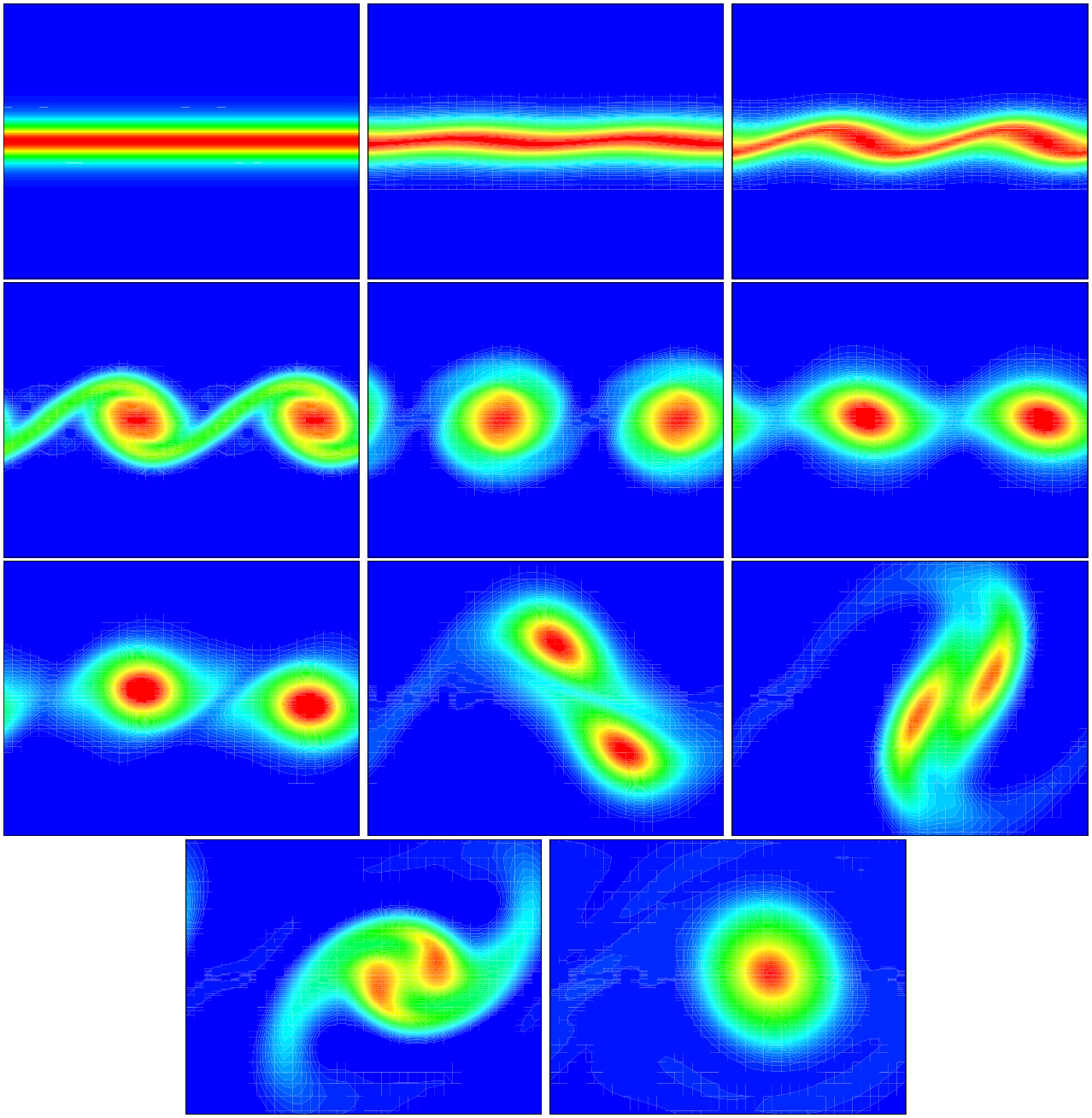

Figure 10: The linear and nonlinear two-dimensional evolution of disturbance composed of a dominant mode and a subharmonic mode at convective Mach number equals to 0.4. A non-uniform grid in y-direction was used in these simulations. The frames presented correspond to the non-dimensional times 30, 55, 60, 65, 70, 80, 90, 100, 105, 110 and 165.

non-uniform grid. This technique was utilized to remove sound waves produced by the pairing that occurs due a secondary instability. These waves can propagate in normal direction forwards free stream boundaries and might be reflected back contaminating the numerical solution.

The compressible shear layer flow was simulated giving some interesting results. In the linear regime was possible to obtain an good amplification rate with the use of stretching in y-direction. This non-uniform grid allows for a high resolution in the interior of the domain. The growth rate for uniform and non-uniform grids was analyzed and the cases with a grid stretching show the best results. Also, the effect of the convective Mach number on the growth rate of two-dimensional disturbances was analysis. The results confirm a reduction in the growth rate for high convective Mach numbers as also predicted linear theory stability.

For simulations in the non-linear regime the results were very interesting and it was possible reproduce some

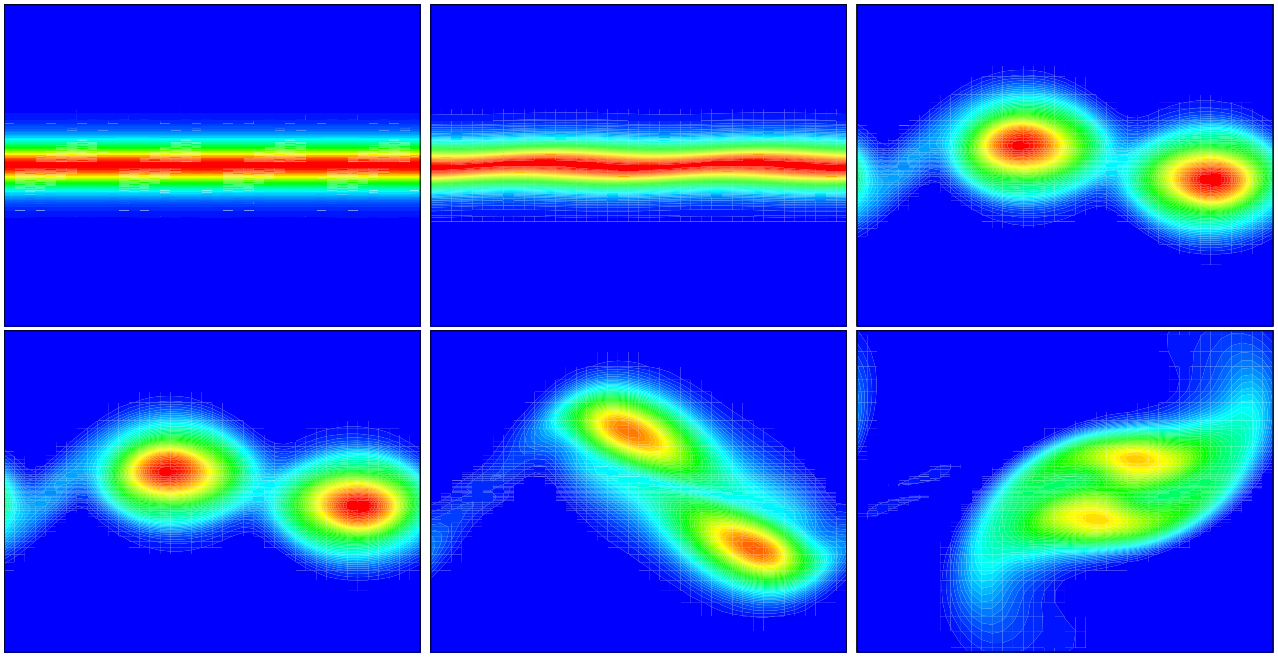

Figure 11: The linear and nonlinear two-dimensional evolution of disturbance composed of a dominant and a subharmonic mode at convective Mach number equals to 0.6. A non-uniform grid in y-direction was used in these simulations. The frames presented correspond to the non-dimensional times 55, 73, 85, 110, 117 and 128.

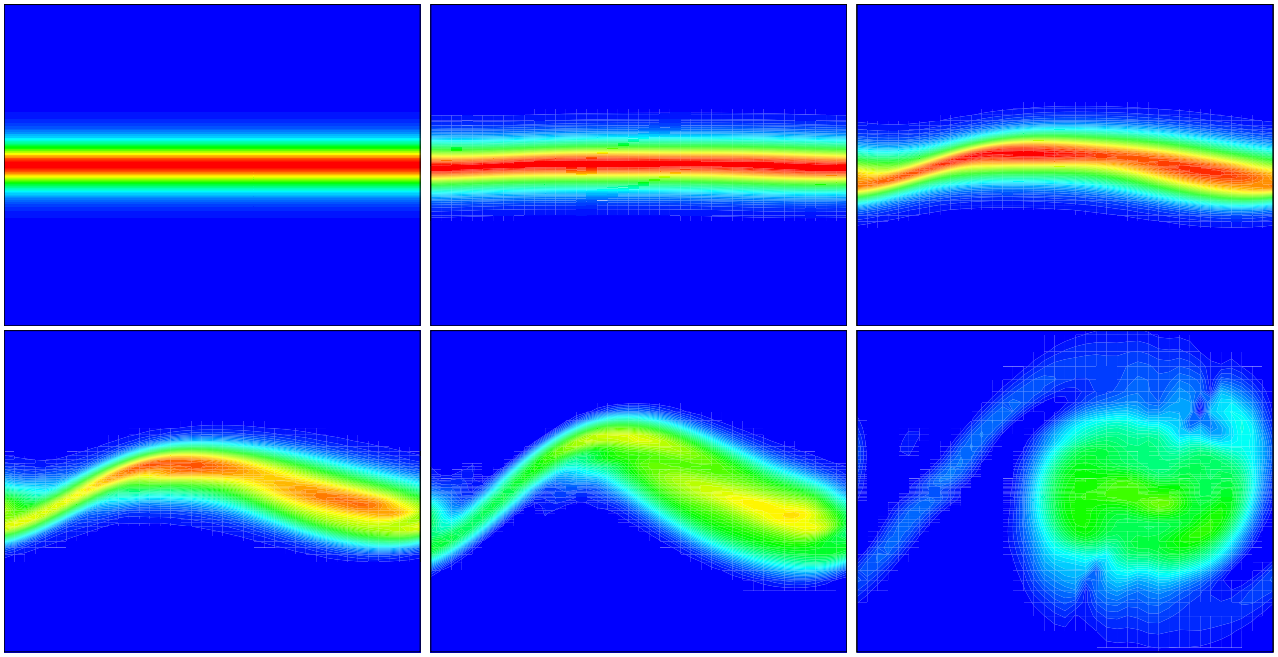

Figure 12: Linear and nonlinear two-dimensional evolution of disturbances composed of a fundamental mode and a subharmonic mode at convective Mach number equal 0.8. A non-uniform grid in y-direction was used in these simulations. The frames presented correspond to the non-dimensional times 30, 115, 125, 133, 160 and 170.

important physical phenomena. First, the effects of the grid stretching was analyzed. Test was performed to verify the efficiency of grid stretching in damping at undesirable sound waves produced by the shear zone. In this analysis we observed that these waves were strongly reduced in the direction towards the boundaries, if grid stretching was applied.

Following the evolution of disturbances composed of a dominant mode were presented. In these simulations

the two-dimensional disturbances show a sinusoidal pattern and structure of vortices forming until the limit cycle oscillation. Lastly it was introduced a subharmonic mode, and this way, it was possible to reproduced the secondary instability. In this case, a pairing occurs between the two vortices and one large vortice results. From these results it was possible to verify the effect of the convective Mach number on the amplification rate of two-dimensional waves. These results confirm that the growth rate were strongly reduced as the Mach number was increased. This behavior is in agreement with other studies of hydrodynamic instability in compressible shear layers and the authors of this work concluded that the results for all cases were very good.

6. Acknowledgments

The financial support from FAPESP (State of São Paulo Research Support Foundation) – Grant number 02/09256-3 is greatly acknowledged.

7. References

Anderson, D. A., Tannehill, J. C., and Pletcher, R. H., 1984, "Computational Fluids Mechanics and Heat Tranfer", Hemisphere Publishing Corporation.

Bernal, L. and Roshko, A., 1986, Streamwise vortex structure in plane mixing, "J. Fluid Mech.", Vol. 170, pp. 429–525.

Birch, S. F. and Eggers, J. M., 1973, A critical review of the experimental data for developed free turbulent shear layers., "NASA SP", Vol. 321, pp. 11–40.

Blumen, W., Drazin, P. G., and Billings, D. F., 1975, Shear Layer instability of an inviscid compressible fluid. Part 2, "J. Fluid Mech.", Vol. 71, pp. 305–316.

Bogey, C., Bailly, C., and Juve, D., 2000, Numerical Simulation of Sound Generated by Vortex Pairing in a Mixing Layer., "AIAA Journal", Vol. 38, pp. 2210–2218.

Brown, G. L. and Roshko, A., 1974, On density Effects and Large Structure in Turbulent Mixing Layer, "J. Fluid Mech.", Vol. 64, pp. 775–816.

Canuto, C., Hussaini, M. Y., Quarteroni, A., and Zang, T. A., 1987, "Spectral Methods in Fluid Dynamics".

Collatz, L., 1966, "The numerical treatment of differential equations", Springer-Verlag, New York.

Colonius, T., Lele, S. K., and P., M., 1997, Sound generation in a mixing layer, "J. Fluid Mech.", Vol. 330, pp. 375–409.

Eibler, W. and Bestek, H., 1996, Spatial Numerical Simulations of Linear and Weakly Nolinear Wave Instabilities in Supersonic Boundary Layers, "Theoretical and Computational Fluid Dynamics", Vol. 8, pp. 219–235.

Ferziger, J. H. and Peric, M., 1997, "Computational methods for fluid dynamics", Springer.

Fortuné, V., 2000, "Étude par Simulation Numérique Directe du rayonnement acoustique de couches de mélange isothermes et anisothermes", PhD thesis, Université de Poitier.

Germanos, R. A. C. and Medeiros, M. A. F., 2004, Simulação Numérica da Transição para Turbulência em uma Camada Limite Compressível sobre uma Placa Plana, 1º relatório técnico fapesp, Universidade de São Paulo - USP.

Germanos, R. A. C. and Medeiros, M. A. F., 2005, Simulação Numérica da Transição para Turbulência em uma Camada Limite Compressível sobre uma Placa Plana, 2º relatório técnico fapesp, Universidade de São Paulo - USP.

Germanos, R. A. C. and Medeiros, M. A. F., 2006, Simulação Numérica da Transição para Turbulência em uma Camada Limite Compressível sobre uma Placa Plana, 4º relatório técnico fapesp, Universidade de São Paulo - USP.

Germanos, R. A. C., Medeiros, M. A. F., and de Souza, L. F., 2004, Development of a computational code for studying compressible shear layer flow instabilities, "IV school of transition and turbulence".

Herbert, T., 1988, Secondary instability of boundary layers, "Ann. Rev. Fluid Mech.", Vol. 20, pp. 487–526.

Kloker, M., Rist, R., and Fasel, H., 1993, Outflow boundary conditions for spatial Navier-Stokes simulations of boundary layer transition, "AIAA J.", Vol. 31, pp. 620–628.

Kopal, Z., 1961, "Numerical Analysis", Wiley, New York.

Lele, S. K., 1992, Compact finite difference schemes with spectral-like resolution, "J. Comp. Phys.", Vol. **103**, pp. 16–42.

Lesieur, M., 1997, "Turbulence in fluids, (third edition)", Kluwer Academic Publisher.

Lessen, M., Fox, J. A., and Zien, H. N., 1966, Stability of the laminar Mixing of two Parallel Streams with respect to Supersonic Disturbances, "J. Fluid Mech.", Vol. 25, pp. 737–742.

Mahesh, K., 1998, A Family of High Order Finite Difference Schemes Spectral Resolution, "J. Comp. Phys.", Vol. **145**, pp. 332–358.

Medeiros, M. A. F., 2000, nonlinear hydrodynamic instability, "II school of transition and turbulence", pp.

312–357, Uberlândia – Brazil. in portuguese.

Medeiros, M. A. F., Silvestrini, J. H., and Mendonça, M. T., 2000, Using Linear and non Linear Stability Theory for Evaluating Code Accuracy, "II school of transition and turbulence".

Metcalfe, R., Orszag, S., Brachet, M., Menon, S., and Riley, J., 1987, Secondary instability of a temporally growing mixing layer, "J. Fluid Mech.", Vol. 184, pp. 207–243.

Michalke, A., 1964, On the instability of the hyperbolic-tangent velocity profile, "DVL-Institut für Turbulenzforschung, Berlin", pp. 543–556.

Papamoschou, D. and Roshko, A., 1988, The compressible turbulent mixing layer: an experimental study, "J. Fluid Mech.", Vol. **197**, pp. 453–477.

Rayleigh, L., 1880, On the stability, or instability, of certain fluid motions, "Proc. London Math. Soc.", Vol. 11, pp. 57–70.

Sandham, N. D. and Reynolds, W., 1989, Compressible Mixing Layer: Linear Theory and Direct Simulation, "AIAA Journal", Vol. 28, pp. 618–624.

Sandham, N. D. and Reynolds, W., 1991, Three-dimensional simulations of large eddies in the compressible mixing layer, "Journal of Fluids MEchanics", Vol. 224, pp. 133–158.

Souza, L. F., 2003, "Instabilidade centrífuga e transição para turbulência em escoamentos laminares sobre superfície côncava.", PhD thesis, Instituto Tecnológico de Aeronaútica, São José dos Campos - SP.

Souza, L. F., Mendonça, M. T., de Medeiros, M. A. F., and Kloker, M., 2002a, Analisys of Tollmien-Schlichting waves propagation on a flat plate with a Navier-Stokes solver, "9th brazilian congress on thermal engineering and sciences".

Souza, L. F., Mendonça, M. T., de Medeiros, M. A. F., and Kloker, M., 2002b, Three dimensional code validation for transition phenomena, "III Escola de Transição e Turbulência".

Souza, L. F., Mendonça, M. T., and Medeiros, M. A. F., 2002c, Assessment of Different Numerical Schemes and Grid Refinement for Hydrodynamic Stability Simulations, "ENCIT 2002", Campinas - SP.

Strang, G., 1988, "Linear Algebra and its applications.", HBJ.

Thompson, K. W., 1987, Time depedent boundary conditions for hyperbolic systems, "J. Comput. Phys.", Vol. 68, pp. 1–24.

White, F. M., 1974, "Viscous Fluid Flow, (First Edition)", McGraw-Hill.

Williamson, J. H., 1980, Low-storage Runge-Kutta Schemes, "J. Comp. Phys.", Vol. 35, pp. 48–56.

Proceedings of the 11th Brazilian Congress of Thermal Sciences and Engineering -- ENCIT 2006
Braz. Soc. of Mechanical Sciences and Engineering -- ABCM, Curitiba, Brazil, Dec. 5=8, 2006

Paper CIT06-0317

APLICAÇÃO DO MÉTODO DA ESTEIRA DE VÓRTICES GENERALIZADO A UM AEROFÓLIO SUJEITO A RAJADAS E MOVIMENTO HARMÔNICO

Fabiano Hernandes
Instituto Tecnológico de Aeronáutica
12228-900 São José dos Campos - SP
f_hernandes@bol.com.br

Paulo Afonso de Oliveira Soviero
Instituto Tecnológico de Aeronáutica
12228-900 São José dos Campos - SP
soviero@ita.br

Resumo. *São estudados os efeitos aerodinâmicos (coeficientes de pressão e sustentação) em um perfil fino penetrando em rajadas discretas dos tipos um-menos-cosseno e senoidal, e também cargas devido movimento harmônico de translação lateral. Análises aeroelásticas de resposta a rajada requerem um modelo aerodinâmico para aeronave a medida que esta penetra numa rajada atmosférica. Tradicionalmente dois métodos são usados para cálculo das cargas aerodinâmicas: os de domínio no tempo e os de domínio na frequência. O presente trabalho usa uma abordagem numérica, no domínio do tempo, baseada na singularidade vórtice.Os resultados hoje disponíveis na literatura são baseados em equações exponenciais aproximadas ou cálculados via Dinâmica do Fluidos Computacional (CFD). Assim, o método proposto pretende um cálculo mais acurado em relação aos que utilizam equações aproximadas e bem mais rápido do que aqueles feitos via CFD. Resultados são obtidos para escoamento em um meio compressível subsônico e supersônico.*

Palavras chave: rajada um-menos-cosseno, rajada senoidal, movimento harmônico, singularidade vórtice, escoamento não permanente.

1. Introdução

Ao longo da década passada o Método de Rede Turbilhonar Generalizado (Generalized Vortex Lattice Method) foi desenvolvido para o caso não estacionário, inicialmente no regime subsônico (Soviero, 1993) e posteriormente nos regimes supersônico (Soviero e Ribeiro, 1995) e transônico (Soviero e Pinto, 2001). Em todos os casos anteriores o movimento do perfil, tanto em translação lateral como em movimento angular de arfagem, é restrito ao movimento harmônico e, deste modo, o cálculo é efetuado no domínio da freqüência e não do tempo.

Se o objeto de estudo for à previsão de cargas aerodinâmicas devidas a movimentos arbitrários a única maneira prática de obtê-las é, segundo Bisplinghoff *et al*. (1955), através da superposição de integrais de Fourier dos resultados obtidos para movimentos harmônicos. No entanto, tal metodologia não é adequada para movimentos bruscos os quais podem ocorrer durante manobras de aviões de alto desempenho, rajadas ou deflexões rápidas de superfícies de comando, tais como os ailerons, pois nestes casos o número de termos da série a serem empregados pode se tornar proibitivamente elevados em função da lenta convergência da resposta ao movimento estudada.

No regime incompressível são clássicos os estudos de Wagner (1925) e Küssner (1936) que obtiveram a evolução com o tempo da sustentação em perfis finos para a variação instantânea do ângulo de ataque e da penetração do perfil em uma rajada de canto vivo; ambas, de fato, respostas indiciais. No regime compressível tanto subsônico quanto supersônico uma série de respostas indiciais são apresentadas por Bisplinghoff *et al.* (1955) em função do número de Mach para perfis finos. No entanto a obtenção analítica destas respostas indiciais é longa e tediosa sugerindo a busca por soluções numéricas suficientemente rápidas e gerais.

Assim, o estudo e desenvolvimento de um método numérico que permita a obtenção das forças e momentos aerodinâmicos para um perfil em movimento arbitrário são atrativos. A fim de preencher essa lacuna foi desenvolvida (Hernandes e Soviero, 2004) uma metodologia baseada na singularidade vórtice para obtenção das forças aerodinâmicas para um movimento qualquer. Neste trabalho, Hernandes e Soviero calcularam as chamadas respostas indiciais do perfil, sendo elas a função degrau unitário e a rajada de canto vivo. Posteriormente (Hernandes e Soviero, 2005), utilizando mesma metodologia, foram estudados os efeitos aerodinâmicos de um perfil fino penetrando em uma rajada de canto vivo (para diversas razões de velocidades de rajada) e também estudado a interação do perfil com um vórtice livre que passa sob o perfil – fenômeno conhecido na literatura como AVI (*Airfoil-Vortex Interaction*).

No presente trabalho é utilizada a mesma metodologia (Hernandes e Soviero, 2004) com adequações nas condições de contorno aplicadas. Condições de contorno são estabelecidas para os movimentos das rajadas discretas um-menos-

cosseno e menos-seno, e também para movimento harmônico de translação lateral. São resultados os coeficientes de pressão e sustentação ao longo do tempo.

Até a década de 50 o critério para cálculo de cargas devido à presença de rajadas em aeronaves (ou perfis) era baseado no modelo de rajada de canto vivo, ou seja, a aeronave abruptamente sofre um acréscimo de velocidade vertical com intensidade definida. Com a evolução das aeronaves, crescimento das dimensões e aumento das velocidades, ficou evidente a necessidade de considerar uma resposta dinâmica-estrutural. Foi definido um perfil mais adequado de rajada discreta (representando melhor as rajadas existentes na atmosfera) para análises de corpo rígido e dinâmica-estrutural. O perfil definido foi o chamado um-menos-cosseno, que é o perfil aqui estudado. Alguns autores também estudam o perfil menos-seno, e este também é aqui calculado. Noback (1986), Pratt e Walker (1954), Flomenhoft (1994) e Fuller (1995) são boas referências da evolução histórica dos perfis de rajada utilizados nos projetos de aeronaves.

Ainda no presente trabalho é estudado o movimento harmônico de translação lateral, isto é, um perfil fino rígido submetido, sem variação de seu angulo de ataque, a um movimento harmônico. No presente trabalho foi calculada somente a parcela real dos coeficientes aerodinâmicos. Estudos estão sendo realizados para completar os resultados com a parcela imaginária, visto que a maior parte dos métodos no domínio da freqüência e resultados disponíveis na literatura calculam ambas parcelas: real e imaginária. Resultados existentes na literatura para o assunto são os clássicos Theodorsen (1935) e Bisplinghoff *et al.* (1955).

2. Rajadas Discretas

2.1. Rajada um-menos-cosseno (1-cos)

Considere um perfil fino, com ângulo de incidência nulo, imerso num meio com velocidade uniforme U. O perfil então é submetido a uma rajada de intensidade, $U_{1-\cos}(s)$, conforme perfil chamado um-menos-cosseno. O perfil da rajada discreta um-menos-cosseno é definido como:

$$U_{1-\cos}(s) = \begin{cases} \dfrac{\overline{U}_{1-\cos}}{2}\left[1-\cos\left(\dfrac{2\pi s}{2H}\right)\right] & ,\ 0 \le s \le 2H \\ 0 & ,\ s > 2H \end{cases} \tag{1}$$

Onde s denota a distância adimensional de penetração da rajada, $s = Ut/c$. A intensidade da rajada é definida por $\overline{U}_{1-\cos}$, sendo no presente trabalho adotado $U = \overline{U}_{1-\cos}$. Em projetos de aeronave essa intensidade tem valores da ordem de 30 ft/s a 350 ft/s. H denota o gradiente de rajada, ou seja, a distância paralela ao eixo de deslocamento da rajada onde ocorre a intensidade máxima da rajada, e possui no presente estudo a mesma dimensão da corda do perfil, c. Em projetos deve-se usar um número significativo de valores de H, de forma a determinar valores críticos que maximizam a carga no perfil (ou aeronave). Nos problemas aqui estudados serão usados valores de $2H = 5$ e $2H = 25$. Os resultados são comparados com dados obtidos por Raveh e Zaide (2005) onde foram obtidos resultados para rajada um-menos-cosseno a partir de um processo de convolução de dados obtidos por CFD (dinâmica dos fluidos computacional) para rajada de canto vivo. A Fig. 1 ilustra o problema da rajada um-menos-cosseno.

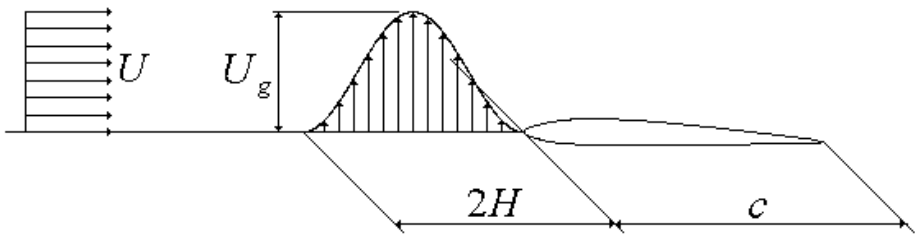

Figura 1. Rajada um-menos-cosseno.

2.1. Rajada menos-seno (-sen)

Analogamente a rajada um-menos-cosseno seja um perfil fino, com ângulo de incidência nulo, imerso num meio com velocidade uniforme U. O perfil então é submetido a uma rajada de intensidade, $U_{-sen}(s)$, conforme perfil chamado menos-seno. O perfil da rajada discreta menos-seno é definido como:

$$U_{-sen}(s) = \begin{cases} \dfrac{\overline{U}_{-sen}}{2}\left[-\text{sen}\left(\dfrac{2\pi s}{2H}\right)\right] & ,\ 0 \le s \le 2H \\ 0 & ,\ s > 2H \end{cases} \tag{2}$$

Onde s denota a distância adimensional de penetração da rajada, $s = Ut/c$. A intensidade da rajada é definida por $\overline{U}_{-sen}$, sendo no presente trabalho adotado $U = \overline{U}_{-sen}$. H denota o gradiente de rajada, e possui a mesma dimensão da corda do perfil, c. Nos problemas aqui estudados serão usados valores de $2H = 5$ e $2H = 25$. Os valores calculados são novamente comparados com dados obtidos por Raveh e Zaide (2005). A Fig. 2 ilustra o problema da rajada um-menos-cosseno.

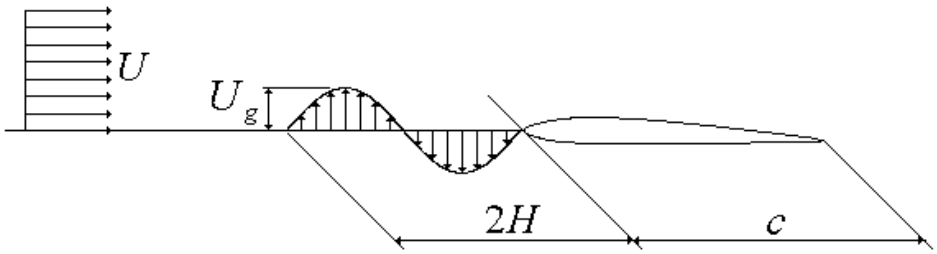

Figura 2. Rajada menos-seno.

2. Movimento Harmônico

Estuda-se o movimento harmônico de translação de um perfil fino, num meio com velocidade uniforme U, que oscila verticalmente, sem angulo de ataque, segundo a função $h(t)$ definida como segue:

$$h(t) = h_0 \text{sen}(wt) \tag{3}$$

A freqüência de oscilação é definida por $w = 2k_r U/c$, sendo k_r a freqüência reduzida de oscilação. No presente trabalho adotou-se $h_0 = U/2$ e $k_r = \pi/5$ (adotado este valor apenas como referência, visto implicar num período igual da rajada menos-seno). A Fig. 3 ilustra o movimento harmônico de translação.

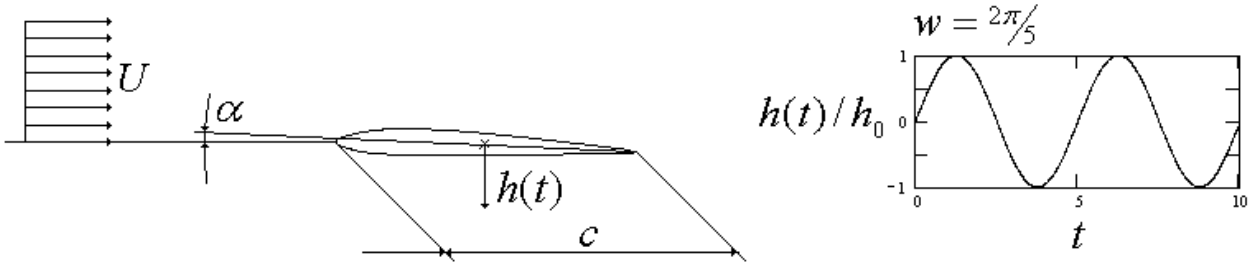

Figura 3. Movimento harmônico de translação.

4. Modelo Numérico

Utiliza-se o modelo desenvolvido por Hernandes e Soviero (2004) sujeito às condições de contorno descritas para os problemas de rajada de canto vivo com velocidade variável e AVI.

São hipóteses do modelo o fluido não viscoso, portanto as forças atuam normais a superfície (não existindo forças tangenciais); o escoamento ser irrotacional; e admite-se o conceito de pequenas perturbações ($u', v', w' << U$). O estudo então é restrito a equação do potencial de velocidades, ϕ, para regime não permanente:

$$\phi_{tt} + 2U\phi_{xt} + U^2\phi_{xx} = a^2\nabla^2\phi \tag{4}$$

Onde a é a velocidade do som. O perfil é dividido em um número conveniente de n painéis. A medida que o perfil está sujeito a condição de contorno ($U_n \neq 0$) surge sobre o perfil (nos painéis onde a condição $U_n \neq 0$ é preenchida) um salto potencial de perturbação, $\delta\phi$, associado a cada painel, que pode ser determinado através da Teoria do Pistão (Bisplinghoff et al., 1955). Num instante imediatamente seguinte esses salto são substituídos por pares de vórtices contra-rotativos de intensidades Γ e $-\Gamma$ (onde Γ é numericamente igual a $\delta\phi$).

A velocidade U_n, após a condição inicial, é constituída da condição de contorno inicial somado às velocidades normais induzidas pelos vórtices emitidos nos instantes anteriores. Os vórtices que são introduzidos em substituição aos saltos de potencial são definidos em dois tipos: os vórtices ligados ao perfil e os vórtices livres (que se deslocam com a velocidade do escoamento não perturbado).

A seqüência de eventos pode ser entendida na Fig. 4. Tem-se sobre os painéis, num instante qualquer, os saltos gerados pela condição de contorno daquele instante somado aos vórtices emitidos em todos os passos de tempo anteriores. Na junção dos painéis é feito um balanço entre os vórtices emitidos resultando num somatório nas extremidades esquerdas de cada painel. Os saltos de potencial estão intimamente relacionados à parcela impulsiva do movimento e a vorticidade gerada a parcela circulatória.

A seqüência de eventos para escoamento supersônico é análoga ao subsônico diferindo apenas que não há emissão de vórtices criados impulsivamente pelo bordo de fuga, sendo todos os vórtices ligados ao perfil, visto que a esteira não influenciaria o escoamento sobre o perfil. Os vórtices contrarotativos originários dos saltos de potenciais de perturbação de velocidade para o escoamento supersônico são todos eles ligados ao perfil, pois a condição de Kutta não necessita ser respeitada neste regime. Para o escoamento subsônico o vórtice do bordo de fuga do perfil (de intensidade $-\Gamma_1^k$ localizado na extremidade direita do painel $j=1$) é, por imposição do modelo, livre para criar automaticamente uma esteira e satisfazer o teorema de Kelvin.

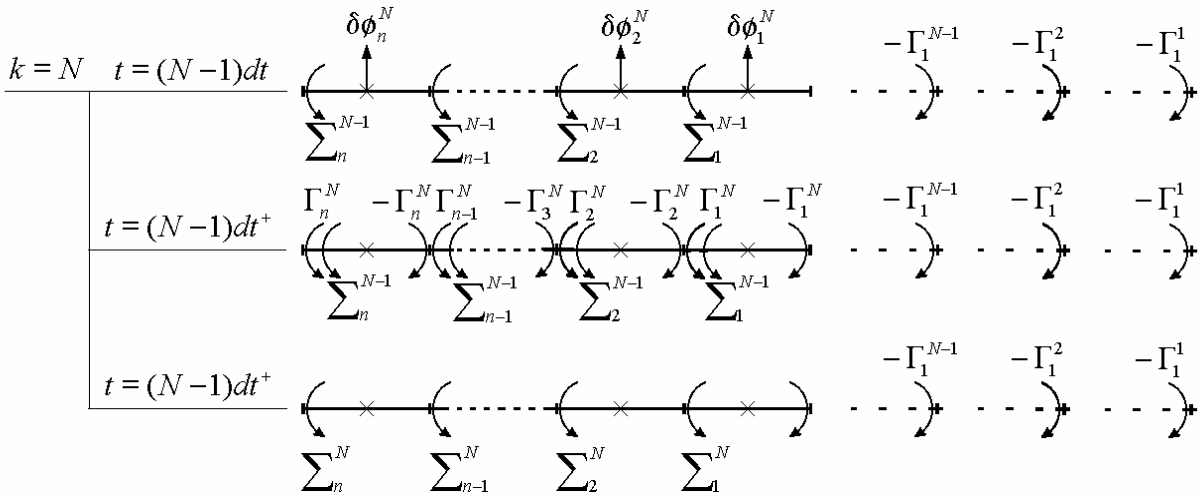

Figura 4. Modelo numérico

A solução do problema se dá através da solução de um sistema linear onde temos uma matriz $[A]$ de coeficientes tal que multiplicada pela matriz dos saltos de potenciais $[\delta\phi]^k$ para o instante k considerado resulta na matriz da condição de contorno $[W]^k$ (velocidade normal sobre os painéis).

$$[A][\delta\phi]^k = [W]^k \tag{5}$$

A matriz $[A]$ está associada a influência dos vórtices gerados num dado instante k e sua influência no próprio instante. Devemos ainda somar aos elementos da diagonal principal a parcela referente a impulsão do próprio painel, dada por $1/(2adt)$.

Para escoamento subsônico a matriz das velocidades $[W]^k$ é função da velocidade normal ao perfil devido ao movimento ($U\alpha$) somado as velocidades induzidas pelos vórtices emitidos nos instantes anteriores ao considerado. Para o correto funcionamento do método no regime supersônico é essencial considerar o elemento fundamental do método – a singularidade vórtice. No regime subsônico é possível calcular a velocidade induzida pelo vórtice em qualquer ponto da área afetada por ele. Já para o regime supersônico o ponto de origem do vórtice é singular não sendo

possível calcular a velocidade induzida neste ponto. Deste modo é necessário definir a contribuição da singularidade para o campo de velocidade. Esse conceito é explorado por Miranda et al. (1977). A parcela relativa à velocidade induzida devido à singularidade é definida a partir da velocidade induzida no regime permanente.

A partir da solução do sistema (matriz $[\delta\phi]^k$) podemos calcular os coeficientes aerodinâmicos.

5. Resultados

São apresentados os coeficientes aerodinâmicos de um perfil sujeito às rajadas um-menos-cosseno e menos-seno bem como um perfil sujeito a um movimento harmônico de translação, calculados numericamente, para ambos regimes, subsônico e supersônico. Os resultados numéricos das rajadas são comparados com soluções disponíveis na literatura. Para o estudo de rajadas os resultados são comparados com Raveh e Zaide (2005) no regime subsônico; no regime supersônico não foi encontrada referência para comparação. As comparações dos resultados obtidos para o movimento harmônico lateral são deixadas como estudo futuro - uma boa referência é Timman *et al.* (1951).

A Fig. 5 apresenta os resultados das rajadas comparadas com Raveh e Zaide (2005). Observa-se boa concordância dos resultados. Nessas rajadas especificamente foi considerado um gradiente de rajada de $2H = 25$.

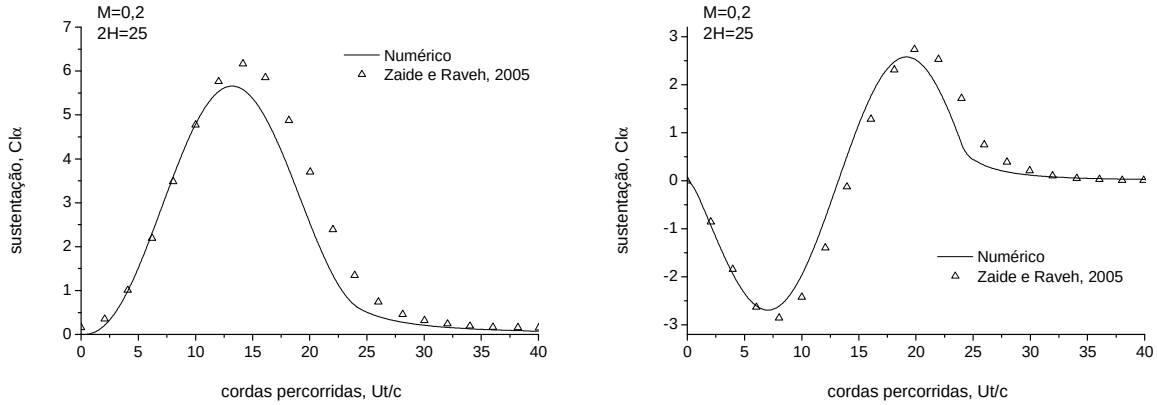

Figura 5. Comparativo com referência. Esq.: rajada um-menos-cosseno. Dir.: rajada menos-seno.

A Fig. 6 mostra os resultados obtidos, para o coeficiente de sustentação, da rajada um-menos-cosseno para regime subsônico considerando-se um gradiente de rajada de $2H = 5$. De maneira análoga na Fig. 7 são apresentados os resultados no regime supersônico. Os resultados estão divididos em partes circulatória e impulsiva. As mesmas também são chamadas de permanente e não-permanente respectivamente. A parcela permanente está associada à circulação total presente sobre o perfil no momento considerado e a parcela não-permanente está associado à parcela não-circulatória, ou seja, que surge imediata a presença de um potencial de perturbação de velocidade sobre o perfil. Nota-se que a parcela impulsiva é a responsável para que não tarde o surgimento de sustentação sobre o perfil, já que a circulação leva um tempo para se desenvolver - é percebida uma defasagem entre a sustentação total e a sustentação circulatória (esta está atrasada da total). Percebe-se também uma diferença de fase entre parcelas circulatória e impulsiva. Isso também se observa nos outros movimentos aqui estudados e será discutida à frente. Uma observação se faz com relação ao movimento supersônico, onde a sustentação retorna a seu valor de origem (no caso nula), já no escoamento subsônico esse retorno é assintótico sendo, portanto, os efeitos da rajada no regime supersônico finitos.

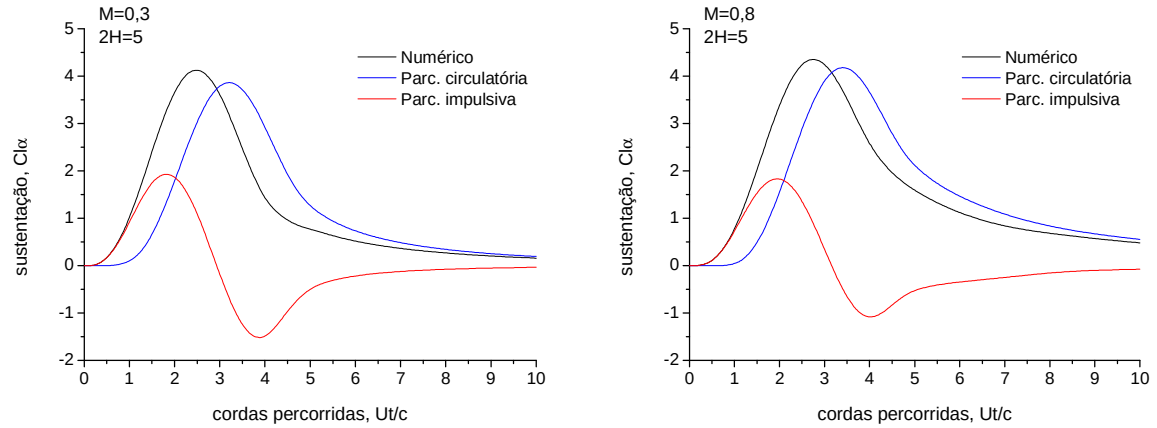

Figura 6. Rajada um-menos-cosseno. Escoamento subsônico.

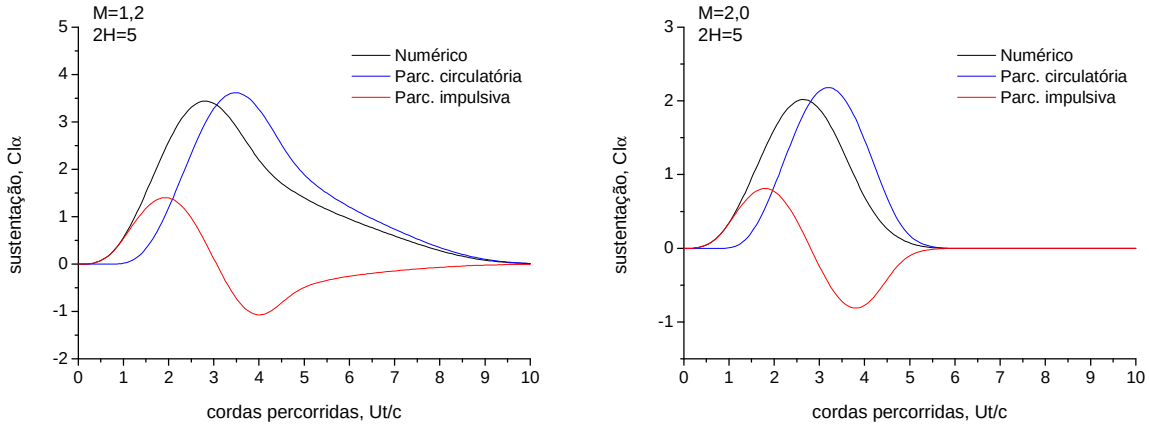

Figura 7. Rajada um-menos-cosseno. Escoamento supersônico.

A Figuras 8 e 9 mostram os resultados obtidos, para o coeficiente de sustentação, da rajada menos-seno para regime subsônico e supersônico respectivamente, considerando-se um gradiente de rajada de $2H = 5$. Novamente, os resultados estão divididos em partes circulatória e impulsiva. As mesmas observações com relação à defasagem das parcelas e comportamento finito do regime supersônico verificadas na rajada um-menos-cosseno são aqui verificadas.

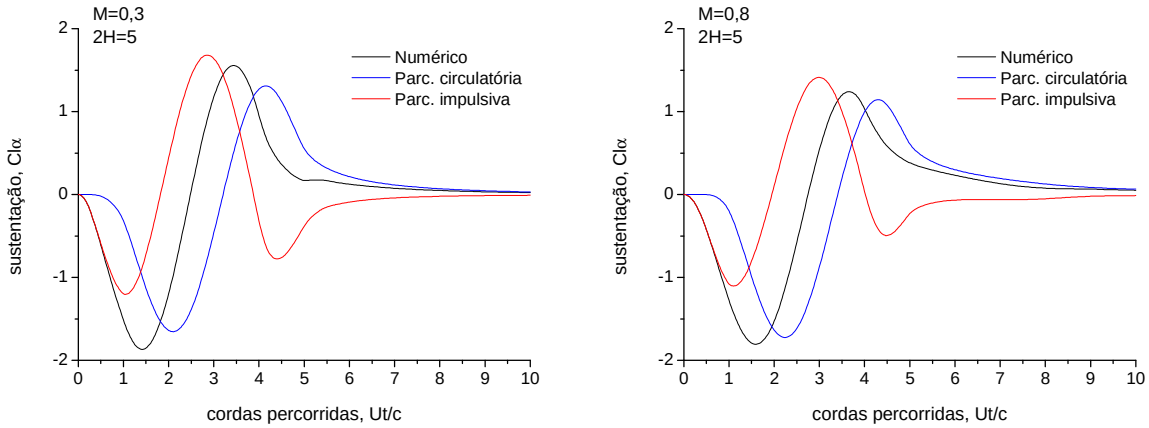

Figura 8. Rajada menos-seno. Escoamento subsônico.

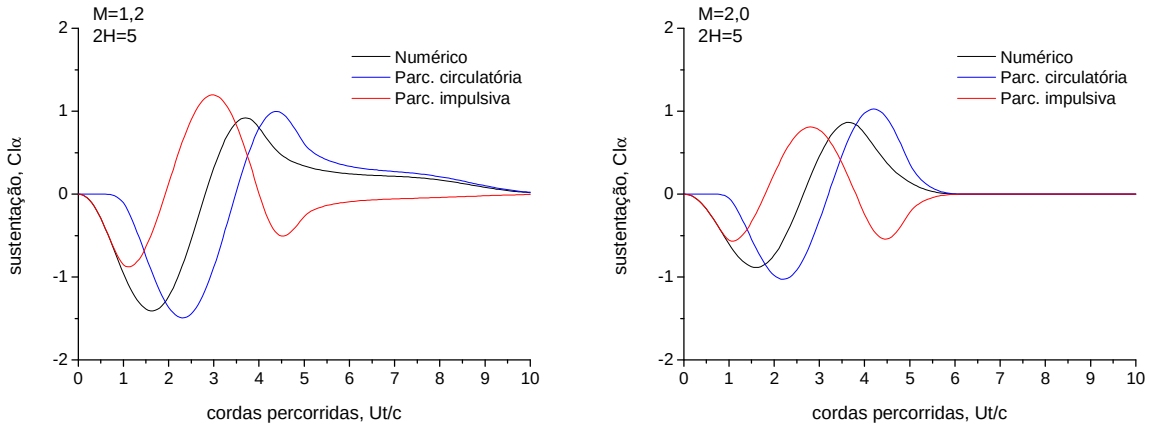

Figura 9. Rajada menos-seno. Escoamento supersônico.

Resultados comparativos de ambas rajadas para várias velocidades são mostrados na Fig. 10. Verifica-se que ambos regimes (subsônico e supersônico) que quanto mais próxima à velocidade da rajada estiver da velocidade do som mais lento se dá o retorno ao valor de sustentação de origem.

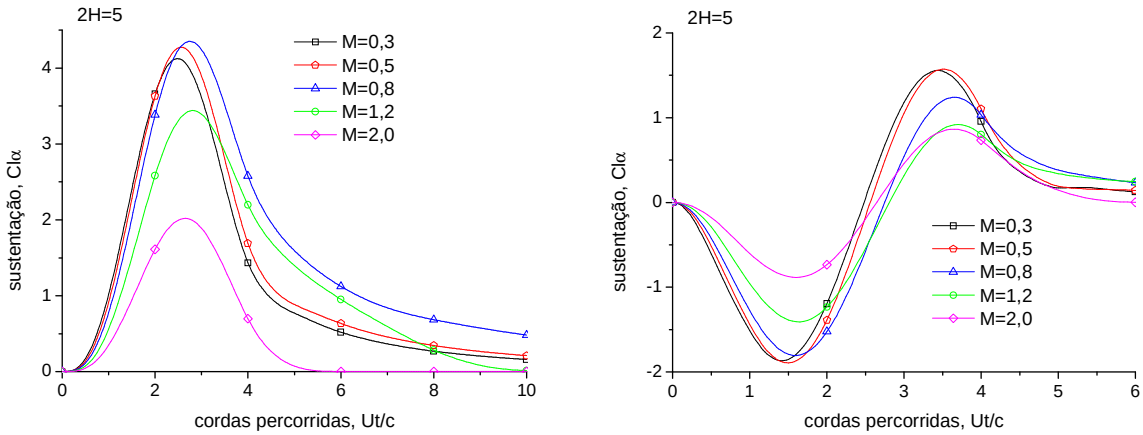

Figura 10. Resultado para várias velocidades de rajada. Esq.: rajada um-menos-cosseno. Dir.: rajada menos-seno.

A Fig. 11 mostra os resultados obtidos, para o coeficiente de sustentação, do perfil sujeito a movimento harmônico de translação, considerando-se um gradiente de rajada de $2H = 5$. De maneira análoga na Fig. 12 são apresentados os resultados no regime supersônico. Aqui é nítida a defasagem entre parcelas circulatória e impulsiva. Essa característica foi mostrada por Theodorsen (1935), onde se verifica a parcela circulatória ser uma função da primeira derivada no tempo da função, e a parcela impulsiva (não-circulatória) ser função da segunda derivada no tempo. Observa-se também um pico da parcela impulsiva no início do movimento. Esse comportamento de deve ao fato que o perfil parte do repouso e instantaneamente inicia o movimento oscilatório. Essa característica, de existir um salto inicial de sustentação, se observa na função degrau (Hernandes e Soviero, 2004).

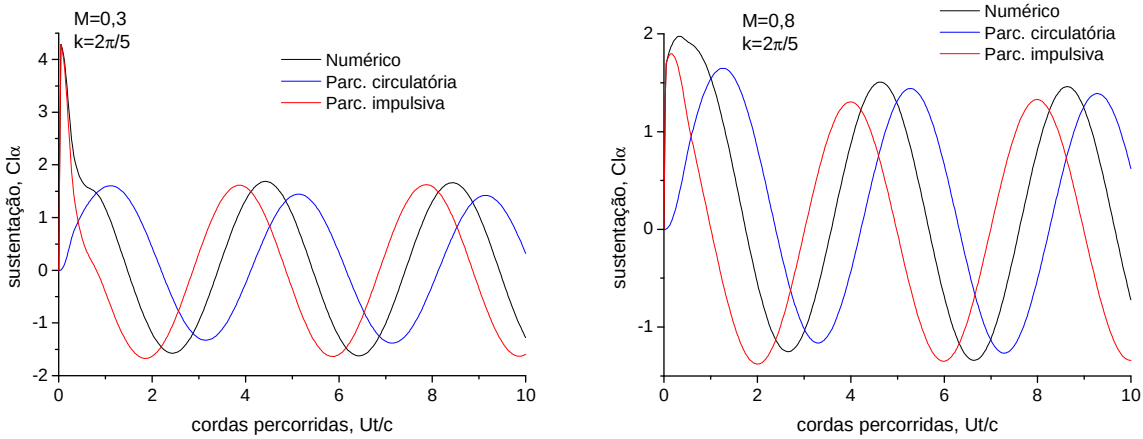

Figura 11. Movimento harmônico. Regime subsônico.

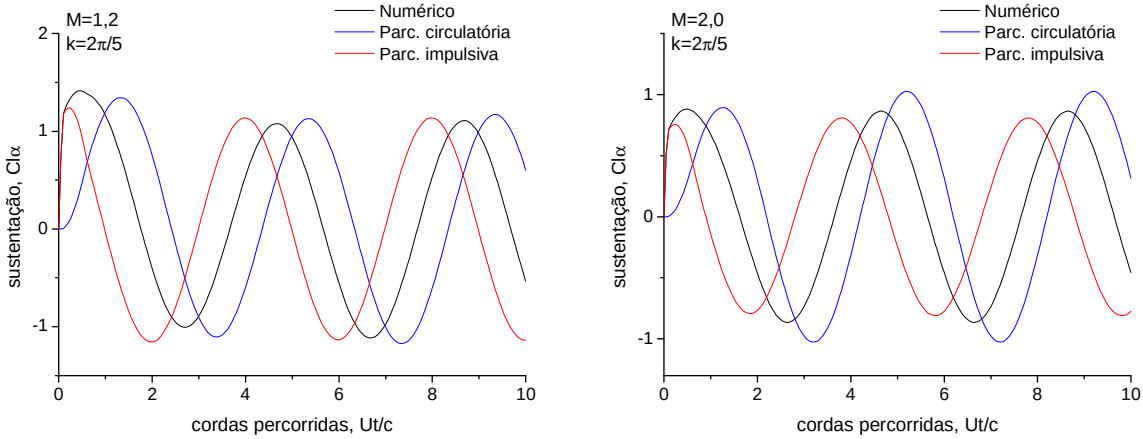

Figura 12. Movimento harmônico. Regime supersônico.

A Fig. 13 apresenta os resultados do movimento harmônico para vários números de Mach.

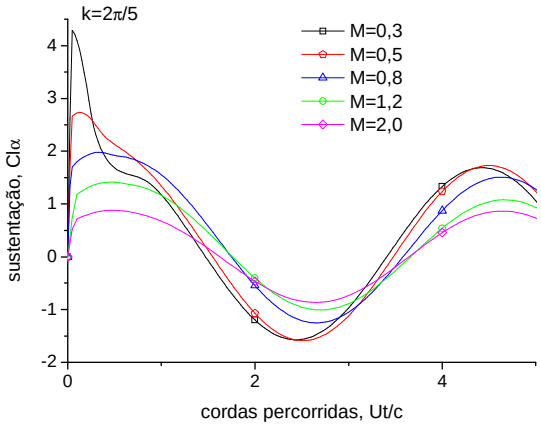

Figura 13. Escoamento harmônico. Vários números de Mach.

As figuras 14 a 16 mostram a evolução da distribuição do salto do coeficiente de pressão sobre o perfil em função do tempo adimensional.

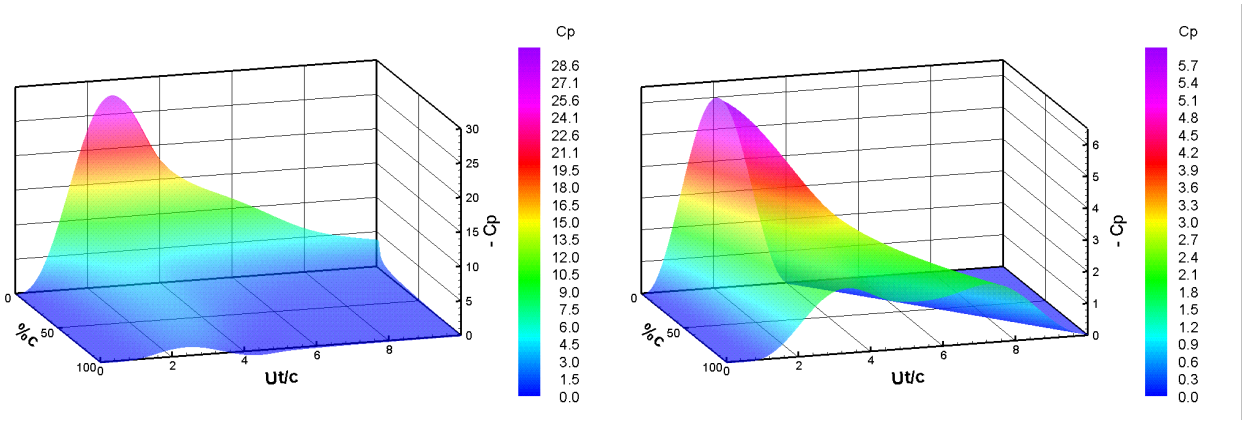

Figura 14. Distribuição do salto do coeficiente de pressão Rajada um-menos-cosseno. Esq.: M=0,8. Dir.: M=1,2.

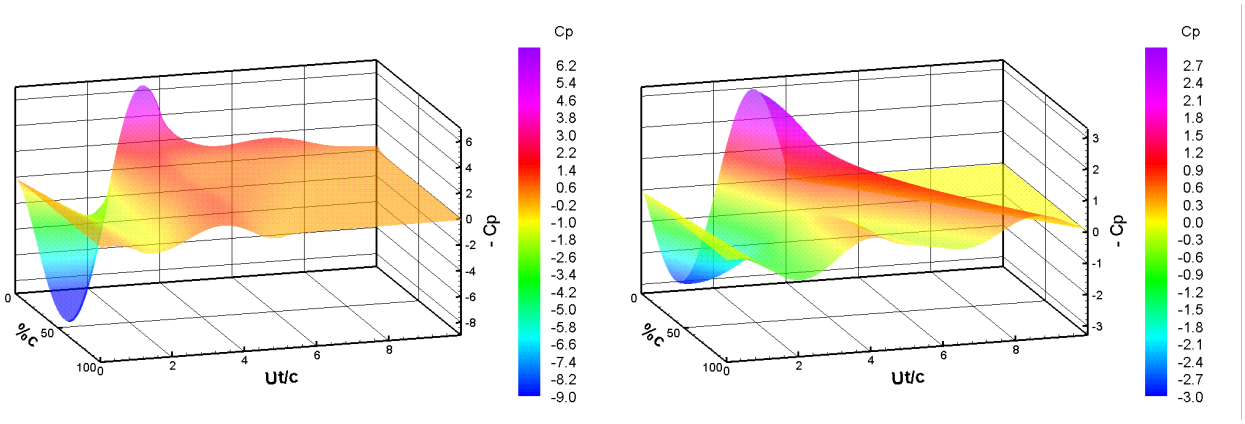

Figura 15. Distribuição do salto do coeficiente de pressão Rajada menos-seno. Esq.: M=0,8. Dir.: M=1,2.

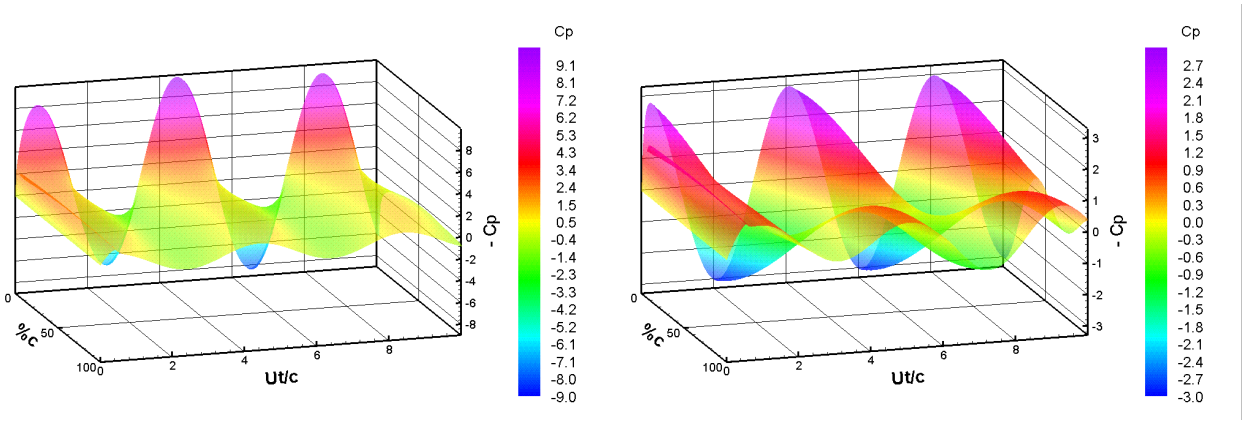

Figura 16. Distribuição do salto do coeficiente de pressão Movimento harmônico. Esq.: M=0,8. Dir.: M=1,2.

6. Conclusões

Foram obtidas numericamente as forças aerodinâmicas para um perfil sujeito a rajadas discretas, de perfis um-menos-cosseno e menos-seno, e forças resultante do movimento harmônico de translação de um perfil. O método proposto abrange todo regime compressível, excetuando a faixa transônica onde as hipóteses que levam a linearização da Eq. (4) não são mais válidas. Comparações com a literatura foram realizadas a fim de validar os resultados e mostrar a precisão do método utilizado. Os resultados mostram os efeitos da compressibilidade nesses problemas, bem como esses movimentos são afetados pela velocidade de propagação da rajada. O estudo de rajadas discretas é fundamental no projeto de aeronaves modernas, sendo o método pela sua velocidade (aproximadamente 10000 vezes mais rápido que CFD) uma excelente ferramenta no projeto preliminar de aeronaves. A evolução natural do método é sua extensão ao tridimensional, de modo a permitir cálculos com modelos simplificados de aeronaves, que é a atual metodologia utilizada em projetos. Estudos futuros devem ser feitos visando completar os resultados obtidos para o movimento harmônico com sua parcela imaginária permitindo comparação com estudos disponíveis na literatura.

7. Agradecimentos

Este trabalho teve o apoio parcial do Conselho Nacional de Desenvolvimento Científico e Tecnológico (CNPq), Brasília, DF, através Bolsa de Produtividade em Pesquisa (Processo No. 302352/2002-3).

8. Referências

Bisplinghoff, R. L., Ashley, H., e Halfman, R. L.,1955, Aeroelasticity, Addison-Wesley, Reading, MA.

Flomenhoft, H. I., 1994, "Brief History of Gust Models for Aircraft Design", Journal of Aircraft, Vol. 31, No. 5, pp. 1225-1227.

Fuller, J. R., 1995, "Evolution of Airplane Gust Loads Design Requirements", Journal of Aircraft, Vol. 32, No. 2, pp. 235-246.

Hernandes, F., e Soviero, P.A.O., 2004, "Modelo Numérico Para Perfis Finos Em Escoamento Compressível Não Permanente", Proceedings of the 10th Brazilian Congress of Thermal Engineering and Sciences. Rio de Janeiro, Brazil, 12p.

Küssner, H. G., 1936, "Zusammenfassender Bericht Under den Instationarem Auftreib von Flugeln", Luftfahrtforschung, Vol. 13, No. 20, pp. 410-424.

Miranda, L. R., Elliot, R. D., Baker, W. M., 1977, "A Generalized Vortex Lattice Method for Subsonic and Supersonic Flow Applications", NASA Contractor Report 2865

Noback, R., 1986, "Comparison of Discrete and Continuous Gust Methods for Airplane Design Loads Determination", Journal of Aircraft, Vol. 23, No. 3, pp. 226-231.

Pratt, K. G., e Walker, W. G., 1954, "A Revised Gust-load Formula and a Re-evaluation of V-G Data Taken on Civil Transport Airplanes From 1933 to 1950", NACA Technical Report 1206.

Soviero, P. A. O., 1993, "Generalized Vortex Lattice Method for Oscillating Thin Airfoil in Subsonic Flow", AIAA Journal, Vol. 31, No. 12, pp. 2380-2382

Soviero, P. A. O., e Ribeiro, M. V., 1995,"Panel Method Formulation for Oscillating Airfoils in Supersonic Flow", AIAA Journal, Vol. 33, No. 9, pp. 1659-1666.

Soviero, P. A. O., e Pinto, F. H. L., 2001, "Panel Method Formulation for Oscillating Airfoils in Sonic Flow", Journal of the Brazilian Society of Mechanical Sciences, Vol. 23, No. 4, pp. 401-409.

Theodorsen, T., 1935, "General Theory of Aerodynamic Instability and the Mechanism of Flutter", NACA Technical Report 496.

Timman, R., *et al.*, 1951, "Aerodynamic Coefficients on an Oscillating Airfoil in Two-dimensional Subsonic Flow", Journal of the Aeronautical Sciences, Vol. 18, No. 12.

Wagner, H., 1925, "Uber die Entstehung des Dynamischen Auftriesbes von Tragflugeln", Zeitschrift für Angewandte Mathematik und Mechanik, Vol. 5, No. 1, pp. 17-35.

Zaide, A., e Raveh, D., 2005, "Numerical Simulation and Reduced-Order Modeling of Airfoil Gust Response" AIAA 2005-5128, 17th AIAA Computacional Fluid Dynamics Conference, 6 a 9 Junho de 2005, Toronto, Canada.

APPLICATION OF THE GENERALIZED VORTEX LATTICE METHOD TO AN AIRFOIL UNDER GUSTS OR HARMONIC MOTION

Fabiano Hernandes
Instituto Tecnológico de Aeronáutica
12228-900 São José dos Campos - SP
f_hernandes@bol.com.br

Paulo Afonso de Oliveira Soviero
Instituto Tecnológico de Aeronáutica
12228-900 São José dos Campos - SP
soviero@ita.br

Abstract

Aerodynamic effects are studied (lift and pressure coefficients), on a thin profile penetrating into a one-minus-cosine gust and sinusoidal gust, and also oscillating airfoil.. Such predictions are mainly relevant in modern aircrafts. Aeroelastic gust-response analysis requires an aerodynamic model of the unsteady forces that develop on the aircraft as it travel through atmospheric gust. Tradiotionally, two methods are used for the aerodynamic loads: time-domain and frequency-domain. The present work uses a time-domain numerical approach based on vortex singularity. The results now avaiable in literature are based on approximated exponential equations, or computed via Computational Fluid Dynamics (CFD). Thus, the method intends a more accurate computation compared to those of approximated equations, and quite faster than those done via CFD. Results are obtained for subsonic and supersonic compressible flows.

Keywords: one-minus-cosine gust, sinusoidal gust, harmonic motion, vortex singularity, unsteady flow.

Proceedings of the 11th Brazilian Congress of Thermal Sciences and Engineering -- ENCIT 2006
Braz. Soc. of Mechanical Sciences and Engineering -- ABCM, Curitiba, Brazil, Dec. 5-8, 2006

Paper CIT06-0330

PASSIVE, ACTIVE, AND ADAPTATIVE SYSTEMS FOR WING VORTEX DRAG REDUCTION

Hernán Darío Cerón-Muñoz
Aerodynamic Laboratory EESC-USP. Av. Trabalhador São-Carlense 400 São Carlos SP, Brazil
hernan@sc.usp.br

Rogério de Faria Coimbra
IFI-CTA. Av. Brigadeiro Faria Lima, 1.941 São José dos Campos SP, Brazil
rogerio@ifi.cta.br

Fernando Martini Catalano
Aerodynamic Laboratory EESC-USP. Av. Trabalhador São-Carlense 400 São Carlos SP, Brazil
catalano@sc.usp.br

Abstract. *A group of experimental studies were conducted to investigate the effects of different wing tip devices on the reduction of induced drag. The tests were conducted at the Aircraft Laboratory of São Carlos Engineering School (EESC) , and at the Aeronautical Laboratory of the Aeronautical Technical Institute (ITA), Brazil. In this work, wind tunnel test were made, the results are analzed in terms of lift and drag. The experiments were conducted in three stages:*

- *An analysis of the effect of delta tip, winglet, and "Hoerner" devices, concerning the aerodynamic chararacteristics of an agricultural airplane wing.*
- *The effect of wing tip blowing on vortex drag. This study tested lateral wing tip blowing device in which the jet flow exit was from three longitudinal slots on a wing tip model.*
- *Experimental Analysis of the aerodynamic characteristics of adaptative multi-winglets was performed. The aim of this stage is to study the potential use of adaptative multi-winglets for the reduction of induce drag using variations of winglet cant angle.*

Results showed that a delta tip wing is more promising for agricultural aircraf and the potential benefits in combining both the three jets and multi-winglets configurations with the aerodynamic characteristics of a wing.

Keyword: Induced drag, wing tip, winglets, blowing

1. Introduction

The vortices produced at the wing-tip are the inevitable products of the presence of lift, that is to say, they may be considered to be side effect due to the force that supports the aircraft in the air. These vortices are responsible for the appearance of induced drag. In cruise conditions the induced drag may be responsible for approximately 30% of the entire aircraft drag and close to 50% in high lift conditions (Henderson and Holmes, 1989). With the intention of reducing the induced drag, an expansive investigation was made of the methods that have been used to produce favourable effects in the flow existent over the wing tip, including devices that reduce the induced drag. Modifications of the wing tip can either move the vortices away in relation to the aircraft longitudinal axis or reduce their intensity (Kravchenco, 1996). Some of these devices such as winglets (Whitcomb, 1976), tip-sails (Spillman et al., 1978; 1979; 1984; 1987) and multi-winglets (Smith et al, 2001) take advantage of the spiralling airflow in this region to create an additional traction, and reducing the induced drag. Drawings of these previous devices are shown in Fig. (1).

Whitcomb (1976) showed that winglets could increase wing efficiency by 9% and reduce induced drag by 20%. Other devices break up the vortices into several parts, each with less intensity facilitating dispersion, which is important, for instance, for the decrease of the interval time between takeoff and landings in large airports (La Roche and Palffy, 1996). Kravchenco (1996) tested and compared different shapes of wing tips: winglets and tip-sails. The winglets presented higher aerodynamics benefits up to Mach 1.0, however they also presented structural problems for the aircraft due to the increase in bending moment at the wing root. Tip-sails, at low lift coefficient (C_L), provided the same benefits; nevertheless, the bending moment at the wing root was less. Research with agricultural aircraft has also been made comparing wing-tip devices (Coimbra and Catalano, 1999). For this category of aircraft, besides both aerodynamic and structural advantages, the influence of the vortices created during the mission of the aircraf is an added parameter in the analysis.

Winglets have been used to improve sailplane performance. Smith at al (2001) mentions the development work on winglets for sailplanes tested in a wind tunnel with scale models. It was mentioned that winglets with symmetric airfoils are considered better for general aviation use; yet, they are less efficient when applied to tapered wings. Projects of new airfoils for winglets used on sailplanes have been developed and tested. Due to the low Reynolds number flow at

the winglet; a spanwise variation of the airfoil is of fundamental importance for optimizing winglet performance. Maughmer (2002) presented a methodology for the design of winglet airfoils.

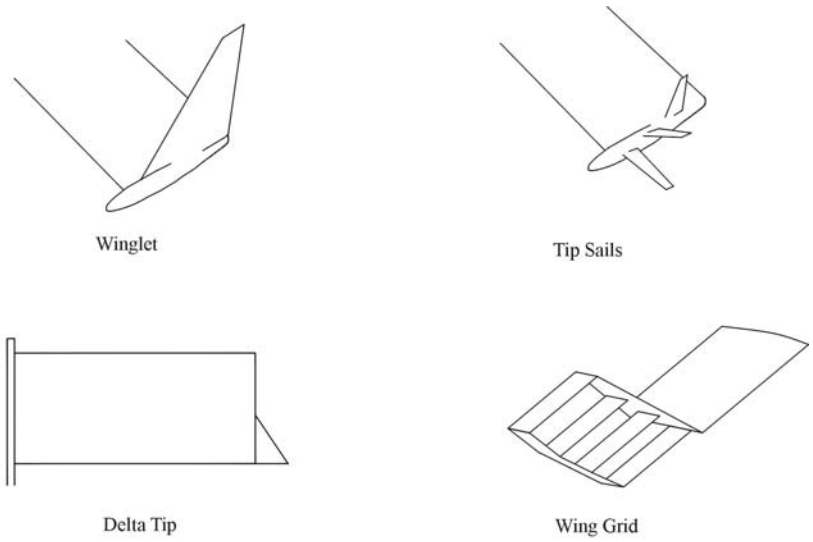

Figure. 1 Wing tip devices

Spillman et al.(1978, 1979, 1984, 1987), realized a series of studies of small aerodynamic devices named tip-sails. These devices took advantage of the direction of the flow existent over the wing tips to create a thrust force, and they also present a reduction in the vortex intensity. The conclusion is, once a particular flight condition has been chosen, the geometry of the tip-sail must present twist and taper ratio. The airfoil must be highly curved at the root and symmetric at the tip. This is due to the behavior of the flow over the wing tips where flow inclination angle decreases with radial distance from the wing tip. Spillman et al. (1978, 1979, 1984, 1944) also investigated the use of tip-sails installed on the tip-tank of a Paris MS 760 Trainer Aircraft (Spillman et al., 1978, 1979). Better results were found using 3 tip-sails. The flight tests confirmed the results achieved in wind tunnel tests such as take off distance and fuel consumption (Spillman et al., 1979). Also flight tests of a Cessna Centurion (Spillman and McVite, 1984) and a Piper Pawnee 235 (Spillman, 1987) were performed using tip-sails. All of these tests presented benefits to the aircraft performance. Tip-sails are the only device that can reduce fuel consumption as well as present structural advantages for the wings.

On the other hand, active systems can be optimized for each maneuver requirement as their effect can be changed and also switched off when necessary. A large number of studies (Tavella, 1985, 1986; Wu and William, 1984 and Mineck, 1995) have been carried-out in order to show the potential benefits of wing tip blowing as an active vortex attenuating system. These tests usually involved large jet momentum coefficients and the jet sizes were a large fraction of the wingtip chord. Also, the required jet mass-flow rates and momentum coefficients were large. In most cases, the jets were exhausted in the plane of the wing and normal to the free-stream direction. Recently, Simpson et al. (2000) introduced a different type of jet system, which was based on the Coanda effect. This type of jet is able to direct the mass flow against the vortex and the mass flow rate is small as is the size compared with the tip chord. In this work, the proposed system consists of three independent Coanda jets, which can be vectored in different directions (see Fig. 2) in a tentative to oppose mass flow against the vortex flow in a similar manner to that of Spillman (1978) with his tip sails.

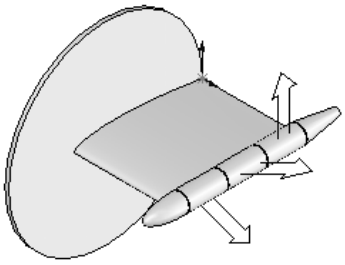

Figure. 2 Three wing tip “coanda” jets

2. An analysis of the effect of delta tip, winglet, and "Hoerner" devices, concerning the aerodynamic chararacteristics of an agrigultural airplane wing

In this stage, wind tunnel tests were made in order to study the influence on aerodynamic characteristics and vortex position, for Brazilian agricultural aircraft, using the following types of wing tips: delta tip, winglet and down curved. The down curved tip was better for total drag reduction, but not good with reference to vortex position. The delta tip gave moderate improvement on aerodynamic characteristics and on vortex position. The winglet had a better vortex position and lift increment, but caused an undesirable result with reference to the wing root bending moment. However, the winglet showed better development potential for agricultural aircraft.

2.1. Experimental Configuration

The tests were made at the University of São Paulo, Aircraft Laboratory, in an open circuit wind tunnel which has a hexagonal test section with a cross section area of 0,526 m² and 1,63 m length. The wing profile used was a NACA 23015 with drooping leading edge, which increases the maximum lift of the original airfoil. The wing model used a rectangular planform, without end caps, and it has 0,138m chord, 0,389m half span and no geometric twist. The aspect ratio (AR) of the basic wing was 5,63.

The delta tip was selected because of the good results shown recently (Traub, 1994), and for its structural simplicity. The winglet was chosen to be tested because of its successful use in commercial airplanes. The down curved tip was chosen to be compared, due to use in Brazilian agricultural aircraft. Figure 3 shows the tested models. The winglet, which was canted outward 20°, was tested at 5° incidence angle; and was constructed with a GA(W)-2 airfoil section, from wood, with a total winglet area of 12% of the wing area. The winglet planform was tapered with 15° leading edge sweep angle; its root chord and span had the same geometric value: 66.6% of the wing chord. It should be noted that the winglet test was exploratory and limited in scope; no attempt was made to optimize winglet geometry for maximum aerial application benefits. The delta tip was made from 1mm thick aluminum plate and had a leading edge sweep angle of 70°. This tip had 0.91% of the wing area and the root chord corresponded to 37.7% of the wing chord. The leading edge of the delta tip was sharp to enforce flow separation. Both configurations were positioned near the wing trailing edge. The down curved tip was made from styrofoam®, and had 8,6% of the wing area. This tip device equipped the second generation of Brazilian agricultural aircraft (from EMB- 201A to EMB-202, all called Ipanema). The aerodynamic forces were measured with a strain gauge balance. The forces from the tests were corrected for blockage (Pope and Rae, 1984). Tare and interference effects, as well as the tunnel flow angularity, were established using an image system (Pope and Rae, 1984). The balance was unable to measure pitching moment. Tests were conducted at a freestream velocity of 28m/s. The set angle of attack was varied from 0 to 15 degrees. Wing Reynolds number was 2,7 x 10^5, based on chord length. A boundary-layer transition strip was fixed at 5% of the chord on the upper and lower surface along the entire wing span.

Wing root bending moments measurement were made also, to check any structural overloading or damage, using the same strain gage balance.

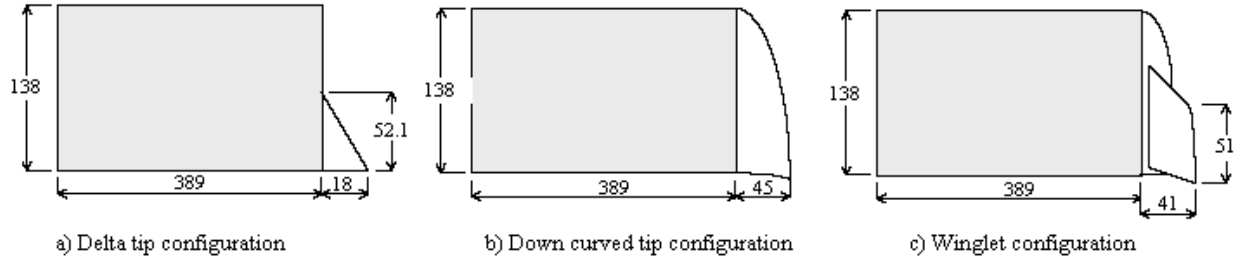

Figure. 3 Wing tip configurations

2.2. Results and Discussion

Table 1 contains a summary of the aerodynamic results. Figure (4) presented the aerodynamic characteristics of all configurations tested and shows the structural results. Figure (4) (a) presents the lift curves and shows an increase in lift coefficient for all tip configurations compared to the basic wing. Figure (5) (a) shows drag polar curves.

Table 1 Aerodynamics increments (%) due to win tip devices referring to basic wing

Parameters	Delta Tip	Down Curved Tip	Winglet
$dC_L/d\alpha$	+3.9	+11.1	+17.29
e	+1.63	+17.45	+45.43
C_{Lmax}	+1.75	+8.87	+8.96
L/D_{max}	+19.63	+34.21	+20.85
$C_L^{1.5}/C_D$ (max)	+17.32	+33.62	+22.41

To quantify the induced drag performance in the most useful lift range, the drag polar may be approximated using equation Eq. (1).

$$C_D = C_{D\min} + C_L{}^2 \big/ \pi \cdot AR \cdot e \tag{1}$$

Where C_D is the drag coefficient, C_{Dmin} is the minimum drag coefficient, AR is the wing aspect ratio, and e is the Oswald efficiency factor. The shape of the tip, including the sharpness of the edge and the trailing edge of the wing tip are all important in directing the vortex as far outward as possible, thus increasing the span efficiency. The constant *e* incorporates both vortex and profile drag, which are difficult to separate as both vary with CL^2 . To calculate values of the Oswald efficiency for each of the wing tips tested, the relationship used was Eq. (2) (Nicks, 1983).

$$e = 57.3 \cdot \frac{dC_L}{d\alpha_\infty} \cdot \left[(\varphi - 1)\pi \cdot AR\right]^{-1} \tag{2}$$

Where φ is the lift curve slope ratio.

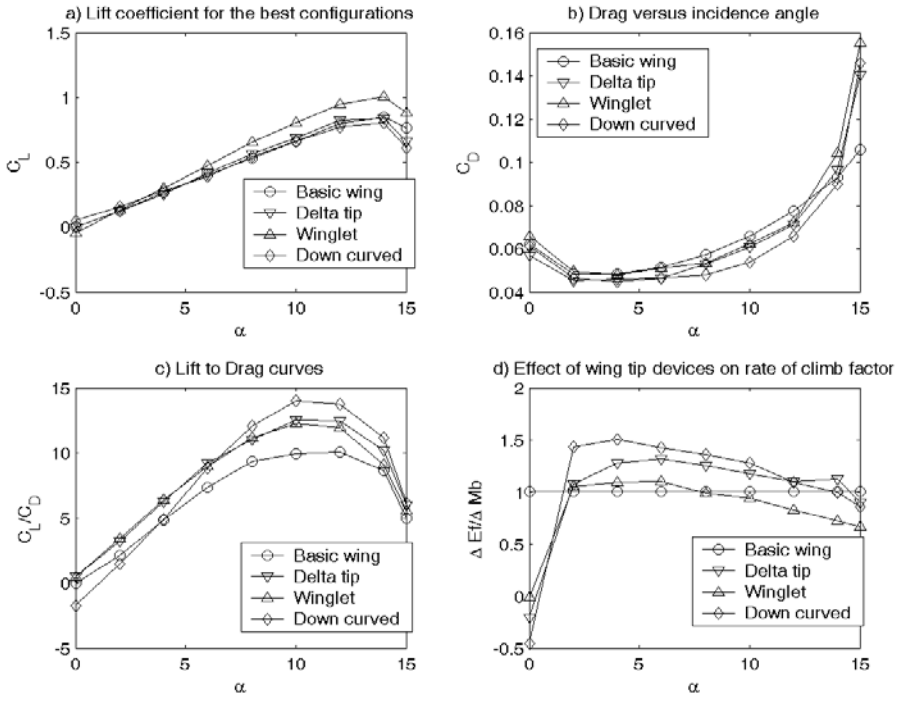

Figure. 4 Aerodynamics characteristics of Ipanema wing tip

Improvements in factor *e* directly affect the performance of the airplane, especially at high lift conditions. In Fig. (4) (b), at small angles of attack ($\alpha < 6°$), the delta tip device shows less drag than the other wing-tip configurations; at higher incidences, the down curved tip presents smaller drag coefficients. In Fig. (5) (a) drag polar shows the same pattern presented in Fig (4) (b), at lift coefficients of less than 0,4 for delta tip and higher for down curved tip. Winglet presented higher drag than the others tip devices, at lift coefficients smaller than 0,4; at *CL*'s from 0,4 to 0,8 the winglet drag is equal to the delta tip values. At much higher lift coefficients, the winglet has a small advantage over the down curved tip. It should be noted that the addition of the tested tips increased the geometric aspect ratio of the basic wing and this was taken into consideration for the Oswald efficiency factor calculations.

The aerodynamic efficiency is presented in Fig. (4) (c) versus incidence. At angles of attack less than 7°, the winglet shows a better L/D ratio; after this incidence, the down curved tip presents better aerodynamic efficiency. The improvements in wing performance with the new wing tips can be related to the increase in aspect ratio, improvements in span efficiencies and changes in the zero lift-drag coefficients. Figure (5) (b) shows rate of climb.

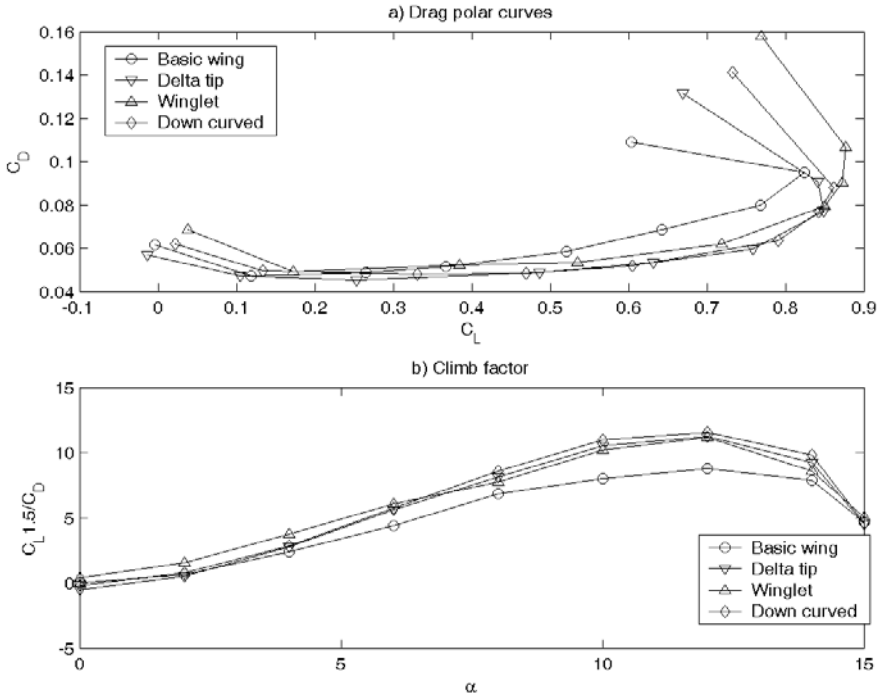

Figure. 5 Polar and range factor of Ipanema wing tip

All aerodynamic benefits had their importance reduced, if structural damages are caused on the wing by the addition of the wing tips, then structural reinforcements are needed, increasing the wing weight and reducing fuel capacity and payload. Figure (4) (d) presents the parameter $\Delta Ef / \Delta Mb$. This parameter, called the *aerodynamic structural efficiency factor* (ASEF) is used to measure the relation between the beneficial increment on wing aerodynamic efficiency to the detrimental increment on wing root bending moment, caused by the addition of the wing tips. The variation of wing efficiency and its root bending moment is compared with the basic wing at each incidence angle; then the basic wing has its parameter equal to the unity at all angles of attack range. It can be noted, in Fig. (4) (d), that only the winglet presents *ASEF* less than the unit for angles of attack higher than 8°.

3. Effect of wing tip blowing on the vortex drag

Experimental work was performed for a large combination of jet flow lateral angles and positions of the tip chord for incidence angles from –4 to 22 degrees always comparing with that of the blowing off (no tip blowing) case.

3.1. Experimental Configuration

The experimental model was a semi- span wing of 0.29m with a 0.25m chord. The wing profile was a NACA 65_3-18 and the model was attached to a horizontal three-component balance as is shown in Fig. 6. The three Coanda jet modules were fixed to a cylindrical “tip tank” for the convenience of providing enough space for the air manifolds and

internal plenum chambers to assure as uniform a jet as possible. Each Coanda Jet module has an air supply manifold with mass flow controlled by a flow meter. Details of the jet dimensions and chambers are shown in Fig. 6.

Tests were conducted at the Aeronautical Laboratory of the Aeronautical Technical Institute in an open circuit wind tunnel with a 0.6 x 0.6 m test section at an average Reynolds Number of $4x10^5$. Turbulence intensity was 0.5% at 30m/s. All the results were corrected for wall interference.

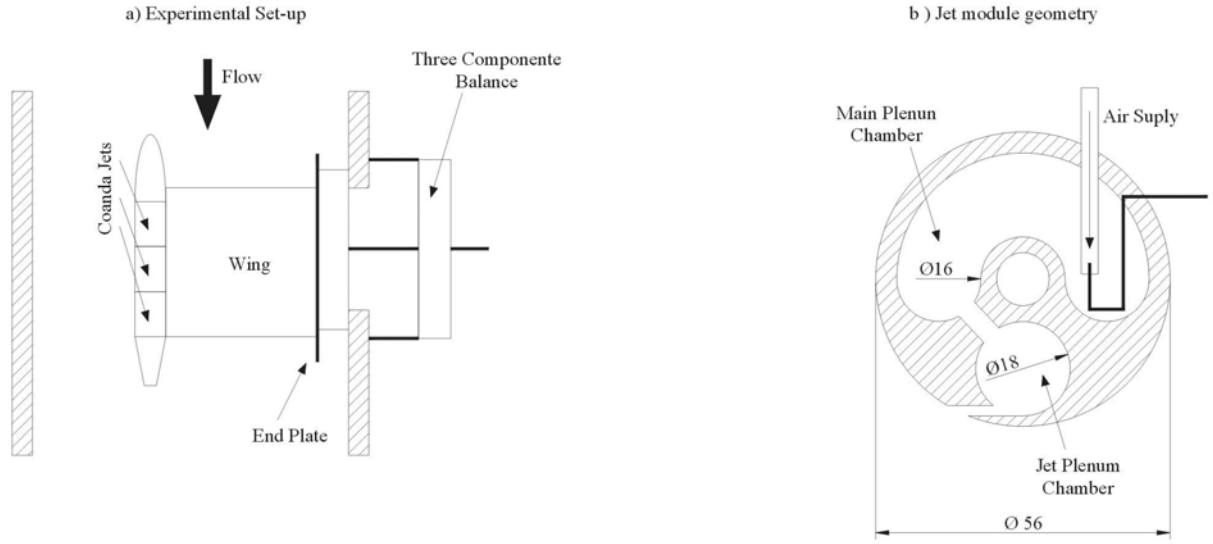

Figure. 6 Experimental set-up and jet module geometry

Limited smoke flow visualization tests were performed with a small wing model in a smoke wind tunnel in order to pre-select the best jet configuration, avoiding in this way a large number of useless tests. It was thus decided to test lateral angles in steps of 5° from 0° to 45° for the first module, 0° to 30° for the central module and 0° to 15° for the rear module. The configuration nomenclature and reference positions are shown in Fig. (7). For example: tip blowing 1CY means that the first module is blowing at 0°, central module at 30° and rear module at 15°.

Lateral Angle	Front Module	Central Module	Rear Module
0°	1	A	X
15°	2	B	Y
30°	3	C	
45°	4		

Figure. 7 Tip jet modules nomenclature

The three-component balance of strain gage type was used. Jet momentum coefficient C_μ was calculated using the Eq. (3)

$$C_\mu = 2\frac{P_e}{q_\infty}\frac{S_j}{S_W} \tag{3}$$

Where P_e is the total pressure in the module plenum chamber, q_∞ the free stream dynamic pressure and S_j and S_W are the jet and wing area respectively.

3.2. Results and Discussion

Because of the large number of configurations tested, data reduction of the best results will be presented. The data presented always includes the blowing off case as a reference. Fig. (8) shows C_L x α and drag polar curves of the best results. As expected from previous work (Tavella et al 1985) (Simpson, et al 2000) jets located at the rear of the chord tip are more effective in Lift enhancement as occurs with a winglet. This is probably due to the shift of the lift produced by the Coanda effect in the downstream direction when the interaction between jet and vortex increases at high incidences.

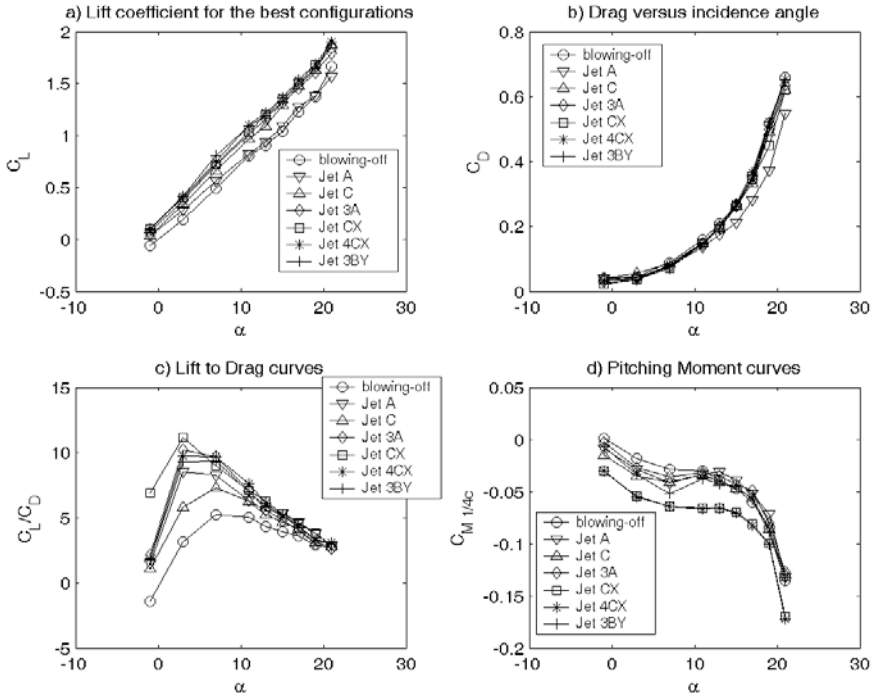

Figure. 8 Aerodynamics characteristics of win-tip blowing

Both configurations, 3A and CX, are the double jet configurations, whit presented best performance. Jet CX presents reasonably large Lift enhancement as can be seen in Fig. (8)(a). At jet 3A the effect was still large but lift slope decreased. Drag results also shown in Fig. (8)(b) are also very similar at low incidences but best overall performance is achieved with Jet CX for which induced drag reductions are larger. Therefore, Jet CX also shows the best aerodynamic performance enhancement as shown in Fig. (8)(c).

The triple jet configurations selected are: 3CX and 3BY. Both Jet 3CX and 3BY show a slightly greater increase in Lift as shown in Fig. (8)(a) . This could be a result of an increase in effective aspect ratio but the weak shift of C_Lx α curve indicates that lift has increased by both the Coanda effect and then increase in effective aspect ratio with probably a greater contribution from the first. The Drag polar also shows a large improvement for all jets especially at high incidences as shown in Fig. (9). The potential flexibility of operation of an active system as that proposed is shown in Fig. (9). It is possible to change the positions of the jets from 3A or 3BY to CX in order to maintain best performance with reference to climb rate and maximum range. The lift enhancement due to the Coanda effect at the tip is a non-circulation born lift force justified by the fact the drag has not increased induced by the lift. Oswald factor has increased to values larger than that obtained in a similar manner with the winglets to an average value of 1.7 for all configurations tested.

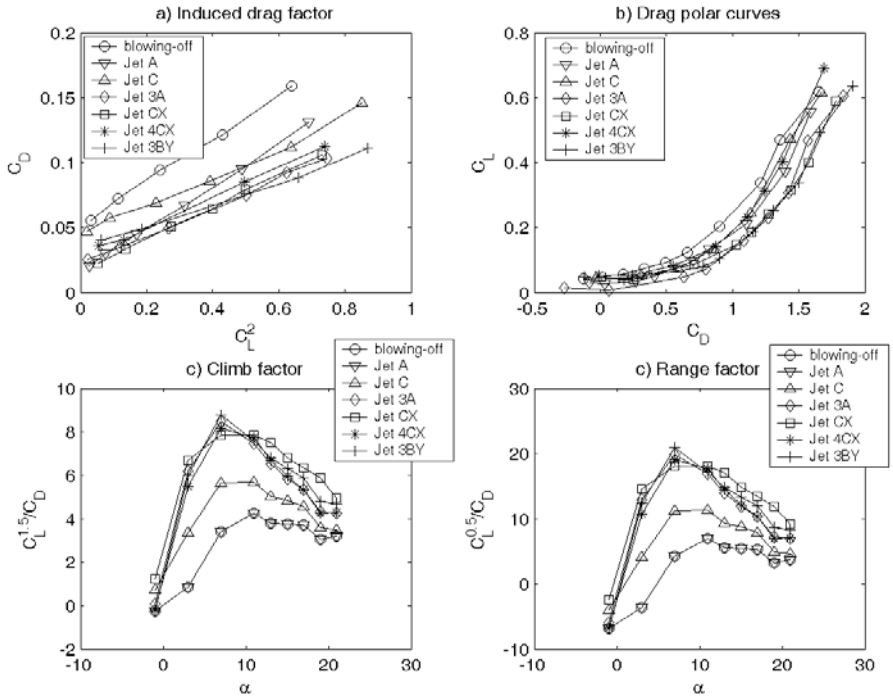

Figure. 9 Aerodynamics curves (wing tip blowing)

4. Experimental Analysis of the aerodynamic characteristics of adaptative multi-winglets

The aim of this research is to study the potential use of adaptive multi-winglets for the reduction of induced drag through variations of winglet cant angles. The model tested is composed of a rectangular wing using a NACA 65_3-018 profile with three winglets called "tip-sails"', which are small wings without sweep along the 25% chord line. The tests were made at a Reynolds number of 350,000. The results are analysed in terms of lift and drag. Results show that it is possible to find the best configuration of the three winglets in order to obtain the optimum aerodynamic performance for each flow regime in climb and cruise.

4.1. Experimental Configuration

The experimental model was a rectangular semi-span wing of 0.49 m with a chord of 0.25 m. For this study a tip tank with three vectorable cylindrical Coanda jets was developed (Coimbra and Catalano 2005). The wing airfoil used was a NACA 65_3-018. Three winglets were added to three cylindrical modules at the tip-tank. The winglets have different airfoil sections along their span. At the root the airfoil is based on the Eppler 387 with 0.05 m chord with a camber of approximated 20%. At the wing tip, the Eppler 387 airfoil was used again, but modified for a symmetric geometry with a chord of 0.023 m. The Eppler 387 is actually an asymmetric airfoil, which can couple very well with the low Reynolds flow at the wing tip. Due to the dimensions of the cylindrical modules of the tip tank, the winglet root chord was fixed at 0.05m. Also, a taper ratio of 0.46 was adopted fixing the winglet tip chord as a function of span. The wind tunnel used was closed circuit with a test section of 1.3 m x 1.75 m, a turbulence level of 0.25% and a maximum speed of 50 m/s (Catalano 2001).

Spillman (1978) got the best results for the tip-sails with 20% camber at the root. The camber decreases rapidly with the distance from the root to the winglet tip lessening approximately to a half part at each distance of 6% of the wing tip chord. In this way, it was established that the winglets would have a span of 0.105 m. It was also established that the winglets would not have sweep at the 1/4 chord. The final winglet geometrical configuration can be seen in Fig. (10).

The lift and drag forces and aerodynamic efficiency were compared and better configurations were chosen, based on improvements in aerodynamic efficiency. Lift and drag forces were measured by a two-component balance. Due to the comparative analysis of the results no wall interference corrections were considered. The two-component balance used is of the strain gage type.

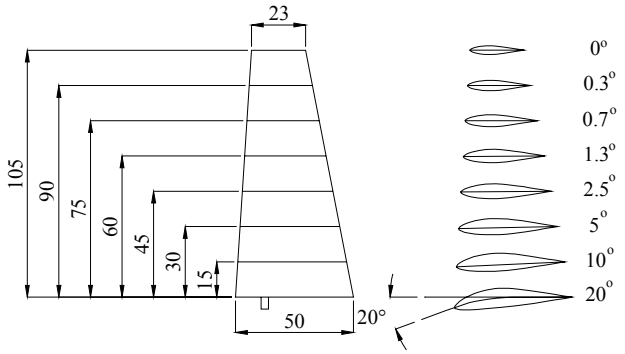

Figure. 10 Winglet final geometry

4.2. Results and Discussion

Only specific results are shown below, presenting the best results in induced drag reduction. Further details can be found in Cerón-Muñoz and Catalano (2006).

. However, a discussion will be presented with reference to the negative effects of each configuration. The results presented are always compared to the winglets-off case. The configurations selected are: Configuration 19: +30^o*A*; 0^o*B*;+30^o*C;* Configuration 48: +45^o*A*;+15^o*B*;-15^o*C,* Configuration 47: +60^o*A*;+30^o*B*; 0^o*C;* Configuration 40: +45^o*A*;+30^o*B*;+15^o*C;* Configuration 11: -30^o*A*;-15*oB*; 0^o*C;* Configuration 44: -15^o*A*;-30^o*B*;-45*oC* An increase in lift was achieved for all the selected configurations. This increase is larger for high incidence angles as shown in Fig. (11). The effect is almost independent of the configurations. Also lift curve inclination increased for all configurations up to 12 degrees, showing that the winglets increase both geometric and effective aspect ratio.

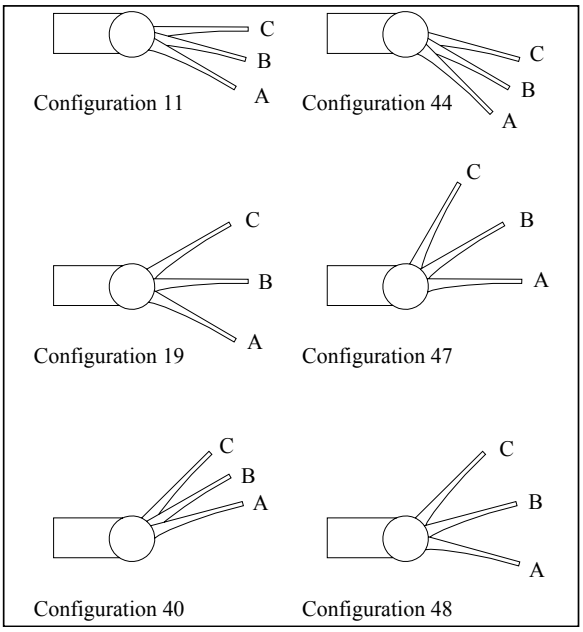

Figure. 11 Configurations considered better, A is the leading winglet, B is the central and C is the trailing one

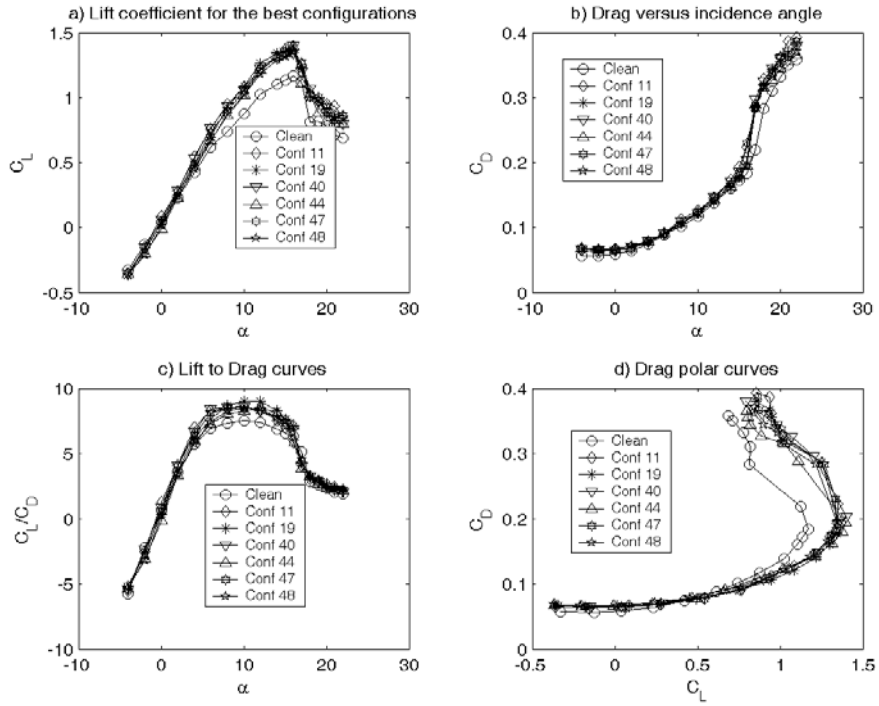

Figure. 12 Aerodynamics characteristics of multi-winglets

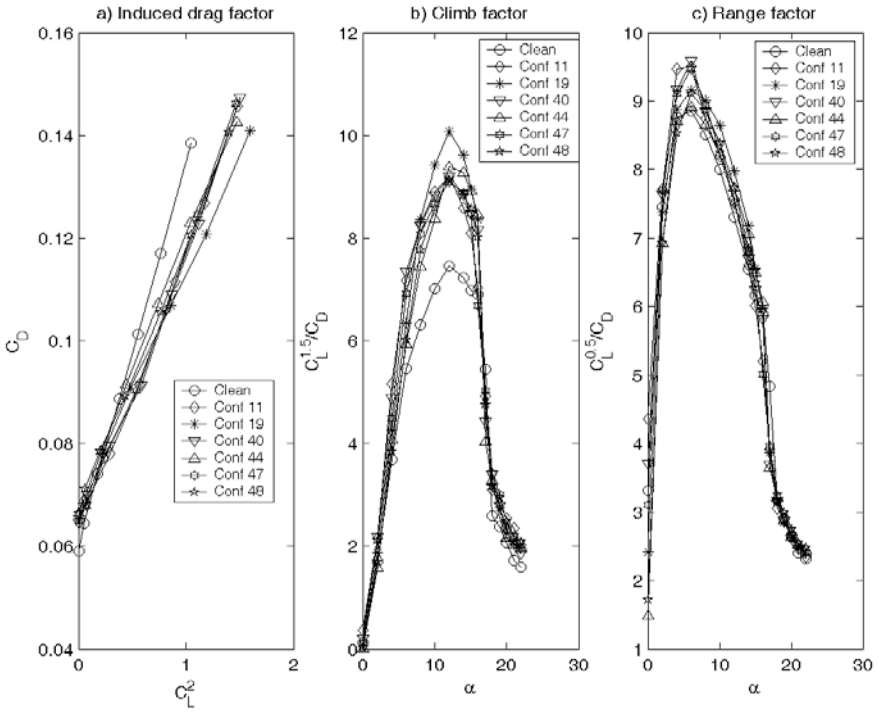

Figure. 13 Aerodynamics factors of multi-winglets

The selected configurations presented curves such as C_D x α similar to those existent for the wing without winglet. However, more drag is produced at low incidence due to the increase in the aspect ratio with the presence of the winglets. Also for incidence angles above 16° the configurations showed larger drag coefficients as shown in Fig. (12), probably due to separation. The increase in effective aspect ratio with the gain in lift led to a dramatic increase in the aerodynamic wing model efficiency as shown in Fig. (12)(c). In Fig. (12)(d), the Drag polar also shows a great improvement for all configurations especially at high values of α..

In Fig. (13)(a) the major parameter is the gradient dC_D/dC_L^2 taken from the linear part of the curve, this relates directly to the lift dependent induced drag C_{Di}. All the configurations improved the performance of wing induced drag and the curves are close and show a higher C_D for negative incidence angles. For these angles the configurations presented small dC_L/dC_L^2 gradients for the base tip. Also from Fig. (13)(b), it is clear that configuration 48 produced the smallest gradient and shows more advantages. The potential flexibility of operation of the adaptive multi-winglet system proposed is shown in Fig.(13). It is possible to change the positions of the configurations in order to maintain the best performance with reference to climb rate and maximum range.

5. Conclusions

A group of experimental studies to investigate the effects of different wing tip devices on the reduction of induced drag were presented. From the experimental data the following conclusions can be drawn.

1). Whit regard to the use of delta tip, winglet, and "Hoerner" devices, concerning the aerodynamic characteristics of an agricultural airplane wing, all tip devices showed improvements to the aerodynamic characteristics of the wing. The best results were presented by the down curved tip, that equips up-to-date the Brazilian agricultural aircraft (EMBRAER-IPANEMA). Winglets improved the aerodynamic characteristics and the resultant tip vortex is very adequate for agricultural use but this device produces an undesirable increase of wing root bending moment. The Delta tip device produced moderate improvements on wing efficiency and is an economical choice for the increase of aircraft performance. However this tip is not adequate for agricultural applications because of the small vortex displacement in relation to other tip devices presented here. Therefore, the winglet offers the best potential capabilities for the development of a specific wing tip design for agricultural aircraft.

2). Wing tip blowing using a three vectored Coanda Jets combination was investigated. Results showed potential benefits in combining the three Jets with the aerodynamic characteristics of a wing. The optimization of the tip Jet flow for each operational maneuver may result in improvements for the whole flight envelope from climb to maximum range. However, some tests are still required at cruise configuration and low jet coefficients in order to accurately study the potential benefit of the three Coanda vectored Jets. Also some consideration and evaluation is still necessary to adapt this concept to the real world aircraft, such as the power bleeded from the engines to maintain efficient blowing; to low aspect ratio wings, a smart vectored system for the jets and so on.

3.) An adaptive multi-winglet system was investigated using wind tunnel experiments in order to show the effect of the system on the aerodynamic characteristics of a low aspect ratio wing. Results showed potential benefits in combining a three winglet configuration with the particular aerodynamic characteristics of a wing. The optimization of the adaptive multi-winglet system for each operational mission may result in an improvement for the whole flight envelope from climb to maximum range. However, some tests are still required for the cruise configuration in order to accurately assess the potential benefits.

6. References

Catalano, F., 2001, "The New Closed Circuit Wind Tunnel of the Aircraft Laboratory of University of São Paulo", 16th Brazilian Congress of Mechanical Engineering. Vol.6, pp 306-312.

Cerón-Muñoz, H. D. and Catalano, F. M., 2006, "Experimental Analysis of the Aerodynamic Characteristics Adaptive of Multi-winglets", Journal of Aerosapce Engineering, Vol 220, No 3, pp. 209-216

Coimbra, R. and Catalano, F., 1999, "Estudo Experimental Sobre Pontas de Asa Para Uma Aeronave Agrícola", Revista Revista Brasileira de Engenharia Agrícola e Ambiental, Vol 3, No 1, pp. 99-105, 1999.

Coimbra, R. and Catalano, F., 2002, "Effect of wing tip blowing on the vortex drag", ICAS 2002 proceedings, Toronto, Canada.

Herderson, W. P. and Holmes, B. J., 1989, "Induced Drag: Historical Perspective", SAE paper n. 892341, Warrendale, PA. USA.

Kravchenco, S. A., 1996, "The Aplication of the Wing tip Lifting Surfaces for Practial Aerodynamic", ICAS-96-4.6.4, Sorrento Italy, pp. 1338-1349.

La Roche, U. And Palffy, S., 1996, "Wing-grid, a Novel Device for Reduction of Induced Drag on Wings",. ICAS-96-2.10, Sorrento Italy, pp. 2303-2309.

Maughmer, M. D., Swan, T. S. and Willits, S. M., 2002, "Design and Testing of a Winglet Airfoil for Low-speed Aircraft", Journal of Aircraft, Vol 39, No 4, pp. 654-661.

Mineck, R. E., 1995, "Stydy of Potential Aerodynamic Benefits from Spanwise Blowing at Wing tips", NASA TP No. 3515, pp. 97.

Nicks, O. W., 1983, " Wing Extension for Improving Climb Performance", AIAA paper 83-2556.

Pope, A. and Rae, W. H., 1984, "Low Speed Wind Tunnel Testing", Wiley, New York.

Simpson, G., Ahmed, N. A. and Archer, R. D., 2000, "Improvement of a Wing's Aerodynamic Efficiency Using Coanda Tip Jets", Journal of Aircraft, Vol. 37 No.1, pp. 183-184.

Smith, M. J. et al., 2001, "Performance Analysis of a Wing with Multiple Winglets", AIAA paper 2001-2407.

Spillman, J. J., 1978, "The Use of Wing tip Sails tu Reduce Vortex Drag", Aeronautical Journal, Vol 82, No 813, pp. 387-395.

Spillman, J. J., Ratcliffe, H.Y. and McVitie, A. 1979, "Flight Experiments to Evaluate the Effect of Eing-tip Sails on Fuel Consumption and Handling Characteristics", Aeronautical Journal, Vol. 83, No. 823, pp. 279-281.

Spillman, J, J. and McVitie, M. 1984, "Wing tip Sails Which Give Lower Drag at All Normal Flight Speeds", Aeronautical Journal, Vol. 88, No. 878, pp. 362-369.

Spillman, J. J., 1987, "Wing tip Sails; Progress to Date and Future Developments", Aeronautical Journal, Vol 91 No 910, pp 445-543.

Tavella, D., 1985, "Measurements on Wing Tip Blowing", NASA CR-176930, pp. 36.

Tavella, D., et al., 1986, " The Iinfluence of Tip Blowing on Rectangular Wings", AIAA paper no. 85-5001.

Traub, L. W., 1994, "Aerodynamics Effects of Delta Planform Tip Sail on Wing Performance", Journal of Aircraft, Vol.31, No 5, pp. 1156-1159.

Whitcomb, R. T., 1976, "A Design Approach and Selected Wind-tunnel Results at High Subsonic Speeds for Wing tip Mounted Winglets", NASA Technical note D-8260, pp. 3-27.

Wu, J. M., Vakili, A. D., and William, F., 1984, "Aerodynamic Interaction of Wing Tip Flow With Discrete Wing tip Jets", AIAA paper no. 84-2206.

Proceedings of the 11th Brazilian Congress of Thermal Sciences and Engineering -- ENCIT 2006
Braz. Soc. of Mechanical Sciences and Engineering -- ABCM, Curitiba, Brazil,- Dec. 5-8, 2006

Paper CIT06-0336

EFFECTIVE USE OF VORTEX GENERATORS TO IMPROVE THE PERFORMANCE OF SUBMERGED AIR INLETS FOR AIRCRAFT

César Celis Pérez, Luis Fernando Figueira da Silva
Department of Mechanical Engineering, Pontificia Universidade Catolica do Rio de Janeiro,
Rua Marquês de São Vicente, 225, Rio de Janeiro, RJ, 22453-900, Brazil.
{ccelis, luisfer}@mec.puc-rio.br

Sandro Barros Ferreira
Institute of Energy, Pontificia Universidade Catolica do Rio de Janeiro,
Rua Marquês de São Vicente, 225, Rio de Janeiro, RJ, 22453-900, Brazil
sandro@ituc.puc-rio.br;

Antonio Batista de Jesus, Guilherme Lara Oliveira
Empresa Brasileira de Aeronáutica SA – EMBRAER,
Avenida Brigadeiro Faria Lima, 2170, São José dos Campos, SP, 12227-901, Brazil
{antonio.jesus, guilherme.oliveira }@embraer.com.br

Abstract. *In this computational work, the influence of the use of a delta wing vortex generator upon the boundary layer that develops upstream a submerged air intake is studied. Firstly, the flow in a conventional NACA inlet is analyzed numerically and its results are considered as a reference for the comparisons with the cases in which the vortex generator is included. Then, a delta wing vortex generator is designed and assembled to the conventional NACA inlet, and the result of this assembling is studied numerically. Finally, a support mast of the vortex generator is designed, and simulations are performed of the ensemble NACA inlet with vortex generator and mast for three sideslip angles of the support. The results show that the use of the delta wing vortex generator is responsible for considerable reductions of the boundary layer thickness and, consequently, significant improvements of the performance parameters of the NACA inlet. The improvements, relative to the conventional NACA intake, in terms of ram recovery ratio and mass flow rate, are of up to 53% and 19%, respectively. The contribution of the drag induced by the vortex generator with support on the total drag of the ensemble is only about 10%.*

Keywords: *Air inlets, vortex generator, aerodynamics.*

1. Introduction

NACA inlets, Figure 1, have been widely used in aircraft as a low drag source of external flow for air conditioning, ventilation and cooling systems. The design criteria of these intakes have been established during the 1940's and 50's. Recently, classical aircraft intakes have been revisited with the use of Computational Fluid Dynamic techniques (CFD), aiming to improve their performance. Performance improvements have been sought with the use of the following techniques: (i) vortex generators (Nogueira de Faria and Oliveira, 2002 and Devine *et al.*, 2002), (ii) flow deflectors (Hall and Barclay, 1948 and Delany, 1948), (iii) parametric geometric optimization (Taskinoglu and Knight, 2004), and (iv) pulsating jets (Gorton *et al.*, 2004). None of the performance enhancement techniques explored to date has shown decisive advantage with respect to the others.

Figure 1. Conventional NACA inlet (Nogueira de Faria and Oliveira, 2002).

The boundary layer thickness upstream the air intake is the key parameter governing the performance of this type of inlets (Devine *et al.*, 2002; Hall and Barclay, 1948 and Mossman and Randall, 1948). These works show that the larger the boundary layer thickness, the poorer the performance of the air inlet. Delta wings are usually employed in supersonic airplanes, because they induce low wave drag while yielding high values of lift coefficient. These high values of lift coefficient are associated to the high levels of vorticity produced by the vortices generated along the suction side of the delta wing. In this work, the vortices generated by a delta wing vortex generator will be used to

reduce the boundary layer thickness through the mixing of high momentum air from the freestream flow with the low energy boundary layer air. The goal of this work is to evaluate the influence of the use of the delta wing vortex generator without and with support on the development of the boundary layer upstream the inlet, and, more specifically, on the performance parameters of the NACA intake. The performance parameters considered are the ram recovery ratio, the mass flow ratio or mass flow rate, and the drag coefficient. The ram recovery ratio of the NACA inlet is defined as the ratio between the dynamic pressure at the throat of the air inlet and the freestream dynamic pressure, whereas the mass flow ratio is the ratio of the actual mass flow ingested by the inlet to the mass flow that would enter to the intake at freestream conditions. The drag coefficient is computed as the ratio between the total drag, which is the component force at the direction of the freestream flow, and the freestream dynamic pressure multiplied by the throat area of the air inlet. A review of the state-of-the-art of submerged inlets, and the results of the influence of parametric variations of the vortex generator geometry were presented in previous publications (Hime *et al.*, 2005 and Celis *et al.*, 2006). This work extends the previous studies by discussing the results obtained from numerical simulations of the ensemble NACA inlet with vortex generator and support. Also, a mesh sensibility study is presented. A support mast of the vortex generator is designed, and then simulations are performed of the ensemble for three sideslip angles of the support.

2. Modeling aproach

2.1. Description of the geometric configurations

In this numerical study are simulated and analyzed three generic configurations. The conventional NACA intake, which geometric characteristics are shown in Figure 2(a), is the first configuration studied in this work. This configuration corresponds to a typical one used in a regional transport aircraft. The flow conditions analyzed correspond to a Mach number of 0.31, an altitude of 9,000 ft and a temperature of -2.83 °C. The results of this configuration will be used as a reference to evaluate the performance of the NACA intake when the vortex generator, without and with support, is utilized.

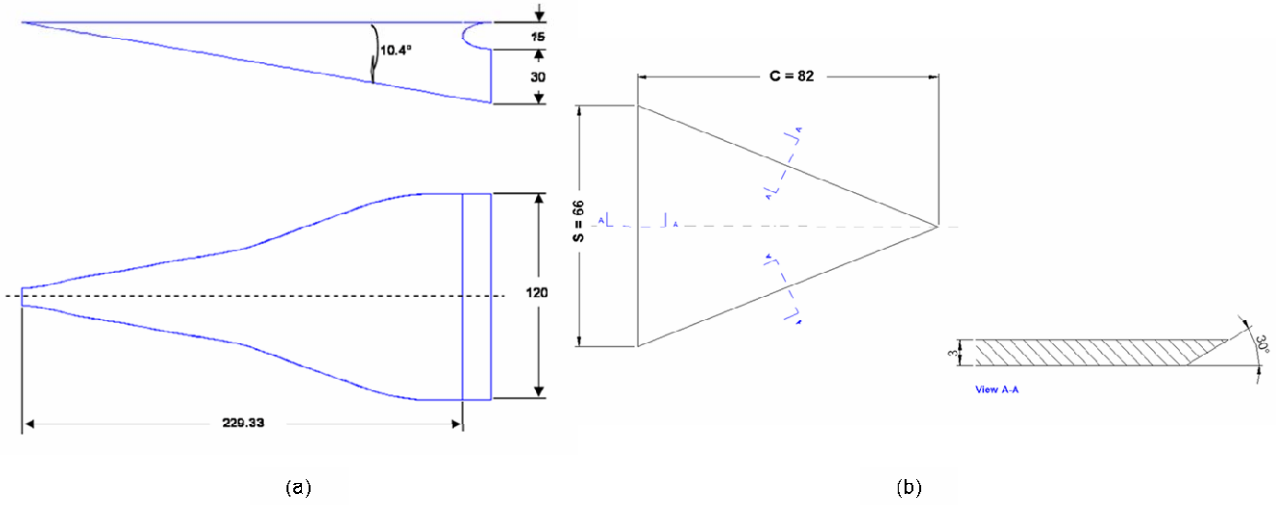

Figure 2. (a) NACA air inlet geometry, (b) Vortex generator geometry (dimensions in mm).

This conventional NACA intake is placed at the center of a flat plate of 10,000x2,000 mm^2. The inlet is positioned at a distance of 5,000 mm of the beginning of the flat plate. Aiming to simulate actual flow conditions, a duct of rectangular cross section 120x30 mm^2 and 500 mm length is coupled to the NACA inlet throat. Since the assembly NACA inlet, flat plate, and exit duct is symmetrical with respect to the center line of the NACA inlet, the configuration studied only considers half of the model. Thus, the computational domain used in the simulations consists of a parallelepiped of 10,000x1,000x1,000 mm^3, where freestream conditions are established.

The configuration resulting from the assembly of the conventional NACA inlet to the vortex generator type delta wing without support, and that in which the support mast is utilized constitute the other two generic configurations studied in this work. The main geometric characteristics of the delta wing vortex generator utilized are shown in Figure 2(b). The positioning of the vortex generator with respect to the NACA intake was defined using results from simulations of the isolated vortex generator, which will not be shown here.

2.2. Mesh generation

Grid generation of the studied configurations was performed using the commercial software ANSYS ICEM CFD, Version 5.0. All the meshes used in this work were structured meshes composed by hexahedral elements. The mesh of

the conventional NACA intake, whose shell characteristics are shown in Figure 3, was composed of about 255,000 elements.

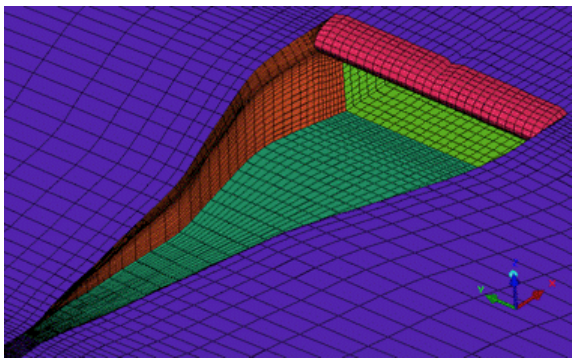

Figure 3. Shell mesh of the conventional NACA inlet.

An a priori evaluation of the quality of the elements was performed using as mesh quality parameters (i) the aspect ratio, and (ii) the angle of the elements. For hexahedral elements, the aspect ratio is defined as the ratio of the distances between diagonally opposite vertices, longer diagonal/shorter diagonal. Thus, an aspect ratio of 1 corresponds to a perfectly regular element, and an aspect ratio of infinity indicates that the element has zero volume. The angle quality parameter measures the maximum internal angle deviation from 90° for each cell. If the cells are distorted and the internal angles are small, the accuracy of the solution could be affected.

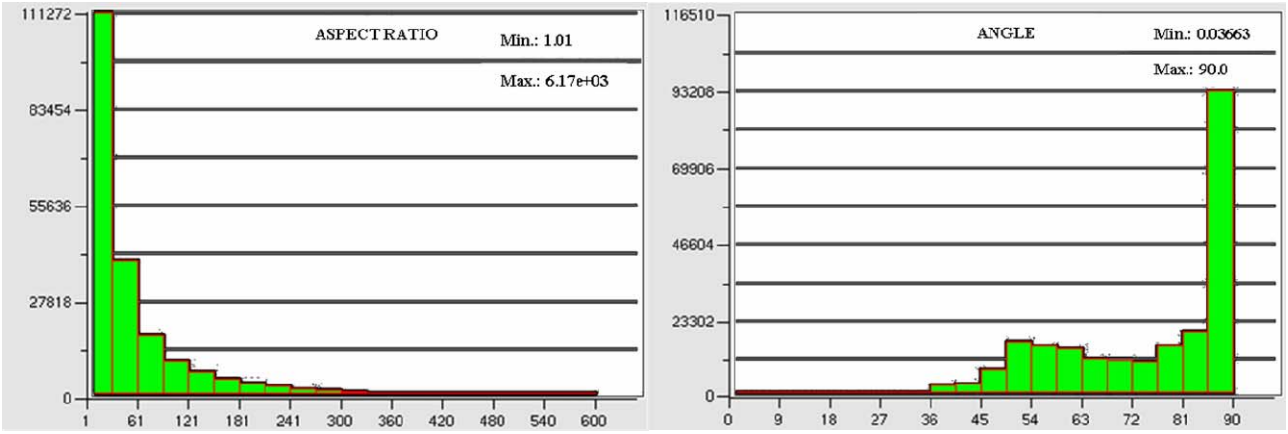

Figure 4. Mesh quality of the conventional NACA inlet.

Figure 4, which shows the histogram of distribution of the number of elements as a function of the quality parameters aspect ratio and angle, illustrates the quality of the mesh of the conventional NACA intake according to these two quality parameters. In this figure it is possible to note that the most of the elements of this mesh have an acceptable quality, aspect ratio near 1 and internal angle near 90°. However, it is clear that there are some elements (< 1%) with a quality smaller than could be desirable. These elements are located on regions of the flow where the mesh is very refined. In the results section it will be shown that the quality of this small group of elements does not affect the solution.

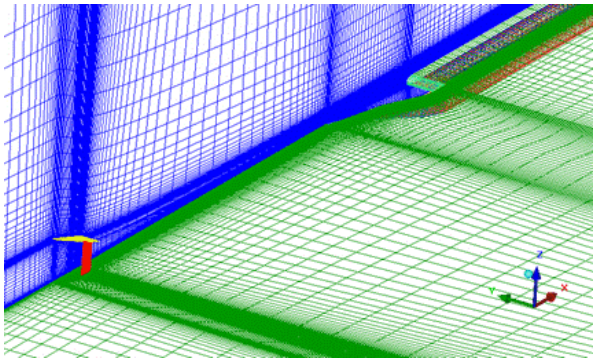

Figure 5. Computational mesh, NACA inlet with vortex generator and support.

The computational mesh used to simulate the flow on the configurations of NACA inlet with vortex generator without support consisted of nearly 1,100,000 elements. The details of the meshes used to simulate the flow on these configurations will not be shown because their similarity with those used at the configurations of NACA intake with vortex generator and support. The meshes used at these configurations of NACA intake with vortex generator and support, one of which is shown in Figure 5, consisted of approximately 1,700,000 elements. On all the configurations corresponding to the NACA inlet with vortex generator without and with support an analysis of mesh quality, similar to that performed on the conventional NACA inlet, was performed in order to verify the quality of the meshes utilized, and thus to ensure an appropriate description of the flow around the NACA inlet and the vortex generator.

2.3. Flow solver

All the numerical simulations were conducted using the commercial CFD package FLUENT, Version 6.1. For the resolution of the governing equations of the compressible flow, Fluent uses a control-volume-based technique, which consists of the division of the domain into discrete control volumes using a computational grid. The integration of the governing equations on the individual control volumes allows constructing algebraic equations for the discrete dependent variables. The linearization of the discretized equations and solution of the resultant linear equation system yields updated values of the dependent variables.

In this work, an implicit segregated solver was used to solve the governing equations along with a Spalart-Allmaras (Spalart and Allmaras, 1994) turbulence model. The interpolation scheme used for the convection term was the Second-Order Upwind Scheme, and the Second-Order for calculating face Pressure. The algorithm applied for Pressure-Velocity Coupling was SIMPLE (Semi-Implicit Method for Pressure-Linked Equations).

2.4. Boundary and initial conditions

Figure 6 illustrates the computational domain zones where the boundary conditions were set. At the farfield, zone 1 (dashed blue lines), freestream conditions with a given Mach number, static pressure and temperature were specified. At the duct exit section, zone 2 (green line), a constant static pressure was specified. No-slip adiabatic boundary conditions were set at the solid walls, zone 3 (red lines). Finally, symmetry conditions were set at the symmetry plane of both the conventional NACA intake and the vortex generator.

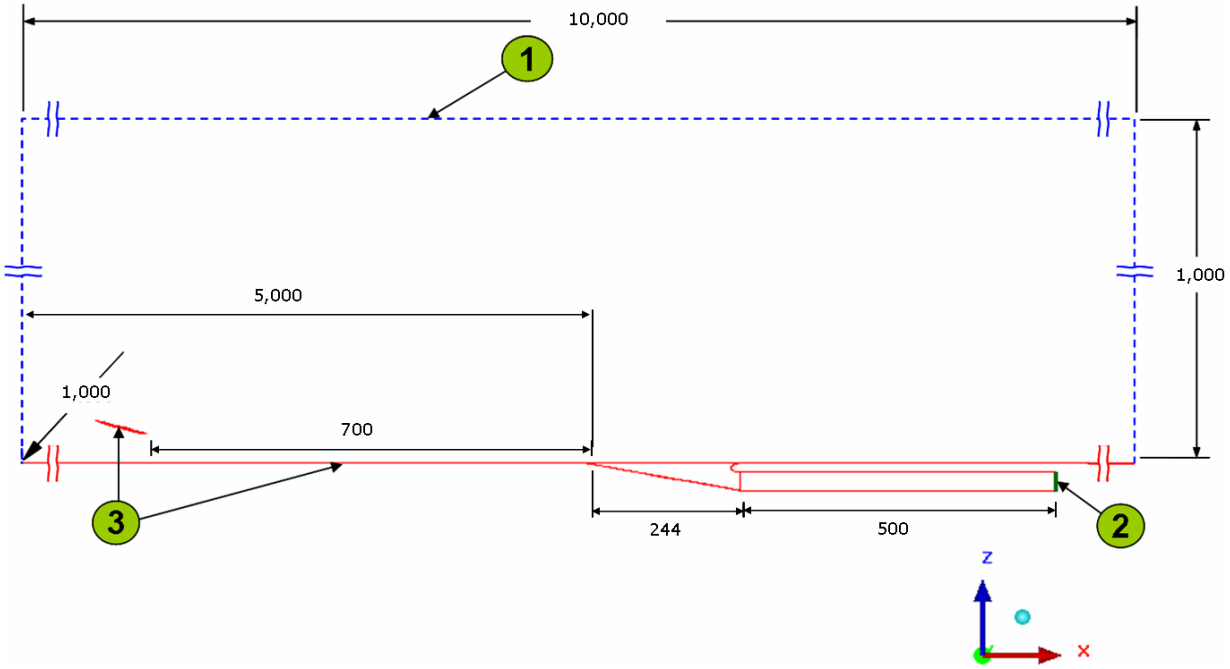

Figure 6. NACA inlet with vortex generator and support – Symmetry plane (dimensions in mm).

The computations were initialized from freestream flow conditions given in Table 1.

Table 1. Freestream flow conditions.

Pressure (p)	Pa	72,428
Temperature (T)	K	270.3
Mach number (M)	-----	0.31
Modified Turbulent Viscosity	m^2/s	0.001

3. Results and discussion

Table 2 summarizes the configurations studied in this work. In this table, β represents the sideslip angle of the support of the vortex generator. In all the configurations of NACA intake with vortex generator showed in this work, the horizontal distance between the trailing edge of the vortex generator and the beginning of the ramp of the NACA inlet was 700 mm, the angle of attack (α) of the vortex generator was 15°, and the vertical distance between the trailing edge of the vortex generator and the flat plate was 50 mm. The area of the vortex generator was A = 2,706 mm^2. For the sake of simplicity, the results will be referenced to their respective codes indicated in Table 2.

Regarding the convergence criterion of the simulated cases in this work, it is important to emphasize that, in all the computations performed here, the solver execution was interrupted only after the residuals of all the computed variables achieved their complete stabilization. The residual levels of all the variables after the stabilization were of the order of 10^{-4} or lesser, except in the case of the mass conservation in which the residuals were of the order of 10^{-2}. The approximated iterations number necessary to achieve the complete stabilization of the residual was of 6,000, 10,000, and 25,000, for the configurations corresponding to the conventional NACA inlet, the NACA inlet with vortex generator, and the NACA inlet with vortex generator and support, respectively.

Table 2. Summary of the configurations simulated.

Case	β (°)
N1A-1	DATUM
NGVA	VG without support
NGVAM-0	0
NGVAM-5	5
NGVAM-10	10

3.1. Conventional NACA inlet

3.1.1. Flow structure

It is well known that the boundary layer thickness is a determinant parameter of the efficiency of a NACA inlet. So, in order to characterize the influence of the vortex generator upon the boundary layer, plots representing the boundary layer development upstream the NACA inlet will be analyzed throughout the paper. Moreover, since conventional NACA inlets have their design based on the generation of vorticity on the divergent ramp walls, contours illustrating the level of vorticity will be also shown. Figure 7 shows cross sections, in transversal planes to the external flow direction, of the longitudinal velocity contours for the configuration of the conventional NACA inlet, case N1A-1. This figure allows verifying the thick boundary which develops upstream the NACA inlet. From computations it was determined that the boundary layer thickness at the beginning of the ramp of the NACA intake is about 50 mm. Also, it is clear that the inlet ingests mostly low energy fluid.

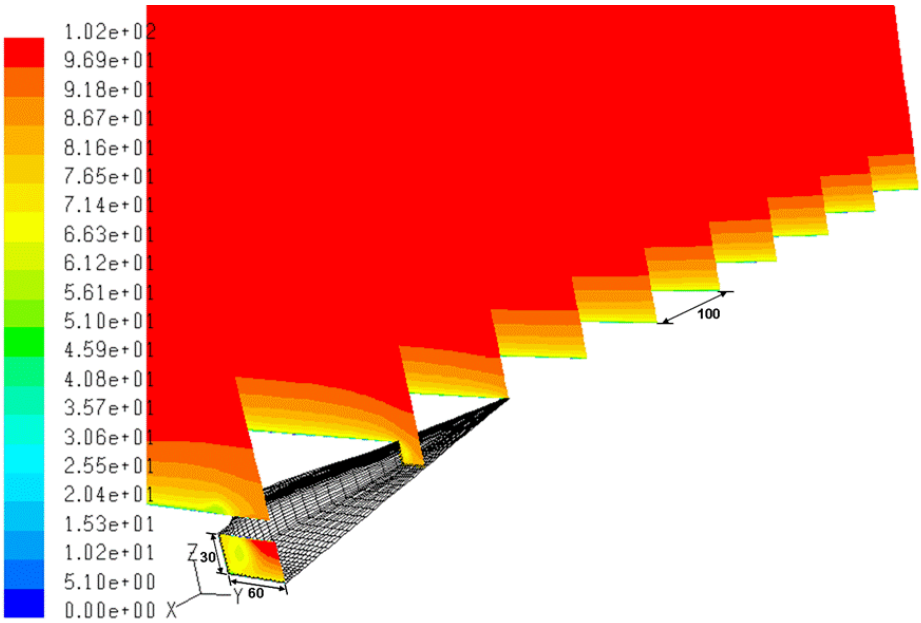

Figure 7. Longitudinal velocity (m/s) – Case N1A-1 (dimensions in mm).

Figure 8 shows the evolution of the longitudinal component of the vorticity for the case of the conventional NACA inlet, case N1A-1, in the same transversal planes to the external flow direction. In this figure, it is possible to see, clearly, the high levels of vorticity originated at the regions close to ramp walls of the NACA inlet. Note that the operation of this type of inlet is based on the generation of vortices on the ramp walls as a consequence of its particular geometry. Consequently, the flow on the throat of NACA inlet is tridimensional.

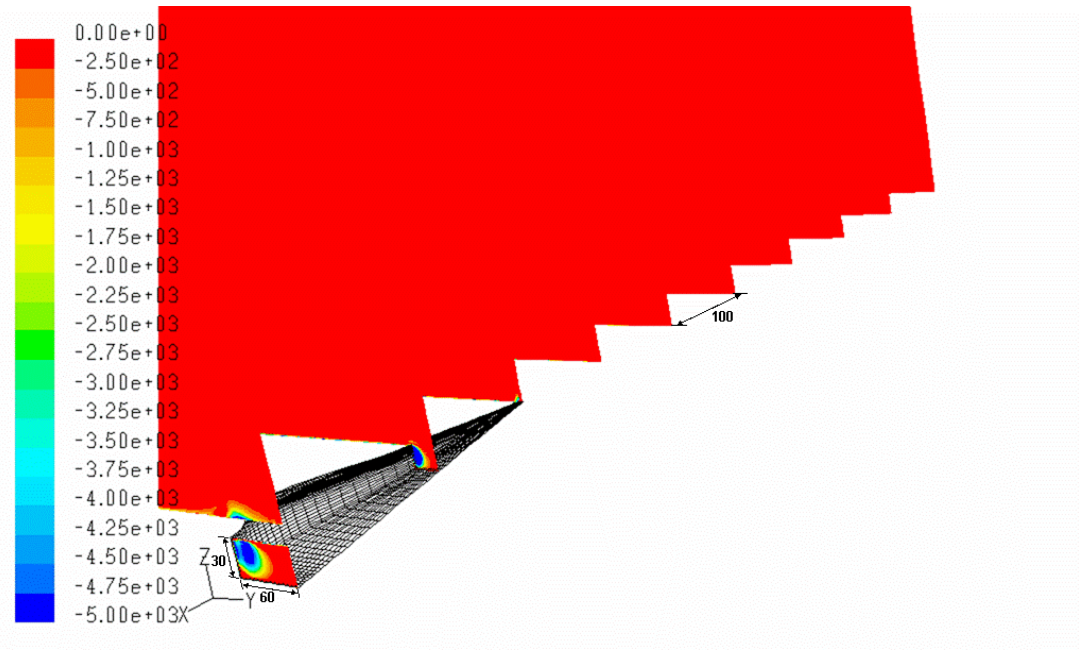

Figure 8. Longitudinal vorticity (1/s) – Case N1A-1 (dimensions in mm).

3.1.2. Influence of the level of refinement of the computational mesh

In order to analyze the influence of the level of refinement of the computational mesh used in the numerical simulations of the conventional NACA inlet on the values of its performance parameters, the mesh utilized was refined using one of the methods of solution-adaptive refinement available in Fluent. The adaptive refinement process utilized is based on the use of a gradient adaption function, which is defined as a function of the element volume and the Euclidean norm of the gradient of the selected solution variable. Trough the use of this gradient adaption function it is assumed that maximum error occurs in high-gradient regions. This particular adaptive refinement process requires (i) the choice of the solution variable from which the adaption function will be constructed, and (ii) for this solution variable, the refine threshold from which the mesh will be refined by subdivision of its elements. Two adaptive refinement processes were performed in this work. The first refinement process was performed using, as solution variable, the longitudinal component of the velocity. In this case, the refine threshold was specified as equal to 5, i.e., elements with gradient values above this value were refined. In the second refinement process the static pressure was considered as solution variable. In this second case, the refine threshold was specified as equal to 10. Modifications of these refinement thresholds in order to assess their influence of the obtained results were not performed.

The number of elements on the mesh after the adaptive refinement process based on the velocity gradients was about 998,000 and about 770,000 after the refinement process based on the static pressure gradients, whereas the original mesh contained about 255,000 elements. From analyses of the meshes obtained after the refinement processes, it was verified that the refinement processes increased the number of elements of the mesh at the regions where the longitudinal component of the velocity and the static pressure present the greatest gradients, i.e., exit duct, ramp, and lip angle of the NACA inlet.

Regarding the performance parameters of the conventional NACA inlet, Table 3 shows the values of these parameters, which were computed using the results obtained from the numerical simulations, for the configuration of the conventional NACA intake, N1A-1, and for the cases in which the adaptive refinement processes was utilized. This table also shows the data used to design this particular NACA inlet. It is important to highlight that the values of ram drag, shown in this table, were computed from equations 3.18 and 6.1 of the ESDU 86002 (Engineering Sciences Data Unit, ESDU, 1996). The friction drag was calculated as the integral wall shear stress of the NACA inlet. Neither the flat plate nor the duct was considered for this drag calculation. The mass flow rate was obtained by a direct integration at the duct exit section of the NACA intake.

Table 3 allows verifying that a good agreement was obtained between the computed values of the performance parameters and the design data. Note, also, that the value of the computed friction drag is negligible when compared to the value of the ram drag of the NACA inlet. Even though the adaptive mesh refinement process more than doubles the

number of elements, the resulting values of the performance parameters of the NACA inlet do not show significant discrepancies, such as can be seen in Table 3. The results reported in this table show that the original mesh used to simulate the NACA inlet, i.e., the mesh without refinement, is already satisfactory to describe the flow behavior through the NACA inlet. When the mesh adaption process was performed, variations of only 1%, in terms of ram recovery ratio, drag coefficient and mass flow rate, were found. Therefore, the level of refinement used on the baseline mesh is considered satisfactory and will be applied to the different meshes used in the computations where the vortex generator is included.

Table 3. Performance parameters – Conventional NACA inlet without and with adaptive refinement.

Parameters	Design Data	N1A-1	Refinement: X velocity	Refinement: S. pressure
Ram-recovery ratio	0.550	0.513	0.511	0.519
Mass-flow rate [kg/s]	0.260	0.260	0.259	0.261
Mass-flow ratio, MFR	----	0.76	0.76	0.76
Total drag, Td = Rd+Fd [N]	16.41	18.60	18.45	18.59
Ram drag, Rd = a+b+c [N]	----	18.13	17.97	18.11
(a) NACA	----	18.13	17.97	18.11
(b) VG	----	0.00	0.00	0.00
(c) Support	----	0.00	0.00	0.00
Friction drag, Fd = d+e+f [N]	----	0.47	0.48	0.47
(d) NACA	----	0.47	0.48	0.47
(e) VG	----	0.00	0.00	0.00
(f) Support	----	0.00	0.00	0.00
Drag coefficient	0.93	1.06	1.06	1.06

3.1.3. Validation of the numerical results

It is important to emphasize that literature on submerged intakes is practically inexistent between the mid 1950s and the end of the 1990s. Apparently, during this period no works were developed related to the submerged inlets. The work performed on the 1940s and 1950s is, as it could be expected, focused on experiments. The main goal of these works, which were conducted by the National Advisory Committee for Aeronautics (NACA), was to determine the influence of both the flow parameters and the geometric configuration on the performance parameters of this type of intakes. Within the references reviewed (Hime *et al.*, 2005), few had detailed information about the flow field, what makes the comparison between the results described and a Computational Fluid Dynamics (CFD) simulation impossible. In particular, among the references reviewed, velocity measurements were not available. Roughly speaking only total pressure is measured. Such an experimental flowfield characterization is insufficient for the purpose of choosing the most appropriate turbulence model. Then, since detailed experimental results are not available to validate the numerical results obtained in this work, design data obtained from ESDU will be used as a reference to validate these computational results and to select the more appropriate turbulence model to simulate the flow in the NACA intake. Thus, Figure 9 shows curves of ram recovery ratio, for the results obtained from the ESDU 86002, and from numerical simulations performed using as turbulence model both the Spalart-Allmaras and the k-ε Realizable (Shih *et al.*, 1995) turbulence model.

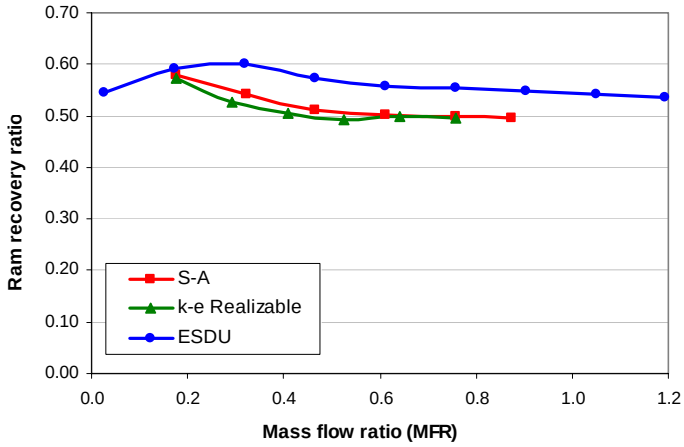

Figure 9. Ram recovery ratio of the conventional NACA intake as a function of the mass flow ratio.

In Figure 9 it is possible to verify that the numerical simulations under-estimate the values of the ram recovery ratio of the NACA inlet. Furthermore, the value of the mass flow ratio of maximum ram recovery ratio is under predicted by the computations. However, in this figure one can observe that the performance trends computed with both turbulence models are quite similar to each other, even if the semi-empirical figures computed from ESDU always exhibit higher values. Considering that the computed values of ram recovery ratio using the Spalart-Allmaras turbulence model showed the smallest discrepancies, about 8%, when compared to the design data obtained from ESDU, and that this turbulence model was specifically developed for aerodynamical applications, it was decided to use only this model on the simulations performed in this work.

3.2. NACA inlet with vortex generator

The influence of the use of the delta wing vortex generator upon the development of the boundary layer upstream the NACA inlet and, consequently, on the performance parameters of this type of intakes, is analyzed using the same plots used to describe the flow structure in the case of the conventional NACA intake.

Figure 10 shows cross sections, in transversal planes to the external flow direction, of the longitudinal velocity contours for the basic configuration of NACA inlet with vortex generator, called NGVA. In this figure, considering that the free-stream velocity at x-axis direction is equal to 102 m/s, it is possible to see, accordingly to the color scale, that the downwash effect of the vortices generated by the delta wing vortex generator leads to a considerable reduction of the boundary layer thickness upstream the air intake, which occurs mainly at the central region of the flat plate. One immediate consequence of the reduction of the boundary layer thickness is the larger amount of external air ingested by the NACA intake, which leads to increases of the ram recovery ratio and the mass flow rate, such as will be demonstrated later.

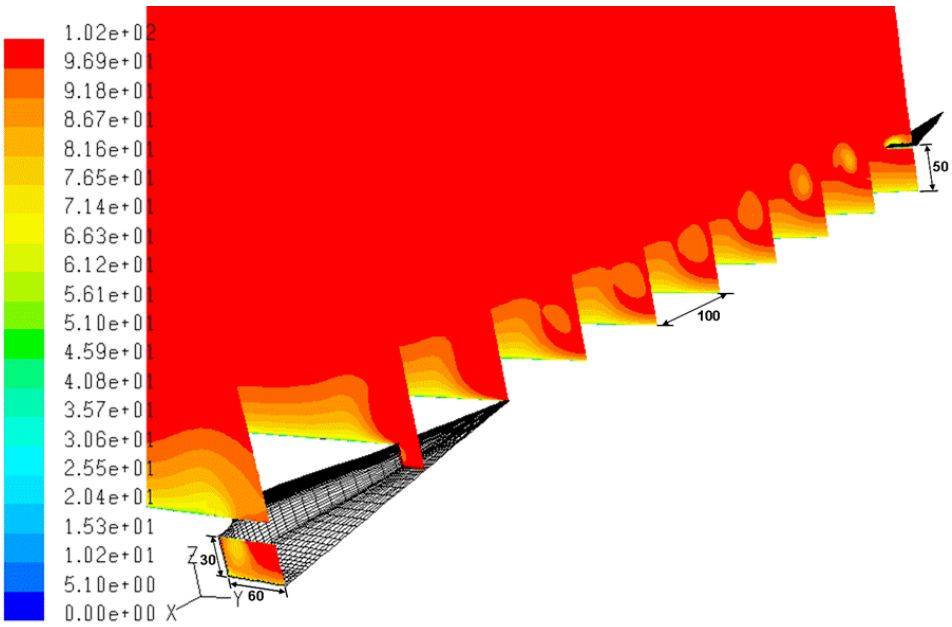

Figure 10. Longitudinal velocity (m/s) – Case NGVA (dimensions in mm).

The considerable reduction of the boundary layer thickness upstream the air intake observed in Figure 10 is originated, as mentioned previously, by the downwash effect of the vortices generated at the suction side of the vortex generator, which are shown in Figure 11. This figure shows the evolution of the longitudinal component of the vorticity for the case of the basic configuration of NACA inlet with vortex generator, case NGVA, in the same transversal planes to the external flow direction. Figure 11, which clearly shows the development of these vortices and the high levels of vorticity associated with them, allows observing that the vortex cores are not ingested by the intake. This particular behavior avoids the negative effects that the vortices ingestion could originate. Comparing this figure with Figure 8, case N1A-1, it is possible to see that the presence of the vortex generator originates, at the throat plane of the NACA inlet, a greater region affected by the vorticity. However, these higher levels of vorticity are not detrimental to the inlet performance, as shown further on.

3.3. NACA inlet with vortex generator and support

The next stage on the development of our work was to design the support of the vortex generator which is used to maintain the desired relative position with respect to the NACA intake. To this end, it was considered that the support should, if possible, contribute to the reduction of boundary layer thickness upstream the NACA intake and downstream

the vortex generator. Considering this aspect, what one intends is that the wake generated by the support can contribute positively to the effect of the counter-rotating vortices generated on the suction side of the vortex generator, and specifically, to supplement the effect of these vortices on the reduction of the boundary layer thickness. Since the reduction of the boundary layer thickness occurs mainly on the central region of the flat plate, it was decided to use a pair of tip-mounted supports. Another possibility considered was the use of a ventral support, which was cast aside since the wake generated by this type of support could (i) negatively influence the process of reduction of the boundary layer thickness, and (ii) be ingested by the NACA intake, degrading its performance parameters.

The basic configuration of NACA intake with vortex generator, called NGVA, was used as the configuration on which the support was designed. The designed support was obtained as a result of the extrusion, at the normal direction to the flat plate, of a NACA 0012 profile, whose chord is 25 mm. The distance, in the lateral direction, between the leading edge of the support and the symmetry plane of the vortex generator is 21 mm. Defining the angle formed by the chord of the support and the symmetry plane of the vortex generator as "sideslip angle", β, it was decided to perform computations for different values of the sideslip angle, in order to evaluate its influence on the performance parameters of the NACA inlet. Note that it is expected that the actual flow sideslip angle should be different from the geometrical sideslip, since the pressure difference between the suctions and the pressure side of the vortex generator induces lateral flow.

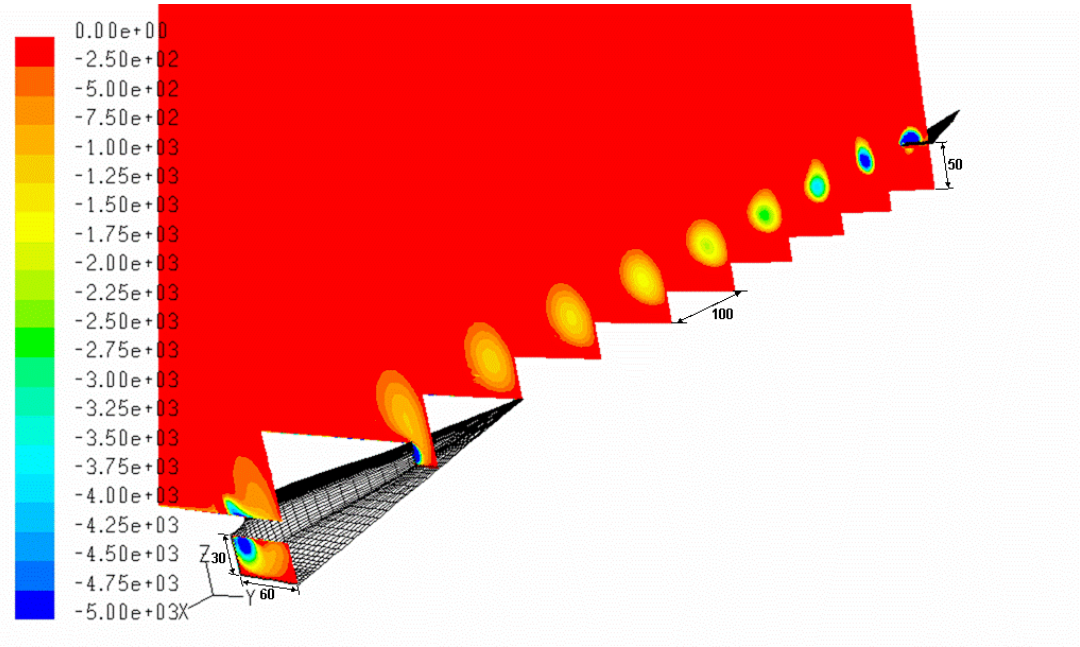

Figure 11. Longitudinal vorticity (1/s) – Case NGVA (dimensions in mm).

3.3.1. Flow structure

Figure 12 shows cross sections, in transversal planes to the external flow direction, of the longitudinal velocity contours for the basic configuration of NACA inlet with vortex generator and support, NGVAM-0. Comparing this figure with Figure 10, corresponding to the basic configuration of NACA inlet with the freely standing vortex generator, it is possible to see that that the boundary layer development upstream the NACA inlet and downstream the vortex generator is slightly influenced by the presence of the support of the vortex generator. This influence seems to be restricted to the first 200 mm downstream the vortex generator, where occurs a reduction of the velocity due to the wake generated by the support. Further downstream the vortex generator, the boundary layer thickness does not present significant variations originated by the presence of the support. Thus, the use of the vortex generator and its support continues to lead to a considerable reduction of the boundary layer thickness upstream the air intake, and, consequently, significant improvements of the performance parameters of the NACA intakes are obtained, such as will be shown further on.

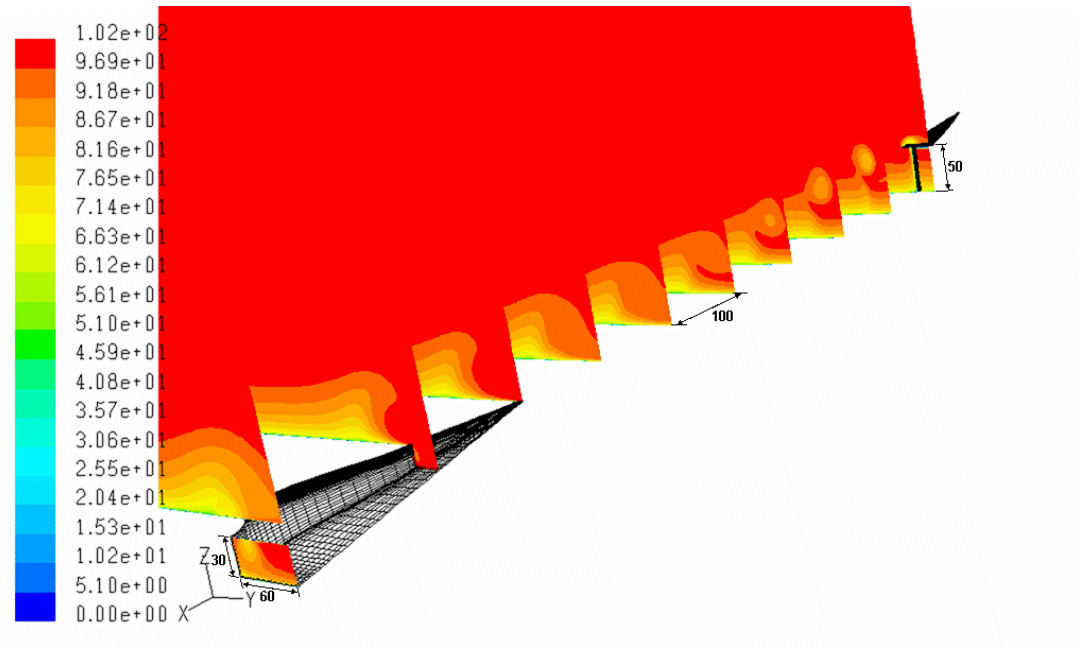

Figure 12. Longitudinal velocity (m/s) – Case NGVAM-0 (dimensions in mm).

The longitudinal vorticity contours for the basic configuration of NACA inlet with vortex generator and support, NGVAM-0, which allows observing the behavior of the vortices wake generated by the support, is shown in Figure 13. This figure clearly shows that the intensity of the vorticity at the wake generated by the support is small when compared to the vortices generated on the suction side of the vortex generator. In this figure, also it is possible to see that support wake is displaced away from the symmetry plane due to the effect of the vortex generator wake and completely dissipated upstream the beginning of the ramp of the NACA inlet.

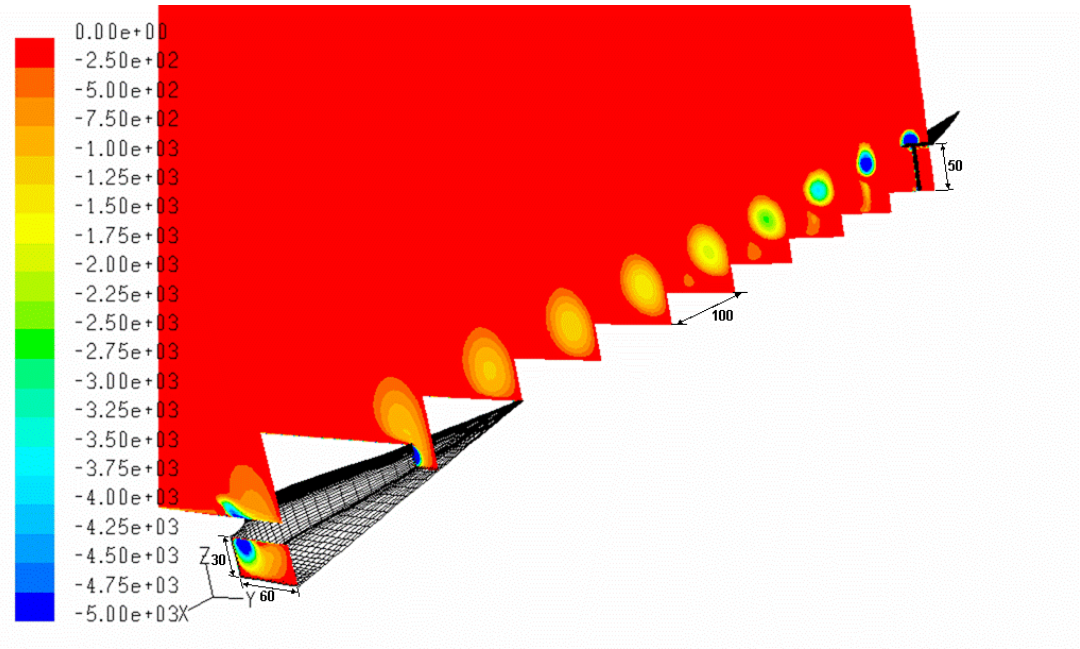

Figure 13. Longitudinal vorticity (1/s) – Case NGVAM-0 (dimensions in mm).

3.3.2. Influence of the sideslip angle of the support of the vortex generator

With the aim of assessing the influence of the sideslip angle of the vortex generator support on the performance parameters of the NACA intake, two different values of the sideslip angle of the support, 5° and 10°, configurations NGVAM-5 and NGVAM-10, respectively, were studied. Figure 14 and Figure 15 show cross sections, in transversal planes to the external flow direction, of the longitudinal velocity contours for the configurations NGVAM-5 and NGVAM-10, respectively. In these figures it is possible to verify that for the two values of the sideslip angle of the support, i.e., β = 5° and 10°, the reduction of the boundary layer thickness at the central region of the flat plate remains

practically unaltered. These figures also show that the wake of the support seems to enhance the lateral motion of the fluid downstream the vortex generator.

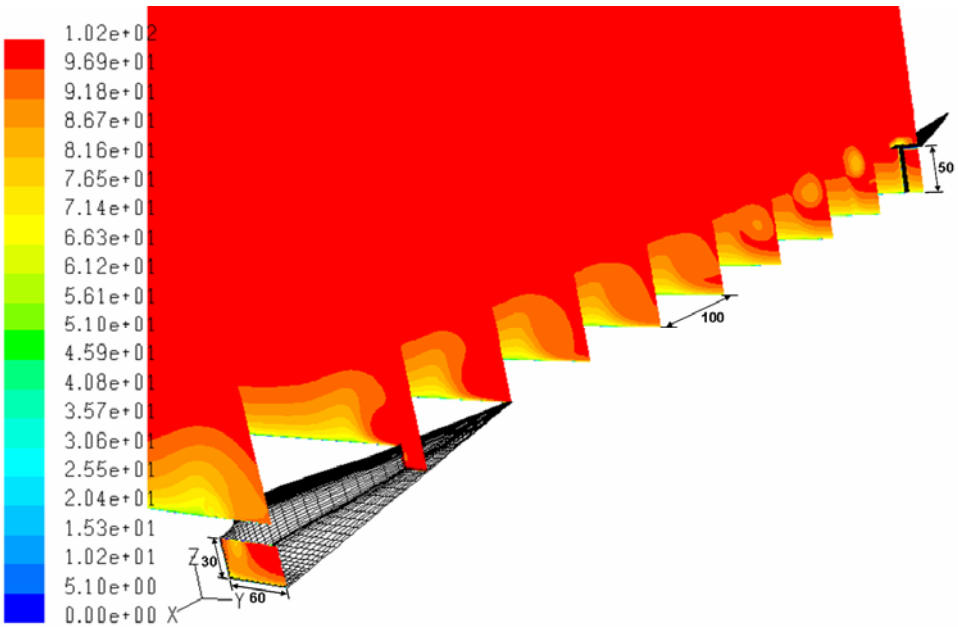

Figure 14. Longitudinal velocity (m/s) – Case NGVAM-5 (dimensions in mm).

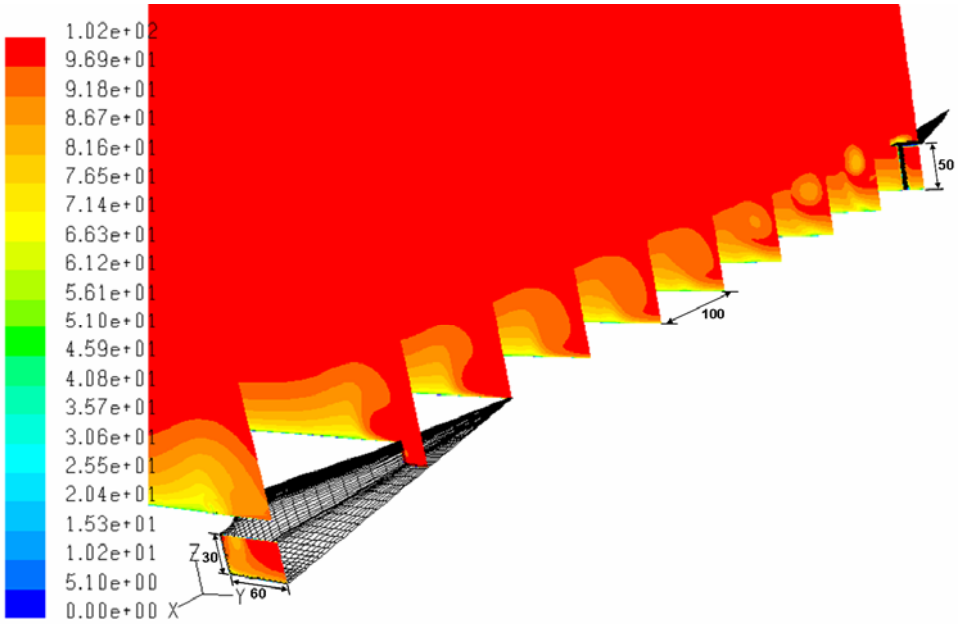

Figure 15. Longitudinal velocity (m/s) – Case NGVAM-10 (dimensions in mm).

Figure 16 and Figure 17 show the longitudinal vorticity contours, in the same transversal planes to the external flow direction, for the configurations of NACA inlet with vortex generator and support which are being analyzed, i.e., NGVAM-5 and NGVAM-10. In these figures it is possible to verify that the longitudinal component of the vorticity practically disappears with the increase of the sideslip angle of the support to 10°. This result is in accordance with design specifications of the support, which intended to minimize the negative effects of the presence of the support on the performance parameters of the NACA intake. Indeed, at the sideslip angle of 10°, the mast profile is aligned with the local flow deflection angle at the suction side of the vortex generator, thus leading to a lesser interference.

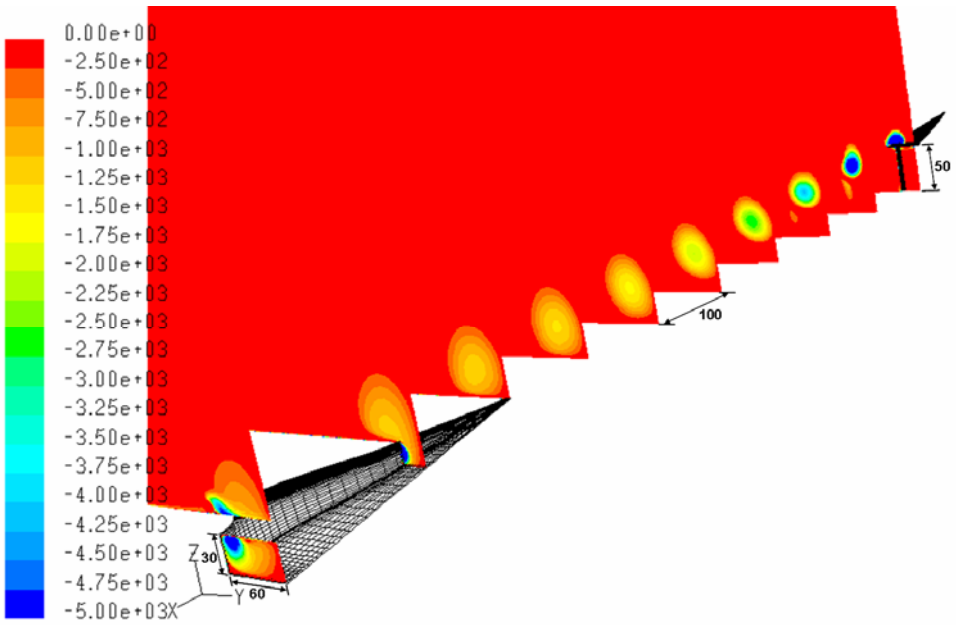

Figure 16. Longitudinal vorticity (1/s) – Case NGVAM-5 (dimensions in mm).

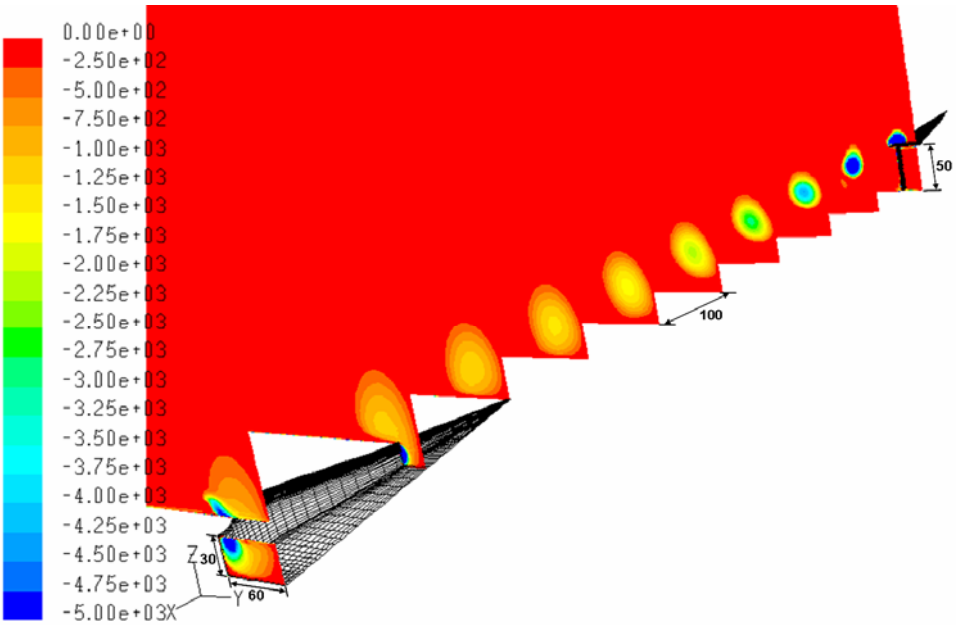

Figure 17. Longitudinal vorticity (1/s) – Case NGVAM-10 (dimensions in mm).

Table 4 shows the values of the performance parameters for the conventional NACA intake, for the basic configuration of NACA inlet with vortex generator without and with support, and for the two configurations of NACA inlet with vortex generator and support called NGVAM-5 and NGVAM-10, which are being analyzed. These parameters were computed following the same procedures used for the conventional NACA inlet, but now accounting for the contribution of the vortex generator and its support to both the ram drag and the friction drag. In this table, the percentage increases related to the values of the performance parameters corresponding to the conventional NACA inlet are indicated in the parentheses.

The results shown in Table 4 indicate that the considerable reduction of the boundary layer thickness upstream the air intake, observed in Figure 10, Figure 12, Figure 14 and Figure 15, leads to significant improvements of the ram recovery ratio and the mass flow rate. This is a direct consequence of the larger amount of external air ingested by the NACA intake. Table 4 also indicates that the presence of the support does not negatively affect the values of the performance parameters of the NACA intake. On the contrary, it contributes to slightly increase the overall performance of the intake. Thus, this table shows that the three configurations of the NACA inlet with vortex generator and support

exhibit improvements for the computed values of mass flow rate and ram recovery ratio. The largest increases in these performance parameters are obtained for a sideslip angle of the support of 10°.

Table 4. Performance parameters – Influence of the sideslip angle of support of the vortex generator.

Parameters	Design Data	N1A-1	NGVA	NGVAM-0	NGVAM-5	NGVAM-10
Ram-recovery ratio	0.550	0.513	0.741 (44.4 %)	0.749 (46 %)	0.774 (50.9 %)	0.787 (53.3 %)
Mass-flow rate [kg/s]	0.260	0.260	0.302 (16 %)	0.303 (16.5 %)	0.307 (18.1 %)	0.309 (18.9 %)
Mass-flow ratio, MFR	----	0.76	0.88 (16 %)	0.88 (16.5 %)	0.9 (18.1 %)	0.9 (18.9 %)
Total drag, Td = Rd+Fd [N]	16.41	18.60	32.43 (74.4 %)	33.18 (78.4 %)	33.67 (81 %)	34.31 (84.5 %)
Ram drag, Rd = a+b+c [N]	----	18.13	31.69 (74.7 %)	32.34 (78.3 %)	32.8 (80.9 %)	33.45 (84.4 %)
(a) NACA	----	18.13	29.68 (63.7 %)	29.81 (64.4 %)	30.22 (66.7 %)	30.43 (67.8 %)
(b) VG	----	0.00	2.01	2.35	2.21	2.09
(c) Support	----	0.00	0.00	0.18	0.37	0.93
Friction drag, Fd = d+e+f [N]	----	0.47	0.74 (60 %)	0.84 (80.1 %)	0.86 (85.8 %)	0.87 (86 %)
(d) NACA	----	0.47	0.59 (26.5 %)	0.58 (24.2 %)	0.59 (26.8 %)	0.6 (29.2 %)
(e) VG	----	0.00	0.16	0.15	0.15	0.15
(f) Support	----	0.00	0.00	0.11	0.13	0.11
Drag coefficient	0.93	1.06	1.86 (74.4 %)	1.9 (78.4 %)	1.93 (81 %)	1.96 (84.5 %)

Besides, in Table 4 it can be seen that in the three configurations of NACA inlet with vortex generator and support, the drag coefficient values only exhibit a small increase when compared to the corresponding values of the case called NGVA. The reason behind this slight increase observed is related to the fact that the contribution to the ram drag, the main component of the total drag, due to the presence of the support is negligible when compared to that of the NACA inlet. However, when the values of the drag coefficient of the configurations of NACA inlet with vortex generator without and with support are compared to that of the conventional NACA inlet, it is possible to verify that the obtained increases are considerable. This is a direct consequence of the increase of mass flow rate that follows the reduction of the boundary layer thickness. Even so, the drag contribution due to the vortex generator with support is only about 10% of the total drag of the ensemble. In this case, 7% corresponds to the drag produced by the vortex generator and 3% to the support of the vortex generator. It is worthy to highlight that the contribution of this 10% relative increase on the drag due the vortex generator with support on the total drag of the aircraft is insignificant. This type of performance enhancement device should be used only in certain NACA inlets, such as that corresponding to the Auxiliary Power Unity.

4. Conclusions and perspectives

In this computational work the influence of the use of a delta wing vortex generator upon the boundary layer that develops upstream the air intake, with the aim of decreasing its thickness and thus to improve the performance of a NACA inlet, was investigated. The values of the ram recovery ratio of the conventional NACA inlet computed from the results obtained from numerical simulations show that there is a good agreement when compared to their respective design data. Regarding the adaptive refinement process of the computational mesh utilized, the results show that the adopted refinement process does not have a significant influence on the obtained results. The differences obtained with relation to the original mesh, which are about 1%, allow concluding that, regarding the performance parameters, the obtained results present mesh convergence.

The computational results show that the presence of the freely standing vortex generator is responsible for considerable reductions of the boundary layer thickness and, consequently, significant improvements of the performance parameters of the NACA inlet. The obtained improvements, relative to the conventional NACA intake, in terms of ram recovery ratio and mass flow rate, are 44% and 16%, respectively. When the support of vortex generator was utilized, additional improvements of the performance parameters of the NACA inlet were obtained. For the this case, improvements of up to 53%, in terms of ram recovery ratio, and 19%, in terms of mass flow rate ingested by the intake, were achieved. The contribution of the drag induced by the presence of the vortex generator with support on the total drag of the ensemble is small, only about 10%. The choice of using – or not – vortex generators to increase NACA inlet performance is, obviously, a designer choice.

In order to validate the results obtained in this work, an associated experimental study is needed, in which detailed measurements would allow validating the numerical results obtained. Also, future work should involve the study of other parametric variations, including combinations of those already studied, in order to optimize the vortex generator geometry.

5. Acknowledgements

The authors wish to thank Embraer, CNPq and Fapesp for the support provided for this work. During this work Luís Fernando Figueira da Silva was on leave from the Laboratoire de Combustion et de Détonique (Centre National de la Recherche Scientifique, France). Mesh generation was performed by Mr. Rodrigo Ferraz, from ESSS (Engineering Simulation and Scientific Software Ltda).

6. References

Celis, C. P., Figueira da Silva, L. F., Ferreira, S. B., Batista de Jesus, A., and Oliveira, G. L., "Numerical Study of the Performance Improvement of Submerged Air Intakes using Vortex Generators", 25th ICAS Congress, Hamburg, Germany, Sept. 2006.

Delany, N. K., "An Investigation of Submerged Air Inlets on a ¼-scale Model of a Fighter-type Airplane", NACA RM A8A20, June 1948.

Devine, R. J., Watterson, J. K., Cooper, R. K., and Richardson, J., "An Investigation into Improving the Performance of Low Speed Auxiliary Air Inlets using Vortex Generators", 20th AIAA Applied Aerodynamics Conference, AIAA 2002-3264, St. Louis - Missouri, June 2002.

Engineering Sciences Data Unit, ESDU, "Drag and Pressure Recovery Characteristics of Auxiliary Air Inlets at Subsonic Speeds", Item Nº 86002 with amendments A and B, London 1996.

Gorton, S. A., Owens, L. R., Jenkins, L. N., Allan, B. G., and Schuster, E. P., "Active Flow Control on a Boundary-Layer Ingesting Inlet", 42nd AIAA Aerospace Sciences Meeting and Exhibit, AIAA 2004-1203, Reno - NV, Jan. 2004.

Hall, C. F., and Barclay, F. D., "An Experimental Investigation of NACA Submerged Inlets at High Subsonic Speeds. I-Inlets Forward of the Wing Leading Edge", NACA RM A8B16, June 1948.

Hime, L., Celis, C. P., Figueira da Silva, L. F., Ferreira, S. B., Batista de Jesus, A., Takase, V. L., and Vinagre, H. T. M., "A Review of the Characteristics of Submerged Air Intakes", 18th International Congress of Mechanical Engineering, COBEM2005-1016, Ouro Preto - MG - Brazil, Nov. 2005.

Mossman, E. A., and Randall, L. M., "An Experimental Investigation of the Design Variables for NACA Submerged Duct Entrances", NACA RM A7130, Jan. 1948.

Nogueira de Faria, W., and Oliveira G. L., "Análise de Entradas de Ar tipo NACA com Gerador de Vórtices", 9th Brazilian Congress of Thermal Engineering and Sciences - ENCIT 2002, CIT02-0758, Caxambu - MG - Brazil, Nov. 2002.

Shih, T. H., Liou, W. W., Shabbir, A. and Zhu, J., "A New k-Eddy-Viscosity Model for High Reynolds Number Turbulent Flows - Model Development and Validation", Computers and Fluids, Vol. 24, No. 3, 1995, pp. 227-238.

Spalart, P. R., and Allmaras, S. R., "A One-Equation Turbulence Model for Aerodynamic Flows", La Recherche Aérospatiale, No. 1, 1994, pp. 5-21.

Taskinoglu, E. S., and Knight, D. D., "Multi-Objective Shape Optimization Study for a Subsonic Submerged Inlet", Journal of Propulsion and Power, Vol. 20, No. 4, 2004, pp.620-633.

Paper CIT06-0357

Experimental and numerical study of the wake of a simplified automobile model with a variable rear slant angle

Claudia Vergueiro Massei
Instituto Tecnológico de Aeronáutica - ITA
claudia.massei@gmail.com

Valérie Ferrand
École Nationale Supérieure de l'Aéronautique et de l'Espace – Supaéro (Toulouse, France)

Paulo Afonso de Oliveira Soviero
Instituto Tecnológico de Aeronáutica - ITA
soviero@ita.br

Abstract. *This work studies the critical geometry case of the rear slant angle of a simplified car model together with the influence of the moving floor. Initially, the literature results concerning the drag of the critical geometry were experimentally validated. Next, the same experiments were carried out in the presence of a moving ground. To better understand the flow around the model and how the moving ground affects it, it was used the technique known as PIV – Particle Image Velocimetry. Last, the assembly was modeled on CFD software and the same tests were simulated, so that it would be possible to compare experimental and numerical results.*

Keywords*. automobile, rear slant, drag, PIV, CFD*

1. Introduction

Among the objectives of subsonic aerodynamics research is the determination of overall pressure forces – mainly, lift and drag. For streamlined bodies, the major interest is generally in lift. On the other hand, in the bluff-body case there are always regions of separation generating pressure drag. In this situation, drag, rather than lift, is the major unknown and there is no general theoretical model to predict it, as there are the non-viscous flow models used for streamlined bodies. The existence of "critical geometries" is one of the reasons for systematic experiments. This concept is related to the drag exhibiting a local maximum with respect to some geometrical parameter of a body shape. Usually, the critical geometries are found by chance with no prior expectation of their behavior. As drag overshoots are often unsuspected and tend to involve complex types of flow, one has to rely on systematic experimental studies to identify critical geometries and analyze them. One case of critical geometry concerning road vehicles was reported by Janssen and Hucho (1974). Changing the angle of the rear slanted portion of the roof of a car, they observed that, for a small range of angles (25-35), overall drag exhibited a large overshoot. There was also an effect on the after body flow separation: the separation line was either at the top of the slanted surface, or at its bottom, depending on the angle. This case of critical geometry inspired this work. Nevertheless, when studying flows around vehicles in wind tunnels, it should be considered the use of a moving floor, in order to carry out the simulations in a more realistic way. Measurements show that floor movement reduces drag and lift and computational fluid dynamics can predict differences in the flow fields.

1.1. Literature review

There is a great dependence between the vehicle drag and its rear slant angle. Around 30°, drag increases considerably and is drastically reduced around 40°, remaining reasonably constant from there on. This observation has made car designers avoid the critical rear slant angles on their vehicles. As a result, passenger cars can be classified into three categories: squarebacks, fastbacks and notchbacks. It should be mentioned that the wake originated in each of the three cases has a different structure, which will be discussed further.

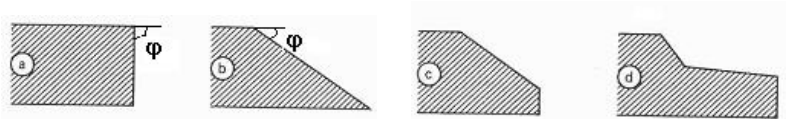

Figure 1. Different rear ends, schematic: squareback (a), fastback (b) (c), notchback (d).

The flow round a car body is characterized by separation and its drag is primarily pressure drag. There are typically two forms of separation at the rear end of vehicles: the quasi-two-dimensional, in the form of a wake, and the three-dimensional, as a longitudinal vortex pair. Frequently, both forms occur simultaneously; however, they are first discussed separately, on simplified models.

In Fig.(1), the primary rear end shapes are illustrated schematically. Shape (a), the full rear end (φ>30°), most commonly called 'squareback', is typical for the quasi-two-dimensional separation bubble. This is because the boundary

layer cannot follow the steep pressure increase – at the rear edge – according to potential flow theory, and separates from the contour. This results in a considerably lower mean pressure coefficient Cp, than in friction-free flow, on the rear vehicle surface. A classical example for this is the airflow around a sphere: the difference of the pressures occurs only on the rear side of it and the pressure drag, therefore, is generated only there.

The three-dimensional separation with the formation of a pair of longitudinal vortices occurs on rear end shape (b) and (c), whose inclination are lower than the squareback one ($\varphi<30°$). These kinds of shape are known as 'fastback'. A quasi-two-dimensional wake is also present at the perpendicular basis. Therefore, both types of separation can occur at the same time in this rear end shape.

The flow field for each of these configurations is illustrated in Fig.(2).

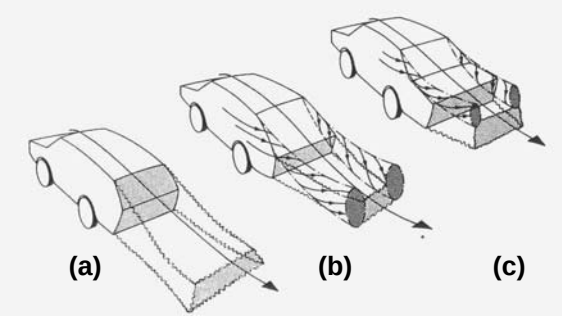

Figure 2. Flow pattern for different rear end configurations, schematic (Hucho, 1977).

In the light gray areas (a), the separation has a quasi-two-dimensional character. In this case, the line of separation tends to run perpendicular to the local flow direction. If reattachment occurs, separation bubbles are formed. The flow in these separation bubbles is unsteady, but there is a macrostructure with circulation in which the axes of the vortices run primarily perpendicular to the undisturbed flow, parallel to the line of separation. In some not very clarified way, the vortices of the separation bubble 'double back' in the shape of a horseshoe – see Fig.(4) – in the main flow direction at the side boundaries of the bubble and somehow they interfere with the exterior flow. The lower vortex rotates counterclockwise and the upper vortex, in the opposite sense. After the separation bubble closes, a pair of counter-rotating longitudinal vortices forms in the trailing wake. This produces an upwash in the case of a squareback, and induces a downwash in the trailing wake flow on a notchback or fastback.

Of course the flow inside the bubble, which is shed from a three-dimensional body, is three-dimensional in nature. However, since the separation itself is mainly two-dimensional, with the separation line normal to the flow and vortex axes parallel to separation line, it is designated 'quasi-two-dimensional'. This type of flow can occur at the leading edge of the front hood, at the sides on the fenders, on the cowl and on the front spoiler, and possibly in the notch of a notchback. Wakes are also formed on the blunt rear of a squareback. Depending on the outer flow field, long wakes are formed, which extend far downstream, or the wakes are short and closed – this will be explained right away.

The other type of separation, shown in Fig.(2) (b) and (c) by the dark gray areas, is three-dimensional in nature. A strong vortex pair – also known as C-pillar – is formed at the rear of the vehicle, depending on the inclination of the rear end. These rear vortices interact with the external flow field and with the quasi-two-dimensional wake and are similar to the tip vortices of a wing of low aspect ratio. They induce a downwash field in the space between their axes, which increases the tendency of reattachment in the central portion of the slanted surface and determines the position of the separation line for the wake. If the downwash is induced by a strong vortex pair, the separation line is quite low and a short wake is formed. If not, the flow separates at the upper edge of the roof and a long wake is formed. Last, it should be mentioned that this kind of separation isn't present in the squareback case.

The interaction between the C-pillar vortex pair ('tip vortices') and the vortex system of the quasi-two-dimensional separation bubble also depends on the rear slant angle.

With the squareback configuration, say 0° (or 90°), there are no 'tip vortices', but the stronger lower vortex in the wake, which rotates counterclockwise in the vicinity of the vehicle, generates an upwash with its developing horseshoe vortex, as explained above.

At a higher angle of inclination of the rear end, say 15°, the C-pillar vortex pair has developed. It induces a downwash, which forces the external flow downward in the area of the rear end and keeps it attached. This type of structure is responsible for a higher value of drag.

At 30°, the C-pillar vortices are highly pronounced, which induces very low pressure on the slanted part of the back and, consequently, increases drag considerably; the flow separates at the top or the bottom of the inclined rear end – depending upon the curvature of the rear edge of the roof.

At angles greater than 30°, the vortex burst increases the base pressure and the flow separates at the upper edge of the roof. C-pillar vortices are no more formed and a squareback flow regime is again present (with a limited recirculation zone), which makes the drag values become lower.

Between 10° and 15° the effect of the downwash-inducing C-pillar vortex pair and the upwash-inducing horseshoe vortex from the separation bubble counteract one another. The drag coefficient is at a minimum at these angles. However,

for 30° the C_D is at a maximum: the C-pillar vortices are so strong that flow remains attached over almost all of the sloping back, despite the large angle of inclination. This attached flow pattern is maintained by a supply of fluid from the sides of the body, which passes over the longitudinal vortices onto the slanted base, relieving the pressure rise along the central part of the inclined surface. Near the side edges of this surface, the wall pressure is expected to be much lower than in the center, due to the proximity of the rolled-up stream vortices – which usually have low pressure in their cores. The contribution to drag from these low-pressure regions is a manifestation of the energy continuously supplied into the edge-vortices. The evolution of the drag coefficient with the rear end slope angle is illustrated in Fig.(3) along with the schemas of separation line and wake for both fastback and squareback shapes.

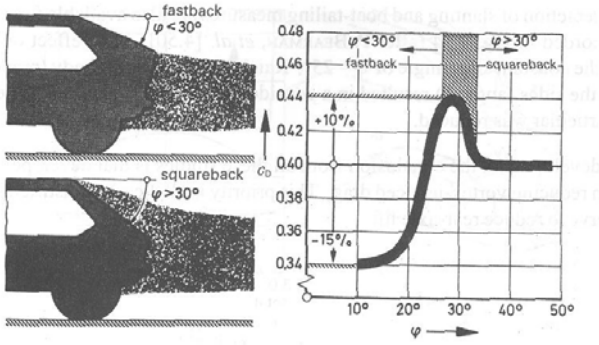

Figure 3. Influence of rear slant angle on drag, separation line and wake, measured on VW Golf (Janssen and Hucho, 1975)

The 'profile drag' of the three different rear end shapes is not equal because the position of the separation line changes when the flow pattern is changed from the fastback type into a squareback type and vice versa, i.e. the properties of the flow field around the 'profile' are significantly different. Therefore the profile drag will also change.

It is possible to summarize the vortex pattern for a sloping rear end as sketched in Fig.(4). In principle, there are three different vortex systems. Vortex C, emanating at the C-pillars, presents a 'potential flow' character. With the exception of a small viscous core area, its circumferential speed increases with decreasing radius (measured from the vortex centre). Its strength increases with the slant angle and, if the slant angle exceeds 30°, this vortex bursts and the flow pattern changes to the squareback flow regime. Vortex A and vortex B are the so called horseshoe vortices, generated in the quasi-two-dimensional manner at the edges A and B, respectively. They are of the viscous type and their vorticity is low. With inclined rearwards, as shown in Fig.(2), they are either dissipated or somehow merged into C-pillar vortices.

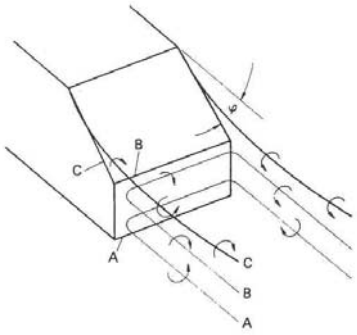

Figure 4. Vortex system for a sloping rear end, schematic (Hucho, 1977).

Finally, the flow along the underside of the vehicle is particularly unclear and suggests comparison with that on a very rough plate or with that in a narrow channel with one very rough wall.

Concerning the ground effect, the flow can be described by that around the body and its imaginary mirror image beneath the ground. As a result of the high speed, a force of attraction develops between the body and its mirror image – thus, a negative lift – which increases as the distance decreases. Circulation develops on the body due to friction effect, which results in a positive lift component. When considering three-dimensional flows, it should not be forgotten the lift induced by side and trailing vortices. This portion of the lift can be linked with the drag also induced by these vortices. As the vortices approach the ground they move slowly to the outside, as a result of the induction effect of their mirror image.

The experiments would be carried out with a simplified automobile model. The simplest model found in the literature consisted on an axisymmetric body (Bearmann (1979)). So, it was used a cylinder with a frontal disc as a model. The frontal disc played the role of assuring the reattachment of the flow at the beginning of the cylinder, avoiding, thus, a separation region over it. In the literature, there were only results available for the axisymmetric body off ground. This way, it is only possible to compare the off ground experiments results. The curve below (Fig.(5)) was extracted from Bearmann (1979) and, for this case, $Re = 10^6$.

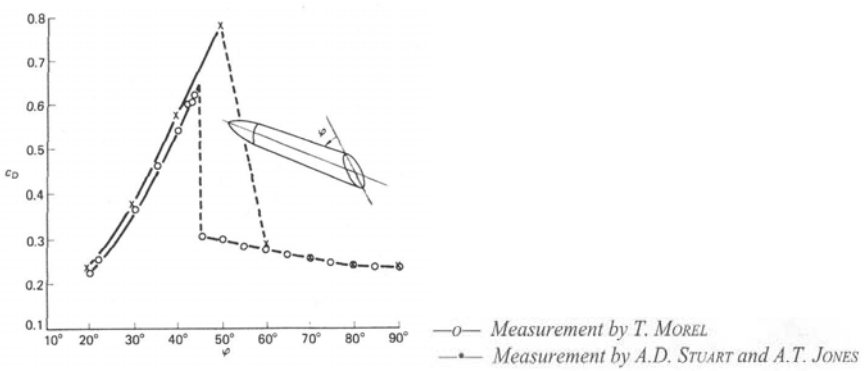

Figure 5. Effect of rear end slope angle φ on drag of an axisymmetric body off ground Bearmann (1979).

A study about the influence of a moving floor has been previously done by Bearmann, De Beer, Hamidy and Harvey (1988). Their conclusions were, basically, the following:

"The recirculation region is seen to be slightly longer above the moving floor and there are differences in flow direction beyond the region of reversed flow. Just downstream of the base and near the floor, the flow is seen to be nearly parallel with the moving floor, whereas the stationary floor data has a velocity component towards the floor. In this case, fluid appears to be being entrained into the boundary layer developing along the floor. Turbulence measurements indicate that the shear layer separating from the lower edge of the base spreads more rapidly in the stationary floor case and merges with the floor boundary layer."

However, "the flow immediately downstream of the base, within the wake, appears insensitive to floor movement."

2. Experimental methodology

The wind tunnel used in this work was equipped with a moving belt with a boundary layer suction system located upstream the belt, avoiding the problem of the wind tunnel inner boundary layer. To study the effects of this facility – especially its influence on the drag – all the experiments were carried out first with the belt off and, afterwards, with the belt on. In the latter case, the belt would always run at the same speed as the flow. The speed range of the experiments was from 10 m/s to 30 m/s, with the Reynolds number varying from $3.5\ 10^4$ to $1.5\ 10^5$.

It was used a cylinder linked to a frontal disc to simulate a simplified road vehicle. The position of this frontal disc also had an influence on drag. So, its distance was varied in order to find the optimal one – the one that would produce the minimum drag. The dimensions of the model (without its rear part) were as follows (Fig.(6)):

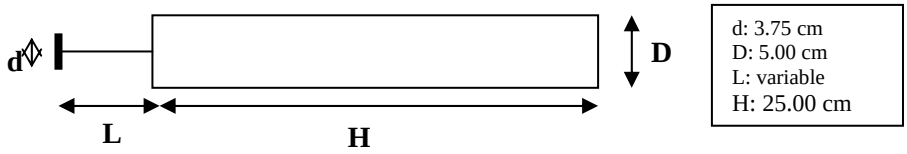

Figure 6. Geometric configuration of the model.

The rear part of the model was removable, in order to test different rear slant angles (φ). There were 7 possible configurations: 0°, 10°, 20°, 30°, 40°, 50°, 90° (without the rear part).

The cylinder was sustained by a vertical mast connected to the balance above the tunnel. It must be mentioned that, before calculating the drag coefficient in every case, it would be necessary to suppress the drag value of the mast – obtained by testing only the mast, without the model – from the value of total drag obtained by the balance. By doing this, it would be possible to obtain the value of drag on the model only (without the influence of the mast). Figure (7) illustrates the wind tunnel (with the moving belt) and the model with one of its removable rear parts, by the time of the calibration of the balance.

The drag forces were measured by a balance with a pair of wire strain gages connected to a computer. By calibrating the balance, it was possible to find the relation between the forces applied to the model and the strain-gage signals produced by the change in their length. The range of calibration – from 0 to 200 grams – was estimated based on C_D values extracted from Bearmann (1979) for cylinders in the same conditions as ours and on known values of velocity, air density and reference area of the cylinder.

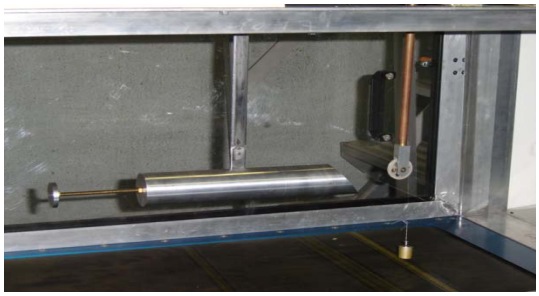

Figure 7. Assembly, with a rear slant angle of 50^o, by the time of the calibration of the balance.

The Particle Image Velocimetry (PIV) is used to measure the velocity all over the flow field – even in the presence of high frequency oscillations of the fluid – without bringing a probe into it; thus, without disturbing the flow. Like the Laser Doppler Velocimetry, the Particle Image Velocimetry is based on the measurement of the velocity of tracer particles carried by the fluid. The advantage of the PIV-technique is that a complete section of the flow under investigation is illuminated, not only one single point of it. Images of the illuminated seeding particles are recorded, so that their displacement can be determined through the analysis of the records.

Initially, it was essential to define the type of seeding that would be used in the experiments: it was chosen to inject fluid-produced smoke into the wind tunnel. The illumination was provided by two pulsing laser beams located above the test section. First, PIV was carried out on the longitudinal plan; afterwards, on the transversal plan. To do that, it was necessary to turn the laser sheet and install a mirror inside the wind tunnel. The laser employed was the double-cavity Q-switched Nd: YAG type. The CCD camera was placed by the side of the wind tunnel, so that it would be perpendicular to the laser sheet. The camera faced the laser sheet directly in the case of the longitudinal plan. For the transversal plan, the mirror was placed at the end of the test section, at 45°, so that the camera would face the mirrored image directly and would record it. Next, it was necessary to regulate the focus of the camera – according to the position of the laser sheet, in order to properly see the particles in the illuminated section. After that, the scale factor was determined – the ratio between the real size of the object and the size of the image acquired by the camera. The necessary time between two pulses also had to be estimated in order to avoid loss-of-pairs in the longitudinal case. Since the scale factor was known, as well as the dimensions of the interrogation area in pixels, it was possible to calculate its dimensions regarding the wind tunnel. With this data and the wind velocity, the maximum time interval between two pulses necessary to photograph twice (on the two frames) the same particle in the same interrogation area could be estimated. For a better precision, this maximum time interval was used in the recordings. To avoid loss-of-pairs in the transversal case, it was necessary to work on the thickness of the laser sheet. A 3-milimeter sheet thickness was employed – a little bit more than twice the side of an interrogation area – to ensure that the particles wouldn't be able to completely cross the sheet in a 2-pulse time interval. A hundred images were recorded for each configuration tested, say 10°, 30° and 90° – with the moving belt both on and off – for both the longitudinal and transversal plans (the transversal plans were two: one at 1 cm from the cylinder and the other at 4 cm).

After recording the images, all of them were analyzed with the cross correlation method. This resulted in many instantaneous vector maps, which were validated with a peak validation process. With the validated maps, it was obtained an average vector field. This originated the vorticity fields together with the streamlines for all the maps. Only for the transversal tests, the velocity vertical component fields were obtained as well. For the longitudinal tests, the velocity maps inside the boundary layer were plotted – in order to specially compare the influence of the moving ground. It should also be mentioned that tests without the model were carried out in order to analyze only the test section with the PIV method.

3. Experimental results and analysis

3.1. Determination of the optimal distance disc-cylinder

"The position of the disc influences the intensity of the vortex wake. A turbulent boundary layer (in the absence of the disc, for example) generates a strong diffusion that makes the vortex sheet more spread and the vortices themselves less intense. This phenomenon affects drag directly, increasing it." (Morel, 1978).

By knowing that the position of the disc has an influence on drag, it would be interesting to find the optimal distance, this is, the distance that produces the minimum drag.

Figure (8) shows the behavior of the flow for different distances disc-cylinder. The first case, (a), illustrates the situation when the distance is less than the optimal one. The last one, (c), when the distance is greater than the optimal one. The other one, (b), is the optimal distance. This distance corresponds to the one for which the flow separates at the disc and reattaches right at the beginning of the cylinder, avoiding, thus, a separation region over the cylinder – as it is possible to observe in cases (a) and (c) – and a turbulent boundary layer, which would consequently increase drag, as explained above.

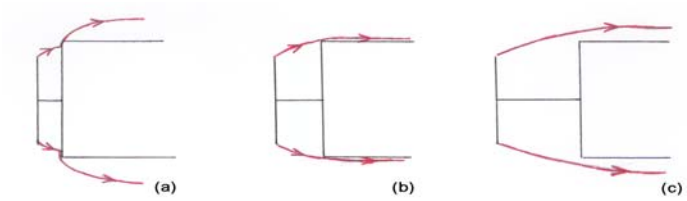

Figure 8. Possible distances disc-cylinder and flow behavior, schematic.

As a reference in the search of this optimal distance, it was used a previous study made by A. Roshko and K. Koenig in their book "Aerodynamic drag mechanism". Their purpose was to understand the behavior of the flow over two objects (cylinder and disc) placed one behind the other. They have observed that the interaction between the objects was positive and capable to lessen total drag. The minimum drag was achieved for the following geometry: d/D=0.75 and L/D=0.375. This information was withdrawn from the graph shown below in Fig.(9).

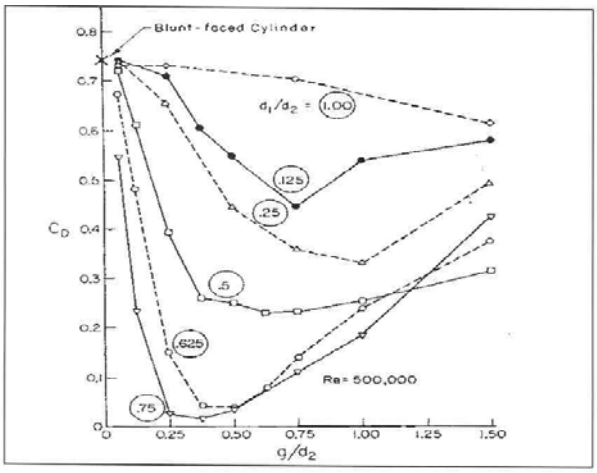

Figure 9. Drag coefficient evolution by A. Roshko and K. Koenig (Roshko and Koenig, 1974).

It must be noticed that the Reynolds number used to build this curve was 5.10^5, while the Reynolds in our case is around 5.10^4 or 7.10^4. Also, the cylinder of Roshko and Koenig wasn't placed near the ground as ours is. This implies one more reason to carry out this experiment and verify if the information found applies to this case.

So, with a disc to cylinder ratio d/D=0.75, drag was measured for different positions of the disc (L/D) and different velocities of the flow (10, 15, 20 and 30 m/s), either with and without the moving ground (moving at the same speed of the flow, for each case). The cluster was placed 5 mm from the ground and the rear slant angle of the cylinder was a right angle.

Since this study was a little bit more refined than that of Roshko and Koenig, 0.32 was found as the optimal L/D ratio for all the velocities tested – with and without the moving ground. One of the graphs obtained is plotted below on Fig.(10).

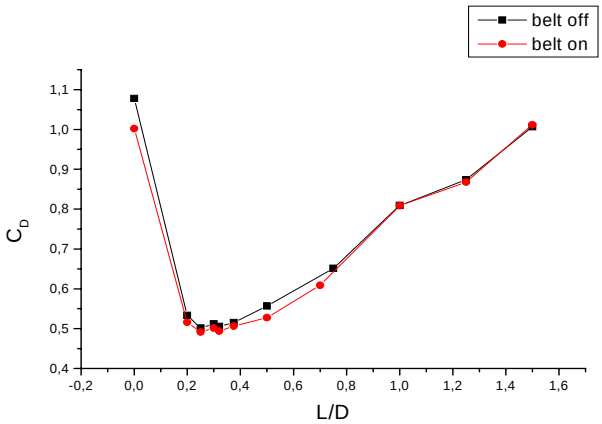

Figure 10. Determination of the optimal ratio L/D (flow velocity: 15 m/s).

Eventually, visualization tests with smoke were used to check and validate the optimal distance disc-cylinder found.

3.2. Influence of the rear slant angle and ground effect

With the ratio L/D = 0.32 fixed, the model was tested with the different rear parts to study the influence of the rear slant angle on drag. The cylinder was placed 5 mm from the ground and was tested at the same previous conditions (flow velocities of 10, 15, 20 and 30 m/s, both with and without the moving ground). Like this, it would be also possible to investigate the influence of the Reynolds number and the ground motion on the drag produced.

In order to analyze the influence of the ground on the previous experiments, the model was tested in the middle of the section – avoiding, thus, the ground effect – at those same velocities. The tests were made with the moving belt off to assure the symmetry of the section. These experimental results would be compared to the ones from Bearmann (1979).

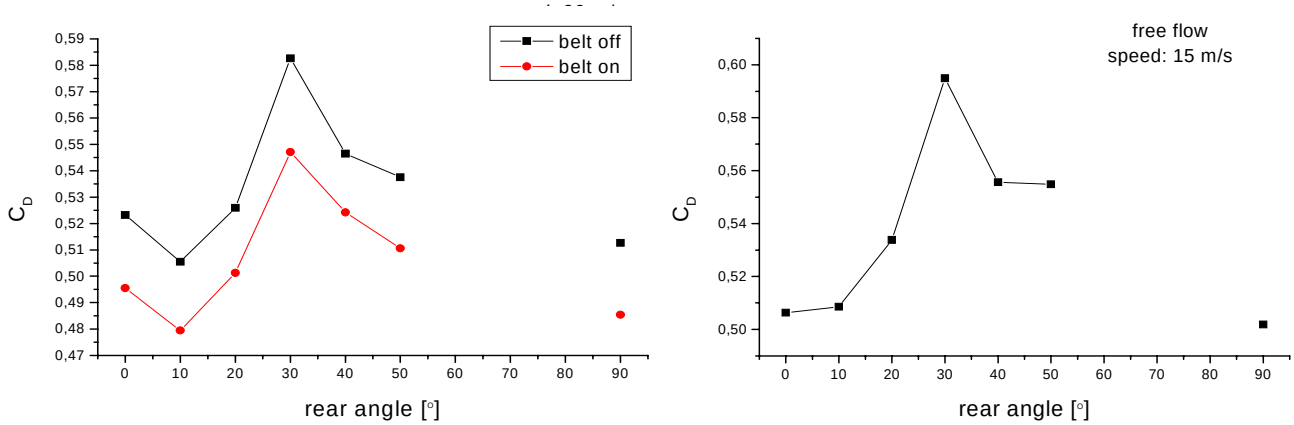

Figure 11. Influence of rear slant angle on drag near the ground and in free flow (Re: 5.5 10^4).

The curves present themselves according to the expected, based on theory. The 30-degree rear slant angle is the one responsible for the greatest value of drag coefficient, being, thus, its critical value. Also, C_D evolution follows two opposing trends that change at the critical value. In addition, it is remarkable that the 10-degree rear slant angle is the one that implies the least drag coefficient. Therefore, it can be evidenced a similar qualitative behavior between the curves that result from the measurements and the curves related to road vehicle tests found in the literature. Quantitatively, though, the C_D values found are higher than the literature ones. This might be due to the fact that a cylinder is less aerodynamic than a road vehicle and, being so, it is natural that its drag be higher. Furthermore, it is possible to notice that the C_D range of variation is practically the same, near 0.1, in both cases – measurements and literature.

Moreover, the C_D values for a 0-degree and a 90-degree rear slant angles are really close, which evidences that the cylinder's length doesn't influence its drag (the 90-degree rear slant angle corresponds to the cylinder without its rear part).

Evolution of the C_D values in free flow resembles, qualitatively, a lot that found in the literature (see Fig.(5)). The drag coefficients for 0-degree and 90-degree rear angles are basically the same; there is a monotonic crescent trend before the critical value; and, after the critical value, drag coefficient remains barely constant. Quantitatively, it is not possible to establish a comparison, once the shapes of the two bodies are different and the Reynolds numbers of the flows are completely different – the C_D values depend also on it.

3.3. Influence of the moving ground

The moving belt causes somewhat higher pressures near the front of the model. Because of the suppression of the lower boundary layer and the kinetic energy brought in by the moving belt, a larger volume of flow rate develops under the cylinder. Due to the continuity condition, a smaller volume of flow rate with higher pressures emerges above the cylinder, then. This change in the pressure distribution, according to further studies of Geropp and Odenthal (1996), affects drag directly, in a way that it always decreases when the ground is in motion.

3.4. Particle Image Velocimetry

3.4.1. Longitudinal tests

By analyzing the vector maps and, specially, the streamlines, it can be observed that the presence of the moving belt makes the fluid approach the ground. This is due to the fact that the lower boundary layer exists no longer (the velocity of the flow right above the belt is 15 m/s instead of 0 m/s), since the ground "pushes" the flow (this will be better exploited later) and makes it nearly parallel to the floor, "leaving room" for the fluid from above to come down. This makes the wake approach the ground as well. Sometimes the presence of the moving ground may influence as well the shape of the wake, "stretching" it - say, making it longer and less wide. This happens because the moving belt helps to develop the lower part of the wake – as can be seen for the case of the 0-degree slant angle cylinder.

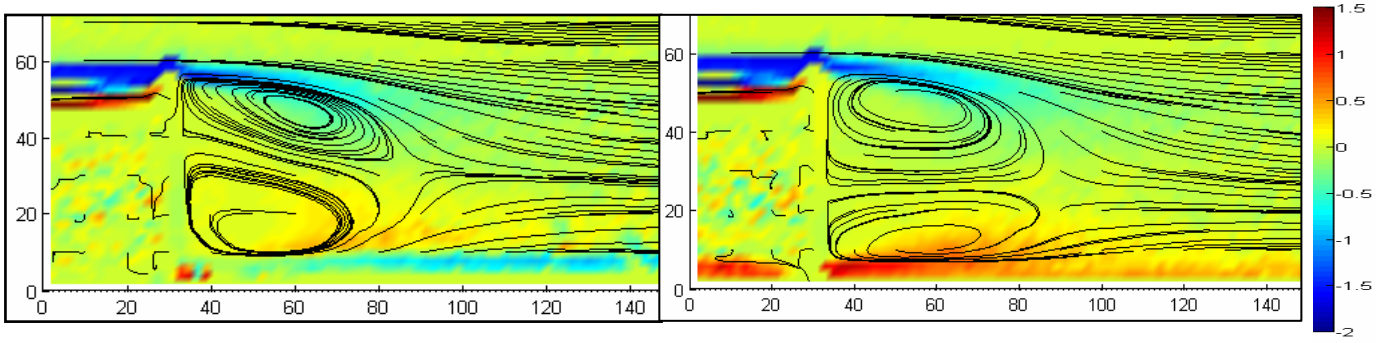

Figure 12. Streamlines and vorticity (10^4 s^{-1}) map for a 0-degree rear slant angle, belt off and on.

For the 0-degree slant angle cylinder, the flow separates completely at the end of the cylinder (as expected for a squareback car model) and the bubble closes practically at the same distance from the cylinder, not mattering whether the ground moves or not. Even though, the structures of both wakes are not the same. By analyzing the streamlines in Fig.(12), one can well remark that, with the belt on, the wake presents itself in a much more symmetric way.

In the case of the 10-degree slant angle, it is clear that the flow follows the rear slant, separating only at its end – just like for a fastback car model. It is also possible to identify that the recirculation bubble closes a little bit closer to the cylinder comparing to the 0-degree case.

In the case of the 30-degree slant angle, the flow remains attached to the rear slant until its end and there is an even smaller recirculation region. Figure (13) clarifies this difference.

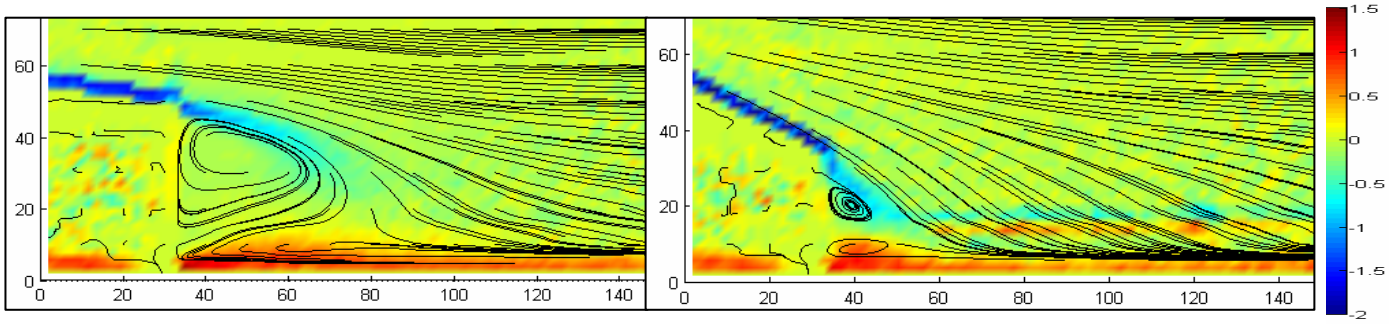

Figure 13. Streamlines and vorticity (10^4 s^{-1}) map for a 10 and a 30-degree rear slant angle, belt on.

It is also remarkable the upwash in the case of the right angle and the downwash in the 10-degree slant angle case, as previewed by theory (see “Introduction) for squarebacks and fastbacks, respectively. There is also a downwash in the case of the 30-degree slant angle. This fastback behavior makes sense once the flow has remained attached to the rear slant, just as it would remain on a fastback model.

Moreover, the vorticity maps show that the belt movement increases the vorticity of the flow near the ground – especially right after the cylinder, which is explained by the movement of the belt bringing vibration into the test section.

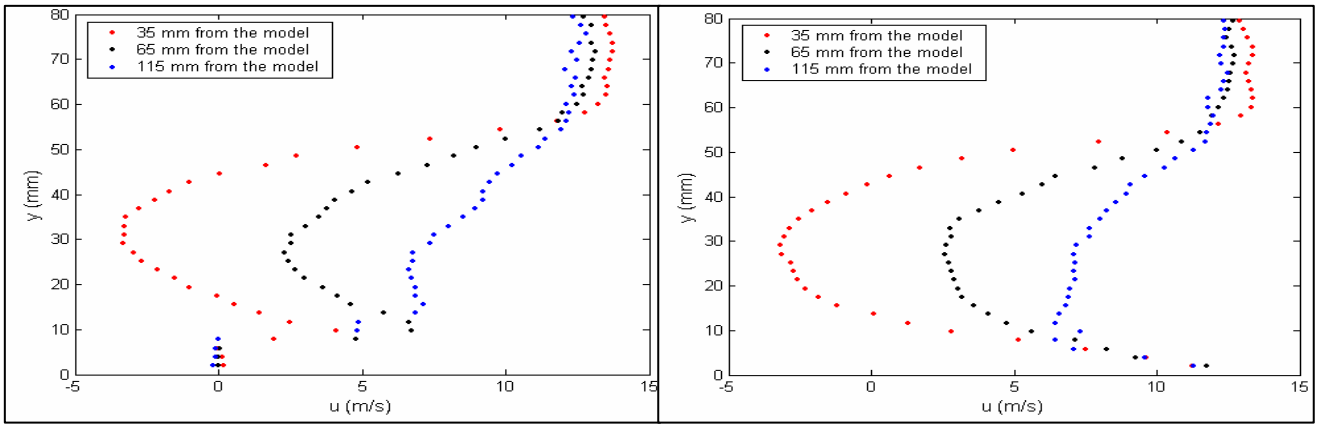

Figure 14. Velocity profiles for a 0-degree rear slant angle, belt off and on.

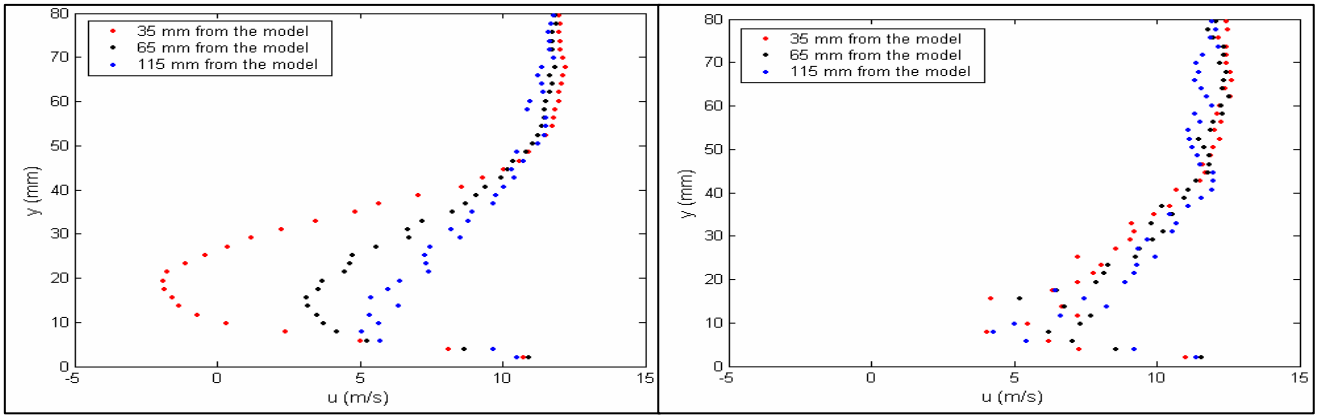

Figure 15. Velocity profiles for a 10-degree and a 30-degree rear slant angle, belt on.

The velocity profile maps evidence the fact already mentioned that the moving belt "pushes" the flow, once the velocity of the flow near the ground with the belt off is 0 m/s and with the belt on is near 12 m/s. The differences between the profiles at different distances from the model can also be remarked. The recirculation region impels to the fluid a lower (sometimes, even negative) velocity than the velocity of the flow. Since the recirculation bubble is larger closer to the cylinder, this effect is stronger the closer the point analyzed is to the model. This is also valid when comparing the profiles for different rear slant angles. For larger recirculation zones, lower velocities of the fluid are observed. This explains why the 0-degree slant angle model is the one that presents the lower velocity values. For values of height of 55 mm – the top of the cylinder – and greater, the velocity profiles present values of 12 m/s approximately constant. It is also possible to observe the velocity slightly greater as the point analyzed approaches the model and, consequently, the section entrance.

3.4.2. Transversal tests

First of all, it must be mentioned that the mirror placed in the section was responsible for deviating the flow; that is why the vector maps obtained presented the top vectors pointing to the left. This was also evidenced by the streamlines and the vector maps corresponding to the tests without the model. In the latter, it could also be verified that the deviation was not uniform in the section, which makes it even harder for its effects to be withdrawn.

By analyzing the vector maps, it has been possible to observe that, with the belt on, there was a greater vertical velocity component towards the floor at the bottom part of the field around the cylinder – in comparison with the belt off case. This could be justified by the fact – already explained – that the belt impels the longitudinal streamlines towards the ground, which decreases the fluid vertical velocity, making it more negative.

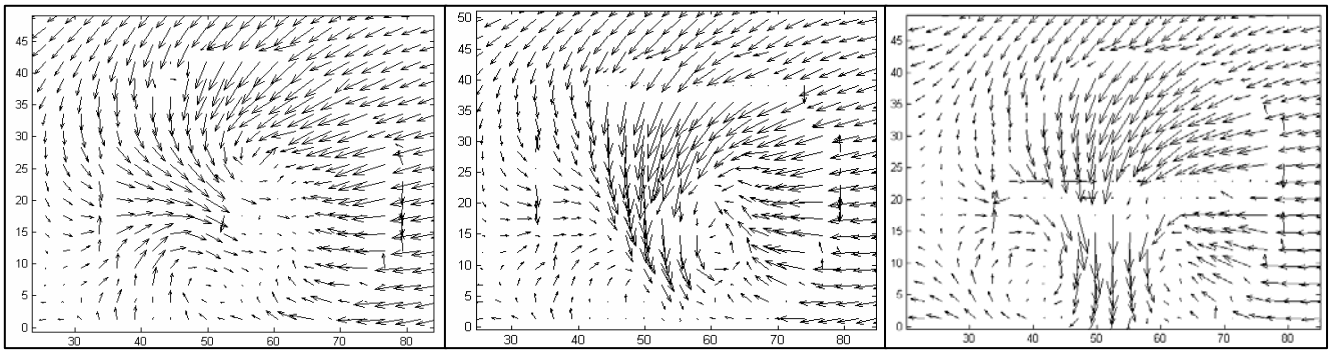

Figure 16. Vector maps for 0, 10 and 30-degree rear slant angles, belt on.

Figure (16) shows that, for the 0-degree slant angle cylinder, it is impossible to distinguish the vortex pair. It is only possible to see the movement of the particles that joined the recirculation bubble. In the case of the 10-degree one, it becomes possible to see the vectors at the bottom of the cylinder pointing towards the top and some vectors at mid-height pointing towards the center of the cylinder, indicating the vortex pair. Eventually, for the 30-degree case, one can already clearly visualize the vortex pair.

The vertical velocity maps were, then, analyzed in order to assure their symmetry. With the belt on, the vertical velocity all over the section was lower than it would be with the belt off. This was expected, just as explained above. For the 0-degree slant angle cylinder, the map was definitely not symmetric, which indicated the inexistence of a vortex pair. In the 10-degree case, it was possible to identify two symmetric steams that stood for high velocity values and indicated, approximately, the location of the vortex pair. Also for the 30-degree cylinder, but, in this case, the steams were larger.

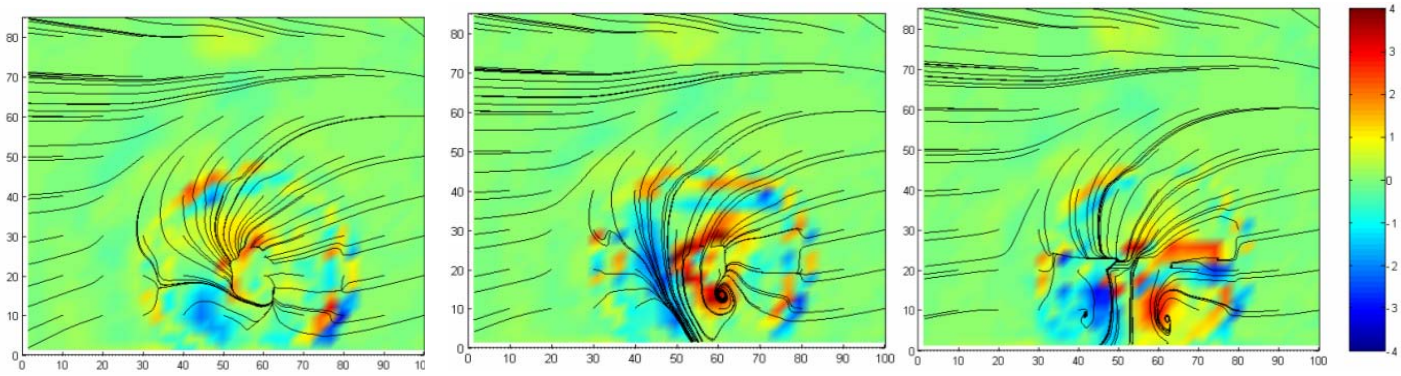

Figure 17. Streamlines and vorticity (10^3 s^{-1}) map 0, 10 and 30-degree slant angles, belt on.

The vorticity maps, illustrated in Fig.(17) led, basically, to the same conclusions as the vertical velocity ones. There was no vortex pair defined for the 0-degree rear angle cylinder. For the 10-degree one, there were, clearly, two steams – one blue and one red – that indicated the counter-rotating vortex pair. In the case of the 30-degree one, once again, the blue and red steams could be observed. This time, though, they presented themselves greater and more symmetric. The vortex pair was so intense that it could be distinguished from the streamlines as well.

This variation on the vortices intensity – already exploited in the introduction, explains the increase in drag when the rear slant angle is modified from 0 to 30 degrees. The more the vortices are pronounced, the lower the pressure they induce on the slanted part of the back – which contributes to a greater value of drag. For angles greater than 30 degrees, for example the right angle case, there are no longer vortices. This increases the base pressure and makes the flow separate, lowering drag at the same time.

The figures above result from tests at 4 cm from the cylinder. The same tests were carried out at the distance of 1 cm from the cylinder and the same effects, in less intensity, though, were observed. Even though the wake is larger closer to the cylinder, the structure of the vortex pair is not so well defined at this point. Concerning the analysis of the vector maps at 1 cm, for the 10-degree rear angle case, it was possible to see the vectors at mid-height of the cylinder pointing rearwards its center and some vectors near its edge pointing towards the top. This indicates that the vortex pair vertical position, at 1 cm from the model, is higher than the one at 4 cm from it; which shows that the vortices go down as they move away from the cylinder. As well, for the 30-degree slant angle cylinder, at 1 cm, it was possible to distinguish the vortex pair, vertically located a bit higher than in the 4 cm case. Coherently, on the vertical velocity maps, the vertical position of the steams that stood for high velocity values was higher than in the 4 cm case. In addition, the size of the steams was much smaller in the 1 cm case. This indicates that the vortices spring out as they move away from the cylinder – exactly as previewed in the theoretical part of this work. Concerning the vorticity maps at 1 cm, there were red and blue spots that fairly indicated the position of the counter-rotating vortex pair starting to develop. They were, again, smaller and vertically located a little bit higher than in the 4 cm case.

3.4.3. Tests without the model

The vector maps obtained evidenced that, with the belt on, there was a greater vertical velocity component towards the floor at the bottom part of the field. And, from the vorticity maps, one could tell that free flow had hardly any vorticity; this means that all the vorticity observed before was due to the presence of the model.

4. Computational Fluid Dynamics Method

Once having experimental results for three different rear slant angles, the next step would be obtaining the computational ones for the 30-degree rear slant angle cylinder. For such a task, it was necessary to build a mesh that would be solved later for the same boundary conditions as the ones from the experiments. The results obtained will be compared and commented in the next part of this work.

Producing a mesh starts by the conception of the virtual model geometry. This latter was done on the program CATIA. The geometry was, then, exported to the CFD program ICEM. Only after ensuring the good quality of the mesh, this one was exported to a solver; in this case, FLUENT.

4.1. CFD results and analysis

Regarding the longitudinal vector maps, the flow had a slight tendency of separating at the top of the rear slant base. On the other hand, it was remarkable that it remained attached to the base at its bottom. This instable behavior can be explained by the fact of dealing with a critical geometry – the 30-degree rear slant angle.

Just like observed experimentally, it was evidenced the downwash of the flow. Nevertheless, the recirculation region after the cylinder was not as evident as it was in the experimental maps.

Observing the velocity maps, it could be evidenced that the flow remained attached to the cylinder at its beginning, right after passing by the disc, just as it happened experimentally. It was also possible to compare the wakes obtained in each of the methods. Defining the wake as the region with velocity lower than 30% of free flow velocity, the wake obtained numerically was more stretched (narrower and longer) than the experimental one – which was more like an isosceles triangle. Nevertheless, their areas were pretty much the same.

Considering the vorticity maps, it was observed the same kind of difference there was between the belt on and belt off experimental cases. In the belt on case, there was more vorticity at the bottom base of the cylinder and in the region near the ground right after the cylinder than in the belt off case. In addition, the vorticity region after the cylinder follows the behavior of the wake, which is "stretched" by the action of the moving belt. So, this vorticity area after the cylinder is more "stretched" for the belt on configuration.

Concerning the effects of the moving floor, it can be stated that, without it, the flow under the cylinder presented two boundary layers: one attached to the cylinder and the other on the floor. Moreover, at the end of the cylinder, the flow below it presented almost zero velocity. However, when the belt was moving, the flow below the cylinder presented only one boundary layer – the one attached to it.

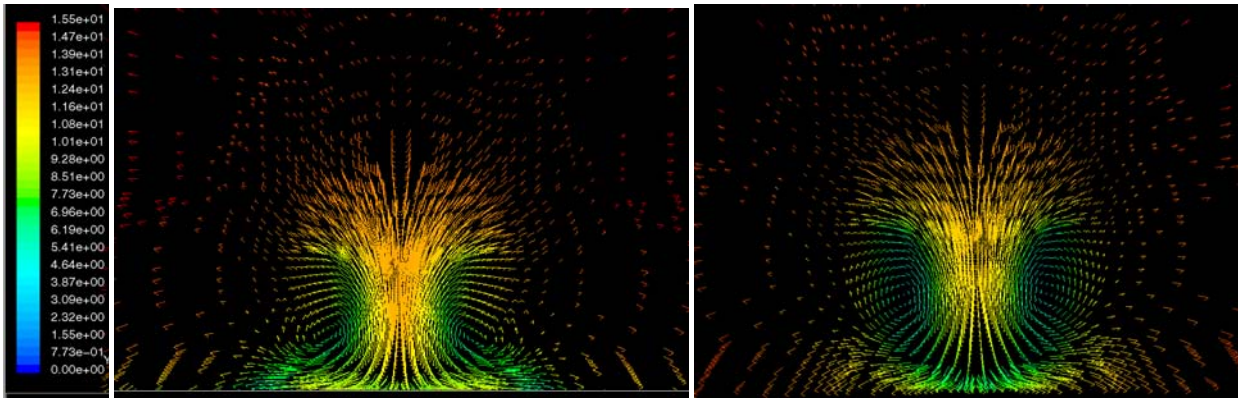

Figure 18. Vector map at 4 cm from the cylinder colored by velocity (m/s), belt off and on.

Concerning the transversal vector maps – shown in Fig.(18) and colored according to the total velocity magnitude – one could see that the counter-rotating vortices turned in the same sense as the experimental ones. In addition, it must be mentioned that, with the belt on, on a same given region of the section (except for below the cylinder), the velocity of the flow tends to be lower than it would be with the belt off. This can be explained by the continuity condition. With the belt on, there is more fluid that passes under the cylinder at a time. Consequently, there is less fluid that passes through the rest of the section, which makes a lower velocity all over this region. It could also be observed the fact that the vortices go down and spring out as they move away from the cylinder, as mentioned in the experimental results.

Regarding the vertical velocities maps, it was possible to evidence downwash from a region above the cylinder that presented negative vertical velocities. There were also two red steams and a blue central one, which showed the position of the vortices. Their analysis on both plans (1 cm and 4 cm from the cylinder) assures the fact that the vortices go down and spring out as they move away from the cylinder.

In the vorticity maps, Fluent gives only the vorticity amplitude, this is, only positive values. This way, it wasn't expected to have symmetric steams of different colors as there were in the experimental transversal vorticity maps, for example. It could be noticed, though, just like in the experimental results, that, for the 1 cm maps, the greater values of vorticity were concentrated at the edge of the cylinder; while for the 4 cm maps, they were concentrated at its center. Moreover, on the 1 cm maps, one could notice, again, that the action of the moving belt helped to increase vorticity near the ground right after the cylinder.

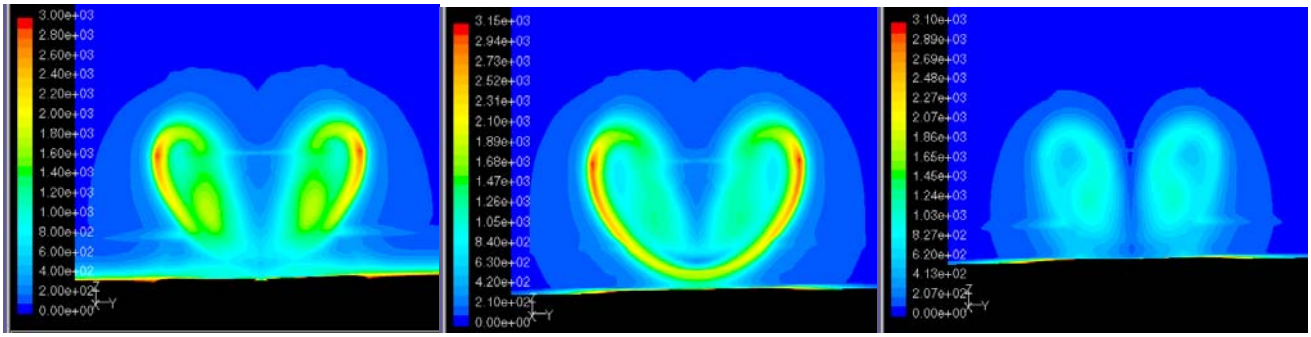

Figure 19. Vorticity (s^{-1}) map at 1 cm from the cylinder, belt off; belt on; and at 4 cm from the cylinder, belt on.

It must be mentioned that, although the qualitative behavior was likely for both experimental and numerical cases, the values of vorticity obtained numerically were not exactly compatible with the experimental ones. These latter are greater – even 3 times greater, especially for the longitudinal and the 4 cm cases. In fact, this might be due to experimental imperfections, such as irregularities on the belt surface that might bring in more vibration to the test section, image resolution problems in the PIV method, or even to the three-dimensionality of the flow, which might compromise the vorticity calculation, for example. At this point, the reader must be careful when considering the experimental results, since they don't agree with the numerical ones and it hasn't been possible to deeply investigate this issue.

5. Final remarks

It has been possible to evidence experimentally the results regarding the drag behavior when the rear slant angle of the model is modified. The obtained results were quite satisfactory and compatible with the existing literature data.

The Particle Image Velocimetry was useful to understand this behavior. The variation on the vortices intensity explains the increase in drag when modifying the rear slant angle from 0 to 30 degrees. The more the vortices are pronounced, the lower the pressure they induce on the slanted part of the back – which contributes to a greater value of drag. For angles greater than 30 degrees, for example the right angle case, there were no longer vortices. This increases the base pressure and makes the flow separate, lowering drag at the same time.

The CFD simulations were useful to compare the experimental data with the numerical one and to better analyze the influence of the moving ground. When comparing both methods, it is possible to notice that there are some "reality imperfections" – such as the mirror inside the wind tunnel, which generates a yawed flow, the real moving belt, the PIV system resolution – that keep one from obtaining the same data that could be obtained numerically. It is important to have these imperfections in mind not to absolutely thrust the experimental results. Regarding the influence of the moving ground, it could be evidenced a phenomenon described in the literature, but not experimentally measured. The reduction of drag by the movement of the belt is due to a change in the pressure distribution over the model. The action of the moving belt increases a lot the Cp values and also reduces, relatively, their range, making the pressure distribution more uniform. In addition, with the belt on, there were no longer negative values for Cp, as there were for the belt off case.

6. References

Bearmann, P.W., 1979, "Bluff body flows applicable to vehicle aerodynamics", Aerodynamics of Transportation, ASME-CSME-Conf. Niagara Falls, June 18th to 20th.

Bearmann, P.W., De Beer, D., Hamidy, E. and Harvey, J. K., 1988, "The effect of a moving floor on wind-tunnel simulation of road vehicles", SAE Technical Paper Series, International Congress and Exposition. Detroit, Michigan, February 29 – March 4.

Geropp, D. and Odenthal, H.J., 1996, "Drag reduction of motor vehicles by active flow control using the Coanda effect", Stanford.

Hucho, W.-H., 1977, "Aerodynamics of road vehicles from fluid mechanics to vehicle engineering".

Janssen, L.J. and Hucho, W.-H., 1975, "Aerodynamische Entwicklung von VW Golf und VW Scirocco", ATZ, Vol.77, pp 1-5.

Morel, T., 1978, "The effect of base slant on the flow pattern and drag of three-dimensional bodies with blunt ends", General Motors Research Laboratories, Warren, Michigan.

Roshko, A. and Koenig, K., 1974, "Aerodynamic drag mechanism".

7. Copyright notice

Proceedings of the 11th Brazilian Congress of Thermal Sciences and Engineering -- ENCIT 2006
Braz. Soc. of Mechanical Sciences and Engineering -- ABCM, Curitiba, Brazil, Dec. 5-8, 2006

Paper CIT06-0413

ANALYSIS OF COMPRESSIBLE POTENTIAL FLOW OVER NONLIFTING AIRFOILS USING THE DUAL RECIPROCITY METHOD

André Valdetaro Gomes Cavalieri
Instituto Tecnológico de Aeronáutica
São José dos Campos – SP
CEP 12228-900
andre@ita.br
Paulo Afonso de Oliveira Soviero
Instituto Tecnológico de Aeronáutica
São José dos Campos – SP
CEP 12228-900
soviero@ita.br

Abstract. *The use of the linearized potential model for the analysis of compressible flows is quite popular, and provides good results for subsonic and supersonic flows. However, the calculation of airfoils and wings subject to transonic flows requires a non-linear model, such as the transonic small-disturbance (TSD) potential equation. The solution of the problem by a singularity distribution requires singularities over the field, as well as panels on the boundary, characterizing the procedure known as field panel method. The present work shows results of calculations of the transonic small-disturbance potential equation, with the use of the dual reciprocity method (DRM), which permits calculation of integrals only at the boundary of the problem, without the need of field distributions. This approach, compared to the field panel methods, takes considerably less computer time. The results show very good agreement with other methods found in literature.*

Keywords. *transonic aerodynamics, panel methods, dual reciprocity method.*

1. Introduction

Calculation of subsonic and of supersonic flows over airfoils and wings by potential methods is possible with a linear theory, which provides accurate results for the pressure distribution. However, transonic flows cannot be modeled by a linear equation, and the linear potential theory, well developed for purely subsonic and supersonic flows, is not capable to describe a transonic flow.

Since Mach numbers of the transonic range are usually commercially interesting for transport aircraft, considerable attention has been given to the study of transonic flows. The use of an approach similar to the panel methods developed by Hess and Smith (1967) would be of much importance, since it allows the determination of pressure distribution over bodies of arbitrary geometry, without a need of extensive calculations. Panel methods have proven to be useful tools to design airfoils and wings, with less computer time required than Euler or Navier-Stokes calculations, since only calculations along the surface of the wings (the boundary of the problem) are required in a panel method formulation.

The work of Spreiter and Alksne (1955) is an attempt to solve the non-linear problem which is characteristic of transonic flows. The approach is based on the integral equation, and is similar to the panel methods mentioned. However, the application of Green's theorem to the transonic equation results in an integral equation, with integrals evaluated along the boundary and along the field. The solution of this equation is found by an approximation of the velocity profile along the field, which can reduce the integral along the field to an integral along the boundary. A similar method was developed by Nixon (1974), but with a different approximation of the velocity profile.

With faster computers available, it became possible to solve the integral equation with an integral along the domain, which resulted on field panel methods. Ribeiro and Soviero (1987) presented a field panel method for the solution of the transonic flow over an airfoil, based on the transonic small-disturbances equation. The results are very good; however, much more computer time is required by a field panel method than by a regular panel method.

A transformation of the domain integral to surface integrals is desired if one wishes to decrease the computer time required for the calculation of transonic flows. The appearance of the Dual Reciprocity Method (DRM), presented by Partridge et al (1992), gives a new alternative for the study of transonic flows. This method allows the calculation with panels distributed only along the boundary of the problem. The application of DRM for transonic flows was presented in the work of Uhl et al (1999), where wings at transonic speed had their pressure distributions calculated with good results.

This work focuses on the application of the Dual Reciprocity Method to airfoils, modeled by the transonic small-disturbances equation. This model is of interest because of its simplicity, since all the singularities are distributed along the chord. Rapid calculations can thus be performed, providing good estimations of the pressures on the airfoil surface.

2. Mathematical model

The full potential equation for a two-dimensional compressible flow can be written as:

$$\left(1-M_\infty{}^2\right)\phi_{xx}+\phi_{yy}=M_\infty{}^2\left[(\gamma+1)\frac{\phi_x}{V_\infty}+\frac{\gamma+1}{2}\frac{\phi_x{}^2}{V_\infty{}^2}+\frac{\gamma-1}{2}\frac{\phi_y{}^2}{V_\infty{}^2}\right]\phi_{xx}+$$
$$+M_\infty{}^2\left[(\gamma-1)\frac{\phi_x}{V_\infty}+\frac{\gamma-1}{2}\frac{\phi_x{}^2}{V_\infty{}^2}+\frac{\gamma+1}{2}\frac{\phi_y{}^2}{V_\infty{}^2}\right]\phi_{yy}+ \tag{1}$$
$$+M_\infty{}^2\left[\frac{\phi_y}{V_\infty}\left(1+\frac{\phi_x}{V_\infty}\right)\left(\phi_{xy}+\phi_{yx}\right)\right]$$

With the hypothesis of small disturbances, the right hand side of Eq. (1) can be approximated by zero if the undisturbed Mach number is less than 5, and is outside of the transonic range. In these cases, Eq. (1) becomes:

$$\left(1-M_\infty{}^2\right)\phi_{xx}+\phi_{yy}=0 \tag{2}$$

This is a linear partial differential equation, much simpler than Eq. (1). Its type depends on the undisturbed Mach number. If M_∞ is less than 1, which means the incident flow is subsonic, Eq. (2) is of the elliptic kind; if M_∞ is greater than 1 (supersonic incident flow), the equation is hyperbolic.

Equation (2) is not a good mathematical model for transonic flows over an airfoil. When a flow has Mach number close to unity, there are subsonic and supersonic zones in the flow. In order to describe the different character of the subsonic and supersonic zones, a mixed-type differential equation must be used. The simplest one is known as Transonic Small Disturbance (TSD) equation, and is presented in Eq. (3).

$$\left(1-M_\infty{}^2\right)\phi_{xx}+\phi_{yy}=\frac{(\gamma+1)M_\infty}{V_\infty}\phi_x\phi_{xx} \tag{3}$$

It is possible to define:

$$\beta^2=1-M_\infty{}^2 \tag{4}$$

$$k=\frac{(\gamma+1)M_\infty}{V_\infty} \tag{5}$$

Thus, Eq. (3) becomes:

$$\beta^2\phi_{xx}+\phi_{yy}=k\phi_x\phi_{xx} \tag{6}$$

The usual boundary conditions for eq. (6) are that values of the potential vanish at infinity, and that the velocity normal to the surface of the airfoil is zero. This second condition is linearized when small disturbances are assumed, and is satisfied at the chord. Written using the velocity potential, the boundary conditions at the surface are given in Eq. (7).

$$\frac{\partial y_S}{\partial x_S}=\frac{\phi_y}{V_\infty} \tag{7}$$

Since the coefficients of Eq. (3) are constant, it is possible to transform its variables, to obtain a simpler equation in a transformed plan. The transformed variables X and Y and the transformed potential Φ can be obtained using Eqs. (8)-(10).

$$X=x \tag{8}$$

$$Y=\beta y \tag{9}$$

$$\Phi=\frac{k}{\beta^2}\phi \tag{10}$$

Equation (6) in the transformed plan becomes:

$$\Phi_{XX} + \Phi_{YY} = \nabla^2 \Phi = \Phi_X \Phi_{XX} \tag{11}$$

The equation above is in the transformed plan. The boundary conditions also need to be transformed; the resulting boundary conditions at the transformed plan are given in Eq. (12).

$$\frac{\partial y_S}{\partial x_S} = \frac{1}{V_\infty} \frac{\beta^3}{k} \Phi_Y \tag{12}$$

Equation (11) is non-linear, and its solution is more difficult than that of the linear problem. The application of Green's theorem with eq. (11) leads to eq. (13).

$$c\Phi(x_i) = -\int \frac{\partial \Phi}{\partial n} G d\Gamma + \int \Phi \frac{\partial G}{\partial n} d\Gamma + \iint \Phi_X \Phi_{XX} G d\Omega \tag{13}$$

In the equation above, G is the fundamental solution of Laplace's equation, which is, for the two-dimensional case, $ln\ r$, being r the distance between x_i, the point of interest, and any other point x. The first two integrals are calculated at the boundary of the problem. However, the third integral is calculated at the field.

The solution of the problem described by Eq. (11) can be found using a field panel method; this solution was found by Ribeiro and Soviero (1987). This approach is similar to the panel method proposed by Hess and Smith (1967), but the field panel method requires a distribution of sources in the field and of sources and dipoles on the surface of the airfoil. These distributions are done by a proper discretization of the domain on panels; consequently, a field panel method for a two-dimensional problem consists on a division of the surface of the airfoil into segments with unknown distributions of sources and dipoles, and a division of the field into small areas with unknown source distributions. The distributions can be found by an iterative process.

The requirement of panels in the field to calculate the potential is due to the presence of the double integral in Eq. (13). Since panels must be distributed in the field, there is a notable increase on computer time for the calculations. Panel methods for incompressible flow require only panels at the surface of the airfoil. Since we have to deal with a much greater number of unknown distributions of singularities, a solution of a transonic flow with a field panel method takes much more time than an incompressible solution found with a panel method based on Hess and Smith's work.

The Dual Reciprocity Method (DRM), such as presented by Partridge et al (1992), can be applied to the present problem, in order to eliminate the double integral in Eq. (13). With only integrals calculated at the surface of the airfoil, it is not required to divide the field into panels. Consequently, the solution takes less computer time.

If the right hand side of Eq. (11) can be expressed by

$$\Phi_X \Phi_{XX} = \sum_{j=1}^{n} \alpha_j f_j \ , \tag{14}$$

being f_j a set of n appropriate functions, and being ϕ_j functions defined as

$$\nabla^2 \phi_j = f_j \ , \tag{15}$$

it is possible to apply Green's theorem with ϕ_j, resulting on Eq. (16).

$$c\phi_j(x_i) = -\int \frac{\partial \phi_j}{\partial n} G d\Gamma + \int \phi_j \frac{\partial G}{\partial n} d\Gamma + \iint f_j G d\Omega \tag{16}$$

Equation (16) is valid for the whole set of functions defined on Eqs. (14) and (15). Consequently, it is possible to write Eq. (17).

$$\sum_{j=1}^{n} \alpha_j c\phi_j(x_i) = \sum_{j=1}^{n} \alpha_j \left(-\int \frac{\partial \phi_j}{\partial n} G d\Gamma + \int \phi_j \frac{\partial G}{\partial n} d\Gamma \right) + \iint \sum_{j=1}^{n} \alpha_j f_j G d\Omega \tag{17}$$

Using the definition of the functions f_j, Eq. (17) becomes

$$\sum_{j=1}^{n}\alpha_j c\phi_j(x_i)=\sum_{j=1}^{n}\alpha_j\left(-\int\frac{\partial\phi_j}{\partial n}Gd\Gamma+\int\phi_j\frac{\partial G}{\partial n}d\Gamma\right)+\iint\Phi_X\Phi_{XX}Gd\Omega\,. \tag{18}$$

Thus, the double integral of Eq. (13) can be transformed to line integrals.

$$\iint\Phi_X\Phi_{XX}Gd\Omega=\sum_{j=1}^{n}\alpha_j c\phi_j(x_i)+\sum_{j=1}^{n}\alpha_j\left(\int\frac{\partial\phi_j}{\partial n}Gd\Gamma-\int\phi_j\frac{\partial G}{\partial n}d\Gamma\right) \tag{19}$$

With equations (13) and (19), it is possible to write de potential at the point xi with only integrals calculated at the boundary of the problem, as shown in Eq. (20).

$$c\Phi(x_i)=-\int\frac{\partial\Phi}{\partial n}Gd\Gamma+\int\Phi\frac{\partial G}{\partial n}d\Gamma+\sum_{j=1}^{n}\alpha_j c\phi_j(x_i)+\sum_{j=1}^{n}\alpha_j\left(\int\frac{\partial\phi_j}{\partial n}Gd\Gamma-\int\phi_j\frac{\partial G}{\partial n}d\Gamma\right) \tag{20}$$

Equation (20) allows the determination of the velocity potential of transonic flows. However, new unknowns (α_j) appear at the integral equation. Once the values of the interpolation coefficients α_j are determined, the potential can be calculated in the whole domain.

In this work, only symmetrical nonlifting airfoils were analyzed. Thus, Eq. (20) can be solved without distributions of normal dipoles; this simplifies the problem, leading to Eq. (21), which is the final form of the integral equation to be solved.

$$c\Phi(x_i)=-\int\frac{\partial\Phi}{\partial n}Gd\Gamma+\sum_{j=1}^{n}\alpha_j\left[c\phi_j(x_i)+\int\frac{\partial\phi_j}{\partial n}Gd\Gamma\right] \tag{21}$$

The expression presented above shows that the velocity potential of a nonlifting transonic flow can be calculated with two additional terms. These terms come from the dual reciprocity method. It should be noted that the first term of Eq. (21) is identical to that of the linear theory. Consequently, the distribution of sources along the chord can be calculated with linear theory. The calculation of the remaining two terms is explained in the next section.

3. Numerical implementation

The functions f_j employed in the Dual Reciprocity Method can be any set of functions that can provide an adequate expansion of the right hand side of Eq. (11). Uhl et al (1999) have proposed the functions

$$f_j=1+r \tag{22}$$

as the interpolation functions.

Application of Eq. (15) with the chosen functions results

$$\phi_j=\frac{r^2}{4}+\frac{r^3}{9} \tag{23}$$

The n functions defined in Eqs. (22) and (23) are centered at n nodes distributed at the boundary and at the field. These nodes are chosen in order to represent well the variations of $\Phi_X\Phi_{XX}$ along the domain with the set of f_j functions. The functions chosen are very simple, but can provide good expansions of the non-linear part of Eq. (11).

If the values of $\Phi_X\Phi_{XX}$ are calculated at the n nodes, it is possible to write a system with n equations and n unknowns.

$$\begin{bmatrix}\Phi_X\Phi_{XX}(x_1)\\ \Phi_X\Phi_{XX}(x_2)\\ \vdots\\ \Phi_X\Phi_{XX}(x_n)\end{bmatrix}=\begin{bmatrix}f_1(x_1) & f_2(x_1) & \cdots & f_n(x_1)\\ f_1(x_2) & f_2(x_2) & \cdots & f_n(x_2)\\ \vdots & \vdots & \ddots & \vdots\\ f_1(x_n) & f_2(x_n) & \cdots & f_n(x_n)\end{bmatrix}\begin{bmatrix}\alpha_1\\ \alpha_2\\ \vdots\\ \alpha_n\end{bmatrix} \tag{24}$$

If the f matrix is inverted, it can be used to determine the values of the interpolation coefficients αj based on the calculated values of $\Phi_X\Phi_{XX}$.

$$\begin{bmatrix} \alpha_1 \\ \alpha_2 \\ \vdots \\ \alpha_n \end{bmatrix} = \begin{bmatrix} f_1(x_1) & f_2(x_1) & \cdots & f_n(x_1) \\ f_1(x_2) & f_2(x_2) & \cdots & f_n(x_2) \\ \vdots & \vdots & \ddots & \vdots \\ f_1(x_n) & f_2(x_n) & \cdots & f_n(x_n) \end{bmatrix}^{-1} \begin{bmatrix} \Phi_X \Phi_{XX}(x_1) \\ \Phi_X \Phi_{XX}(x_2) \\ \vdots \\ \Phi_X \Phi_{XX}(x_n) \end{bmatrix} \tag{25}$$

Based on this approach, it is possible to define the calculation steps.

a. The intensities of the sources distributed along the chord are calculated according to linear theory. The solution is considered a first guess for the potential in the whole field;
b. The right hand side of eq. (10) is calculated based on the current calculated potential;
c. Values of α_j are calculated with eq. (25).
d. A new potential can be obtained if the values of α_j are used with eq. (x);
e. This new potential becomes the current one, and steps b-d are repeated until convergence is attained.

The method outlined above has a rapid convergence for Mach numbers below the critical value. When M_∞ is increased above its critical value, and supersonic regions appear in the flow, the iterative process diverges. In order to allow convergence for higher Mach numbers, finite-difference methods make use of schemes with different forms of calculation for subsonic and supersonic velocities. Ribeiro and Soviero (1987) suggest the use of a function of artificial viscosity for the calculation of finite differences at points with supersonic velocities, in order to allow the convergence of the method at higher Mach numbers and to provide a good representation of zones with large velocity gradients, which represent shock waves. It should be noted that this method avoids the appearance of expansion shocks. The finite-difference scheme becomes, for points with local Mach number greater than one:

$$\sigma(x_i) = \Phi_X \Phi_{XX}(x_i) - \nu(x_i)\left[fv(x_i)\Phi_{XX}(x_i)\right] + \nu(x_{i-1})\left[fv(x_{i-1})\Phi_{XX}(x_{i-1})\right] \tag{26}$$

In Equation (26), x_{i-1} is a point upwind of the reference point x_i; consequently, the scheme presented in Eq. (26) adds a term of upwind differences in order to represent adequately a supersonic flow. The function *fv* is an arbitrary function of artificial viscosity. In the present work, *fv* was given by (Φx-1), which was the expression used by Ribeiro and Soviero (1987); the same function was chosen to provide a validation of the present method with the results shown on that work. The function *v* is equal to 1 for points with supersonic speeds, and equal to 0 for points with subsonic speeds.

Equation (26) is an example of a conservative scheme of artificial viscosity. It is possible to use a non-conservative scheme, such as the one given by Eq. (27).

$$\sigma(x_i) = \Phi_X \Phi_{XX}(x_i) - \nu(x_i)\left[fv(x_i)\Phi_{XX}(x_i) - fv(x_{i-1})\Phi_{XX}(x_{i-1})\right] \tag{27}$$

5. Results

The calculations were performed using a circular biconvex airfoil, with 6 percent of maximum thickness. Figure (1) shows the airfoil, as well as the nodes distributed along the domain.

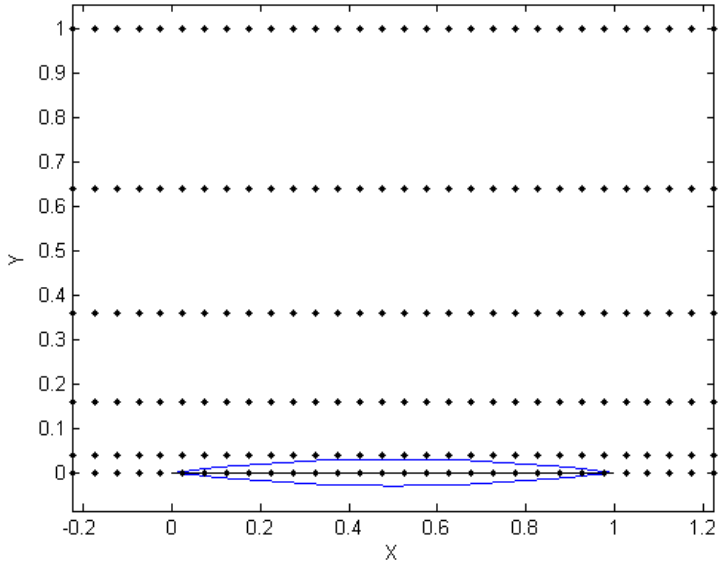

Figure 1. Discretization of the airfoil and position of the nodes.

The nodes shown on Fig. (1) are equally spaced along the X axis, and are distributed using a quadratic function along the Y axis, allowing a node clustering near the surface of the airfoil.

In the present work, the chord of the airfoil was divided into 20 panels, with control points placed at the center of each panel. The intensities of the sources are calculated in order to fulfill the boundary conditions at the control points. It should be noted that there are nodes that are coincident with the control points. This coincidence does not cause any problem with the numerical calculations, and provide a better representation of the nonlinear term of the governing equation.

The nodes were distributed only along the positive y direction, taking advantage of the symmetry of the problem in order to decrease computer time. The results of the present work were obtained using six nodes along the y axis, extended until one chord above the x axis.

In order to validate the method, a comparison with the field panel method of Ribeiro and Soviero (1987) was made. Since the work performed by this reference was based on the same equation, and the same airfoil was used, its results can be used to test if the dual reciprocity method is valid.

The pressure coefficient can be obtained with the expression for small disturbances, presented on Eq. (28).

$$C_P = -\frac{2\phi_x}{V_\infty} \tag{28}$$

The non-linear expression of the pressure coefficient was also tested, with little change on the values of C_P. This was expected, for the disturbances are small; consequently, the application of Eq. (28) is recommended for its simplicity.

Figures (2) to (4) show the comparison between dual reciprocity and field panel methods, for Mach numbers equal to 0.8, 0.85 and 0.87.

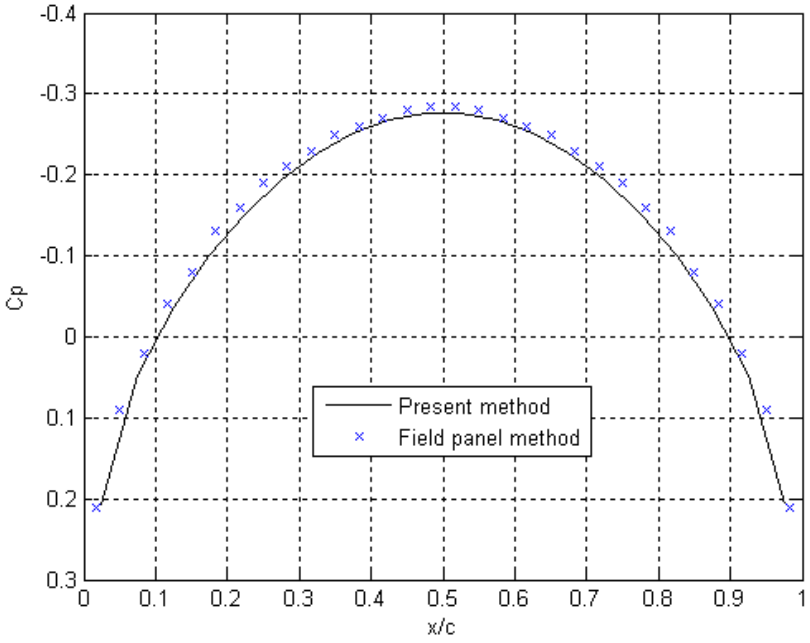

Figure 2. Pressure distribution for the circular-arc profile, M=0.8.

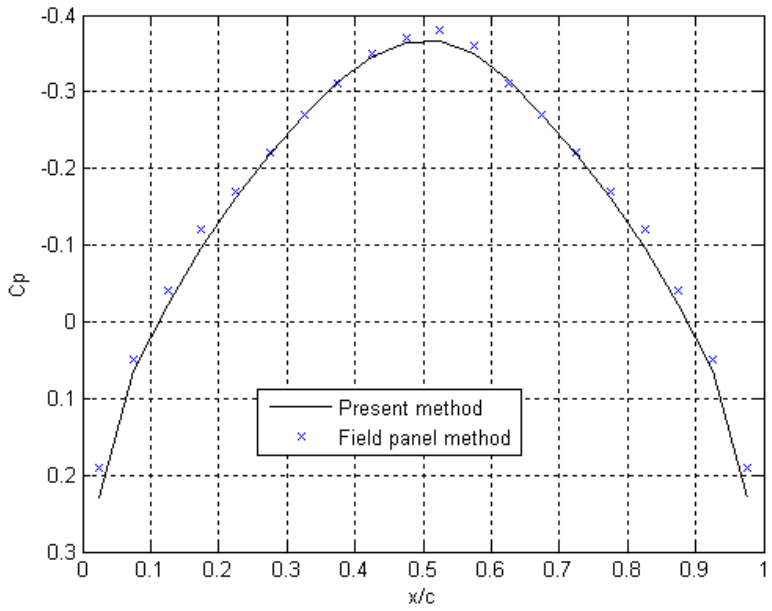

Figure 3. Pressure distribution for the circular-arc profile, M=0.85.

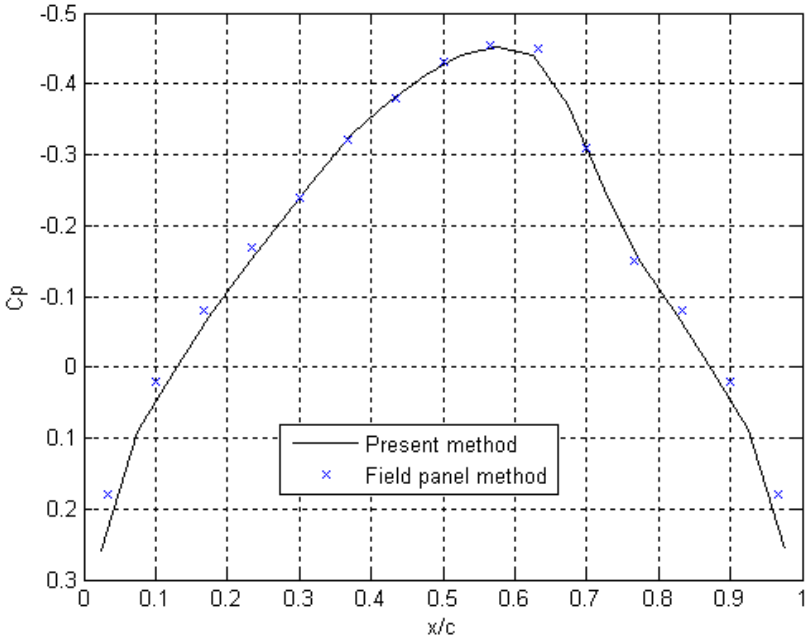

Figure 4. Pressure distribution for the circular-arc profile, M=0.87.

The results show good agreement between both methods. The differences are probably due to the nature of each method. The field panel method takes the source intensity at a control point and uses it as a constant value for the whole panel; and the dual reciprocity method uses interpolation functions, and thus gives a different approximation to the distribution along the field. However, it should be noted that the results are very similar, showing that the dual reciprocity method can be a substitute for field panel methods, giving accurate results that require less computer time.

The results shown on Figs. (3) and (4) are characteristic of transonic flows, since the minimum value of CP is more negative than its critical value. Convergence for both methods was obtained using the conservative version given by Eq. (26).

Figure (5) shows the results of the method for Mach number equal to 0.806, as well as experimental results taken from the work of Knechtel (1959).

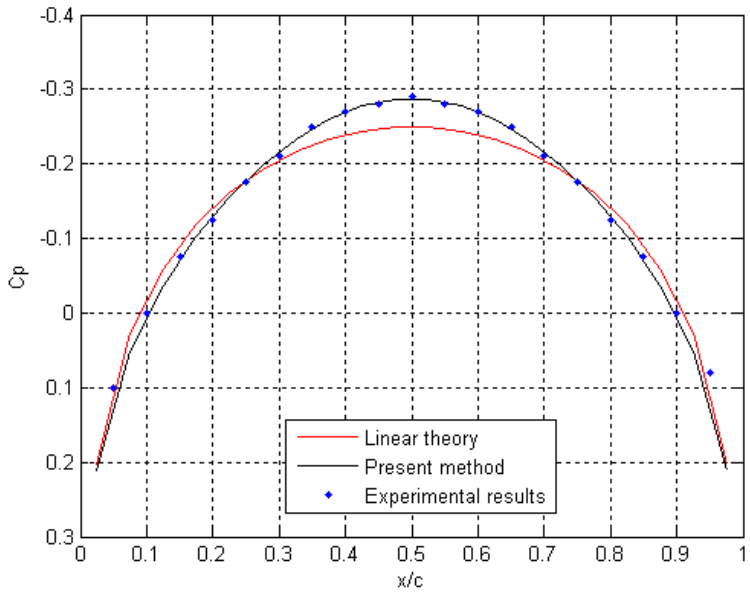

Figure 5. Pressure distribution on circular biconvex profile at Mach number 0.806.

The flow surrounding the airfoil in this case is entirely subsonic; thus, for the results presented on Fig. (5), the scheme presented by Eq. (26) was not used. Examination of Fig. (2) shows that the results of the present method agree very closely with the experimental values obtained by Knechtel (1959).

The close agreement found here cannot be expected to happen every time, since real flows have viscous effects, and their magnitude can cause differences between pressure distributions found by experiment and by the present method. However, the results shown on Fig, (5) show that the dual reciprocity method captures very well the tendencies of the real flow. The present method gives a more accurate value of the minimal C_P, which is valuable for the determination of the critical Mach number; and provides a better representation of the shape of the pressure distribution.

Figure (6) shows the results for Mach 0.861 for the conservative version, based on Eq. (26); and Figure (7) shows the results for the same Mach number, but with the non-conservative version, with calculations done such as shown on Eq. (27).

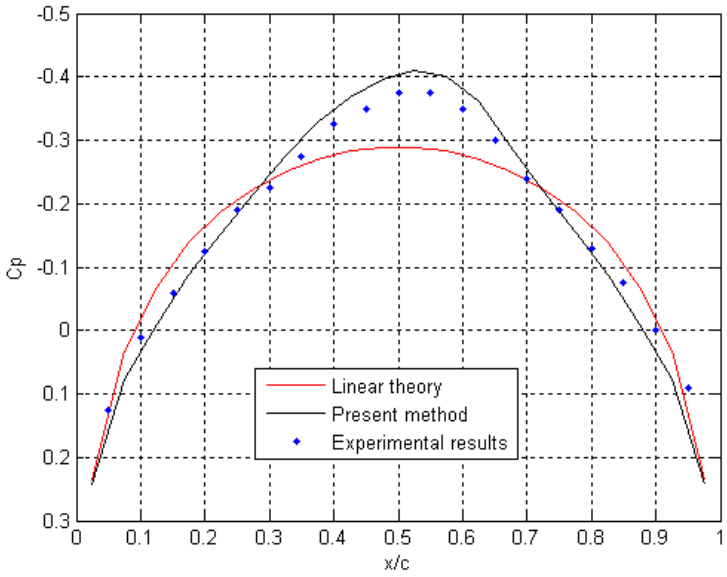

Figure 6. Pressure distribution on circular biconvex profile at Mach number 0.861 – conservative version.

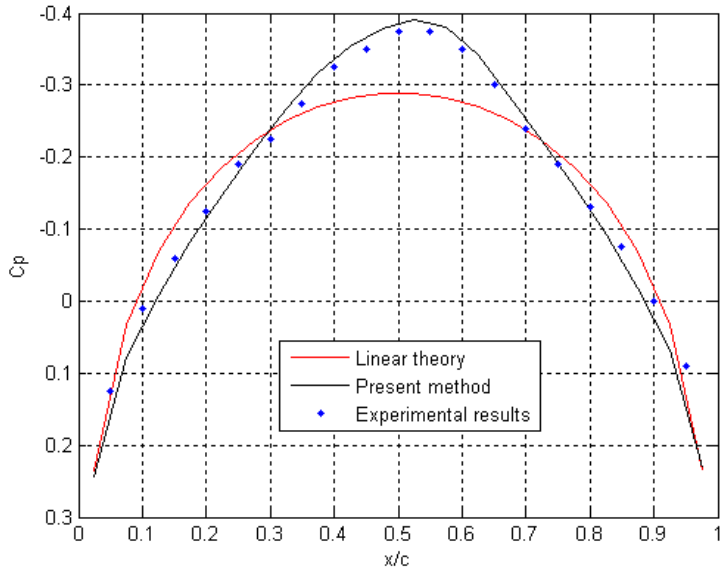

Figure 7. Pressure distribution on circular biconvex profile at Mach number 0.861 – non-conservative version.

The results show that the present method provides a good prediction of the pressure distribution over the airfoil. Linear theory prove to be inadequate for transonic flows, giving a shape of the distribution which is not close to the actual one.

The non-conservative version gives results closer to the experimental values. However, the conservative version gives a steeper pressure gradient on the region of the shock wave. The comparison of the two versions for a Mach number of 0.87 is shown on Fig. (8).

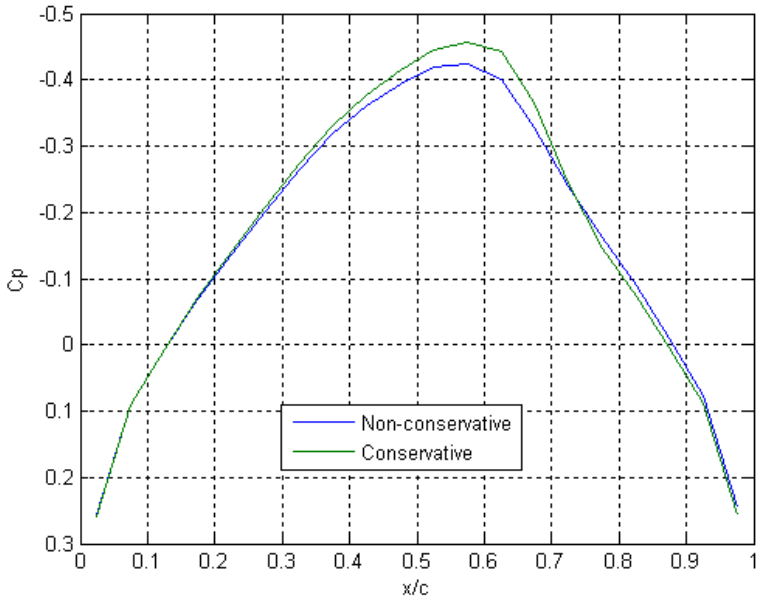

Figure 8. Comparison between non-conservative and conservative versions.

6. References

Hess, J. L., Smith, A. M. O., "Calculation of Potential Flow About Arbitrary Bodies", Progress in Aeronautical Sciences, 1967.

Knechtel, E. D., 1959, "Experimental Investigation at Transonic Speeds of Pressure Distributions over Wedge and Circular-Arc Airfoil Sections and Evaluation of Perforated-Wall Interference", NASA Technical Note D-15.

Nixon, D., 1974, "Transonic Flow around Symmetric Aerofoils at Zero Incidence", Journal of Aircraft vol. 11, no. 2.

Partridge, P.W., Brebbia, C.A. and Wrobel, L. C., 1992 "The Dual Reciprocity Boundary Element Method", Computational Mechanics Publications.

Ribeiro, R. S. and Soviero, P. A. O., 1987, "Análise do Escoamento Transônico Através do Método das Singularidades", Master Thesis, ITA.

Ribeiro, R. S. and Soviero, P. A. O., 1987, "Calculation of Transonic Flow About Airfoils by a Field Panel Method", Boundary Element Techniques: Applications in Fluid Flow and Computational Aspects, Computational Mechanics Publications.

Spreiter, J. R. and Alksne, A., 1955, "Theoretical prediction of pressure distributions on nonlifting airfoils at high subsonic speeds", NACA Report 1217.

Uhl, B., Ostertag, J., Guidati, G. and Wagner, S., 1999, "Application of the Dual-Reciprocity Method to Three-Dimensional Compressible Flows Governed by the Full-Potential Equation", 37th AIAA Aerospace Sciences Meeting and Exhibit, January 11-14, 1999, Reno, NV.

Proceedings of the 11th Brazilian Congress of Thermal Sciences and Engineering -- ENCIT 2006
Braz. Soc. of Mechanical Sciences and Engineering -- ABCM, Curitiba, Brazil, Dec. 5-8, 2006

Paper CIT06-0414

EXTENSÃO DO MÉTODO DOS PAINÉIS PARA O REGIME COMPRESSÍVEL ATRAVÉS DA DISTRIBUIÇÃO DE SINGULARIDADES UNICAMENTE NA FRONTEIRA DE PERFIS AERODINÂMICOS

Aline Sousa da Silveira
Instituto Tecnológico de Aeronáutica – ITA
alinesilveira4@yahoo.com.br

André Valdetaro Gomes Cavalieri
Instituto Tecnológico de Aeronáutica – ITA
andre@ita.br

Paulo Afonso de Oliveira Soviero
Instituto Tecnológico de Aeronáutica – ITA
soviero@ita.br

Este trabalho consiste na aplicação de um método de resolução da equação do potencial do escoamento transônico sobre um perfil por meio de integrais unicamente sobre a corda desse perfil. Nesse método, usado neste trabalho para perfis simétricos sem sustentação, é calculada uma distribuição de singularidades sobre essa corda tal que o campo de velocidades induzidas por essa distribuição satisfaça as condições de contorno necessárias. Um dos componentes da solução são as fontes, que satisfazem a equação de Laplace e, sozinhas, resolveriam o problema incompressível. As outras singularidades, que fazem a correção para o compressível, são funções meta-harmônicas e são denominadas metafontes de ordem i. Ao transformar a integral referente à parte compressível em uma integral de linha usando o Teorema de Green, obtém-se uma série infinita dessas metafontes, e são determinados pelo método os termos necessários à exatidão pretendida.
Entretanto, o método tem uma limitação: nem sempre a série de metafontes converge. Ela divergiu ao se tentar resolver o escoamento em torno de um perfil parabólico. Apesar disso, esse método pode ser usado em vários casos, tanto em aerodinâmica, em caso de problemas não-singulares, como em transferência de calor e muitas outras áreas.

Palavras chave: aerodinâmica transônica, método dos painéis, método da reciprocidade dual.

1. Introdução

Este trabalho consiste em usar o Teorema de Green, que será enunciado mais adiante, para transformar integrais de área em integrais de linha, a fim de que se possa determinar o campo de velocidades sobre um perfil aerodinâmico unicamente por meio de integrais sobre sua fronteira. Esse método, o método das singularidades, já tem uma variedade, o método dos painéis, largamente utilizada para o regime incompressível, cuja equação regente é a equação de Laplace:

$$\nabla^2 \phi = 0 \tag{1}$$

onde ϕ é o potencial de velocidade, definido por $\nabla \phi = \vec{V}$.

Contudo, o objetivo deste trabalho é estender o método das singularidades para o regime compressível transônico, regido por uma equação de Poisson. A forma geral dessas equações é a seguinte:

$$\nabla^2 \phi + R(\phi, P) = 0 \tag{2}$$

onde P é um ponto do domínio de ϕ e terá tantas coordenadas quantas forem as dimensões desse domínio (ex: P = (x, y, z) para três dimensões).

Primeiramente, foi feita a dedução, a partir do Teorema de Green, do método de resolução de uma equação de Poisson arbitrária conhecendo apenas informações sobre os pontos da fronteira do domínio, de acordo com a referência [6]. Essa dedução foi feita para a forma tridimensional, mas o método é análogo para qualquer número de dimensões. Em seguida, trabalhou-se com o problema da condução do calor em regime permanente, que também é descrito por uma Equação de Poisson, em sua forma mais simples: unidimensional e linear (R apenas função de x). A resolução desse problema por esse método está descrita na referência [1].

A seguir, foi mostrada a equação de Poisson que rege o regime transônico e, depois disso, foram apresentadas as equações necessárias à execução de um método iterativo para resolver essa equação, seguindo o procedimento descrito como Método da Reciprocidade Múltipla na referência [10]. Finalmente, foi criado um programa que utiliza esse método, cujo algoritmo está descrito no último tópico deste artigo.

2. Dedução da fórmula de integração sobre a fronteira

O Teorema de Green, enunciado na referência [2], é dado por:

$$\iiint_{V(S)} \phi_1 \nabla^2 \phi_2 - \phi_2 \nabla^2 \phi_1 = \oiint_{S(V)} (\phi_1 \nabla \phi_2 - \phi_2 \nabla \phi_1) \cdot \hat{n}\, dS \tag{3}$$

onde ϕ_1 e ϕ_2 são campos escalares quaisquer. Como $\nabla\phi \cdot \hat{n} = \partial\phi/\partial n$, tem-se:

$$\iiint_{V(S)} \phi_1 \nabla^2 \phi_2 - \phi_2 \nabla^2 \phi_1 = \oiint_{S(V)} (\phi_1 \frac{\partial \phi_2}{\partial n} - \phi_2 \frac{\partial \phi_1}{\partial n})\, dS \tag{4}$$

Definindo:

$$\begin{aligned} &\nabla^2 G_i(P,Q) = G_{i-1}(P,Q) \\ &\nabla^2 G_0(P,Q) = \delta(P,Q) \end{aligned} \tag{5}$$

onde δ(P, Q) é a função Delta de Dirac definida em P e centrada em Q.

Multiplicando (2) por G_0(P,Q), obtém-se:

$$G_0(P,Q)\nabla^2\phi(P) + R(\phi,P)\,G_0(P,Q) = 0 \tag{6}$$

E ainda, a integração da equação anterior na variável P para Q constante resulta em (em três dimensões):

$$\iiint_V G_0(P,Q)\nabla^2\phi(P)\, dV + \iiint_V R(\phi,P)\,G_0(P,Q)\, dV = 0 \tag{7}$$

Para aplicar o Teorema de Green ao primeiro termo da equação (7), precisa-se calcular o valor de

$$\iiint_V \phi(P)\nabla^2 G_0(P,Q)\, dV \tag{8}$$

$\nabla^2 G_0(P,Q)$ só é diferente de zero em Q:

$$\rightarrow \iiint_V \phi(P)\nabla^2 G_0(P,Q)\, dV = \phi(Q)\iiint_V \nabla^2 G_0(P,Q)\, dV \tag{9}$$

$$\nabla^2 G_0(P,Q) = \delta(P,Q) \rightarrow \iiint_V \nabla^2 G_0(P,Q)\, dV = C \tag{10}$$

onde C é o valor principal de Cauchy, que depende do ângulo sólido em torno do ponto. C vale 1 nos pontos do interior do domínio, ½ nos pontos de fronteira suave e, nos pontos onde a fronteira tiver quinas ou vértices, tem o valor da razão entre o ângulo sólido em torno do ponto e o ângulo sólido máximo (4π).

$$\rightarrow \iiint_V \phi(P)\nabla^2 G_0(P,Q)\, dV = C\phi(Q) \tag{11}$$

Subtraindo (7) de (10), tem-se:

$$\iiint_v (\phi\nabla^2 G_0 - G_0\nabla^2\phi)\, dV - \iiint_v (R G_0)\, dV = C\phi(Q)$$

$$\rightarrow C\phi(Q) = \oiint_S \left(\phi(P)\frac{\partial G_0(P,Q)}{\partial n} - G_0(P,Q)\frac{\partial \phi(P)}{\partial n} \right) dS - \iiint_V R(\phi,P)G_0(P,Q)\, dV \tag{12}$$

Definindo:

$$\begin{aligned} f_i &= \nabla^2 f_{i-1} \\ f_1 &= R(\phi, P) \end{aligned} \tag{13}$$

Tem-se:

$$\begin{aligned} &\iiint_V R(\phi,P)G_0(P,Q)\,dV = \iiint_V f_1(\phi,P)G_0(P,Q)\,dV = \iiint_V f_1\nabla^2 G_1\,dV = \\ &\iiint_V (f_1\nabla^2 G_1 - G_1\nabla^2 f_1)dV + \iiint_V G_1\nabla^2 f_1\,dV = \oiint_S \left(f_1 \frac{\partial G_1}{\partial n} - G_1 \frac{\partial f_1}{\partial n} \right) dS + \iiint_V f_2 G_1\,dV \end{aligned} \tag{14}$$

Para um i arbitrário, obtém-se:

$$\begin{aligned} \iiint_V f_i G_{i-1}\,dV &= \iiint_V f_i\nabla^2 G_i\,dV = \iiint_V f_i\nabla^2 G_i - G_i\nabla^2 f_i\,dV + \iiint_V G_i\nabla^2 f_i\,dV = \\ &\oiint_S f_i \frac{\partial G_i}{\partial n} - G_i \frac{\partial f_i}{\partial n} dS + \iiint_V f_{i+1} G_i\,dV \end{aligned} \tag{15}$$

Utilizando os resultados (14) e (15), por indução, tem-se:

$$\iiint_V R(\phi,P)G_0(P,Q)\,dV = \sum_{i=1}^{\infty} \oiint_S \left(f_i(\phi,P) \frac{\partial G_i(P,Q)}{\partial n} - G_i(P,Q) \frac{\partial f_i(\phi,P)}{\partial n} \right) dS \tag{16}$$

Substituindo (16) em (12), chega-se à expressão final:

$$C\phi(Q) = \oiint_S \left(\phi(P) \frac{\partial G_0(P,Q)}{\partial n} - G_0(P,Q) \frac{\partial \phi(P)}{\partial n} \right) dS - \sum_{i=1}^{\infty} \oiint_S \left(f_i(\phi,P) \frac{\partial G_i(P,Q)}{\partial n} - G_i(P,Q) \frac{\partial f_i(\phi,P)}{\partial n} \right) dS \tag{17}$$

A equação (17) fornece um resultado importante: é possível a resolução da equação de Poisson se forem conhecidos os valores do campo escalar ϕ *e de todas as suas derivadas* apenas sobre a fronteira. A necessidade de se conhecer esses valores leva a um método iterativo, exceto no caso linear, que será tratado na próxima parte deste relatório. Porém, esse método já economiza bastante esforço computacional devido ao fato de não ser preciso fazer uma discretização de todo o campo, mas somente da fronteira.

Entretanto, o conhecimento apenas dos valores na fronteira só é suficiente se o campo escalar ϕ for de classe C^{∞} (tiver todas as derivadas contínuas) em todos os pontos do domínio e nem sempre a série convergirá, mesmo se o campo escalar atender essa condição.

3. Condução de calor unidimensional

O problema da condução estacionária com geração de calor também é regido por uma equação de Poisson. Aqui, será tratado o caso unidimensional e linear, cuja equação está escrita abaixo:

$$\frac{d^2T}{dx^2} + R(x) = 0 \tag{18}$$

Nesse caso, R(x) = g(x)/k, onde g (x) é a potência de geração de calor na posição x e k, a condutividade térmica do material.

As condições de contorno podem ser de três tipos: temperatura na fronteira especificada, fluxo de calor na fronteira ($-k\,\partial T/\partial x$) especificado ou condição de contorno de convecção, $-\partial T/\partial x = Bi(T - T_f)$, onde:

- T_f: Temperatura do fluido circundante
- Bi: Número de Biot, dado por hL/k, onde:
  - L: Comprimento característico do domínio, dado por V/A (V é o volume desse domínio e A, a área da fronteira)

- h: Coeficiente de convecção do fluido. Depende tanto da natureza quanto do campo de velocidades desse fluido.

Sem perda de generalidade, foi feita a mudança de variável $\theta = T - T_f$. Com isso, a equação permaneceu a mesma, já que $d^2T/dx^2 = d^2\theta/dx^2$, e a condição de contorno de convecção ficou mais simples.

A equação (18) é facilmente solúvel por dupla integração de R(x), mas o objetivo deste item é aplicar a equação (17) ao caso mais simples possível para depois estendê-la a problemas mais complexos. Enquanto no caso tridimensional esse método resolve a equação de Poisson por meio de uma integral de superfície sobre a fronteira, no caso unidimensional ele substitui a integração por um simples cálculo algébrico com os valores de R(x) e suas derivadas nos limites do domínio.

A equação (17), no caso unidimensional para a condução de calor, já que o valor principal de Cauchy é sempre 1 em problemas unidimensionais, é escrita como:

$$\theta(\xi) = \left[\theta(x) \frac{dG_0(x,\xi)}{dx} - G_0(x,\xi) \frac{d\theta(x)}{dx} - \sum_{i=1}^{\infty} f_i(x) \frac{dG_i(x,\xi)}{dx} - G_i(x,\xi) \frac{df_i(x)}{dx} \right]_{x_1}^{x_2} \tag{19}$$

onde x_1 e x_2 são os limites inferior e superior do domínio e as funções f_i são definidas como:

$$\begin{aligned} f_i(x) &= \frac{d^2 f_{i-1}(x)}{dx^2} \\ f_1(x) &= R(x) \end{aligned} \tag{20}$$

Ainda no caso unidimensional, as funções G_i serão definidas por:

$$G_i(x,\xi) = \begin{cases} -\frac{1}{2}\frac{1}{(2i+1)!}(x-\xi)^{2i+1} \; para \; x < \xi \\ \frac{1}{2}\frac{1}{(2i+1)!}(x-\xi)^{2i+1} \; para \; x > \xi \end{cases} \tag{21}$$

Serão mostrados dois exemplos de funções R(x), no domínio $0 < x < 1$, com as condições de contorno: extremidade $x = 0$ isolada e $x = 1$ com convecção, descritas abaixo:

$$\frac{d\theta}{dx} = 0 \qquad \text{em } x = 0 \tag{22}$$

$$\frac{d\theta}{dx} + Bi\theta = 0 \qquad \text{em } x = 1 \tag{23}$$

3.1. R(x) = sen 2πx

$$\begin{aligned} f_i(x) &= (-1)^{i-1}(2\pi)^{2i-2} \, sen\,(2\pi x) \\ \frac{df_i(x)}{dx} &= (-1)^{i-1}(2\pi)^{2i-1} \cos(2\pi x) \end{aligned} \tag{24}$$

Substituindo (24) e as condições de contorno (22) e (23) em (19), tem-se:

$$\theta(\xi) = \frac{1}{2}\left[\theta(1)\left(1 + Bi(1-\xi)\right) + \theta(0)\right] - \sum_{i=1}^{\infty} \frac{(-1)^{i-1}}{2} \frac{(2\pi)^{2i-1}}{(2i+1)!}\left[\xi^{2i+1} - (1-\zeta)^{2i+1}\right] \tag{25}$$

A série infinita pode ser escrita como:

$$\frac{1}{8\pi^2}\left(\sum_{i=1}^{\infty} (-1)^{i-1} \frac{(2\pi\xi)^{2i+1}}{(2i+1)!} - \sum_{i=1}^{\infty} (-1)^{i-1} \frac{(2\pi(1-\xi))^{2i+1}}{(2i+1)!} \right) = \frac{4\pi\xi - 2\pi + sen\,2\pi(1-\xi) - sen\,2\pi\xi}{8\pi^2} \tag{26}$$

Substituindo (26) em (25) e fazendo $\xi = 0$ e $\xi = 1$, obtém-se o seguinte sistema de equações:

$$\begin{cases} \theta(0) = \dfrac{1}{2}\left[\theta(1)(1+Bi) + \theta(0)\right] + \dfrac{1}{4\pi} \\ \theta(1) = \dfrac{1}{2}\left[\theta(1) + \theta(0)\right] - \dfrac{1}{4\pi} \end{cases} \tag{27}$$

cuja solução é:

$$\left(\theta(0) = \frac{1}{2\pi}, \theta(1) = 0\right) \tag{28}$$

Substituindo (26) em (25) e a solução (28) na equação resultante e fazendo sen(2π-2πξ) = sen(-2πξ) = -sen(2πξ), tem-se:

$$\theta(\xi) = \frac{1-\xi}{2\pi} + \frac{sen\,2\pi\xi}{4\pi^2} \tag{29}$$

Essa é a mesma solução que seria obtida se tivesse sido usado o método clássico de dupla integração unidimensional. A diferença é que, no método que agora foi usado, não foi necessário fazer integração alguma, apenas derivações, cálculos algébricos e o uso das funções pré-definidas G_i. Neste caso, a integração unidimensional foi substituída por uma "integração de dimensão zero". Generalizando, esse método sempre reduz em uma dimensão a integração que seria feita pelo método convencional.

Nesse caso, foi possível encontrar a solução exata. Entretanto, em problemas onde R também é função de θ (ou ϕ, no caso do problema aerodinâmico), sua forma não é conhecida a priori, sendo, pois, necessário o uso da série, com um número de termos satisfatório. Devido a isso, foi feita uma análise da convergência da série do problema resolvido acima. Está mostrada abaixo uma comparação entre os gráficos das soluções desse problema com diversos números de elementos da série e o da solução exata:

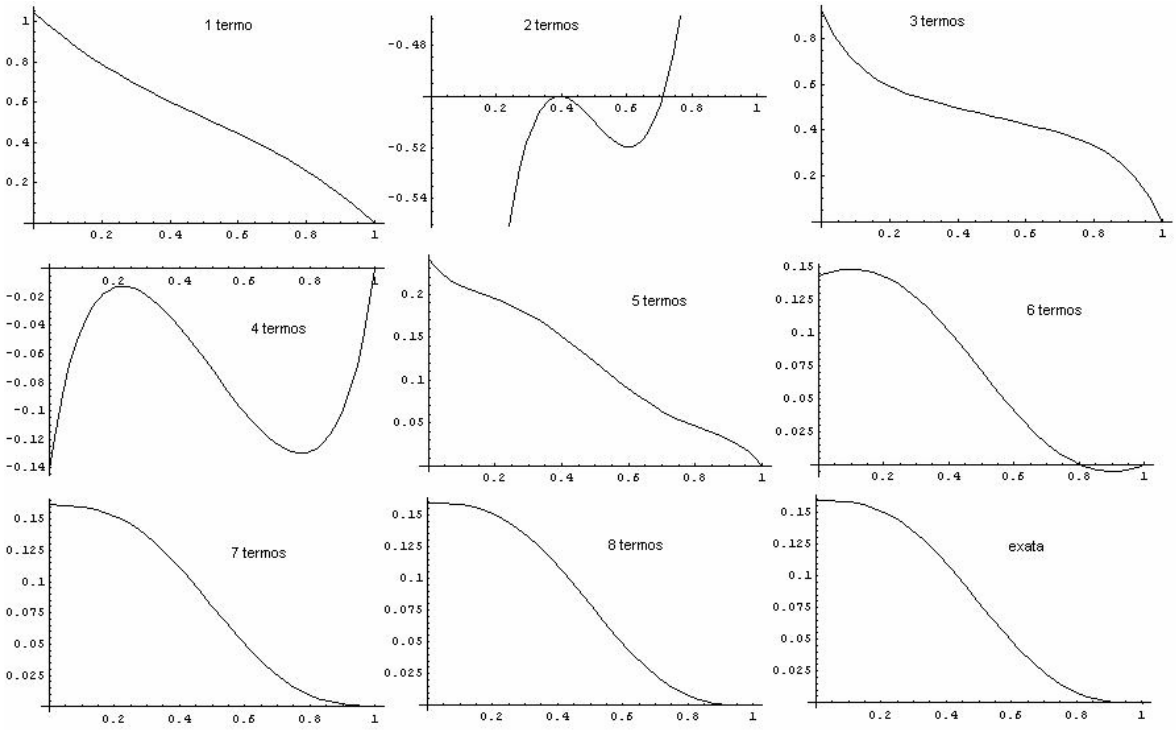

Figura 1. Convergência da solução de R(x) = sen 2πx.

Nota-se que, com oito termos da série, o gráfico ficou praticamente indistinguível do da solução exata. Deve haver erros da ordem de 1%, pois a capacidade de visualização no gráfico é limitada. Isso dá uma idéia do número de termos necessário nos problemas não-lineares: aproximadamente oito, ou mais, dependendo da exatidão pretendida.

3.2. R(x) = $1/(x+1/2)$

$$f_i(x) = \frac{(2i-2)!}{(x+1/2)^{2i-1}}$$
$$\frac{df_i(x)}{dx} = -\frac{(2i-1)!}{(x+1/2)^{2i}} \tag{30}$$

Fazendo a substituição na equação (19), tem-se:

$$\theta(\xi) = \frac{1}{2}\left[\theta(1)(1+Bi(1-\xi)) + \theta(0)\right] - \sum_{i=1}^{\infty}\left[\begin{array}{l} \frac{1}{2}\left(\frac{2}{3}\right)^{2i-1}\frac{1}{2i(2i-1)}(1-\xi)^{2i} - 2^{2i-2}\frac{1}{2i(2i-1)}\xi^{2i} \\ -\frac{1}{2}\left(\frac{2}{3}\right)^{2i}\frac{1}{2i(2i+1)}(1-\xi)^{2i+1} + 2^{2i-1}\frac{1}{2i(2i+1)}\xi^{2i+1} \end{array}\right] \tag{31}$$

Substituindo ξ = 0 e ξ = 1, é formado o sistema de equações abaixo:

$$\begin{cases} \theta(0) = \frac{1}{2}\left[\theta(1)(1+Bi) + \theta(0)\right] - \sum_{i=1}^{\infty}\left[\frac{1}{2}\left(\frac{2}{3}\right)^{2i-1}\frac{1}{2i(2i-1)} - \frac{1}{2}\left(\frac{2}{3}\right)^{2i}\frac{1}{2i(2i+1)}\right] \\ \theta(1) = \frac{1}{2}\left[\theta(1) + \theta(0)\right] + \sum_{i=1}^{\infty}\left[2^{2i-2}\frac{1}{2i(2i-1)} - 2^{2i-1}\frac{1}{2i(2i+1)}\right] \end{cases} \tag{32}$$

Será analisada agora a convergência da série da segunda equação. Para isso, será aplicado o critério da razão, que consiste em calcular $\lim_{i\to\infty}\left|a_{i+1}/a_i\right|$, onde os a_i são os termos da série. Se esse limite for menor que 1, a série converge, se for maior, ela diverge e, se for igual, nada se pode afirmar.

$$a_i = 2^{2i-2}\frac{1}{2i(2i-1)} - 2^{2i-1}\frac{1}{2i(2i+1)} = 2^{2i-2}\frac{-2i+3}{2i(2i+1)(2i-1)} \tag{33}$$

$$\left|\frac{a_{i+1}}{a_i}\right| = \left|4\frac{(2i-1)^2}{(2i-3)(2i+2)}\right| = \left|4\frac{4i^2-2i+1}{4i^2-2i-6}\right| \tag{34}$$

$$\lim_{i\to\infty}\left|4\frac{4i^2-2i+1}{4i^2-2i-6}\right| = \lim_{i\to\infty}\left|4\frac{1-\frac{1}{2i}+\frac{1}{4i^2}}{1-\frac{1}{2i}-\frac{3}{2i^2}}\right| = 4 \tag{35}$$

Logo, essa série diverge. As séries obtidas por esse método são, na verdade, as séries de Taylor das funções que seriam obtidas a partir do método convencional de solução feitas em torno de um dos extremos e avaliadas no outro. A série divergiu porque o outro extremo não estava em seu raio de convergência. Essa é uma limitação do método: é possível que séries de funções limitadas e de classe C^{∞} no domínio divirjam em seus extremos. Isso é típico para funções do tipo $(x - a)^{-n}$, nas quais, perto da singularidade, as derivadas sucessivas vão aumentando muito.

4. A equação do regime transônico para pequenas perturbações

A equação do potencial para o regime incompressível, a equação de Laplace (equação (1)), é derivada da equação da continuidade para esse regime:

$$\nabla \cdot \vec{V} = 0 \tag{36}$$

Já no regime compressível, cuja característica é possuir a concentração mássica, ρ, variável, a equação da continuidade toma a seguinte forma:

$$\nabla \cdot (\rho\vec{V}) = 0 \tag{37}$$

Definem-se $\hat{u}$ e $\hat{v}$, as velocidades de perturbação, como:

$$\begin{aligned} \hat{u} &= u - V_\infty \\ \hat{v} &= v \end{aligned} \tag{38}$$

onde u = V_x, v = V_y, e V_∞ é a velocidade do escoamento não-perturbado. Além disso, define-se $\hat{\phi}$, o potencial de perturbação, como:

$$\begin{aligned} \frac{\partial \hat{\phi}}{\partial x} &= \hat{u} \\ \frac{\partial \hat{\phi}}{\partial y} &= \hat{v} \end{aligned} \tag{39}$$

Após a aplicação de alguns princípios aerodinâmicos, é possível, de acordo com a referência [3], chegar a partir da equação (37) à equação bidimensional do potencial de perturbação para o regime compressível:

$$\begin{aligned} &\left(1 - M_\infty^2\right)\hat{\phi}_{xx} + \hat{\phi}_{yy} = M_\infty^2\left[\frac{\gamma+1}{V_\infty}\hat{\phi}_x + \frac{\gamma+1}{2V_\infty^2}\hat{\phi}_x^2 + \frac{\gamma-1}{2V_\infty^2}\hat{\phi}_y^2\right]\hat{\phi}_{xx} + \\ &M_\infty^2\left[\frac{\gamma-1}{V_\infty}\hat{\phi}_x + \frac{\gamma+1}{2V_\infty^2}\hat{\phi}_y^2 + \frac{\gamma-1}{2V_\infty^2}\hat{\phi}_x^2\right]\hat{\phi}_{yy} + M_\infty^2\left[\frac{\hat{\phi}_y}{V_\infty}\left(1 + \frac{\hat{\phi}_x}{V_\infty}\right)\left(\hat{\phi}_{xy} + \hat{\phi}_{yx}\right)\right] \end{aligned} \tag{40}$$

onde γ é a razão entre os calores específicos a pressão constante e a volume constante e M_∞ é o número de Mach do escoamento não-perturbado, definido por $M_\infty = V_\infty / a_\infty$, onde a_∞ é a velocidade do som no escoamento não-perturbado.

A equação (40) é exata para qualquer escoamento não-viscoso. Entretanto, ela é extremamente não-linear e, por isso, de difícil solução. Se fizermos uma aproximação para pequenas perturbações, para números de Mach fora das faixas transônica e hipersônica, então essa equação se transforma em:

$$\left(1 - M_\infty^2\right)\hat{\phi}_{xx} + \hat{\phi}_{yy} = 0 \tag{41}$$

A equação (41) é elíptica no regime subsônico e hiperbólica no regime supersônico, logo, quando o regime muda, há também uma mudança no tipo da equação e de sua solução. Não obstante, com números de Mach do escoamento não-perturbado entre 0.8 e 1.2, que é a faixa transônica, há uma coexistência dos dois regimes no campo de velocidades, que não pode ser descrita satisfatoriamente por uma equação unicamente elíptica ou hiperbólica. Dessa forma, um dos termos que foram abandonados ao se passar da equação (40) para a (41) não é desprezível e deve ser considerado. Com isso, a equação mais simples para o regime transônico é a seguinte:

$$\left(1 - M_\infty^2\right)\hat{\phi}_{xx} + \hat{\phi}_{yy} = \frac{M_\infty^2(\gamma+1)}{V_\infty}\hat{\phi}_x\hat{\phi}_{xx} \tag{42}$$

Fazendo:

$$\begin{aligned} \beta^2 &= 1 - M_\infty^2 \\ K &= \frac{M_\infty^2(\gamma+1)}{V_\infty} \\ \tilde{x} &= x \\ \tilde{y} &= \beta y \\ \tilde{\phi} &= \frac{K\hat{\phi}}{\beta^2} \end{aligned} \tag{43}$$

chega-se a uma expressão mais simples:

$$\tilde{\phi}_{\tilde{x}\tilde{x}} + \tilde{\phi}_{\tilde{y}\tilde{y}} = \tilde{\phi}_{\tilde{x}}\tilde{\phi}_{\tilde{x}\tilde{x}} \tag{44}$$

A resolução da equação (44) é um dos objetivos principais deste trabalho e será a próxima tarefa. Doravante, o símbolo "~" será suprimido e, quando se fizer referência à equação do regime transônico, deve-se entender que se está trabalhando com as variáveis transformadas.

5. Singularidades bidimensionais

No método que será utilizado na resolução bidimensional da equação (44) para perfis, será feita uma distribuição de singularidades sobre a corda do perfil de forma que sua fronteira seja uma linha de corrente. A rigor, ela não será uma fronteira propriamente dita e o valor principal de Cauchy em todo o plano xz será 1.

A equação (16), aplicada nesse caso, toma a seguinte forma:

$$\phi(Q) = \oint_C \left(\phi(P) \frac{\partial G_0(P,Q)}{\partial n} - G_0(P,Q) \frac{\partial \phi(P)}{\partial n} \right) ds - \sum_{i=1}^{\infty} \oint_C \left(f_i(\phi,P) \frac{\partial G_i(P,Q)}{\partial n} - G_i(P,Q) \frac{\partial f_i(\phi,P)}{\partial n} \right) ds \tag{45}$$

Em duas dimensões, a função $G_0(P,Q)$, que é a função cujo laplaciano é o Delta de Dirac centrado em Q, é a solução fonte da equação de Laplace: $\ln r/(2\pi)$, onde r é o módulo de $\vec{r}$, o vetor que liga Q a P. $\partial G_0(P,Q)/\partial n$ é a solução dipolo orientada na direção de $\hat{n}$.

Devido à definição das funções G_i, $\nabla^2 G_i = G_{i-1}$, cada função G_i é denominada *metafonte de ordem i*, por ser solução da equação $\nabla^{2(i+1)}\phi = 0$ (por exemplo, $\nabla^4\phi = \nabla^2(\nabla^2\phi)$, e assim por diante). Suas derivadas são denominadas *metadipolos de ordem i*.

Para encontrar uma fórmula geral para as metafontes, será usado o laplaciano em coordenadas polares:

$$\nabla^2 G_i(r,\theta) = \frac{1}{r}\frac{\partial}{\partial r}\left(r \frac{\partial G_i}{\partial r} \right) + \frac{1}{r^2}\left(\frac{\partial^2 G_i}{\partial \theta^2} \right) \tag{46}$$

Como as funções G_i são apenas funções de r, será usado apenas o primeiro termo. Além disso, nos cálculos abaixo, será omitido o termo $1/(2\pi)$, que será acrescentado na expressão final.

$$\frac{1}{r}\frac{\partial}{\partial r}\left(r \frac{\partial G_1}{\partial r} \right) = \ln r \tag{47}$$

$$G_1 = \frac{r^2}{4}\ln r - \frac{r^2}{8} - \frac{r^2}{8} = \frac{r^2}{4}(\ln r - 1) \tag{48}$$

$$\frac{1}{r}\frac{\partial}{\partial r}\left(r \frac{\partial G_{i+1}}{\partial r} \right) = r^{2i}(C_i \ln r - D_i) \tag{49}$$

$$G_{i+1} = r^{2(i+1)}\left[\frac{C_i}{4(i+1)^2}\ln r - \frac{C_i}{4(i+1)^3} - \frac{D_i}{4(i+1)^2} \right] \tag{50}$$

Usando os resultados (49) e (50), por indução, chega-se à forma recursiva geral:

$$G_i = \frac{1}{2\pi} r^{2i}(C_i \ln r - D_i), C_0 = 1, D_0 = 0, C_{i+1} = \frac{C_i}{4(i+1)^2}, D_{i+1} = \frac{C_i}{4(i+1)^3} + \frac{D_i}{4(i+1)^2} \tag{51}$$

6. Solução do escoamento incompressível

A primeira integral da equação (45), referente apenas à função G_0 e sua derivada, ou seja, à fonte e ao dipolo, é uma forma de resolver a equação de Laplace (equação (1)), por conter apenas singularidades que são suas soluções. Já que essa equação rege o escoamento incompressível, a aplicação apenas da primeira integral da equação (45) fornece uma solução para esse regime e a série infinita faz as correções necessárias para o escoamento compressível.

Na verdade, a solução por esse método não é única, se forem usados os dipolos e metadipolos. São esses termos que fornecem a sustentação, a qual, para ser univocamente determinada, precisa da aplicação da condição de Kutta, que determina que a velocidade no bordo de fuga deve ser finita. Por ora, entretanto, só será resolvido o problema sem sustentação, ou seja, só serão usadas as fontes e metafontes.

Será encontrada agora uma maneira de resolver o problema incompressível por meio de uma distribuição de fontes sobre a corda de um perfil simétrico, que está descrita na referência [5]. Utilizar-se-á o volume de controle abaixo, que

compreende duas seções transversais separadas por uma distância dx, um elemento de fronteira sobre o extradorso, que será uma linha de corrente, e um elemento de corda com uma intensidade de fonte por unidade de comprimento λ:

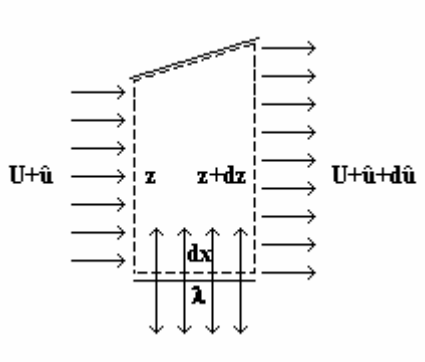

Figura 2. Volume de controle.

Fazendo o balanço de fluxos na fronteira do volume de controle, como ρ não varia, tem-se:

$$\frac{1}{2}\lambda\, dx + (U+\hat{u})z - (U+\hat{u}+d\hat{u})(z+dz) = 0 \tag{52}$$

$$\frac{1}{2}\lambda\, dx = (U+\hat{u})z + z\, d\hat{u} + (U+\hat{u})dz - (U+\hat{u})z = U\, dz + \hat{u}\, dz + z\, d\hat{u} \tag{53}$$

$$\lambda = 2U\frac{dz}{dx} + 2\hat{u}\frac{dz}{dx} + 2z\frac{d\hat{u}}{dx} \tag{54}$$

Fazendo a hipótese de pequenas perturbações, $\hat{u}$ e $d\hat{u}/dx$ são desprezíveis e é obtida a expressão final:

$$\lambda = 2U\frac{dz}{dx} \tag{55}$$

A equação acima é uma forma direta de encontrar a distribuição de fontes conhecendo apenas a velocidade não-perturbada e a forma do perfil, desde que as perturbações sejam realmente pequenas.

7. Velocidades induzidas

Ao substituir a equação do potencial transônico (equação (44)) na equação (45), nota-se que é necessário calcular os laplacianos sucessivos do termo $\phi_x\phi_{xx}$, ou uu_x, onde u é a componente x da velocidade de perturbação. As funções $G_i(P,Q)$ fornecem o potencial induzido por uma metafonte de ordem i localizada no ponto P sobre o ponto Q. Para encontrar a velocidade induzida, basta aplicar o gradiente em coordenadas polares,

$$\frac{\partial G_i}{\partial r}\hat{r} + \frac{1}{r}\frac{\partial G_i}{\partial \theta}\hat{\theta} \tag{56}$$

do qual só será usado o primeiro termo porque G_i é apenas função de r. Portanto, derivando a expressão de G_i dada em (51), tem-se que a velocidade induzida por uma metafonte pontual é dada por:

$$\vec{V} = \frac{1}{2\pi} r^{2i-1}\left(2iC_i \ln r - (2iD_i - C_i)\right)\hat{r} \tag{57}$$

No método numérico, a corda é dividida em painéis com distribuição de intensidade de metafonte por unidade de comprimento constante A_i ou linear, $a_i s + b_i$, onde s é a variável de comprimento ao longo do painel. Para calcular a velocidade induzida por um painel da corda sobre um ponto também na corda, basta fazer uma integral simples na variável r e a velocidade induzida estará na direção do eixo x. Para intensidade constante, temos:

$$V = -\frac{A_i}{2\pi}\int_{r_1}^{r_2} r^{2i-1}\left(2iC_i \ln r - (2iD_i - C_i)\right) dr = -\frac{A_i}{2\pi} r^{2i}\left(C_i \ln r - D_i\right)\Big|_{r_1}^{r_2} \tag{58}$$

onde r_1 e r_2 são as distâncias do ponto onde está sendo calculada a velocidade induzida (ponto de controle) aos limites inferior e superior do painel. O sinal negativo ocorre porque a velocidade induzida por um ponto do painel tem sentido oposto ao do vetor que vai do ponto de controle a esse ponto. Para distribuição linear, temos, para painéis à esquerda do ponto de controle:

$$V = -\frac{1}{2\pi}\left[-a_i r^{2i+1}\left(\frac{2i}{2i+1}C_i \ln r - \left(\frac{2i}{2i+1}D_i - C_i\right)\right) + (a_i r_1 + b_i) r^{2i}\left(C_i \ln r - D_i\right)\right]\Bigg|_{r_1}^{r_2} \tag{59}$$

E, para painéis à direita do ponto de controle:

$$V = -\frac{1}{2\pi}\left[a_i r^{2i+1}\left(\frac{2i}{2i+1}C_i \ln r - \left(\frac{2i}{2i+1}D_i - C_i\right)\right) + (b_i - a_i r_1) r^{2i}\left(C_i \ln r - D_i\right)\right]\Bigg|_{r_1}^{r_2} \tag{60}$$

As equações (58), (59) e (60) podem ser estendidas a painéis de orientação arbitrária (que formem um ângulo α com o eixo x) induzindo velocidade em um ponto localizado em sua mesma reta. Agora, será calculada a velocidade induzida em um ponto de localização também arbitrária, ou seja, fora da reta do painel. Seja o ponto de controle a origem do sistema de coordenadas polares (r, θ). Então o vetor velocidade induzida por um elemento de painel ds com intensidade de metafonte constante A_i é dado por:

$$\left(-\frac{A_i}{2\pi} r^{2i-1}\left(2iC_i \ln r - \left(2iD_i - C_i\right)\right) ds,\, \theta\right) \tag{61}$$

Logo, o vetor total é:

$$\vec{V} = \left(-\frac{A_i}{2\pi}\int_{(r_1,\theta_1)}^{(r_2,\theta_2)} r^{2i-1}\left(2iC_i \ln r - \left(2iD_i - C_i\right)\right) ds,\, \theta\Big|_{\theta_1}^{\theta_2}\right) \tag{62}$$

Escrevendo ds em função de dr e dθ:

$$ds = \sqrt{dr^2 + r^2 d\theta^2} = \sqrt{r^2 + \left(\frac{dr}{d\theta}\right)^2}\, d\theta \tag{63}$$

Sendo (r_0, θ_0) o limite inferior do painel (ou um ponto arbitrário sobre o painel), obtém-se:

$$\begin{aligned} r(\theta) &= r_0 \cos(\theta_0 - (\pi/2 + \alpha))\sec(\theta - (\pi/2 + \alpha)) \\ \frac{dr}{d\theta} &= r_0 \cos(\theta_0 - (\pi/2 + \alpha))\sec(\theta - (\pi/2 + \alpha))\tan(\theta - (\pi/2 + \alpha)) \end{aligned} \tag{64}$$

Logo, o vetor velocidade induzida em coordenadas polares será dado por:

$$\left(-\frac{A_i}{2\pi}\left(r_0 r^{2i-1}(2iC_i \ln r - (2iD_i - C_i))\cos(\theta_0 - (\pi/2 + \alpha))\int_{\theta_1}^{\theta_2} \sec^2(\theta - (\pi/2 + \alpha))\, d\theta\right)\Bigg|_{r_1}^{r_2}, \theta_2 - \theta_1\right) \tag{65}$$

Portanto:

$$\vec{V} = \left(-\frac{A_i}{2\pi}\left(r_0 r^{2i-1}(2iC_i \ln r - (2iD_i - C_i))\cos(\theta_0 - (\pi/2 + \alpha))\tan(\theta - (\pi/2 + \alpha))\right)_{(r_1,\theta_1)}^{(r_2,\theta_2)}, \theta_2 - \theta_1\right) \tag{66}$$

A equação (66) só pode ser usada se o ponto de controle não estiver sobre a reta que passa pelo painel, caso contrário, ela gerará uma indeterminação do tipo $0.\infty$ e, na verdade, a integração não poderia ser feita em θ porque θ

não varia. Nesses casos, deve-se usar a equação (58) e o vetor terá a direção do painel e, se o resultado for positivo, o sentido painel – ponto de controle.

Para uma distribuição linear $a_i s + b_i$, tem-se:

$$\frac{ds}{d\theta} = r_0 \cos(\theta_0 - (\pi/2+\alpha)) \sec^2(\theta - (\pi/2+\alpha)) \tag{67}$$

$$\Rightarrow s = r_0 \cos(\theta_0 - (\pi/2+\alpha))\left[\tan(\theta - (\pi/2+\alpha)) - \tan(\theta_1 - (\pi/2+\alpha))\right] \tag{68}$$

E a velocidade induzida é:

$$V = -\left[\frac{1}{2\pi} r_0 \cos(\theta_0 - (\pi/2+\alpha)) r^{2i-1} (2iC_i \ln r - (2iD_i - C_i)) \left(\begin{array}{l} \frac{a_i}{2} \tan^2(\theta - (\pi/2+\alpha)) \\ + (b_i - a_i \tan(\theta_1 - (\pi/2+\alpha))) \tan(\theta - (\pi/2+\alpha)) \end{array} \right)\right]_{(r_1,\theta_1)}^{(r_2,\theta_2)} \tag{69}$$

O ângulo θ de orientação da velocidade induzida também será dado por $\theta_2 - \theta_1$ e o sentido dessa velocidade, pelo sinal do resultado da expressão (69), que fornece sua intensidade. No caso particular de G_0, cuja velocidade induzida por fonte pontual é dada por $1/(2\pi r)\hat{r}$, temos que a velocidade induzida em um ponto localizado fora da reta do painel com uma distribuição constante A_i é dada por:

$$\vec{V} = \left(-\frac{A_i}{2\pi} \left(\frac{r_0}{r} \cos(\theta_0 - (\pi/2+\alpha)) \tan(\theta - (\pi/2+\alpha)) \right)\Bigg|_{(r_1,\theta_1)}^{(r_2,\theta_2)}, \theta_2 - \theta_1 \right) \tag{70}$$

E, com uma distribuição linear, por:

$$\vec{V} = \left(-\left[\frac{1}{2\pi} \frac{r_0}{r} \cos(\theta_0 - (\pi/2+\alpha)) \left(\begin{array}{l} \frac{a_i}{2} \tan^2(\theta - (\pi/2+\alpha)) \\ + (b_i - a_i \tan(\theta_1 - (\pi/2+\alpha))) \tan(\theta - (\pi/2+\alpha)) \end{array} \right)\right]_{(r_1,\theta_1)}^{(r_2,\theta_2)}, \theta_2 - \theta_1 \right) \tag{71}$$

8. Método iterativo para a resolução da equação do regime transônico

Será descrito agora o algoritmo do método que foi utilizado em um programa para a resolução da equação (44), $\phi_{xx} + \phi_{yy} = \phi_x \phi_{xx}$, para um escoamento sem sustentação sobre um perfil simétrico. Essa implementação foi feita usando o software Matlab, que oferece uma linguagem computacional que facilita bastante os cálculos, e pode, inclusive, trabalhar com números complexos.

- Entrar com as variáveis np (número de painéis) e m (número de metafontes). Considerar velocidade não-perturbada U = 1, sem perda de generalidade.
- Sendo ps o vetor de pontos sobre a corda que separam cada painel de seus vizinhos (corda variando de zero a um) e p = x + iz (i é a unidade imaginária) o vetor de pontos sobre o extradorso que possuem as mesmas coordenadas x que os pontos do vetor ps, calcular o vetor t, de vetores tangentes unitários: $t_j = p_{j+1} - p_j \big/ \left\| p_{j+1} - p_j \right\|$.
- Atribuir a pc a matriz de pontos de controle sobre a corda, no centro dos painéis, e fora da corda, em algumas coordenadas z acima dos pontos anteriores, de modo que todos os pontos sejam separados de seus vizinhos pela mesma distância.
- Calcular o vetor n, de vetores normais unitários: $n_j = it_j$ e calcular a distribuição de fontes sobre a corda $s_0 = A_0$ ou $s_0 = (a_0, b_0)$, sendo A_0 calculado pela equação (55) do regime incompressível, fazendo $(dz/dx)_j = \mathrm{Im}(t_j)/\mathrm{Re}(t_j)$, e a_0 e b_0 como $a_{0,j} = (dA_0/dx)\big|_{pc_{j,1}}$ e $b_{0,j} = A_{0,j} - a_{0,j}(pc_{j,1} - ps_j)$. A derivada de A_0 é calculada no primeiro painel como $dA_0/dx\big|_{pc_{1,1}} = (A_{0,2} - A_{0,1})/(pc_{2,1} - pc_{1,1})$, e nos painéis centrais e no último como $dA_0/dx\big|_{pc_{j,1}} = (A_{0,j+1} - A_{0,j-1})/(pc_{j+1,1} - pc_{j-1,1})$ e $dA_0/dx\big|_{pc_{np,1}} = (A_{0,np} - A_{0,np-1})/(pc_{np,1} - pc_{np-1,1})$. Todas as outras derivações são feitas de modo análogo.
- Ir calculando as velocidades induzidas por cada um dos painéis sobre a corda (usando os pontos ps) em cada um dos pontos da matriz pc de pontos de controle, usando a equação (58), (59) ou (60) nos pontos da corda e (66) ou (69) nos pontos fora. Fazer o somatório das componentes x da velocidade induzida por cada

painel no ponto de controle e gravar o resultado na variável correspondente da matriz v0. Fazer isso com todos os pontos de controle.

- Atribuir à matriz v2 os valores da matriz v0.
- Para q variando de 1 a m:
  - Para ni variando de 1 a 50 (ou outro número de iterações):
    - Atribuir o valor zero à variável de controle *convergiu*
    - Atribuir à matriz v1 os valores da matriz v2
    - Derivar em relação a x o campo v2 pelo método já descrito e gravar na matriz ux. Multiplicar cada elemento de v2 pelo correspondente de ux e gravar na matriz uux. Gravar na matriz f_1 da matriz tridimensional f os valores da matriz uux.
    - Calcular o gradiente de f_1 sobre a corda pelo método de derivação já descrito, guardar num vetor de variáveis complexas dl e calcular a intensidade de metafonte A_1 como $A_{1,j} = \mathrm{Re}(\overline{n}_j \times dl)$, onde $\overline{n}_j$ é o complexo conjugado da normal externa ao perfil já calculada. Esse cálculo é o resultado de $\frac{\partial f_1}{\partial n}$ (vide equação (45)), dado pelo produto escalar $\hat{n} \cdot \nabla f_1$, que pode ser calculado da maneira descrita.
    - Se for distribuição linear de metafontes, calcular a_1 e b_1 a partir de A_1, como foi feito com a_0 e b_0 a partir de A_0
    - Para k variando de 2 a q:
      - Fazer $f_k = \nabla^2 f_{k-1}$. O laplaciano é calculado numericamente pelo Matlab usando o comando 4*del2(f_{k-1},1/np), onde del2(u, h) calcula $\frac{1}{4h}(u_{i+1,j} + u_{i-1,j} + u_{i,j+1} + u_{i,j-1}) - u_{i,j}$ e faz o mesmo nas bordas com uma extrapolação cúbica.
      - Calcular $A_k = \hat{n} \cdot \nabla f_k$, como já foi feito com A_1 e, se necessário, calcular a_k e b_k.
    - Atribuir à matriz v2 os valores da matriz v0
    - Ir calculando as velocidades induzidas por cada metafonte de cada painel em cada ponto de controle usando a equação (58), (59) ou (60) nos pontos sobre a corda e (66) ou (69) nos pontos fora e calculando os C_k e D_k pelas fórmulas recursivas (51). Em cada ponto, ir somando as componentes x das velocidades à variável correspondente de v2 e gravar na própria matriz v2.
    - Calcular o erro relativo médio entre v1 e v2 e, se ele for menor que 0.000001 (ou outro valor, dependendo da precisão desejada), atribuir à variável de controle *convergiu* o valor 1 e sair do loop.
  - Mostrar os valores de v2 e todas as metafontes s_k.
  - Se a variável *convergiu* tiver o valor zero, sair do loop.
- Mostrar o valor da variável *convergiu*.
- Fim

Da maneira acima, o programa vai resolvendo iterativamente a equação (44) com um número de metafontes de cada vez até chegar ao número desejado, o que é feito para facilitar a convergência, visto que, desde que não seja um caso similar ao do problema 3.4 de condução do calor, a solução estará mais próxima da exata após a introdução de cada metafonte.

Como já foi constatado ao se tentar resolver o problema 3.4, a série infinita pode divergir, o que aconteceu quando foi feita uma tentativa de se resolver a equação (44) para um perfil parabólico, $z = 2tx - 2tx^2$, $0 \le x \le 1$, sendo t a espessura relativa do perfil e uma entrada do programa. No caso desse perfil, a equação (55) do regime incompressível, com sua aproximação para pequenas perturbações, se mostrou inadequada nos bordos de ataque e fuga e gerou uma solução de velocidades induzidas pelas fontes com singularidades nesses bordos. Dessa forma, a série divergiu.

9. Conclusão

Foi apresentado aqui um método que simplifica bastante a resolução numérica de equações de Poisson, em particular a equação do potencial do regime transônico, por substituir a discretização do campo por uma discretização da fronteira (ou da corda), já que basta aplicar as equações deduzidas na seção 7 aos valores das metafontes calculados pelo programa para encontrar a velocidade em qualquer ponto do campo.

No entanto, o método tem uma limitação: nem todas as distribuições de velocidade produzem uma série convergente de metafontes, fato que foi constatado no problema 3.4 e na aplicação do algoritmo descrito na seção 8 a um perfil parabólico. Apesar dessa restrição, freqüente em problemas aerodinâmicos devido às singularidades decorrentes de linearizações em pontos de estagnação, o método tem muitas aplicações se a solução for bem-

comportada. Uma delas são os problemas de transferência de calor, os quais podem ser resolvidos facilmente dessa maneira, mesmo nos casos bi e tridimensional.

10. Referências

Nowak, A.J., 1988, "Temperature Fields in Domains with Heat Sources using Boundary-Only Formulation", Proceedings of the 10th BEM Conference, Southampton, Springer, Berlin, pp. 233-247

Hildebrand, F.B., 1948, "Advanced Calculus for Applications", Prentice-Hall

Anderson Jr., J.D., 1984, "Fundamentals of Aerodynamics", McGraw-Hill

Shapiro, A.H., 1953, "The dynamics and termodynamics of compressible flow", The Ronald Press, New York

Schilichting, H., Truckenbrodt, E., 1979, "Aerodynamics of the airplane", McGraw-Hill, New York

Zuosheng, Y., 1988, "A complete boundary integral formulation for steady compressible inviscid flows governed by non-linear equations", Int. Journal for Numerical Methods in Fluids, Vol. 16, pp. 231-237

Silva, B.G.O., 2001, "Estudo de perfis aerodinâmicos em alta velocidade", Trabalho de Graduação, ITA

Spreiter, J.R., Alksne, A., 1955, "Theoretical prediction of pressure distributions on nonlifting airfoils at high subsonic speeds" NACA, Washington D.C. (NACA Report 1217)

Ribeiro, R.S., 1987, "Análise do escoamento transônico através do método das singularidades", Tese de Mestrado, ITA

Partridge, P.W., Brebbia, C.A. and Wrobel, L. C., 1992, "The Dual Reciprocity Boundary Element Method", Computational Mechanics Publications.

EXTENSION OF THE PANEL METHOD TO COMPRESSIBLE FLOW BY DISTRIBUTING SINGULARITIES ONLY OVER THE BOUNDARY OF AERODYNAMIC PROFILES

Aline Sousa da Silveira
Instituto Tecnológico de Aeronáutica – ITA
alinesilveira4@yahoo.com.br

André Valdetaro Gomes Cavalieri
Instituto Tecnológico de Aeronáutica – ITA
andre@ita.br

Paulo Afonso de Oliveira Soviero
Instituto Tecnológico de Aeronáutica – ITA
soviero@ita.br

Abstract
This work presents a method for solving the potential equation of transonic flow over a profile by integrating only over this profile's chord. This method, applied in this work for non-lifting symmetric profiles, computes a singularity distribution over the chord whose induced velocity field satisfies the necessary boundary conditions. One of the solution's components are the sources, which satisfy Laplace's equation and, if applied alone, they would solve the incompressible problem. The other singularities are meta-harmonic functions and are called meta-sources. When the compressible area integral is converted into a line integral using Green's theorem, an infinite series of meta-sources is obtained, and the method calculates the necessary terms for the wanted accuracy. However, the method has a restriction: the meta-source series is not always convergent. It diverged when a solution over a parabolic profile was tried. In spite of that fact, this method can be used in many cases, such as non-singular problems in aerodynamics, or heat transfer and many other areas.
Keywords: transonic aerodynamics, panel method, Dual-Reciprocity Method

Paper CIT06-0427

AERODYNAMIC ANALYSIS OF AN AXIAL FLOW TURBINE STAGE FOR A 5 kN TURBOJET ENGINE

Marco Aurélio B. Santin
ITA - Praça Marechal Eduardo Gomes, 50 - Vila das Acácias - São José dos Campos, SP - Brasil - 12228-900
marcoabs@ita.br

João Roberto Barbosa
ITA - Praça Marechal Eduardo Gomes, 50 - Vila das Acácias - São José dos Campos, SP - Brasil - 12228-900
barbosa@ita.br

Abstract. *A stage of axial flow turbine is designed for the application in a gas turbine engine and its three-dimensional flow field is analyzed. The baseline turbomachinery is designed based on a mean line zero-dimensional approach. The off-design performance is predicted with a mean line methodology based on the loss correlations suggested by Ainley-Mathieson and Kacker-Okapuu and the axial turbine performance curves are generated. The 3-D blade geometry is established by using 3 and 5 arcs MCA profiles. A mesh of about 600,000 hexahedral elements is constructed and the solution is obtained for steady state by using periodic boundary conditions and a mixing plane for stator-rotor interaction. RANS equations with Spalart-Allmaras turbulence model are solved by using a commercial CFD software. The simulation in several operating points allowed the construction of the turbine performance curves, which were compared to those generated by using the correlations of Ainley-Mathieson and Kacker-Okapuu. The CFD results show that mass flow is under-predicted by the mean line methodology while efficiency and power are over-predicted.*

keywords: *Gas Turbines, Axial Flow Turbines, CFD, Turbojets, Turbine Performance Maps*

1. Introduction

Worldwide gas turbine production amounted to a total of US$25.6 billion in 2005 (Langston, 2006), demonstrating the importance of this engine nowadays. Most commercial and military aircrafts employ it for propulsion and auxiliary power generation, mainly thanks to its high power/weight ratio. The fundamental module that describes a gas turbine is constituted by compressor, combustor and turbine. The working fluid, usually air, enters the compressor and receives energy in a process of compression. In the combustor, more energy is added by burning the fuel. Turbine extracts from the combustion gases the energy necessary to drive the compressor. In a turbojet engine, after leaving the turbine, the flow passes through a nozzle creating the jet that propels the aircraft.

An axial turbine stage is composed by a stator followed by a rotor. The first one's function is to convert pressure energy into kinetic energy and to drive the flow towards rotor inlet. In this last one, a part of the flow energy is converted into shaft power.

The efficiency of the current turbines is usually over 90%, making further improvements more difficult to obtain. Advances are still possible, not only in efficiency, but by lowering the cost to obtain this performance, by a more precise comprehension of the flow physical characteristics (Denton, 1993). The application of CFD analysis in the main gas turbine components is in agreement with this philosophy as it makes possible to refine the design with a comparatively less expensive tool and to reduce the development work done in test rigs, resulting in lower design cost.

Until about 1940, the design of an axial flow turbine was based only on an one-dimensional point of view, by the velocity triangles. At the beginning of the 1950s, the blade-to-blade flow characteristics were well understood; even so, design was mainly based on correlations (Cumpsty and Greitzer, 2004). From the 1970s, two-dimensional calculation methods became widespread, like the *Actuator Disc* and *Throughflow* approaches, which solve the flow considering axial symmetry. The usage of CFD as a turbomachinery design tool began in the 1970s for two-dimensional solutions and passed then to three-dimensional Euler solutions, in the 1980s, and to Navier-Stokes, in the 1990s. These developments were stimulated by the work done by J. Denton in the UK, about 1975, using Euler models; by R. Ni in the USA, in 1982, and W. Dawes, in 1988, using Navier-Stokes models (Hirsch and Demeulenaere, 2003).

The main objectives of this work were to design an axial flow turbine for a turbojet, to obtain its performance map, using three-dimensional viscous CFD simulation, and to compare this map with those obtained by using a performance prediction methodology that applies the loss correlations of Ainley and Mathieson, 1952, and Kacker and Okapuu, 1982.

The CFD software employed in this work was FLUENT for Linux, version 6.2.16. ICEM CFD, version 5.1, was applied to generate geometries and computational meshes. Turbine design and performance prediction were obtained by

using codes developed at ITA, initially as a part of the work of Bringhenti, 2003 (related to whole engine performance) and after for the work of Jesus, 2003 (related to variable geometry turbines).

2. Turbine Design

The baseline turbomachinery was designed by using the code mentioned previously. It is based on a mean line zero-dimensional approach and properties are determined along the blade by using the free vortex method. This code was implemented following the design recommendations of Saravanamuttoo *et al.*, 2001. The losses at design point, and therefore the efficiency, were estimated by using the model of Ainley and Mathieson, 1952.

At the design point of the proposed turbojet engine, the turbine operating conditions are as follows:

Inlet total temperature:	1123 K
Outlet total temperature:	940.9 K
Inlet total pressure:	471,668 Pa
Mass flow:	8.34 kg/s

From compressor design, shaft rotational speed N was defined as 25,500 rpm. The blade tip velocity was limited to 400 m/s, for structural issues.

Several authors define criteria for evaluating an axial turbine design, as can be found in Mattingly, 1996; Wilson and Korakianitis, 1998; Saravanamuttoo *et al.*, 2001. It is recommended to ensure that stator outlet angle be less than 70^o to avoid high deviation, which result in increased profile losses. When the absolute outlet angle of the last stage is high, it results in high losses in the nozzle, therefore it must be less than 20^o. It is recommended to do not allow a loading factor greater than 1.8 at mean diameter, to avoid high losses. The relation between tip and hub radius must be less than 1.4, to avoid structural and assembly problems; but must be greater than 1.2 to avoid that tip losses become predominant. The angle of divergence between the walls must be less than 25^o to avoid flow detachment on endwall. To avoid vibration, it is recommended that the stator-rotor spacing be greater than 20% of stator axial chord. It is imposed that reaction at hub be greater than zero to avoid recompression.

Turbine preliminary design characteristics are:

Stator with cylindrical hub and casing
Rotor with cylindrical casing

Stator blade number:	31	Reaction degree (mean diameter):	0.444
Rotor blade number:	41	Reaction degree (root):	0.153
Isentropic efficiency:	0.909	Expansion ratio:	2.2
Stator losses:	0.0578	Stator blade height:	34.3 mm
Rotor losses:	0.0755	Rotor outlet blade height:	42.7 mm
Rotor outlet relative Mach :	0.981	Casing radius:	149.7 mm
Loading factor:	1.658	Tip clearance:	0.0 mm
Flow coeficient:	0.843		

3. Performance Prediction

Off-design performance was predicted with the mean line methods suggested by Ainley and Mathieson, 1952, and Kacker and Okapuu, 1982, and the axial turbine performance curves were generated by an in-house developed software. The performance prediction methodology implemented by Jesus, 2003, is a modification of the methodology suggested by Ainley and Mathieson, 1952; which estimates efficiency by calculation of *loss coefficients*.

Losses are any phenomena that reduce turbine efficiency, which can be associated to viscous friction, non equilibrium process and heat transfer across finite temperature differences (Denton, 1993). The loss coeficient Y can be related to pressure losses by Eq.(1), where the subscripts *i* and *o* indicate cascade inlet and outlet, respectively.

$$Y = \frac{P_{ti} - P_{to}}{P_{ti} - P_o} \tag{1}$$

Frequently, the losses related to distinct phenomena are modeled separately and are then combined to result in a total loss. The form of how this division is made is not a consensus between different authors, but generally there are: *profile losses*, related to blade boundary layer, detachment, wake and shock waves; *clearance losses*, related to flow leakage over the tips of rotor blades and the hub clearance of stator blades; and *secondary losses*, related to secondary flow and to endwall boundary layer. The contribution of these components can vary from a turbomachinery to another, but in most machines each one contributes with a third part of the total loss.

The loss method of Ainley and Mathieson, 1952, is based on experimental data of turbines of the 1950s and was widely used since then. In this method it is assumed that the losses are not influenced by the flow Mach number and that exit flow angle is not influenced by the incidence angle. The total loss coefficient Y is calculated by Eq.(2), where Y_P

is related to profile losses; Y_T is related to clearance losses; Y_S is related to secondary losses and $f\left(t_{te}\right)$ is a function of trailing edge thickness.

$$Y = \left(Y_P + Y_S + Y_T\right) f\left(t_{te}\right) \tag{2}$$

The loss method of Kacker and Okapuu, 1982, is a modernization of the method of Ainley-Mathieson. The difference from de former is the structure of the loss system and the introduction of compressibility and shock waves influences (Wei, 2000). The total loss coefficient for this method is calculated by Eq.(3), where $f\left(Re\right)$ is a function of Reynolds number and the part of the profile losses related to wake is accounted by *trailing edge losses* Y_{te}.

$$Y = f\left(Re\right) Y_P + Y_S + Y_T + Y_{te} \tag{3}$$

The off-design performance simulation code, which includes these two methods, was used to predict the behavior of the designed turbine. Results provided by the design code, allied to geometrical data of the blade at mean diameter, were inserted into the performance code. The performance of the turbojet turbine was predicted for 14 operating points, seven for 100% and seven for 80% of the design speed N, varying outlet pressure.

4. CFD Simulation

The test case DLR cascade, presented in AGARD-AR-355 report (Dunham, 1998), was studied with purpose of familiarization with the problem of turbine cascade simulation and to evaluate the applied methodology. This cascade is an annular turbine stator with cylindrical hub and casing tested by the German Aerospace Research Center, DLR. Workgroup 26 from AGARD compared DLR's experimental data to several CFD simulations from different research groups. Flow data at cascade outlet were measured using a 5-hole probe and a 3D laser-two-focus (3D-L2F). The simulation done for the work here presented is more deeply described in Santin, 2006. Some of the results for circumferentially averaged values at cascade outlet are presented in Fig. (1).

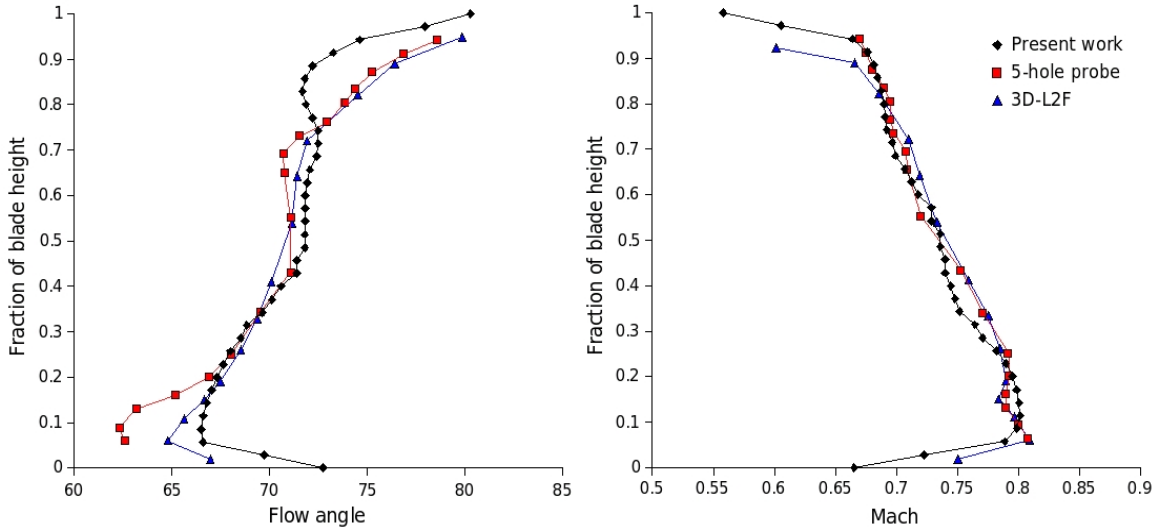

Figure 1: Circumferentially averaged values of cascade outlet flow angle and Mach number.

The CFD simulation methodology used in this work was chosen due to its feasibility on a personal computer. Aiming at the low computational cost, the turbine was simulated by the solution of RANS equations with Spalart-Allmaras turbulence model (Spalart and Allmaras, 1992), at steady state, using periodic boundary conditions and a mixing plane for the stator-rotor interaction.

The solver uses the finite volume method with second-order upwind scheme, is coupled, explicit, and uses one level of FAS (*Full-Approximation Storage*) multigrid to accelerate convergence (further details can be found in Fluent Inc., 2003).

The Spalart-Allmaras turbulence model is based on the Boussinesq hypotesis and uses one equation to solve the turbulent viscosity. As it includes only one more equation, it is seen as a low computational cost model. An analysis of the application of turbulence models to cascades is shown in Dunham, 1998. This model showed acceptable performance for obtainment of global parameters. It also showed good performance in regions of adverse pressure gradient (Menter, 2003). The turbulence model implemented in this solver does not account for the boundary layer transition (Fluent Inc., 2003), therefore in all operating points the flow was considered fully turbulent.

The turbine was simulated as a single channel of stator plus a single channel of rotor, supposing that flow properties in other channels of the row are similar. This consideration difficults the prediction of the real phenomenon, mainly in the

rotor, but should be sufficiently accurate for the construction of a performance map. The domain is then reduced to 1/31 for the stator and to 1/41 for the rotor, what reflects in a similar reduction of the computational cost .

The choice of steady state simulation neglects the unsteady phenomena related to stator-rotor interaction. These phenomena affect turbine performance, but it is supposed that time averaged properties are similar to that obtained in a steady simulation. By using the mixing plane model, total pressure, total temperature, turbulent viscosity and flow direction at stator outlet are circumferentially averaged and used as rotor inlet boundary condition. Similarly, static pressure at rotor inlet is circumferentially averaged and applied as stator outlet boundary condition.

Average Mach number of the studied cases is around 0.6 and usually assumes supersonic values at cascade outlet, evidencing the importance of the effects of compressibility. The density variation was obtained by using ideal gas model and the temperature distribution was determined by solving the energy equation.

A great part of the losses is due to the tip clearance of the rotor, however it was not considered and its influence on the turbine performance map will be evaluated in a future work.

The blade geometry is established by an in-house developed software capable of designing 3 and 5 arcs MCA profiles. A group of computational tools makes possible to generate and change reasonably easily the blade geometry and mesh. This automated procedure is obtained via scripts, which are read by ICEM CFD. This is a manner to reduce the turn-around time of this phase that is usually long. The details of the domain are presented in Fig. (2).

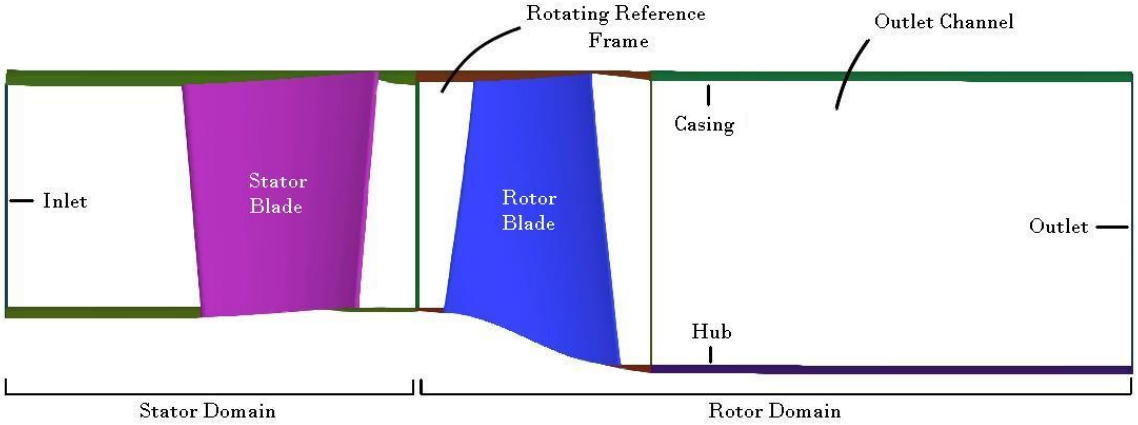

Figure 2: Computational domain used for the simulation of the turbine stage.

The mesh generated for this study presents 584,288 cells (276,830 in the stator, 196,230 in the rotor and 111,228 in the outlet channel) and is composed by 29 blocks (13 in the stator, 13 in the rotor e 3 in the outlet channel). Mesh quality was verified initially by its values of minimum angle of 28.2^o, minimum determinant of 0.52, maximum aspect ratio of 2.28 and minimum volume of 4,1$\cdot 10^{-12}$ m^3.

For solid surfaces, the boundary condition was set for null heat transfer and no slip. The fluid inside the rotor channel was set as a rotating reference frame and rotor blade and hub were set as moving walls (seen as static by the rotating frame). Outlet boundary condition was defined by setting the static pressure at hub and distributing along the height by Eq. (4) of radial equilibrium, where v_t is tangential flow velocity, ρ is density and r is radial position.

$$\frac{1}{\rho}\frac{dP}{dr} = \frac{v_t^2}{r} \tag{4}$$

The inlet boundary condition was defined with constant values of total pressure, total temperature, static pressure (for initial calculation) and turbulent intensity. The influence of the turbulent intensity is important, but depends on upstream information, unknown at this phase of the engine design. Therefore, a value of 5% was established based on the value used by Dunham, 1998. The settings for the inlet boundary condition was the following:

Total pressure:	472 kPa
Total temperature:	1123 K
Flow direction:	axial
Static pressure (initial):	440 kPa
Turbulence intensity:	5%
Hydraulic diameter:	0.0061 m

Fourteen cases were studied; seven for 100%N and seven for 80%N, changing the pressure at the outlet boundary condition (pressure at the hub). The operating points (OP) that were evaluated are presented in Tab. (1).

The inlet measuring plan (section 1) was positioned at a distance from the stator leading edge of 0.3 times its axial chord; while the outlet measuring plan (section 3) was positioned at a distance from the rotor trailing edge equal to 1.2 times its axial chord.

Table 1: Operating points simulated by CFD

OP	0	1	2	3	4	5	6	7	8	9	10	11	12	13
Pressure at Outlet (kPa)	120	180	220	250	280	320	360	120	180	220	250	280	320	360
Speed (rpm)	25,500 (100%N)							20,400 (80%N)						

The power W of the axial turbine was calculated from total enthalpy H_t drop in the flow along an adiabatic process by Eq. (5), where n_B is number of blades, v_a is axial velocity, A is cross section area, and the subscripts *I* and *O* indicate turbine inlet and outlet, respectively.

$$W = H_{tI} - H_{tO}\ , \quad \text{where} \quad H_t = n_B \int \rho v_a h_t dA \tag{5}$$

Turbine efficiency was calculated from the relation between real and ideal powers. The ideal power is given by the total enthalpy drop along an isentropic process. The temperature drop along this isentropic process for an ideal gas can be represented by the Eq. (6), where a_1, a_2, a_3 e a_4 are the constants of a specific heat polynomial variation with temperature of third order.

$$a_1\ ln\left(\frac{T_{tOs}}{T_{tI}}\right) + a_2\left(T_{tOs} - T_{tI}\right) + \frac{a_3}{2}\left(T_{tOs}^2 - T_{tI}^2\right) + \frac{a_4}{3}\left(T_{tOs}^3 - T_{tI}^3\right) - R\ ln\left(\frac{P_{tO}}{P_{tI}}\right) = 0 \tag{6}$$

Oulet isentropic total temperature T_{tOs} can be obtained numerically, based on mean properties at inlet and outlet. Therefore, outlet total enthalpy in an isentropic process is calculated by Eq. (7), where $\dot{m}$ is the mass flow.

$$H_{tOs} = \dot{m}\ h_{tOs}, \quad \text{where} \quad h_{tOs} = a_1\ T_{tOs} + \frac{a_2}{2}\ T_{tOs}^2 + \frac{a_3}{3}\ T_{tOs}^3 + \frac{a_4}{4}\ T_{tOs}^4 \tag{7}$$

5. Results and Discussions

The simulations demanded 770 MB of RAM and the average time per iteration was 24.7 s with an Intel Pentium 4 HT 2.4 GHz processor. The first case demanded 4300 iterations and the subsequent cases were obtained from this after 3000 more iterations each.

The convergence was detected by the stabilization of the mass flow. The difference between the inlet and the outlet mass flow was no more than 0.02% $\dot{m}$ (with oscillation of 0.05%) for the stator and no more than 0.01% $\dot{m}$ (with oscillation of 0.1%) for the rotor.

The average values of y^+ obtained with the simulation were no more than 64, and on most parts of the blade the values were close to the 50, which is adequate for the application of wall functions.

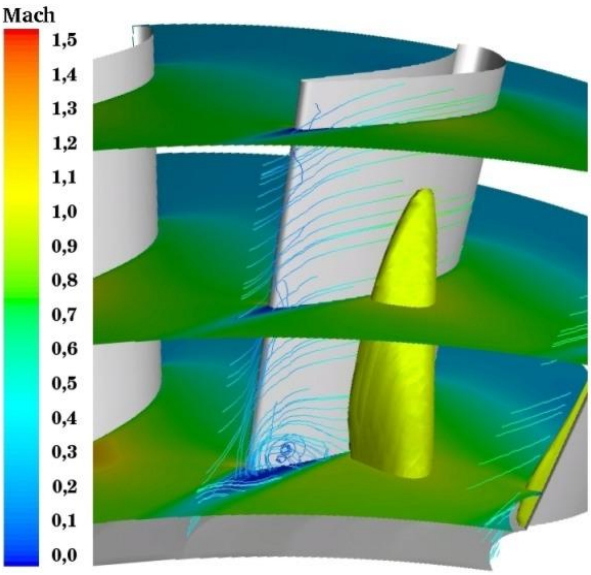

Figure 3: Mach distributions in the stator at OP 1.

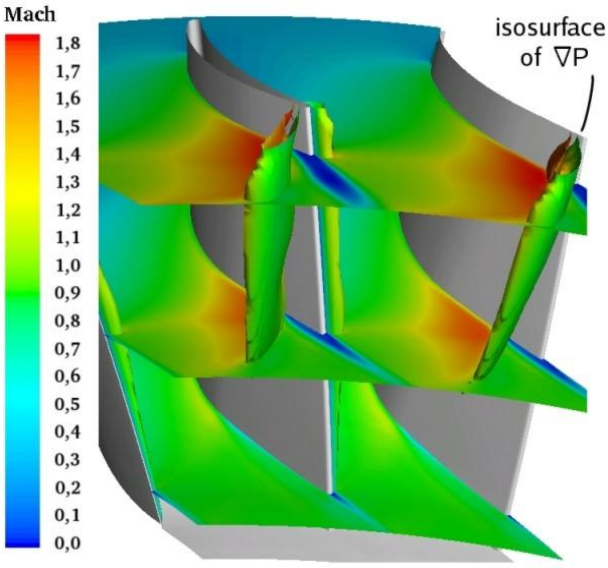

Figure 4: Mach distributions in the rotor at OP 1.

The main flow characteristics in the stator are shown in Fig. (3). The Mach number contours are shown on three surfaces along the blade height and on an isosurface of Mach equal to 1. There are also path lines originated close to the suction side of the blade. The main flow characteristics in the rotor are shown in Fig (4), with similar Mach number contour surfaces along the blade height and with an isosurface indicating high values of pressure gradient.

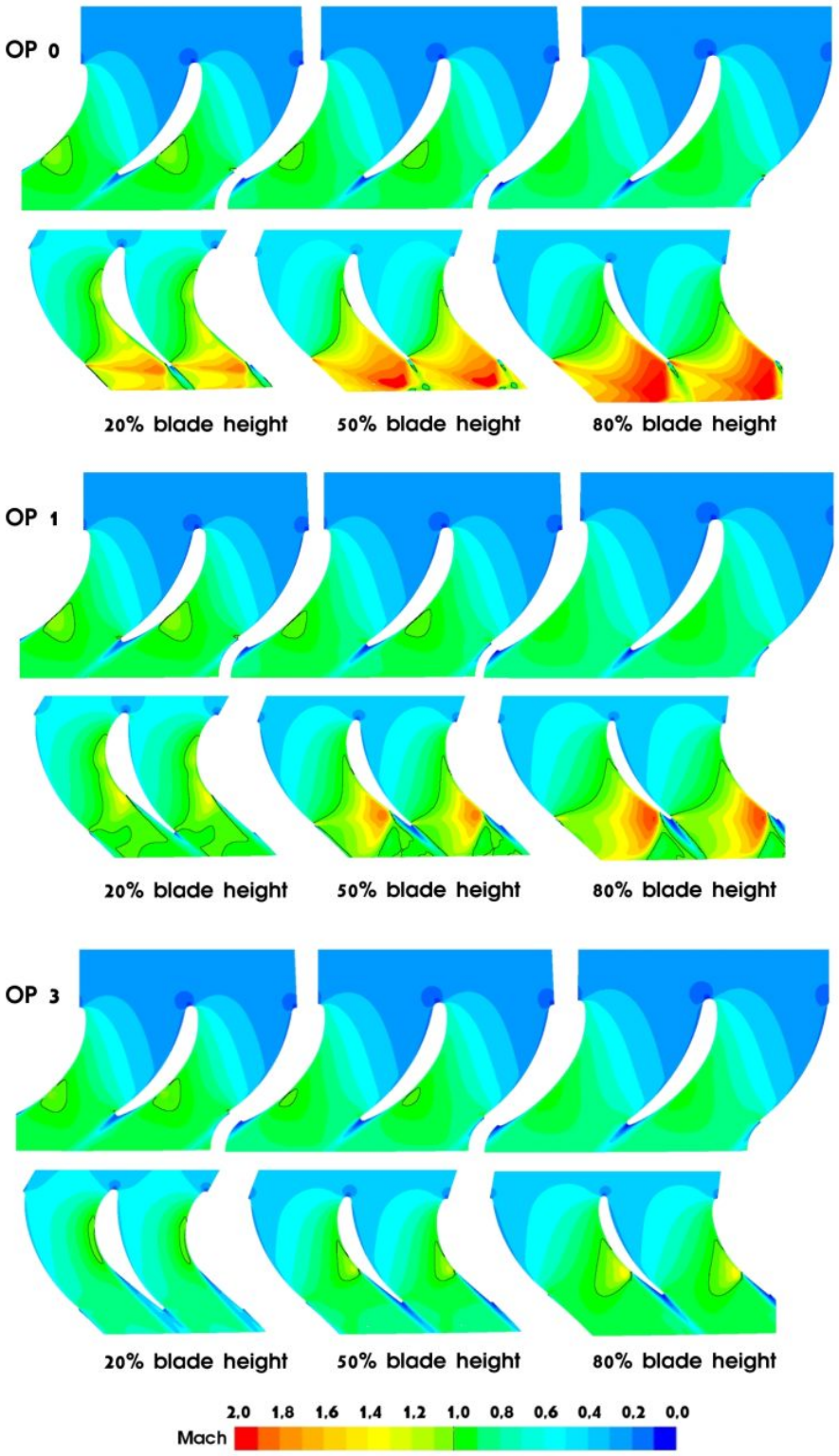

Figure 5: Contours of Mach on stator and relative Mach on rotor at OP 0, OP 1 and OP 3.

Figure (5) shows contours of Mach number on stator and relative Mach number on rotor at OP 0, OP 1 and OP 3. Rotor relative Mach numbers are much higher than stator absolute Mach numbers, which allows concluding that the stage choke initiates at rotor. From the point that the rotor is choked, the flow in stator stabilizes and alterations only occur at rotor outlet region.

At high expansion ratios, the fluid enters the stator at subsonic velocities, Mach around 0.3, and accelerate creating a supersonic region close to hub on the suction side rear portion that can reach Mach 1.2. On the corner between hub and suction side there is a region of boundary layer detachment. In this region, as can be seen in Fig. (6), occur an increase of static temperature, specific entropy and turbulent viscosity; occur a decrease of density and also a variation of radial velocity.

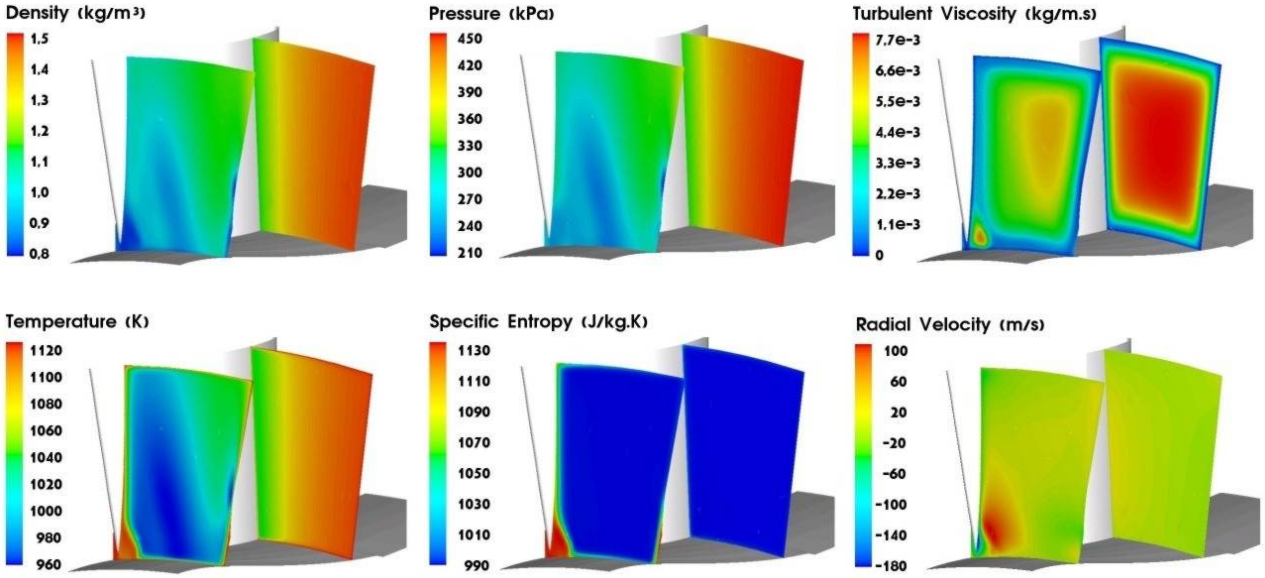

Figure 6: Rear view of the cross section contours in the stator at OP 1.

The flow enters the rotor at Mach numbers no more than 0.5 and reaches supersonic conditions in all operating conditions but those of lower expansion ratios. As the expansion ratio increases, the choke starts at tip and goes down the blade, as can be seen in Fig. (5). A shock wave arises at suction side and is followed by boundary layer detachment, caused by the adverse pressure gradient of the wave. The fluid from the hub goes up in this detachment region, leaving the blade in trailing edge vortices close the tip. As the expansion ratio increases, the shock wave moves toward the trailing edge of the suction side, reducing the detachment region. Fig. (7) illustrates wake and vortex formation at rotor trailing edge, indicated by regions of high static temperature, specific entropy and turbulent viscosity.

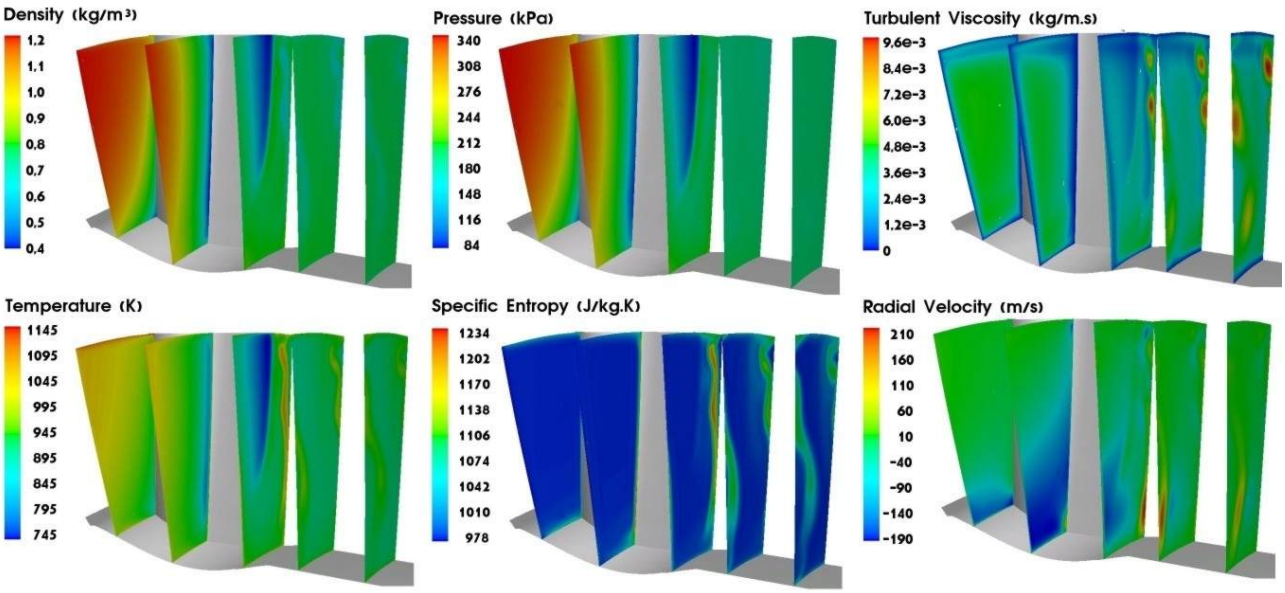

Figure 7: Rear view of the cross section contours in the rotor at OP 1.

Circumferentially averaged values of stator inlet angle and rotor inlet and outlet relative angles are shown in Fig. (8). The results indicate that stator flow deviation is approximately constant (around 10^o) along the upper half of the blade, increasing on the bottom half due to boundary layer detachment on the trailing edge. Close to the tip, it is possible to

notice a decrease of deviation, probably related to the endwall boundary layer. The incidence is bellow 5^o on a great portion of the blade height, achieving the design expectation. Due to relative motion, as mass flow decreases, incidence decreases; and as rotational speed decreases, incidence increases. The influence of the stator detachment can be clearly noticed on the bottom portion of the rotor leading edge, as it causes negative angles of incidence. Rotor flow deviation at mean height is around 8^o, but can reach 15^o in some regions. The deviation is high on tip due to the endwall boundary layer that is stationary in the absolute reference frame. At root there is a strong secondary flow from pressure side to suction side, resulting in high angle values.

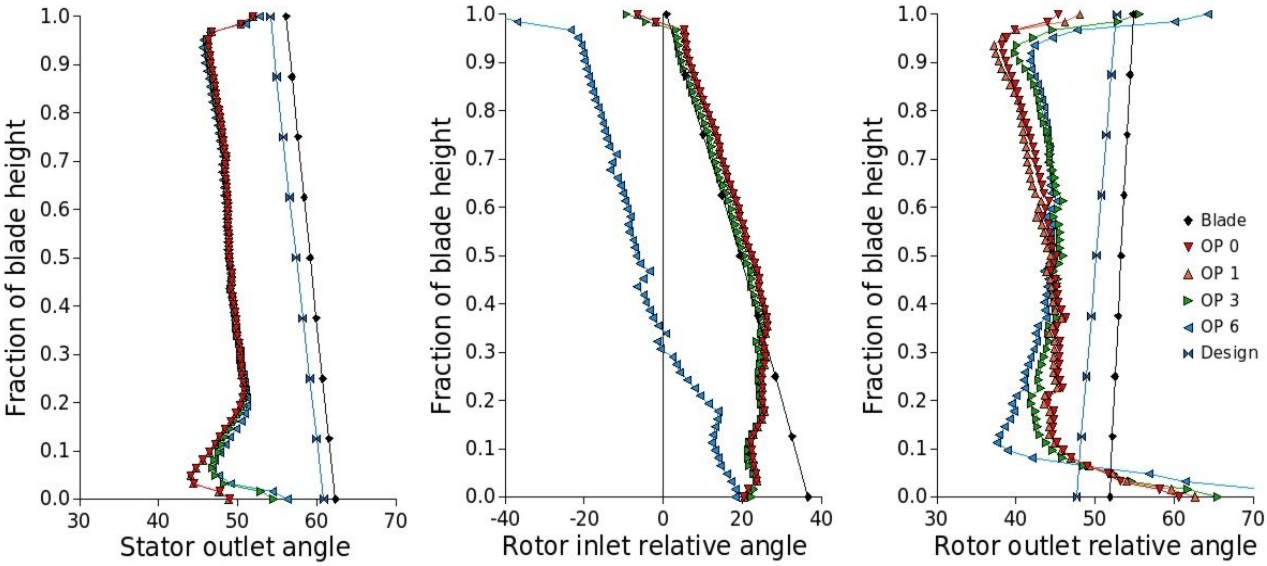

Figure 8: Circumferentially averaged values of stator inlet angle and rotor inlet and outlet relative angles.

Total enthalpy development along the axial length is shown in Fig. (9) for several operating points. From the first law of thermodynamics, total enthalpy must remain constant in adiabatic processes without work transference and must decrease when work leaves the control volume. The data show that there are small oscillations along the domain, probably due to numerical uncertainties. In a region just after the rotor, these oscillations become noticeable, mainly at OP 0. This effect can be related to the high gradients associated to the shock waves that can produce errors due to poor refinement. At OP 6, total enthalpy is increased close to rotor leading edge, what is probably caused by the poor flow incidence, as was shown in Fig. (8). There is a small leap of total enthalpy when crossing the mixing plane, caused by uncertainty on passing flow informations from one domain to other.

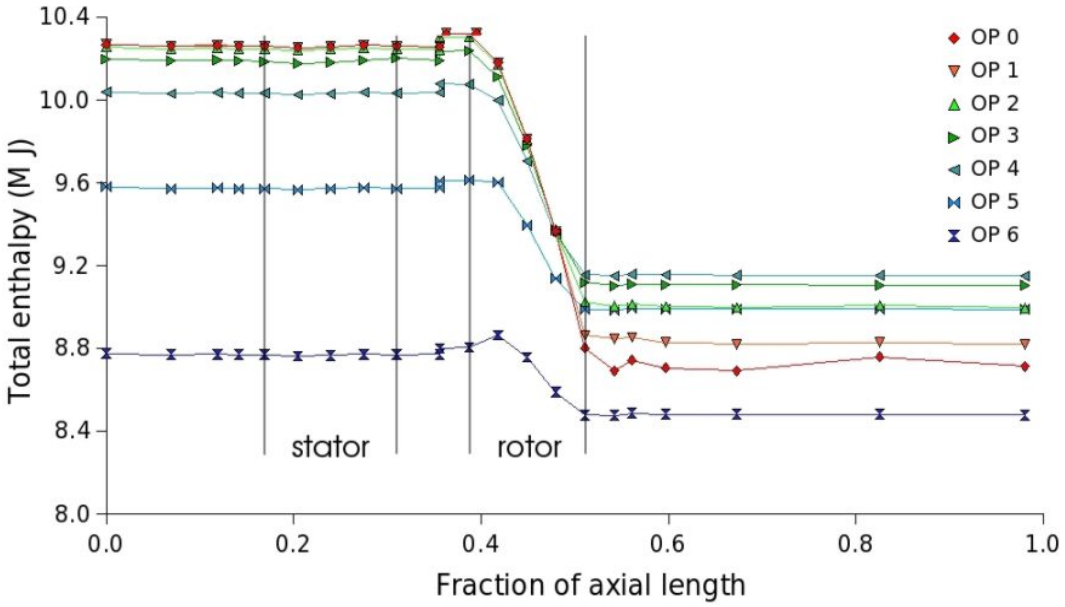

Figure 9: Total enthalpy along the axial length.

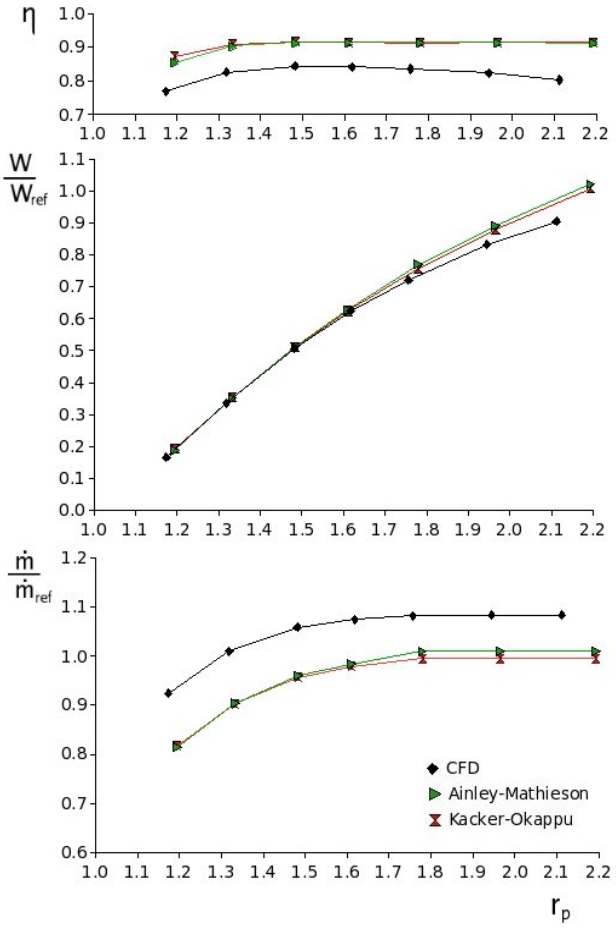

Figure 10: Performance map of the turbine for 100% N.

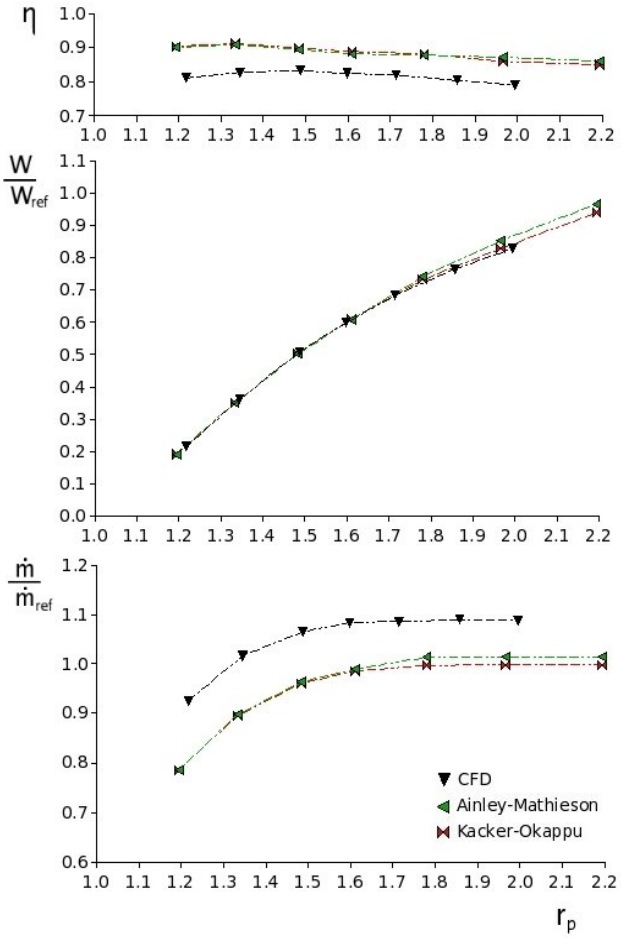

Figure 11: Performance map of the turbine for 80% N.

The performance maps obtained by CFD simulation and by using the mean line methodology are presented in Fig. (10) and Fig. (11), for 100% and 80% of the design speed, where η is efficiency. Non-dimensional power and mass flow were obtained by dividing the calculated values by the design values of power W_{ref} and mass flow $\dot{m}_{ref}$. The choking was established when the mass flow variation was reduced below 0.5%$\dot{m}$. The results of the CFD simulation indicate agreement with the results obtained by using the mean line methodology concerning the expansion ratio that occurs choking.

At choke region, the mass flow obtained by CFD was 8.3% grater than the design mass flow for 100%N and 8.7% grater for 80%N, what is probably caused by the error of mean density estimation in the area calculation of the mean line design approach.

The efficiency predicted by CFD is noticeably lower than that obtained by using the loss correlations of Ainley-Mathieson and Kacker-Okapuu. At an expansion ratio of 2, for 100%N, the differences in efficiency were in order of 10%.

The power predicted by CFD also is lower than the obtained by using the loss correlations; however the differences are not as great as those of the efficiency due to the greater mass flow of the CFD simulations.

By using Eq. (8) from Kacker and Okapuu, 1982, the efficiency reduction due to the presence of a tip clearance can be calculated. The parameter h_B is blade height and k is tip clearance. Supposing a tip clearance of 1mm, the efficiency would be reduced by 0.045.

$$\Delta\eta = 0,93 \left(\frac{r_{tip}}{r_{mean}}\right) \left(\frac{\Delta k}{h_B cos\alpha_s}\right) \eta_{(k=0)} \tag{8}$$

6. Concluding Remarks

A commercial CFD software was employed on the analysis of the flow in an axial turbine for a gas turbine engine. The performance maps of the turbine were generated and compared to the maps generated by using a mean line methodology for performance prediction that uses the loss correlations of Ainley-Mathieson and Kacker Okapuu.

The test case *DLR Cascade* of AGARD AR-355 report was simulated to familiarize with the study of flows in turbine cascades and to evaluate the methodology employed. The results indicate a good representation of the physical phenom-

enon that was measured. In global terms, the values of the properties agree with the measurements, even if there are some local discrepancies.

The CFD simulation of the axial turbine indicates that the mass flow calculated by the mean line methodology was underestimated. By the use of the Ainley-Mathieson and Kacker-Okapuu correlations, the mean line methodology lead to overestimate power and efficiency.

The softwares for design and performance prediction of axial flow turbines are essential tools for its preliminary design, even if these methodologies present the deficiencies of a zero-dimensional modeling. At this initial phase, the design must be redone hundreds or thousands of times, evidencing the necessity for simpler models. The employment of the CFD simulations is interesting at a second design phase, in which the redesign times are larger, giving good quantitative informations of the flow field and indicating regions where the loss generation is undesirably high. To seek the improvement of the precision of the preliminary design tools is important to avoid the usage of CFD simulations to correct global problems of the design.

7. Acknowledgements

The authors thank CAPES (*Coordenação de Aperfeiçoamento de Pessoal de Nível Superior*) for the support to the research on gas turbine, developed at the *Centro de Referência em Turbinas a Gás* with support of ANEEL projects. Thanks also to Genival Sena de Jesus for the assistance with the design and performance softwares.

8. References

Ainley, D. G. and Mathieson, G. C. R., 1952, A Method of Performance Estimation for Axial-Flow Turbines, Technical Report R.111, NTGE.

Bringhenti, C., 2003, "Variable Geometry Gas Turbine Performance Analysis", Ph. d., Instituto Tecnológico de Aeronáutica, São José dos Campos.

Cumpsty, N. A. and Greitzer, E. M., 2004, Ideas and methods of turbomachinery aerodynamics: a historical view, "Journal of Propulsion and Power".

Denton, J. D., 1993, Loss Mechanisms in Turbomachines, "The 1993 IGTI Scholar Lecture".

Dunham, J., 1998, CFD Validation for Propulsion System Components, Technical Report AR-355, AGARD.

Fluent Inc., 2003, FLUENT 6.1 User's Guide.

Hirsch, C. and Demeulenaere, A., 2003, State of the art in the industrial CFD for turbomachinery flows, "QNET-CFD Network Newsletter".

Jesus, G. S., 2003, Projeto e Análise de Desempenho de Turbinas Axiais de Vários Estágios com Geometria Variável, M. sc., Instituto Tecnológico de Aeronáutica, São José dos Campos.

Kacker, S. C. and Okapuu, U., 1982, A Mean Line Prediction Method for Axial Flow Turbine Efficiency, "Journal of Engineering for Power".

Langston, L. S., 2006, Wild Blue Yonder, "Mechanical Engineering, Focus on Power and Energy", Vol. 128, No. 5.

Mattingly, J. D., 1996, "Elements of Gas Turbine Propulsion", McGraw-Hill.

Menter, F. R., 2003, Turbulence Modelling for Turbomachinery, "QNET-CFD Network Newsletter".

Santin, M. A. B., 2006, Simulação Numérica de Escoamento em Turbinas Axiais de Alto Desempenho, M. sc., Instituto Tecnológico de Aeronáutica, São José dos Campos.

Saravanamuttoo, H. I. H., Rogers, G. F. C., and Cohen, H., 2001, "Gas Turbine Theory", Prentice Hall, 5 edition.

Spalart, P. R. and Allmaras, S. R., 1992, A One-Equation Turbulence Model for Aerodynamic Flows, "AIAA - 30th Aerospace Sciences Meeting and Exhibit", AIAA-92-0439.

Wei, N., 2000, "Significance of Loss Models in Aerothermodynamic Simulation for Axial Turbines", PhD thesis, Royal Institute of Technology.

Wilson, D. G. and Korakianitis, T., 1998, "The design of high-efficiency turbomachinery and gas turbines", Prentice-Hall, EUA, 2 edition.

Proceedings of the 11th Brazilian Congress of Thermal Sciences and Engineering – ENCIT 2006
Braz. Soc. of Mechanical Sciences and Engineering – ABCM, Curitiba, Brazil, Dec. 5-8, 2006

Paper CIT06-0432

Numerical Solution of 2-Dimensional Linearized Euler Equations for Acoustic Waves in Flow

Leandro Dantas de Santana
SMM – EESC – USP Av. Trabalhador Sancarlense, 400, CEP:13566-590 São Carlos - SP
dantas@sc.usp.br

Leandro Franco de Souza
SME – ICMC – USP Av. Trabalhador Sancarlense, 400, CEP:13560-970 São Carlos - SP
lefraso@icmc.usp.br

Abstract. *Aeroacoutics is a relatively new area of study derived from Mechanic of Fluids. Its study had made fantastic advances on the last fifteen years. The noise levels requirements for certificating an aircraft are gradually more restrictive and the study in this area is increasing. This industrial need, brought attention of academic community to this field. In this way this paper shows a review and comparison of the most used optimized finite difference with a 4th order Runge-Kutta scheme. A new finite difference scheme, based on spectral optimization is proposed. A 2-dimensional linearized Euler code is verified. For verification a benchmark case of a Gaussian pulse propagation was performed. As boundary conditions the non-reflective Perfectly Matched Layer (PML) zone is implemented and analyzed. The results shows that the proposed finite difference scheme gives better results in 1D propagation than in 2D propagation. The analysis of the PML zone shows that the reflections are very small.*

keywords: *Computational Aeroacoustics, Linearized Euler equations, Low dispersion, Low dissipation, Perfectly Matched Layer*

1. Introduction

The actual concern with environmental problems caused by noise generation in regions near airports imposed more restrictives environmental laws. These restrictions are the more severe noise criteria for certification of aircrafts. There are estimates that, if the Brazilian aircraft industry keeps its actual state of technology, in the next 15 years the most of the Brazilians airplanes will not be able to operate in the most important Europe and USA airports.

Computational Aeroacoustics (CAA) is the area that studies the noise generated aerodynamically. The most common approach of CAA is to divide the problem on two secondary problems. The first one, concerns on simulating the airflow using traditional CFD techniques: RANS, DNS, LES, etc. The second problem is to study the acoustic field for a given airflow. in this problem the viscosity effects are non considered and the Navier-Stokes equations are rewritten in a wave form.

The first research in the area of aeroacoustics began with two seminal papers of Sir James Lighthill, 1952; Lighthill, 1954. Lighthill focus was on find sources of sound in turbulent flows. This was achieved by an acoustic analogy. The basic idea of this approach is to consider the viscosity terms negligible and rewrite the Navier-Stokes equations on the form of compressible Euler's equations. At this way the left-hand side consisted of a second-order wave-equation, representing the sound propagation. All other terms were moved to the right hand side and were considered sources. The resulting wave equation, for the density ρ, is:

$$\frac{\partial^2 \rho}{\partial t^2} + c_0^2 \frac{\rho}{\partial x_j \partial x_j} = \frac{\partial T_{ij}}{\partial x_i \partial x_j}, \tag{1}$$

where c_0 is the ambient sound speed and $T_{ij} = \rho v_i v_j + (p - \rho c_0^2)\delta_{ij} - \tau_{ij}$ is the Lighthill stress tensor, and v_i, p, τ_{ij} and δ_{ij} are the velocity, pressure, viscous stress tensor and Kronecker delta, respectively.

An extension of Lighthill's acoustic analogy, to incorporate the effect of solid surfaces was published by Curle, 1955 and generalized by Williams, 1963. The effect of convection on directivity was introduced by Williams, 1969. From the middle sixties to the early nineties all aeroacoustics development were theoretical. On nineties Tam and Webb, 1993 published an optimized finite difference scheme and simulated linearized Euler Equations submitted to a Gaussian pulse on pressure and density fields and re-stated the aeroacoustic study.

One of the most significant difficulties of aeroacoustic solutions is to represent correctly the aeroacoustic quantities. Normally these quantities are so small when compared with fluid dynamic quantities that for

traditional CFD codes the acoustic effects could be neglected. To transport correctly the aeroacoustic quantities, the Navier-Stokes equations can be simplified. The first simplification is to neglect the viscosity terms, since the Reynolds numbers given by:

$$Re_\lambda \approx \frac{|\rho\frac{\partial u'}{\partial t}|}{|\mu\frac{\partial^2 u'}{\partial x^2}|} \approx \frac{\lambda^2 f}{\mu/\rho}, \tag{2}$$

for these cases are very large. Here λ is the wave length, f is the frequency and μ/ρ is the kinematic viscosity. For a typical problem of sound propagation in air these parameters are:

- $\nu = \mu/\rho = 1.4 \times 10^{-5} m^2/s$;
- $f = 1kHz$;
- $c_0 = 340m/s$;
- $\lambda = c_0/f = 34.4m$ and

these values leads to a typical Reynolds number of aeroacoustic problems of $Re_\lambda = 1 \times 10^7$. Using the fact that the Reynolds number is so high, the viscosity terms are very small when compared with dynamic terms, that the viscosity terms can be neglected. This simplification leads to the Euler equations. The second simplification adopted here is the linearization of the Euler equations. This simplification can be done without loss of physical behavior, since the amplitude of the disturbances are very small.

The present paper study the numerical propagation of a 1D and 2D waves. The equations adopted for these verifications are the 1D hyperbolic equation and 2D Linearized Euler Equations (LEE). The discretizations are done by Optimized Finite Difference schemes (Tam and Webb, 1993; Bogey and Bailly, 2004) and a proposed Spectral Optimized SO finite difference scheme. A 4th order 4 steps Runge-Kutta scheme was adopted for time integration. Effects of reflections at the boundaries are tested with Perfectly Matched Layer (PML) zone.

The work is divided as follows: the first section shows formulation used; the finite-difference schemes, the time integration scheme and the PML zone are shown in the second section; the third section shows the Numerical results and the last section shows the conclusions of the present study.

2. Formulation

This section was divided in two subsections: 1D transport equation and 2D transport equation. Both formulations were used in the current study. The details of each formulation is given bellow.

2.1. 1D transport equation

To analyze one dimensional characteristics of finite difference schemes a wave transport, the 1D hyperbolic equation used was:

$$\frac{\partial f}{\partial t} + \frac{\partial f}{\partial x} = 0, \tag{3}$$

where the initial condition adopted was:

$$f(x, t = 0) = \sin\left(\frac{2\pi x}{30}\right) \qquad \text{for} \qquad 10 \leq x \leq 30, \tag{4}$$

for $x < 10$ and $x > 30$ the value of $f(x, t = 0) = 0$ was settled.

2.2. 2D transport equation

The high Reynolds number of acoustic terms suggest that viscous terms are negligible when compared with others terms. Another important fact to be considered is that the order of the terms related to acoustic propagation is very small when compared with the order of the terms of the fluid dynamic motion. This leads to a linearization on full Euler equations. Colonius *et al.*, 1993 shows that this approach solves the problem, with a smaller computational cost, without loosing the quality of the numerical solution.

A way to improve the generality of the computational code simulation is to implement the non-dimensional form of LEE. To perform this we introduce the non-dimensional scales: Length scales $= \Delta x = \Delta y$, Velocity scales $= c_0$, Time scales $= \Delta x/c_0$, Density scales $= \rho_0$, Pressure scales $= \rho_0 c_0^2$, where $\Delta x = \Delta y$ are the distance between two consecutive points in the x and y directions, respectively, and c_0 is the sound velocity given by $c_0 = \sqrt{\gamma p_0/\rho_0}$. Using these parameters, the non-dimensional LEE can be written as:

$$\frac{\partial \mathbf{u}}{\partial t} + \mathbf{A}\frac{\partial \mathbf{u}}{\partial x} + \mathbf{B}\frac{\partial \mathbf{u}}{\partial y} = \mathbf{H}^*, \tag{5}$$

where $\mathbf{H}^*$ is the non-dimensional source term, and

$$\mathbf{u} = \begin{pmatrix} \rho' \\ u' \\ v' \\ p' \end{pmatrix}, \qquad \mathbf{A} = \begin{pmatrix} M & 1 & 0 & 0 \\ 0 & M & 0 & 1 \\ 0 & 0 & M & 0 \\ 0 & 1 & 0 & M \end{pmatrix}, \qquad \mathbf{B} = \begin{pmatrix} 0 & 0 & 1 & 0 \\ 0 & 0 & 0 & 0 \\ 0 & 0 & 0 & 1 \\ 0 & 0 & 1 & 0 \end{pmatrix}, \tag{6}$$

are the respectively matrices, that are used for computational simulation for next sections.

2.2.1. The analytical solution for LEE

This subsection presents the exact solution of the test case of a Gaussian pulse on density and pressure fields used at the present paper. This solution is used on future section to analyze characteristics of the finite difference schemes.

Tam and Webb, 1993 presents the analytical solution, based on Green function presented by Williams, 1969, for the LEE on a Cartesian grid with constant mesh size when the initial condition is a Gaussian pulse on pressure and density field. This initial condition is defined as:

$$\begin{aligned} t &= 0, \\ p &= \rho = \epsilon_1 e^{-\alpha_1 r^2}, \\ u &= 0, \\ v &= 0, \end{aligned} \tag{7}$$

and the boundary conditions are:

$$\begin{aligned} \text{at} \quad x = X_{max}, \quad y = Y_{min} \quad \text{and} \quad y = Y_{max} \quad &: \quad p = 0, \\ \text{at inflow} \quad x = X_{min} \quad &: \quad p = \rho = v = 0, \end{aligned} \tag{8}$$

applying these physical boundary conditions, one could reach the exact solution for the velocity components (u and v) and the pressure and density field (p, ρ) as:

$$u(x,y,t) = \frac{\epsilon_1 (x - Mt)}{2\alpha_1 \eta} \int_0^\infty e^{-\xi^2/4\alpha_1} \sin(\xi t) J_1(\xi\eta) \xi d\xi, \tag{9}$$

$$v(x,y,t) = \frac{\epsilon_1 y}{2\alpha_1 \eta} \int_0^\infty e^{-\xi^2/4\alpha_1} \sin(\xi t) J_1(\xi\eta) \xi d\xi, \tag{10}$$

$$p(x,y,t) = \rho = \frac{\epsilon_1}{2\alpha_1} \int_0^\infty e^{-\xi^2/4\alpha_1} \cos(\xi t) J_0(\xi\eta) d\xi, \tag{11}$$

where $\eta = [(x - Mt)^2 + y^2]^{1/2}$, J_0 e J_1, and J_0 and J_1 are respectively, the Bessel functions of first kind and zeroth and first order, respectively.

3. Numerical method

In the present section the optimized finite difference schemes, the time integration method and the PML zone are shown. The equations adopted here (1D Hyperbolic equation and LEE) needs only the evaluation of first order derivatives, and the current paper concerns only the finite difference schemes that treat these derivatives. There are two main kinds of finite difference schemes: explicit schemes and implicit ones. The implicit schemes uses smaller stencils when compared with explicit ones, for the same truncation error, with the drawback to obtain the inverse of a coefficient matrix. Explicit schemes, otherwise, needs greater stencils. This can be a problem near boundaries, but as will be shown in a future section, the application of PML zone reduces the importance of the non-centered finite difference technique.

In present section, the first subsection presents a general presentation of finite difference schemes, and its first subsection presents the DRP and FDo finite difference schemes, the next one presents the proposed SO finite difference scheme. The next subsection presents the Runge-Kutta scheme adopted. The last subsection shows the details of the PML zone.

3.1. Finite difference schemes

The standard approach finite difference method evaluates the spatial derivative of a function in a uniform grid points equally spaced by Δx using the following approximation, for a symmetric (2N+1)-point stencil, one can write:

$$\frac{\partial f}{\partial x}(x) \simeq \sum_{j=-N}^{N} a_j f(x + j\Delta x) \tag{12}$$

where a_j are the weight coefficients, defined for a given finite difference method. To reach great orders one could find greater stencils. Tam, 1995 shows that traditional finite difference schemes are not the better approximation for aeroacoustics derivatives calculations. The following section shows two optimized finite difference schemes presented in literature.

3.1.1. DRP and FDo finite difference schemes

Tam and Webb, 1993 shows that the improvement of formal order on finite difference scheme is not as important as its spectral characteristics. Looking for better characteristics for their finite difference schemes, Tam and Webb, 1993 applied the Fourier transform to Eq. 12 and minimized the spectral absolute error in the range of $0 \leq \pi/2$. By doing that they obtained optimized schemes called Dispersion-Relation-Preserving (DRP) finite difference method.

Bogey and Bailly, 2004 present an improvement to DRP method. They show that a better way to obtain the finite difference coefficients is not to minimize the absolute error, but to minimize the relative absolute error. They adopted the range $\pi/16 \leq \pi/2$, for schemes of 9 and 11 points and $\pi/16 \leq 3\pi/5$ for schemes of 13 points. Their proposed scheme was called Finite Difference Optimized (FDo). Tab. 1 presents the coefficients of this both methods.

Table 1: Coefficients for finite difference schemes, where $a_0 = 0$ and $a_j = -a_{-j}$.

Coef.	DRP	FDo9p	FDo11p	FDo13p
a_1	0.79926643	0.8415701254	0.8727569939	0.9076465913
a_2	-0.18941314	-0.2446786317	-0.2865111739	-0.3370483932
a_3	0.02651995	0.0594635847	0.0903200012	0.1334428853
a_4		-0.0076509040	-0.0207794058	-0.0452464802
a_5			0.0024845946	0.0111692941
a_6				-0.0014565017

3.1.2. Spectral Optimized finite difference scheme

A new finite difference scheme is proposed in the current work. It is based on Spectral Optimization (SO). This method is based on Lele, 1992 technique of optimization for compact schemes, and was adapted here to optimize explicit finite difference methods.

Differently from Tam and Webb, 1993 and Bogey and Bailly, 2004, the technique does not try to optimize an objective function. It is defined a family of straight forward constraints that defines the formal order of the scheme, and find a some points on spectrum where the relation $k'\Delta x = k\Delta x$ results in a good spectral characteristics.

Using this approach, the $k'\Delta x = k\Delta x$ condition, for centered explicit schemes with $2N + 1$ stencil points can be rewritten as:

$$k = 2 \times \sum_{j=0}^{M} a_j \sin(jk), \tag{13}$$

to best representative the condition presented in Eq. (13) and the constraint condition the following matrix

form is presented:

$$\begin{pmatrix} \sin m & \sin 2\times m & \cdots & \sin k\times m \\ \sin n & \sin 2\times n & \cdots & \sin k\times n \\ \vdots & \vdots & \ddots & \vdots \\ \sin z & \sin 2\times z & \cdots & \sin k\times z \\ CCtt_1 1 & CCtt_1 2 & \cdots & CCtt_1 k \\ \vdots & \vdots & \ddots & \vdots \\ CCtt_k 1 & CCtt_k 2 & \cdots & CCtt_k k \end{pmatrix} \times \begin{pmatrix} a_1 \\ a_2 \\ \vdots \\ a_j \\ a_l \\ \vdots \\ a_k \end{pmatrix} = \begin{pmatrix} m \\ n \\ \vdots \\ z \\ 0 \\ \vdots \\ 0 \end{pmatrix}, \tag{14}$$

where $m, n, \ldots, z$ are points conveniently choose on spectrum where the relation $k'\Delta x = k\Delta x$ is valid. $CCtt_u v$ are the coefficient of the constraint condition and a_j are the finite difference coefficients.

To define a sixth order finite difference scheme with 11 stencil points the values of m, n, p, q and r adopted are:

$$\begin{aligned} m = 0.2\pi, \quad n = 0.35\pi, \quad p = 0.45\pi, \\ q = 0.5\pi, \quad r = 0.6\pi, \end{aligned} \tag{15}$$

applying this method, the sixth order SO coefficients are:

$$\begin{aligned} a(1) = 0.89862767688255, \quad a(2) = -0.32385996447943, \quad a(3) = 0.12047995924059, \\ a(4) = -0.03334363299405, \quad a(5) = 0.00458628520861. \end{aligned} \tag{16}$$

3.2. Runge-Kutta scheme

Runge-Kutta schemes are by far the most commonly used scheme for time integration on computational aeroacoustics. The time evolution equation can be written as:

$$\frac{\partial \mathbf{U}}{\partial t} = F(\mathbf{U}), \tag{17}$$

where $\mathbf{U}$ represents the vector containing the solution values of the spatial functions and finite difference derivatives. An explicit low-storage *p-stage* Runge-Kutta scheme advance the solution from time level t_n to $t_n + \Delta t$ in the form:

$$\begin{aligned} u^0 &= u^n, \\ u^l &= u^n + \alpha_l \Delta t F(u^{u^{l-1}}) \quad \text{for l=1,..,p,} \\ u^{n+1} &= u^p. \end{aligned} \tag{18}$$

To analyze and compare the effect of the accouplement of the Runge-Kutta scheme with the finite difference scheme the Figs. 1 and 2 presents the modulus of the amplification factor of the 4^{th}-order Runge-Kutta scheme, for the DRP and SO finite difference schemes, respectively. Comparing the the Figs. 1 one can note that for

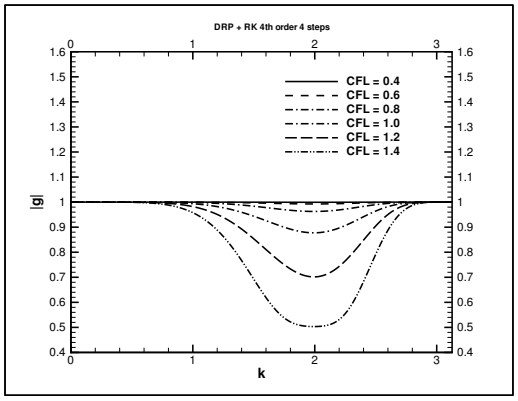

Figure 1: Dissipation factor of a RK 4^{th}-order with DRP method.

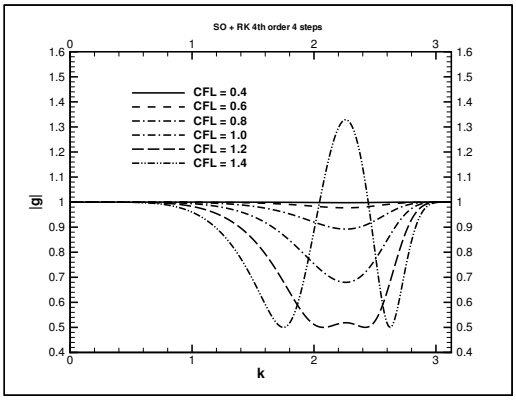

Figure 2: Dissipation factor of a RK 4^{th}-order with SO method.

small wave-number the two schemes gives similar answers. As the CFL number increases some dissipation is noted. DRP scheme is dissipative but stable for all wave-numbers and CFL numbers on the range analyzed, and SO scheme can be unstable for CFL > 1.3.

3.3. Numerical treatment of the boundaries

Nowadays one of the most relevant topic of discussion on computational aeroacoustics is the correct used of numerical schemes at and near the boundaries of the computational domain. A good numerical scheme on the boundary should be able to absorb all disturbances (far-field boundary condition) without any reflection to the interior of the domain. There are several schemes on literature, one scheme that seems to be the best of them is presented by Hu, 2001. This scheme applies a dumping zone near the boundary of the computational domain. The main advantage of this technique when compared with others is that this approach do not need stretching on the mesh near the boundary and its computational cost is not so high. The equation for this scheme is:

$$\frac{\partial \mathbf{u}}{\partial t} + \mathbf{A}\frac{\partial \mathbf{u}}{\partial x} + \mathbf{B}\frac{\partial \mathbf{u}}{\partial y} + \sigma_y \mathbf{A}\frac{\partial \mathbf{q}}{\partial x} + \sigma_x \mathbf{B}\frac{\partial \mathbf{q}}{\partial y} + (\sigma_x + \sigma_y)\mathbf{u} + \\ + \sigma_x \sigma_y \mathbf{q} + \frac{\sigma_x M}{1 - M^2}\mathbf{A}(\mathbf{u} - \sigma_y \mathbf{q}) = 0, \tag{19}$$

where σ_x and σ_y are dumping factors in the x and y directions, respectively, and $\mathbf{q}$ is a vector of auxiliary variables. Analyzing the Eq. 19 one could note that if $\sigma_x = \sigma_y = 0$ we go back to equation to LEE on its non dimensional for (Eq. 5). Hu, 2001 defines the dumping factors as:

$$\sigma_x = \sigma_m (1 - M^2) |\frac{x - x_l}{D}|^\beta, \quad \sigma_y = \sigma_m |\frac{y - y_l}{D}|^\beta, \tag{20}$$

where x_l and y_l represents the set of points where the PML zones starts and D is the length of the PML zone. Completing the procedure, one could note that in the horizontal region of PML zone $\sigma_x = 0$ and for the vertical region of PML zone $\sigma_y = 0$. Leading to some simplifications on PML equations represented respectively by:

$$\frac{\partial \mathbf{u}}{\partial t} + \mathbf{A}\frac{\partial \mathbf{u}}{\partial x} + \mathbf{B}\frac{\partial \mathbf{u}}{\partial y} + \sigma_x \mathbf{B}\frac{\partial \mathbf{q}}{\partial y} + \sigma_x \mathbf{u} + \frac{\sigma_x M}{1 - M^2}\mathbf{A}\mathbf{u} = 0, \tag{21}$$

$$\frac{\partial \mathbf{u}}{\partial t} + \mathbf{A}\frac{\partial \mathbf{u}}{\partial x} + \mathbf{B}\frac{\partial \mathbf{u}}{\partial y} + \sigma_y \mathbf{A}\frac{\partial \mathbf{q}}{\partial x} + \sigma_y \mathbf{u} = 0. \tag{22}$$

Hu, 1996 shows that the choice of the parameters σ_m and β have to be according to the length of the computational domain. He also shows that, for a uniform square mesh with a minimal dimension of 201 x 201 grid points on domain, the parameters $\sigma_m \Delta x = 2$ and $\beta = 2$ should be adopted and give good results.

4. Numerical Results

This section presents results of the 1D and 2D wave propagation comparing the DRP, FDo and SO finite difference schemes. The first subsection uses the 1D hyperbolic equation and verify the error with different finite difference schemes. The second subsection presents the effect of the finite difference scheme along the time. The next subsection compare the finite difference schemes effect for a given instant on time comparing the pulse shape. The following section presents the effect of PML on numerical results.

4.1. Analysis and results for finite difference schemes

To analyze the performance of finite difference schemes, its spectrum is analyzed. With the spectrum analysis, the family of wave number where there is transport without significant dispersion can be seen. The region where, the modified wavenumber of a finite difference scheme gives the same value of the wave number, is free of dispersion error. Since only centered schemes are evaluated no dissipation is introduced via finite difference schemes. The spectrum of the schemes and their dispersion error are shown in Figs. 3 and 4, respectively. Observing Figs. 3 and 4 one can note that SO scheme of 11-stencil-points presents almost the same spectral quality of the FDo13p (scheme with 13-stencil-points). Comparing the dispersion error versus number of points-per-wave one can note that for a small number of points-per-wave, says 5, the SO scheme presents a small dispersion error when compared with other schemes showed in present work.

All calculations where carried out, using the formula and the initial conditions given in subsection 2.1. 400 steps were integrated in time, on a non-dimensional domain with length 500. No outflow boundary conditions was added to the code because the information does not reaches this boundary. For each calculation the following discretization constants was adopted: $\Delta t = \Delta x = 1$. This constants implies on a CFL (Courant-Friedrichs-Lewy) number equal to 1. For each calculation performed on present paper the residue error is defined as:

$$E_{RMS} = \sqrt{\sum_{j=1}^{N} \frac{\left(u_j - u'_j\right)^2}{(n-1) \times n}} \tag{23}$$

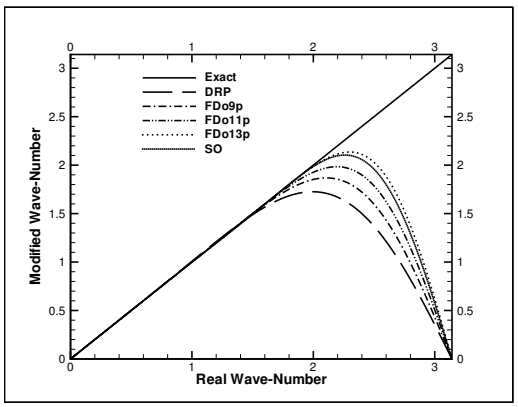

Figure 3: Spectrum of finite difference schemes.

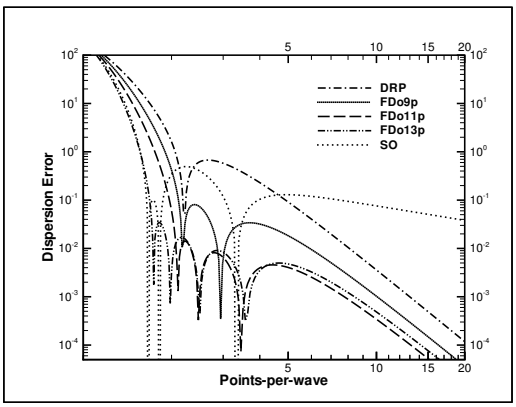

Figure 4: Finite difference dispersion error.

where u_j is the exact solution and u'_j is the numerical result and N is the number of points in the spatial domain. For time integration the traditional fourth-order four steps Runge-Kutta schemes was adopted.

The Tab. 2 presents the E_{RMS} for the DRP, FDo9p, FDo11p, FDo13p and SO finite difference schemes. Analyzing the results present on Tab. 2 it can be seen that for one dimensional wave propagation the SO finite

Table 2: E_{RMS} for the finite difference schemes analyzed at present paper.

Scheme	DRP	FDo9p	FDo11p	FDo13p	SO
E_{RMS}	1.556×10^{-3}	1.701×10^{-3}	1.663×10^{-3}	1.681×10^{-3}	0.847×10^{-3}

difference schemes presents better results when compared with other ones.

4.2. The effect of the finite difference scheme along the time

For this subsection on, the results were obtained using the LEE (subsection 2.2). For all calculations presented on the next subsections the following numerical constants were adopted:

- $\Delta x = \Delta y = 1$;
- $Mach = 0.5$;
- $\Delta t = 1/(1 + Mach)$.

To evaluate numerical results along time the L_2-norm is computed:

$$L_2(t) = \left[\frac{1}{N^2} \sum_{i,j}^{N^2} p'^2_{i,j}(t) \right]^{1/2}, \tag{24}$$

The Fig. 5 presents the L2 norm along the time for the exact solution. This figure is useful to explain how the sound intensity is dissipated, although aeroacoustic problems have no viscosity. Along the time, the propagation of the acoustic wave causes a reduction on its intensity, dissipating the noise. To evaluate along the time the effect of the finite difference scheme on solution along the time the Figs. 6 and 7 presents details of two regions of Fig. 5. Comparing the figures one can note that for all time range there are errors. comparing the results on time 54 to 64 and 95 to 100 one can note that the errors added to the code are improved. Comparing the finite difference results with the exact solution one can note that all finite difference presents similar results. The family of FDo finite difference schemes presents the best results. The results of FDo9p, FDo11p and FDo13p gave almost the same result. The proposed SO scheme has results similar to DRP finite difference scheme present on literature.

4.3. Comparison of finite difference schemes

To compare the real efficiency of finite difference schemes a 2-dimensional pulse propagation was carried out. The results on Figs. 8 and 9 show the general characteristics of the analyzed pulse and the details of the region marked with a circle, respectively. The region marked with a circle in Fig. 8 was chosen for analysis because it is the region that presents the worse results along all domain. Comparing the results that the tested finite

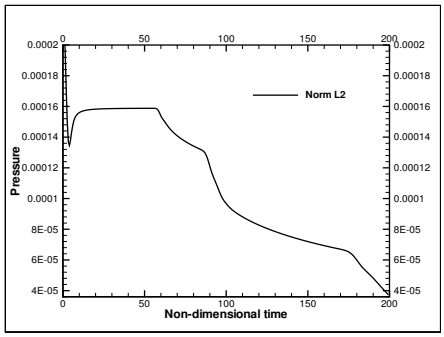

Figure 5: Exact L2 norm along non-dimensional time.

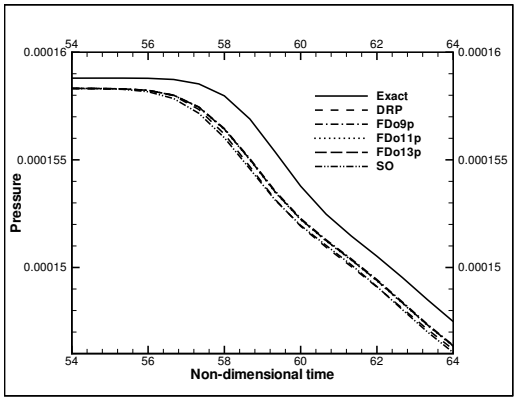

Figure 6: Details of L2 norm on non-dimensional time 54 to 64.

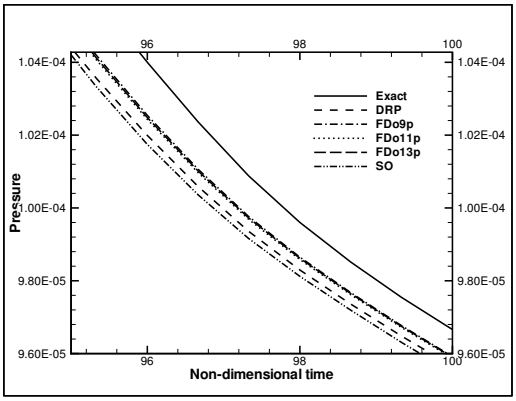

Figure 7: Details of L2 norm on non-dimensional time 95 to 100.

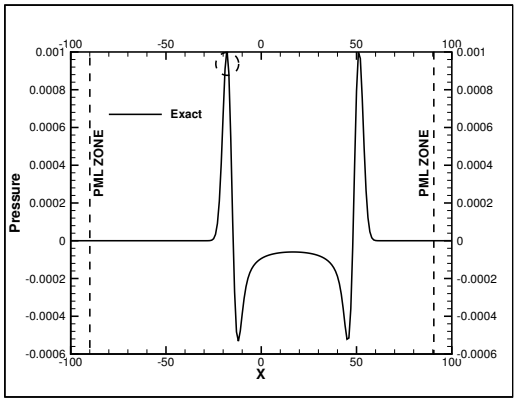

Figure 8: General characteristics of the pulse on t = 50/3.

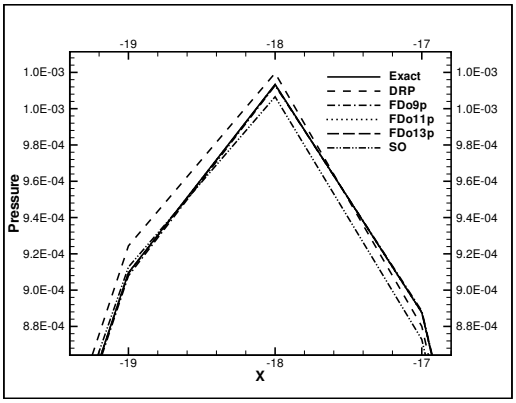

Figure 9: Detail of the pulse on the region marked with a circle of Fig. 8.

difference schemes presents in Fig. 9 one can note that the finite difference schemes FDo9p, FDo11p, FDo13p, presents results almost equal to the exact solution. On other hand the DRP and SO finite difference schemes presents some errors when compared with the exact solution. Comparing these results with the presented in Figs. 3 and 4, one can note that the the errors presented in Fig. 9 can be caused mainly by waves with many points-per-wave. This suggests that a finite difference scheme should not be optimized to transport waves with a great range of points-per-wave, but to transport waves with a small number of points-per-wave, giving a smaller dispersion error in these cases.

4.4. The effect of PML on the main pulse

To analyze the effect of PML on the main pulse the wave propagation is carried out with the same conditions presented on previous sections. The 11 points SO scheme was used for the calculations of the spatial derivatives.

A first study is done with the intention to characterize the need of the PML zone coupled with the physical

boundary conditions of the problem. The Figs. 10 and 11, presents respectively, the pulse propagation on time $t = 400/3$. The left figure shows a case that there is no application of the PML zone and the right presents a figure where this zone is added to the numerical code. Comparing the figures one can note that the pulse

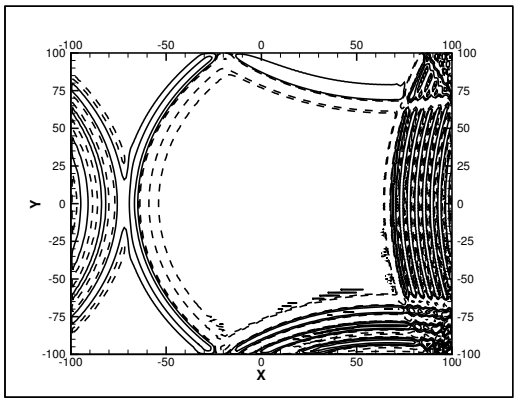

Figure 10: Wave transport with the physical boundary condition but without PML region.

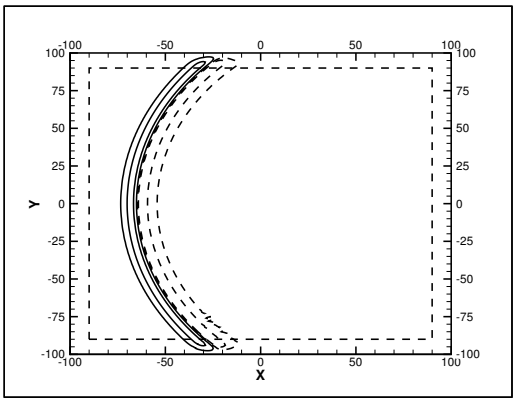

Figure 11: Wave transport with physical boundary condition and PML region.

transport without the use of PML zone implies on a very reflective boundary. These reflections do not represent the physical condition of a rigid wall reflection, they are only numerical spurious reflections.

In order to analise the effects of the PML zone, two simulations were carried out, changing width and height of the computational domain. This was done by using a domain with 201 x 201 points and another with 401 x 401 points. The results after integrating some steps in time for both simulations are shown if Figs. 12 and 13. Fig. 13 shows the details of the region that is marked with a circle in Fig. 12. Observing the Fig. 13 one can

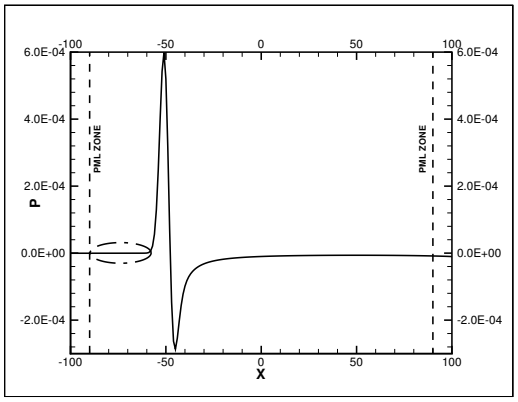

Figure 12: General characteristics of the analyzed pulse.

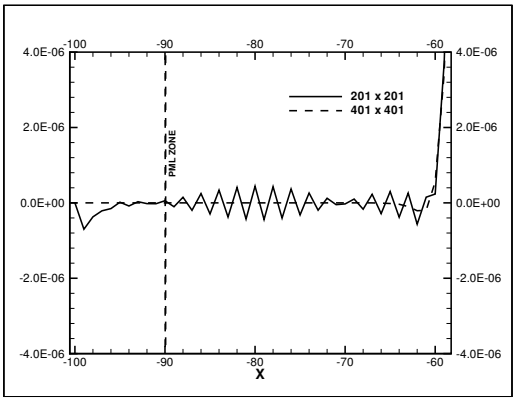

Figure 13: Detail of the circled region on the left figure.

note that the boundary introduces a perturbation error on the order of error of 1.0×10^{-7}, while the intensity of the main pulse is on the order of 1.0×10^{-4}. Comparing the relation of intensity on can note that the intensity of the main pulse on the order of 1000 times greater than the perturbations. This amplitude is acceptable for most of the cases studied.

To analyze the effect of the number of points on PML zone, three different number of points were adopted in the PML region: 6, 10 and 16 points. The simulations were integrated 150 steps in time. The numerical results are shown in Fig. 14 and its details showed in Fig. 15. The results presented on Fig. 15 shows that for 6 points on PML zone there is an introduction of a error, when the solution is compared with the exact. For transports with 10 and 16 points in the PML zone, one can note that the both solutions gave almost the same result. This result coupled with the presented on Fig. 13 lead to the conclusion that for square domains with more than 201 x 201 points, 10 points on PML zone is enough.

5. Conclusions

In this paper a review and comparison of the DRP, FDo, and a new finite difference scheme, based on spectral optimization – SO schemes were done. The 1D results showed that, for a sine function propagation, the SO scheme has the lowest error if compared with the others. A LEE code was used for a 2D verification. For this

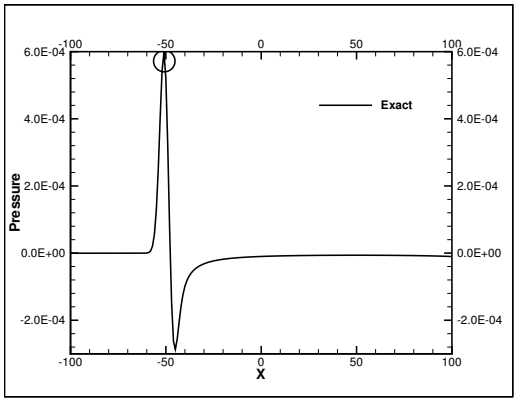

Figure 14: General view of the pulse used to analyze the effect of the number of point on PML zone.

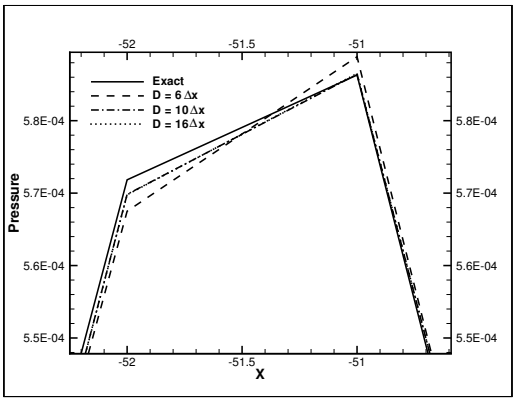

Figure 15: Detail of the left figure.

verification a benchmark case of a Gaussian pulse propagation was performed. In these cases the FDo schemes were better than the others. The result obtained with SO scheme in this case was almost the same of the DRP scheme. An analisys of the SO scheme accoupled with 4th order Runge-Kutta scheme showed that this scheme can be unstable for CFL > 1.3. As boundary conditions the non-reflective Perfectly Matched Layer (PML) zone was implemented and analyzed. The analysis of the PML zone shows that the reflections are of order 0.1% of the maximum wave amplitude, and therefore is a good technique to avoid reflections at the boundaries.

6. Acknowledgments

The authors acknowledge the financial support given by FAPESP under grants 05/00001-0 and 04/07507-4.

7. References

Bogey, C. and Bailly, C., 2004, A Family of Low Dispersive and Low Dissipative Explicit Schemes for Flow and Noise Computation, "Journal of Computational Physics", Vol. 194, pp. 194–214.

Colonius, T., Lele, S. K., and Moin, P., 1993, Boundary Conditions for Direct Computation of Aerodynamic Sound Generation, "AIAA Journal", Vol. 31, pp. 1574–1582.

Curle, J., 1955, The Influence of Solid Boundaries Upon Aerodynamic Sound, "Proc. Roy. Soc.", Vol. 231, pp. 505–514.

Hu, F. Q., 1996, On Absorbing Boundary Conditions for Linearized Euler Equations by a Perfectly Matched Layer, "Journal of Computational Physics", Vol. 129, pp. 201–219.

Hu, F. Q., 2001, A Stable, Perfectly Matched Layer for Linearized Euler Equations in Unsplit Physical Variables, "Journal of Computational Physics", Vol. 173, pp. 455–480.

Lele, S. K., 1992, Compact Finite Differences Schemes with Spectral-like Resolution, "Journal of Computational Physics", Vol. 103, pp. 16–42.

Lighthill, M. J., 1952, On Sound Generated Aerodynamically, i. general theory, "Proc. Roy. Soc.", Vol. 211, pp. 564–587.

Lighthill, M. J., 1954, On Sound Generated Aerodynamically, ii. turbulence as source of sound, "Proc. Roy. Soc.", Vol. 222, pp. 1–32.

Tam, C. K. W., 1995, Computational Aeroacoustics: Issues And Methods, "AIAA Journal", Vol. 33, pp. 1788–1796.

Tam, C. K. W. and Webb, J. C., 1993, Dispersion-Relation-Preserving Finite Difference Schemes for Computational Acoustics, "Journal of Computational Physics", Vol. 107, pp. 262–281.

Williams, J. E. F., 1963, The Noise from Turbulence convected at High Speed, "Philos. Trans. Roy. Soc.", Vol. 255, pp. 496–503.

Williams, J. E. F., 1969, Sound Generation by Turbulence and surfaces in Arbitrary Motion, "Philos. Trans. Roy. Soc.", Vol. 264, pp. 321–342.

Proceedings of the 11th Brazilian Congress of Thermal Sciences and Engineering -- ENCIT 2006
Braz. Soc. of Mechanical Sciences and Engineering -- ABCM, Curitiba, Brazil,- Dec. 5-8, 2006

Paper CIT06-0474

MESH TOPOLOGY INFLUENCE ON SUPERSONIC BLUNT BODY FLOW SOLUTIONS

Fábio Rodrigues Guzzo
CTA/ITA – Instituto Tecnológico de Aeronáutica
fabio@guzzo.com.br

João Luiz F. Azevedo
CTA/IAE – Instituto de Aeronáutica e Espaço
azevedo@iae.cta.br

Abstract. *The present work is concerned with studying the mesh topology influence on supersonic blunt body flow numerical solutions. The work is motivated by previous difficulties the authors experienced when trying to compute very high speed flows with chemical reactions over blunt bodies. Some test cases led to property oscillations, rendering, solutions without physical meaning, in a chemically reacting mixture flow context. Recently, however, the authors observed that the regularity and the smoothness of the computational meshes have a very positive effect on the quality of the solutions obtained for such cases. Hence, in this context, the work here reported considers the solutions of axisymmetric flows over blunt bodies using three different mesh topologies: triangular and quadrilateral unstructured grids and quadrilateral structured grids. The flowfields of interest are modeled by the axisymmetric Euler equations, and ideal gases are considered. The flow equations are solved by a cell centered finite volume method, in which Liou's AUSM+ flux-vector splitting scheme is used for flux computations at cell interfaces. Time march uses a fully explicit, 5-stage, Runge-Kutta time stepping scheme. The numerical methodology employed has performed considerably better for the quadrilateral grids and for the structured meshes, in opposition to the triangular grid and the unstructured meshes, respectively.*

Keywords. *CFD, Mesh Influence, Blunt Body Flow Solutions, AUSM+ scheme.*

1. Introduction

Unstructured meshes, specifically triangular grids in 2-D or tetrahedral grids in 3-D, are preferable when treating complex geometries, and have received considerable attention of the Computational Fluid Dynamic (CFD) community in the past few years. Due to the geometric flexibility and the availability of well-defined algorithms for good-quality mesh generation, general grid generation and remeshing adaptation are easier to conceive for unstructured meshes composed by triangular elements. However, it is important to mention that general systems that incorporate the possibility for generating and remeshing quadrilateral and hybrid meshes over arbitrary domains are feasible. Lyra *et al*. (2000) describe the main features of an integrated computational system for automatic two-dimensional mesh generation and remeshing adaptation for triangular, quadrilateral or mixed meshes.

The present work is concerned with the study of the mesh topology influence over the quality of supersonic blunt body CFD solutions. One unstructured triangular grid, one unstructured quadrilateral grid and two structured quadrilateral grids are considered. It is known that certain formulations perform better with quadrilateral elements than with triangular elements (Lyra *et al*., 2000). The numerical code used herein was already validated by Strauss and Azevedo (2001).

The governing formulation employed comprises the dimensionless, axisymmetric Euler equations. The constitutive relation is the ideal gas equation. Specific heats, at constant volume and pressure, are assumed to be constant. The spatial discretization is performed in a cell centered, face-based finite volume procedure on unstructured meshes. An upwind scheme, AUSM+ (Advection Upstream Splitting Method), proposed by Liou (1994; 1996) for structured meshes, is used. The reinterpretation of the formulation for unstructured meshes follows Azevedo and Korzenowski (1998). Boundary conditions are set through the use of ghost cells attached to the boundary faces. A fully explicit, second order accurate, five stage Runge-Kutta method was used as the time-stepping scheme. Since the problem of interest is steady state, a local time stepping option has been implemented, *i.e.*, the CFL number is kept constant throughout the field.

The configuration studied is a supersonic flow over a semi-spherical blunt body. Four solutions for this configuration are generated using different meshes, one for triangular unstructured grid, one for quadrilateral unstructured grid and two for structured quadrilateral grids. The solutions are presented, compared and discussed.

2. Theoretical Formulation

The flow is modeled by the dimensionless azimuthal-invariant Euler equations in cylindrical coordinates. Perfect gas and constant specific heat, at constant volume and pressure, are considered. The equations employed are written as

$$\frac{\partial \mathbf{Q}}{\partial t}+\frac{\partial \mathbf{E}r}{\partial z}+\frac{\partial \mathbf{F}r}{\partial r}+\mathbf{H}=0. \tag{1}$$

The vector of conserved variables, $\mathbf{Q}$, the convective flux vectors, $\mathbf{E}$ and $\mathbf{F}$, and the axisymmetry source term, $\mathbf{H}$, are given by

$$\mathbf{Q}=\begin{bmatrix}\rho\\ \rho u_z\\ \rho u_r\\ \rho e\end{bmatrix},\quad \mathbf{E}=\begin{bmatrix}\rho u_z\\ \rho u_z^2+p\\ \rho u_z u_r\\ u_z(\rho e+p)\end{bmatrix},\quad \mathbf{F}=\begin{bmatrix}\rho u_r\\ \rho u_z u_r\\ \rho u_r^2+p\\ u_r(\rho e+p)\end{bmatrix},\quad \mathbf{H}=\begin{bmatrix}0\\ 0\\ -p/r\\ 0\end{bmatrix}. \tag{2}$$

The nomenclature used herein is the standard one, such that ρ is the density, u_z and u_r are the velocity components, e is the total energy per unit of mass and p is the pressure. Equation (1) is supplemented by the following constitutive equation:

$$p=(\gamma-1)\rho\left[e-\frac{1}{2}\left(u_z^2+u_r^2\right)\right], \tag{3}$$

where γ is the ratio of specific heats. γ equals to 1.4 was assumed. In this work, the properties are made dimensionless according to the following equations

$$t=t_d\frac{a_\infty}{l_0},\ z=\frac{z_d}{l_0}, r=\frac{r_d}{l_0},\ u_z=\frac{u_{zd}}{a_\infty},\ ur=\frac{u_{rd}}{a_\infty},\ p=\frac{p_d}{\rho_\infty a_\infty^2},\ e=\frac{e_d}{a_\infty^2}. \tag{4}$$

The subscript d denotes the dimension properties. l_0 is the reference length, a_∞ is the freestream speed of sound and ρ_∞ is the freestream density.

3. Numerical Formulation

The governing equations are discretized in a stationary mesh. Finite volume cell centered method is employed. The formulation is obtained by integrating the equations in each finite volume and assuming that the convective flux vectors, $\mathbf{E}$ and $\mathbf{F}$, are constant in each face of the control volume. The equations employed at each cell are written as

$$\frac{\partial \mathbf{Q}_i}{\partial t}+\frac{1}{Vi}\left[\sum_{k=1}^{nf}\left(\mathbf{E}_{ik}r_{ik}\Delta r_{ik}-\mathbf{F}_{ik}r_{ik}\Delta z_{ik}\right)+\mathbf{D}(\mathbf{Q}_i)\right]+\mathbf{H}_i=0. \tag{5}$$

Here, nf is the number of neighboring cells of the i-th cell and $\mathbf{D}(\mathbf{Q}_i)$ is the artificial dissipation operator. The subscript ik denotes the property values at the interface between the i-th cell and its k-th neighbor. r_{ik} was defined as the average r at the interface. A scheme of the edge nomenclature of the *ik* interface is presented in the Fig. 1. The discrete value of the vector of conserved variables for the i-th cell, $\mathbf{Q}_i$, and of the axisymmetry source term, $\mathbf{H}_i$, are defined as the mean value of the continuous properties in the volume. The summation term of the Eq. (5), $\sum_{k=1}^{nf}\left(\mathbf{E}_{ik}r_{ik}\Delta r_{ik}-\mathbf{F}_{ik}r_{ik}\Delta z_{ik}\right)$, is also called as the convective operator, $\mathbf{C}(\mathbf{Q}_i)$:

$$\mathbf{C}(\mathbf{Q}_i)=\sum_{k=1}^{nf}\left(\mathbf{E}_{ik}r_{ik}\Delta r_{ik}-\mathbf{F}_{ik}r_{ik}\Delta z_{ik}\right). \tag{6}$$

An upwind scheme, AUSM+ (Advection Upstream Splitting Method), proposed by Liou (1994; 1996), was used. $\mathbf{E}$ and $\mathbf{F}$ can be expressed as a sum of the convective and pressure terms:

$$\mathbf{E}=u_z\mathbf{\Phi}+\mathbf{P}_z=M_z a\mathbf{\Phi}+\mathbf{P}_z, \tag{7}$$

$$\mathbf{F}=u_r\mathbf{\Phi}+\mathbf{P}_r=M_r a\mathbf{\Phi}+\mathbf{P}_r, \tag{8}$$

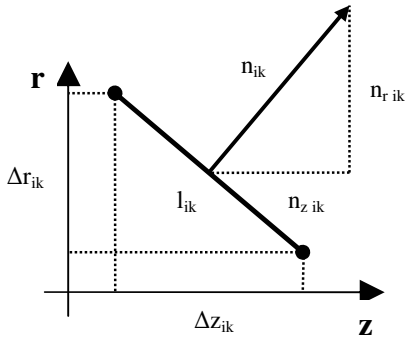

Figure 1. Edge Nomenclature.

where $\mathbf{\Phi}$, $\mathbf{P}_z$, $\mathbf{P}_r$ vectors are defined as

$$\mathbf{\Phi} = \begin{bmatrix} \rho \\ \rho u_z \\ \rho u_r \\ (\rho e + p) \end{bmatrix}, \ \mathbf{P}_z = \begin{bmatrix} 0 \\ p \\ 0 \\ 0 \end{bmatrix}, \ \mathbf{P}_r = \begin{bmatrix} 0 \\ 0 \\ p \\ 0 \end{bmatrix}. \tag{9}$$

In these expressions, a is the speed of sound, $M_z = u_z / a$ and $M_r = u_r / a$. The term $\mathbf{E}_{ik} r_{ik} \Delta r_{ik} - \mathbf{F}_{ik} r_{ik} \Delta z_{ik}$ of the Eq. (6) can be then written as

$$\mathbf{E}_{ik} r_{ik} \Delta r_{ik} - \mathbf{F}_{ik} r_{ik} \Delta z_{ik} = \left(\mathbf{F}_{ik}^{(c)} + \mathbf{P}_{ik} \right) r_{ik} l_{ik}, \tag{10}$$

where the vectors $\mathbf{F}_{ik}^{(c)}$ and $\mathbf{P}_{ik}$ are defined as

$$\mathbf{F}_{ik}^{(c)} = \left(u_{z\,ik} n_{z\,ik} \mathbf{\Phi}_{ik} + u_{r\,ik} n_{r\,ik} \mathbf{\Phi}_{ik} \right), \tag{11}$$

$$\mathbf{P}_{ik} = \left(\mathbf{P}_{z\,ik} n_{z\,ik} + \mathbf{P}_{r\,ik} n_{r\,ik} \right). \tag{12}$$

The approach adopted in the present work in order to extend the formulation proposed by Liou (1994; 1996) to unstructured meshes follows Azevedo and Korzenowski (1998) and consists in defining a local one-dimensional system normal to the edge considered. Azevedo and Korzenowski (1998) describe the method to calculate the terms $\mathbf{F}_{ik}^{(c)}$ and $\mathbf{P}_{ik}$ for unstructured meshes. The upwind scheme used herein, AUSM+, does not require the use of additional artificial dissipation in order to control nonlinear instabilities. However, it was introduced in some simulations to analyze and to propose a feasible way to reduce flow oscillations in the field. The artificial dissipation operator, $\mathbf{D}(\mathbf{Q}_i)$, used in the present work, is formed as a blend of undivided Laplacian and biharmonic operators (Jameson and Mavriplis, 1986 and Mavriplis, 1988, 1990). These mimic, in an unstructured mesh context, the concept of using 2nd and 4th difference terms as presented by Jameson *et al.* (1981) and Pulliam (1986). The artificial dissipation is written as

$$\mathbf{D}(\mathbf{Q}_i) = \mathbf{d}^{(2)}(\mathbf{Q}_i) - \mathbf{d}^{(4)}(\mathbf{Q}_i), \tag{13}$$

where $\mathbf{d}^{(2)}(\mathbf{Q}_i)$ represents the contribution of the undivided Laplacian operator, and $\mathbf{d}^{(4)}(\mathbf{Q}_i)$ the contribution of the biharmonic operator. The undivided Laplacian artificial dissipation operator and the biharmonic operator are described by Jameson and Mavriplis, (1986) and Mavriplis, (1988, 1990). The parameters used to adjust the artificial dissipation, i.e. $K^{(2)}$ and $K^{(4)}$, received here the greatest values within the ranges suggested by Jameson *et al.* (1981) and Mavriplis (1990).

The fully explicit, 5-stage, Runge-Kutta method was used as the time-stepping scheme. The time integration for the i-th cell is expressed as

$$
\begin{aligned}
&\mathbf{Q}_i^{(0)} = \mathbf{Q}_i^n, \\
&\mathbf{Q}_i^{(1)} = \mathbf{Q}_i^{(0)} - \alpha_1 \Delta t_i^n \left[\frac{1}{V_i} \left[\mathbf{C}\left(\mathbf{Q}_i^{(0)}\right) - \mathbf{D}\left(\mathbf{Q}_i^{(0)}\right) \right] + \mathbf{H}_i^{(0)} \right], \\
&\mathbf{Q}_i^{(2)} = \mathbf{Q}_i^{(0)} - \alpha_2 \Delta t_i^n \left[\frac{1}{V_i} \left[\mathbf{C}\left(\mathbf{Q}_i^{(1)}\right) - \mathbf{D}\left(\mathbf{Q}_i^{(1)}\right) \right] + \mathbf{H}_i^{(1)} \right], \\
&\mathbf{Q}_i^{(3)} = \mathbf{Q}_i^{(0)} - \alpha_3 \Delta t_i^n \left[\frac{1}{V_i} \left[\mathbf{C}\left(\mathbf{Q}_i^{(2)}\right) - \mathbf{D}\left(\mathbf{Q}_i^{(1)}\right) \right] + \mathbf{H}_i^{(2)} \right], \\
&\mathbf{Q}_i^{(4)} = \mathbf{Q}_i^{(0)} - \alpha_4 \Delta t_i^n \left[\frac{1}{V_i} \left[\mathbf{C}\left(\mathbf{Q}_i^{(3)}\right) - \mathbf{D}\left(\mathbf{Q}_i^{(1)}\right) \right] + \mathbf{H}_i^{(3)} \right], \\
&\mathbf{Q}_i^{(5)} = \mathbf{Q}_i^{(0)} - \alpha_5 \Delta t_i^n \left[\frac{1}{V_i} \left[\mathbf{C}\left(\mathbf{Q}_i^{(4)}\right) - \mathbf{D}\left(\mathbf{Q}_i^{(1)}\right) \right] + \mathbf{H}_i^{(4)} \right], \\
&\mathbf{Q}_i^{n+1} = \mathbf{Q}_i^{(5)}.
\end{aligned}
\tag{14}
$$

The superscript n and $n+1$ refer to the states at the beginning and at the end of a generic n-th time step. The artificial dissipation operator, $\mathbf{D}(\mathbf{Q}_i)$, is evaluated only at the two initial stages is order to reduce timing process. The values used for the α coefficients are

$$
\alpha_1 = \frac{1}{4},\ \alpha_2 = \frac{1}{6},\ \alpha_3 = \frac{3}{8},\ \alpha_4 = \frac{1}{2},\ \alpha_5 = 1. \tag{15}
$$

These values were suggested by Mavriplis (1988; 1990). A specific time stepping value is determined for each i-th cell, Δt_i^n, as

$$
\Delta t_i^n = \frac{(CFL)(\Delta s_i)}{\left(\sqrt{u_z^2 + u_r^2} + a\right)_i^n}. \tag{16}
$$

A constant CFL number was used and attributed throughout the field. (Δs_i) is the characteristic length associated to the i-th cell, and it has been defined as the diameter of the inscribed circle of the element. a is the local speed of sound.

Boundary conditions are set through the use of ghost cells attached to the boundary faces. The flow is made tangent at the wall boundary by imposing the velocity component normal to the wall, in the ghost volume, the same magnitude value and opposite sign of the normal velocity component in its adjacent interior volume, whereas the ghost volume velocity component tangent to the wall is equal in magnitude and sign to its internal volume counterpart. Zero normal pressure and temperature gradients are assumed at the wall. Symmetry boundary is modeled as the wall boundary. The variables in the ghost volumes at the entrance boundary are set equal to the freestream values. For the exit boundary, all properties are extrapolated from the interior information, i.e. the variables of the ghost volume are made equal to the variables of its interior volume counterpart. Initial condition is set by applying the freestream properties over each cell.

4. Results and Discussion

4.1 Supersonic Flow over a Blunt Body

The configuration studied is a supersonic flow over a semi-spherical blunt body. Freestream Mach number equal to 4 and zero flow angle of attack are considered. This configuration was selected because flows over blunt bodies with detached shock waves are widely explored in the literature and their comprehensive study has become important with the advent of ballistic missiles and, specially, reentry vehicles. Artificial dissipation terms are not considered in the simulations here presented. These terms are used in the additional solutions, discussed in the next section, in order to analyze their effects on the reduction of property oscillations. Four simulations are performed and the solutions are herein presented: one for triangular unstructured grid, one for quadrilateral unstructured grid, and two for structured quadrilateral grids. Figure 2 shows the meshes employed. The triangular unstructured mesh is composed of 13456 nodes and 26408 volumes; the quadrilateral unstructured mesh comprises 26939 nodes and 26508 volumes; the quadrilateral structured mesh 1, which is the fine structured mesh, has 18000 nodes and 17641 volumes, in which the distribution is 60 × 300 points in the normal and longitudinal directions, respectively; and the quadrilateral structured mesh 2, which is the coarse structured mesh, has 4500 nodes and 4321 volumes, distributed as 30 × 150 points in the

normal and longitudinal directions. The number of volumes that composes both structured meshes is considerably lower than the number of volumes of the unstructured meshes. The quadrilateral structured mesh 2 has the greatest local mesh spacing throughout the field, even near the symmetry boundary. This mesh was included in order to assure that the analysis presented here is restricted to the mesh topology and the effects are not due to the mesh refinement. The unstructured meshes were generated with ICEM CFD code. The grids were smoothed using the quality criteria (ICEM CFD, 1999). A single mesh spacing was considered through out the field. For the structured meshes, the nodes are equally spaced in the normal and longitudinal directions. In order to assess the qualities of the meshes, Fig. 3 shows details of each mesh, upstream of the body stagnation point, and Fig. 4 shows the angle distribution of the elements of the meshes.

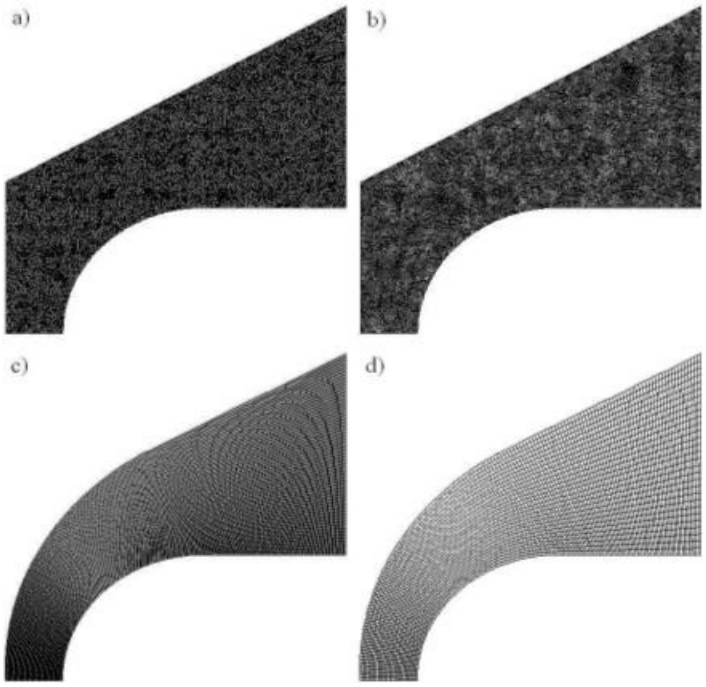

Figure 2. Computational meshes: a) triangular unstructured grid, b) quadrilateral unstructured grid, c) quadrilateral structured grid 1 and d) quadrilateral structured grid 2 .

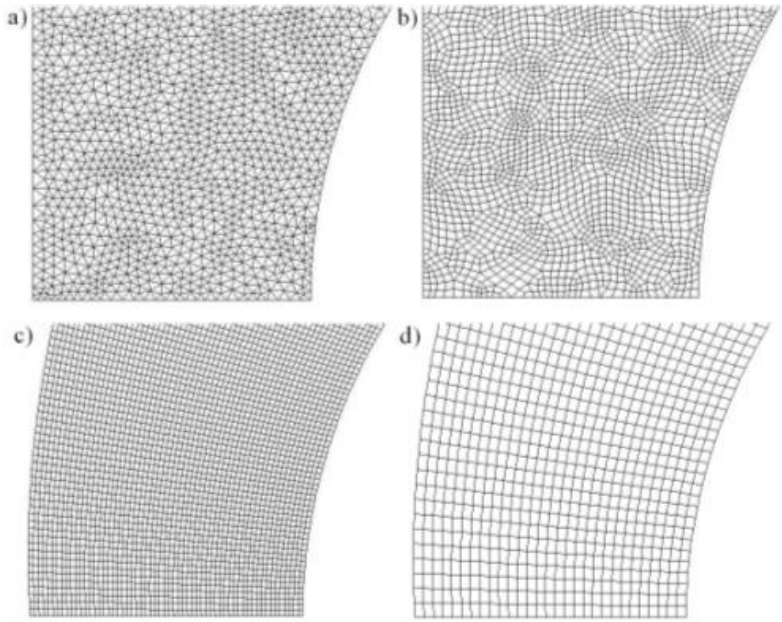

Figure 3. Detailed view of the upstream region of the various meshes: a) triangular unstructured grid, b) quadrilateral unstructured grid, c) quadrilateral structured grid 1 and d) quadrilateral structured grid 2.

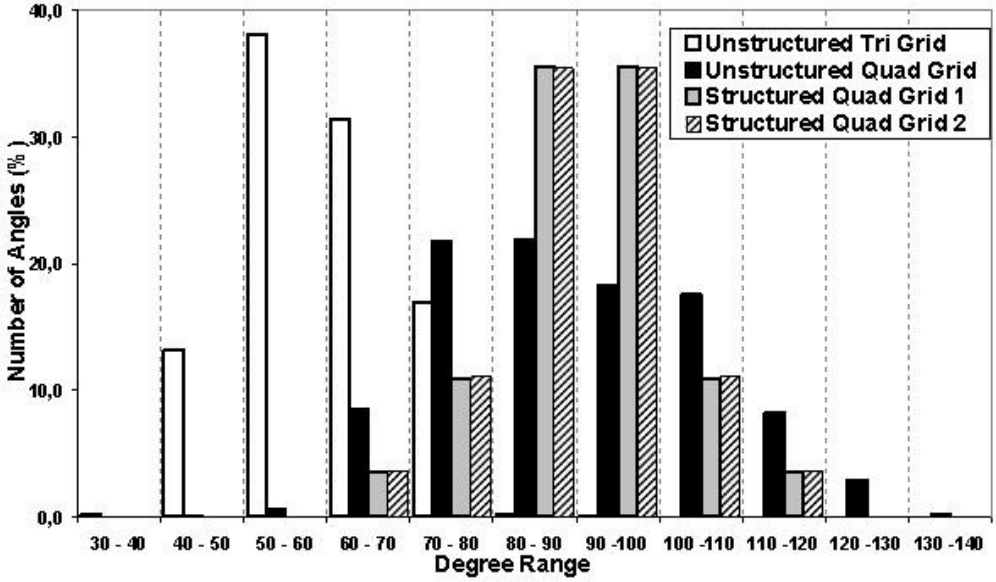

Figure 4. Angle distributions for the various meshes.

Figure 5 shows the density, ρ, and the Mach number, M, contours of the simulations performed using each of the meshes considered. All solutions presented herein are converged. It is possible to note that, although the property contours after the shock wave are similar among the solutions, oscillations of ρ and M are more pronounced for the triangular grid solution in comparison with the quadrilateral grid solutions. Moreover, the same statement can be made for the unstructured mesh results in comparison with the structured mesh calculations. Property oscillations are more perceptive in the solution obtained with the triangular unstructured mesh compared to the quadrilateral unstructured mesh, especially for Mach number, after the region where the variation of the properties is more severe, *i.e.*, after the shock wave and near the symmetry boundary. The solution obtained for the quadrilateral structured meshes presented considerable less oscillation compared to the unstructured meshes, both for density and for Mach number.

Figure 6 shows the contours of constant $M = 3.9$. Since the shock wave in a numerical simulation is not a discontinuity in the solution, the determination of its real position has a certain subjectivity. The contour of constant M equal to 3.9 is considered as the approximate shock wave position because it is simple to compute and it allows consistent comparisons. Although oscillations of the properties are observed, mainly in the solution for the unstructured meshes, as already shown in Fig. 5, differences of the shock wave position are not pronounced among the solutions obtained, as shown in Fig. 6.

Figure 7 shows the pressure distributions along the symmetry and wall boundaries. Oscillations are more perceptive in the solutions obtained with the unstructured meshes in comparison with the structured meshes, as already evidenced in Figs. 5 and 6. Despite the oscillations, the pressure distributions, in the region after the shock wave, are similar for the four simulations. The differences of the shock wave position are not pronounced among the solutions obtained, as also observed in Fig. 6.

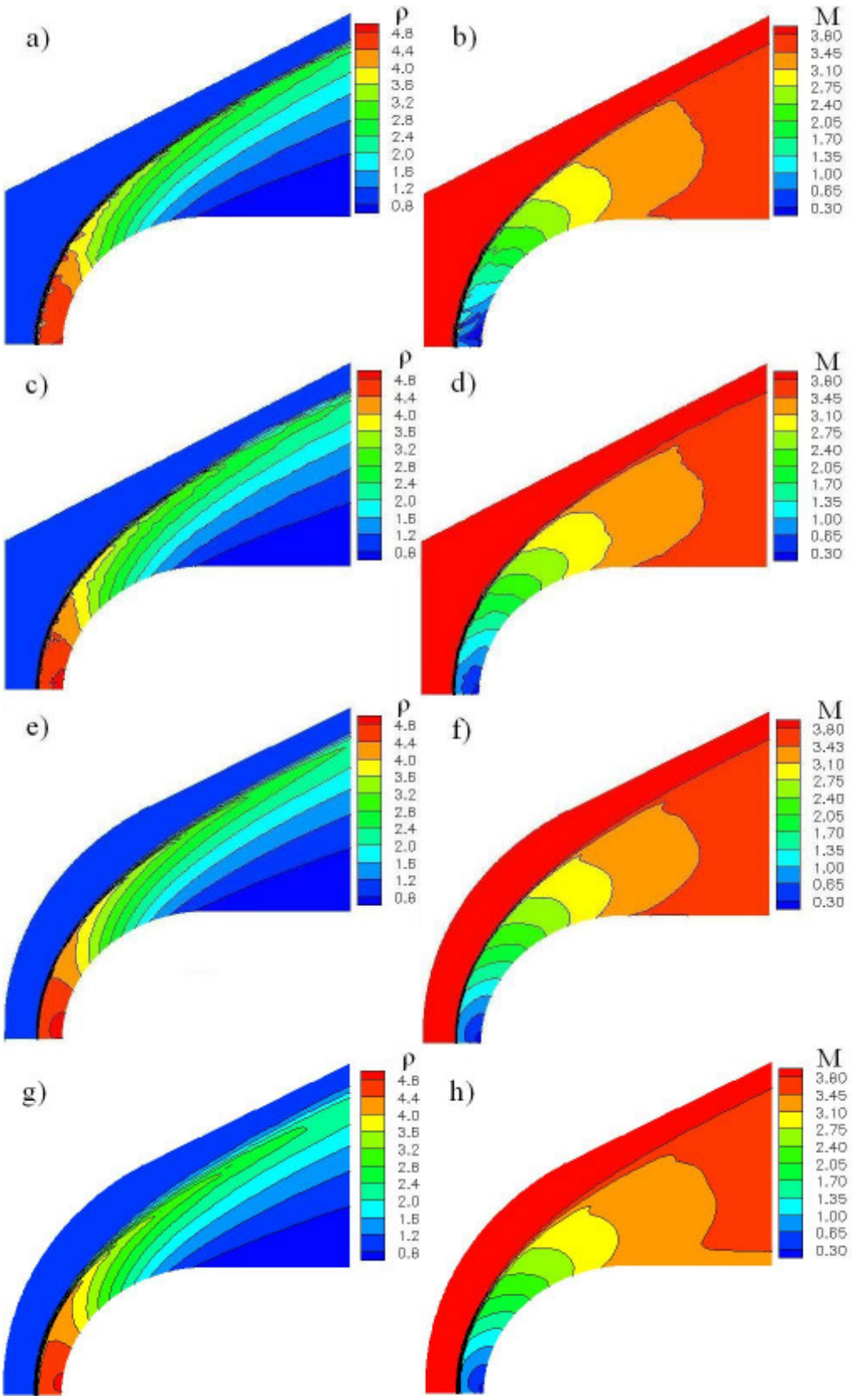

Figure 5. Density, ρ, and Mach number, M, contours: a) and b) for triangular unstructured mesh, c) and d) for quadrilateral unstructured mesh, e) and f) for quadrilateral structured mesh 1, and g) and h) for quadrilateral structured mesh 2. $M_\infty = 4$, zero angle of attack and no artificial dissipation.

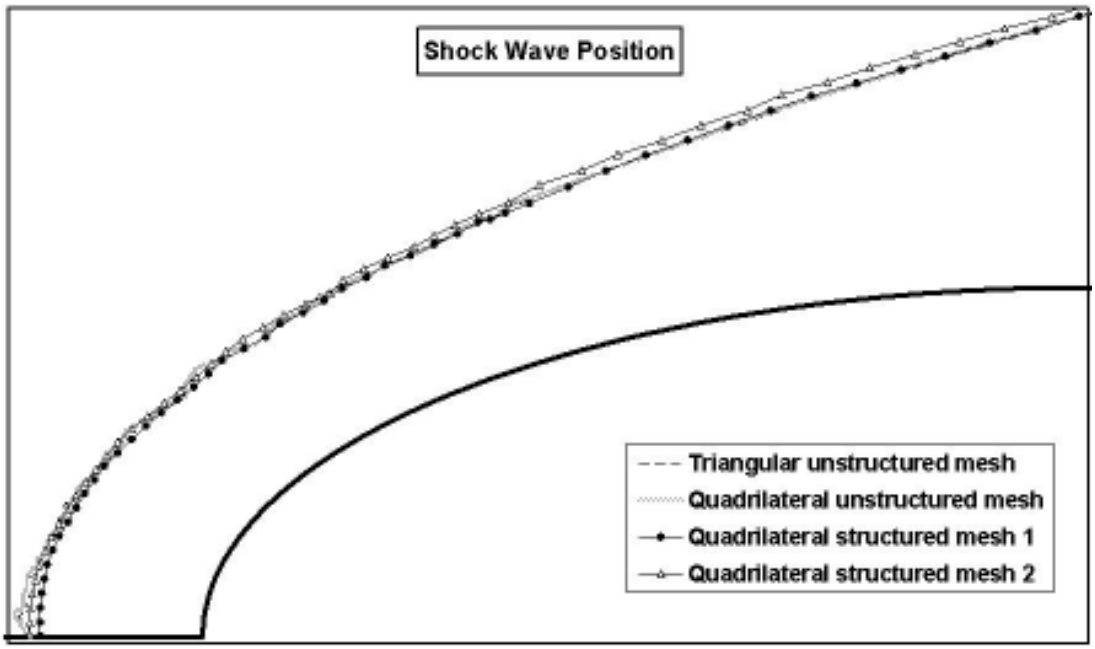

Figure 6. Shock wave position of the simulations performed: contours of constant $M = 3.9$. $M_\infty = 4$, zero angle of attack and no artificial dissipation.

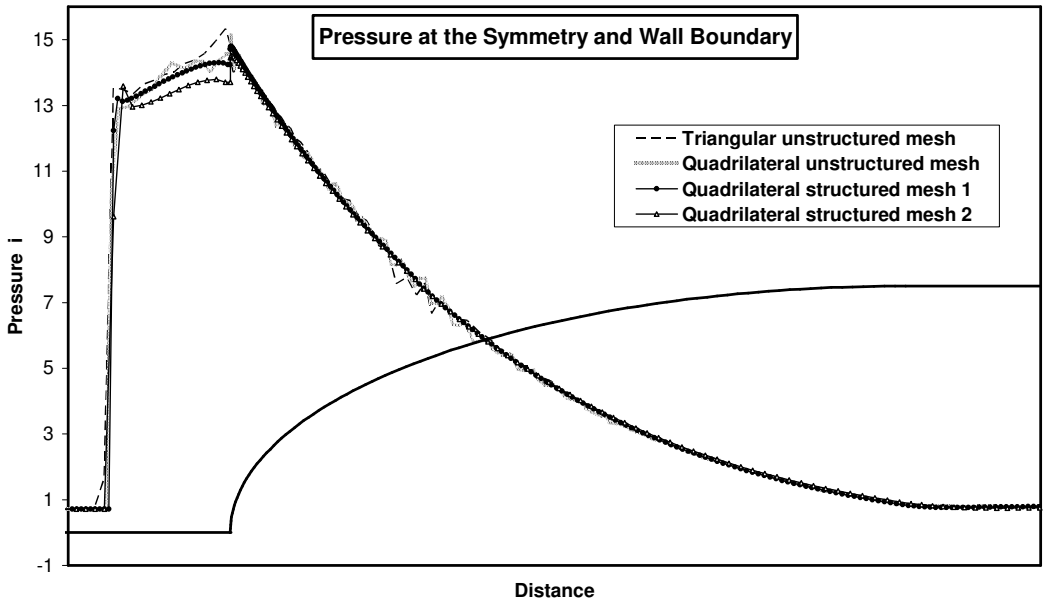

Figure 7. Pressure distributions along the symmetry and wall boundaries. $M_\infty = 4$ and no artificial dissipation.

4.2 Additional Results

Additional solutions are presented here in order to extend the analysis of the mesh topology influence. Simulations are performed over a configuration identical to the previous one, except that the freestream Mach number is equal to 5. Figure 8 shows the density, ρ, and Mach number, M, contours for the meshes considered. Artificial recirculation is observed over the triangular unstructured mesh after the shock wave, near the symmetry boundary. The property oscillations over the field may be led to this artificial recirculation. This solution is not converged and it differs considerably from the solutions obtained for the quadrilateral meshes. Figure 9 shows details of the artificial recirculation observed over the triangular unstructured mesh.

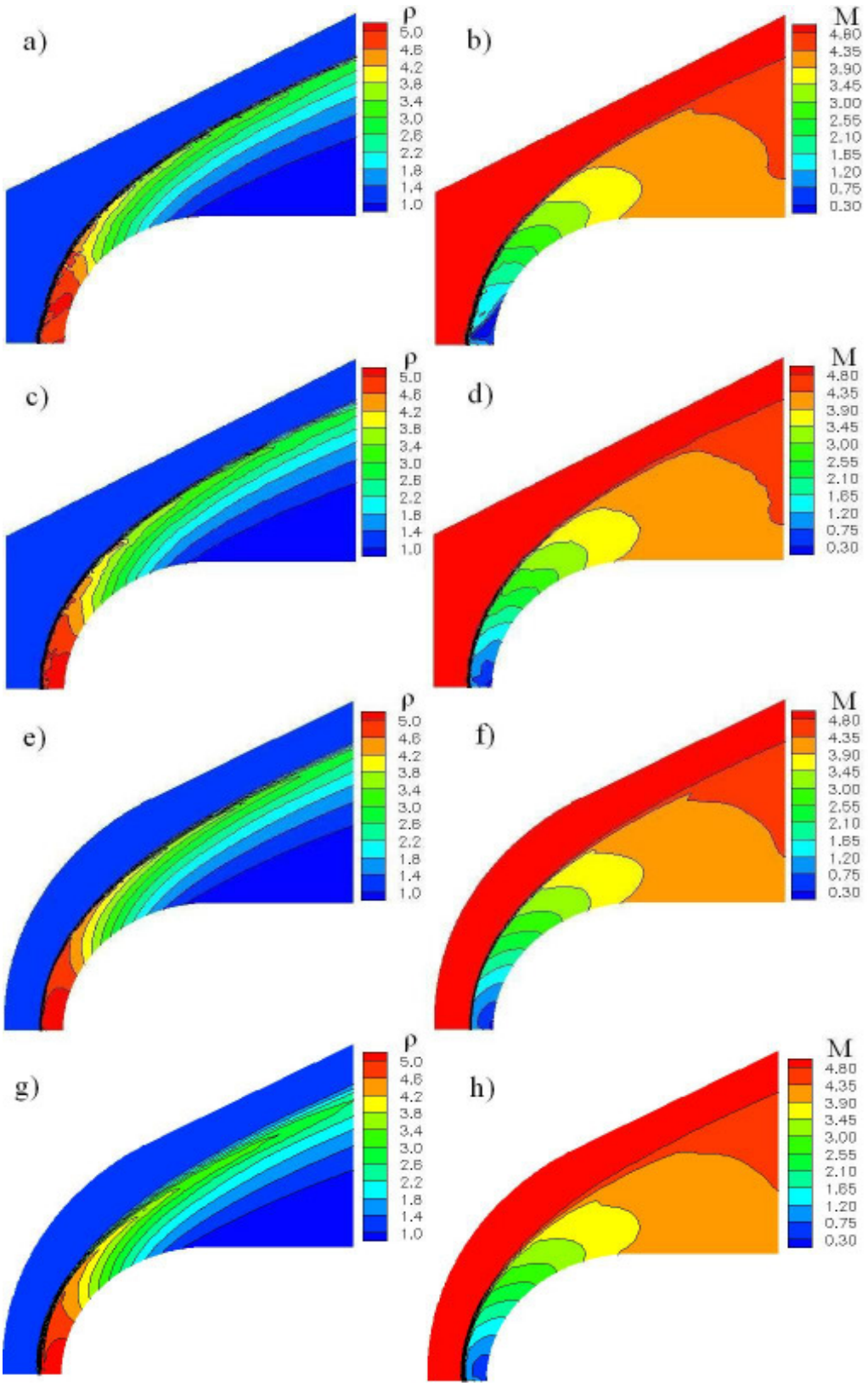

Figure 8. Density, ρ, and Mach number, M, contours: a) and b) for triangular unstructured mesh, c) and d) for quadrilateral unstructured mesh, e) and f) for quadrilateral structured mesh 1, and g) and h) for quadrilateral structured mesh 2. $M_\infty = 5$ and no artificial dissipation.

The property oscillations observed in the simulations performed with the unstructured meshes, shown in the Fig. 8, are considerably reduced and the appearance of artificial recirculation in the solution over the triangular unstructured mesh is eliminated with the use of additional artificial dissipation. Figure 10 shows solutions using the unstructured meshes, in which the artificial dissipation terms are considered. It is important to observe that property oscillations are more pronounced for the solutions obtained with the unstructured meshes, even with the use of artificial dissipation, Figs. 9 (a) to (d), when compared to the solutions obtained for the structured meshes without the use of artificial dissipation, Figs. 8 (e) to (h).

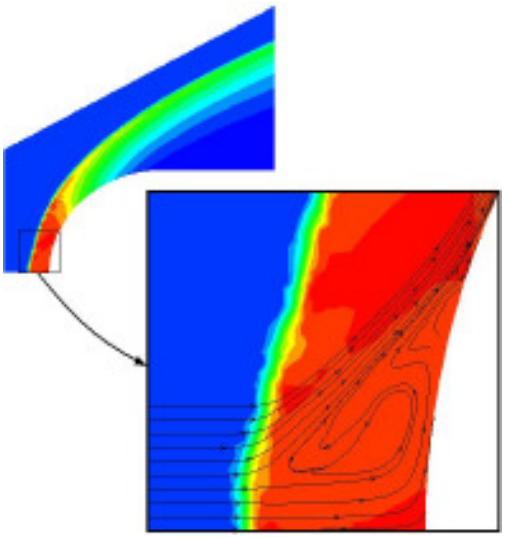

Figure 9. Details with streamtraces of the artificial recirculation observed over the triangular unstructured grid.

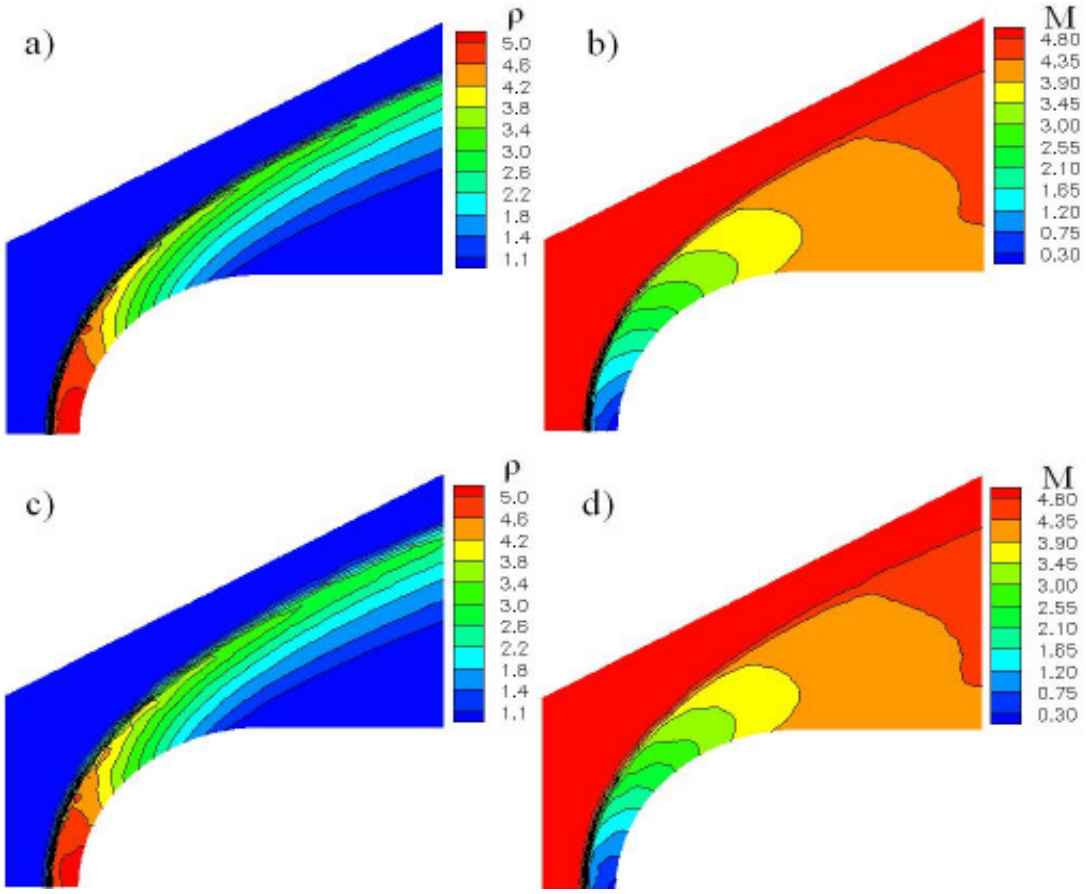

Figure 10. Density, ρ, and Mach number, M, contours: a) and b) for triangular unstructured mesh, and c) and d) for quadrilateral unstructured mesh. $M_\infty = 5$ and with the use of artificial dissipation.

5. Concluding Remarks

The present work has presented supersonic blunt body flow solutions performed using four different meshes. The objective was to address the mesh topology influence on the quality of CFD solutions. The axisymmetric Euler equations and ideal gases were considered. Liou's AUSM+ flux-vector splitting scheme, implemented in the context of a cell centered finite volume method, was used for flux computations at cell interfaces. Time march uses a fully explicit, 5-stage, Runge-Kutta time stepping scheme.

Similar solutions, assessed by the shock wave position and by the property distribution after the shock wave, were obtained for the meshes employed, except that oscillations over the field were more perceptive for the simulations performed with the triangular grid and the unstructured meshes, in opposition to the simulations over the quadrilateral grids and the structured meshes. The results indicated that the use of quadrilateral grids is preferable to triangular grids in the cases tested. Furthermore, better solutions were obtained for the quadrilateral structured meshes when compared to the quadrilateral unstructured mesh. This observation strongly suggests that the regularity and the smoothness of the mesh play an important role on the quality of the solutions. Property oscillations over the field may be led to artificial recirculations for a simulation over the triangular unstructured grid. The oscillations were considerably reduced and the appearance of the artificial recirculation was eliminated with the use of additional artificial dissipation.

It is also important to observe that property oscillations over the flowfield may create additional difficulties to implement second order accurate spatial discretization schemes, since the extrapolation of the properties from the cell center to the interfaces is based on the property values of the cell and of its neighbors. Oscillations may also jeopardize the quality of solutions when the formulation contemplates chemical reactions, even for simple geometries, since a small variation of the flow properties, as temperature, may represent a large variation in the species production rates in the kinetic reaction process.

6. Acknowledgements

The authors acknowledge Conselho Nacional de Desenvolvimento Científico e Tecnológico, CNPq, which partially supported the present research under the Integrated Project Research Grant No. 501200/2003-7

7. References

Azevedo, J. L. F., Korzenowski, H., 1998, "Comparison of Unstructured Grid Fine Volume Methods for Cold Gas Hypersonic Flow Simulations", AIAA Paper No. 98-2629, Proceedings of the 16th AIAA Applied Aerodynamics Conference, Albuquerque, NM, pp. 447-463.

ICEM CFD Engineering, 1999, ICEM CFD Tutorial Manual, Version 4.0.

Jameson, A., Schmidt, W., Turkel, E., 1981, "Numerical Solution of the Euler Equations by Finite Volume Methods Using Runge-Kutta Time-Stepping Schemes", AIAA Paper 81-1259, AIAA 14th Fluid and Plasma Dynamics Conference, Palo Alto, CA.

Jameson, A., Mavriplis, D. J., 1986, "Finite Volume Solutions of the Two-Dimensional Euler Equations on a Regular Triangular Mesh", AIAA Journal, Vol. 24, No. 4, pp. 611-618.

Liou, M.S., 1994 ,"A Continuing Search for a Near-Perfect Numerical Flux Scheme. Part I: AUSM+", NASA TM-106524, NASA Lewis Research Center, Cleveland, OH.

Liou, M.S., 1996 ,"A Sequel to AUSM: AUSM+", Journal of Computation Physics, Vol. 129, No. 2, pp. 364-382.

Lyra, P. R. M., Carvalho, D. K. E., Almeida, R. C., Feijóo, R. A., 2000, "Anisotropic Bidimensional Unstructured Mesh Generation and Adaptation for Finite Element Flow Simulation", CILAMCE.

Mavriplis, D. J., 1988, "Multigrid Solution of the Two-Dimensional Euler Equations on Unstructured Triangular Meshes," AIAA Journal, Vol. 26, No. 7, pp. 824-831.

Mavriplis, D. J., 1990, "Accurate Multigrid Solution of the Euler Equations on Unstructured and Adaptive Meshes," AIAA Journal, Vol. 28, No. 2, pp. 213-221.

Pulliam, T. H., 1986, "Artificial Dissipation Models for the Euler Equations", AIAA Journal, Vol. 24, No 12, pp. 1931-1940.

Strauss, D., and Azevedo, J. L. F., 2001, "Unstructured Multigrid Simulations of Axisymmetric Inviscid Lauch Vehicles Flows," AIAA 19th Applied Aerodynamics Conference, Anaheim, CA.

Proceedings of the 11th Brazilian Congress of Thermal Sciences and Engineering -- ENCIT 2006
Braz. Soc. of Mechanical Sciences and Engineering -- ABCM, Curitiba, Brazil,- Dec. 5-8, 2006

Paper CIT06-0484

NUMERICAL PREDICTION OF THE TRANSITIONAL FLOW PAST POWER-LAW LEADING EDGES

Wilson F. N. Santos
Combustion and Propulsion Laboratory
National Institute for Space Research
12630-000 Cachoeira Paulista, SP, Brazil
wilson@lcp.inpe.br

Abstract. *This work deals with a numerical study of power-law shaped leading edges situated in a hypersonic flow at zero-incidence. The primary aim of this paper is to examine the effect of rarefaction on the flowfield structure. Rarefaction effect on the flowfield structure has been investigated by employing the Direct Simulation Monte Carlo (DSMC) method. The work is motivated by interest in investigating power-law shaped leading edges as possible candidates for blunting geometry of hypersonic leading edges. The sensitivity of the primary flow properties to variations on rarefaction is simulated for altitudes of 70, 80 and 85 km. The analysis shows significant differences on the flowfield properties due to variations not only on the altitude but also on the leading edge shape defined by the power-law exponent. It is found that the upstream effects have different influence on velocity, density, pressure and temperature along the stagnation streamline ahead of the leading edges.*

Keywords. *DSMC, hypersonic flow, rarefied flow, power-law shape, sharp leading edge.*

1. Introduction

Hypersonic waverider configurations have been proposed as promising airframes for high-speed vehicles because they have the highest known lift-drag (L/D) performance. A waverider concept, introduced by Nonweiler (1959), is a lifting body that is derived from a known analytical flowfield, such as a flow over a two-dimensional wedge or a flow over a slender cone. The potential for high L/D ratio on waveriders originates from the high-pressure region between the shock wave and the lower surface. Due to the sharp leading edge, the attached shock wave prevents the high-pressure gas from the lower surface to communicate with the gas on the upper surface. However, as any practical waverider will have some degree of leading edge bluntness for heat transfer, manufacturing and handling concerns, then the predicted performance of waverider configurations may not be achieved. Moreover, because of the viscous effects, the shock wave will be detached from the leading edge and, hence, the aerodynamic performance of the vehicle may be degraded from ideal performance. Typically, a round leading edge with constant radius of curvature near the stagnation point (circular cylinder) has been chosen. Nevertheless, shock detachment distance on a cylinder, with associated leakage, scales with the radius of curvature. Therefore, designing a hypersonic vehicle leading edge involves a tradeoff between making the leading edge sharp enough to obtain acceptable aerodynamic and propulsion efficiency and blunt enough to reduce the aerodynamic heating in the stagnation region.

Certain classes of non-circular shapes, such as power-law shaped leading edges ($y \propto x^n$, $0 < n < 1$), may provide the required bluntness for heat transfer, manufacturing and handling concerns with reduced departures from ideal aerodynamic performance. This concept is based on work of Mason and Lee (1994), who have pointed out, based on Newtonian flow analysis, that power-law shapes exhibit both blunt and sharp aerodynamic properties. They suggested the possibility of a difference between shapes that are geometrically sharp and shapes that behave aerodynamically as if they were sharp.

Santos and Lewis (2002) have investigated the sensitivity of the pressure gradient and the stagnation point heating to shape variations of power-law leading edges by considering two-dimensional rarefied hypersonic flow. Through the use of the DSMC method, they showed that the pressure gradient on the power-law shapes is in surprising agreement with that obtained by Mason and Lee (1994) by employing Newtonian Analysis. They also found that the stagnation point heating scales inversely with the square root of the curvature radius for power-law bodies with finite radius of curvature.

Santos and Lewis (2005a and 2005b) compared power-law shapes to a corresponding circular cylinder in order to determine which geometry would be better suited as a blunting profile. Their analysis also showed that power-law shapes provided smaller total drag than circular cylinder, typically used in blunting sharp leading edges for heat transfer considerations. However, circular cylinder provided smaller stagnation point heating than power-law shapes under the range of conditions investigated.

Based on recent interest in hypersonic waveriders for high-altitude/low-density applications (Anderson, 1990, Potter and Rockaway, 1994, Rault, 1994, Graves and Argrow, 2001, Shvets et al., 2005), the present account deals with a parametric study performed on power-law shapes with emphasis placed on the rarefaction effects. In this context, the primary goal of this paper is to assess the sensitivity of the primary flow properties to variations not only on the rarefaction experienced by the leading edges but also on the leading-edge shapes by means of the power-law exponent.

For the high altitude/high Knudsen number of interest (Kn > 0.1), the flowfield is sufficiently rarefied that continuum method becomes inappropriate. Alternatively, the DSMC method is used in the current study to calculate the rarefied hypersonic two-dimensional flow on the leading edge shapes.

2. Leading Edge Geometry Definition

In dimensional form, the body power-law shapes (Santos and Lewis, 2002) are given by the following expression,

$$y = ax^n \tag{1}$$

where n is the power-law exponent and a is the power-law constant which is a function of n.

The power-law shapes are modeled by assuming a sharp leading edge of half angle θ with a circular cylinder of radius R inscribed tangent to this wedge. The power-law shapes, inscribed between the wedge and the cylinder, are also tangent to them at the same common point where they have the same slope angle. The circular cylinder diameter provides a reference for the amount of blunting desired on the leading edges. It was assumed a leading edge half angle of 10 degrees, a circular cylinder diameter of 10^{-2}m and power-law exponents of 1/2, 2/3, and 3/4. Figure (1a) illustrates schematically this construction for the set of power-law leading edges investigated.

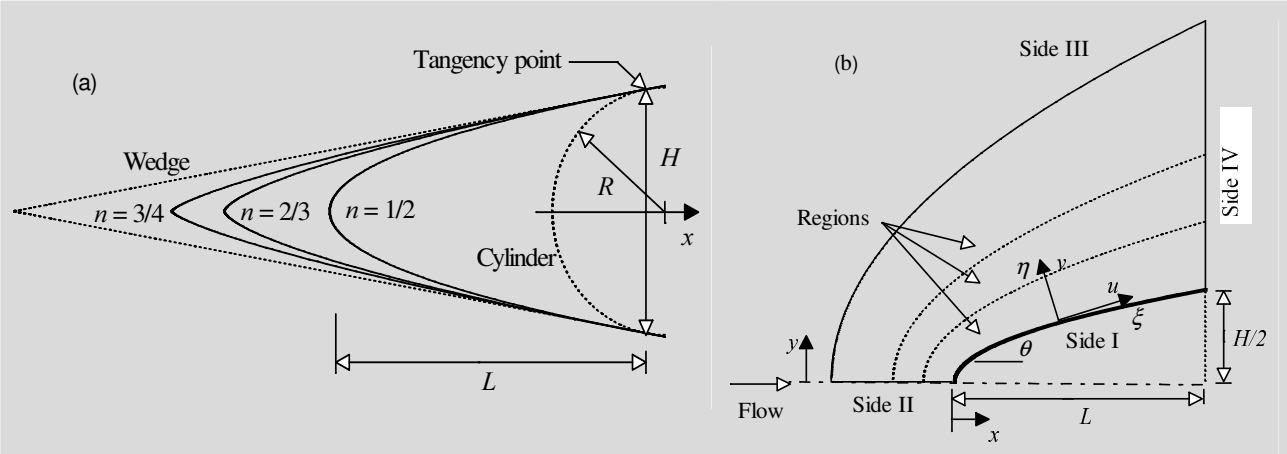

Figure 1: Drawing illustrating (a) the leading edge shapes and (b) the computational domain.

From geometric considerations, the power-law constant a is obtained by matching slope on the wedge, circular cylinder and power-law body at the tangency point. The common body height H at the tangency point is equal to $2R\cos\theta$, and the body length L from the nose to the tangency point in the axis of symmetry is given by $nH/2\tan\theta$. It was assumed that the power-law leading edges are infinitely long but only the length L is considered since the wake region behind the power-law bodies is not of interest in this investigation.

3. Computational Method and Procedure

The most successful numerical technique for modeling complex transitional flows has been the Direct Simulation Monte Carlo (DSMC) method (Bird, 1994). The DSMC method simulates real gas flows with various physical processes by means of a huge number of modeling particles; each particle represents a fixed number of real gas molecules. In the DSMC model, the particle evolution is divided into two independent phases during the simulation; the movement phase and the collision phase. In the movement phase, all particles are moved over distances appropriate to a short time interval, time step, and some of them interact with the domain boundaries in this time interval. Particles that strike the solid wall would reflect according to the appropriate gas-surface interaction model, specular, diffusive or a combination of these. In the collision phase, intermolecular collisions are performed according to the theory of probability without time being consumed. In this context, the intermolecular collisions are uncoupled to the translational molecular motion over the time step used to advance the simulation. Time is advanced in discrete steps such that each step is small in comparison with the mean collision time. The simulation is always calculated as unsteady flow. However, a steady flow solution is obtained as the large time state of the simulation.

The molecular collisions are modeled using the variable hard sphere (VHS) molecular model (Bird, 1981) and the no time counter (NTC) collision sampling technique (Bird, 1989). The energy exchange between kinetic and internal modes is controlled by the Borgnakke-Larsen statistical model (Borgnakke and Larsen, 1975). Simulations are performed using a non-reacting gas model consisting of two chemical species, N_2 and O_2. Energy exchanges between

the translational and internal modes, rotational and vibrational, are considered. Relaxation collision numbers of 5 and 50 were used for the calculations of rotation and vibration, respectively.

In order to easily account for particle-particle collisions, the flowfield is divided into an arbitrary number of regions, which are subdivided into computational cells. The cells are further subdivided into subcells. The cell provides a convenient reference sampling of the macroscopic gas properties, while the collision partners are selected from the same subcell for the establishment of the collision rate.

The computational domain used for the calculation is made large enough so that body disturbances do not reach the upstream and side boundaries, where freestream conditions are specified. A schematic view of the computational domain is depicted in Fig. (1b). Side I is defined by the body surface. Diffuse reflection with complete thermal accommodation is the condition applied to this side. Advantage of the flow symmetry is taken into account, and molecular simulation is applied to one-half of a full configuration. Thus, side II is a plane of symmetry. In such a boundary, all flow gradients normal to the plane are zero. At the molecular level, this plane is equivalent to a specular reflecting boundary. Side III is the freestream side through which simulated molecules enter and exit. Finally, the flow at the downstream outflow boundary, side IV, is predominantly supersonic and vacuum condition is specified (Guo and Liaw, 2001). At this boundary, simulated molecules can only exit.

Application of a numerical method to solve practical problems requires a reliable way in order to estimate the accuracy of the solution. The numerical accuracy in DSMC method depends on the cell size chosen, on the time step as well as on the number of particles per computational cell. In the DSMC algorithm, the linear dimensions of the cells should be small in comparison with the scale length of the macroscopic flow gradients normal to streamwise directions, which means that the cell dimensions should be of the order of or smaller than the local mean free path (Alexander et al., 1998 and Alexander et al., 2000). The time step should be chosen to be sufficiently small in comparison with the local mean collision time (Garcia and Wagner, 2000, and Hadjiconstantinou, 2000). In general, the total simulation time, discretized into time steps, is identified with the physical time of the real flow. Finally, the number of simulated particles has to be large enough to make statistical correlations between particles insignificant.

These effects were investigated in order to determine the number of cells and the number of particles required to achieve grid independence solutions. Grid independence was tested by running the calculations with half and double the number of cells in ξ and η directions (see Fig. (1b)) compared to a standard grid. Solutions (not shown) were near identical for all grids used and were considered fully grid independent. Details on the grid independence effect are shown in Santos and Lewis (2005a and 2005b).

4. Freestream and Flow Conditions

Rarefaction effects are investigated for altitudes of 70, 80 and 85 km. For each one of the altitude investigated, the freestream Mach number M_∞ and the wall temperature T_w are kept to the constant values of 12 and 880 K, respectively. Freestream Mach number M_∞ of 12 corresponds to freestream velocity V_∞ of 3.56, 3.236 and 3.236 km/s for altitudes of 70, 80 and 85 km, respectively.

Table (1) summarizes the freestream and flow conditions used in the present calculations. The gas properties considered in the simulation are those given by Bird (1994) and tabulated in Tab. (2). Referring to Tab. (1), T_∞, p_∞, ρ_∞, n_∞, μ_∞, and λ_∞ stand respectively for temperature, pressure, density, number density, viscosity and mean free path.

Table 1: Freestream Conditions

Altitude (km)	T_∞ (K)	p_∞ (N/m^2)	ρ_∞ x 10^5 (kg/m^3)	n_∞ x 10^{-20} (m^{-3})	μ_∞ x 10^5 (Ns/m^2)	λ_∞ x 10^3 (m)	V_∞ (m/s)
70	220.0	5.582	8.753	18.2090	1.455	0.903	3560
80	181.0	1.040	1.999	4.1586	1.253	3.960	3236
85	181.0	0.414	0.796	1.6550	1.253	9.940	3236

Table 2: Gas Properties

	X *Mole fraction*	m (kg) *Molecular mass*	d (m) *Molecular diameter*	ω *Viscosity index*
O_2	0.237	5.312 x 10^{-26}	4.01 x 10^{-10}	0.77
N_2	0.763	4.65 x 10^{-26}	4.11 x 10^{-10}	0.74

The overall Knudsen number Kn_∞, defined as the ratio of the freestream mean free path λ_∞ to the diameter of the circular cylinder, corresponds to 0.0903, 0.3960 and 0.9940 for altitudes of 70, 80 and 85 km, respectively. Finally, the Reynolds number Re_∞ per unit of meter, based on conditions in the undisturbed stream is 21416.3, 5165 and 2055 for altitudes of 70, 80 and 85 km, respectively.

4. Computational Results and Discussion

The regime of intermediate Knudsen numbers ($0.1 < Kn < 10$), which is difficult to treat analytically, is simulated in the present account by Kn_∞ of 0.0903, 0.3960 and 0.9940, which correspond to the altitudes of 70, 80 and 85 km, respectively. These freestream Knudsen numbers were obtained by considering the diameter of the reference circular cylinder as the characteristic length. In order to assess the dependence of the flowfield structure on the freestream Knudsen number, by way of changing the altitude, the other flow parameters were kept the same as defined in Tab. (1), i.e., freestream Mach number of 12, wall temperature of 880 K, and diffuse reflection with full thermal accommodation. In this way, the purpose of this section is to discuss and to compare differences in the flowfield properties due to variations on the freestream Knudsen number as well as on the leading-edge shape. The flowfield properties of particular interest in the regime of intermediate Knudsen number are velocity, density, pressure and temperature.

4.1. Velocity Profile

Normal velocity profiles along the stagnation streamline and their dependence on rarefaction are illustrated in Figs. (2a), (2b) and (2c) for leading-edge shapes corresponding to power-law exponent n of 1/2, 2/3 and 3/4, respectively. In this set of figures, the normal velocity v is normalized by the freestream velocity V_∞, which is slightly different for each altitude, and the distance x upstream the leading edges is normalized by the radius R of the reference circular cylinder instead of the freestream mean free path λ_∞, since it is different for the altitudes investigated. In addition, in order to emphasize points of interest, this set of figures shows only part of the computational domain of the normal velocity profiles for altitudes of 80 and 85 km.

According to these figures, it is seen that the leading-edge shape as well as the rarefaction influences the flowfield far upstream. This domain of influence increases with increasing both the power-law exponent n and the altitude. By means of the power-law exponent n, the leading-edge shape effect results from the upstream diffusion of particles that are reflected from the nose of the leading edges. Consequently, blunting the nose of the body ($n \rightarrow 1/2$) leads to larger disturbance upstream of the body. On the other hand, the effect of increasing the altitude is to create a more rarefied situation. In this fashion, the presence of the body, propagated by random motion of the molecules, is communicated to a larger distance ahead of the body, since the molecules interact little with each other and collisions among them are less frequent. For comparison purpose, the upstream disturbance for a velocity reduction of 1% ($v/V_\infty = 0.99$) is around $0.95R$, $0.60R$ and $0.54R$ for cases n = 1/2, 2/3 and 3/4, respectively, at an altitude of 70 km. Nevertheless, it changes to around 5.47R, 5.00R and 4.56R for cases n = 1/2, 2/3 and 3/4, respectively, at an altitude of 85 km.

Despite the large upstream influence of the altitude as well as the shape of the leading edge on the normal velocity, the significant reduction in the normal velocity takes place in a small region very close to the stagnation point. As a reference, for altitudes of 70, 80 and 85 km, a reduction of 50% in the normal velocity occurs for the n = 1/2 case around x/R = 0.22, 0.52 and 0.84, and for the n = 3/4 case around x/R = 0.07, 0.17 and 0.29, respectively.

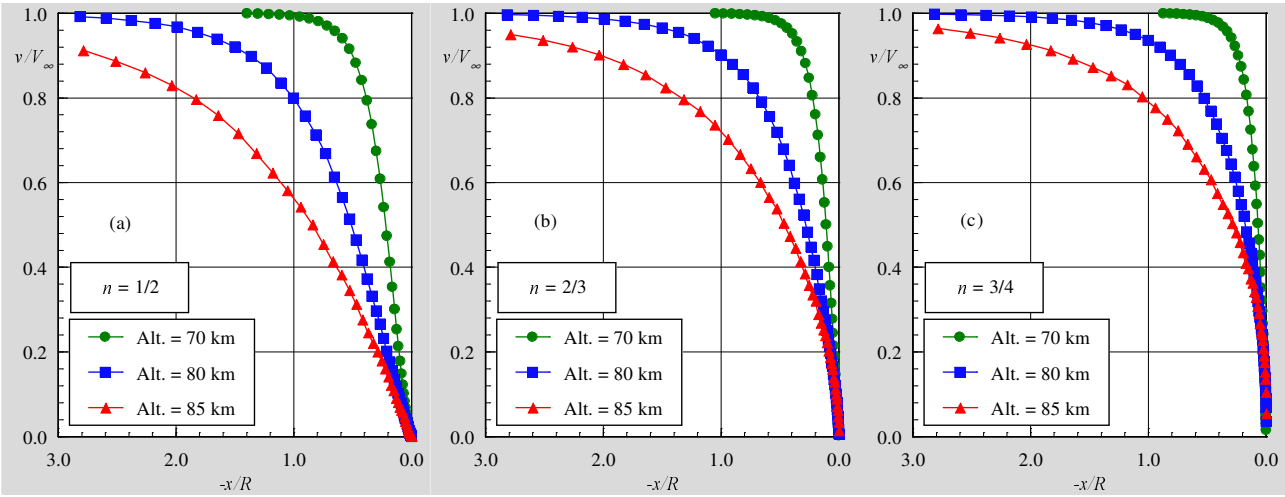

Figure 2: Normal velocity (v/V_∞) profiles along the stagnation streamline as a function of the altitude for leading-edge shape corresponding to power-law exponent n of (a) 1/2, (b) 2/3 and (c) 3/4.

4.2. Density Profile

Rarefaction effects on density along the stagnation streamline are shown as a function of the altitude in Figs. (3a), (3b) and (3c) for power-law exponent n of 1/2, 2/3 and 3/4, respectively. In this set of figures, the density ρ is normalized by the freestream density ρ_∞, which is different for each altitude as shown in Tab. (1).

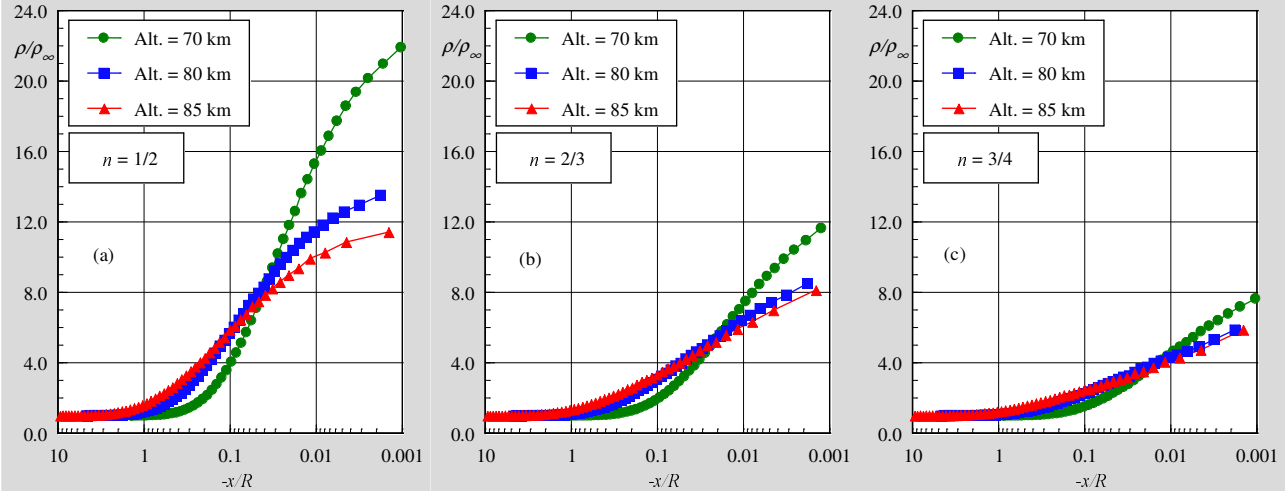

Figure 3: Density (ρ/ρ_∞) profiles along the stagnation streamline as a function of the altitude for leading-edge shape corresponding to power-law exponent n of (a) 1/2, (b) 2/3 and (c) 3/4.

The predictions of density for all of the leading-edge shapes investigated show no sign of a discrete shock wave. Instead, there is a continuous rise in density from the freestream to the nose of the leading edges, rising to well above the continuum inviscid limit for the majority of the cases investigated. As a point of reference, the Rankine-Hugoniot relations give a postshock density that corresponds to the ratio $\rho/\rho_\infty = 5.8$ for freestream Mach number of 12. Near the stagnation point ($x/R \approx 0$), a substantial density increase occurs which is a characteristic of cold-wall entry flow (Haas and Fallavollita, 1994). In typical entry flow, the body surface temperature is low compared to the stagnation temperature. This leads to a steep density gradient near the body surface. For the range of altitude in the present simulation, the ratio of wall temperature to stagnation temperature is from 0.134 to 0.163, which correspond to a cold-wall flow.

Referring to Figs. (3a), (3b) and (3c), it can be recognized that density rises gradually as the flow approaches the nose of the leading edge, indicating the diffuse nature of the shock wave, a characteristic of highly rarefied flows. Also, density increases much more for blunt leading edge ($n \rightarrow 1/2$) than that for sharp leading edge ($n \rightarrow 3/4$) in the stagnation region and reaches its maximum value at the stagnation point. As a result, the buildup of particle density near the nose of the leading edge acts as a shield for the molecules coming from the undisturbed stream. The buildup of particles density at the vicinity of the stagnation point decreases as the altitude increases from 70 to 85 km. This is explained by the fact that the effect of increasing the altitude is to create a more rarefied situation, since the molecules interact little with each other and collisions among them are less frequent. In addition, with the density decrease near the stagnation point, the local mean free path increases resulting in a higher local Knudsen number.

For the flow conditions in this set of simulations, the density ratio ρ/ρ_∞ at the stagnation point by assuming free molecular flow (Bird, 1994) is found to be 9.89, 9.07 and 9.07 for altitudes of 70, 80 and 85 km, respectively. By comparing these density ratios with those presented in the Figs. (3a), (3b) and (3c), one can conclude that the flow approaches the free molecular flow near the nose of the leading edge for power-law exponent of 3/4.

It may be recognized from the density distribution that, unlike normal velocity, density has little effect on the extent of the domain of influence upstream of the body for the leading edge shapes investigated. Much of the density increase in the shock layer occurs after the temperature has reached its postshock value, as will be seen subsequently.

In the following, it proves instructive to illustrate the density behavior adjacent to the body surface. In this fashion, density ratio (ρ/ρ_∞) contours at the vicinity of the nose are displayed in Figs. (4a), (4b) and (4c) for power-law exponent n of 1/2, 2/3 and 3/4, respectively. In this set of contours, the half upper part of leading edge represents the distribution of density at an altitude of 70 km, and the half lower part that for 85 km. In addition, X and Y are the distance x and y normalized by the radius R of the reference circular cylinder. Also, it should be emphasized that the density scale is common for all of the cases, even though the scale for the coordinate axis is different.

By examining the density contours depicted in Figs. (4a), (4b) and (4c), it is observed that the major changes in density occur in a thin region close to the body surface. As mentioned earlier, the pick in density occurs at the stagnation point, and the higher value is attained for the bluntest leading edge investigated, the leading edge corresponding to n of 1/2. As the altitude increases, a reduction on the density level is observed not only at the stagnation point but also adjacent to the body surface.

Also of great significance in Figs. (4a), (4b) and (4c) is the disturbance domain upstream the nose of the leading edges. Similar to the velocity profiles, the density disturbance is more pronounced for the bluntest leading edge investigated. Also it is clearly noticed that the upstream effect increases with the altitude rise, as was pointed previously.

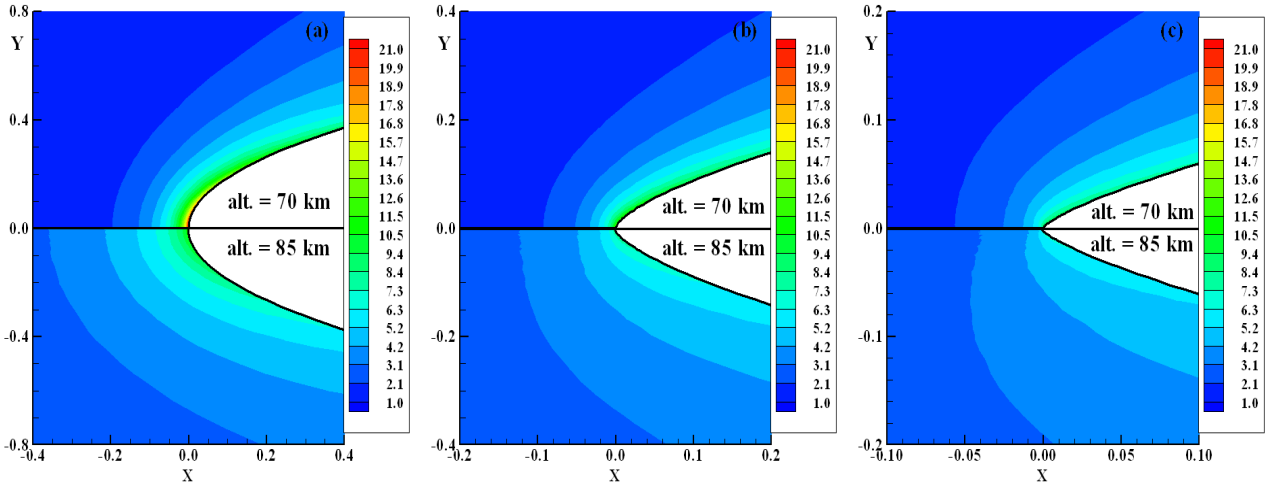

Figure 4: Density ratio (ρ/ρ_∞) contours at the vicinity of the leading-edge nose as a function of the altitude for leading-edge shapes that correspond to the power-law exponents of (a) 1/2, (b) 2/3 and (c) 3/4.

4.3. Pressure Profile

The large amount of kinetic energy present in a hypersonic freestream is converted by molecular collisions into high thermal energy surrounding the body and by flow work into increased pressure. In this respect, the stagnation line is a zone of strong compression, where pressure increases from the freestream to the stagnation point due to the shock wave that forms ahead of the leading edges.

Variations on pressure profiles along the stagnation streamline due to rarefaction effect are displayed as a function of the altitude in Figs. (5a), (5b) and (5c) for power-law exponent n of 1/2, 2/3 and 3/4, respectively. In this set of diagrams, pressure p is normalized by the freestream pressure p_∞. The general shape of the dimensionless pressure profile is preserved even for the highest altitude investigated. In this fashion, the pressure increases from the freestream value toward the stagnation point where the maximum value is attained. The maximum pressure located at the stagnation point decreases with the altitude rise. Also, it decreases as the power-law exponent n increases, since the leading edge becomes sharp. At the stagnation region, the compression produces a maximum pressure that is around two order of magnitude higher that the freestream value for the cases investigated.

The extent of the upstream flowfield disturbance for pressure is significantly different from that presented by density. The domain of influence for pressure is higher than that for density and lower than that presented for temperature. Similar to the density, much of the pressure increase in the shock layer occurs after the translational kinetic temperature has reached its postshock value, as will be shown subsequently.

In what follows, a critical assessment of the flowfield is provided by Figs. (6a), (6b) and (6c) which consider a magnification of the pressure ratio, p/p_∞, at the vicinity of the leading edge for power-law exponent of 1/2, 2/3 and 3/4, respectively.

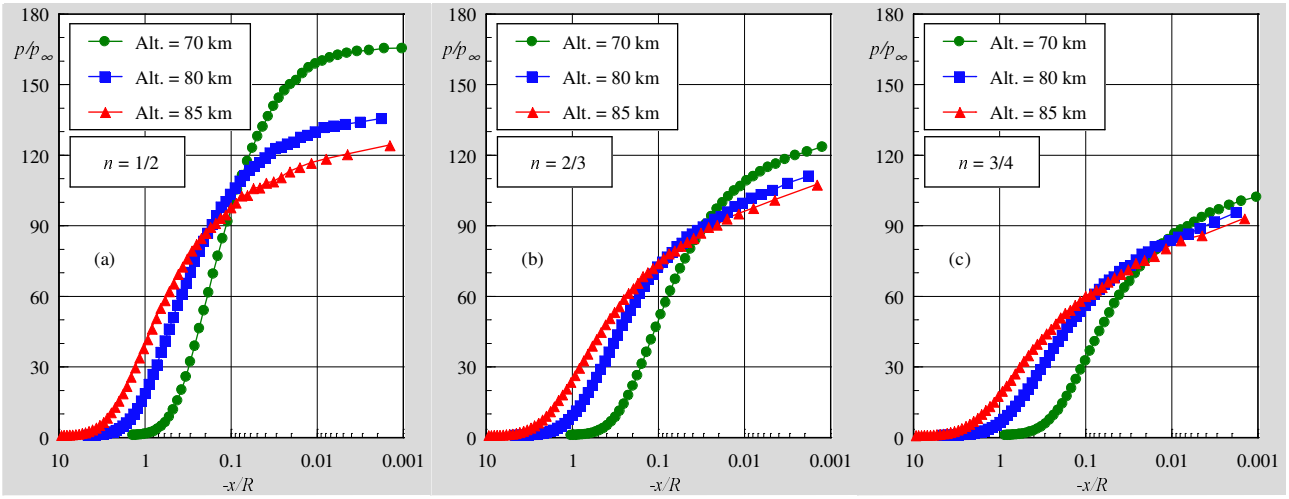

Figure 5: Pressure (p/p_∞) profiles along the stagnation streamline as a function of the altitude for leading-edge shape corresponding to power-law exponent n of (a) 1/2, (b) 2/3 and (c) 3/4.

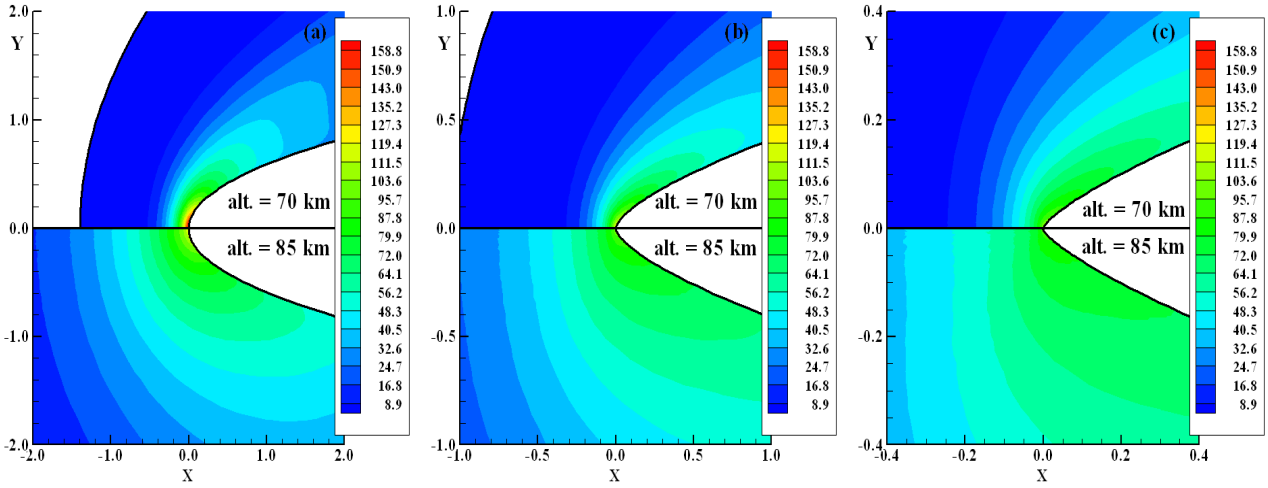

Figure 6: Pressure ratio (p/p_∞) contours at the vicinity of the leading-edge nose as a function of the altitude for leading-edge shapes that correspond to the power-law exponents of (a) 1/2, (b) 2/3 and (c) 3/4.

Referring to Figs. (6a), (6b) and (6c), it is clearly observed that the stagnation region is a zone of strong compression. Moreover, due to the expansion along the body surface, the pressure adjacent to the surface presents a significant reduction as compared to the freestream pressure.

4.4. Temperature Profile

The strong shock wave that forms ahead of a blunt leading edge at hypersonic flow converts part of the kinetic energy of the freestream air molecules into thermal energy. This thermal energy downstream of the shock wave is partitioned into increasing the translational kinetic energy of the air molecules, and into exciting of other molecular energy states such as rotation and vibration.

Kinetic temperature profiles along the stagnation streamline are demonstrated as a function of the altitude in Figs. (7), (8) and (9) for power-law exponent n of 1/2, 2/3 and 3/4, respectively. In this set of plots, temperature ratio accounts for the kinetic temperatures normalized by the freestream temperature T_∞. In addition, T_T, T_R, T_V and T_O stand for translational, rotational, vibrational and overall temperature, respectively. It is apparent from these figures that thermodynamic non-equilibrium occurs throughout the shock layer, as shown by the lack of equilibrium of the translational and internal kinetic temperatures. Thermal non-equilibrium occurs when the temperatures associated with the translational, rotational, and vibrational modes of a polyatomic gas are different.

The overall kinetic temperature shown is defined for a non-equilibrium gas as the weighted mean of the translational and internal temperature (Bird, 1994) as follows,

$$T = \frac{\zeta_T T_T + \zeta_R T_R + \zeta_V T_V}{\zeta_T + \zeta_R + \zeta_V} \tag{2}$$

where ζ is the degree of freedom, and subscripts T, R and V stand for translational, rotational and vibrational modes.

The overall kinetic temperature is equivalent to the thermodynamic temperature only under thermal equilibrium conditions. It is important to mention that the ideal gas equation of state does not apply to this temperature in a non-equilibrium situation.

Referring to Figs. (7), (8) and (9), in the undisturbed freestream far from the body, the translational and internal temperatures have the same value and are equal to the thermodynamic temperature. Approaching the nose of the leading edge, the translational temperature rises to well above the rotational and vibrational temperatures and reaches a maximum value that is a function of the leading edge shape as well as of the altitude. Since a large number of collisions is needed to excite molecules vibrationally from the ground state to the upper state, the vibrational temperature increases much more slowly than rotational temperature. Still further downstream toward the nose of the leading edge, the translational temperature decreases and reaches a value on the wall that is above the wall temperature, resulting in a temperature jump as defined in continuum formulation.

It is evident by comparison with Fig. (3) that, for the altitudes investigated, the translational kinetic temperature rises to a peak well before any substantial increase in density has been experienced. This rise is due to the particles being reflected forward from the compression region into the low-density approaching flow. Energetic collisions between the fast moving freestream particles and reflected ones result in the translational kinetic temperature rising to a peak comparable in magnitude to that behind the bow shock for the equivalent continuum flow.

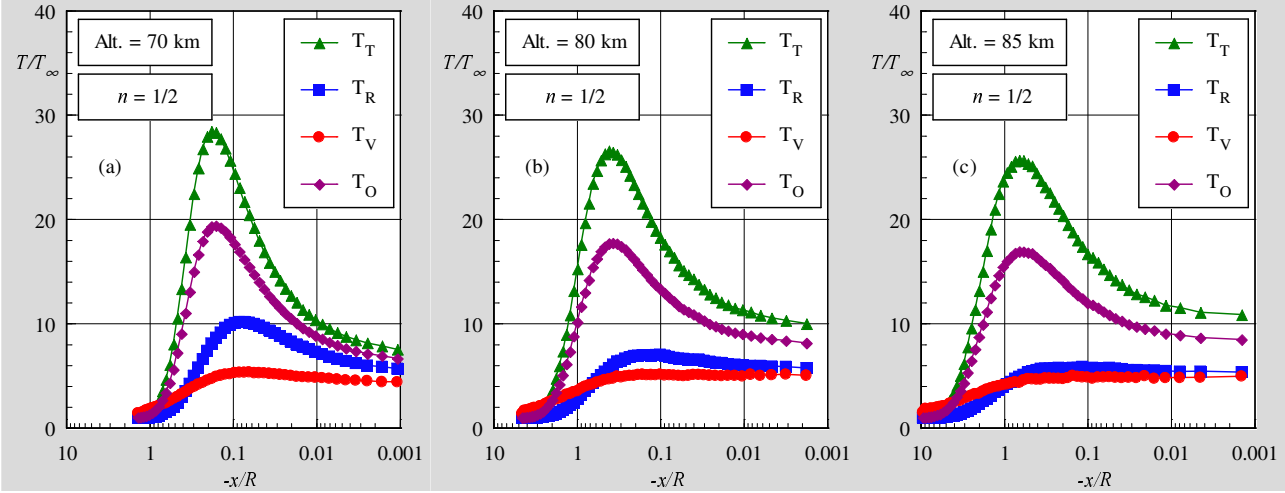

Figure 7: Kinetic temperature (T/T_∞) profiles along the stagnation streamline for leading-edge shape that corresponds to the power-law exponent of 1/2 for altitudes of (a) 70, (b) 80 and (c) 85 km.

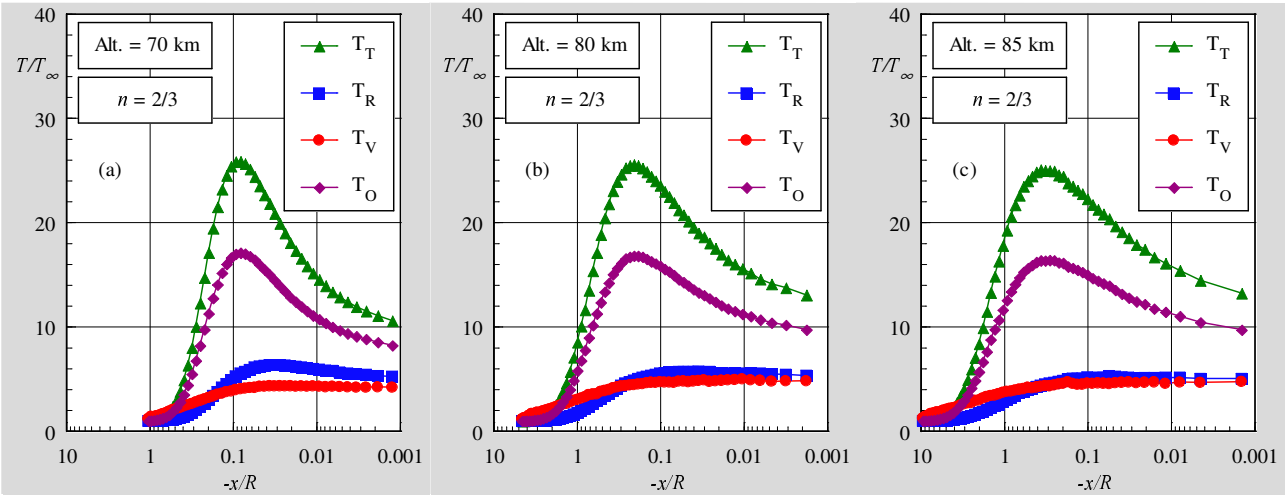

Figure 8: Kinetic temperature (T/T_∞) profiles along the stagnation streamline for leading-edge shape that corresponds to the power-law exponent of 2/3 for altitudes of (a) 70, (b) 80 and (c) 85 km.

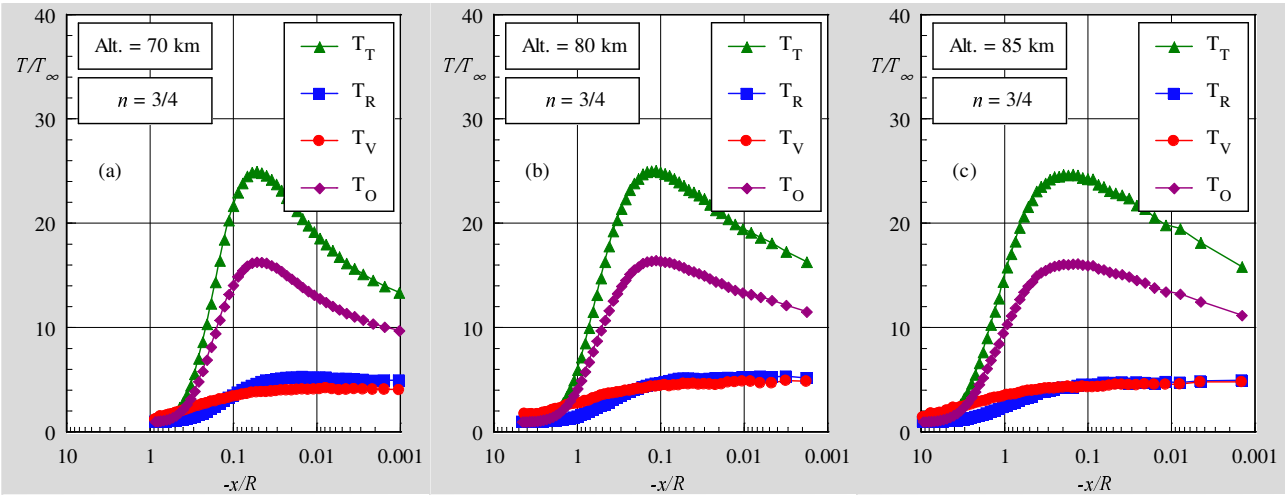

Figure 9: Kinetic temperature (T/T_∞) profiles along the stagnation streamline for leading-edge shape that corresponds to the power-law exponent of 3/4 for altitudes of (a) 70, (b) 80 and (c) 85 km.

The magnitude of the peak for the translational temperature is higher for altitude of 70 km than those for altitudes of 80 and 85 km, since the freestream temperature T_∞ corresponds to 220, 181 and 181 K, for altitudes of 70, 80 and 85 km, respectively. Although the freestream Knudsen number increases around 2.5 times as the altitude increases from 80 to 85 km, very little variation in the translational kinetic temperature peak is seen.

As the density of a flow is reduced from that of continuum conditions, the conditions of temperature continuity adjacent to the body surface are no longer satisfied. This occurs because the state of the molecules adjacent to the body surface is affected not only by the surface but also by the flow conditions at a distance of the order of a mean free path from the surface. Consequently, as the flow becomes more rarefied, the spatial region, which influences the state of the gas adjacent to the body surface, increases and gives rise to a significant temperature jump effect. This effect is more pronounced as the altitude is increased, as shown in Fig. (9). It is worth noting that the wall temperature ratio T_w/T_∞ corresponds to 4.0 for altitude of 70 km and 4.8 for altitudes of 80 and 85 km.

In an effort to provide additional information concerning the flowfield structure, dimensionless overall temperature contours on color maps are illustrated in Fig. (10). This set of plots clearly illustrates the effect of the leading-edge shapes as well as the effect of rarefaction on the flowfield structure.

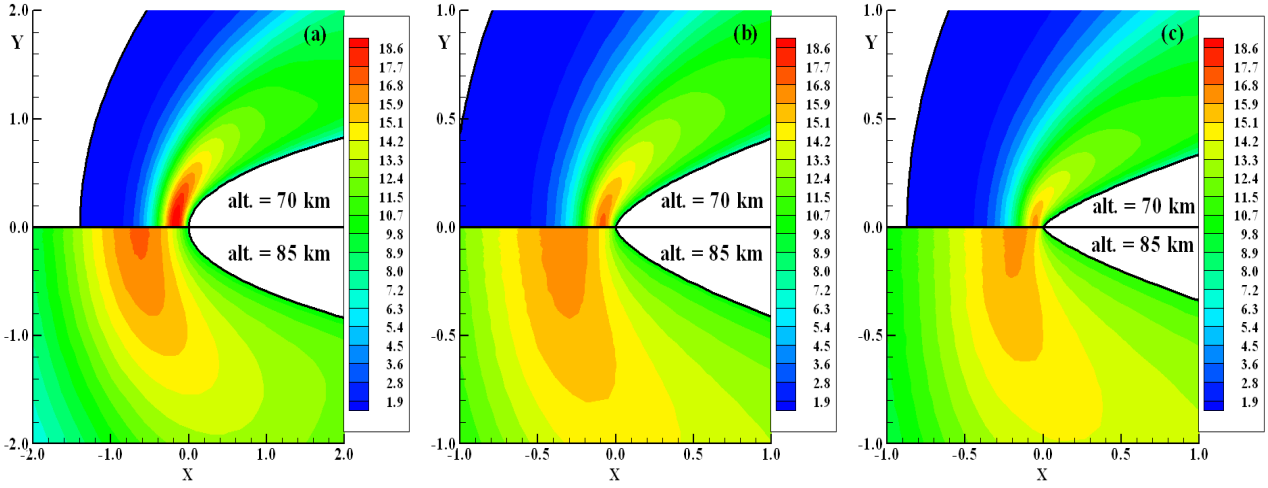

Figure 10: Overall temperature (T_O/T_∞) contours at the vicinity of the leading-edge nose as a function of the altitude for leading-edge shapes that correspond to the power-law exponents of (a) 1/2, (b) 2/3 and (c) 3/4.

5. Concluding Remarks

Computations of a rarefied hypersonic flow on power-law shaped leading edges have been performed by using the Direct Simulation Monte Carlo method. The calculations provided information concerning the nature of the flowfield structure about the primary flow properties at the vicinity of the nose and immediately adjacent to the body surface.

Effects of rarefaction on the velocity, density, pressure, and temperature for a wide range of parameters were investigated. The altitude varied from 70 to 85 km, which correspond to an increase of one order of magnitude on the freestream mean free path. In addition to that, the power-law exponent ranged from 1/2 to 3/4, corresponding blunt and sharp power-law leading edges. Cases considered in this study covered the hypersonic flow on the transitional flow regime.

It was found that changes on the altitude as well as on the shape of the leading edge disturbed the flowfield far upstream, as compared to the radius of the reference circular cylinder, and the domain of influence increased with increasing the altitude, and decreased by increasing the power-law exponent, as the leading edge became sharp. Moreover, the extent of the upstream flowfield disturbance is significantly different for each one of the primary flow properties. The domain of influence for temperature is larger than that observed for pressure and density. Since the extent of the flowfield disturbance is significantly different for each one of the leading edge shapes, this will have important implications in problems that take into account for the gas-phase chemistry and for the gas-surface catalytic activity.

6. References

Alexander, F. J., Garcia, A. L., and, Alder, B. J., 1998, "Cell Size Dependence of Transport Coefficient in Stochastic Particle Algorithms", Physics of Fluids, Vol. 10, No. 6, pp. 1540-1542.

Alexander, F. J., Garcia, A. L., and, Alder, B. J., 2000, "Erratum: Cell Size Dependence of Transport Coefficient is Stochastic Particle Algorithms", Physics of Fluids, Vol. 12, No. 3, pp. 731-731.

Anderson, J. L., 1990, "Tethered Aerothermodynamic Research for Hypersonic Waveriders", Proceedings of the 1st International Hypersonic Waverider Symposium, Univ. of Maryland, College Park, MD.

Bird, G. A., 1981, "Monte Carlo Simulation in an Engineering Context", Progress in Astronautics and Aeronautics: Rarefied gas Dynamics, Ed. Sam S. Fisher, Vol. 74, part I, AIAA New York, pp. 239-255.

Bird, G. A., 1989, "Perception of Numerical Method in Rarefied Gasdynamics", Rarefied gas Dynamics: Theoretical and Computational Techniques, Eds. E. P. Muntz, and D. P. Weaver and D. H. Capbell, Vol. 118, Progress in Astronautics and Aeronautics, AIAA, New York, pp. 374-395.

Bird, G. A., 1994, "Molecular Gas Dynamics and the Direct Simulation of Gas Flows", Oxford University Press, Oxford, England, UK.

Borgnakke, C. and Larsen, P. S., 1975, "Statistical Collision Model for Monte Carlo Simulation of Polyatomic Gas Mixture", Journal of computational Physics, Vol. 18, No. 4, pp. 405-420.

Garcia, A. L., and, Wagner, W., 2000, "Time Step Truncation Error in Direct Simulation Monte Carlo", Physics of Fluids, Vol. 12, No. 10, 2000, pp. 2621-2633.

Graves, R. E. and Argrow, B. M., 2001, "Aerodynamic Performance of an Osculating-Cone Waverider at High Altitudes", Proceedings of the 35th AIAA Thermophysics Conference, AIAA Paper 2001-2960, Anaheim, CA.

Guo, K. and Liaw, G.-S., 2001, "A Review: Boundary Conditions for the DSMC Method", Proceedings of the 35th AIAA Thermophysics Conference, AIAA Paper 2001-2953, Anaheim, CA, 11-14 June.

Haas, B. L., Fallavollita, M. A., 1994, "Flow Resolution and Domain Influence in Rarefied Hypersonic Blunt-Body Flows", Journal of Thermophysics and Heat Transfer, Vol. 8, No. 4, pp. 751-757.

Hadjiconstantinou, N. G., 2000, "Analysis of Discretization in the Direct Simulation Monte Carlo", Physics of Fluids, Vol. 12, No. 10, pp. 2634-2638.

Mason, W. H. and Lee, J., 1994, "Aerodynamically Blunt and Sharp Bodies", Journal of Spacecraft and Rockets, Vol. 31, No. 3, pp. 378-382.

Nonweiler, T. R. F., 1959, "Aerodynamic Problems of Manned Space Vehicles", Journal of the Royal Aeronautical Society, Vol. 63, Sept, pp. 521-528.

Potter, J. L. and Rockaway, J. K., 1994, "Aerodynamic Optimization for Hypersonic Flight at Very High Altitudes", Rarefied gas Dynamics: Space Science and Engineering, eds. B. D. Shizgal and D. P. Weaver, vol. 160, pp. 296-307, Progress in Astronautics and Aeronautics, AIAA New York.

Rault, D. F. G., 1994, "Aerodynamic Characteristics of a Hypersonic Viscous Optimized Waverider at High Altitude", Journal of Spacecraft and Rockets, Vol. 31, No. 5, pp. 719-727.

Santos, W. F. N. and Lewis, M. J., 2002, "Power Law Shaped Leading Edges in Rarefied Hypersonic Flow", Journal of Spacecraft and Rockets, Vol. 39, No. 6, pp. 917-925.

Santos, W. F. N. and Lewis, M. J., 2005a, "Aerothermodynamic Performance Analysis of Hypersonic Flow on Power Law Leading Edges", Journal of Spacecraft and Rockets, Vol. 42, No. 4, pp. 588-597.

Santos, W. F. N. and Lewis, M. J., 2005b, "Calculation of Shock Wave Structure over Power Law Bodies in Hypersonic Flow", Journal of Spacecraft and Rockets, Vol. 42, No. 2, pp. 213-222.

Shvets, A. I., Voronin, V. I., Blankson, I. M., Khikine, V., & Thomas, L., 2005, "On Waverider Performance with Hypersonic Flight Speed and High Altitudes", Proceedings of the 43rd AIAA Aerospace Sciences Meeting and Exhibit, AIAA Paper 2005-0512, Reno, NV.

Proceedings of the 11th Brazilian Congress of Thermal Sciences and Engineering -- ENCIT 2006
Braz. Soc. of Mechanical Sciences and Engineering -- ABCM, Curitiba, Brazil, Dec. 5-8, 2006

Paper CIT06-0487

BANCADA EXPERIMENTAL PARA TESTE DO SISTEMA PROPULSIVO DO VANT DO ITA

[1]Cristiane Aparecida Martins
Departamento de Propulsão, Instituto Tecnológico de Aeronáutica
Centro Técnico Aeroespacial, São José dos Campos, CEP 12228-210, SP, Brazil
cmartins@ita.br

[2]Carlos Guedes Neto
Departamento de Propulsão, Instituto Tecnológico de Aeronáutica
Centro Técnico Aeroespacial, São José dos Campos, CEP 12228-210, SP, Brazil
guedes@ita.br

[3]Pedro Teixeira Lacava
Departamento de Propulsão, Instituto Tecnológico de Aeronáutica
Centro Técnico Aeroespacial, São José dos Campos, CEP 12228-210, SP, Brazil
placava@ita.br

[4]Amilcar Porto Pimenta
Departamento de Propulsão, Instituto Tecnológico de Aeronáutica
Centro Técnico Aeroespacial, São José dos Campos, CEP 12228-210, SP, Brazil
amilcar@ita.br

Resumo
Este projeto foi definido no âmbito do projeto VANT do ITA. O primeiro objetivo foi selecionar os elementos do sistema propulsivo. O próximo passo consta da construção da bancada seguida de testes das propriedades relevantes ao sistema, concluindo-se com o acoplamento do sistema propulsivo a aeronave. Neste trabalho se aterá às duas primeiras etapas sem realização dos testes. Ressalta-se que o projeto VANT está sendo realizado junto a outros domínios sendo, portanto, um projeto que envolve diferentes equipes de trabalho.

Palavras Chaves: VANT, bancada para teste de motor, UAV.

1. Introdução

Veículos autônomos não tripulados (VANT) tornaram-se objetos de interesse tecnológico, civil e militar, principalmente a partir do emprego bem-sucedido por Israel, durante as operações no Líbano, em 1982 (Bone e Bolkcom, 2003). Sua maior projeção ocorreu na campanha dos Estados Unidos no Afeganistão (2001), onde além de realizarem sua missão primordial de coleta de informações começaram a ser utilizados no ataque de alvos. (Somerville, 2006). Da definição de UAV (Unmanned Aerial Vehicle) ou para o português VANT (Veículo Autonômo Não-Tripulado) "veículo aéreo motorizado que não transporta operador humano, usa forças aerodinâmicas para a sustentação aérea, pode voar de maneira autônoma ou ser pilotado por controle remoto, pode ser descartável ou recuperável e pode transportar uma carga útil letal ou não-letal."(DOD, 2006) tem como maior vantagem o fato de não expor a riscos a vida de um eventual piloto. Isso o torna bem mais barato por dispensar o sofisticado e dispendioso sistema de ejeção. Finalmente, elimina a necessidade das operações de busca e resgate que, em certas circunstâncias, são extremamente arriscadas e imprevisíveis.

O presente trabalho, tal como o título indica, insere-se no projeto VANT do ITA. Para esta aeronave o objetivo geral é realizar o imageamento (na parte visível do espectro) de elementos de linhas de transmissão de energia elétrica. Na presente fase desta pesquisa, uma aeronave prova de conceito será projetada, construída e testada para verificar se um veículo leve, sujeito a rajadas atmosféricas, é capaz de substituir um helicóptero na tarefa de fiscalização de linhas de transmissão de energia elétrica. O escopo do projeto corresponde a inspeção visual das linhas de transmissão com os seguintes objetivos: (a) Detectar proximidades de vegetação; (b) Detectar isolamentos quebrados; (c) Verificar a ocorrência de roubo de cabo e (d) Verificar queda de estrutura.

Segue abaixo a descrição do sistema propulsivo, partindo da lógica operacional que conduz a três etapas principais. Inicialmente a seleção do conjunto motor/hélice, seguido do planejamento e construção da bancada de ensaios e finalmente a implementação / integração do motor a fuselagem da aeronave. Os parágrafos seguintes estarão restritos a detalhes das duas primeiras etapas.

2. Sistema Propulsivo

Basicamente o sistema propulsivo pode ser dividido nas seguintes partes: motor, hélice, sistema de combustível e conjunto motor-hélice. A grande dificuldade na seleção e escolha de itens foi a escassez de informação. Para esta escala de aeronave não existem informações provenientes da literatura resultando na busca de soluções através da Internet e contato com alguns aeromodelistas.

Considerando-se itens similares, com resposta operacional compatível, as decisões tiveram como critério de relevância máxima o fator "confiabilidade" seguido pela facilidade de aquisição e custo. A facilidade de aquisição se justifica uma vez que neste segmento grande parte dos itens é importada, o que torna muitas vezes determinada escolha inviável pela demora que acarretará ao prosseguimento do projeto.

Nesta etapa deverão ser detalhados cada item com os respectivos parâmetros mostrados na Tabela 1. Assim serão fornecidas informações necessárias aos grupos responsáveis pela estrutura, aerodinâmica, mecânica do vôo e sistemas.

Tabela 1: Parâmetros do Sistema Propulsivo - Configuração A-1

Elemento	Parâmetro	
Motor	Peso	
	Dimensão longitudinal	
	Dimensão Transversal	
	Dimensão Vertical	
	Consumo específico	
	Potência máxima com escapamento	
	Requisitos do atuador p/ controle do motor	Torque
		Velocidade
Hélice (24 x10)	Peso	
	Diâmetro	
	Passo	
	Rotação máxima	
	Eficiência	
	Tração máxima	
	Posição longitudinal do eixo da hélice (X)	
	Posição vertical do eixo da hélice (Z)	
	Momento de inércia da hélice	
Sistema de Combustível	Peso do combustível (30 minutos de operação)	
	Densidade do combustível	
	Volume de combustível	
	Peso do tanque de combustível (seco)	
	Dimensão longitudinal do tanque	
	Dimensão transversal do tanque	
	Dimensão vertical do tanque	
	Posição longitudinal do CG do tanque (X)	
	Posição vertical do CG do tanque (Z)	
Conjunto Motor-hélice	Torque transmitido p/ a aeronave (max)	

2.1 Seleção do Motor

A primeira fase de seleção dos motores foi precedida pela definição das características gerais do VANT e, com base nesses pressupostos de projeto, estimativa da potência necessária. O grupo de mecânica de vôo nos forneceu o valor da potência necessária. Deveríamos selecionar um motor com estrutura simples, leve e compacto para atender as exigências da estrutura e aerodinâmica. Optou-se de imediato pela solução de motor de combustão interna, principalmente por apresentar melhor relação peso / potência. Outras possibilidades seriam motor elétrico e turbina. Motor elétrico, em geral é solução utilizada em aeronaves de pequena dimensão, devido a restrição decorrente do

elevado peso de um conjunto motor elétrico e bateria capaz de fornecer maior potência e autonomia. A solução menos convencional para a aplicação prevista que é o caso das turbinas, ainda possui alto custo.

Basicamente para escolha do motor**,** quatro itens foram levados em conta: segurança (carga valiosa), potência necessária para cumprir a missão em qualquer fase do envelope de vôo, incluído situações inesperadas (ex: rajadas), baixo consumo de combustível (isso interfere no peso de tanque molhado ou no alcance da missão) e peso do motor. Considerando tais critérios de escolha a configuração final deveria representar uma solução de compromisso entre eles.

Dentre os quatros requisitos citados no parágrafo anterior, alguns parâmetros mínimos foram especificados e são listados na seqüência.

Potência no eixo: Segundo as simulações de mecânica de vôo, em condições de rajada pode-se necessitar do motor uma potência de eixo de até 5hp; assim, por segurança, definiu-se como potência máxima de eixo no mínimo 6hp.

Cilindros: dois dispostos lado a lado. A presença de dois cilindros suaviza o funcionamento do motor, ou seja, induz menos vibração. Também aumenta a segurança, pois no caso de uma falha de abastecimento ou pane na ignição de um dos cilindros, será possível "trazer" a aeronave.

Tipo de ciclo de funcionamento: dois tempos. Motores mais simples e sem a presença de válvulas (menos peso).

Combustível e ignição da mistura: gasolina e centelha. Os motores a gasolina são mais econômicos e sofrem menos problemas de apagamento. O combustível é mais barato, mas será necessária uma atenção especial para o problema de a centelha interferir nos equipamentos eletrônicos. Outra questão importante é que esse tipo de motor estar mais próximo do funcionamento de motor aeronáutico de maior escala. Assim sendo, haveria maior confiança nos modelos.

Peso do motor: não superior a 4kg.

Refrigeração: pelo fluxo de ar, o que torna o motor mais leve e evita a presença de um sistema de refrigeração fechado (radiador, mangueiras, etc.), acarretando em uma maior peso.

Motores de diferentes fabricantes foram analisados entre estes os da marca Moki, OS Engines, Kroma (fabricante nacional) e Zenoah. Após seleção de motores com desempenho teóricos similares restringimos a escolha entre dois deles. Ambos, em princípio, atenderiam ao projeto. O primeiro, da marca Kroma modelo 100i, e segundo, da marca Zenoah modelo 80GT. A Fig. 2 os mostra lado a lado.

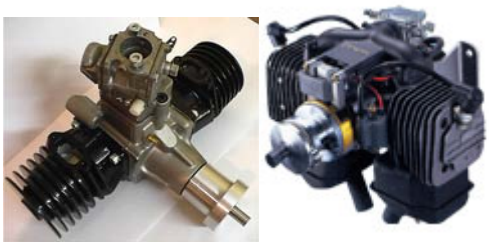

Figura 2 : Motor Kroma 100i / Zenoah 80GT, respectivamente, (Kroma, 2006 e Zenoah, 2006)

O fabricante nacional tem como principal vantagem a facilidade de aquisição e contato. Muito embora, dúvidas e informações requisitadas ao fabricante japonês tenham sido sempre prontamente respondidas. Outra observação é que por possuir representante no Brasil, não precisaríamos esperar pela importação do motor, uma vez que seu representante possuía o equipamento na prateleira. Desta forma foi possível nos fixarmos apenas nas características técnicas dos motores. A Tabela II apresenta as principais características de ambos. Destas encontramos diferenças consideráveis no peso e no sistema de ignição. A Zenoah teve a seu favor também a maior quantidade de informação sobre o desempenho e característica do motor, nos fornecendo, por exemplo, a curva característica do motor.

Tabela 2 - Características dos motores -

Características	Kroma 100i	Zenoah 80 GT	Unidade
Fabricante	Nacional	Japonês	
Tipo	Bi-cilindrico	Bi-cilindrico	
Potência Máx	10.0 valor bruto	6.0 (4.41), valor líquido	hp (kW)
Torque Máx (valor líquido)	----	0.54	kg.m

Deslocamento	100	80	cm^3
Peso	2,3 (s/escape)	3,6 (c/ escape)	kg
rotação	máxima 7400	1800-10000	rpm
Partida		Sistema de mola	
Combustível	Pré mistura, 25 (Gasolina): 1 (óleo sintético)	Pré mistura, 25 (Gasolina): 1 (óleo sintético)	
Dimensões (CxLxA)		192 x 257 x 205	mm
Ignição	centelha (eletrônica)	centelha (magneto)	
Preço	R$ 2850.00 (c/ escape)	US$ 1300.00	

Abaixo segue a ponderação sobre a principal diferença entre os dois motores (sistema de ignição). Num motor de combustão interna de ignição por centelha, a inflamação da mistura carburada é produzida por uma faísca que sai entre os dois eletrodos da vela. Para que haja faísca, isto é, para que a corrente atravesse a mistura fortemente comprimida, é necessário que uma tensão de 6.000 a 12.000 volts seja desenvolvida. Esta corrente de ignição pode ser produzida de dois modos diferentes:

1) Com a ajuda de um sistema de ignição por bateria. É um conjunto de aparelhos utilizando a corrente fornecida pela bateria de acumuladores (6 ou 12 volts). Esta corrente de bateria é transformada em corrente de alta tensão e, depois, distribuída às velas do motor. (motor Kroma)

2) Com a ajuda de um sistema de ignição por magneto. O magneto é um aparelho que transforma a energia mecânica em energia elétrica a alta tensão, assegurando igualmente a distribuição desta corrente às velas do motor. (motor Zenoah)

Optamos pelo motor Zenoah, uma vez que o sistema por magneto possui, teoricamente, menor possibilidade de falha. Muito embora apresente maior atraso no tempo de resposta. Até serem feitos testes efetivos não podemos afirmar se tal atraso irá influenciar sobremaneira na aeronave.

2. Hélices

Hélice tem a tarefa de transformar potência do motor em empuxo da melhor maneira possível. Devido a alta velocidade de rotação, e a alta potência, em geral são fabricadas em madeira ou material composto. Ao serem fabricadas com material composto (resina epoxi, por exemplo) são utilizados moldes os quais permitem reprodução exata através de uma hélice mestra. Hélices de madeira são mais leves e reduzem o nível de vibração, mas são mais delicadas no manuseio, além de não serem de fácil reprodução. As de material composto são mais facilmente ajustadas na parte fina do aerofólio no topo do hélice.

A pesquisa realizada indicou que o modelo tri-pá possui maior estabilidade, entretanto, este tipo de hélice é pouco comercial. Os modelos de hélice sugeridos pelo fabricante são 22x12 e 24x10 bi-pá. Adquirimos hélice de madeira da marca Zinger 24 x8, Zinger 24 x 10, JC 26 x 8, JC 22 x12, JC 24 x 12. Serão ainda realizados testes.

3. Sistema de Combustível

Considerando-se o consumo especifico do motor, o tempo de operação e a segurança, a escolha foi de dois tanques com a dimensão tanque de 50 oz (~1500 cc) modelo Du-Bro (DUBR 692), mostrado na Fig. 3.

Figura 3: Tanque de combustível - DU-BRO 692, dimensões (CxLx A) = 212,7 x 111,1x 88,9 mm

Finalmente temos a partir de dados gerados pelo próprio grupo de propulsão ou determinado pelos outros grupos a Tabela 1 com seus respectivos valores, mostrada como Tab. 3.

Tabela 3: Parâmetros do Sistema Propulsivo - Configuração I - completa

Elemento	Parâmetro		Valor	Unid.
Motor	Peso		3,6	kg
	Dimensão longitudinal		0,192	m
	Dimensão Transversal		0,257	m
	Dimensão Vertical		0,205	m
	Consumo específico (CSF) @7200 rpm, 5,5 hp		0,49	kg/(hp h)
	Potência máxima com escapamento		6	hp
	Requisitos do atuador p/ controle do motor	Torque	0,54	kgf. m
		Velocidade	7200	rpm
Hélice (24 x10)	Peso		0,5	kg
	Diâmetro		0,6096	m
	Passo		0,254	m
	Rotação máxima		10000	rpm
	Eficiência (pior caso)		0,6	
	Tração máxima			
	Posição longitudinal do eixo da hélice (X)		0	
	Posição vertical do eixo da hélice (Z)		0	
	Momento de inércia da hélice			
Sistema de Combustível	Peso do combustível (30 minutos de operação)		1,5	kg
	Densidade do combustível		0,74	kg/l
	Volume de combustível		2	l
	Peso do tanque de combustível (seco)		0,2	Kg
	Dimensão longitudinal do tanque		212,2	mm
	Dimensão transversal do tanque		88,9	mm
	Dimensão vertical do tanque		111,1	mm
	Posição longitudinal do CG do tanque (X)			
	Posição vertical do CG do tanque (Z)			
Conjunto Motor-hélice	Torque transmitido p/ a aeronave (max)		0,54 @7200rpm	kgf. m

Com a Tab. 3 finaliza-se a descrição geral do sistema propulsivo. Na seção seguinte será descrita a bancada de testes.

3. Bancada

O desempenho de um motor, combustão interna ou elétrico, é usualmente dado pela potência P (w ou hp) versus rotação n (rotações por minuto). Primeiramente efetua-se a seleção dos instrumentos de medidas seguida pela montagem da bancada.

3.1 Sistemas de Medidas

3.1.1 Velocidade de Rotação - [1/min]

As opções para obtenção deste parâmetro são tacômetros digitais, luz estroboscópica ou uso de circuito utilizando sistema ótico.

Ao utilizarmos o tacômetro nos deparamos com duas desvantagens. Primeiro foi necessário aproximarmos muito o instrumento da hélice, o que causa certo desconforto no critério de segurança em seguida percebemos certa interferência com relação à luz ambiente. Já a luz estroboscópica resulta em valores de medida bastante precisos, entretanto no túnel de vento, onde serão realizados os testes, sua utilização é pouco prática. Resta-nos, portanto, o circuito com sistema ótico. O medidor de rotação foi projetado baseado em um circuito óptico (no espectro infravermelho). Obtivemos com tal sistema resultados similares aos dois métodos anteriores tendo a facilidade de segurança em relação a proximidade da hélice sem interferência eletrônica e mais facilmente adaptável ao sistema de túnel de vento.

3.1.2 Tração - [N]

A tração da aeronave pode ser obtida posicionando de forma adequada uma célula de carga, de modo que ao tracionarmos, empurrando para frente ou para trás, esta força seja obtida. Um esquema é mostrado na Fig.4.

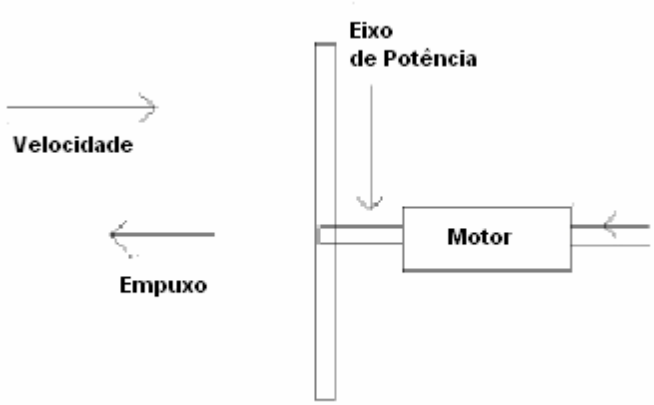

Figura 4 - Esquema do sistema de medida de tração

3.1.3 Torque - [Nm]

O torque pode ser obtido de diferentes formas. Um arranjo experimental relativamente simples pode ser construído. A idéia geral é fixar o motor a um eixo, o qual está em paralelo com o virabrequim. Acoplar um braço com certa distância D sendo que a esse braço acoplaremos uma balança de prato. Nesta balança serão colocados os pesos para calibração. Deslocado do centro a uma pequena distância d, está acoplada uma célula de carga que será responsável pela medição do torque imposto a aeronave pelo peso ou posteriormente pelo giro da hélice. Atente-se que a força medida pela célula de carga não é a mesma força imposta a balança, mas o torque sim, este é de mesmo valor. Este mesmo princípio pode ser utilizado para diferentes tamanhos de motores, bastando utilizar diferentes braços de alavanca. A Fig. 5 mostra um esquema do princípio utilizado para medição de torque.

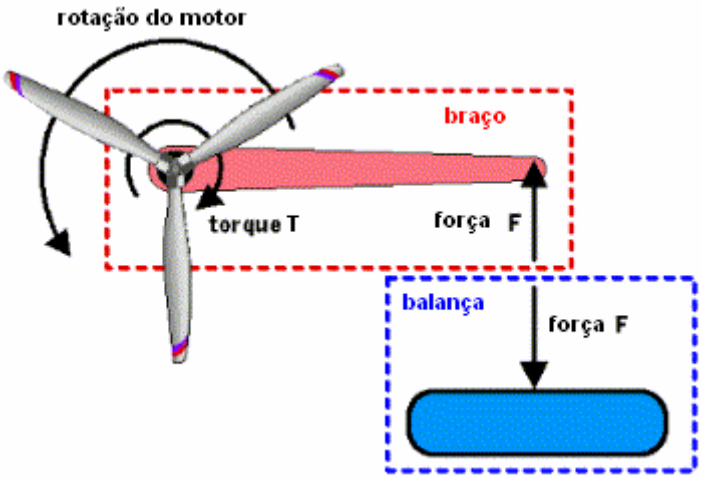

Figura 5: Esquema das forças e momento atuando no braço e balança (Figura adaptada http://www.mh-aerotools.de/airfoils/engingeperformance.htm)

Para o motor Zenoah 80 GT com torque máximo de 0.54 kg.m se utilizarmos um braço de 250 mm, por exemplo, teremos que calibrar com pesos até 2,20 kg. Os testes de bancada resultarão na curva torque vs. rpm. Esses resultados rearranjados resultam na curva potência versus torque, através da equação:

$P = T / (n/60 \cdot 2\pi)$, onde P = Potência, T = torque e n rotações.

3.1.4. Sistema de aquisição de dados

Os sistemas de medida serão acoplados a um sistema de aquisição de dados baseado em placas de aquisição e módulos de condicionamento (SCXI) da National Instruments tendo como software de trabalho o LabVIEW.

3.2 - Montagem experimental

A montagem experimental completa consta do acoplamento de um sistema de medida de torque, tração, pressão dinâmica e rotação. A medida de pressão dinâmica será realizada com tubo de Pitot e manômetro Betz adequadamente conectado ao túnel de vento. Serão realizadas as calibrações de cada sistema de medida, antes do início dos testes. Tanto as medidas de tração quanto de torque serão realizadas utilizando células de carga. Tais células foram construídas no próprio laboratório e serão realizados testes de sensibilidade, uma vez que as mesmas deverão ter capacidade de perceber a força aplicada de forma adequada. Caso contrário, pode ocorrer que não seja sensibilizada ou o oposto. Testes serão ainda realizados de forma que o sinal gerado fique entre 0 - 10 volts. A Fig. 6 mostra o sistema projetado e construído, com detalhe para sensor de força para medida de tração, sensor de força para torque e o montante para fixação do motor.

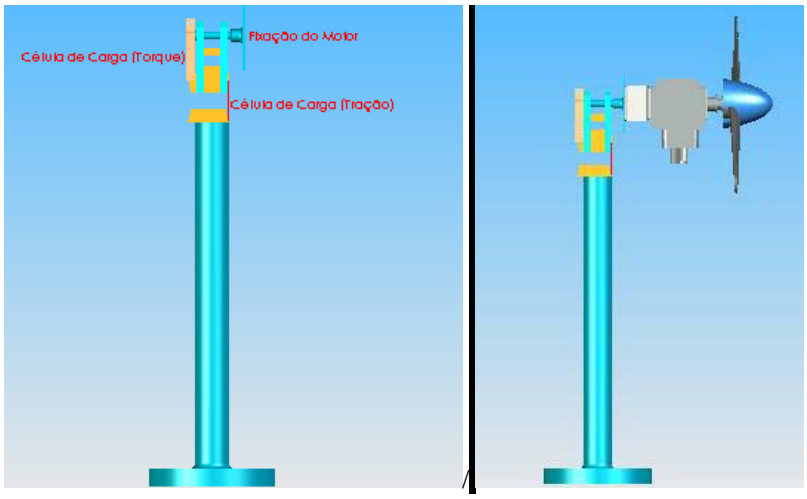

Figura 6: Montagem experimental para medida de torque e tração: (a) detalhe das partes, (b) motor acoplado.

Para maior detalhamento de cada detalhe da cabeça da montagem, abaixo a Fig. 7 (a), (b) e (c).

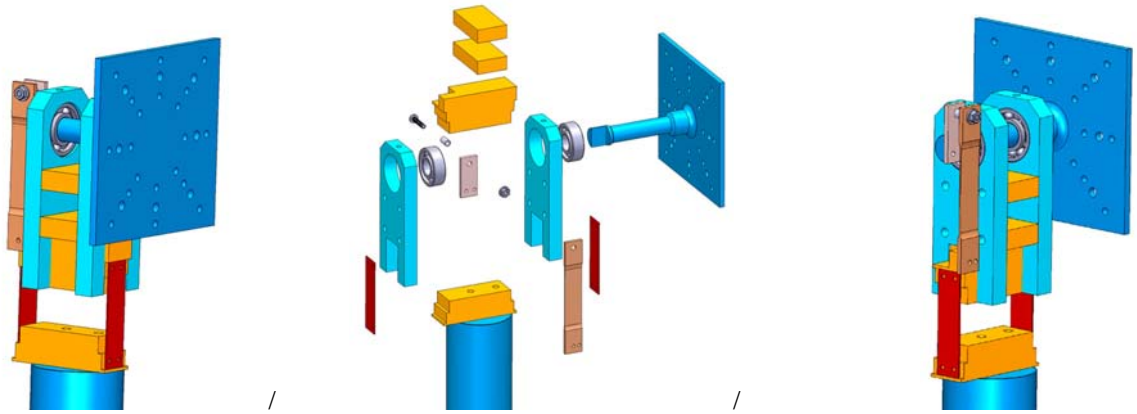

Figura 7: Cabeça da montagem: (a) vista frontal (b) Vista explodida e (C) Vista traseira.

4. Conclusão

O trabalho descreveu desde a escolha do motor e dos outros componentes do sistema propulsivo até a montagem da bancada experimental. A construção da bancada já se finalizou. Na próxima fase serão realizados testes do motor propriamente ditos, juntamente com alguns ajustes na bancada, caso necessário.

5. Agradecimentos

Ao MCT/FINEP/Ação Transversal - Cooperativos - no. 243/2004. Ao Sr. Gilberto Simão, desenhista.

6. Bibliografia

Bone E. e Bolkcom C., *Unmanned Aerial Vehicles: Background and Issues for Congress*, 25 April 2003, 2. Disponível em: www.fas.org/irp/crs/RL31872.pdf.

DOD- "Dictionary of Military and Associated Terms", Disponível em http://www.dtic.mil/doctrine/jel/doddict/data/u/05642.html, consultado em 25/05/2006.

Kroma, 2006, http://www.lem.com.br.

Somerville K., "US Drone Takes Combat Rol*e*", BBC News Online, 5 November 2002. Disponível em: http://news.bbc.co.uk/1/hi/world/2404425.stm.

Zenoah, 2006, http://www.zenoah.net.

EXPERIMENTAL BENCH OF PROPULSION SYSTEM OF UAV-ITA

[2]Cristiane Aparecida Martins
Departamento de Propulsão, Instituto Tecnológico de Aeronáutica
cmartins@ita.br

[2]Carlos Guedes Neto
Departamento de Propulsão, Instituto Tecnológico de Aeronáutica
guedes@ita.br

[3]Pedro Teixeira Lacava
Departamento de Propulsão, Instituto Tecnológico de Aeronáutica
placava@ita.br

[4]Amilcar Porto Pimenta
Departamento de Propulsão, Instituto Tecnológico de Aeronáutica
amilcar@ita.br

Abstract
In this project was defined within the ambit of the VANT from ITA project. The first goal was to select of propulsion elements. The next step would have been the bench test of the relevant properties of the selected engines and system. The last goal would have been the implementation of the propulsion elements (the engines) on the VANT, in which are included several aspects. Although these were the three main goals, much more was done in other domains, because making an VANT project involves team work in the design, coordination and logistics of the project, which went far beyond what was expected at first.

Keywords: VANT, Propulsion System Characterization, UAV

Proceedings of the 11th Brazilian Congress of Thermal Sciences and Engineering -- ENCIT 2006
Braz. Soc. of Mechanical Sciences and Engineering -- ABCM, Curitiba, Brazil,- Dec. 5-8, 2006

Paper CIT06-0490

COMPRESSIBILITY EFFECT ON AERODYNAMIC HEATING AND DRAG OF HYPERSONIC FLOW OVER FLAT-NOSE LEADING EDGES

Wilson F. N. Santos
Combustion and Propulsion Laboratory
National Institute for Space Research
12630-000 Cachoeira Paulista, SP, Brazil
wilson@lcp.inpe.br

Abstract. *In designing rarefied hypersonic vehicles one fundamental problem that must be solved regards the aerodynamics of re-entry. This challenging problem is nowadays handled by using the Direct Simulation Monte Carlo (DSMC) method In this work, the hypersonic two-dimensional flow around a family of blunt leading edges at an altitude of 70 km is investigated by using the DSMC method. The effect of compressibility on the aerodynamic surface quantities is investigated for flat-nose leading edges. Numerical simulations were performed for freestream Mach numbers of 5, 8 and 12. The aerothermodynamic performance of the flat-nose leading edges is assessed by using the pressure, skin friction, heat transfer and total drag coefficients. The calculation results depict a weak effect of the leading-edge thickness on total drag, while predict a significant dependence of drag on the freestream Mach number over the range examined. The data generated in the present account is part of an investigation in order to determine and to quantify the benefits and disadvantages of using these new blunt shapes over circular cylinder shapes.*

Keywords. *DSMC, aerodynamic heating, hypersonic flow, rarefied flow, blunt leading edge.*

1. Introduction

Hypersonic vehicles experience severe aerothermodynamic heating during the atmospheric entry path. As a result, the design of a thermal protection system in order to protect the vehicles from the intense heat load is a critical task. The selection of material type depends on the surface temperature, which is determined from the local heat transfer rate. In addition, the nose radius or nose tip for hypersonic vehicles is determined so that the maximum surface temperature does not exceed the upper limit temperature of the material used for thermal protection system. Due mainly to improvements in the material used for thermal protection system, the radius of the leading edges or nose tips can be reduced significantly. Consequently, the wave drag is reduced and the aerodynamic efficiency is improved.

A method of designing low heat transfer bodies is devised on the premise that the rate of heat transfer to the nose will be low if the local velocity is low, while the rate of heat transfer to the afterbody will be low if the local density is low (Reller, 1957). A typical body that results from this design method consists of a flat nose followed by a highly curved, but for the most part slightly inclined, afterbody surface. Due mainly to manufacturing problems and the extremely high temperatures attained in hypersonic flight, flat-nose leading edges have been considered (Santos, 2003, 2004, and 2005) as especially promising bluntness for hypersonic configurations.

Santos (2003) has investigated the effect of the leading-edge thickness on the flowfield structure over these flat-nose leading edges. The thickness effect was examined for a range of Knudsen number, based on the thickness of the flat nose, covering from the transitional flow regime to the free molecular flow regime. The emphasis of the work was to compare the heat transfer and drag of these new flat-nose leading edges with those obtained for circular cylinder shape, typically assumed as the appropriate blunting geometry for heat transfer considerations. It was found that flat-nose leading edges provided much smaller drag than round leading edges. Nevertheless, round leading edge still presented smaller stagnation point heating than flat-nose leading edges for the conditions investigated. Nevertheless, flat-nose bodies have more volume than round leading edges. In this respect, the overall heat transfer to these leading edges may be tolerate if there is an active cooling, since additional coolant may be placed in the leading edge.

Santos (2004) has extended the analysis presented by Santos (2003) by performing a parametric study on these shapes with a great deal of emphasis placed on the wall temperature effects. In this scenario, the primary aim was to assess the sensitivity of the pressure, skin friction, heat transfer and drag coefficients to variations on the body surface temperature. Calculations showed that the heat transfer coefficient decreased with increasing the wall temperature. It was also found that the total drag slightly increased by increasing the wall temperature.

The works of Santos (2003 and 2004) have been concentrated primarily on the analysis of the flowfield structure by considering the diffuse reflection model as being the gas-surface interaction. Nonetheless, as a space flight vehicle is exposed to a rarefied environment over a considerable time, a departure from the fully diffuse model is observed, resulting from the colliding molecules that clean the surface of the vehicle, which becomes gradually decontaminated. In this scenario, Santos (2005) has performed a parametric study on these shapes with a great effort placed on the gas-surface interaction effects. The primary idea of the paper was to assess the sensitivity of the flowfield structure to variations on the surface accommodation coefficients experienced by the leading edges.

In order to provide information on how well these shapes stand up as possible candidates for blunting geometries of

hypersonic leading edges, the present account extends the analysis presented by Santos (2003, 2004 and 2005) by performing a parametric study on these shapes with a great deal of emphasis placed on the compressibility effects. In this connection, this study will objectively assess the sensitivity of the aerodynamic surface quantities, such as pressure, skin friction, heat transfer and drag coefficients, to variations on the freestream Mach number.

The study at hand focuses on the low-density region in the upper atmosphere. High-speed flows under low-density conditions deviate from a perfect gas behavior because of the excitation of rotation, vibration and possible dissociation. At high altitudes, and therefore, low density, the molecular collision rate is low and the energy exchange occurs under non-equilibrium conditions. In such a circumstance, the degree of molecular non-equilibrium is such that the Navier-Stokes equations are inappropriate. Therefore, the Direct Simulation Monte Carlo method will be employed to calculate the hypersonic two-dimensional flow on the leading edges.

2. Leading-Edge Configuration

In dimensionless form, the contour that defines the shape of the afterbody surface (Santos, 2003, 2004 and 2005) is as following,

$$\bar{x} = \int_{\bar{y}=1}^{\bar{y}=\bar{y}_{\max}} \sqrt{\bar{y}^{k} - 1}\, d\bar{y} \tag{1}$$

where $\bar{x} = x/y_{nose}$ and $\bar{y} = y/y_{nose}$.

The blunt shapes are modeled by assuming a sharp leading edge of half angle θ with a circular cylinder of radius R inscribed tangent to the wedge. The blunt shapes, inscribed between the wedge and the cylinder, are also tangent to them at the same common point where they have the same slope angle. It was assumed a leading edge half angle of 10 degrees, a circular cylinder diameter of 10^{-2}m and flat-nose thickness t/λ_∞ of 0.01, 0.1 and 1, where $t = 2y_{nose}$ and λ_∞ is the freestream mean free path. Figure (1a) illustrates this construction for the set of shapes investigated. From geometric considerations, the exponent k in Eq. (1) is obtained by matching slope on the wedge, circular cylinder and on the body shapes at the tangency point. For dimensionless thickness t/λ_∞ of 0.01, 0.1 and 1, the exponent k corresponds to 0.501, 0.746 and 1.465, respectively. The common body height H and the body length L are obtained in a straightforward manner. It was assumed that the leading edges are infinitely long but only the length L is considered, since the wake region behind the leading edges is not of interest in this investigation.

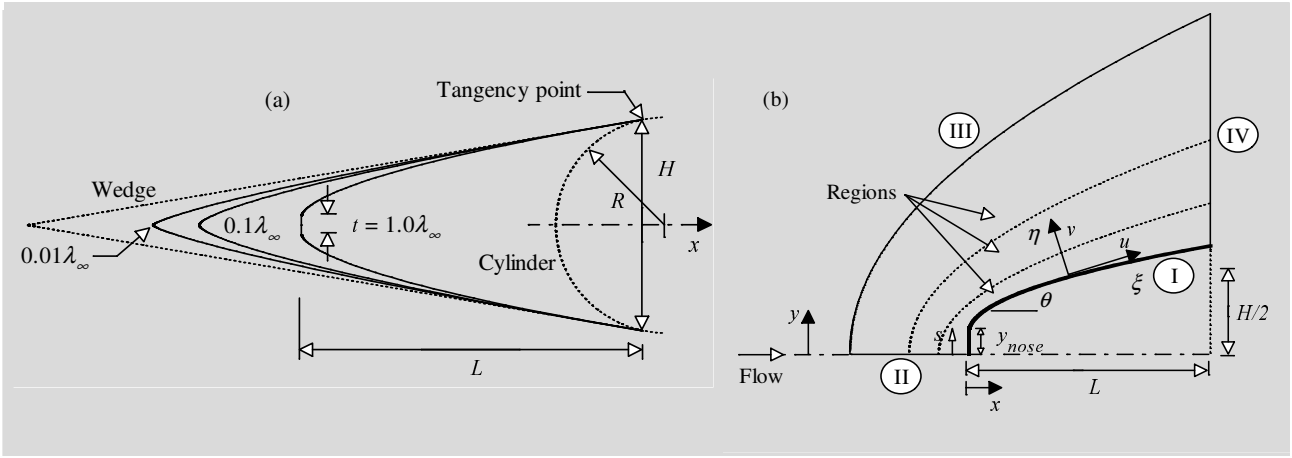

Figure 1: Drawing illustrating (a) the leading edge shapes and (b) the computational domain.

3. Computational Method and Procedure

Navier-Stokes equations, based on the continuum approximation, are adequate to model the fluid behavior for a large class of flows. Continuum approximation implies that the molecular mean free path λ is much smaller than the characteristic length l of interest. It means that the Knudsen number $Kn = \lambda/l << 0.1$. Nevertheless, for a variety of flows, the Knudsen number Kn is of $O(1)$, and the continuum assumption is not valid. In this type of flows, the gas is neither completely in the continuum regime nor in the free molecular flow regime. In this fashion, the flows have been categorized as transitional flows. Examples of such flows are the hypersonic flows about space vehicles or flows in microchannels of microelectro-mechanical (MEMS) devices. In high altitude hypersonic flows, the high Knudsen numbers are mainly due to low density, while in microscale flows the small characteristic length scale results in regions of high Knudsen number, since the flows occur at atmospheric conditions.

Nowadays, the Direct Simulation Monte Carlo (DSMC) method (Bird, 1994), pioneered by Bird in 1960's, has been considered as the most accurate and widely used technique for computation of low density flows. In the DSMC method, the real gas is modeled by thousands or millions of simulated molecules in a computer. The positions, energies and velocity components of the molecules are stored by the computer and are modified over time as the molecules undergo representative intermolecular collisions and boundary interactions in the simulated physical space. Particles that strike the solid wall would reflect according to the appropriate gas-surface interaction model, specular, diffusive or a combination of these. In the collision phase, intermolecular collisions are performed according to the theory of probability without time being consumed. In this context, the intermolecular collisions are uncoupled to the translational molecular motion over the time step used to advance the simulation. Time is advanced in discrete steps such that each step is small in comparison with the mean collision time (Garcia and Wagner, 2000, and Hadjiconstantinou, 2000). All simulations are of an unsteady nature and the time parameter in the simulations may be identified with physical time. For a steady flow problem, the solution is the asymptotic limit of the unsteady flow.

The molecular collisions are modeled using the variable hard sphere (VHS) molecular model (Bird, 1981) and the no time counter (NTC) collision sampling technique (Bird, 1989). The energy exchange between kinetic and internal modes is controlled by the Borgnakke-Larsen statistical model (Borgnakke and Larsen, 1975). Simulations are performed using a non-reacting gas model consisting of two chemical species, N_2 and O_2. Energy exchanges between the translational and internal modes are considered. For a given collision, the probabilities are designated by the inverse of the relaxation numbers, which correspond to the number of collisions necessary, on average, for a molecule to relax. In this simulation, the relaxation number is 5 for rotation and 50 for vibration.

The simulated physical space is divided into an arbitrary number of regions, which are subdivided into computational cells. The cells are further subdivided into four subcells, two subcells/cell in each Coordinate direction. The cell provides a convenient reference sampling of the macroscopic gas properties, whereas the collision partners are selected from the same subcell for the establishment of the collision rate. As a result, the flow resolution is much higher than the cell resolution. The dimensions of the cells must be such that the change in flow properties across each cell is small. The linear dimensions of the cells should be small in comparison with the scale length of the macroscopic flow gradients normal to the streamwise directions, which means that the cell dimensions should be of the order of the local mean free path or even smaller (Alexander et al., 1998 and Alexander et al., 2000).

The computational domain used for the calculation is made large enough so that body disturbances do not reach the upstream and side boundaries, where freestream conditions are specified. A schematic view of the computational domain is depicted in Fig. (1b). According to this figure, side I is defined by the body surface. Diffuse reflection with complete thermal accommodation is the condition applied to this side. In a diffuse reflection, the molecules are reflected equally in all directions, and the final velocity of the molecules is randomly assigned according to a half-range Maxwellian distribution determined by the wall temperature. Advantage of the flow symmetry is taken into account, and molecular simulation is applied to one-half of a full configuration. Thus, side II is a plane of symmetry. In such a boundary, all flow gradients normal to the plane are zero. At the molecular level, this plane is equivalent to a specular reflecting boundary. Side III is the freestream side through which simulated molecules enter and exit. Finally, the flow at the downstream outflow boundary, side IV, is predominantly supersonic and vacuum condition is specified (Guo and Liaw, 2001). At this boundary, simulated molecules can only exit.

Numerical accuracy in DSMC method depends on the grid resolution chosen as well as the number of particles per computational cell. Both effects were investigated to determine the number of cells and the number of particles required to achieve grid independence solutions. Grid independence was tested by running the calculations with half and double the number of cells in ξ and η directions (see Fig. (1b)) compared to a standard grid. Solutions (not shown) were near identical for all grids used and were considered fully grid independent.

4. Computational Conditions

The freestream and flow conditions used in the present calculations are those given by Santos (2003) and summarized in Tab. (1). The gas properties considered in the simulation are those given by Bird (1994) and tabulated in Tab. (2).

In order to simulate the compressibility effects, the freestream velocity V_∞ was assumed to be constant at 1.49, 2.38 and 3.56 km/s, which correspond to freestream Mach number M_∞ of 5, 8, and 12, respectively. The temperature T_w on the leading-edge surfaces is assumed constant at 880 K, which corresponds to 4 times the freestream temperature T_∞. This temperature is chosen to be representative of the surface temperature near the stagnation point.

Table 1: Freestream Conditions

Temperature T_∞ (K)	Pressure p_∞ (N/m^2)	Density ρ_∞ (kg/m^3)	Number density n_∞ (m^{-3})	Viscosity μ_∞ (Ns/m^2)	Mean free path λ_∞ (m)
220.0	5.582	8.753×10^{-5}	1.8209×10^{21}	1.455×10^{-5}	9.03×10^{-4}

Table 2: Gas Properties

	Mole fraction X	Molecular mass m (kg)	Molecular diameter d (m)	Viscosity Index ω
O_2	0.237	5.312×10^{-26}	4.01×10^{-10}	0.77
N_2	0.763	4.65×10^{-26}	4.11×10^{-10}	0.74

The overall Knudsen number Kn_t, defined as the ratio of the freestream mean free path λ_∞ to the leading edge thickness t, corresponds to 100, 10 and 1 for leading edge thickness t/λ_∞ of 0.01, 0.1 and 1, respectively. The Reynolds number Re_t covers the range from 0.193 to 19.3, based on conditions in the undisturbed stream with leading edge thickness t as the characteristic length.

5. Computational Results and Discussion

In order to assess the overall performance of the leading edges, this section will discuss and compare differences on the aerodynamic surface quantities due to the compressibility effects. Aerodynamic surface quantities of particular interest in the transition flow regime are number flux, heat transfer rate, wall pressure, wall shear stress and drag.

5.1. Number Flux

The number flux N is calculated by sampling the molecules impinging on the surface by unit time and unit area. The sensitivity of the dimensionless number flux to variations on the leading-edge thickness and on the freestream Mach number is illustrated in Figs. (2a), (2b) and (2c) for leading-edge thicknesses t/λ_∞ of 0.01, 0.1 and 1, which correspond to thickness Knudsen number Kn_t of 100, 10 and 1, respectively. In this set of figures, the dimensionless number flux N_f stands for the number flux N normalized by $n_\infty V_\infty$, where n_∞ is the freestream number density and V_∞ is the freestream velocity. Also, S is the arc length s along the body surface, measured from the stagnation point, normalized by the freestream mean free path λ_∞.

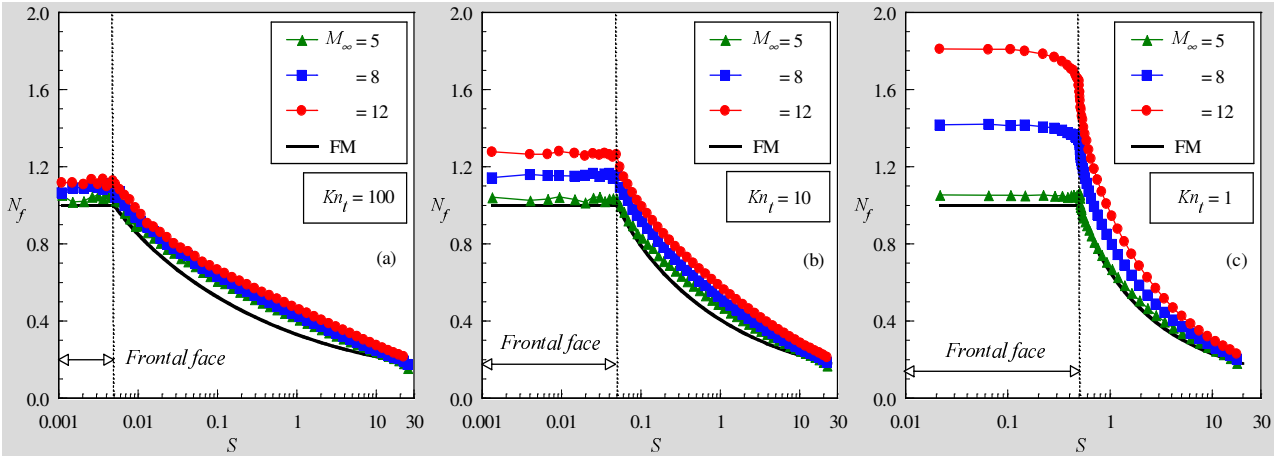

Figure 2: Dimensionless number flux N_f along the body surface as a function of the freestream Mach number for leading-edge thickness corresponding to Knudsen number Kn_t of (a) 100, (b) 10 and (c) 1.

According to these figures, the dimensionless number flux to the surface depends not only on the freestream Mach number but also on the leading-edge thickness. For a sharp leading edge, Kn_t of 100 ($t/\lambda_\infty = 0.01$), the dimensionless number flux is low and constant along the frontal surface and decreases gradually along the afterbody surface. A similar behavior is seen for the slightly blunt leading edge case, Kn_t of 10 ($t/\lambda_\infty = 0.1$). Nevertheless, for the bluntest leading edge case investigated, Kn_t of 1 ($t/\lambda_\infty = 1$), the dimensionless number flux is large on the frontal surface. It presents a constant value along the first half of the frontal face and decreases at the vicinity of the shoulder for the largest freestream Mach number investigated. After that, it decreases significantly along the afterbody surface. The dimensionless number flux rise with increasing the leading-edge thickness may be related to the collisions of two groups of molecules; the molecules reflecting from the body and the molecules oncoming from the freestream. The molecules reflecting from the body surface, which have a lower kinetic energy, interact with the oncoming freestream molecules, which have a higher kinetic energy. Thus, the surface-reflected molecules recollide with the body surface, which produce an increase in the dimensionless number flux in this region. It should be mentioned in this context that,

this behavior is more pronounced with increasing the freestream Mach number, since the molecules oncoming from the freestream have larger kinetic energy. As a result, the net buildup of particle density near the body surface is enhanced.

Free-molecular flow or collisionless flow is the limiting case in which the Knudsen number tends to infinity. It is the subdivision of rarefied gas dynamics corresponding to the lowest densities, therefore with very high mean free paths, or with very small characteristic dimensions. The basic assumption is that intermolecular collisions can be neglected. The fluxes of mass, momentum and energy incident on and reflected from a surface element can be treated separately and do not interfere with each other. The incident flux is entirely unaffected by the presence of the surface. Analytical expressions for number density of the gas just above the surface, number flux, pressure coefficient, heat transfer coefficient and skin friction coefficient have been derived (Bird, 1994) by assuming that the flow past the surface element is in Maxwellian equilibrium with freestream number density n_∞, temperature T_∞, macroscopic velocity V_∞ inclined at an angle of incidence β to the unit normal vector to the surface element, and diffuse reflection. However, the body slope angle θ is related to the angle of incidence β of the element surface by $\pi/2$-β, and it seems to be more appropriate for this work. In this fashion, the number density by considering free molecular flow is given by the following expression,

$$\frac{N}{n_\infty V_\infty} = \frac{1}{2\sqrt{\pi} U_\infty}\left[\exp(-\chi^2) + \sqrt{\pi}\chi(1 + erf\chi)\right] \tag{2}$$

where U_∞ is the speed ratio of the freestream defined by $V_\infty\sqrt{2RT_\infty}$ and $\chi = U_\infty sin\theta$ with R standing for the gas constant.

For comparison purpose, the dimensionless number flux by considering free molecular flow is also displayed in Figs. (2a), (2b) and (2c). It is seen from this set of figures that, for freestream Mach number of 5, the dimensionless number flux along the frontal surface approaches the limit value, $N/n_\infty V_\infty$, = 1, obtained by the Eq. (2). By analyzing Eq. (2), the dimensionless number flux for free molecular flow tends to $sin\theta$ as the freestream speed ratio $U_\infty \to \infty$. As the freestream Mach number increases from 5 to 12, the freestream speed ratio increases from 4.18 to 9.44. As the slope angle θ is 90 degrees for the frontal surface, then the dimensionless number flux becomes independent of the freestream speed ratio or freestream Mach number for free molecular flow.

5.2. Heat Transfer Coefficient

The heat transfer coefficient C_h is defined as being,

$$C_h = \frac{q_w}{\frac{1}{2}\rho_\infty V_\infty^3} \tag{3}$$

where q_w is the net heat flux to the body surface and ρ_∞ is the freestream density.

The heat flux q_w to the body surface is calculated by the net energy flux of the molecules impinging on the surface. A flux is regarded as positive if it is directed toward the surface. The net heat flux q_w is related to the sum of the translational, rotational and vibrational energies of both incident and reflected molecules as defined by,

$$q_w = q_i + q_r = \sum_{j=1}^{N}\left\{\left[\frac{1}{2}m_j v_j^2 + e_{Rj} + e_{Vj}\right]_i + \left[\frac{1}{2}m_j v_j^2 + e_{Rj} + e_{Vj}\right]_r\right\} \tag{4}$$

where N is the number of molecules colliding with the surface by unit time and unit area, m is the mass of the molecules, v is the velocity of the molecules, e_R and e_V stand for the rotational and vibrational energies, respectively. Subscripts i and r refer to incident and reflected molecules.

Distribution of heat transfer coefficient C_h along the body surface is displayed in Figs. (3a), (3b) and (3c) for thickness Knudsen numbers Kn_t of 100, 10 and 1, respectively, and parameterized by the freestream Mach number. It is observed from Fig. (3a) to Fig. (3c) that the heat transfer coefficient is sensitive to the leading-edge thickness as well as to the freestream Mach number. The heat transfer coefficient remains essentially constant over the first half of the frontal surface, and then it decreases sharply and continues to decline along the afterbody surface. However, for the bluntest case investigated, Kn_t = 1 (t/λ_∞ = 1), the heat transfer coefficient increases at the vicinity of the flat-face/afterbody junction, in contrast to the sharpest case investigated, Kn_t = 100. As would be expected, the blunter the leading edge is the lower the heat transfer coefficient at the stagnation point. Moreover, the higher the freestream Mach number the larger the heat transfer coefficient along the frontal surface and at the vicinity of the stagnation region. For the purpose of reference, the heat transfer coefficient at the stagnation point for shapes represented by Kn_t = 100, 10 and 1 at M_∞ = 12 corresponds, respectively, to 2.1, 2.2 and 2.6 times the heat transfer coefficient for the same shapes at M_∞ = 5.

As the freestream Mach number increases from 5 to 12, the kinetic energy of the freestream molecules increases.

As a result, the heat flux to the body surface increases. An understanding of this behavior can be gained by Eq. (4). The incident component of the velocity v of the molecules is a function of the freestream Mach number. However, the reflected component of the molecular velocity is not a function of the freestream Mach number. Due to the diffuse reflection model, the reflected component of the molecular velocity is obtained from a Maxwellian distribution that only takes into account for the temperature of the body surface, which has the same value for the freestream Mach number cases investigated. It should also be emphasized that the number of molecules colliding with the surface by unit time and unit area, N, which appears in Eq. (4), is the same for the incident and reflected components of the heat transfer coefficient C_h. Nevertheless, N dramatically increases on the front surface of the leading edges with increasing the freestream Mach number as shown from Fig. (2a) to Fig. (2c).

Of particular interest in Fig. (3c) is the behavior of the heat transfer coefficient at the vicinity of the flat-face/afterbody junction. As the number of molecules impinging on the body surface decreases (see Fig. (2c)) at the vicinity of the leading edge shoulder, then the velocity of the molecules increases in this region in order to increase the heat transfer coefficient in this region, based on Eq. (4). It should be mentioned in this context that the increase on the molecular velocity in this region is expected due to the flow expansion along the shoulder of the leading edges.

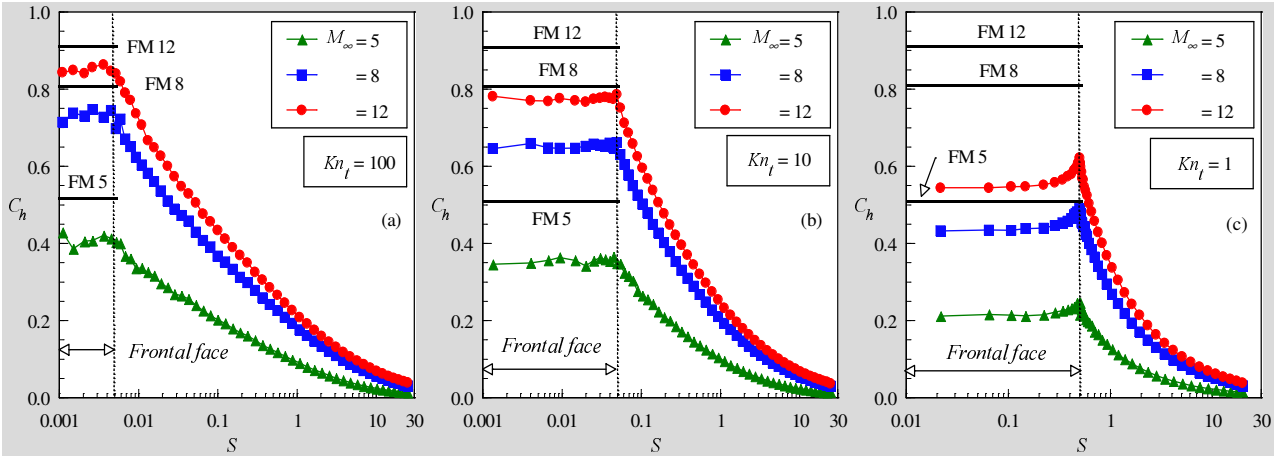

Figure 3: Heat transfer coefficient C_h along the body surface as a function of the freestream Mach number for leading-edge thickness corresponding to Knudsen number Kn_t of (a) 100, (b) 10 and (c) 1.

For completeness, the computations on heat transfer coefficient discussed above are compared to those by considering free molecular flow. The analytical expression (Bird, 1994) for the heat transfer coefficient is given as follows,

$$C_h = \frac{1}{2\sqrt{\pi}U_\infty^3}\left\{\left[U_\infty^2 + \frac{\gamma}{\gamma-1} - \frac{\gamma+1}{2(\gamma-1)}\frac{T_w}{T_\infty}\right]\left[\exp(-\chi^2) + \sqrt{\pi}\chi(1+erf\chi)\right] - \frac{1}{2}\exp(-\chi^2)\right\} \tag{5}$$

where γ specific heat ratio.

By considering free molecular flow, the heat transfer coefficient along the frontal surface, based on Eq. (5), is 0.514, 0.810 and 0.916 for freestream Mach number of 5, 8 and 12, respectively. For purpose of reference, these limit values (FM) are shown in Figs. (3a), (3b) and (3c). It is noticed from these figures that the heat transfer coefficients for the sharpest leading edge investigated, $t/\lambda_\infty = 0.01$, approach those values obtained by considering free molecular flow. As matter of fact, this is an expected behavior since this leading edge corresponds to a thickness Knudsen number Kn_t of 100. In contrast, the flow is far from the free molecular limit for the bluntest leading edge, Kn_t of 1, as shown in Fig. (3c).

5.3. Pressure Coefficient

The pressure coefficient C_p is defined as being,

$$C_p = \frac{p_w - p_\infty}{\frac{1}{2}\rho_\infty V_\infty^2} = \frac{p_w/p_\infty - 1}{\frac{1}{2}\gamma M_\infty^2} = \frac{p_w/p_\infty - 1}{U_\infty^2} \tag{6}$$

where p_w is the pressure acting on the body surface and p_∞ is the freestream pressure.

The pressure p_w on the body surface is calculated by the sum of the normal momentum fluxes of both incident and reflected molecules at each time step as follows,

$$p_w = p_i + p_r = \sum_{j=1}^{N} \left\{ \left[m_j v_{\eta j}^2 \right]_i + \left[m_j v_{\eta j}^2 \right]_r \right\} \tag{7}$$

where v_η is the velocity component of the molecules in the normal direction, i.e., η-direction as shown in Fig. (1b).

The effect on pressure coefficient due to variations on the freestream Mach number and on the leading-edge thickness is demonstrated from Fig. (4a) to Fig. (4c) for thickness Knudsen number Kn_t of 100, 10 and 1, respectively.

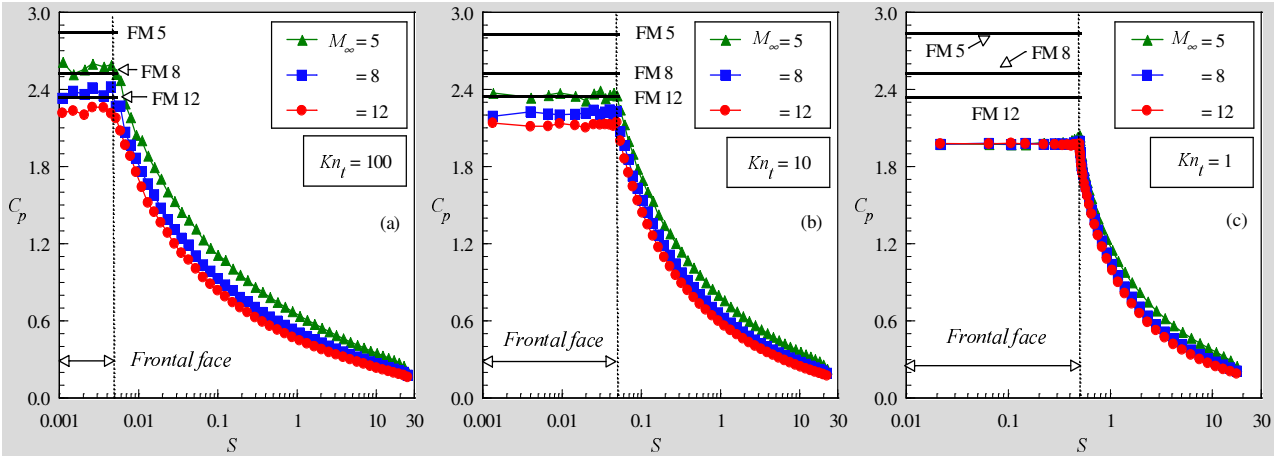

Figure 4: Pressure coefficient C_p along the body surface as a function of the freestream Mach number for leading-edge thickness corresponding to Knudsen number Kn_t of (a) 100, (b) 10 and (c) 1.

Referring to Figs. (4a), (4b) and (4c), it is noted that the pressure coefficient basically present a constant value along the frontal surface and the constant value increases with increasing the freestream Mach number. Subsequently, the pressure coefficient decreases dramatically along the afterbody surface for the cases investigated. In addition, it is clearly noticed in Fig. (4c) that the freestream Mach number rise investigated has no expressive effect on the pressure coefficient for the bluntest leading edge, Kn_t = 1. At this point, it is important to recognize from the number flux distribution in Fig. (2) that significant changes in the number flux occur due to variations not only on the leading edge thickness but also on the wall temperature.

Plotted along with the computational solutions for pressure coefficient is the pressure coefficient limit predicted by the free molecular flow. These values, obtained from Eq. (8) are 2.85, 2.53 and 2.35 for freestream Mach number of 5, 8 and 12, respectively. As expected, the pressure coefficient along the frontal surface for the Kn_t = 100 case approaches the free molecular limit, as shown in Fig. (4a).

$$C_p = \frac{1}{U_\infty{}^2} \left\{ \left[\frac{\chi}{\sqrt{\pi}} + \frac{1}{2} \left(\frac{T_w}{T_\infty} \right)^{1/2} \right] \exp\left(-\chi^2\right) + \left[\frac{1}{2} + \chi^2 + \frac{1}{2} \left(\frac{T_w}{T_\infty} \right)^{1/2} \sqrt{\pi}\chi \right] \left[1 + erf\chi \right] - 1 \right\} \tag{8}$$

Before proceeding with the discussion in this paper, care must be taken with the pressure coefficient changes due to the compressibility effects. The pressure coefficient rise, observed in Figs. (4a) and (4b) as the freestream Mach number decreases, are not associated to a pressure rise on the wall. Equations (6) and (7) provide the necessary assistance in order to understand this behavior. As the freestream Mach number decreases from 12 to 5, the number of particles impinging on the body surface diminishes, as shown in Figs. (2a-c). As a result, the wall pressure, given by Eq. (7), also diminishes. Thus, the numerator of Eq. (6) grows progressively less while the denominator ($\propto M_\infty{}^2$) decreases faster than the numerator and results in a pressure coefficient rise, as shown in Figs. (4a-c).

In what follows, for convenience, the sensitivity of the wall pressure to variations on the freestream Mach number is demonstrated in Figs. (5a), (5b) and (5c) for thickness Knudsen number Kn_t of 100, 10 and 1, respectively. In this set of figures, the wall pressure p_w is normalized by the freestream pressure p_∞. It is noted that the pressure basically present a constant value along the frontal surface and the constant value increases with increasing the freestream Mach number. It can also be seen that the front surface experiences a remarkable pressure compared to the freestream pressure; it is one order of magnitude larger than the freestream pressure for those simulations with M_∞ = 5, and two orders of magnitude larger than the freestream pressure for the other two freestream Mach number cases investigated. It should be mentioned in this context that the large amount of kinetic energy presented in a hypersonic freestream is converted by molecular collisions into high thermal energy surrounding the body and by flow work into increased pressure. In this way, the region at the vicinity of the front surface is a zone of strong compression.

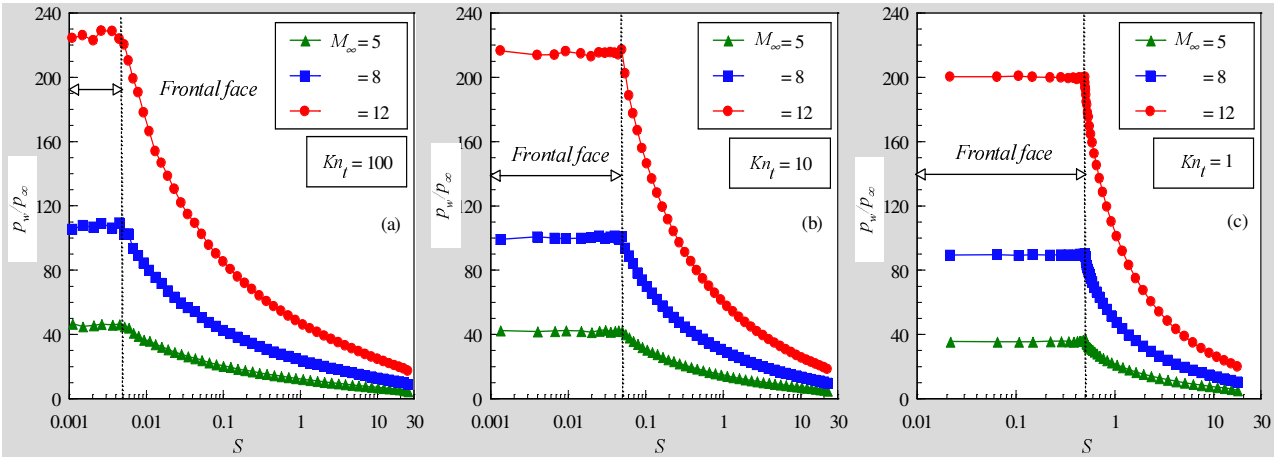

Figure 5: Pressure ratio (p_w/p_∞) along the body surface as a function of the freestream Mach number for leading-edge thickness corresponding to Knudsen number Kn_t of (a) 100, (b) 10 and (c) 1.

5.4. Skin Friction Coefficient

The skin friction coefficient C_f is defined as being,

$$C_f = \frac{\tau_w}{\frac{1}{2}\rho_\infty V_\infty^2} = \frac{\tau_w / p_\infty}{\frac{1}{2}\gamma M_\infty^2} = \frac{\tau_w / p_\infty}{U_\infty^2} \tag{9}$$

where τ_w is the shear stress acting on the body surface.

The shear stress τ_w on the body surface is calculated by averaging the tangential momentum transfer of the molecules impinging on the surface. For the diffuse reflection model imposed for the gas-surface interaction, reflected molecules have a tangential moment equal to zero, since the molecules essentially lose, on average, their tangential velocity component. In this context, the tangential momentum flux of the incident molecules is defined as follows,

$$\tau_w = \sum_{j=1}^{N} m_j v_{\xi j}^2 \tag{10}$$

where v_ξ is the velocity component of the molecules in the tangential direction, i.e., ξ-direction as shown in Fig. (1b).

The variation of skin friction coefficient C_f with the freestream Mach number is depicted from Figs. (6a) to (6c) for Kn_t of 100, 10 and 1, respectively. It is noted that the skin friction coefficient is zero at the stagnation point and slightly increases along the frontal surface up to the flat-face/afterbody junction of the leading edges. After that, it increases dramatically to a maximum value that depends on the leading-edge thickness, and decreases downstream along the afterbody surface. Smaller thickness t (larger Kn_t) leads to higher peak value for the skin friction coefficient. Also, smaller thickness t displaces the peak value to near the flat-face/afterbody junction.

The compressibility effect on the skin friction coefficient can also be seen in a different way by comparing the DSMC computational results along the body surface with that calculated by assuming free molecular flow. For comparison purpose, the skin friction coefficient predicted by the free molecular flow, Eq. (11), is also displayed in Figs. (6a-c).

$$C_f = \frac{\cos\chi}{\sqrt{\pi} U_\infty}\left[\exp(-\chi^2) + \sqrt{\pi}\chi(1 + erf\chi)\right] \tag{11}$$

The skin friction coefficient presents interesting features as it is plotted as a function of the body slope angle θ. Figures (7a), (7b) and (7c) illustrate these features for thickness Knudsen number Kn_t of 100, 10 and 1, respectively. In addition, this set of diagrams displays the skin friction coefficient by assuming a free molecular flow, as defined by Eq. (11). Also, in these figures, 90 degrees correspond to the station at the flat-face/afterbody junction, and 10 degrees correspond to the tangent point common to all of the shapes as shown in Fig. (1a). As can be seen, the skin friction coefficient predicted by free molecular flow exhibits its maximum value at 45 degrees. From Eq. (11), it is found that the maximum skin friction coefficient occurs at 45 degrees when the speed ratio U_∞ is very high, but at zero incidence as the speed ratio U_∞ is extremely small. Similarly, the maximum values for the leading edges obtained by DSMC occur very close to the same station, i.e., 45 degrees.

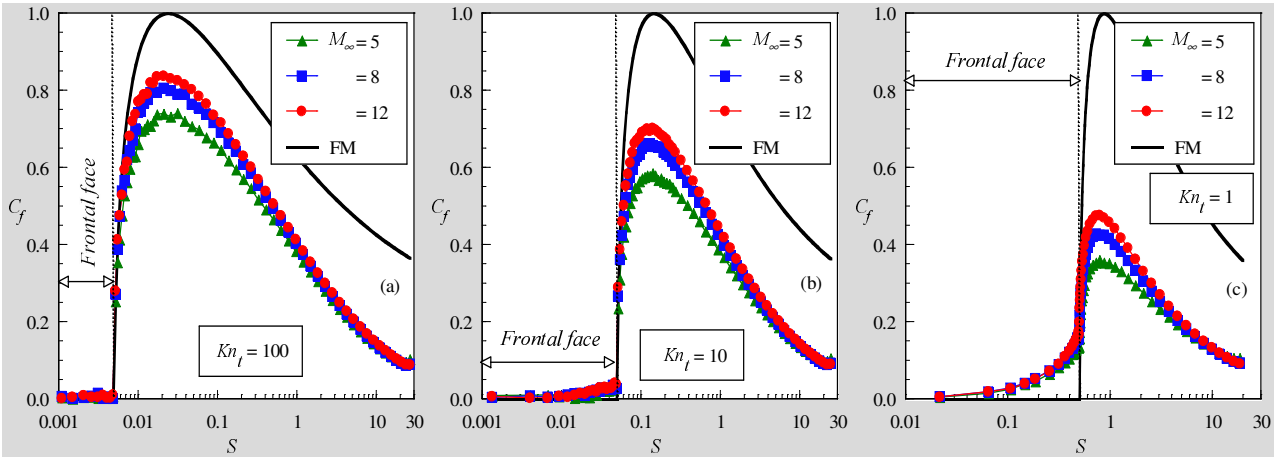

Figure 6: Skin friction coefficient C_f along the body surface as a function of the freestream Mach number for leading-edge thickness corresponding to Knudsen number Kn_t of (a) 100, (b) 10 and (c) 1.

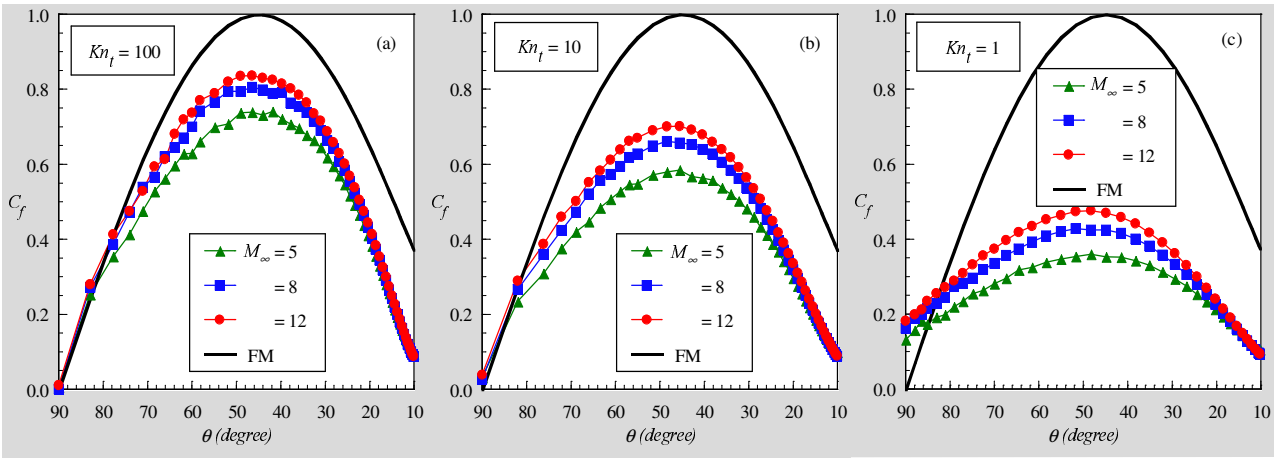

Figure 7: Skin friction coefficient C_f along the afterbody surface as a function of the body slope angle for leading-edge thickness corresponding to Knudsen number Kn_t of (a) 100, (b) 10 and (c) 1.

5.5. Drag Coefficient

The total drag coefficient C_d is defined as being,

$$C_d = \frac{F}{\frac{1}{2}\rho_\infty V_\infty^2 H} \tag{12}$$

where F is the resultant force acting on the body surface and H is the height at the matching point common to the leading edges (see Fig. (1a)).

The drag force is obtained by the integration of the pressure p_w and shear stress τ_w distributions from the stagnation point of the leading edge to the station L, which corresponds to the tangent point common to all of the body shapes, as shown Fig. (1a). It is important to mention that the values for the total drag presented in this section were obtained by assuming the shapes acting as leading edges. Consequently, no base pressure effects were taken into account on the calculations.

The impact of the compressibility effect on the total drag coefficient C_d is displayed in Figs. (8a), (8b) and (8c) for thickness Knudsen number Kn_t of 100, 10 and 1, respectively. In this set of figures, the contributions of the pressure C_{pd} and skin friction drag C_{fd} to the total drag coefficient are also illustrated. It is apparent from this set of diagrams that as the leading edge becomes blunter, i.e., the nose becomes flatter, the contribution of the pressure drag to the total drag increases and the contribution of the skin friction drag decreases, and the net effect results in a slightly increase in the total drag. It is also seen that the total drag decreases with increasing the freestream Mach number.

As a reference, for freestream Mach number of 5, the pressure drag is 39.5%, 45.7% and 61.3% of the total drag for the leading edges defined by Kn_t of 100, 10 and 1, respectively. Consequently, the skin friction contribution decreases from 60.5% to 39.7% for the same cases. On the other hand, for freestream Mach number of 12, the pressure drag is

28.2%, 34.6% and 53.7% of the total drag for the leading edges defined by Kn_t of 100, 10 and 1, respectively. This behavior appears to be fully explained through the changes in pressure and shear stress shown from Figs. (5) to (8). Note that on the front surface, for the same freestream Mach number, the wall pressure decreases as the leading-edge thickness increases, while it increases on the afterbody surface of leading edges. In contrast, the shear stress basically has no contribution on the frontal surface. However, it decreases on the afterbody surface.

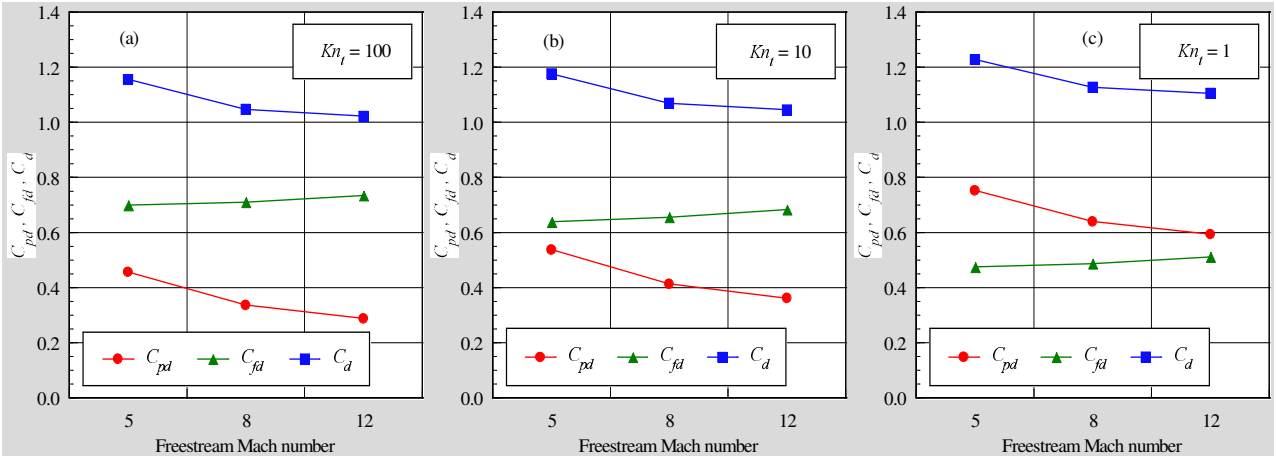

Figure 8: Pressure drag C_{pd}, skin friction drag C_{fd} and total drag coefficient C_d as a function of the freestream Mach number for leading-edge thickness corresponding to Knudsen number Kn_t of (a) 100 and (b) 10 and (c) 1.

For completeness, the total drag coefficient for the cases investigated is tabulated in Tab. (3). Significant differences in the total drag coefficient between freestream Mach number of 5 and 12 are seen on the leading-edge shapes. By referring to Tab.(3), the total drag coefficient for leading edge corresponding to Kn_t of 1decreases around 11% as the freestream Mach number increases from 5 to 12, despite of the fact that the wall pressure and shear stress significantly increase with freestream Mach number, as depicted from Figs. (5) to (8). In order to understand this behavior, Eq. (12) provides the necessary assistance. The numerator of Eq. (12) grows with wall pressure and shear stress, while the denominator ($\propto M_\infty^2$) increases faster than the numerator and results in a total drag coefficient decrease.

Table 3: Total drag coefficient for the flat-nose leading edges.

M_∞	$Kn_t = 100$	$Kn_t = 10$	$Kn_t = 1$
5	1.156	1.176	1.228
8	1.047	1.069	1.127
12	1.022	1.046	1.105

6. Concluding Remarks

The Direct Simulation Monte Carlo method is used to numerically simulate the rarefied hypersonic flow on blunt leading edges. The calculations provided information concerning the nature of the aerodynamic surface quantities for a family of contours composed by a flat nose followed by a highly curved afterbody surface. Effects of compressibility on the number flux, heat transfer coefficient, pressure coefficient, skin friction coefficient and total drag coefficient for a wide range of parameters are investigated. The freestream Mach number was varied from 5 to 12. In addition, the leading-edge thicknesses investigated correspond to thickness Knudsen number of 1, 10 and 100. These cases cover the hypersonic flow from the transition regime to the free molecular one.

Performance results for leading-edge thickness corresponding to thickness Knudsen number of 100 indicated that the aerodynamic surface quantities approach those values predicted by the free molecular flow equations on the frontal surface for the flow conditions considered. Calculations showed that the heat transfer coefficient decreases with increasing the frontal surface of the leading edges, since the leading edge changes from a sharp leading edge to a blunt one. It was found that the heat transfer coefficient increases with the freestream Mach number rise. The analysis also showed that the total drag slightly increases by increasing the leading-edge thickness, and decreases with increasing the freestream Mach number, as would be expected.

7. References

Alexander, F. J., Garcia, A. L., and, Alder, B. J., 1998, "Cell Size Dependence of Transport Coefficient in Stochastic Particle Algorithms", Physics of Fluids, Vol. 10, No. 6, pp. 1540-1542.

Alexander, F. J., Garcia, A. L., and, Alder, B. J., 2000, "Erratum: Cell Size Dependence of Transport Coefficient is Stochastic Particle Algorithms", Physics of Fluids, Vol. 12, No. 3, pp. 731-731.

Bird, G. A., 1981, "Monte Carlo Simulation in an Engineering Context", Progress in Astronautics and Aeronautics: Rarefied gas Dynamics, Ed. Sam S. Fisher, Vol. 74, part I, AIAA New York, pp. 239-255.

Bird, G. A., 1989, "Perception of Numerical Method in Rarefied Gasdynamics", Rarefied gas Dynamics: Theoretical and Computational Techniques, Eds. E. P. Muntz, and D. P. Weaver and D. H. Capbell, Vol. 118, Progress in Astronautics and Aeronautics, AIAA, New York, pp. 374-395.

Bird, G. A., 1994, "Molecular Gas Dynamics and the Direct Simulation of Gas Flows", Oxford University Press, Oxford, England, UK.

Borgnakke, C. and Larsen, P. S., 1975, "Statistical Collision Model for Monte Carlo Simulation of Polyatomic Gas Mixture", Journal of computational Physics, Vol. 18, No. 4, pp. 405-420.

Garcia, A. L., and, Wagner, W., 2000, "Time Step Truncation Error in Direct Simulation Monte Carlo", Physics of Fluids, Vol. 12, No. 10, 2000, pp. 2621-2633.

Guo, K. and Liaw, G.-S., 2001, "A Review: Boundary Conditions for the DSMC Method", Proceedings of the 35th AIAA Thermophysics Conference, AIAA Paper 2001-2953, Anaheim, CA, 11-14 June.

Hadjiconstantinou, N. G., 2000, "Analysis of Discretization in the Direct Simulation Monte Carlo", Physics of Fluids, Vol. 12, No. 10, pp. 2634-2638.

Reller Jr., J. O., 1957, "Heat Transfer to Blunt Nose Shapes with Laminar Boundary Layers at High Supersonic Speeds", NACA RM-A57FO3a.

Santos, W. F. N., 2003, "Aerodynamic Heating on Blunt Nose Shapes in Rarefied Hypersonic Flow", Proceedings of the 17th International Congress of Mechanical Engineering COBEM 2003, 10-14 Nov, São Paulo, SP, Brazil.

Santos, W. F. N., 2004, "Surface Temperature Effects in Low-Density Flow over Flat-Nose Bodies at Hypersonic Speed. Part II: Aerodynamic Suface Quantities", Proceedings of the 10th Brazilian Congress of Thermal Sciences and Engineering ENCIT 2004, 29 Nov – 3 Dec, Rio de Janeiro, RJ, Brazil.

Santos, W. F. N., 2005, "Gas-Surface Interaction Impact on Aerodynamic Surface Quantities of Low-Density Hypersonic Flow over Flat-Nose Bodies", Proceedings of the 18th International Congress of Mechanical Engineering COBEM 2005, 6-11 Dec, Ouro Preto, MG, Brazil.

Proceedings of the 11th Brazilian Congress of Thermal Sciences and Engineering -- ENCIT 2006
Braz. Soc. of Mechanical Sciences and Engineering -- ABCM, Curitiba, Brazil,- Dec. 5-8, 2006

Paper CIT06-0491

RAREFACTION EFFECTS ON SHOCK-WAVE STRUCTURE OF HYPERSONIC FLOW OVER POWER-LAW LEADING EDGES

Wilson F. N. Santos
Combustion and Propulsion Laboratory
National Institute for Space Research
12630-000 Cachoeira Paulista, SP, Brazil
wilson@lcp.inpe.br

Abstract. *This work deals with a numerical study of power-law leading edges situated in a hypersonic flow. The primary aim of this paper is to examine the effect of rarefaction on the shock-wave structure. The rarefaction effect on the shock wave has been investigated by employing the Direct Simulation Monte Carlo (DSMC) method. The work is motivated by interest in investigating power-law shaped leading edges as possible candidates for blunting geometry of hypersonic leading edges. The sensitivity of shock standoff distance, shock thickness and shock wave shape to variations on rarefaction are simulated for altitudes of 70, 80 and 85 km. The analysis shows significant differences on the shock wave structure due to variations not only on the altitude but also on the leading-shape defined by the power-law exponent. It was found that the shock standoff and the shock thickness increased with increasing the altitude.*

Keywords. *DSMC, hypersonic flow, rarefied flow, power-law shape, shock standoff distance, shock wave thickness.*

1. Introduction

Hypersonic waveriders are advanced hypersonic lifting bodies which generate the highest known lift-to-drag (*L/D*) ratio at high Mach number. A waverider (Nonweiler, 1959) is designed from an inverse process which involves the initial selection of a shock wave and a known analytic flowfield, such as flow over a two-dimensional wedge or flow around a slender cone, followed by the determination of a vehicle geometry which corresponds to the desired flowfield. The potential of generating high lift is obtained by using the attached shock wave as a barrier in order to prevent air flow from the high pressure windward side to the low leeward side. In principle, there is no leakage of high pressure from the bottom surface around the leading edge to the top surface. Nevertheless, in practice, waveriders tend to surfer from viscous effects. As a result, the full potential of waveriders has never been fulfilled, as viscous forces tend to displace the shock wave, and the displacement effect has some influence on the *L/D* performance.

The successful design of high-lift, low-drag hypersonic configurations will depend on the ability to incorporate relatively sharp-leading edges that combine good aerodynamic properties with acceptable heating rates. However, for practical applications, these sharp leading edges must be blunted for heat transfer, manufacturing, and handling concerns, with associated departures from ideal performance. Typically, a round leading edge with constant radius of curvature (circular cylinder) near the stagnation point has been chosen. Nevertheless, shock detachment distance on a cylinder, with associated leakage, scales with the radius of curvature. Certain classes of non-circular shapes may provide the required bluntness with smaller shock separation than round leading edges, thus allowing manufacturing, and ultimately heating control, with reduced aerodynamic losses.

In this scenario, power-law shaped leading edges ($y \propto x^n$, $0 < n < 1$) may provide the required bluntness for heat transfer, manufacturing and handling concerns with reduced departures from ideal aerodynamic performance. This concept is based on work available in the literature that pointed out, based on Newtonian flow analysis, that these shapes exhibit both blunt and sharp aerodynamic properties.

Numerous studies have been done with the power-law form representing blunt geometries. For the purpose of this introduction, it will be sufficient to describe only a few of these works. The major interest in these works had gone into finding solutions to the hypersonic small disturbance form of the inviscid adiabatic-flow equations. The equations of motion for hypersonic flow over slender bodies can be reduced to simpler form by incorporating the hypersonic slender-body approximations (Van Dyke, 1954). The reduced equations are valid provided $\tau^2 << 1$ and $(M_\infty \tau)^{-2}$ is not near one, where M_∞ is the freestream Mach number and τ is a characteristic shock slope. Lees and Kubota (1957) observed that similarity exists for hypersonic flows whenever the shock shape follows a power-law variation with the streamwise distance, provided the hypersonic slender body equations are considered in the limit as $(M_\infty \tau)^{-2} \rightarrow 0$. According to their work, energy considerations combined with a detailed study of the equations of motion show that flow similarity is possible for a class of bodies of the form x^n, provided that $2/3 < n < 1$ for a two dimensional body and $1/2 < n < 1$ for an axisymmetric body. The similarity solutions referred herein are solutions for self-similar flows, i.e., flows in which the flowfield between the shock wave and the body can be expressed in terms of functions which, in suitable coordinates, are independent of one of the coordinate directions.

Mason and Lee (1994) pointed that, for certain exponents, power law shapes exhibit aerodynamic properties similar to geometrically sharp shapes. They suggested the possibility of a difference between shapes that are geometrically

sharp and shapes that behave aerodynamically as if they were sharp. They showed that for values of $0 < n < 1/2$, the leading-edge radius of curvature goes to infinite at the nose, a characteristic of a blunt shape. For values of $1/2 < n < 1$ the leading-edge radius of curvature approaches zero at the nose, a characteristic of a sharp shape. Furthermore, for $2/3 < n < 1$, their computational investigation predicts that the derivative of the pressure coefficient with respect to the body coordinate dC_p/ds approaches $-\infty$ at $x = 0$, a characteristic of a sharp body. In this way, there is a class of body shapes given by $1/2 < n < 2/3$, for which the leading edge may behave aerodynamically like a blunt body, even though the leading-edge radius of curvature is zero, and another one given by $2/3 < n < 1$ for which the leading edge may behave like aerodynamically sharp body even though the leading edge bluntness is infinite. Their analysis describes the details of the geometry and aerodynamics of low-drag axisymmetric bodies by using Newtonian theory. Nonetheless, one of the important aspects of the problem, stagnation point heat transfer, was not considered.

Based on recent interest in hypersonic waveriders for high-altitude/low-density applications, Santos and Lewis (2002) have investigated the sensitivity of the pressure gradient and the stagnation point heating to shape variations of power-law leading edges by considering two-dimensional rarefied hypersonic flow. Through the use of the DSMC method, they showed that the pressure gradient on the power-law shapes is in surprising agreement with that obtained by Mason and Lee (1994) by employing Newtonian Analysis. They also found that the stagnation point heating scales inversely with the square root of the curvature radius for power-law bodies with finite radius of curvature.

Santos and Lewis (2005a) compared power-law shapes to a corresponding circular cylinder in order to determine which geometry would be better suited as a blunting profile. Their analysis also showed that power-law shapes provided smaller total drag than circular cylinder, typically used in blunting sharp leading edges for heat transfer considerations. However, circular cylinder provided smaller stagnation point heating than power-law shapes under the range of conditions investigated. The power-law exponent effect on shock-wave was examined by Santos and Lewis (2005b).

In an effort to obtain further insight into the nature of the shock-wave structure on power-law leading edges under hypersonic transitional flow conditions, a parametric study is performed on these leading edges with a great deal of emphasis placed on the rarefaction effects. In this connection, the primary goal of the present account is to assess the sensitivity of the shock standoff distance, shock wave thickness and shock wave shape to variations not only on the rarefaction experienced by the leading edges but also on the shape of the leading edges via power-law exponent.

For the high altitude/high Knudsen number of interest ($Kn > 0.1$), the flowfield is sufficiently rarefied that continuum method becomes inappropriate. Alternatively, the DSMC method is used in the current study to calculate the rarefied hypersonic two-dimensional flow on the leading edge shapes.

2. Leading Edge Geometry Definition

In dimensional form, the body power-law shapes (Santos and Lewis, 2002) are given by the following expression,

$$y = ax^n \tag{1}$$

where n is the power-law exponent and a is the power-law constant which is a function of n.

The power-law shapes are modeled by assuming a sharp leading edge of half angle θ with a circular cylinder of radius R inscribed tangent to this wedge. The power-law shapes, inscribed between the wedge and the cylinder, are also tangent to them at the same common point where they have the same slope angle. The circular cylinder diameter provides a reference for the amount of blunting desired on the leading edges. It was assumed a leading edge half angle of 10 degrees, a circular cylinder diameter of 10^{-2}m and power-law exponents of 1/2, 2/3, and 3/4. Figure (1a) illustrates schematically this construction for the set of power-law leading edges investigated.

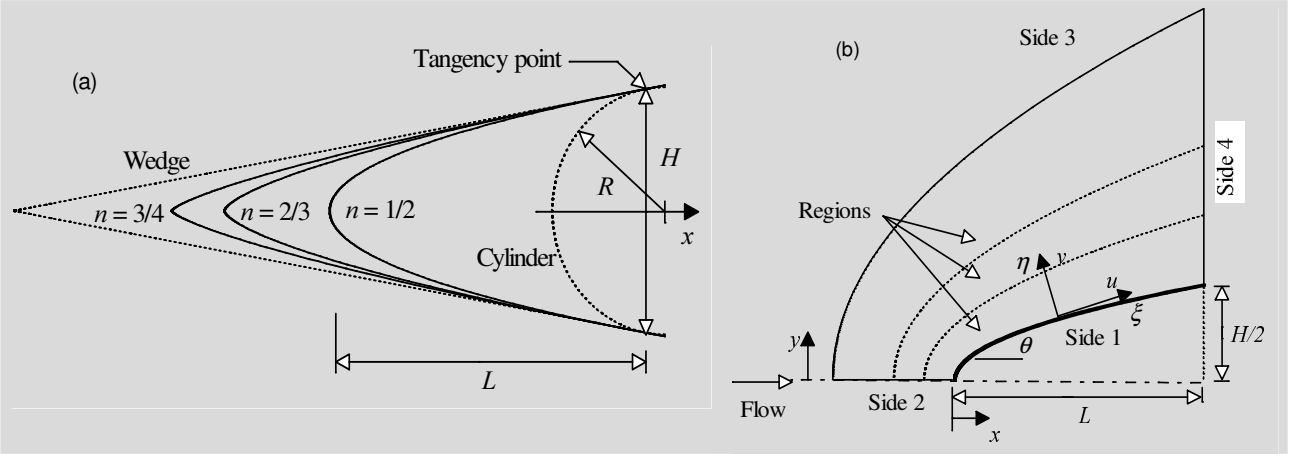

Figure 1: Drawing illustrating (a) the leading edge shapes and (b) the computational domain.

From geometric considerations, the power-law constant a is obtained by matching slope on the wedge, circular cylinder and power-law body at the tangency point. The common body height H at the tangency point is equal to $2R\cos\theta$, and the body length L from the nose to the tangency point in the axis of symmetry is given by $nH/2\tan\theta$. It was assumed that the power-law leading edges are infinitely long but only the length L is considered since the wake region behind the power-law bodies is not of interest in this investigation.

3. Computational Method

The DSMC method (Bird, 1994) has proved to be an extremely useful and flexible tool in the analysis of rarefied hypersonic non-equilibrium gas flows. In this study, the particle simulations were performed by using the DSMC method developed by Bird (1994). The DSMC method simulates fluid flow by using thousands to millions of particles. These particles are tracked as they move, collide and undergo boundary interactions in simulated physical space. In addition, particle motions are assumed to be decoupled from particle collisions and each process is computed independently during a time step used to advance the simulation. This time step must be sufficiently small in comparison with the local mean collision time (Garcia and Wagner, 2000, and Hadjiconstantinou, 2000) such that the assumption of decoupled particle motions and collisions is not violated.

The reliability of the method is entirely dependent on the accuracy of the collision models used to simulate particles interactions. The molecular collisions are modeled using the variable hard sphere (VHS) molecular model (Bird, 1981) and the no time counter (NTC) collision sampling technique (Bird, 1989). The VHS model employs the simple hard sphere angular scattering law so that all directions are equally possible for post-collision velocity in the center-of-mass frame of reference. However, the collision cross section is a function of the relative energy in the collision. The energy exchange between kinetic and internal modes is controlled by the Borgnakke-Larsen statistical model (Borgnakke and Larsen, 1975). Simulations are performed using a non-reacting gas model consisting of two chemical species, N_2 and O_2. Energy exchanges between the translational and internal modes are considered. For this study, the relaxation numbers of 5 and 50 were used for the rotation and vibration, respectively.

4. Computational Flow Domain and Grid

The computational domain is made large enough so that the upstream and side boundaries can be specified as freestream conditions. Figure 1(b) depicts the physical extent of the computational domain for the present simulations. Advantage of the flow symmetry is taken into account, and molecular simulation is applied to one-half of a full configuration. The computational domain is divided into an arbitrary number of regions, which are subdivided into computational cells. The cells are further subdivided into four subcells, two subcells/cell in each coordinate direction. The linear dimensions of the cells should be small in comparison with the scale length of the macroscopic flow gradients normal to the streamwise directions, which means that the cell dimensions should be of the order of or even smaller than the local mean free path (Alexander et al., 1998 and 2000). In the current DSMC code, the cell provides a convenient reference for the sampling of the macroscopic gas properties, while the collision partners are selected from the same subcell. As a result, the flow resolution is much higher than the cell resolution.

Referring to Fig. (1b), side 1 is defined by the body surface. Diffuse reflection with complete thermal surface accommodation is the condition applied to this side. Side 2 is a plane of symmetry, where all flow gradients normal to the plane are zero. This plane is equivalent to a specular reflecting boundary at the molecular level. Side 3 is the freestream side through which simulated molecules enter and exit. Finally, the flow at the downstream outflow boundary, side 4, is predominantly supersonic and vacuum condition is specified (Guo and Liaw, 2001). At this boundary, simulated molecules can only exit.

Numerical accuracy in DSMC method depends on the grid resolution chosen as well as on the number of particles per computational cell. Both effects were investigated to determine the number of cells and the number of particles required to achieve grid independence solutions. The grid generation scheme used in this study follows that procedure presented by Bird (1994). Along the outer boundary (side 3) and the body surface (side 1) (see Fig. (1b)), point distributions are generated in such way that the number of points on each side is the same (ξ-direction in Fig. (1b)). Then, the cell structure is defined by joining the corresponding points on each side by straight lines and then dividing each of these lines into segments which are joined to form the system of quadrilateral cells (η-direction in Fig. (1b)). The distribution can be controlled by a number of different distribution functions that allow the concentration of points in regions where high flow gradients or small mean free paths are expected.

A grid independence study was made with three different structured meshes in each coordinate direction. The effect of altering the cell size in the ξ-direction was investigated with grids of 35(coarse), 70(standard) and 105(fine) cells, and 50 cells in the η-direction for power-law exponent of 1/2. In analogous fashion, an examination was made in the η-direction with grids of 25(coarse), 50(standard) and 75(fine) cells, and 70 cells in the ξ-direction for power-law exponent of 1/2. Each grid was made up of non-uniform cell spacing in both directions. The effect (not shown) of changing the cell size in both directions on the heat transfer, pressure and skin friction coefficients was rather insensitive to the range of cell spacing considered, indicating that the standard grid, 70x50 cells, for the power-law shape defined by $n = 1/2$ is essentially grid independent. A similar procedure was performed for the two other cases

investigated. Results indicated that a grid of 80x50 and 90x50 for power-law exponents of 2/3 and 3/4 respectively, were considered fully independent. Of particular interest is the number of cells in the η-direction for the three power-law cases investigated. It should be emphasized that, even though the number of cells is the same, the computational domain size is different for each one of the cases; side 2 shown in Fig. (1b) corresponds to $8\lambda_\infty$, $6\lambda_\infty$ and $5\lambda_\infty$ for power-law exponents of 1/2, 2/3 and 3/4, respectively, where λ_∞ is the freestream mean free path.

In a second stage of the grid independence investigation, a similar examination was made for the number of molecules. The standard grid for power-law exponent of 1/2, 70x50 cells, corresponds to, on average, a total of 121,000 molecules. Two new cases using the same grid were investigated. These two new cases correspond to 108,000 and 161,000 molecules in the entire computational domain. As the three cases presented approximately the same results (see Santos and Lewis, 2002) for the heat transfer, pressure and skin friction coefficients, hence the standard grid with a total of 121,000 molecules is considered enough for the computation of the shock wave structure.

5. Freestream and Flow Conditions

Rarefaction effects are investigated for altitudes of 70, 80 and 85 km. For each one of the altitude investigated, the freestream Mach number M_∞ and the wall temperature T_w are kept to the constant values of 12 and 880 K, respectively. Freestream Mach number M_∞ of 12 corresponds to freestream velocity V_∞ of 3.56, 3.236 and 3.236 km/s for altitude of 70, 80 and 85 km, respectively.

Table (1) summarizes the freestream and flow conditions used in the present calculations. The gas properties considered in the simulation are those given by Bird (1994) and tabulated in Tab. (2). Referring to Tabs (1) and (2), T_∞, p_∞, ρ_∞, n_∞, μ_∞, and λ_∞ stand respectively for temperature, pressure, density, number density, viscosity and mean free path, and X, m, d and ω account respectively for mole fraction, molecular mass, molecular diameter and viscosity index.

Table 1: Freestream Conditions

Altitude (km)	T_∞ (K)	p_∞ (N/m^2)	ρ_∞ x 10^5 (kg/m^3)	n_∞ x 10^{-20} (m^{-3})	μ_∞ x 10^5 (Ns/m^2)	λ_∞ x 10^3 (m)	V_∞ (m/s)
70	220.0	5.582	8.753	18.2090	1.455	0.903	3560
80	181.0	1.040	1.999	4.1586	1.253	3.960	3236
85	181.0	0.414	0.796	1.6550	1.253	9.940	3236

Table 2: Gas Properties

	X	m (kg)	d (m)	ω
O_2	0.237	5.312 x 10^{-26}	4.01 x 10^{-10}	0.77
N_2	0.763	4.65 x 10^{-26}	4.11 x 10^{-10}	0.74

The overall Knudsen number Kn_∞, defined as the ratio of the freestream mean free path λ_∞ to the diameter of the circular cylinder, corresponds to 0.0903, 0.3960 and 0.9940 for altitude of 70, 80 and 85 km, respectively. Finally, the Reynolds number Re_∞ per unit of meter, based on conditions in the undisturbed stream is 21416.3, 5165 and 2055 for altitude of 70, 80 and 85 km, respectively.

6. Computational Procedure

The knowledge of the shock wave displacement is especially important in waverider configurations (Nonweiler, 1959), since these hypersonic configurations usually rely on shock wave attachment at the leading edge to achieve their *L/D* ratio at high-lift and low drag coefficients. In addition, the ability to predict the shape and location of shock waves is of primary importance in the analysis of aerodynamic interference.

In the present account, the shock wave structure, defined by shape, thickness and detachment of the shock wave, is predicted by employing a procedure based on the physics of the particles. In this scenario, the flow is assumed to consist of three distinct classes of molecules: those molecules from the freestream that have not been affected by the presence of the leading edge are denoted as class I molecules; those molecules that, at some time in their past history, have struck and been reflected from the body surface are denoted as class II molecules; and finally, those molecules that have been indirectly affected by the presence of the body are defined as class III molecules. For illustration purpose, Fig. (2a) displays the definition for the molecular classes adopted in this simulation.

According to Fig. (2a), it is assumed that the class I molecule changes to class III molecule when it collides with class II or class III molecule. Class I or class III molecule is progressively transformed into class II molecule when it interacts with the body surface. Also, a class II molecule remains class II regardless of subsequent collisions and

interactions. Hence, the transition from class I molecules to class III molecules may represent the shock wave, and the transition from class III to class II may define the boundary layer.

A typical distribution of class III molecules along the stagnation streamline for blunt leading edges is displayed in Fig. (2b), together with the definition used to determine the thickness, displacement and shape of the shock wave. In this figure, the distance x along the stagnation streamline is normalized by the radius of the reference circular cylinder (see Fig. (1b)) and f_{III} is the number of molecules for class III to the total amount of molecules inside each cell.

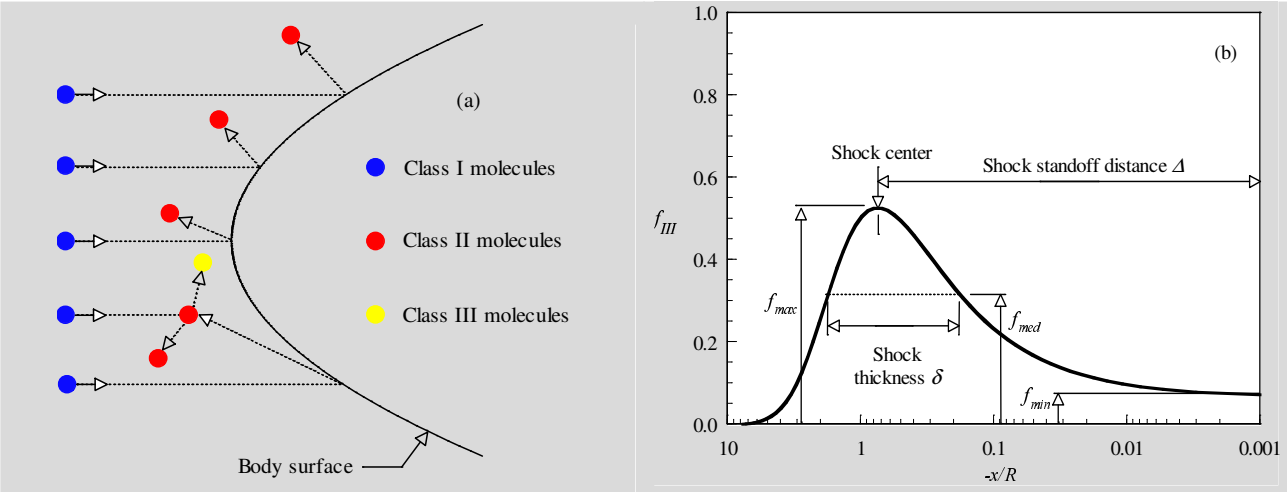

Figure 2: (a) Drawing illustrating the classification of molecules and (b) Schematic of shock wave structure.

In a rarefied flow, the shock wave has a finite region that depends on the transport properties of the gas, and can no longer be considered as a discontinuity obeying the classical Rankine-Hugoniot relations. In this context, the shock standoff distance Δ is defined as being the distance between the shock wave center and the nose of the leading edge along the stagnation streamline. As shown in Fig. (2b), the center of the shock wave is defined by the station that corresponds to the maximum value for f_{III}. The shock wave thickness δ is defined by the distance between the stations that correspond to the mean value for f_{III}. Finally, the shock wave shape (shock wave "location") is determined by the coordinate points given by the maximum value in the f_{III} distribution along the lines departing from the body surface, i.e., η-direction as shown in Fig. (1b).

7. Computational Results and Discussion

Having presented the definition for the shock-wave structure, it becomes instructive to focus on the computational results. In this connection, the purpose of this section is to discuss and to compare differences on the shape, thickness and displacement of the shock wave due to variations on rarefaction as well as on the power-law exponent, which defines the leading-edge shape. Before proceeding with the presentation of the shock-wave properties, it is desirable to discuss the results related to the molecular class distribution.

7.1. Molecular Class Distribution

The distribution of molecules for classes I, II and III along the stagnation streamline is displayed in Figs. (3), (4) and (5) for power-law exponent n of 1/2, 2/3 and 3/4, respectively. In this set of plots, f_I, f_{II} and f_{III} are the ratio of the number of molecules for class I, II and III, respectively, to the total amount of molecules inside each cell along the stagnation streamline. Also, the flow is from left to right and the distance x along the stagnation streamline is normalized by the radius R of the reference circular cylinder.

Interesting features are observed in Figs. (3), (4) and (5). Of great significance in these figures is the behavior of the class I molecules for sharp and blunt leading edges. It should be noticed that molecules from freestream, represented by class I molecules, do not reach the nose of the leading edge for that case illustrated in Fig. (3a), which represents a blunt leading edge at an altitude of 70 km. In contrast, class I molecules collide with the nose of the leading edge, even after the establishment of the steady state, for that case shown in Fig. (5a), which represents a sharp leading edge at the same altitude. This is explained by the fact that density increases much more for blunt leading edges in the stagnation region and reaches its maximum value at the stagnation point. In this connection, the buildup of particle density near the nose of the leading edge acts as a shield for the molecules coming from the undisturbed stream.

The buildup of particles density at the vicinity of the stagnation point decreases as the altitude increases from 70 to 85 km. As a result, the class I molecules reach the nose of either blunt or sharp leading edges, as displayed by Figs. (3c), (4c) and (5c). The effect of increasing the altitude is to create a more rarefied situation in which the shock standoff

increases and the shock wave center locates more away from the body, since the Kn_∞ increases. The presence of the body, propagated by random motion of the molecules, is communicated to a larger distance ahead of the body, since the molecules interact little with each other and collisions among them are less frequent.

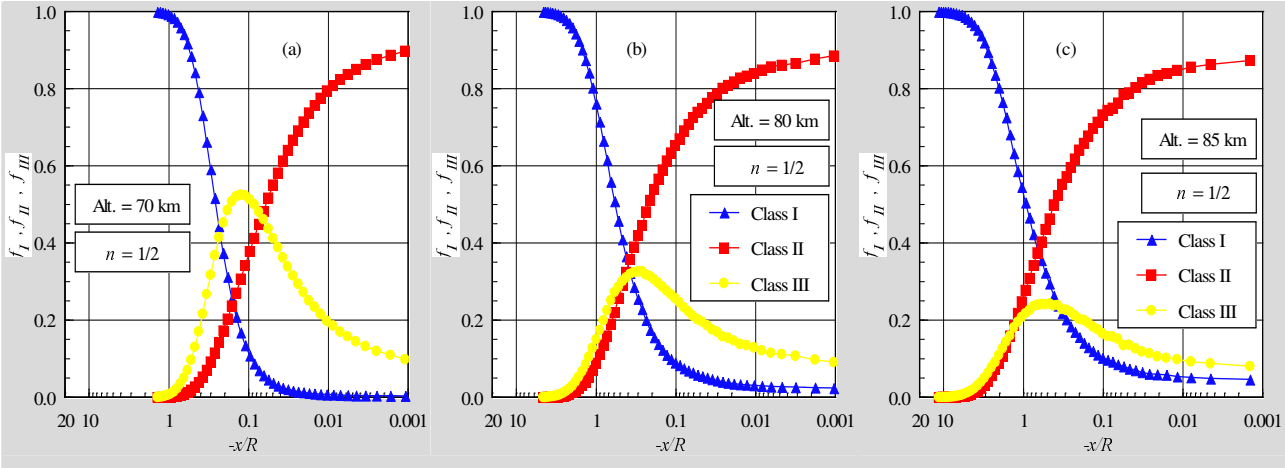

Figure 3: Distributions of molecules for classes I, II and III along the stagnation streamline for power-law exponent n of 1/2 and altitude of (a) 70, (b) 80 and (c) 85 km.

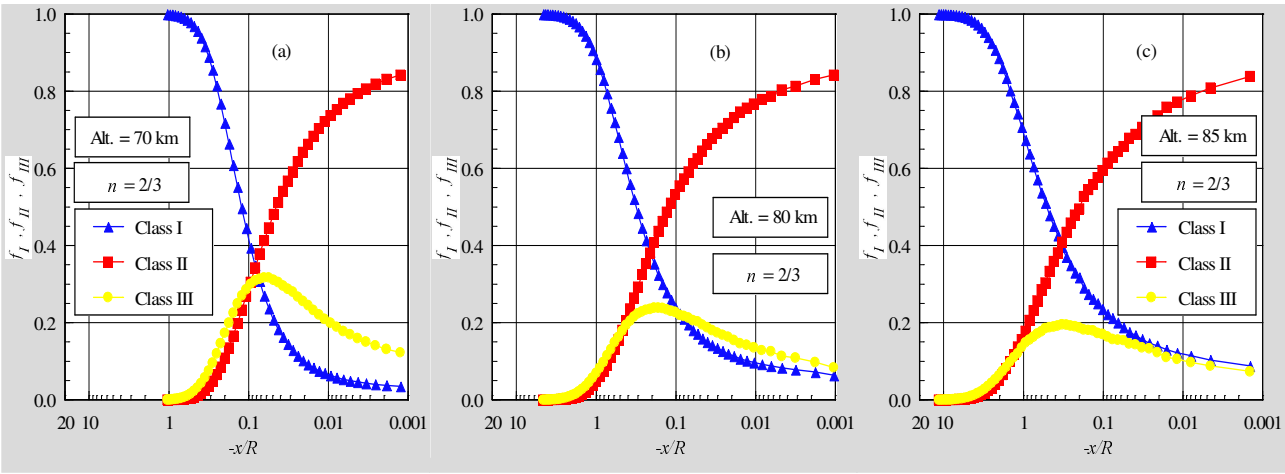

Figure 4: Distributions of molecules for classes I, II and III along the stagnation streamline for power-law exponent n of 2/3 and altitude of (a) 70, (b) 80 and (c) 85 km.

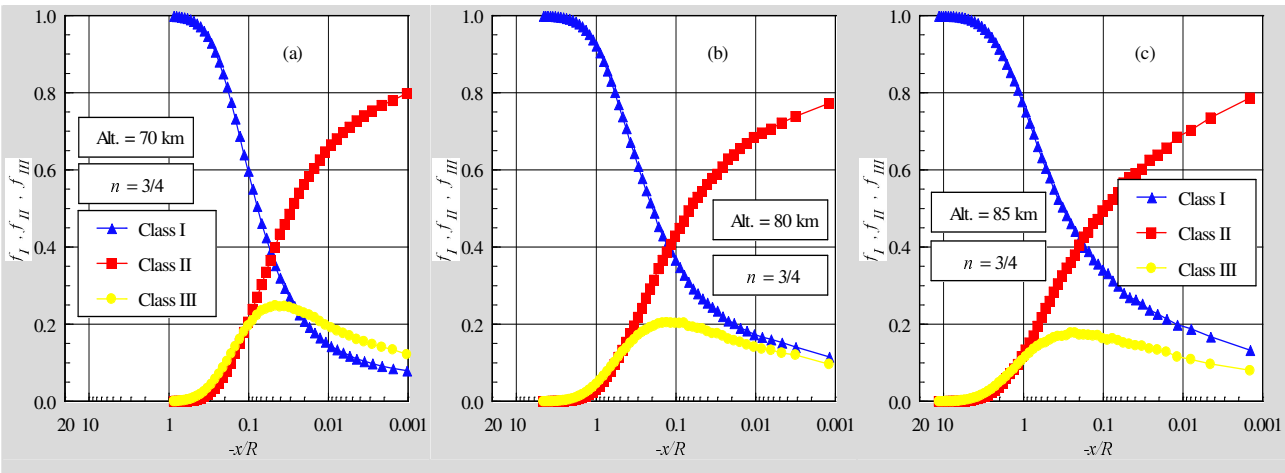

Figure 5: Distributions of molecules for classes I, II and III along the stagnation streamline for power-law exponent n of 3/4 and altitude of (a) 70, (b) 80 and (c) 85 km.

In this connection, of particular interest in Figs. (3), (4) and (5) is the upstream disturbance of the flowfield. It is clearly seen in this set of figures that the flowfield upstream disturbance increases with increasing the altitude. As an illustrative example, for power-law exponent of 1/2, the class I molecules defined by f_I, = 0.99 is located at an upstream distance x/R of around 1.0, 3.1 and 6.0 for altitudes of 70, 80 and 85 km, respectively. As a reference, for power-law exponent of 3/4, the class I molecules defined by f_I, = 0.99 is located at an upstream distance x/R of around 0.5, 2.2 and 5.0 for altitudes of 70, 80 and 85 km, respectively. Therefore, it is observed that the rarefaction effect on the upstream disturbance is less pronounced as the leading edge becomes aerodynamically sharp.

7.2. Shock Wave Standoff Distance

The shock wave standoff distance Δ for the leading edges corresponding to n of 1/2, 2/3 and 3/4 can be observed in Figs. (3) (4) and (5), respectively. It is apparent from these plots that there is a discrete shock standoff distance for the cases shown. In conformity with the definition presented in Fig. (2b), the calculated shock wave standoff distance Δ, normalized by the radius R of the reference circular cylinder, is tabulated in Tab. (3) for the cases investigated. As would be expected, the shock standoff distance increases with increasing the altitude. By increasing the altitude, or increasing in the Knudsen number Kn_∞, the presence of the leading edge is communicated to a lager distance ahead of the nose of the leading edge since the molecules interact little with each other and collisions among them are less frequent. As a result, the center of the shock wave is located more away from the nose, resulting in a shock standoff rise. Moreover, the shock standoff distance decreases by increasing the power-law exponent n. This is explained by the fact that, as the power-law exponent n increases from 1/2 to 3/4 the leading edge changes from blunt to sharp one. As a result, the leading edge becomes more streamlined, and the presence of the leading edge is communicated to a smaller distance ahead of the leading edge. As a reference, for the n = 1/2 case, the shock standoff distance for altitudes of 70, 80 and 85 km is around 2.9, 2.5 and 2.3 times, respectively, larger than those for the n = 3/4 case.

Table 3: Dimensionless shock wave standoff distance Δ/R for power-law leading edges.

Altitude (km)	n = 1/2	n = 2/3	n = 3/4
70	0.122	0.062	0.042
80	0.296	0.172	0.119
85	0.525	0.311	0.230

Before proceeding with the analysis, it is desirable to compare the shock standoff distance for power-law shapes with that for the circular cylinder, shown in Fig. (1a). According to Santos and Lewis (2005a), the circular cylinder provides a larger shock standoff distance, i.e., Δ/R of 0.297 for an altitude of 70 km. This value is about 2.4, 4.8 and 7.1 times larger than that for power-law exponent n of 1/2, 2/3 and 3/4, respectively, for the same altitude. The results tend to confirm the expectation that the shock standoff distance for sharp leading edge is smaller than that for blunt leading edge. In fact, the power-law bodies behave as if they had a sharper profile than the representative circular cylinder, as shown in Fig.(1a).

It is important to mention that shock standoff distance becomes important in hypersonic vehicles such as waveriders, which depend on leading edge shock attachment to achieve their high lift-to-drag ratio at high lift coefficient. In this connection, power-law shapes seem to be more appropriate than the circular cylinder, since they present reduced shock wave detachment distances. Nevertheless, smaller shock detachment distance is associated with a higher heat load to the nose of the body. According to Santos and Lewis (2002), the heat transfer coefficient C_{ho} (= $2q_w/\rho_\infty V_\infty^2$) at the stagnation point for power-law shapes defined by n of 1/2, 2/3 and 3/4, at an altitude of 70 km, is around 1.7, 2.1 and 2.3 times larger than the heat transfer coefficient for the circular cylinder at the same conditions. Consequently, it should be notice from this comparison that the ideal blunting leading edge depends on the context. If shock standoff distance is the primary issue in leading edge design of hypersonic waveriders, then power-law shapes are superior to round leading edges (circular cylinder). In contrast, if the stagnation point heating is the important parameter in the hypersonic vehicle design, then round shapes seem to be superior to the power-law shapes.

7.3. Shock Wave Thickness

The shock wave thickness δ along the stagnation streamline can be obtained from Figs. (3), (4) and (5) for the power-law shapes based on the definition of the shock wave thickness shown in Fig. (2b). As a result of the calculation, Tab. (4) tabulates the shock-wave thickness δ, normalized by the radius R of the reference circular cylinder, for the cases investigated.

The circular cylinder provides a much larger shock thickness, i.e., δ/R, of 0.605 for an altitude of 70 km. Compared to the power-law shapes, this value is about 2.1, 3.8 and 5.2 times larger than that for power-law exponent n of 1/2, 2/3 and 3/4, respectively, for the same altitude.

Table 4: Dimensionless shock wave thickness δ/R for power-law leading edges.

Altitude (km)	n = 1/2	n = 2/3	n = 3/4
70	0.285	0.161	0.117
80	0.732	0.514	0.391
85	1.390	1.034	0.800

7.4. Shock Wave Shape

The shock wave shape, defined by the shock wave center location, is obtained by calculating the position that corresponds to the maximum f for class III molecules in the η-direction along the body surface (see Fig. (1b)). Figures (6a), (6b) and (6c) display the shock-wave shape on power-law bodies defined by n of 1/2, 2/3 and 3/4, respectively, as a function of the altitude. In this set of plots, the Cartesian coordinates x and y are normalized by the radius R.

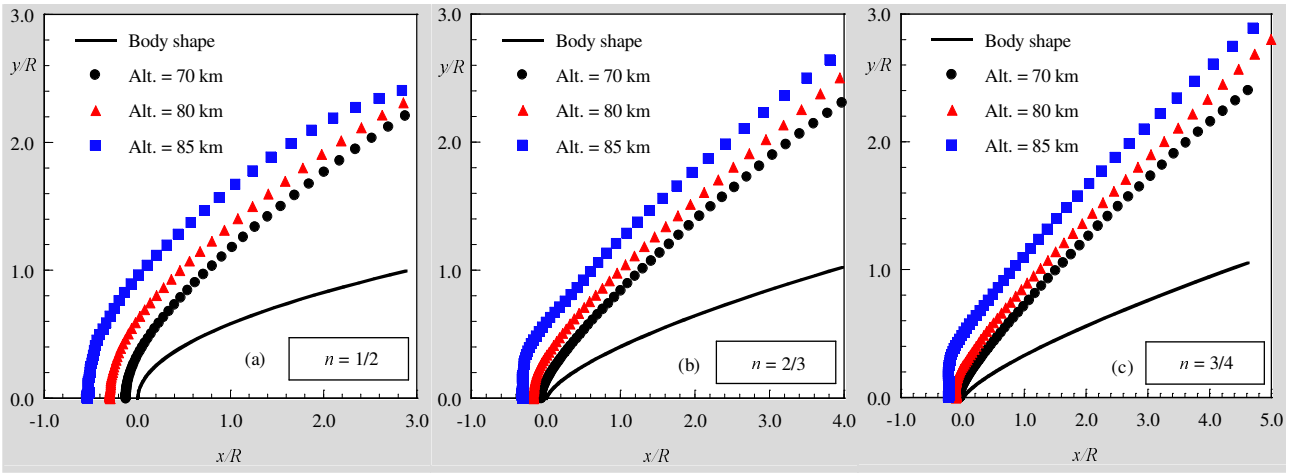

Figure 6: Shock wave shapes on power-law bodies as a function of the altitude for power-law exponent n of (a) 1/2, (b) 2/3 and (c) 3/4.

It was pointed out by Lees and Kubota (1957) that when the freestream Mach number M_∞ is sufficiently large, the hypersonic small-disturbance equations admit similarity solutions for the asymptotic shock wave shapes over power-law bodies ($y \propto x^n$, $0 < n < 1$), where asymptotic refers to the flowfield at large distances downstream of the nose of the body. The hypersonic small-disturbance theory states that, for certain exponent n, a body defined by x^n produces a shock wave of similar shape and profiles of flow properties transverse to the stream direction that are similar at any axial station not too near the nose. At or near the nose, the surface slope, the curvature, and the higher derivatives are infinite, and the similarity solutions break down. In the more general case for $0 < n < 1$, the shock wave grows as x^m. When n grows from zero, m begins by keeping the constant value $m = 2/3$, and if n keeps on growing towards unity, m remains equal to n.

By assuming that power-law bodies generate power-law shock waves in accordance with hypersonic small-disturbance theory, the shock location coordinates shown in Fig. (6) were used to approximate the shape of the shock wave with a curve fit. A fitting algorithm was performed over these points to approximate the shock shape as a power law curve of the following form,

$$y = A(x + B)^m \tag{2}$$

where A is the shock-wave power-law constant, B is the distance from the nose of the leading edge to the shock wave curve fit along the stagnation streamline, and m is the shock-wave power-law exponent.

For comparison purpose, two forms of the curve fit were considered in defining the shock shape: (1) A and B were found by keeping $m = 2/3$ for $n < 2/3$ cases, (2) $m = n$ for $n \geq 2/3$ cases, and (3) A, B and m were found to provide the best curve fit solutions where n and m stand for body and shock wave power-law exponents, respectively.

It is important to mention that the fitting process was performed over the points yielded by DSMC simulations located far from the nose region, say $x/R > 1.0$, where it is expected that the blunt nose effects are not significant. It is also important to recall that the shock wave shape at the vicinity of the nose is not correctly predicted by the theoretical solutions, since the hypersonic slender body approximations are violated close to or at the nose of the leading edges as explained above.

Curve fit solutions for shock shape over the body power-law exponent n of 1/2 are displayed in Fig. (7a) for altitude of 70 km. In this figure, the solutions given by m = 2/3 and m = 0.670 represent, respectively, two forms of the curve fit solutions mentioned above. For comparison purpose, the form $m = n$ = 1/2 is also displayed in this figure. It is apparent from Fig. (7a) that, except for the form $m = n$ = 1/2, the curve fit solutions present a good agreement, by visual inspection, with those solutions provided by the DSMC simulation. Nevertheless, as the maximum absolute error between the DSMC solutions and the curve fit solutions are calculated for coordinate points located at $x/R > 1.0$, it is found that the best fit is obtained for that form of the fitting process where A, B and m were found in order to yield the best solution.

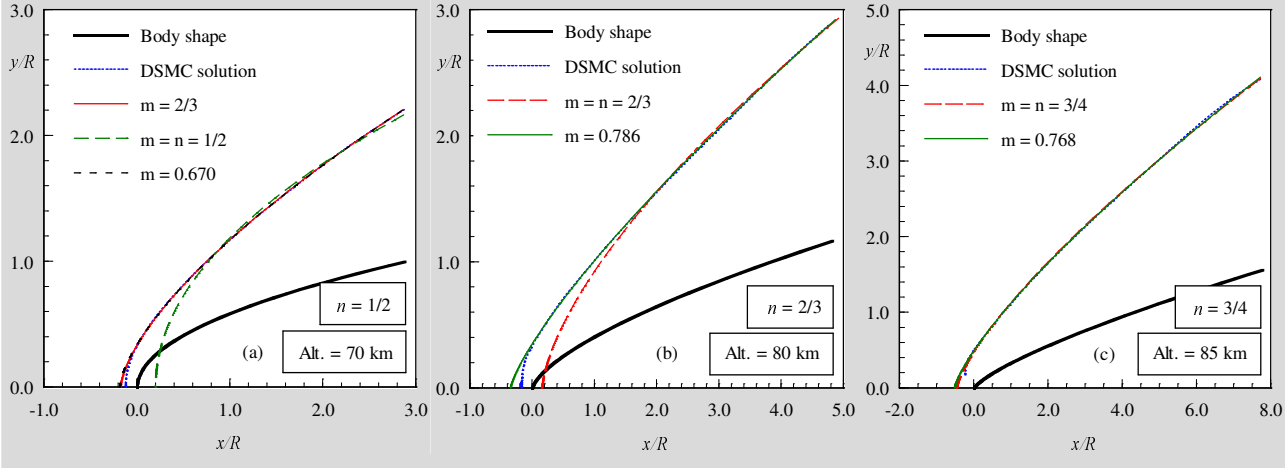

Figure 7: Shock wave shapes on power-law bodies for power-law exponent n of (a) 1/2 and altitude of 70 km, (b) 2/3 and altitude of 80 km, and (c) 3/4 and altitude of 85 km.

Shock shape curve fit solutions for body power-law exponent n of 2/3 are displayed in Fig. (7b) for altitude of 80 km. The curve fit solutions shown in this set of figures were obtained according to Eq.(2) by two different forms; in the first form, A and B were found by keeping m equal to the body shape, $m = n$; in the second form, A, B and m were found in order to obtain the best fit.

Referring to Fig. (7b), it is noted that the curve fit given by $m = n$ = 2/3 present a reasonable agreement far from the nose of the leading edge. Nonetheless, the curve fit solution given by m equal to 0.786 present an excellent agreement with those solutions provided by the DSMC simulation. Once again, the curve-fitted solution deviates from the DSMC solution close to the nose of the leading edge, as would be expected.

Finally, curve fit solutions for shock shape over the body power-law exponent n of 3/4 are displayed in Fig. (7c) for altitude of 85 km. In this figure, the solutions given by $m = n$ = 3/4 and m = 0.768 represent, respectively, two forms of the curve fit solutions mentioned above. It is clearly seen in this figure that the curve fit solutions given by present a remarkable agreement with those solutions provided by the DSMC simulation.

According to Figs. (7a), (7b) and (7c), it is observed that, in general, the solutions are in qualitative agreement with the Lees and Kubota (1957) findings in the sense that the shock wave shape would follow the shape of the body for body power law exponent $n > 2/3$.

At this point, it should be emphasized that the curve fit exponents are very sensitive to the number of coordinate points, which define the shock wave, used in the fitting process. In addition, these coordinate points present fluctuations, originated from the DSMC simulations.

8. Concluding Remarks

This study applies the Direct Simulation Monte Carlo method to investigate the shock wave structure for a family of power-law leading edges. The calculations have provided information concerning the nature of the shock wave detachment distance, shock wave thickness and shock wave shape resulting from variations on the power-law exponent and on the freestream Knudsen number for the idealized situation of two-dimensional hypersonic rarefied flow.

The analysis showed that the shock wave structure was affected by changes on the rarefaction via altitude. It was found that the shock wave standoff and the shock wave thickness increased with the altitude rise. In addition, the shock wave was displaced further upstream the nose of the leading edges with increasing the altitude. It was also found that the shock wave standoff distance and the shock wave thickness for the power-law bodies are lower than that for the circular body with the same tangency to a wedge of specified oblique angle. Moreover, the computational results indicated that the shock wave shape grows with power law form ($\propto x^m$), for the power-law bodies investigated.

9. References

Alexander, F. J., Garcia, A. L., and, Alder, B. J., 1998, "Cell Size Dependence of Transport Coefficient in Stochastic Particle Algorithms", Physics of Fluids, Vol. 10, No. 6, pp. 1540-1542.

Alexander, F. J., Garcia, A. L., and, Alder, B. J., 2000, "Erratum: Cell Size Dependence of Transport Coefficient is Stochastic Particle Algorithms", Physics of Fluids, Vol. 12, No. 3, pp. 731-731.

Bird, G. A., 1981, "Monte Carlo Simulation in an Engineering Context", Progress in Astronautics and Aeronautics: Rarefied gas Dynamics, Ed. Sam S. Fisher, Vol. 74, part I, AIAA New York, pp. 239-255.

Bird, G. A., 1989, "Perception of Numerical Method in Rarefied Gasdynamics", Rarefied gas Dynamics: Theoretical and Computational Techniques, Eds. E. P. Muntz, and D. P. Weaver and D. H. Capbell, Vol. 118, Progress in Astronautics and Aeronautics, AIAA, New York, pp. 374-395.

Bird, G. A., 1994, "Molecular Gas Dynamics and the Direct Simulation of Gas Flows", Oxford University Press, Oxford, England, UK.

Borgnakke, C. and Larsen, P. S., 1975, "Statistical Collision Model for Monte Carlo Simulation of Polyatomic Gas Mixture", Journal of computational Physics, Vol. 18, No. 4, pp. 405-420.

Garcia, A. L., and, Wagner, W., 2000, "Time Step Truncation Error in Direct Simulation Monte Carlo", Physics of Fluids, Vol. 12, No. 10, 2000, pp. 2621-2633.

Guo, K. and Liaw, G.-S., 2001, "A Review: Boundary Conditions for the DSMC Method", Proceedings of the 35th AIAA Thermophysics Conference, AIAA Paper 2001-2953, Anaheim, CA, 11-14 June.

Hadjiconstantinou, N. G., 2000, "Analysis of Discretization in the Direct Simulation Monte Carlo", Physics of Fluids, Vol. 12, No. 10, pp. 2634-2638.

Lees, L. and Kubota, T., 1957, "Inviscid Hypersonic Flow over Blunt-Nosed Slender Bodies", Journal of Aeronautical Sciences, Vol. 24, No. 3, pp. 195-202.

Nonweiler, T. R. F., 1959, "Aerodynamic Problems of Manned Space Vehicles", Journal of the Royal Aeronautical Society, Vol. 63, Sept, pp. 521-528.

Mason, W. H. and Lee, J., 1994, "Aerodynamically Blunt and Sharp Bodies", Journal of Spacecraft and Rockets, Vol. 31, No. 3, pp. 378-382.

Santos, W. F. N. and Lewis, M. J., 2002, "Power Law Shaped Leading Edges in Rarefied Hypersonic Flow", Journal of Spacecraft and Rockets, Vol. 39, No. 6, pp. 917-925.

Santos, W. F. N. and Lewis, M. J., 2005a, "Aerothermodynamic Performance Analysis of Hypersonic Flow on Power Law Leading Edges", Journal of Spacecraft and Rockets, Vol. 42, No. 4, pp. 588-597.

Santos, W. F. N. and Lewis, M. J., 2005b, "Calculation of Shock Wave Structure over Power Law Bodies in Hypersonic Flow", Journal of Spacecraft and Rockets, Vol. 42, No. 2, pp. 213-222.

Van Dyke, M. D., 1954, "A Study of Hypersonic Small-Disturbance Theory", NACA TN-3173.

Proceedings of the 11th Brazilian Congress of Thermal Sciences and Engineering -- ENCIT 2006
Braz. Soc. of Mechanical Sciences and Engineering -- ABCM, Curitiba, Brazil, Dec. 5-8, 2006

Paper CIT06-0498

MODELO DE DESEMPENHO DO SISTEMA PROPULSIVO DO VANT-ITA

Pedro Teixeira Lacava
Instituto Tecnológico de Aeronáutica – São José dos Campos - SP
placava@ita.br

Cristiane Aparecida Martins
Instituto Tecnológico de Aeronáutica – São José dos Campos - SP
cmartins@ita.br

Amílcar Porto Pimenta
Instituto Tecnológico de Aeronáutica – São José dos Campos - SP
amílcar@ita.br

Carlos Guedes Neto
Instituto Tecnológico de Aeronáutica – São José dos Campos - SP
guedes@ita.br

Gustavo Violato
Instituto Tecnológico de Aeronáutica – São José dos Campos - SP
gustavoviolato@redecasd.ita.br

Resumo. Nos dias de hoje existem diversas aplicações para Veículos Aéreos não Tripulados - VANT e essa é uma importante área de desenvolvimentos aeroespaciais. Algumas dessas aplicações são muito dependentes do desempenho do veículo para concluir a satisfatoriamente a missão. Assim, são necessárias simulações de desempenho baseadas em modelos de mecânica de vôo no estágio de projeto do veículo. Uma parte específica do modelo global de mecânica de vôo é o modelo de desempenho do sistema propulsivo, cuja idéia é obter informações para tração, torque, consumo de combustível e consumo específico de combustível, como função da rotação do motor, altitude e velocidade de vôo. Desta forma, o presente trabalho mostra o desenvolvimento de um modelo de sistema propulsivo para motor a pistão dois tempos/hélice para uma aplicação de VANT.

Palavras chave: *veículo aéreo não tripulado, VANT, modelo de sistema propulsivos.*

1. Introdução

Uma das áreas que mais cresce no setor aeroespacial é o desenvolvimento de veículos aéreos não tripulados, comumente chamados de VANTs. Impulsionados inicialmente por aplicações militares, os VANTs começam a ganhar aplicações em diversas áreas como agricultura, segurança, patrulhamento de áreas, ajuda a resgates, entre outras. Atualmente há diversos grupos em todo mundo trabalhando no desenvolvimento não só de aeronaves não tripuladas, mas aeronaves autônomas, ou seja, de aeronaves que sejam capazes de executarem sua missão sem a interferência humana, apenas através de um sistema de posicionamento e controle.

Em função de algumas missões de um VANT serem extremamente sensíveis ao desempenho da aeronave em condições normais de operação e muitas vezes estarem sujeitas a condições intempestivas como a possibilidade de fortes rajadas. Sendo assim, são necessárias várias simulações baseadas em modelos de mecânica de vôo para prever o desempenho da aeronave durante a fase de projeto desta. Embutido no modelo global de mecânica de vôo deve estar previsto um modelo específico para o sistema propulsivo que seja possível descrever os comportamentos do empuxo, torque transmitido à aeronave, consumo de combustível e consumo específico de combustível, em função da rotação do motor, velocidade de vôo e altitude. Contudo, em função de muitas vezes a potência de eixo do motor exigida para cumprir o envelope de vôo da aeronave não tripulada é de apenas alguns hp, fazendo com que seja muito difícil encontrar dados dos motores e hélices dessa classe de motores.

Dentro desse contexto, o objetivo do presente trabalho foi o de apresentar a metodologia desenvolvida para se obter um modelo propulsivo constituído de um motor a pistão a gasolina dois tempos e hélice, para uso na simulação de desempenho em um VANT cuja missão é a inspeção de linhas de transmissão de energia elétrica através do uso de termo-câmeras para identificação de sinistros na linha. O desenvolvimento desse modelo faz parte do projeto "Inspeção de Linhas de Transmissão Utilizando Aeronaves não Tripuladas Autônomas", Financiada pela Financiadora de Estudos e Projetos – FINEP, desenvolvida pelo Instituto Tecnológico de Aeronáutica – ITA, C.E.S.A.R. e Companhia Hidrelétrica do São Francisco – CHESF (Finep, 2005).

O presente artigo limita-se a comentar as considerações sobre a escolha do sistema propulsivo e desenvolvimento do seu modelo de desempenho, não entrando em detalhes sobre o projeto da aeronave, apenas quando necessário para o contexto do sistema propulsivo.

2. Escolha do Motor

Para escolha do motor**,** quatro itens foram levados em conta: segurança (carga valiosa), potência necessária para cumprir a missão em qualquer fase do envelope de vôo, incluído situações inesperadas (ex: rajadas), baixo consumo de combustível (o que interfere no peso de tanque molhado ou no alcance da missão) e peso do motor. Assim, tais critérios de escolha foram levados em conta e a configuração escolhida representa uma solução de compromisso entre eles.

Dentre esses quatro requisitos citados no parágrafo anterior, alguns parâmetros mínimos foram especificados e são listados na seqüência.

- *Potência no eixo*: segundo as simulações de mecânica de vôo, em condições de rajada pode-se necessitar do motor uma potência de eixo de até 5hp; assim, por segurança, definiu-se como potência máxima de eixo no mínimo 6hp.
- *Cilindros*: dois dispostos lado a lado. A presença de dois cilindros suaviza o funcionamento do motor, ou seja, induz menos vibração.
- *Tipo de ciclo de funcionamento*: dois tempos. Motores mais simples e sem a presença de válvulas (menos peso).
- *Combustível e ignição da mistura*: gasolina de aviação e centelha. Os motores a gasolina são mais econômicos e sofrem menos problemas de apagamento. O combustível é mais barato, mas é necessária uma atenção especial para o problema de a centelha interferir nos equipamentos eletrônicos.
- *Peso do motor*: não seja superior a 4kg.

Acrescido às características citadas, outro ponto importante é a performance do motor, ou seja, as curvas de potência de eixo, torque e consumo específico em função da rotação de operação. Apesar dessas informações serem triviais para motores aeronáuticos e automotivos de maior potência, para a potência desejada a falta dessas informações passou a ser o maior "gargalo" para especificar o motor. O contato com os fabricantes mostrou que grande maioria dos usuários desse tipo motor, não busca informações tão refinadas e que os números apresentados em catálogos são uma mera estimativa.

Dentro dos motores pré-selecionados, a escolha convergiu para o motor Zenoah G800BPU, pois, além de obviamente cumprir com as especificações desejadas, dois pontos foram fundamentais para sua escolha: 1) segurança de funcionamento, ou seja, baixo registro de falhas (informação de usuários); 2) fácil relacionamento com o fabricante, o que permitiu obter a curva de potência em função da rotação. A Tab. 1 apresenta as principais características do motor. A Fig. 1 apresenta as curvas de potência e torque do motor.

Tabela 1. Características do motor escolhido.

Tipo: 2-Cilindros Deslocamento: 4.88 cu in (80 cc) Diâmetro interno: 40.5 mm (1.60 in) Curso: 31 mm (1.22 in) Cilindros: 2 - Cromo platinado Peso Total: 123 oz (3,487 kg) Peso do motor (somente): 108 oz (3,06 kg) Peso abafador: 15 oz *Crankshaft Threads*: M10 x 1.25 Hélice na bancada: 24 x 10 APC @ 7,400 Hélice faixa: 22"x12" – 24"x10" RPM - faixa: 1,800 - 10,000 Combustível: Gasolina / mistura óleo Dimensões: 192 x 257 x 205 mm Tipo de cilindro: anel Tipo de Carburador: Walbro WJ-64 Refrigeração: ar	

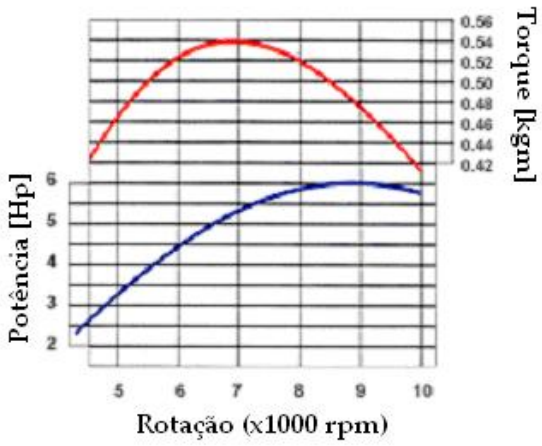

Figura 1. Curvas de Torque e Potência do motor.

3. Modelo de Funcionamento do Motor

Basicamente três informações sobre o funcionamento do motor são necessárias em função da rotação e da altitude de vôo: a potência de eixo, o torque e o consumo específico.

3.1. Potência do Motor (no eixo)

A potência do motor foi obtida diretamente da curva potência de eixo versus rotação do motor, conforme Fig. 1. Para inclusão da variação da potência em um programa de simulação de mecânica de vôo, a curva apresentada pelo fabricante foi escrita como um polinômio do terceiro grau.

$$N = -0{,}772066 + 0{,}00647169.(rot) + 0{,}266071.(rot)^2 - 0.020243.(rot)^3, \quad [hp] \tag{1}$$

onde, N = potência a 1atm e 288K em hp e rot = rotação em rpm/1000.

A Fig.2 apresenta a concordância do polinômio com os resultados apresentados pelo fabricante do motor.

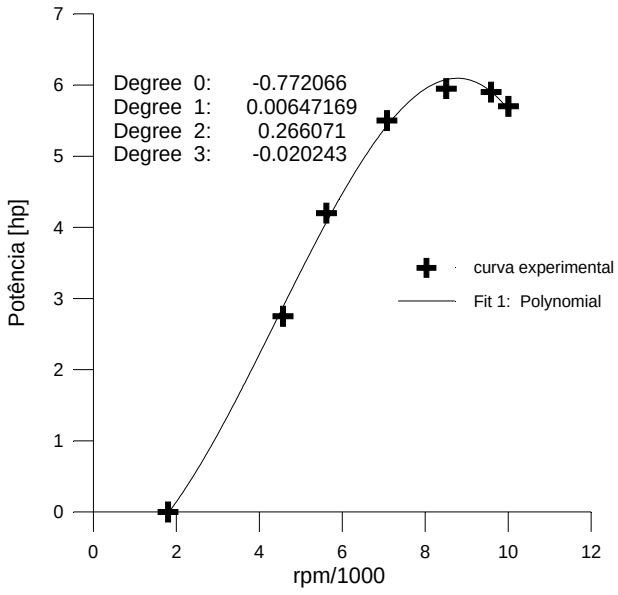

Figura 2. Concordância do polinômio com o resultado apresentado pelo fabricante.

3.2. Correção da Potência (no eixo) com as condições ambientais.

Como a capacidade de aspiração do motor diminui com a altitude, a potência de eixo corrigida em hp (Nc) em relação à potência ao nível do mar fica:

$$Nc = (N.p)/(T/288)^{1/2} \quad [hp] \tag{2}$$

p = pressão ambiente em atm.
T = temperatura ambiente em K.

3.3. Torque de reação na aeronave

Modelo de torque (Torq) baseado no valor da potência de eixo do motor.

$$Torq = 0{,}00712.(Nc/rot) \quad [kN.m] \tag{3}$$

ou

$$Torq = 0{,}7255.(Nc/rot) \quad [kgm] \tag{4}$$

Lembrado que Nc é a potência corrigida em hp e rot a rotação em rpm/1000. A Fig. 3 apresenta o resultado do torque calculado e o experimental apresentado pelo fabricante do motor ao nível do mar e diferentes rotações.

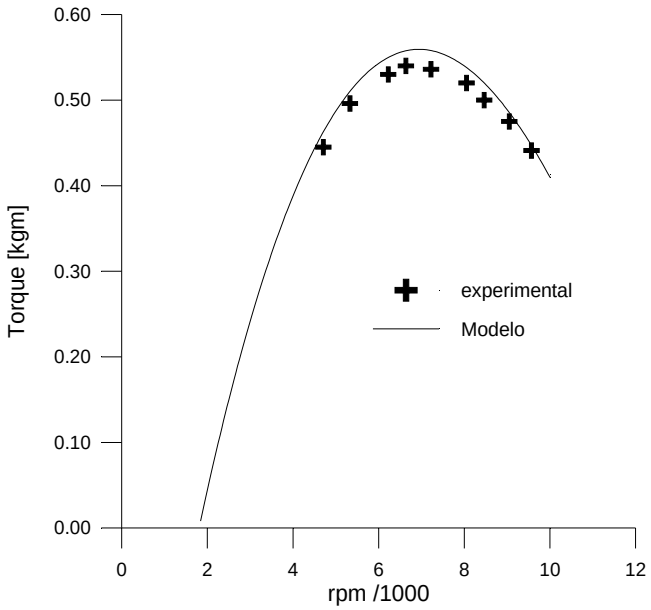

Figura 3. Comparação entre os resultados do modelo e os apresentados pelo fabricante do motor.

3.4. Consumo Específico de Combustível

Para calcular o consumo específico são necessários os valores da quantidade de ar aspirado pelo motor, da razão ar combustível e do consumo de combustível, todos em função da rotação.

A quantidade de ar aspirada é calculada como:

$$m_{ar} = (p/T).V_c.rot.21{,}1 \quad [kg/h] \tag{5}$$

onde, p = pressão ambiente em atm, T = temperatura ambiente em K, V_c = cilindrada total do motor em cm^3, rot = rotação rpm/1000. Para se determinar a razão ar combustível, baseou-se na curva típica do sistema de injeção de combustível de motores a pistão (curva de demanda), conforme Fig.4 (Garcia e Brunetti, 1992).

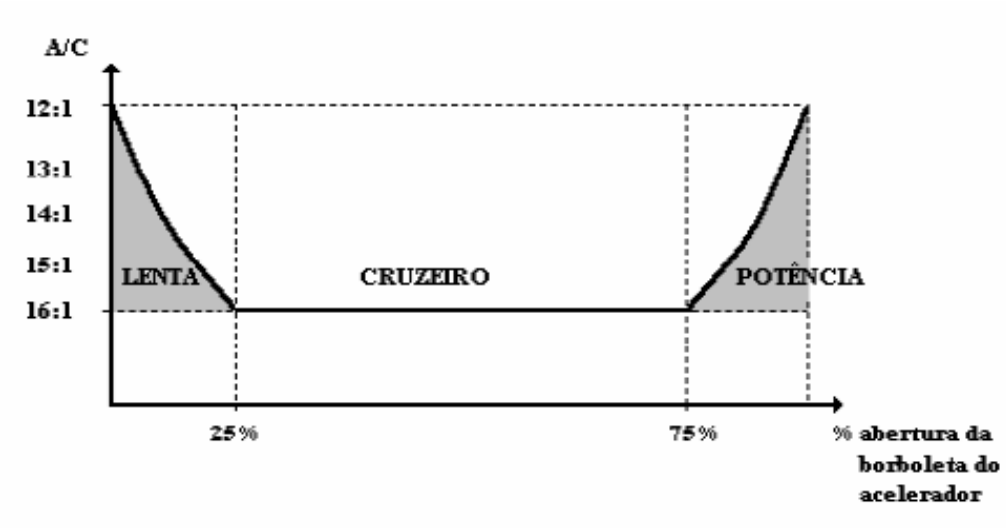

Figura 4. Curva de demanda de um motor a pistão.

Com os dados fornecidos pelo fabricante e as informações da Fig. 4, calculou-se a razão ar/combustível (F(A/C)) para alguns pontos de operação do motor e montou-se a curva de demanda desse motor, Fig.5. Ajustou-se a curva de demanda como um polinômio do quarto grau.

$$F(A/C) = 0{,}0154667.\text{rot}^4 - 0{,}327264.\text{rot}^3 + 2{,}06074.\text{rot}^2 - 3{,}47031.\text{rot} + 13{,}3461 \quad (6)$$

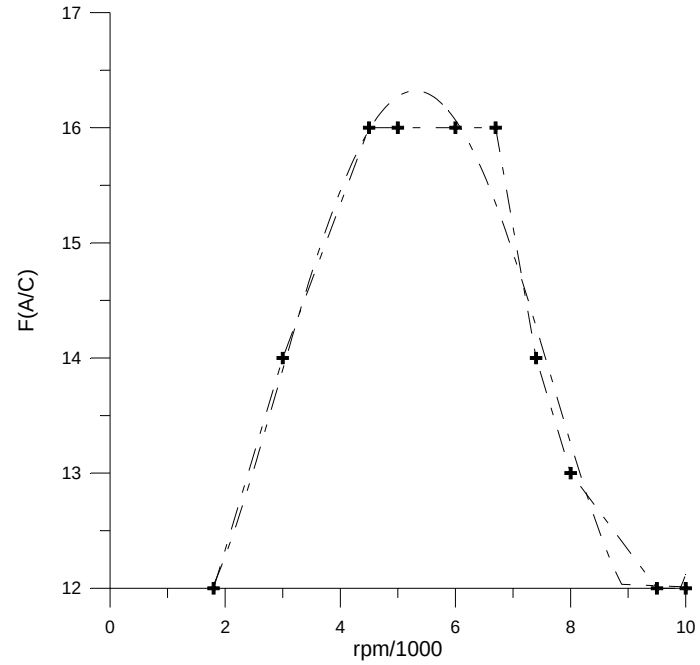

Figura 5. Curva de demanda do motor e ajuste por polinômio do quarto grau.

Com a vazão de ar e razão ar/combustível como funções da rotação, calcula-se o consumo de combustível e o consumo específico de combustível pelas equações (7) e (8), respectivamente.

$m_f = m_{ar} / F$ [kg/h]. (7)

$$SFC = m_f / N_c \quad [kg/(hp.h)] \quad . \tag{8}$$

4. Modelo de Eficiência de Hélice

A eficiência de uma hélice é definida como sendo o quanto da potência de eixo fornecida pelo motor é transformada em potência de empuxo (definida adiante). A eficiência dessa transformação depende basicamente do desenho aerodinâmico da hélice, da rotação do eixo onde ela é acoplada e da velocidade de vôo (Solomon, 1953). Normalmente os fabricantes apresentam a eficiência da hélice em função do coeficiente de avanço (j) dessa. Contudo, para as dimensões pretendidas de diâmetro e passo da hélice (24"x10", conforme Tab. 1) não existe esse tipo de informação por parte dos fabricantes, provavelmente por ser um produto de baixo valor agregado e pelos consumidores não exigirem esse tipo de informação.

No entanto, para que as variações das condições de operação da aeronave e do motor pudessem ser contabilizadas nessa fase do projeto, decidiu-se desenvolver um modelo empírico baseado nos ensaios de várias hélices com diferentes razões diâmetro/passo realizados no túnel de vento do ITA. O resultados desses ensaios estão reunidos na Fig. 6. e, baseado nesses resultados, decidiu-se descrever a eficiência da hélice em função do coeficiente de avanço como um polinômio do segundo grau.

$$\eta_{pr} = a + b.j + c.j^2 \, , \tag{9}$$

onde j = coeficiente de avanço = u/(n.D), u = velocidade de vôo (m/s), n = rotação (rps) e D = diâmetro da hélice (m).

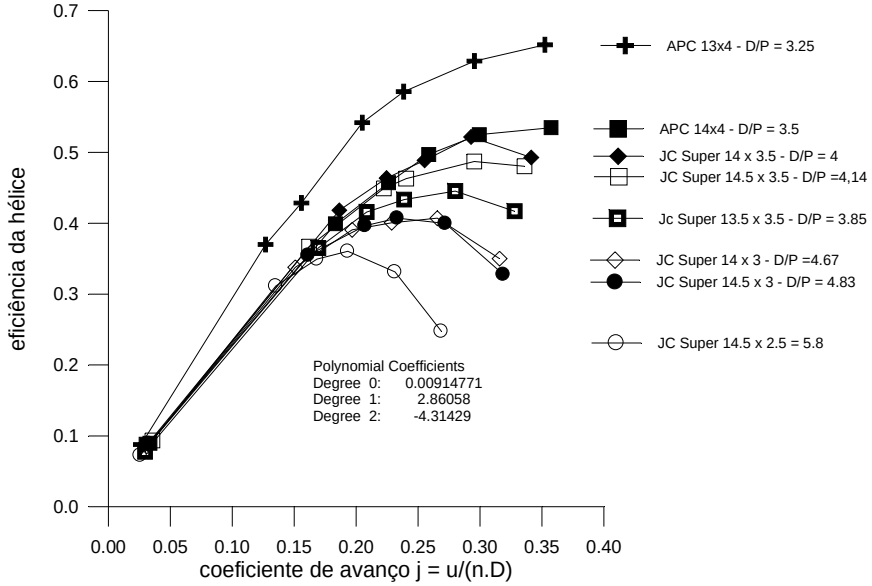

Figura 6. Eficiência das hélices em função do coeficiente de avanço.

Para se determinar os coeficientes do polinômio da Eq. (9) ajustou-se a curva de cada hélice ensaiada como um polinômio do segundo grau e aí gerou-se curvas da variação dos graus dos polinômios em função razão diâmetro/ passo das hélices (D/P), conforme Fig. 7. Assim os coeficientes dos graus da Eq. (9) foram escritos como polinômios de terceiro grau em função da razão (D/P), sendo:

$$a = 0 \quad , \tag{10}$$

$$b = 36.063-22.0861.(D/P)+4.80604.(D/P)^2-0.335109.(D/P)^3 \quad , \tag{11}$$

$$c = -95.9898+63.3504.(D/P)-13.9935.(D/P)^2+0.96083.(D/P)^3 \quad , \tag{12}$$

onde P = passo da hélice.

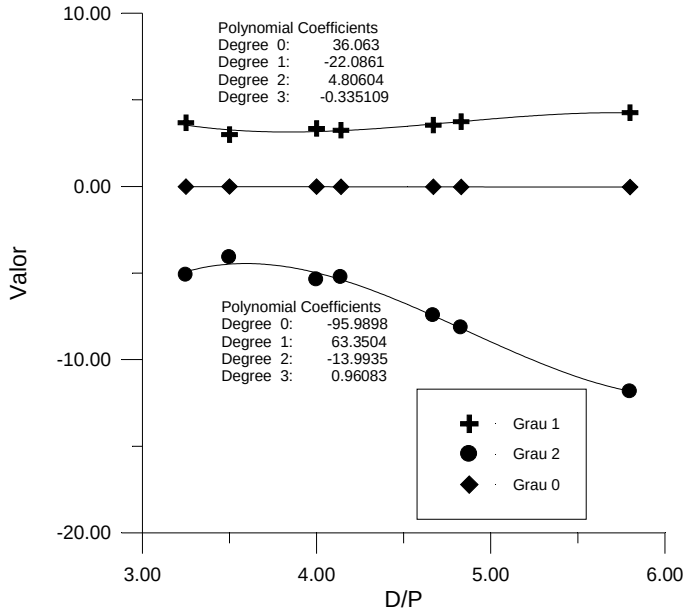

Figura 7. Variação dos graus do polinômio da Eq. (5) em função da razão diâmetro/ passo da hélice (D/P).

A Fig. 8 compara o modelo com o resultado de duas hélices ensaiadas no túnel de vento.

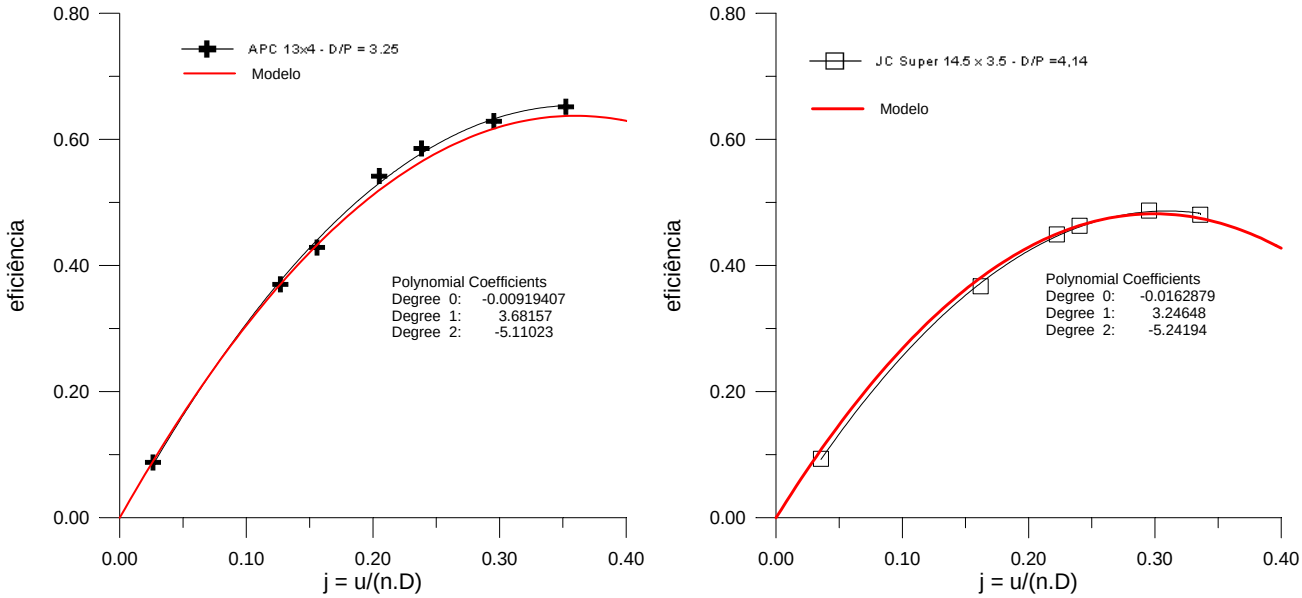

Figura 8. Eficiência da hélice em função do coeficiente de avanço – modelo e experimental.

5. Potência Disponível para Hélice (Nd) e Tração do Sistema Propulsivo em Vôo (Tra)

$$Nd = Nc.\eta_{pr} \quad [hp] \tag{13}$$

$$Tra = (Nd/1{,}341)/u \quad [kN] \tag{14}$$

Com a seqüência de cálculos apresentados até aqui é possível descrever o desempenho do sistema propulsivo (motor + hélice) em vôo em função da rotação do motor, velocidade de vôo e altitude. Os seguintes parâmetros devem ser previamente conhecidos para que os cálculos sejam executados:

p = pressão ambiente em atm.
T = temperatura ambiente em K.
u = velocidade de vôo em m/s.

n = rotação do motor em rps
V_c = cilindrada total do motor em cm^3 (para o presente projeto $80cm^3$)
D = diâmetro da hélice em m (para o presente projeto 0,61m)
D/P = razão diâmetro/ passo da hélice (para o presente projeto 2,4)

Com esses dados, seqüência de cálculos que deve ser executada é apresentada na Tab.2.

Tabela 2. Seqüência de cálculos para se obter a tração e o consumo específico do motor.

	Parâmetro	**Equação**	**unidade**
1	j	u/(n.D)	-
2	b	$36.063-22.0861.(D/P)+4.80604.(D/P)^2-0.335109.(D/P)^3$	-
3	c	$-95.9898+63.3504.(D/P)-13.9935.(D/P)^2+0.96083.(D/P)^3$	-
4	η_{pr}	$a + b.j + c.j^2$	-
5	rot	n.(60/1000)	rpm/1000
6	N	$-0,772066 + 0,00647169.(rot) + 0,266071.(rot)^2-0.020243.(rot)^3$	hp
7	Nc	$(N.p)/(T/288)^{1/2}$	hp
8	Torq	0,00712.(Nc/rot)	kN.m
9	Nd	$Nd = Nc.\eta_{pr}$	hp
10	Tra	(Nd/1,341)/u	kN
11	m_{ar}	$m_{ar} = (p/T).V_c.rot.21,1$	kg/h
12	F	$0,0154667.rot^4 - 0,327264.rot^3 + 2,06074.rot^2 - 3,47031.rot + 13,3461$	-
13	m_f	m_{ar} / F	kg/h
14	SFC	$m_f /(\eta_{pr}.N_c)$	kg/(hp.h)

6. Modelo Geral para Tração do Sistema Propulsivo

No item anterior apresentou-se como resultado para tração gerada pelo sistema propulsivo como sendo a razão entre a potência disponível para hélice e a velocidade de vôo, conforme Eq (14). Contudo, quando a velocidade de vôo se aproximando do valor nulo a tração tende ao infinito. Assim, o modelo de tração apresentado no item anterior seria apenas aconselhado para situações, como exemplo, vôo em cruzeiro. Contudo, para a correta previsão do desempenho da aeronave a estimativa em baixa velocidade de vôo, inclusive nula, é muito importante para se prever o comportamento de decolagem.

Dados obtidos no portal de Internet (2006) http://www.mh-aerotools.de/airfoils/javaprop.htm mostram como é o comportamento da tração obtida pelo sistema propulsivo em função da velocidade de vôo para diferentes modelos e tamanho de hélices, conforme Fig. (9). Desta forma, buscou-se um modelo que descrevesse comportamentos qualitativamente semelhantes ao da Fig. (15).

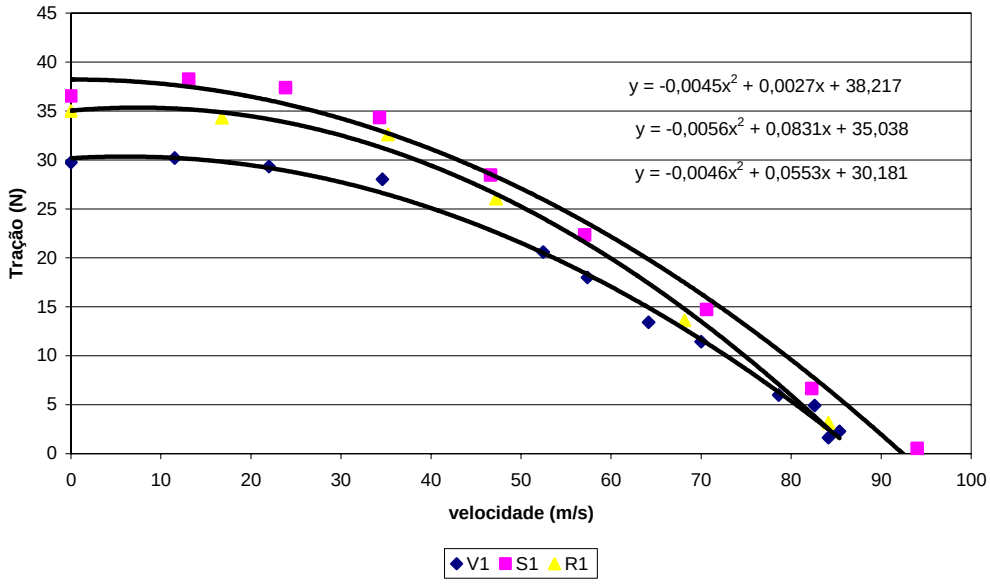

Figura 9. Comportamento da tração para sistemas propulsivos com as hélices V1, S1 e R1 em função da velocidade de vôo.

Para prever o comportamento estático da tração (velocidade de vôo u = 0) utilizou-se o modelo apresentado em Naca 447 (1932), onde a tração estática é dada por:

$$Tra^0 = (K_{T0}.Nc)/(rpm.D) \quad , \tag{15}$$

onde Tra^0 é a tração estática em lbf, Nc a potência de eixo corrigida em hp, rotação em rpm, D em pés e K_{T0} é o coeficiente de empuxo estático que é obtido através de dados experimentais variando-se a razão passo/diâmetro (Naca 447).

$$K_{T0} = 112400 - 57000.(P/D) \quad . \tag{16}$$

Utilizando uma hélice com diâmetro de 24" e passo de 10", que é a recomendada para o motor escolhido, obtém-se K_{T0} = 88460. Assim calculou-se a tração estática para diferentes rotações com essa hélice. Além disso, utilizou-se o modelo de tração em vôo para essas mesmas rotações em diferentes velocidades de vôo e aproveitaram-se os resultados coerentes para se traçar curvas de tendência acoplando o resultado de tração estática com o resultado coerente de tração em vôo, conforme Fig. (10). Os resultados foram obtidos para o nível do mar e temperatura ambiente de 288,15K. Nota-se um comportamento qualitativo semelhante ao da Fig. (9).

Os polinômios de ajuste das curvas de tendência foram escritos como polinômios do segundo grau, conforme Tab. (3). Assim, a tração ao nível do mar e a 288,15K ($Tra|_0$) é dada por:

$$Tra|_0 = a.u^2 + b.u + c \quad , \quad [N] \tag{17}$$

onde u é a velocidade de vôo em m/s e os coeficientes dos polinômio são funções da rotação (rpm), ajustando os dados da Tab. (3).

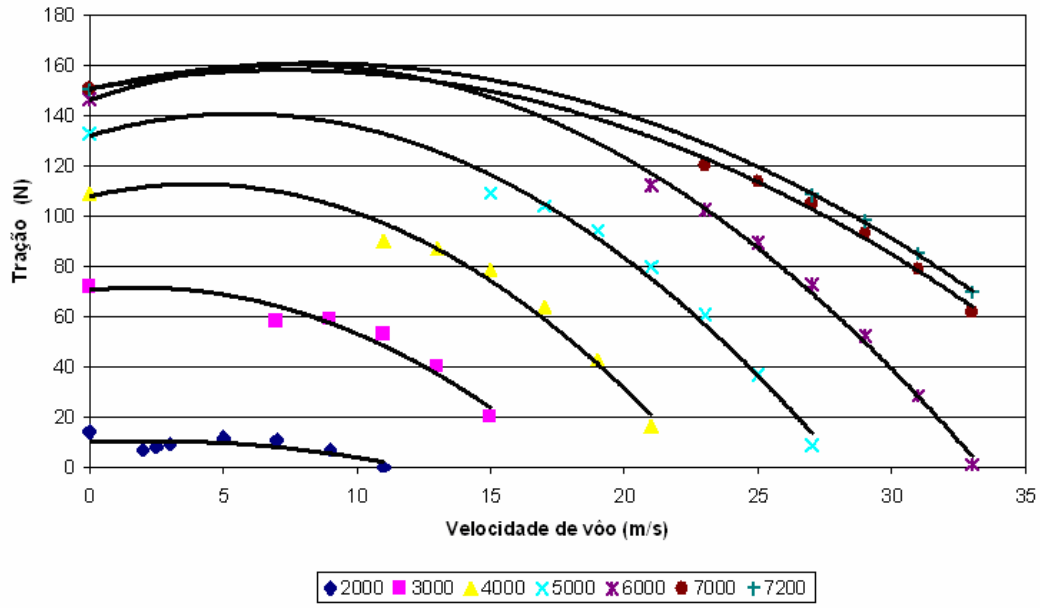

Figura 10. Comportamento da tração em função da velocidade para as rpm´s 2000, 3000, 4000, 5000, 6000, 7000 e 7200 ao nível do mar temperatura ambiente de 288,15K.

Tabela 3. Tração em função rotação.

rpm	y = tração e x = velocidade de vôo
2000	$y = -0{,}1071.x^2 + 0{,}4437.x + 10{,}239$
3000	$y = -0{,}278.x^2 + 1{,}0456.x + 70{,}541$
4000	$y = -0{,}3165.x^2 + 2{,}5148.x + 107{,}74$
5000	$y = -0{,}2782.x^2 + 3{,}1387.x + 131{,}88$
6000	$y = -0{,}2422.x^2 + 3{,}7051.x + 146{,}04$
7000	$y = -0{,}1425.x^2 + 2{,}0842.x + 150{,}46$
7200	$y = -0{,}1489.x^2 + 2{,}4899.x + 150{,}36$

$$a = -6.10^{-3}.rpm^3 + 1.10^{-7}.rpm^2 - 0{,}0006.rpm + 0{,}6839 \quad (18)$$

$$b = -9.10^{-11}.rpm^3 + 1.10^{-6}.rpm^2 - 0{,}0023.rpm + 1{,}9293 \quad (19)$$

$$c = 7.10^{-10}.rpm^3 - 2.10^{-5}.rpm^2 + 0{,}1243.rpm - 180{,}67 \quad (20)$$

Para se calcular a tração em uma condição qualquer, primeiramente calcula-se a constante k:

$$k = Tra|_0/N \quad , \quad (21)$$

onde N é a potência de eixo ao nível do mar e temperatura ambiente de 288,15K, calculado na Eq. (1). A Tração em qualquer altitude pode ser calculada como:

$$Tra = k.Nc \quad , \quad (22)$$

sendo Nc a potência de eixo corrigida pela altitude, seguindo a Eq. (2). É importante observar que a metodologia empregada nesse item já embute o comportamento particular da hélice, portanto não pode ser generalizado.

7. Conclusões

O presente trabalho apresentou um modelo de sistema propulsivo baseado em motor a pistão de dois tempos e hélice para aplicação em uma aeronave não tripulada para inspeção de sinistros em linhas de distribuição de energia elétrica.

O desenvolvimento de veículos aéreos autônomos para aplicações com exigências específicas, como a do presente caso, requer simulações do desempenho da aeronave durante a fase de projeto da mesma para que essas exigências sejam atendidas. Desta forma, a disponibilidade de um modelo que simule a comportamento do sistema moto-propulsor da aeronave passa a ser fundamental para as simulações de mecânica de vôo e controle. Contudo, para as exigências de baixa potência como a do presente caso é muito difícil encontrar algo já desenvolvido para literatura; exigindo uma certa criatividade do grupo de propulsão para encontrar um modelo que seja capaz de apresentar resultados com razoável descrição de comportamento, sendo que esse foi o enfoque do presente trabalho.

É evidente que um modelo que leva em conta dados fornecidos pelo fabricante do motor sem condição de uma verificação desses valores, dados empíricos de hélice levantado em túnel de vento e razão ar/combustível baseado em uma curva de demanda média para motores a pistão é bastante aproximado, não excluindo a necessidade de ensaios específicos para o motor e a hélice, o que será feito na próxima etapa desse projeto.

8. Agradecimentos

A Financiadora de Estudos e Projetos – FINEP, pelo apoio financeiro ao projeto “Inspeção de Linhas de Transmissão Utilizando Aeronaves não Tripuladas Autônomas”.

9. Referências

Financiadora de Estudos e Projetos, Finep, “Inspeção de Linhas de Transmissão Utilizando Aeronaves não Tripuladas Autônomos”, Relatório de Trabalho (2005).

Garcia, O., Brunetti, F., 1992, “Motores de Combustão Interna”, Faculdade de Engenharia Industrial, São Bernardo dos Campos.

http://www.mh-aerotools.de/airfoils/javaprop.htm, acesso em 27/04/2006

NACA Report 447 (1932), “Static Thrust of airplane propellers”.

Solomon, W. (1953), “Aerodynamic Characteristics of a Two-Blade Naca 10-(3)(062)-045 Propeller and of Two-Blade Naca 10-(3)(08)-045 Propeller”, Technical Note 2881, National Advisory Committee for Aeronautics (NACA),Langley Aeronautical Laboratory, Langley Field, Va.

PERFORMANCE MODEL OF UAV-ITA PROPULSIVE SYSTEM

Pedro Teixeira Lacava
Instituto Tecnológico de Aeronáutica – São José dos Campos - SP
placava@ita.br

Cristiane Aparecida Martins
Instituto Tecnológico de Aeronáutica – São José dos Campos - SP
cmartins@ita.br

Amílcar Porto Pimenta
Instituto Tecnológico de Aeronáutica – São José dos Campos - SP
amílcar@ita.br

Carlos Guedes Neto
Instituto Tecnológico de Aeronáutica – São José dos Campos - SP
guedes@ita.br

Gustavo Violato
Instituto Tecnológico de Aeronáutica – São José dos Campos - SP
gustavoviolato@redecasd.ita.br

Abstract
Nowadays there is several applications for Unmanned Aerial Vehicles – UAV, and it is a very important area of aerospace developments. Some of these applications are very dependent of vehicle performance to conclude the mission with satisfaction. So that, it is necessary performance simulations based on flight mechanics models during the vehicle design stage. A specific part of the global flight mechanics model is the propulsive system performance model, which the idea is the information for thrust, torque, fuel consumption, and specific fuel consumption, as function of engine rotation speed, altitude, and flight velocity. So, the present work shows the development of two strokes piston engine/propeller propulsion system model for an UAV application.
.

Keywords: Unmanned Aerial Vehicles, UAV, propulsive systems models

Proceedings of the 11th Brazilian Congress of Thermal Sciences and Engineering -- ENCIT 2006
Braz. Soc. of Mechanical Sciences and Engineering -- ABCM, Curitiba, Brazil,- Dec. 5-8, 2006

Paper CIT06-0509

ENTROPY STATISTICS APPLIED TO AIRPLANE EVOLUTION

Andre Bosuqe Monteiro
Technological Institute of Aeronautics (ITA) – São José dos Campos – SP - Brazil
andre.bosque@embraer.com.br

Bento Silva de Mattos
Technological Institute of Aeronautics (ITA) – São José dos Campos – SP - Brazil
bmattos@ita.br

Roberto da Mota Girardi
Technological Institute of Aeronautics (ITA) – São José dos Campos – SP - Brazil
girardi@ita.br

Abstract. *Aeronautical evolution by definition is a technological evolution. As such, like any other form of evolution, it follows certain rules or heuristics. These rules can vary in complexity; from the relatively simple evolution of an arithmetical progression to the more intricate biological evolution of any species, technology belongs somewhere near the complex end of that spectrum. This form of evolution can potentially be lucrative if well understood, especially in the firm level. By employing the entropy statistics methodology, analyses concerning airplane evolution were carried out. The present work is an improved and extended effort regarding the one performed by Frenken and Leydesdorff (1999). Here, proper variables adequately represent the aircraft configuration and its embedded technology. The variables were carefully selected after an extensive study. Both works also differ in range of application. In the present work, two analyses were performed to validate the methodology. One is concerned with the evolution of civil aviation transportation in the jet age (1950-2006) and the other with the evolution of fighter aircraft (1914-2009). A considerable effort was made in order to select the variables used to describe each aircraft. After the creation of the databank, the tool that was developed during this work takes the variables as input to evaluate two important evolutionary indexes: the convergence and the diffusion. Studies analyzing the combination of the diffusion and the convergence indexes, as well as the critical transition of the airplanes were conducted in the present work. A computer tool was also developed, which can be useful in the decision making process in the conceptual design phase of aircraft.*

Keywords *Entropy Statistics, Information Theory, Aircraft design, Conceptual Studies*

Symbols and Abbreviations

WWI	World War One
WWII or WW2	World War Two
MTOW	Maximum Take Off Weight
W/S	Wing Loading
EOW	Empty Operating Weight
T/W	Thrust to Weight Ratio
S	Wing Area
MMO	Maximum Operating Mach Number
C_{Lmax}	Maximum Lift Coefficient
I	Information Content
p_i	*a priori* distribution
qi	*a posteriori* distribution

1. Introduction

1.1. Convergence vs. divergence

It is an amazed experience to observe that the tools and instruments devised by human beings undergo an evolution themselves that is strangely analogous to ordinary evolution, almost as if these artifacts propagated themselves as animals do. Aircraft began as birdlike objects but evolved into fishlike objects for much the same hydrodynamic reasons as those which caused fish to evolve into fishlike objects. Bicycles have evolved and so have motor cars.

The challenge of understanding the dynamics of technological development has long been a concern of every branch of manufacturing enterprises. Two approaches dominates the scene: one suggests that the external requirements of the market (Schmookler, 1966), while the other views the activities and internal capabilities of firms as primary drivers of innovation (Dosi, 1982). Taken in isolation, each approaches highlights key aspects of technological development but, as many have argued, the greatest insight derives from their joint consideration (Movery and Rosenberg, 1979).

Convergence contends that products evolve into unified devices through linear evolutions; whereas divergence disputes this notion, citing innovation is spurred through disruptive revolutions. The Internet was a disruptive technology and the same will certainly occur to the air transportation. A different way to move in the atmosphere will not be called "airplane" anymore.

Convergence captures the imagination, but divergence is tuned to the market. Today many types of aircraft (jet aircraft, propeller-driven airplanes, and helicopters) and many types of automobiles (sedans, convertibles, station wagons, minivans, sport-utility vehicles.) are available. However, no flying car succeeded, although many attempts have been made to bring them into life. Ries (2004) asks the question "Why divergence and not convergence?" According to them, that is because convergence requires compromise and divergence satisfies the evolving needs of different market segments. An automobile needs to be heavy enough to stay on the highway; an airplane needs to be light enough to take off from a runway. No flying car will ever be as drivable as an automobile or as well flyable as an airplane. The autoboat, another convergence concept that has been floating around for decades, suffers from the same flaws.

. The codification of design principles associated with the emergence of a dominant design also implies a convergence of particular design principles that have been developed in the past. Thus, the coming into existence of a scaling trajectory at the industry level is essentially a two-sided phenomenon. It refers both to the diffusion of design principles, and to the convergence of design principles. These phenomena are different: the diffusion of particular design principles does not necessarily imply convergence of design principles, since a design can be scaled in various different and potentially divergent directions. For example, some aircraft firms may scale a dominant design with respect to maximum take-off weight, others with respect to speed, and still others with respect to range. Hence, to test the dominant design hypothesis, one needs to distinguish between the diffusion of design principles through time and the convergence of design principles that can be observed in retrospect.

At this point, it is worthy of mention the different meanings of divergence and diffusion. At first glance, both concepts appear to be the same. Consider the computer. There are supercomputers, network computers, personal computers, laptop computers, tablet computers and handheld computers. That is a typical divergence case, a family of products having the same *common ancestral*. Diffusion is related to different products sharing *common technologies or features*. The fly-by-wire flight and control system appeared in a Western plane in the supersonic Concorde airliner. Since those days, this technology has spread her legs to a large variety of airplanes. Even small to medium capacity airliners like the ENBRAER 170 have adopted such technology. That is a typical example of diffusion.

1.2. Technological evolution modeling

Utterback and Abernathy (1975) have proposed the concept of a product life-cycle to describe technological evolution at the level of an industry. At the start of a product life-cycle, a variety of product designs is being developed. The competition among designs is eventually resolved into a dominant design. Hereafter, innovation concentrates on process and incremental improvement of the product with reference to the dominant design. Nelson and Winter (1977) and Dosi (1982) proposed to describe a series of incremental innovations within a stable design framework as a natural trajectory or technological trajectory, respectively. Along a trajectory, development is guided and constrained by a set of heuristics which make up a technological paradigm. The trajectory concept can be appreciated as the dynamic analogue of the concept of a dominant design.

Nelson and Winter (1977, 1982) and Sahal (1981, 1985) highlighted that trajectories do not only concern periods during which the basic technological principles remain unchanged, but also a stage of incremental scaling of designs. A prime example of a series of scaled models in civil aircraft has been the piston propeller Douglas airliner trajectory. The scaling of the engine power, wing span, and fuselage length have led to improvements in speed by a factor of two, and in maximum take-off weight and range by a factor of five from the introduction of the DC3 in 1936 to that of the DC7 in 1956.

Information theory was first mentioned by Claude E. Shannon in his 1948 paper entitled "A Mathematical Theory of Communication". The main purpose of Shannon's work is to deal with the problem of transmitting information over a noise channel. He could not imagine that a whole new field of mathematics would result from his proposition. Many deep and far reaching mathematical theories were created, such as channel capacity, source-coding and self-information. But Shannon's most important contribution was his use of *entropy* to elaborate most of his theories.

Entropy came into being as *thermodynamic entropy* by Rudolf Clausis in 1850, in his work on Sadi Carnot's 1824 thermodynamic efficiency study. However, the more modern definition of entropy as a measure of "disorder" in a system was introduced by Ludwig Boltzmann in 1877. This "disorder" entropy, or *statistic entropy*, then became the cornerstone of the theory of statistical mechanics and was later used by Shannon in his information theory.

In this context, some textbooks erroneously employ the "student desk increasing disorder with time" as an example of entropy. This can be misleading since the more precise example would be, "which system has higher entropy: the organized desk or the messy one?" The answer would probably be the messy one, because there are many

more ways of arranging the items in a chaotic manner than there are in an organized one. This is the Shannon definition of entropy, and the one used in this paper. Interestingly, some scholars today credit Claude Shannon as the actual architect of entropy, since his definition is a much broader one than the original thermodynamic definition, even though it is a much newer concept. These scholars claim that thermodynamic entropy is a category of information entropy.

How does this statistical entropy relate to the study of technological evolution? Any system that contains a macroscopic state ruled by many different microscopic systems, such as biological evolution, economic growth, image reconstruction and technological evolution; can be studied using entropy.

If a certain technology has established itself over a long period of time without any major breakthroughs, one can conclude that the entropy of that particular era is very low, since there is a low degree of uncertainty. This means that some major breakthrough has occurred in the past and that most of the competitors, if there are any, have borrowed information from that breakthrough. The appearance of a dominant design usually precludes a low entropy era, while an era of experimentation, with high diversity shows no dominant designs, and thus, high entropy.

Therefore, one can use these far reaching theories to study the evolution of technology in a specific sector of industry, such as civil aviation, automobiles, computers, etc. In this study we will analyze the evolution of civil transport aviation of the jet age (1950-2006) and the evolution of fighter aircraft of the 20th century (1914-2009) by using some specific points from information theory and entropy statistics, discussed in the next section. Although many calculations are performed in this analysis, the results can only be interpreted in a qualitative manner. Entropy statistics is best employed, outside of pure information theory and thermodynamics, as a tool for qualitative analysis of a subject.

2. Methodology

A previous work on this subject, written by Frenken and Leydesdorff (1999), will be used as the baseline methodology for the present study. The targeted improvements are the choice of variables for each design, the availability of newer design data and the focus on Embraer airliners, while conducting firm-level analysis. Another expected conclusion for this work is to ascertain how robust the applied theory and methodology really is in this case.

2.1. Data structure

The most effective way to numerically represent a product is to model its various trade-offs, since these are the expression of years of technical development for a product. To model these trade-offs it is necessary to create ratios between every characteristic of a product. Arranging these ratios in matrix form creates a model of the trade-offs. This matrix is a good numerical representation of a product design, but it is not useful in information theory.

Dividing theses ratios by the sum of all the ratios creates a probabilistic distribution ($p_1, p_2, \ldots, p_n \rightarrow$ where n is the total number of ratios). This is called a probabilistic representation for each product and will be used for every calculation in this procedure.

Every product contains some information from previous designs and provides information to future ones. Using information theory we can calculate how much information is passed among designs using the formula below:

$$I(q \mid p) = \sum_{i=1}^{n} q_i \log_2 \left(\frac{q_i}{p_i} \right)_i \qquad (1)$$

Where I is the information-theoretical distance between two product designs, where q is chronologically after p. This is the same as the amount of information passed on from p to q. If no information was passed than I equals zero, because every trade-off is the same, even if the characteristics are not the same. This would be a perfectly scaled version of a previous product. Mathematically this means that $\left(\frac{q_i}{p_i} \right) = 1$ and its log is zero. Interestingly no matter what I is, it will always be positive, this is called probabilistic entropy, and it is due to the fact that every message that change has occurred is expected to contain information.

Lower I means less change has occurred from p to q, in other words, the more similar two products are and vice versa.

After an extensive analysis, some parameters representing the characteristics for the entropy analysis were selected. They are described below and listed according to the aircraft categories under consideration

Airliner

1. Thrust to weight ratio (T/W);
2. Empty to gross weight ratio (EOW/MTOW);
3. Payload to gross weight ratio;
4. Fuel per Passenger Mile [kg/nm];
5. Maximum operating Mach number (MMO);
6. Range with max. payload [nm];
7. Maximum lift coefficient (C_{Lmax});
8. Service ceiling [ft];
9. Wing loading (W/S) [kg/m^2]

Fighter aircraft

1. Wing span [m];
2. Total length [m];
3. Total height [m];
4. Wing area (S) [m^2];
5. Empty weight [kg];
6. Maximum take Off Weight (MTOW) [kg];
7. Maximum speed (VMAX)[km/h];
8. Service ceiling [m];
9. Range [km];
10. Full armament payload coefficient [mm + kg];
11. Thrust to weight ratio (T/W);
12. Wing loading (W/S) [kg/m^2]

In fact, other important parameters shall be taken into account for the calculations. One of them is the lift-to-drag ratio. However, lack of reliable source of information led the authors to drop out some parameters. Further work will take into account them by a more intensive search in the available literature. The computer code that was developed in the present work is able do analyze the evolution of any kind of object. However, the object of the investigation is technological evolution of aircraft. The first step is to gather enough data for the calculations. This is one of the only limitations of the method. It requires dozens of data points to produce an effective and useable result. Naturally, the most important information for each product is its initial service date, without it there can be no study.

2.2. Diffusion and Convergence Values

In the industry level, a certain design may be compared with its successors or predecessors in order to gauge its effect on the competition, for a certain period. A dominant design is one that has a high degree of diffusion of its design into subsequent products, and also one that includes a high degree of convergence of previous design principles into it. Mathematically, this is accomplished by, first, selecting an appropriate time scale to be used, for the civil aviation five years works well. Take a specific product, for diffusion; calculate the average I-values for each product in the succeeding time period. For convergence, calculate the average I-values for each product in the preceding time period. Doing this for every product in the database creates a time based plot of diffusion and convergence I-values. The lower the I, for both diffusion and convergence, the closer a design is to a dominant one for its time.

2.3. Critical Transition

When comparing three designs in chronological order (A→B→C), the information-theoretical distance between all them can be determined. In normal Euclidean space the distance between A and C will be smaller or equal to the sum of the A and B and B and C distances. However, the information-theoretical distance between A and C can be bigger than the sum of the smaller distances. This means that design B has caused enough impact on C and has a lot of influence from A that the information-theoretical distance is smaller. When this happens, the design process A through B through C is called a critical transition, and it is a safe bet that design B is a major success and the following designs are scaled designs. In other words, one can think of design B as a catalyst or amplifier. A firm that creates a product with the characteristics of design B will be able to leap forward in technology faster than its competitors.

$$I(B \mid A) + I(C \mid B) < I(C \mid A) \tag{2.1}$$

$$I(B \mid A) + I(C \mid B) - I(C \mid A) < 0 \qquad (2.2)$$

3. Results

3.1. Commercial airline transportation in the Jet Age

One of the more unusual aspects of the coming of the jet era was the speed with which airlines internationally adopted these new aircraft. Partly because of Pan American's example, airlines from all over the world replaced piston-engine aircraft with jets at an unprecedented pace. The Soviet national airline Aeroflot was part of this explosion. In fact, Aeroflot held the distinction of offering the world's first regularly scheduled and sustained passenger jet service with its Tupolev Tu-104 aircraft. Aeroflot opened service from Moscow to Irkutsk in September 1956. The second jet revolution came into life in the 90s even speedier than the previous one. It ook place after Embraer and Bombardier Aerospace (former Canadair) introduced their regional jet seating 50 passengers. The so-called regional jet replaced turboprop aircraft in many routes. However, their most importation contribution for the aviation was the opening of new routes, with some of then enduring 3 hours or more. The main reason for the success of the regional airlines was their intrinsically low-cost structure.

3.1.1 Diffusion and Convergence Analysis

After calculating the diffusion and convergence values for each aircraft in the airliner database, they were plotted on a time scale and also plotted against each other.

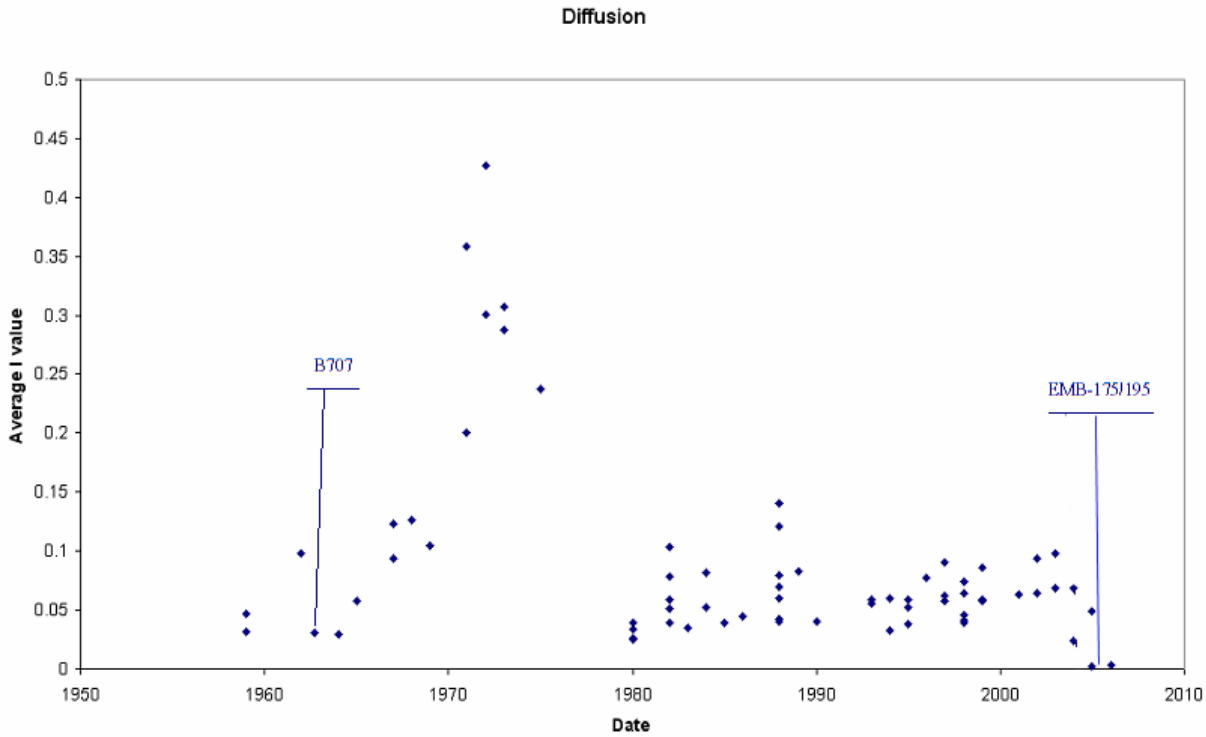

Figure 1 - Diffusion I-values for airliners in the Jet Age.

On the diffusion plot **Figure 1** one can see that the lower I-values (meaning more diffusion) are concentrate after 1980, and that before that higher values (less diffusion) were more common. Studying the history of commercial transport aircraft it is possible to determine the explanation for this occurrence. In the early jet age, all of the designs were breakthroughs from their propeller predecessors. Therefore, a high degree of diffusion of their design principles can be observed because all of the subsequent aircraft were based solely on these pioneers. Observe the low values for Boeing 707 (0.0982), Sud-Aviation Caravelle (0.0465), and Douglas DC-8 (0.0315). As the technology matured, however, firms started experimenting with new design configurations - this can be seen in the early to mid-70s. The tri-reactor series of aircraft are all included in this era, and none can be seen flying nowadays, McDonnell Douglas DC-10 (0.358), Boeing 727-200(0.200) and Lockheed Tristar (0.307). The same can be said about the supersonic aircraft like Concorde (1.204). The supersonic airliner Concorde is not shown in the graph because it dwarfed the other values. The

twin-pusher CBA-123 turboprop (1.224) – a commuter plane for 19 passengers - shows high values and fits the above description. Since the A380 (1.056) has just recently flown it also shows high values, because it is very different from the aircraft it was compared to others that flew recently. After the 1980's the diffusion average drops significantly, this shows the emergence of a dominant aircraft configuration, which is a low wing, high flying, twin turbofan aircraft. Among these are Boeing 767, Airbus A320 and that from Embraer, all of them with high diffusion. Still in diffusion it is interesting to note the extremely low I-values for the EMBRAER 175 – referred to as EMB-175 - (0.00307) and EMBRAER 190 – mentioned as EMB-190 - (0.0025). This can be partially explained by the fact that only these airliners present an entry into service date of year 2005. Additionally, they are scaled versions of each other, and mainly of the EMBRAER 170, which is referred to as EMB-170. The EMB-170 (0.0242) also has a low value, but higher than its bigger companions because it compares with the A380 as well, as a 2004 airplane.

Figure 2 was leased from Frenken's work and is used here for comparison reasons. There is a good matching when the results presented in **Figure 1**. That indicates the robustness of the method, especially with a solid calculation tool such as the one developed for this work. It is important to mention that Frenken's work covered airliners from 1927 to 1997.

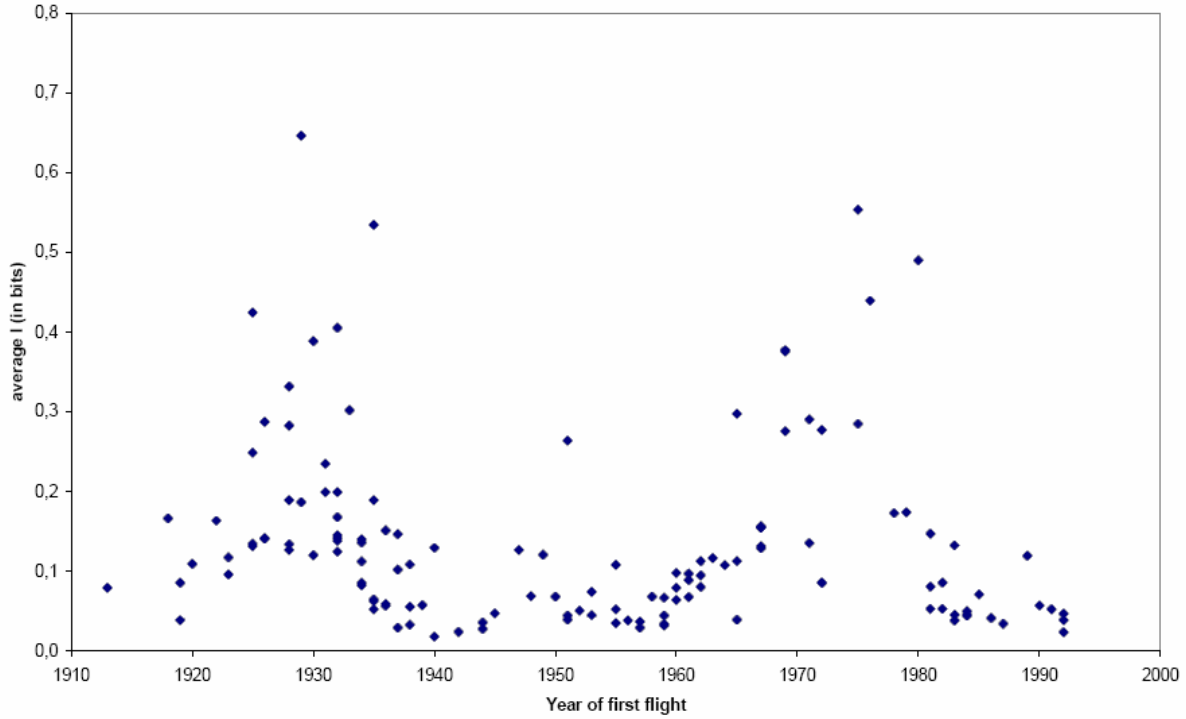

Figure 2 - Diffusion I-value for Civil Air Transport (Frenken).

The same overall behavior of convergence graph can be seen on the diffusion one (**Figure 3)**. In this case, it can be stated that the aircraft designed after the first jet transports show a high convergence of design principles, as can be seen as a small dip in the I-values for the Douglas DC-9-30 twinjet (0.0327), as well as for the DC-9-40 variant (0.0156) and Boeing 747-100 (0.0420). The same rise in I-values on the diffusion graph can also be observed, except this time it occurs about five years later than on the diffusion. This is also mainly due to the major failures like the Concorde (0.902) and the CBA-123 (0.498). The A380 (0.750) presents again high values, but this is due to the fact that it uses little information from previous designs, mainly due to its ultra-large dimensions. If, in the future, the A380's diffusion values lowers it will become a monopoly much like the 747 in its day.

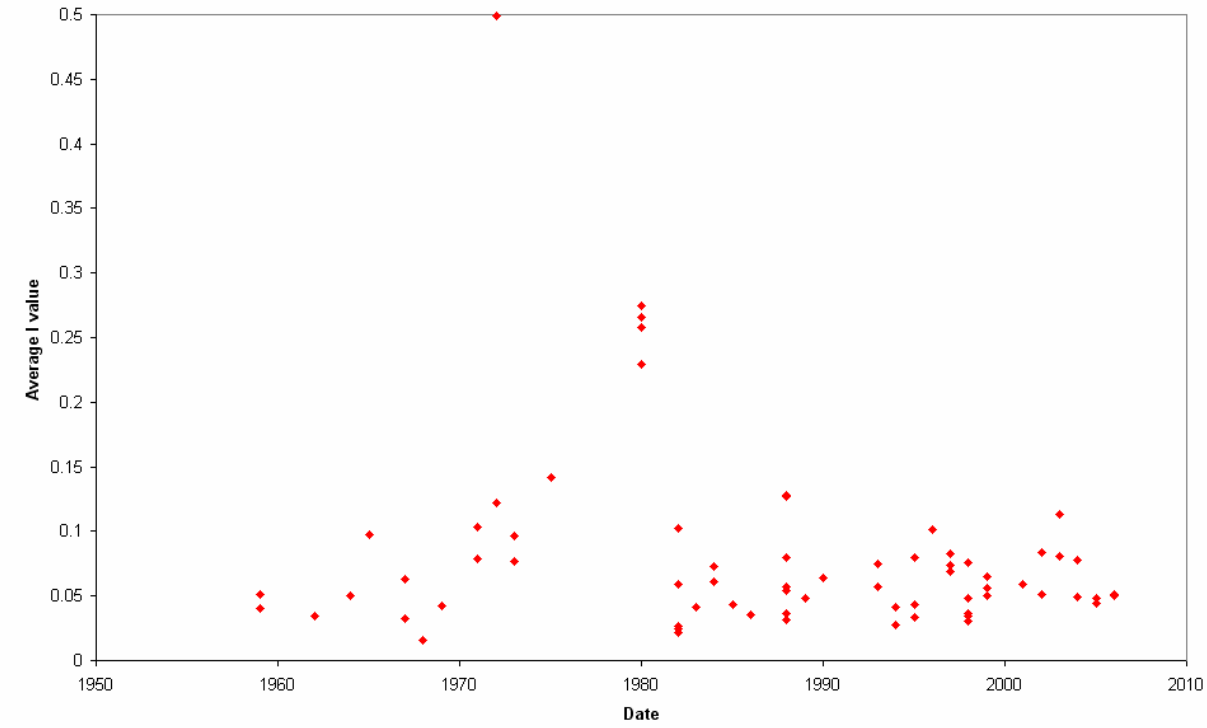

Figure 3 - Convergence I-values for airliners in the Jet Age.

Following the spike, all of the aircraft show a high degree of convergence from previous designs, just as with the diffusion plot. When compared to Frenken's work. **Figure 4** reveals that the similarities are very tight. Even considering the slightly different for some I-values between both works, most aircraft present the same I-values in the graph. Once more, the strength and robustness of the method was accomplished.

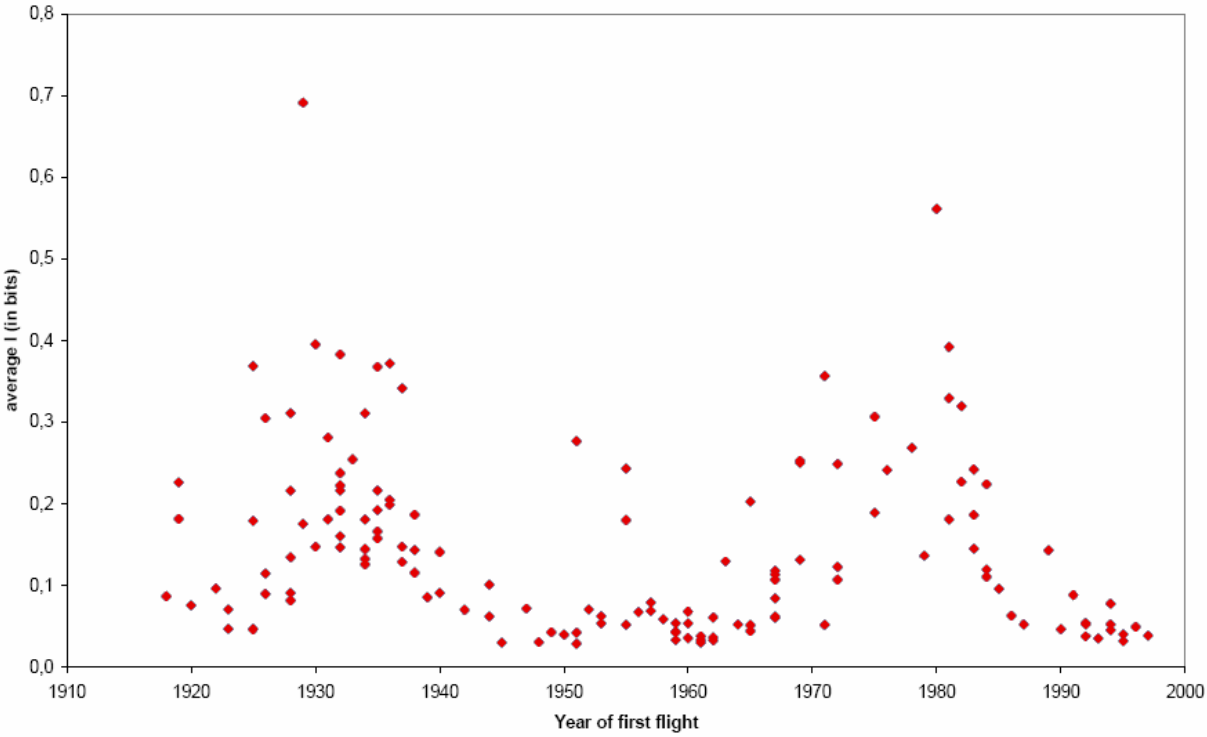

Figure 4 - Convergence I-value for airliners according to Frenken's work.

The last graph in this section is used as an illustrated guide for distinguishing types of innovation. In his paper, Frenken (1999) classifies four types of innovation (**Table I**). In **Figure 5**, it can easily be observed where each aircraft falls within that classification. The SST (Supersonic Transport - Concorde) and the CBA-123 are both failed designs according to the present calculations (high I-values). Even taken into account the Concorde flew for many years as the sole SST. While the McDonnell Douglas DC-10 trijet and Boeing 747 fall into the monopoly category, because of their extra widebody status, they had a lot of influence from previous designs but their influence on later designs was, as is well known, very small. In this study the MD-80 aircraft series reveal themselves as a breakthrough design. This makes sense since they were the first successful mid-range high-bypass turbofan aircraft, their influence on later designs like Fokker 100/70 and the ERJ 145 aircraft family.

Convergence	**High I-values**	Breakthroughs	Failures
	Low I-values	Dominant Designs	Niche, Monopolies
		Low I-values	**High I-values**
		Diffusion	

Table I – Design categories.

The dominant design for the new era of civil aviation transport, according to this study is the EMBRAER 170 family of aircraft. They are the last in a long line of scaled aircraft capitalizing on a sound design and improving on it incrementally to attend market needs. The EMBRAER 170/175 airliners revolutionized the market segment that they are target for. Presenting engines below the wings they enable shorter turnaround times on the ground proving this way a increased daily utilization rate. Besides, their unique cabin dimensions care for a superior comfort and can be compared to widebody revolution pioneered by Airbus in the 70s for the segment of larger capacity.

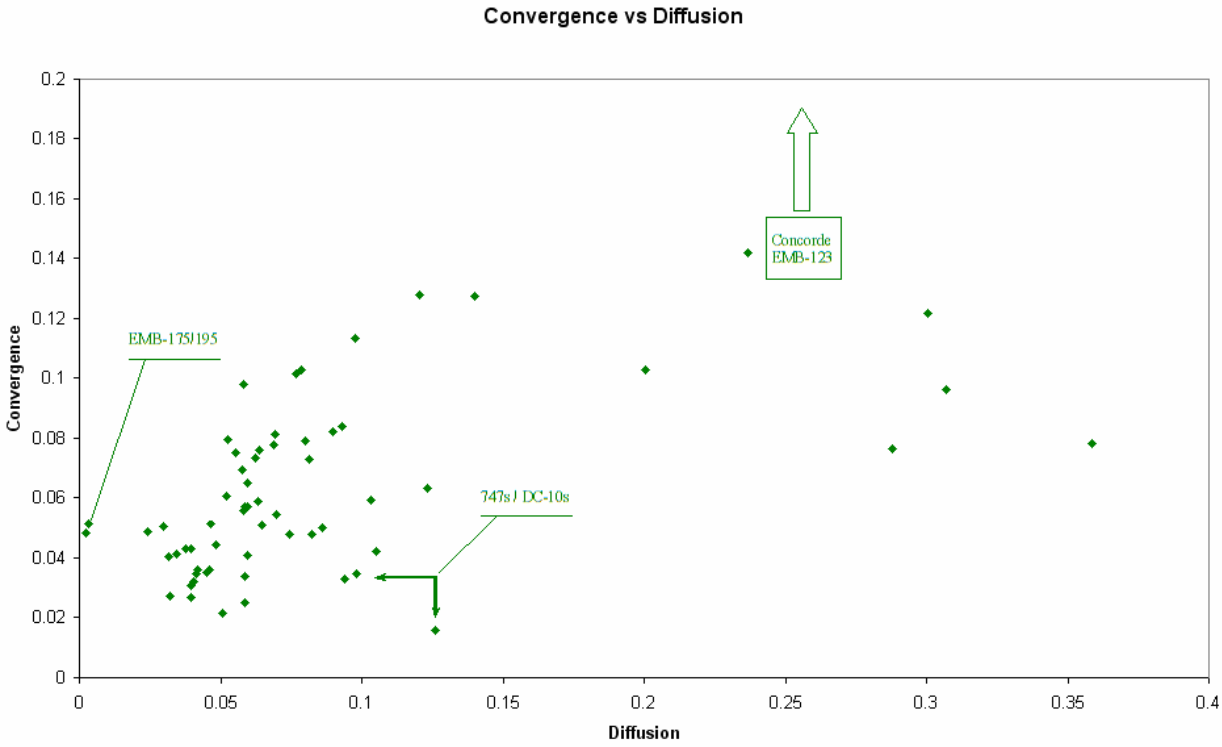

Figure 5 - Diffusion and Convergence for Civil Air Transport in the Jet Age

3.1.2.Critical Transition Analysis for EMBRAER Aircraft

In order to analyze Embraer aircraft evolution we use the critical transition method described in the **Introduction**. This is interesting when considering that Embraer has evolved from the unpressurized EMB-110 Bandeirante twin turboprop, to the ultra-modern EMBRAER 195 airliner (referred to as EMB-195 in Graphs and Tables). The aircraft were used in chronological order as required by this method.

Group	Aircraft Analyzed	Distance
1	EMB-110 -> EMB-120 -> EMB-123	0.0908
2	EMB-120 -> EMB-123 -> EMB-145	0.1119
3	EMB-123 -> EMB-145 -> EMB-135	0.0575
4	EMB-145 -> EMB-135 -> EMB-140	0.0185
5	EMB-135 -> EMB-140 -> EMB-170	-0.0163
6	EMB-140 -> EMB-170 -> EMB-175	-0.0046
7	EMB-170 -> EMB-175 -> EMB-190	-0.0035
8	EMB-175 -> EMB-190 -> EMB-195	-0.0011

Table II - Critical Transition for EMBRAER Aircraft

In **Table II**, the ERJ 145 twinjet is mentioned as EMB-145 and the CBA-123 turboprop is referred to as EMB-123. The value of 0.1119 for the distance related to the Group # 2 is in the spotlight. This result can be explained by the fact that the CBA-123 was a commercial failure, because of the cutting-edge technology that it featured. But even more interesting is the fact that the last for transitions were all considered critical ones. This proves the fact that the EMBRAER 170/190 family of aircraft is destined to become a dominant design in the near future, evidence of that the analyses indicated for the ill-fated Bombardier C-series.

3.2 Results Interpretation for Fighter Aircraft (1914-2009)

3.2.1. Diffusion and Convergence Analysis

The same methodology employed for airliners found an application here. However, there are some differences, which will help to evaluate the robustness of the codification and methodology. First, the number of designs in the fighter databank was considerably larger than that contained in the airliner one: 235 instead of only 74. The number of parameters to model the plane characteristics was also increased from 9 to 13 instead. Considering that the code did not need to be rewritten throughout the analyses indicates that it can handle any type of data, as long as the proper format is provided.

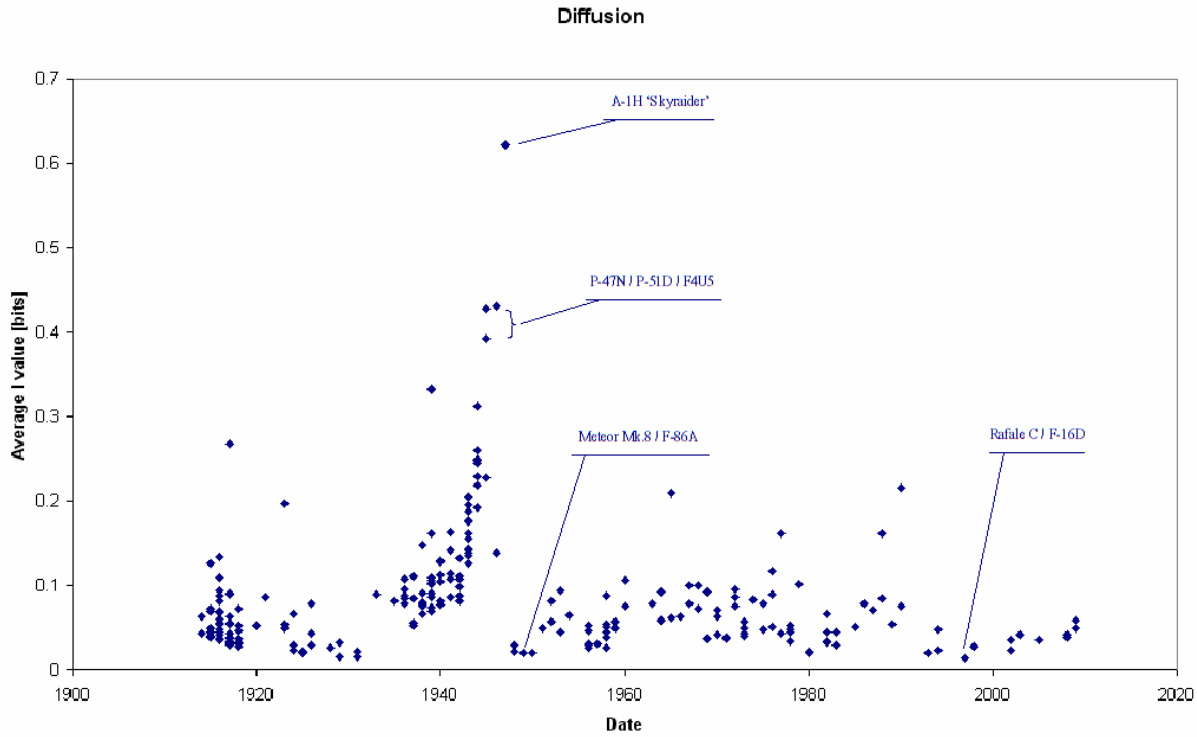

Figure 6 - Diffusion I-values for Fighter Aircraft.

The analysis revealed some important departures regarding the previous study on the commercial aviation. The first difference can be seen in the diffusion graph, shown in **Figure 6**. It can be observed the effects that WWI (1914-1918) and WWII (1939-1945) exerted on fighter design. The very stringent requirements that emerged during those wars tremendously accelerated aircraft development. These periods present a substantial rise in I-values, translating a high degree of diffusion - more pronounced in WWII. This shows that competing countries and firms were producing very different designs, no dominant design is apparent. In WWI it is less visible, however, since it is the beginning of aviation, there isn't much one design can differ from another. After WWII the mean I-value seems to lower as a result of constant technological evolution and also some dominant designs. At the last decade there is a dip in I-values, this shows the presence of a dominant design. The Rafale (0.0135) and the F-16D (0.0193) seem to be the likely candidates.

Many aircraft presented a low degree of diffusion (high I-value) into subsequent designs. This is the case for the A-1H Skyraider (0.621), one of the last piston-powered fighter/attack aircraft developed in WWII. Because it is the last one of its kind, it not diffused its technology onto later designs. Developed to satisfy a US Navy requirement of 1944 for a single-seat carrier-based dive bomber and torpedo carrier, the Douglas AD Skyraider materialized too late for operational service in World War II. Ordered into production alongside the Martin AM Mauler, which has been developed to meet the same specification, it was to continue in production until 1957. The Skyraider reflected the navy's wartime experience gained in the Pacific theatre, where it had been proved that the most important requirement for such aircraft was the ability to carry and deliver a heavy load of assorted weapons. Of low-wing monoplane configuration, a big Wright R-3350 radial engine was selected as the most suitable power to meet the load-carrying requirement, and this more or less dictated the fuselage proportions. The prototype XBT2D-1 flew for the first time on 18 March 1945. When production terminated 3,180 aircraft had been built in many variants. The Skyraider was also employed in the anticipated early warning (AEW) role. Facing with Kamikaze threat during 1944 the United States Navy started the development of an airborne radar system in order to expand the radar horizon under which the Fleet was to operate during the series of campaigns through the Philippines and northwards to Japan. For this reason, the AN/APS-20 radar as fitted to the TBM-3W and PB-1W became the mainstay of AEW aircraft developments following World War Two. While not designed specifically as an AEW aircraft, the Grumman AF-2W Guardian, when fitted with the AN/APS-20 had a secondary capability endowed by this system. Experience with the Guardian led to the development of an AEW variant of Douglas Skyraider. Once again the radar chosen was the AN/APS-20, with a large belly radome being fitted and a crew of three (one pilot and two operators) being carried. The Skyraider AEW was built in three versions, the AD-3W, AD-4W, and AD-5W. AEW aircraft is another example of divergence.

Most of the late propeller fighter designs have low diffusion, P-47N (0.427) F4-U5 (0.4305) and the P-51D (0.311), this also makes sense since they had not much in common with the jets that were being developed at their era. Other corner of the diffusion spectrum is inhabited by some early jets, such as the Meteor Mk.8 (0.020) and the F-86A (0.021). This is likely explained by the fact that a lot of their technology was passed on to later designs. One could expect such aircraft as the P-80 (0.248) and the Me-262 (0.227) to be in this category, but this is not the case because as the pioneers most of their design ideas were not carried through, and the second generation is probably the one that contains the 'good' decisions. This is the price to pay for a breakthrough technology.

Figure 7 - The first early-warning and Control (AEW&C) aircraft of WWII. From left to right: AF-2W Guardian, Grumman TBM-3W Avenger and Douglas EA-1E Skyraider.

The convergence plot, as seen in **Figure 8**, shows the same overall tendency seen in the diffusion figure. The same high I-values during the wars are observed. The main difference here is the fact that the high I-values do not lower as much after the conflicts, especially after WWII, or the birth of the jet age. During the Cold War (1950s-1980s) there is a higher mean as opposed to the diffusion values, this is probably because there are many minor breakthrough designs in this era.

Note, also, that the convergence I-values during WWII are lower than the diffusion ones. This was expected considering that a war boosts technological advances with a great emphasis on improving existing ones. Another factor that contributes to this phenomenon is the invention of the jet engine during the same war, which raises the diffusion I-values. The lower convergence aircraft (high I-values) for these fighters are the P-80C Shooting Star (0.451), the MiG-15 (0.457), the Meteor Mk.8 (0.422), the F-86A (0.362) and the Me-262 (0.393). These are some of the early jet fighters, mostly second generation. This low convergence represents the great leap from the propeller to the jet in air combat, in other words, very little information was passed on to these designs.

The high convergence area is populated by some very old designs, like the P-36 'Peashooter' (0.017) and the Fokker DXXI (0.023) two of the last of the pre-WWII designs. There are some newer fighters as well, the Rafale (0.014), the Chendgu J-10 (0.015) and the F-16C (0.025). All of these fighters have many common design characteristics, they are all light, limited range, very maneuverable aircraft.

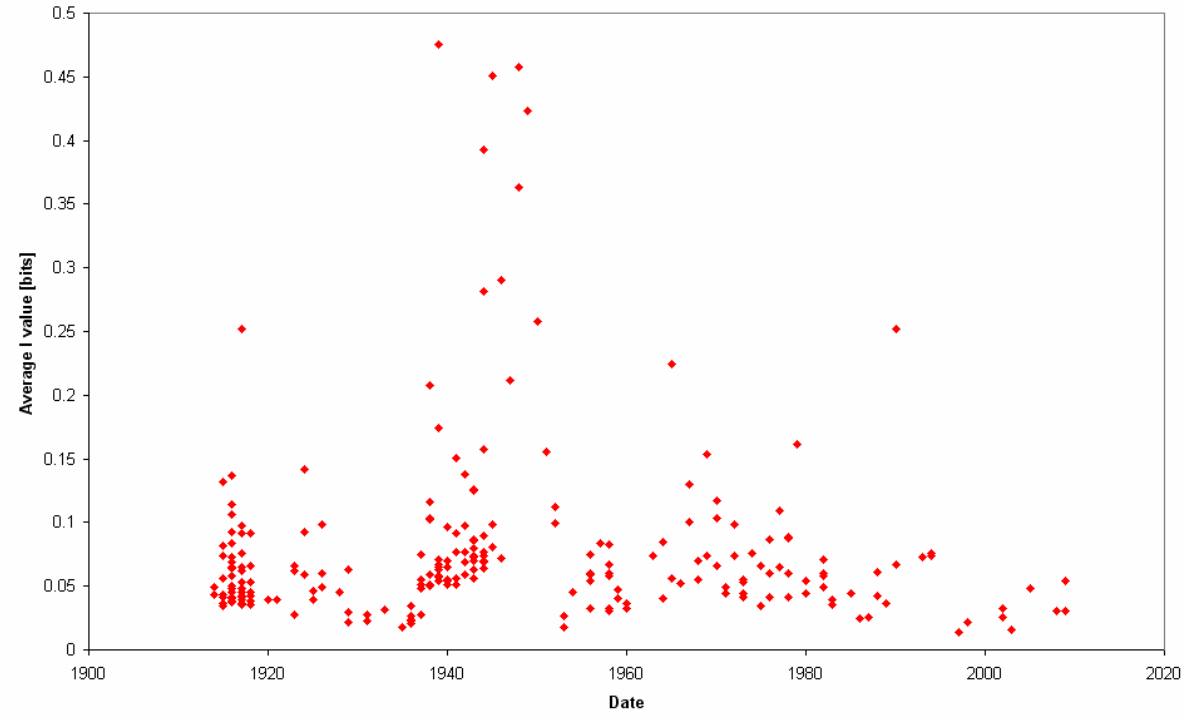

Figure 8 - Convergence I-values for Fighter Aircraft

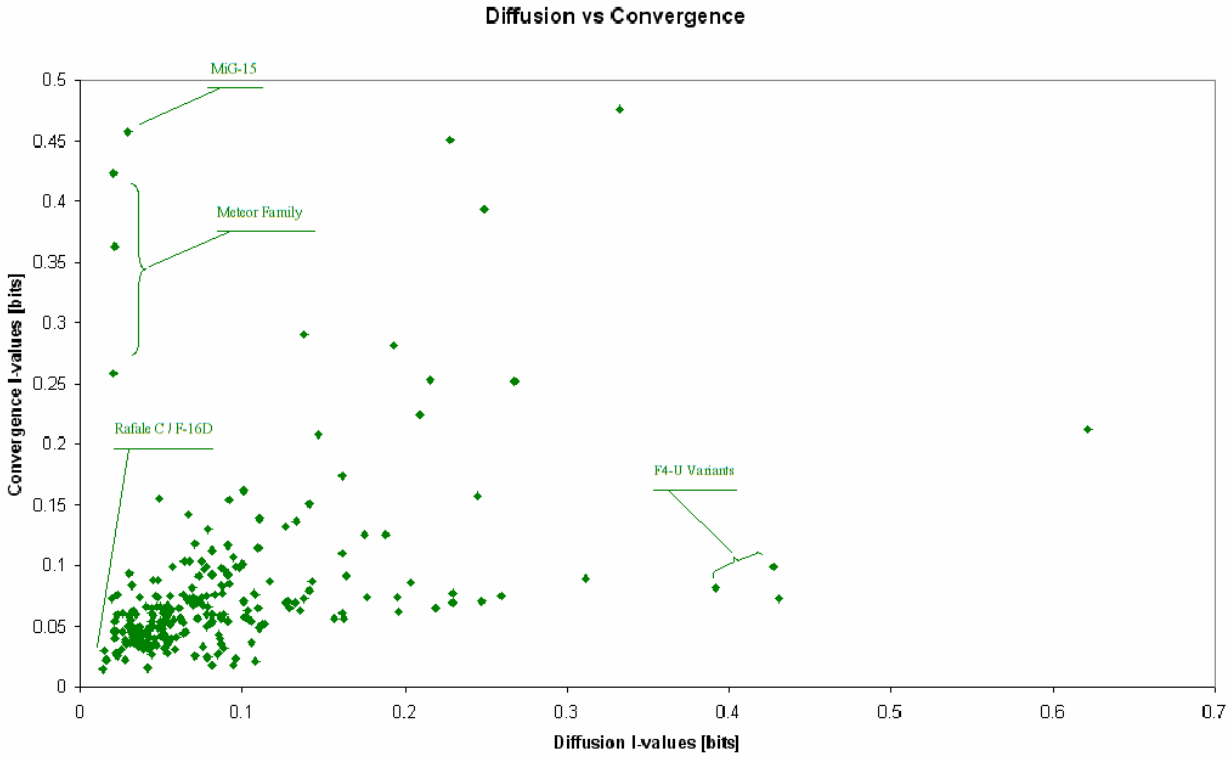

Figure 9 - Diffusion and convergence for fighter aircraft.

Figure 9 displays the combined diffusion/convergence. Using the same classification technique of **Table I**. we can categorize some aircraft. For example, the MiG-15 is undoubtedly one of the major breakthroughs of the early jet age, and it is proven because it shows low convergence and high diffusion. The Meteor variants are all in the same classification as breakthroughs. Now, the F4-U Corsair variants fall into the niche/monopoly category, since they were by far the most advanced carrier based fighter aircraft of their time, and also the last ones, they can be found in the low diffusion, high convergence area of the graph (lower right quadrant).

Some dominant designs, as was mentioned earlier in this section, are the Rafale C for the modern fighter jet, the F8-U Crusader for the Cold War fighters, the Bristol Bulldog for the pre-WWII era, and the Albatross D.III for WWI (not a very dominant design, but considering the effects of war, it is one nonetheless). During WWII no aircraft stands out as a dominant design, due to the high entropy encountered during that period.

4. Concluding Remarks

It was shown that by combining a seemingly unconnected mathematical theory and an empirical study of technological development one can create a very useful qualitative analysis tool. This tool can be used as a technology study aid, in an academic setting, or as part of a firm's decision making process.

As an academic tool, it is very interesting to use it with a variety of seemingly unrelated products in order to study the effects of major events and breakthroughs on the timeline of technological evolution. If the same effect, such as a rise in diffusion or convergence I-values, can be observed for different products in the same time period, they might have some connection, such as events like a major war, or a major discovery. The possibilities are endless as long as the product characteristics are well chosen and organized, and enough data points are gathered. This is particularly important as was seen in out fighter study.

As a corporate instrument, it is particularly desirable. If carefully analyzed, its results can substantially improve the firm's decision making process. The classification method described in this paper allows a company to study how close it can get to its defined goal. With just the convergence results, that are more accurate for modern designs, one can cut some unknowns from the process. It is simpler to think of a decision tree with two branches splitting into smaller branches each. If a strategy is known, say a breakthrough is the desired outcome of a future design, than a firm must aim for a low convergence level. On the other hand if the company cannot afford any risk a high degree of converging technology is desired.

If the firm can estimate the information content on future competitors, and therefore calculate a preliminary diffusion value, a hard but doable task. Subsequently a complete classification can be obtained.

5. Biblography

[1] Frenken, K., Leydesdorff, L., *Scaling Trajectories in Civil Aviation (1913-1997), Research Policy* 29, pp. 331-348, 1999.

[2] Anderson, David A., *Caças Americanos da II Guerra Mundial*, Edições Siciliano, São Paulo, BR, 1984

[3] Cover, T. M., Thomas, J. A., *Elements of Information Theory***,** New York: Wiley, 1991.

[4] Fermi, Enrico, *Thermodynamics*, Prentice Hall, 1937.

[5] Green, W., Swanborough, G., Mowinski, J., *Modern Commercial Aircraft*, Salamander Books, Ltd., London, 1987

[6] Gunston, Bill., *Caças Britânicos da II Guerra Mundial*, Edições Siciliano, São Paulo, BR, 1984

[7] Jackson, P., *Jane's All the World's Aircraft*, Jane's Information Group Coulsdon, Surrey, UK, 1995

[8] Jackson, Robert, *Modern Military Aircraft*, Chartwell Books, Inc., Edison NJ, 2003

[9] MacKay, David J.C., *Information Theory, Inference, and Learning Algorithms*, Cambridge University Press, 2003

[10] Mason, Francis K., *Caças Alemães da II Guerra Mundial*, Edições Siciliano, São Paulo, BR, 1984

[11] Nelson, R.R., Winter, S.G., *An Evolutionary Theory of Economic Change*, Belknap Press of Harvard University Press., Cambridge MA, 1982

[12] Saviotti, P., *Technological Evolution, Variety and Economy***,** Edward Elgar Publishing, Cheltenham UK, May 1996

[13] Shannon, C. E., *A Mathematical Theory of Communication*, *Bell System Technical Journal,* 27, pp.379-423 & 623-656, July & October, 1948.

[14] Utterback, J.M., Abernathy, P., *A dynamic Model of Process and Product Innovations, Omega 3*, pp. 639-656, 1979

[15] Ries, Al & Laura, *The Origin of the Brands*, Harper Business, 2004.

[16] Schmookler, J., *Invention and Economic Growth*, Harvard University Press, Cambridge, MA, 1966.

[17] Dosi, G., *Technological Paradigms and Technological Trajectories*, Research Policy, 11,147-62, 1982.

[18] Movery, D. and Rosenberg, N., *The influence of Market Demand on Innovation: A Critical Review of Some Recent Studies,* Research Policy, 8, 103-53, 1979.

[19] Boeing Co. Website, **www.boeing.com**

[20] Empresa Brasileira de Aeronautica SA – Embraer - Website, **www.embraer.com**

[21] Airbus Industries Website, **www.airbus.com**

[22] Bombardier Aerospace Website, **www.bombardier.com**

[23] Federation of American Scientists Website, **www.fas.org**

[24] Global Security Organization Website, **www.globalsecurity.org**

[25] Wikipedia – The Free Encyclopedia, **www.wikiped**

6. Copyright Notice

Proceedings of the 11th Brazilian Congress of Thermal Sciences and Engineering -- ENCIT 2006
Braz. Soc. of Mechanical Sciences and Engineering -- ABCM, Curitiba, Brazil, Dec. 5-8, 2006

Paper CIT06-0517

PROJETO CONCEITUAL DE UM VEÍCULO AÉREO NÃO TRIPULADO, USADO PARA INSPEÇÃO DE LINHAS DE TRANSMISSÃO DE ENERGIA ELÉTRICA

Roberto da Mota Girardi
Instituto Tecnológico de Aeronáutica (ITA), Praça Mal. Eduardo Gomes, 50, São José dos Campos, SP
girardi@ita.br

Paulo Rizzi
Instituto Tecnológico de Aeronáutica (ITA), Praça Mal. Eduardo Gomes, 50, São José dos Campos, SP
rizzi@ita.br

Resumo. *O veículo Aéreo Não Tripulado (VANT) considerado neste trabalho possui a missão de inspeção dos elementos de uma linha de transmissão de energia elétrica. Este trabalho possui dois objetivos: (i) descrever a metodologia desenvolvida para o projeto conceitual de uma aeronave para cumprir a missão especificada acima e (ii), apresentar os resultados obtidos (evolução da aeronave) durante o processo iterativo que caracteriza o projeto conceitual. Esta aeronave possui algumas características particulares que a distinguem das usualmente projetadas: (i) A velocidade é relativamente baixa, (ii) a construção é feita com técnicas e materiais bem diferentes das aeronaves convencionais e (iii) o peso total é muito baixo e, portanto, a aeronave fica muito suscetível a rajadas atmosférica, dificultando o rastreamento de uma trajetória pré-definida e também, o imageamento dos elementos da linha de transmissão. Uma característica da metodologia desenvolvida é o projeto simultâneo da plataforma aérea e do auto-piloto, com o objetivo de facilitar o imageamento.*

Palavras-chave: Veículo Aéreo Não Tripulado, Metodologia de Projeto, Rastreamento de Linhas de Transmissão

1. Introdução

Veículos aéreos não tripulados (VANT) podem ser usados em inúmeras aplicações civis, tais como: (i) inspeção de linhas de transmissão de energia elétrica e gasodutos, (ii) vigilância de portos, reservas florestais e fronteiras pouco acessíveis, (iii) auxílio no resgate de aeronaves e pessoas desaparecidas, (iv) geração de fotografias aéreas e (v) outros.

Em meados de 2004 o Centro de Estudos de Sistemas Avançados do Recife (CESAR) fez contato com o ITA (Divisão de Engenharia Aeronáutica) e propôs uma cooperação com o objetivo de desenvolver um VANT para inspeção das linhas de transmissão, sob responsabilidade da companhia Centrais Hidrelétricas do São Francisco (CHESF). Para realizar este tipo de tarefa, a aeronave deve voar com uma velocidade baixa (80 km/h). Nesta faixa de velocidades, o efeito de rajadas atmosféricas em aeronaves relativamente leves pode causar problemas de segurança e, também, pode dificultar a obtenção de imagens dos elementos da linha de transmissão, devido a mudanças constantes de atitude da aeronave.

Em Dezembro de 2004 foi iniciado desenvolvimento de uma aeronave prova de conceito, com o objetivo de verificar se uma aeronave leve, voando em baixa velocidade e sujeita a rajadas atmosféricas, é capaz de cumprir a missão de realizar a inspeção de linhas de transmissão.

Logo no início de 2005, foi feita uma análise do tipo de aeronave, mais adaptada para o cumprimento da missão de inspeção da linha de transmissão (Girardi e Rizzi, 2005a). O segundo passo no projeto conceitual foi a definição da configuração mais apropriado para que o veículo (avião) possa satisfazer todos os requisitos associados ao cumprimento da missão (Girardi e Rizzi, 2005b). O projeto conceitual foi realizado por um grupo de professores da Divisão de Engenharia Aeronáutica do ITA (Girardi et alli, 2005c) e, para tanto, foi necessário desenvolver uma metodologia de projeto adaptada para uma aeronave pequena, construída com materiais e técnicas alternativas e que não possui uma tripulação (Girardi e Rizzi, 2006). O objetivo do presente trabalho é descrever suscintamente esta metodologia e, em seguida, fornecer resultados da aplicação da mesma, para o projeto conceitual do VANT especificado anteriormente. Levando em conta o caráter iterativo da atividade de projeto, será mostrada a evolução que a aeronave sofreu durante o projeto conceitual, assim como, serão justificadas algumas das decisões tomadas pela equipe de projeto.

2. Visão geral do desenvolvimento de uma aeronave

O projeto de uma aeronave é iniciado com um conjunto de requisitos que devem ser satisfeitos pelo produto. Para o veículo aéreo não tripulado (VANT) desenvolvido neste trabalho, o objetivo é realizar o imageamento (na parte visível do espectro) de elementos de linhas de transmissão de energia elétrica. A velocidade de cruzeiro deve ser

aproximadamente 120 km/h, a altitude de cruzeiro máxima deve ser em torno de 1000 m, a autonomia mínima é de 30 minutos e a carga paga (constituída por auto-piloto, câmera para imageamento e sistemas de rádio controle e de transmissão de imagens para a estação de terra) deve ser de aproximadamente 6 kgf. Um requisito importante é garantir que a aeronave projetada seja capaz de rastrear uma trajetória pré-definida, levando em conta a questão das rajadas atmosféricas.

O desenvolvimento do produto para satisfazer um requisito como aquele descrito acima segue a seguinte seqüência de atividades (metodologia de projeto de aeronaves), como descrito por Raymer (1999) e Roskam (2000-2003):

(i) **Definição da configuração da aeronave**. Esta configuração é caracterizada por um conjunto de informações que definem o aspecto da aeronave, isto é, a posição da asa em relação a fuselagem, a configuração da empenagem (convencional ou canard), o tipo de trem de pouso e etc. Esta configuração é função dos requisitos estabelecidos, de questões operacionais e de segurança.

(ii) **Dimensionamento da aeronave**. Nesta tarefa, são calculadas as dimensões dos principais elementos (asa, fuselagem, empenagens horizontal e vertical e do trem de pouso) da configuração proposta, de maneira a satisfazer os requisitos mencionados no item anterior. Para tanto, são efetuados cálculos de desempenho, estabilidade, controle e qualidade de vôo. As atividades descritas nos itens (i) e (ii) fazem parte do projeto conceitual da aeronave.

(iii) **Projeto preliminar**. Nesta fase, os elementos dimensionados no item anterior são mais detalhados. Por exemplo, a asa tem sua estrutura interna definida, através das longarinas, das nervuras distribuídas ao longo de sua envergadura, dos reforçadores e do tipo de revestimento. Este tipo de detalhamento é feito para todos os demais elementos da aeronave.

(iv) **Projeto detalhado**. Nesta fase, deve-se detalhar ainda mais cada pequeno elemento da aeronave e estabelecer os métodos de construção e montagem das diversas partes. Ainda nesta fase, devem ser produzidos todos os desenhos utilizados para a fabricação de cada peça da aeronave.

(v) **Construção e montagem da aeronave**. Com base nos desenhos gerados na fase anterior, é feita a construção de cada um dos elementos da aeronave. Em seguida, é feita a integração das partes da aeronave e a instalação dos sistemas requeridos para o funcionamento do produto.

(vi) **Ensaios em solo e em vôo**. Nesta fase são efetuados uma série de ensaios para verificar a segurança da aeronave e para verificar se o produto desenvolvido satisfaz os requisitos estabelecidos inicialmente.

3. Definição da configuração da aeronave

Como mencionado anteriormente, a configuração de uma aeronave é definida pela forma geométrica de cada um dos elementos (asa, fuselagem, empenagens, trem de pouso e etc) e pela posição relativa dos mesmos, como pode ser visto na figura 1. A configuração define o aspecto que a aeronave terá, sem a preocupação com o dimensionamento.

A definição da configuração deve ser feita em função dos requisitos de desempenho, operacionais e de segurança. A configuração é especificada através dos seguintes parâmetros:

(i) **Superfícies sustentadoras**: para a asa e para as empenagens horizontal e vertical devem ser especificados valores numéricos para: (a) Alongamento, (b) Afilamento, (c) Enflechamento, (d) Ângulo de diedro e (e) Espessura relativa dos aerofólios.

(ii) **Fuselagem:** as relações entre as dimensões básicas da fuselagem, assim como, a forma de sua seção transversal.

(iii) **Tipo de trem de pouso**: Neste trabalho foi escolhido o tipo triciclo.

(iv) **Tipo e posição do grupo moto-propulsor**: Motor a pistão com hélice, posicionado no nariz da aeronave.

(v) **Sistemas embarcados**: Neste trabalho são considerados os seguintes sistemas: (a) imageamento, (b) rádio-controle, (c) piloto-automático, (d) recuperação da aeronave (para-queda), (e) ensaios em vôo e (f) geração de energia elétrica.

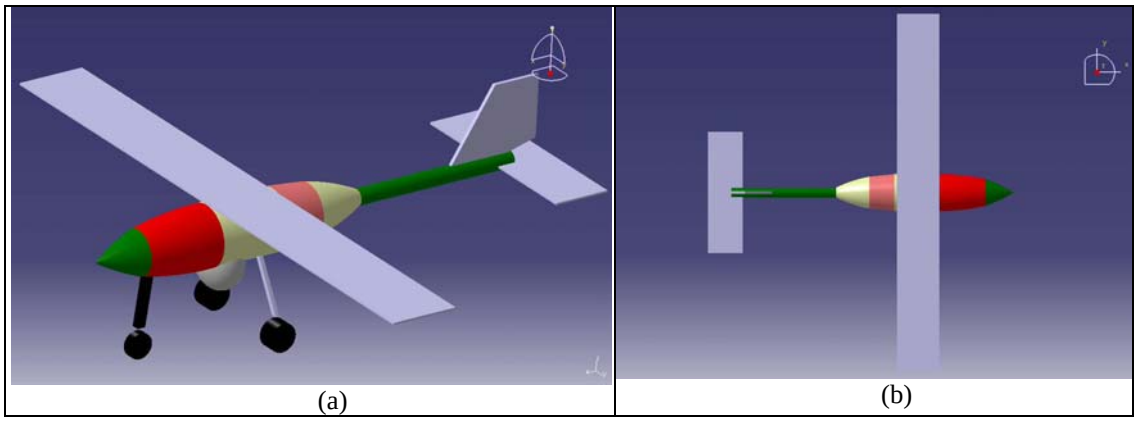

Figura 1: Configuração proposta. Vistas: (a) em perspectiva e (b) em planta.

4. Dimensionamento da aeronave

O dimensionamento de uma aeronave é feito através de um procedimento iterativo, que deve resultar em um produto que satisfaça os requisitos de desempenho, de estabilidade e controle, operacionais e de segurança. No referido procedimento iterativo são realizadas as seguintes atividades:

(i) Inicialmente são feitas estimativas para uma série de parâmetros e, com base nestes, são calculadas todas as dimensões dos elementos da aeronave.

(ii) Em seguida, esta configuração da aeronave é analisada para verificar suas características de desempenho, estabilidade, controle e qualidade de vôo.

(iii) No próximo passo, deve-se verificar se os requisitos especificados inicialmente estão sendo satisfeitos e se a aeronave é capaz de realizar vôos de maneira segura.

(iv) Em geral, após o primeiro ciclo do projeto conceitual, a aeronave dimensionada inicialmente apresenta uma série de problemas que devem ser aprimorados. Devido a isto, deve-se iniciar o próximo ciclo, alterando os valores dos parâmetros estimados no item (i) e refazendo todos os demais passos descritos anteriormente.

(v) O procedimento iterativo descrito acima deve prosseguir até que todos os requisitos sejam satisfeitos e o projeto seja harmônico. Nestas condições pode-se passar para o projeto preliminar da aeronave.

As atividades descritas nos itens (i), (ii) e (iii) podem ser executadas em quatro etapas, como descrito a seguir:

4.1 Etapa # 1: Dimensionamento inicial

Na etapa # 1, o objetivo é estimar a potência do motor e as dimensões principais dos diversos elementos da aeronave, tais como a asa, fuselagem, empenagens horizontal e vertical e do trem de pouso. Para alcançar este objetivo utilizou-se uma metodologia, na qual devem ser realizadas as seguintes atividades:

(i) Fazer estimativas para um conjunto de parâmetros, que permite o dimensionamento de todos os elementos da aeronave. Os parâmetros estimados são: (a) o peso total da aeronave (Wo), (b) o coeficiente de sustentação da aeronave (CL) na fase de cruzeiro, (c) os coeficientes de volume de empenagem horizontal (C_{HT}) e vertical (C_{VT}), (d) a polar de arrasto da aeronave (curva CL x CD) e (e) as relações entre cordas para dimensionamento das superfícies de controle. Em geral, estas estimativas são feitas com base em informações de aeronaves semelhantes.

(ii) Com base nos valores de CL e de Wo é possível determinar a área da asa (S) e, recorrendo-se aos parâmetros adimensionais especificados na configuração da aeronave (vide seção 3), pode-se fazer o dimensionamento completo da asa.

(iii) O comprimento da fuselagem (Lf) pode ser definido inicialmente com base em dados históricos ou através de uma relação entre a envergadura da asa e o comprimento da fuselagem.

(iv) As áreas das empenagens (S_H e S_V) são determinadas em função da área da asa (S), levando em conta as estimativas feitas para C_{HT} e C_{VT}. De maneira análoga ao feito para a asa, os parâmetros adimensionais especificados na seção 3, permitem fazer o dimensionamento completo das empenagens.

(v) Utilizando uma estimativa da polar de arrasto e as variáveis de projeto (dimensões da aeronave) determinadas nos itens anteriores é possível calcular valores aproximados do desempenho da aeronave, tais como: velocidade de "stall", velocidade máxima em vôo nivelado, raio de curvatura mínimo e fator de carga na curva. A potência requerida máxima é um importante resultado que permite o dimensionamento do motor e a estimativa do diâmetro da hélice.

(vi) Os resultados do item anterior permitem avaliar se a aeronave satisfaz os requisitos estabelecidos no início do projeto. Por exemplo, se o raio de curvatura mínimo obtido não é suficiente, então a área da asa deve ser modificada e, para tanto, o CL de cruzeiro deve ser alterado. Deve-se notar que a mudança no dimensionamento da asa acarreta alteração de todo os parâmetros da aeronave. Portanto, todos os passos descritos anteriormente devem ser repetidos e este processo iterativo é interrompido quando todos os requisitos são satisfeitos.

4.2 Etapa # 2: Compatibilização do peso total com os pesos de cada parte da aeronave

Na etapa # 2, o objetivo é fazer uma revisão do valor adotado para o peso total da aeronave na etapa anterior (Wo). A revisão de Wo é realizada através de estimativas dos pesos dos diversos elementos da aeronave. Para tanto, as informações geradas na etapa # 1 (desenhos c/ cotas) devem ser fornecidas para os grupos de propulsão, estruturas e sistemas, os quais devem gerar informações adicionais, como explicado a seguir:

(i) **Grupo de propulsão:** com base na estimativa de potência máxima requerida para a aeronave, é possível especificar o motor e uma hélice. Determinam-se os pesos do motor, da hélice e do combustível requerido, para que a aeronave tenha o alcance especificado no requisito.

(ii) **Grupo de estruturas:** As informações geradas na etapa # 1 contem as dimensões de todos os elementos da aeronave. Desta forma, é possível calcular, de maneira aproximada, os pesos da asa, das empenagens, da fuselagem e do trem de pouso.

(iii) **Grupo de sistemas:** deve determinar o peso e as dimensões dos elementos de cada um dos sistemas que deverá ser embarcado na aeronave. As dimensões de cada elemento permitem que seja verificado se a aeronave possui

espaço interno para acomodar todos os sistemas. Além disto, a determinação do CG necessita da distribuição de cada elemento no interior da aeronave.

Os pesos gerados por cada grupo devem ser somados para a determinação de uma melhor estimativa do peso total da aeronave (W_1). O próximo passo é verificar se existe diferença entre o peso usado na etapa # 1 (Wo) e aquele calculado nesta etapa (W_1). Se uma diferença entre Wo e W_1 for constatada, deve-se retornar para o início da etapa # 1, de maneira a fazer o redimensionamento da aeronave. Deve-se lembrar que o peso estimado na etapa # 1 possui influencia em todas as dimensões da aeronave.

No final da etapa # 2 tem-se uma aeronave cujo peso total é igual a soma dos pesos de cada uma de suas partes e uma aeronave que satisfaz os requisitos de desempenho estabelecidos no início do projeto. Os dados relativos a esta aeronave são registrados em uma tabela (Revisão # 1) e desenhos devem ser feitos. Em seguida, as informações desta nova versão da aeronave são transmitidas para todos os grupos da equipe de projeto.

4.3 Etapa # 3: Ajuste da margem estática da aeronave

Nas duas primeiras etapas desta metodologia foram consideradas as questões de peso e desempenho da aeronave. As dimensões dos elementos isolados (asa, fuselagem e etc) foram ajustadas, porém, a posição relativa dos mesmos não foi analisada. Esta posição relativa é muito importante, pois tem influência sobre a estabilidade e características de qualidade de vôo da aeronave. O objetivo da etapa # 3 é fazer ajustes nas posições relativas dos diversos elementos. Para tanto, deve-se realizar as seguintes atividades:

(i) Com base no conjunto de informações geradas no final da etapa # 2, o grupo de aerodinâmica pode calcular a posição do centro aerodinâmico da aeronave (X_{CA}).

(ii) Para o grupo de estruturas fica a responsabilidade de estimar a posição do centro de gravidade (X_{CG}) da aeronave. Para tanto, os pesos de cada elemento, assim como, as posições relativas do mesmo devem ser conhecidas.

(iii) O grupo de mecânica do vôo deve determinar uma faixa de valores que a margem estática (M-Est), definida como (X_{CA} - X_{CG}), pode assumir de maneira que a aeronave seja estável e tenha boas características de qualidade de vôo. Para a aeronave considerada neste trabalho, o valor mínimo para a margem estática deve ser 10% da corda da asa. Para garantir que a aeronave será estável longitudinalmente basta localizar o CG à frente do CA, isto é, ter-se um valor positivo para M-Est.

(iv) O próximo passo desta etapa é verificar se os valores, determinados nos itens (i) e (ii), para X_{CA} e X_{CG} satisfazem o valor estabelecido para a margem estática no item (iii). Se isto não acontecer, então as posições relativas dos elementos da aeronave (asa, empenagem horizontal e etc) devem ser modificadas para corrigir o problema. Devido a esta modificação pode haver a necessidade de alterar o comprimento da fuselagem e, portanto, pode ser necessário o redimensionamento da aeronave, causado pela modificação do peso total.

4.4 Etapa # 4: Cálculo de desempenho e determinação das características de pilotagem e guiagem da aeronave

No final da etapa # 3, a aeronave que esta sendo projetada tem: (a) as dimensões geométricas de todos os seus elementos, (b) a localização destes elementos, de maneira que o CA e o CG da aeronave estão ajustados e (c) o peso de cada elemento é compatível com as dimensões dos mesmos (asa, fuselagem e etc) e a soma dos pesos dos elementos é compatível com o peso total da aeronave.

Por outro lado, todas as definições mencionadas acima foram obtidas considerando modelos de cálculo simplificados. O objetivo da etapa # 4 é realizar uma análise mais rigorosa das características que a aeronave deverá ter. Para tanto, devem ser aplicados métodos de cálculo mais detalhados e exatos para se analisar: (a) o desempenho em todas as etapas de vôo da aeronave: pouso, decolagem, subida, cruzeiro, velocidade de "stall", desempenho em curva sustentada, teto de serviço e teto máximo, entre outras. (b) a estabilidade e a qualidade de vôo da aeronave, de maneira a tornar a pilotagem o mais fácil possível. (c) a pilotagem e a guiagem da aeronave. Para alcançar os objetivos desta etapa os diversos grupos da equipe de projeto devem gerar as seguintes informações:

(i) Grupo de Propulsão: o motor a ser utilizado na aeronave que esta sendo projetada já foi escolhido em etapa anterior, assim como, uma ou mais hélices. O grupo de propulsão deve gerar informações sobre: (a) potência de eixo, $P(\omega)$ e o consumo específico (C), (b) o rendimento da hélice em função da rotação e da velocidade da aeronave, $\eta(\omega,V)$ e (c) o torque transmitido para a aeronave pelo grupo moto-propulsor, $\tau(\omega,V)$. Os parâmetros mencionados acima permitem a determinação da tração (T) gerada pelo grupo moto-propulsor, que é função da rotação (ω) e da velocidade da aeronave (V).

(ii) Grupo de Aerodinâmica: o maior detalhamento da configuração que esta sendo analisada possibilita a utilização de métodos de cálculo mais aprimorados, para: (a) calcular a polar de arrasto, (b) estimar as derivadas de estabilidade, que permitem modelar a variação das forças e momentos aerodinâmicos que ocorrem por ocasião das manobras ou quando rajadas de vento atmosférico atingem a aeronave e (c) estimar as derivadas de controle, que possibilitam o cálculo das forças e momentos aerodinâmicos que surgem na aeronave devido à deflexão das superfícies de controle primárias, tais como aileron, leme e profundor.

(iii) Grupo de Estruturas: Além do peso total da aeronave e da posição do CG (calculados nas etapas anteriores), os momentos de inércia da aeronave devem ser calculados.

(iv) Grupo de Sistemas: Somente as informações relativas ao piloto automático são requeridas nesta etapa do projeto. O grupo de sistemas deve fornecer as malhas de controle (ou a malha) que são possíveis de serem implementadas na prática. Além disto, o grupo deve fornecer quais são os parâmetros (velocidade, atitude da aeronave e etc) que os sensores poderão fornecer para o piloto automático, para permitir que a guiagem e pilotagem possam ser realizadas.

(v) Grupo de Mecânica do Vôo: Nesta etapa, todos os demais grupos geram resultados para alimentar o grupo de mecânica do vôo, que tem a função de analisar o desempenho, a qualidade de vôo, a guiagem e pilotagem da aeronave. Os resultados desta análise devem mostrar se os requisitos estabelecidos no início do projeto estão sendo satisfeitos de maneira adequada e se a configuração estudada pode realizar a missão proposta em termos de guiagem e pilotagem.

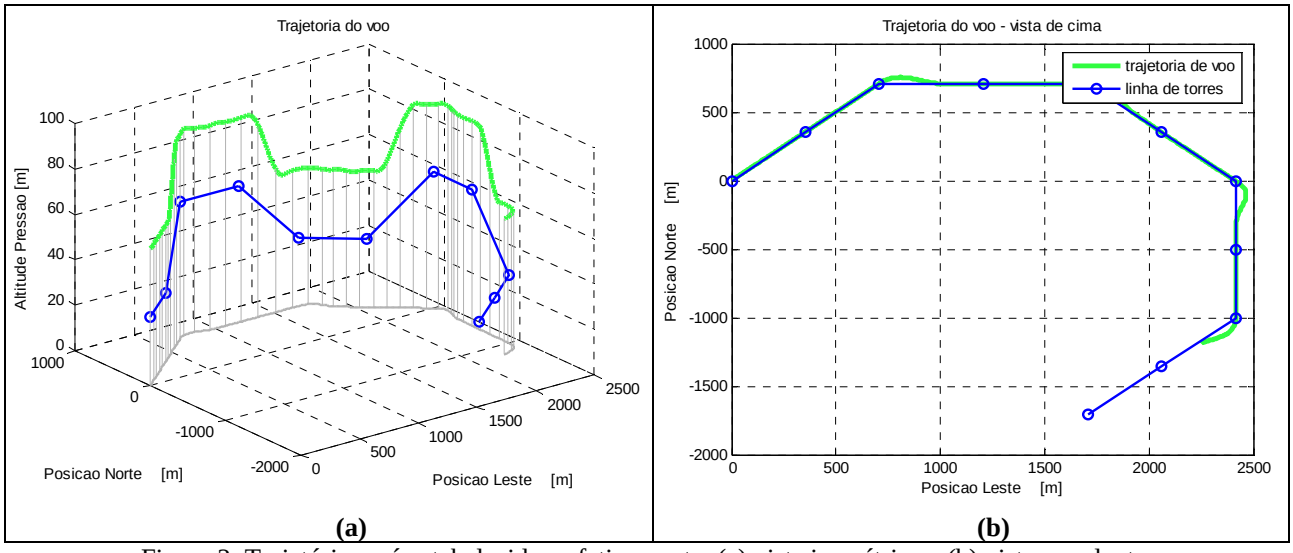

Figura 2: Trajetórias pré-estabelecida e efetivamente: (a) vista isométrica e (b) vista em planta.

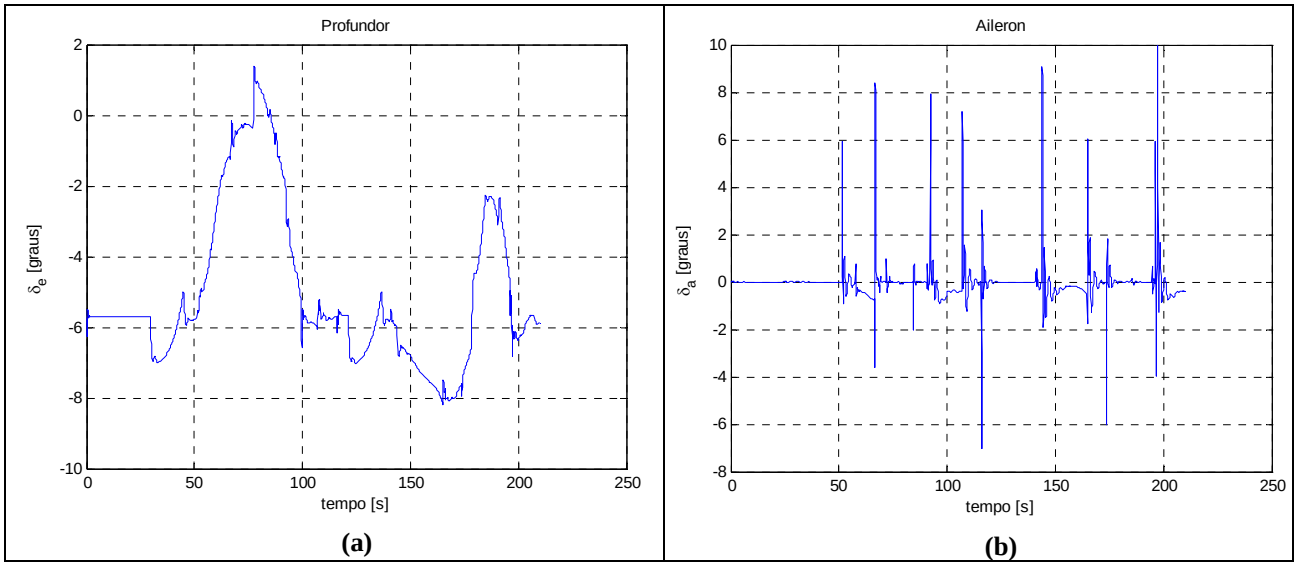

Figura 3: Histórico dos controles da aeronave, durante um vôo em atmosfera turbulenta: (a) profundor e (b) aileron.

Neste trabalho, a pilotagem automática foi analisada em duas condições básicas de vôo: (i) para velocidade de 33 m/s e (ii) para velocidade de 19 m/s (1.2 da velocidade de *stall* da aeronave). Para realizar as simulações, cujos resultados são apresentados nas Figs 2 a 4, utilizou-se o programa MatLab, para realizar uma integração das equações do movimento de uma aeronave. As simulações foram realizadas de maneira que a aeronave sobrevoasse 10 torres. As torres foram posicionadas para que a aeronave percorresse uma missão sofrendo a interferência de vento constante de proa, de cauda, e de través, realizando curvas, subidas e descidas. O posicionamento das torres pode ser verificado na figura 2. Como pode ser visto, foram especificadas duas subidas e duas descidas distintas. Na primeira subida, a aeronave estará sob atuação de vento de cauda. Na segunda subida, a aeronave estará com vento da direita. Da mesma maneira, na primeira descida, a vento estará soprando levemente da direita e de cauda, já na segunda descida, o vento

estará da direita, mas de proa. Todas as curvas especificadas são de 45 graus. É importante salientar, entretanto, que dependendo do vento atuante no momento, a aeronave pode ter mais ou menos dificuldade para realizá-las.

A introdução de ventos e rajadas foi feita de maneira semelhante para as duas condições de vôo citadas acima. O vento introduzido foi constante, com intensidade de 25 km/h soprando na direção nordeste. De forma combinada, foram introduzidas rajadas, definidas em Girardi e Rizzi (2005c).

O auto-piloto usado nas simulações deste estudo é bastante parecido com o auto-piloto disponível para implementação do sistema comercial MicroPilot, o qual será embarcado no VANT desenvolvido neste trabalho. Durante a pilotagem automática, ao longo da trajetória observada na figura 2, os controles da aeronave são variados de maneira a minimizar as diferenças entre as trajetórias efetivamente realizada (linha verde) e aquela pré-estabelecida (linha azul). Os históricos da variação de cada um dos controles da aeronave (aileron, leme de direção, profundor e o controle da rotação do motor) são apresentados nas figuras 3 e 4. Os valores máximos e mínimos são apresentados na tabela 4 e tem grande importância para a avaliação das dimensões das superfícies de controle (vide seção 5).

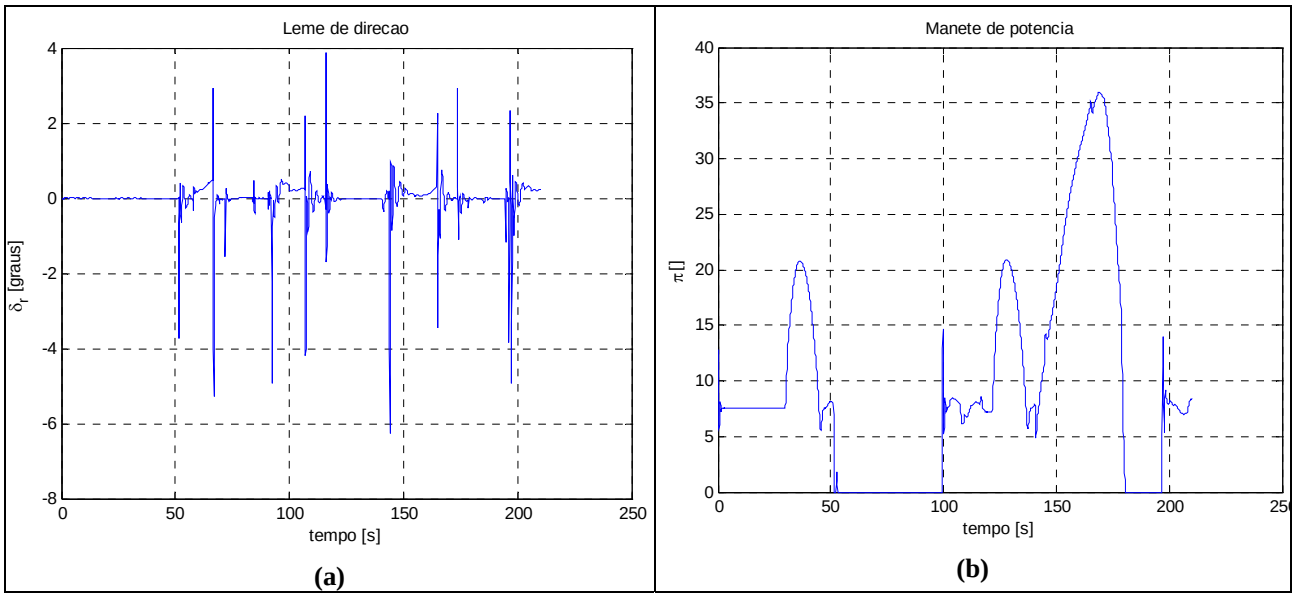

Figura 4: Histórico dos controles da aeronave, durante um vôo em atmosfera turbulenta: (a) leme e (b) manete do motor.

5. Evolução da configuração durante o projeto conceitual

Como mencionado anteriormente, o projeto conceitual é realizado através de um procedimento iterativo, onde as variáveis de projeto são recalculadas até se obter um projeto harmonioso. Na presente seção do trabalho apresenta-se a evolução da aeronave, ocorrida com o transcorrer dos ciclos de projeto conceitual, assim como, os aspectos que demonstram a harmonia do projeto, encontrado na ultima configuração.

Para auxiliar na análise da evolução da aeronave durante a fase de projeto conceitual serão utilizadas tabelas onde são comparadas as variáveis de projeto das três configurações estudadas.

Na tabela 1 são fornecidos os valores adotados para os parâmetros requeridos nos cálculos necessários para o dimensionamento inicial da aeronave (etapa #1).

O peso total da aeronave foi estimado inicialmente (iteração 1, relativa a configuração A-1) com base em informações muito rudimentares sobre o peso de cada um dos elementos principais da aeronave. Após a iteração 1, verificou-se que os pesos dos elementos da aeronave foram super dimensionados e, portanto, o peso total da aeronave analisada na configuração A-1 poderia ser reduzido, caso as dimensões dos elementos fossem mantidas.

Na configuração A-2 foi feita uma redução do CL (vide tabela 1) que resultou em aumento da área da asa (vide tabela 2) e, portanto, incremento das dimensões de toda a aeronave. A equipe de projeto adotou o peso total de 30 kgf para a configuração A-2, analisada na iteração 2, devido aos aspectos conflitantes discutidos anteriormente, a saber: (i) peso menor para os elementos da configuração A-1 e (ii) incremento das dimensões na evolução da configuração A-1 para a A-2. Durante o segundo ciclo, verificou-se que a soma dos pesos dos diversos elementos da aeronave era 25 kgf, porém, este peso estava associado as dimensões calculadas com o peso proposto inicialmente de 30 kgf. O desempenho, a qualidade de vôo e as simulações de guiagem e pilotagem foram feitas para uma aeronave com peso total de 25 kgf e dimensões calculadas com 30 kgf, mostrando claramente uma falta de harmonia do projeto analisado no segundo ciclo.

Para a configuração A-3 a metodologia de projeto foi aprimorada e o peso total proposto inicialmente de 22 kgf foi fruto de um esquema iterativo, no qual a soma dos pesos de cada elemento foi compatibilizado com suas dimensões. Cálculos posteriores, realizados durante o terceiro ciclo, forneceram um peso total de 21 kgf. Esta variação de 1 kgf (aproximadamente 5% do peso total) pode ser compensada por uma pequena variação no valor de CL de cruzeiro, não

havendo necessidade de modificar as dimensões da aeronave considerada na configuração A-3. Para esta configuração pode-se observar que a soma dos pesos das partes é muito próxima do peso total utilizado para o dimensionamento da asa e de toda a aeronave, mostrando uma harmonia entre as variáveis de projeto.

Tabela 1: Valores estimados inicialmente para cada iteração (ciclo do projeto)

Parâmetro	**Valor estimado**		
	Iter. 1	**Iter. 2**	**Iter. 3**
Velocidade de cruzeiro (km/h)	120	120	120
Peso total da aeronave (kgf)	30	30	22
Coeficiente de sustentação em cruzeiro	0,60	0,40	0,40
Coeficiente de volume de empenagem horizontal	0,73	0,80	0,80
Coeficiente de volume de empenagem vertical	0,06	0,05	0,05
Relação entre as cordas do aileron e da asa	0,25	0,20	0,20
Relação entre as envergaduras do aileron e da asa	0,40	0,30	0,30
Relação entre as cordas do profundor e da empenagem horizontal	0,50	0,50	0,50
Relação entre as envergaduras do profundor e da emp. horizontal	1,00	1,00	1,00
Relação entre as cordas do leme e da empenagem vertical	0,40	0,30	0,30
Relação entre as envergaduras do leme e da empenagem vertical	1,00	1,00	1,00

Tabela 2: Parâmetros Geométricos e Potência Requerida p/ cada Iteração

Elemento	Parâmetro Geométrico	Valor		
		Iter. 1	Iter. 2	Iter. 3
Asa	Área (S)	0,80	1,200	0,883
	Envergadura (b)	2,37	2,900	2,486
	Corda (CW)	0,34	0,414	0,355
	Início do aileron, relativo à envergadura	50	60	60
	Final do aileron, relativo à envergadura	90	90	90
	Relação entre as cordas do aileron e asa	0,25	20	20
	Envergadura de cada aileron (BA)	0,474	0,435	0,373
	Corda do aileron (CA)	0,085	0,082	0,071
	Posição do bordo de ataque da asa	-	-	0,510
	Ângulo de incidência da asa na fusel. (Iw)	3	3,7	0,8
Emp. Horiz.	Área (Sh)	0,14	0,275	0,202
	Distância entre o CG e o BA da emp. hor.	-	1,450	1,183
	Envergadura (Bh)	0,74	0,981	0,840
	Corda (Ch)	0,19	0,280	0,240
	Envergadura do profundor (Bp)	0,74	0,981	0,840
	Corda do profundor (Cp)	0,095	0,140	0,120
	Relação entre as cordas Cp/Ch	0,50	50	50
	Ângulo de incidência da empenagem (Ih)	0	2,3	-0,5
Emp. Vert.	Área (Sv)	0,08	0,120	0,098
	Distância entre o CG e o BA da emp. vert.	-	1,320	0,990
	Envergadura (Bv)	0,49	0,347	0,313
	Corda na raiz (Crv)	0,22	0,458	0,422
	Corda na ponta (Crv)	0,11	0,236	0,204
	Enflechamento do bordo de ataque	12,65	32,8	26
	Envergadura do leme (Bl)	0,49	0,347	0,313
	Corda média do leme (Cl)	0,065	0,105	0,094
	Relação entre as cordas Cl/Cv	0,40	30	30
	Ângulo de incidência da empenagem (Iv)	0	0,0	0,0
Fuselagem	Comprimento (Lf)	2,4	2,420	2,055
	Altura máxima (Hf)	0,30	0,300	0,300
	Largura máxima (Bf)	0,30	0,250	0,250
	Comprimento do cone de cauda (Lc)	1,0	0,820	0,905
Motor	Potência Requerida (Tração x Velocidade)	3,0	5,0	2,65

Na tabela 1 pode-se observar que o CL de cruzeiro para a configuração A-1 foi adotado com valor elevado (CL = 0,6), levando em conta os valores históricos encontrados para aeronaves leves. Este valor foi adotado com o objetivo de redução do fator de carga em rajada, de modo a aumentar as chances da aeronave cumprir sua missão, que é a inspeção dos elementos que compõe uma linha de transmissão de energia elétrica. A maior preocupação da equipe de projeto era o arrastamento da aeronave (leve) por ocasião de rajadas atmosféricas. Após a análise do comportamento da aeronave com auto-piloto instalado, verificou-se que durante uma rajada o auto-piloto atua nas superfícies de controle e na potência do motor de maneira a minimizar os erros entre a trajetória pré-estabelecida e a trajetória efetivamente realizada pela aeronave. Devido a isto, a variação do coeficiente de sustentação da aeronave não sofre variações elevadas, não havendo risco da aeronave alcançar o valor máximo de sustentação durante uma rajada, sendo esta uma das preocupações da equipe de projeto, que levou a mesma a escolher um perfil aerodinâmico com valor elevado de CL_{max}.

Com base na discussão apresentada no parágrafo precedente, para a configuração A-2 foi adotado um valor menor para o coeficiente de sustentação em cruzeiro (CL = 0,4). Esta redução implica em: (i) diminuição da velocidade de stall, que melhora a questão da segurança da operação de pouso e (ii) a diminuição do raio de curvatura de curvas coordenadas, que é especialmente interessante para a implementação de uma estratégia alternativa para a realização da inspeção das torres da linha de transmissão. Nesta estratégia, a aeronave faz um vôo reto entre as torres e realiza uma curva de 360 graus ao redor de cada uma das torres. Com isto é possível uma inspeção mais detalhada, como aquela realizada com os helicópteros, que tem a capacidade de pairar.

A redução do CL de cruzeiro acarretou aumento da área da asa (vide tabela 2) e, portanto, de todas as dimensões da aeronave, como discutido anteriormente na análise sobre a evolução do peso.

Após a análise de desempenho (vide tabela 3) da configuração A-2, verificou-se um valor de velocidade de *stall* suficientemente baixo para que a aeronave possa realizar vôos ao longo da linha de transmissão com velocidade próxima àquela requerida para fazer imageamento com termovisão. Como discutido anteriormente, embora a utilização da termovisão não esteja dentro do escopo do presente projeto, a equipe acha importante ganhar alguma experiência em vôos com baixa velocidade, para verificar a questão do impacto de rajadas atmosféricas sobre o comportamento da aeronave e do dispositivo de imageamento e seu suporte (possivelmente uma suspensão de Guimbal mecânica). Na tabela 3 também pode-se observar que o raio mínimo de uma curvatura coordenada que a aeronave pode realizar é um pouco maior que 30 m. A equipe de projeto tentou alcançar este valor de raio de curvatura porque a distancia estabelecida inicialmente, entre a aeronave e os diversos elementos da linha de transmissão, é 30 m. Este valor foi fornecido pelo pessoal da CHESF.

Tendo em vista o bom desempenho da configuração A-2, o mesmo valor de coeficiente de sustentação de cruzeiro foi adotado para a configuração A-3. Pode-se verificar que o desempenho nos quesitos velocidade de *stall* e raio mínimo de curva coordenada são semelhantes para as configurações A-2 e A-3.

Tabela 3: Parâmetros relativos ao desempenho da aeronave

Parâmetro	Iter. 1	Iter. 2	Iter. 3	Unid.
Comprimento de pista de rolamento em decolagem	31.15	11,4	9.70	m
Comprimento de pista de rolamento em pouso	183.00	128.7	143.00	m
Ângulo de ataque de rolamento	-1.9	1.95	2.15	graus
Ângulo máximo de subida	33.68	44.7	89.00	graus
Razão de subida máxima	11.10	14.1	20.84	m/s
Velocidade de stall	20.00	15.4	16.50	m/s
Velocidade máxima de cruzeiro	54.5	52.5	59.00	m/s
Potência máxima disponível (eficiência = 1)	5.0	5.0	6.0	Hp
Potência requerida no cruzeiro (eficiência = 1)	1.5	1.3	1.1	Hp
Quantidade requerida de combustível	0.528	0,2756	0.418	Kg
Tempo de vôo (alcance de 40 km)	1212	1212	1212	s
Teto de serviço	11000	11800	14600	m
Teto máximo	12000	12200	15000	m

Os coeficientes de volume de empenagem horizontal e vertical, assim como, as relações entre cordas das superfícies de controle e das respectivas empenagens foram estimados com base em dados históricos (vide análise crítica apresentada por Lopes e Amaral, 2004) para a configuração A-1 (primeiro ciclo). Após a realização da análise do comportamento dinâmico da aeronave, foi verificado que: (i) a empenagem vertical estava super dimensionada. Devido a isto, a equipe de projeto fez uma redução do coeficiente de volume da empenagem vertical para a configuração A-2. (ii) Foi verificado, através de simulação numérica, que a deflexão máxima requerida pelo leme era muito pequena, sendo mais difícil o controle suave da aeronave, devido a sensibilidade da superfície de controle (pequena deflexão gera grande força) e devido a questão da resolução dos atuadores (servo-motores). Para a configuração A-2 foi feita uma redução da relação entre a corda do leme e a corda da empenagem vertical. (iii) A empenagem horizontal forneceu boas

características de estabilidade longitudinal (estabilidade e qualidade de vôo), porém, ângulos de deflexão elevados (25 graus) foram requeridos para o profundor durante as manobras que a aeronave teve que realizar durante as simulações numéricas. Estes valores de deflexão podem acarretar problemas de descolamento do escoamento e, portanto, falta de efetividade da superfície de controle, principalmente em baixo número de Reynolds, como é o caso da aeronave que esta sendo desenvolvida no presente trabalho. Como a relação entre as cordas do profundor e da empenagem horizontal já tem valor elevado (50%), para a configuração A-2, a equipe de projeto decidiu aumentar o coeficiente de volume de empenagem horizontal e, como conseqüência, a área do profundor. As modificações adotadas para a configuração A-2 deram bons resultados e, para a configuração A-3, foram adotados os mesmos valores para os parâmetros adimensionais discutidos acima.

As simulações da aeronave (configuração A-1) mostraram que curvas bem acentuadas (com baixo raio de curvatura) requeriam apenas alguns graus de deflexão do aileron. Devido a isto, para a configuração A-2, a equipe de projeto decidiu reduzir tanto a relação entre as cordas do aileron e da asa, quanto a envergadura do aileron. Esta alteração forneceu resultado satisfatório e, para a configuração A-3, os parâmetros adimensionais que definem as dimensões do aileron foram adotados com os mesmos valores da configuração A-2.

A discussão relatada nos parágrafos anteriores, mostra que da configuração A-2 para a A-3 não foram feitas modificações nos parâmetros adimensionais que definem as dimensões das empenagens e das superfícies de controle. Esta informação indica uma convergência da configuração adimensionalisada da cauda da aeronave e das superfícies de controle.

Para a configuração A-1 a potência requerida para o motor foi estimada inicialmente com base em simulações numéricas baseadas em modelos simples do desempenho em cruzeiro da aeronave e, também, em uma polar de arrasto estimada de forma grosseira. Não foram feitas considerações sobre a potência requerida para a manutenção da trajetória da aeronave em uma atmosfera turbulenta. Após a realização das primeiras simulações com auto-piloto, verificou-se que a propulsão da aeronave tem um papel muito importante na guiagem e pilotagem da mesma. Observou-se que por ocasião de uma rajada, o auto-piloto modifica a atitude da aeronave e ao mesmo tempo incrementa a tração gerada pelo grupo moto-propulsor, de maneira a evitar o arrastamento da aeronave para fora da trajetória pré-estabelecida. Sem a atuação do motor, a aeronave certamente não poderia cumprir sua missão, pois as rajadas de vento atmosférico arrastariam a aeronave e não haveria possibilidade de se realizar a filmagem dos elementos da linha de transmissão. Os resultados gerados para a configuração A-1 mostram que a potência deste tipo de aeronave deve ser especificada em função dos requisitos de comportamento dinâmico (guiagem e pilotagem em atmosfera turbulenta) e não com base em requisitos de desempenho, como é o caso da maioria das aeronaves existentes.

Tendo em vista a discussão do parágrafo precedente, assim como, o incremento das dimensões da aeronave (como relatado acima), para a configuração A-2 a equipe de projeto decidiu aumentar a potência do motor. Após análise do comportamento dinâmico da aeronave (configuração A-2), verificou-se que a potência de 5 hp foi suficiente para a realização do rastreamento da trajetória pré-definida. Para o ciclo seguinte, a metodologia de projeto foi melhorada e a relação entre a potência e o peso da aeronave, analisada anteriormente, foi utilizada para fazer uma estimativa para a configuração A-3. A aplicação da nova metodologia indicou que a potência requerida pela configuração A-3 deveria ser de 2,70 hp. Após as simulações realizadas pelo grupo de mecânica do vôo, foi verificado que uma potência de 3,3 hp é suficiente para viabilizar o cumprimento da missão. Este resultado mostra que a nova metodologia fornece resultado razoável e, como o motor especificado possuía uma sobra de potência, o pequeno incremento de potência requerida não inviabilizou a utilização do motor especificado pelo grupo de propulsão. Este aspecto é muito importante porque o peso do referido motor é uma parte considerável do peso total da aeronave. Se houvesse necessidade de especificar outro motor, a aeronave deveria ser re-dimensionada devido a modificação do peso total. A não necessidade de alteração do motor é mais um aspecto da harmonia da configuração A-3.

Observando-se a tabela 3 verifica-se que o comprimento de pista de decolagem é bastante reduzido, principalmente para as configurações A-2 e A-3. Este resultado é conseqüência da potência elevada utilizada nesta aeronave, para que a mesma possa rastrear a trajetória pré-estabelecida em uma atmosfera turbulenta. Além disto, o grupo de mecânica do vôo utilizou a potência de eixo do motor, considerando a eficiência da hélice como sendo igual a 1. Na realidade, a potência efetiva é bem menor quando a eficiência da hélice é considerada. Devido a isto, espera-se que o comprimento da pista de decolagem aumente quando condições mais realistas forem consideradas nas simulações, tarefa programada para a próxima fase do projeto. Em termos de desempenho desejado para a aeronave, o comprimento de pista deve ser o menor possível, tendo em vista que a operação de decolagem poderá ser feita em pequenos trechos de estradas locais, muitas vezes não pavimentadas.

Verificou-se que a razão de subida, assim como o ângulo máximo de subida da aeronave, possuem valores muito elevados. Os valores encontrados para a configuração A-3 também são conseqüência do excesso de potência, como discutido no parágrafo anterior. Para a aeronave em estudo neste trabalho, os parâmetros mencionados acima não necessitam ter valores elevados. Este tipo de desempenho em subida pode ser útil em caso de uma rajada vertical arrastar a aeronave para baixo, nas proximidades de uma elevação.

Ainda na tabela 3, pode-se observar que os tetos de serviço e absoluto têm valores muito elevados, sendo isto conseqüência do excesso de potência, discutido acima. Para cumprir a missão de fiscalização de linhas de transmissão não há necessidade da aeronave possuir teto de serviço elevado. Mesmo que trechos da linha de transmissão estejam localizados em regiões montanhosas, os valores para o teto de serviço são muito elevados. Sendo assim, a aeronave,

com as características da configuração A-3, é perfeitamente capaz de cumprir os requisitos de projeto no quesito teto de serviço.

Com relação as características dinâmicas da aeronave (configuração A-3) pode-se dividir a análise em duas partes: (i) resposta dinâmica para a situação onde os controles da aeronaves não são defletidos. Esta situação é considerada como crítica, durante a fase de vôo com piloto humano, pois para rajadas muito rápidas um piloto em terra não terá tempo de resposta suficientemente curto para atuar nos controles e (ii) resposta da aeronave quando controlada pelo auto-piloto. Neste caso, os controles são variados pouco tempo após os sensores embarcados terem detectado variações nos parâmetros que fornecem a atitude da aeronave e, também, sua trajetória.

Considerando a situação mais crítica para a pilotagem à distância, situação (i), as simulações realizadas pelo grupo de mecânica do vôo mostram que a aeronave sofre acelerações da ordem de 5 vezes a aceleração da gravidade, durante rajadas especificadas em regulamento que deve ser seguido pelos fabricantes de aeronaves leves que levam seres humanos. Estes valores são muito importantes para o grupo de estruturas calcular as cargas máximas que os diversos elementos da aeronave (asa, empenagens, fuselagem e trem de pouso) devem resistir. Obviamente, quanto maiores forem estas cargas, mais reforçada deve ser a estrutura da aeronave e, como conseqüência, mais pesados serão os elementos da mesma.

Ainda considerando as fases do vôo, onde a aeronave é controlada por piloto humano, deve-se analisar qualidade de vôo e a controlabilidade da mesma. Para a configuração A-2, que possui coeficientes de volume de empenagens iguais à configuração A-3, verificou-se uma qualidade de vôo muito boa, principalmente para as condições de velocidade de cruzeiro. Foi verificado que o nível de qualidade de vôo ficou um pouco degradado para baixas velocidades, encontradas logo após a decolagem. Ainda neste caso, obteve-se nível razoável. Considerando-se o comportamento da aeronave durante uma rajada, observou-se a ocorrência de valores muito elevados de ângulo de ataque e o conseqüente *stall* da aeronave. No entanto, esta situação somente ocorre para rajadas muito curtas e a aeronave tem a capacidade de continuar seu vôo normal após sair da referida rajada. Para as rajadas mais longas, as simulações do grupo de mecânica do vôo mostraram que é possível uma reação do piloto antes da aeronave assumir atitudes que levem a mesma a cair.

Tabela 4: Parâmetros associados ao comportamento dinâmico da aeronave c/ auto-piloto (configuração A-3)

Parâmetro	Valor Máximo V = 33.3 m/s	Valor Máximo V = 19.0 m/s	Unid.
Erro máximo da velocidade da aeronave	3.00	13.00	m/s
Erro máx. da altura da aeronave, na passagem pelas torres	0.8	0.8	m
Ângulo de ataque máximo da aeronave (α)	+2.00/-2.00	+9.00/0.00	graus
Ângulo de derrapagem máximo da aeronave (β)	+/- 1.50	+/- 1.50	graus
Ângulo de deflexão máximo do profundor (δ_p)	+2.50/-2.00	+2.50/-8.00	graus
Ângulo de deflexão máximo do leme (δ_r)	+12.0/-6.0	+10.0/-6.0	graus
Ângulo de deflexão máximo do aileron (δ_a)	+4.0/-8.0	+4.0/-6.0	graus
Aceleração máxima da aeronave no eixo X (a_x)	+/- 0.8	+/- 0.6	g
Aceleração máxima da aeronave no eixo Y (a_y)	+/- 0.8	+/- 0.4	g
Aceleração máxima da aeronave no eixo Z (a_z)	+0.5/-1.0	+0.15/-0.25	g
Potência requerida máxima (Pmax)	55	35	%

Com relação a fase de vôo controlada pelo auto-piloto, situação (ii) discutida acima, pode-se fazer os comentários formulados abaixo.

Para a configuração A-1, a malha de controle do equipamento que será adquirido para este projeto ainda não era conhecida. O grupo de mecânica do vôo formulou uma malha e fez otimização dos ganhos da mesma. Além disto, foi estabelecido que a aeronave deveria seguir uma trajetória constituída por seguimentos de curvas catenárias, que ligavam uma seqüência de torres da linha de transmissão, com altitudes distintas, para simular a ocorrência de elevações do terreno ao longo da linha de transmissão. Para este tipo de trajetória, existe uma variação brusca da inclinação da mesma exatamente em cada uma das torres. Devido a isto, o auto-piloto requeria deflexões de profundor muito elevadas, fazendo que a equipe de projeto aumentasse a área (coeficiente de volume de cauda) da empenagem horizontal e, como conseqüência, da superfície de controle, como discutido anteriormente.

A partir da configuração A-2, o grupo de mecânica do vôo utilizou a malha de controle capaz de ser implementada no auto-piloto que será embarcado na aeronave (Micro Pilot). Além disto, tendo em vista que no imageamento com câmera sensível a parte visível do espectro, os possíveis problemas ocorrem na região da torre e não no cabo entre as mesmas, o grupo de projeto modificou a trajetória que a aeronave deve seguir, de maneira que a mesma é constituída por seguimentos de "reta", entre as torres, e seguimentos de curva, na região das torres, de maneira que as inclinações da trajetória não sofrem descontinuidades, como na trajetória especificada na configuração A-1. Para esta nova trajetória não há preocupação com os desvios da aeronave na região entre as torres, porém, procura-se minimizar os desvios entre a trajetória efetivamente seguida pela aeronave e aquela pré-estabelecida, somente na região das torres de transmissão.

Nas duas primeiras linhas da tabela 4 (valores obtidos com a configuração A-3) são fornecidos os desvios máximos na velocidade e na altura, lembrando que estes valores são obtidos em uma atmosfera turbulenta, onde são consideradas rajadas com diversas intensidades e durações. Quando as simulações são feitas em atmosfera calma, os desvios são nulos. Pode-se verificar que o desvio na velocidade é bem maior que o desvio encontrado na altura da aeronave (com relação aos parâmetros pré-estabelecidos para a trajetória da aeronave), principalmente em vôo com baixa velocidade. Para o cumprimento da missão (imageamento da região próxima as torres) o parâmetro fundamental é a distância da aeronave com relação a torre, pois desvios neste parâmetro podem acarretar o não imageamento da torre, principalmente porque não haverá dispositivo de apontamento de câmera na aeronave projetada neste trabalho (questão de recursos). Variações de velocidade não são relevantes para a qualidade das imagens obtidas com a câmera embarcada, segundo o grupo de eletrônica, responsável pelo assunto.

Os valores máximos encontrados para os ângulos de ataque e de derrapagem também podem ser encontrados na tabela 4. Observam-se variações muito pequenas na condição de velocidade de cruzeiro (33,3 m/s) e variações um pouco maiores, porém, na faixa linear de comportamento da aeronave, para a condição de vôo com velocidade mais baixa (19 m/s). Estas pequenas variações são conseqüência do controle realizado pelo auto-piloto, como discutido anteriormente, e permitem concluir que os limites de operação da aeronave não serão excedidos, mesmo em uma atmosfera turbulenta.

Uma das preocupações da equipe de projeto é com as deflexões das superfícies de controle primárias: aileron, leme e profundor. Os ângulos de deflexão não podem ser muito altos, porque pode ocorrer o *stall* da superfície sustentadora e a mesma pode perder efetividade, principalmente quando a aeronave esta submetida a um escoamento com baixo número de Reynolds, como é o caso em estudo. Por outro lado, se os referidos ângulos forem muito pequenos, a aeronave fica muito sensível e fica difícil realizar a pilotagem com atuadores convencionais. Como pode ser visto na tabela 4, o leme e o aileron estão trabalhando em uma faixa de variação razoável, porém, o profundor parece estar muito grande e seria interessante estudar a redução desta superfície de controle, tendo em vista a redução da sensibilidade da aeronave com relação a variações na deflexão do profundor. Este pequeno problema não impede que a fase de projeto conceitual seja finalizada com a configuração A-3, porque a alteração da área de qualquer uma das superfícies de controle não tem impacto significativo sobre o peso da aeronave e, portanto, não há necessidade de se fazer re-dimensionamento da mesma. Na fase de projeto preliminar será feito um refinamento das dimensões das superfícies de controle.

Ao contrário do vôo com controles fixados, durante o vôo autônomo a aeronave é submetida a acelerações com intensidade muito baixa (vide tabela 4), mostrando a efetividade do auto-piloto em fazer correções de atitude e de tração, que evitam o aparecimento de forças que tendem a arrastar a aeronave para fora da trajetória pré-estabelecida.

6. Considerações finais

Este trabalho é dividido basicamente em duas partes. Na primeira foi feita uma descrição sucinta da metodologia utilizada para a execução do projeto conceitual de um veículo aéreo não tripulado (VANT). Trata-se de uma adaptação da metodologia aplicada para aeronaves tripuladas, pois o VANT considerado neste trabalho possui características peculiares: (i) vôo em velocidade relativamente baixa (baixo Reynolds), (ii) feito com materiais não convencionais, (iii) peso baixo e, portanto, muito suscetível a rajadas atmosféricas e (iv) deve voar próximo a linha de transmissão. Uma característica muito importante da metodologia proposta é que o projeto da plataforma aérea é feito em função das características do auto-piloto embarcado. Este aspecto teve influência direta na determinação da potência do motor e nas dimensões da empenagem horizontal, pois a situação crítica para estes dois elementos da aeronave (verificado através de simulação numérica) ocorreu durante o vôo da aeronave em uma atmosfera turbulenta.

Na segunda parte é apresentada a evolução da plataforma aérea com o decorrer dos ciclos do procedimento iterativo que caracteriza o projeto conceitual de uma aeronave. Nesta parte são apresentadas justificativas das decisões tomadas pela equipe de projeto e algumas mudanças de filosofia de projeto, ocorridas em função da experiência obtida durante os ciclos do projeto conceitual. Por exemplo, foi verificado que a potência do motor, especificada no primeiro ciclo com base nos requisitos de velocidade máxima de cruzeiro, deveria ser incrementada para satisfazer o requisito de rastreamento da linha de transmissão. Devido ao pequeno peso da aeronave (cerca de 20 kgf) uma rajada de vento tem a tendência de arrastar a aeronave para longe da trajetória pré-determinada (ao longo da linha de transmissão). Para evitar tal problema, o piloto automático, embarcado na aeronave, atua nas superfícies de controle para modificar a atitude da mesma e aumenta a rotação do motor (aumento de potência) para compensar o incremento de velocidade, devido a rajada.

A discussão relatada na seção 5 permite concluir que a configuração A-3 possui um projeto harmonioso, satisfaz os requisitos de desempenho necessários para o cumprimento da missão e possui boas características dinâmicas para as fases de vôo controladas por piloto humano ou pelo auto-piloto, que será adquirido neste projeto.

Na próxima fase (projeto preliminar): (i) serão utilizados modelos mais elaborados (que forneçam resultados mais próximos da realidade) para a determinação das características da aeronave, (ii) serão realizados ensaios para validar e/ou aprimorar estes modelos, (iii) serão feitos ajustes para aprimorar o projeto apresentado na configuração A-3, (iv) maiores detalhes deverão ser levados em consideração, tais como a maneira de fixação dos equipamentos eletrônicos no interior da fuselagem da aeronave entre outros.

Obviamente, existem incertezas nos métodos de cálculo e simulação e o comportamento real da aeronave é determinado na fase de ensaio em vôo, a qual serve para alterar o projeto e melhorar o produto que esta sendo desenvolvido. Além disto, a questão da confiabilidade do novo produto é essencial para que os organismos governamentais possam permitir que aeronaves deste tipo sejam utilizadas. Para tanto, durante a fase de ensaios em vôo serão feitos testes de um sistema de recuperação, constituído por um para-queda e seu dispositivo automático de acionamento.

7. Agradecimentos

A Financiadora de Estudos e Projetos (FINEP) pelo apoio financeiro (protocolo 243/2004) e ao Centro de Estudos de Sistemas Avançados do Recife (CESAR), pela parceria no desenvolvimento do veículo aéreo não tripulado considerado neste trabalho.

8. Referencias bibliográficas

Girardi, R.M. e Rizzi, P., (2005a), "Análise do tipo da aeronave mais adaptada para a inspeção de linhas de transmissão", Relatório de Trabalho, CESAR/ITA, 27 de junho.

Girardi, R.M. e Rizzi, P., (2005b), "Seleção da alternativa mais promissora para prova de conceito, através da construção e testes em vôo", Relatório de Trabalho, CESAR/ITA, 27 de junho.

Girardi, R.M.; Rizzi, P.; Bussanra, F., Lacava,P. & Cavalieri, A.V.G., (2005c), "Projeto conceitual da aeronave, utilizando métodos de cálculo que fornecem boas estimativas, em tempo reduzido, dos parâmetros que definem a aeronave", Relatório de Trabalho, CESAR/ITA, 20 de Dezembro.

Girardi, R.M. e Rizzi, P., (2006), "Desenvolvimento de Metodologia para Projeto Conceitual de um Veículo Aéreo Não Tripulado (VANT), Usado para Inspeção de Linhas de Transmissão de Energia Elétrica", Anais do Congresso Nacional de Engenharia Mecânica (CONEM), Recife, Pe.

Lopes, R.R. e Amaral, R.F.,(2004), "Projeto Conceitual de Aeronave Não-Tripulada para Vigilância de Reservas Florestais". Trabalho de Graduação. Instituto Tecnológico de Aeronáutica (ITA).

Raymer, D.P., (1999), "Aircraft design: a conceptual approach", AIAA Education Series, AIAA, Washington DC.

Roskam, J., (2000-2003), "Airplane design", parts I-VIII, Dar Corporation, Lawrence, Kansas, USA.

9. Direitos autorais

CONCEPTUAL DESIGN OF AN UNMANNED AIRCRAFT VEHICLE, USED TO EXAMINE ELECTRICAL ENERGY TRANSMISSION LINES

Roberto da Mota Girardi
Instituto Tecnológico de Aeronáutica (ITA), Praça Mal. Eduardo Gomes, 50, São José dos Campos, SP
girardi@ita.br

Paulo Rizzi
Instituto Tecnológico de Aeronáutica (ITA), Praça Mal. Eduardo Gomes, 50, São José dos Campos, SP
rizzi@ita.br

Abstract. The unmanned aircraft vehicle (UAV) considered in this work has the specific mission of examining elements of an electric energy transmission line. The present work has two objectives: (i) to describe the developed methodology for the conceptual design of an aircraft, responsible to accomplish the above specified mission and (ii) to present the results obtained during the iterative procedure of a conceptual design (aircraft evolution). Such aircraft has some particular characteristics: (i) a relatively small velocity, (ii) different material and manufacturing techniques are used and (iii) the weight is very low and, therefore, the aircraft will be very sensitive to atmospheric gusts. Such characteristic increases the difficulty to accomplish the mission, that is, performing a pre-defined path along a transmission line and its elements imaging.

Key-words: Unmanned Air Vehicle, Design Methodology, Transmission lines examination

Proceedings of the 11th Brazilian Congress of Thermal Sciences and Engineering -- ENCIT 2006
Braz. Soc. of Mechanical Sciences and Engineering -- ABCM, Curitiba, Brazil,- Dec. 5-8, 2006

Paper CIT06-0546

Wing and Airfoil Optimized Design of Transport Aircraft

J Allan Antunes Lyrio
Technological Institute of Aeronautics (ITA) – São José dos Campos – SP - Brazil
j.antunes@embraer.com.br

Juliano Machado Tenório Cavalcanti
Technological Institute of Aeronautics (ITA) – São José dos Campos – SP - Brazil
Juliano.cavalcanti@embraer.com.br

Bento Silva de Mattos
Technological Institute of Aeronautics (ITA) – São José dos Campos – SP - Brazil
bmattos@ita.br

Nide G. C. R. Fico Junior
Technological Institute of Aeronautics (ITA) – São José dos Campos – SP - Brazil
nide@ita.br

Pedro Paglione
Technological Institute of Aeronautics (ITA) – São José dos Campos – SP - Brazil
paglione@ita.br

Abstract. *An efficient methodology for multi-disciplinary design and optimization of transport was elaborated and developed. The methodology was implemented in a commercial known optimization framework. Semi-empirical methods were employed for wing weight estimation; a multi-block full-potential code was used for drag calculation; Vortex Lattice method was implemented for spanwise lift distribution in order to compute de aircraft maximum-lift coefficient via critical section method; a calibrated single-point Breguet simplified equation was considered for aircraft performance calculation. The optimization design variables are related to the wing planform and airfoil geometry and cruise speed. The design constraints were the fuel tank capacity, flight quality of the aircraft, and takeoff field length. A simple stability augmentation control system was implemented in order to compute its effects on optimal configurations. Multi-objective optimization tasks were performed accomplishing minimization of the block time and block fuel for a specified mission.*

Keywords *Aircraft Design, Multi-Disciplinary Design and Optimization, Evolutionary Algorithms, Wing Design*

1. Symbols and Abbreviations

MDO	=	Multi-disciplinary design and optimization
FPWB	=	Refers to a Full-potential Wing Body code
$L_{1\text{-}LE}$	=	Distance between the first spar and the wing leading edge at the break station
$L_{23\text{-}TE}$	=	Distance between the secondary or auxiliary spar and the wing trailing edge at the break station
AR_w	=	Wing aspect ratio
λ_i	=	Inner wing taper
λ_o	=	Outer wing taper
Y_K	=	break station location coordinate along wingspan
Λ_{LEi}	=	Leading-edge sweep angle of the inner wing
Λ_{LEo}	=	Leading-edge sweep angle of the outer wing
S_w	=	Wing reference area
W_p	=	Wing position at the fuselage
V_{HT}	=	Horizontal tail volume
W_w	=	Wing weight
K_T, K_R	=	Weight estimation calibration factors
S_{ctr}	=	Wing controls surface area
n_{ult}	=	Ultimate load factor
b_w	=	Wingspan
MTOW	=	Maximum takeoff weight
MZFW	=	Maximum zero-fuel weight
MUFW	=	Maximum usable-fuel weight
λ	=	Equivalent wing taper

$(t/c)_{avg}$ = Average thickness of the wing
$(t/c)_r$ = Maximum thickness @ wing-fuselage junction
$\Lambda_{1/4}$ = Equivalent wing quarter-chord sweep
HT = Abbreviation for horizontal tail
CG = Center of gravity
MLG = Main landing gear
CFD = Computational fluid dynamics
AOA = Angle of attack
S_{HT} = Area of the horizontal empennage
Cl(y) = Section lift coefficient
$Cl_0(y)$ = Section zero-lift coefficient
$Cl_3(y)$ = Section lift coefficient @ three degrees angle of attack
$Cl_a(y)$ = Section lift slope
SAS = Stability augmentation system
DOC = Direct Operating Cost
V2 = Takeoff safety speed. Also called takeoff screen speed, the minimum speed in the second segment of a climb following an engine failure.

2. Introduction

There is a need for a software infrastructure in aircraft design that facilitates collaboration and data sharing, while providing comprehensive data management capabilities in line with modern information technologies standards[9]. The present work addresses some issues in that direction. It is concerned with optimal aircraft design. In this context, an efficient framework was built up for the conceptual design of transport aircraft. Since the early 60´s MDO has been a motivation of study for a great number of researches[1,2], However, only with the advent of high-speed computing, its true benefit could be useful to the aeronautical industry. MDO has been at the spotlight of the industry for the last 15 years but its heavy application in the aeronautical industry only started in the last five years. This can be explained by the high complexity of the aeronautical design, and the low automation at all levels of design. Since the 80´s several authors have described numerous techniques on aircraft design[4,5,6]. In 2001, Kroo[2] described several aeronautical process formulations and commented on some process integration. Askin[1], in his 2002 Ph.D. thesis, besides applying MDO for aircraft design, also describes and even intrudes some methodology for aircraft design. Versiani et all[3], in 2004, conducted some aircraft configuration optimization with genetic algorithm for a business jet considering a variant carrying a larger payload with a small range penalty. In his work, the optimization tasks were performed with aircraft fitted with trapezoidal wings only. Cavalcanti et all[11] conducted optimization tasks for complex configurations with fixed airfoil geometry. Besides the more complex wing planform layouts the present considers airfoil geometry variation along optimization. Among other features, it was taken into account feasible structural layout also able to accommodate the main landing gear. A lot of effort was put for the validation of routines to compute configuration parameters such as overall weight of the configuration or of its parts. This was needed in order to evaluate aircraft performance. ESTECO® - modeFrontier package was employed as optimization framework for the present methodology. modeFrontier is a multi-objective optimization and design environment that allow easy coupling to almost any computer aided engineering (CAE) tool.

3. Optimization framework

The MDO workflow considers three areas in the optimization process: aerodynamics, stability and control, weight and balance and performance. A module for configuration management is also part of the framework. This module generates all the necessary data required by the remained ones. The calculation of maximum capacity of the fuel tank is also performed by the geometry management module, which will be appropriately described in next section. **Figure 1** presents the MDO workflow of the present work.

3.1 Geometry management module

The module for the construction of the typical wing planform provides all the required geometric data required for calculations performed by other modules. It was implemented in Microsoft® - Excel software, and a typical wing layout generated with this tool can be seen in **Figure 2**. The structural wing layout is comprised of two main spars and an auxiliary one for the attachment of the main landing gear. Areas of control surfaces as well as that of the high-lift system are also computed in this module. The module also performs some checks concerning the feasibility of the general wing layout.

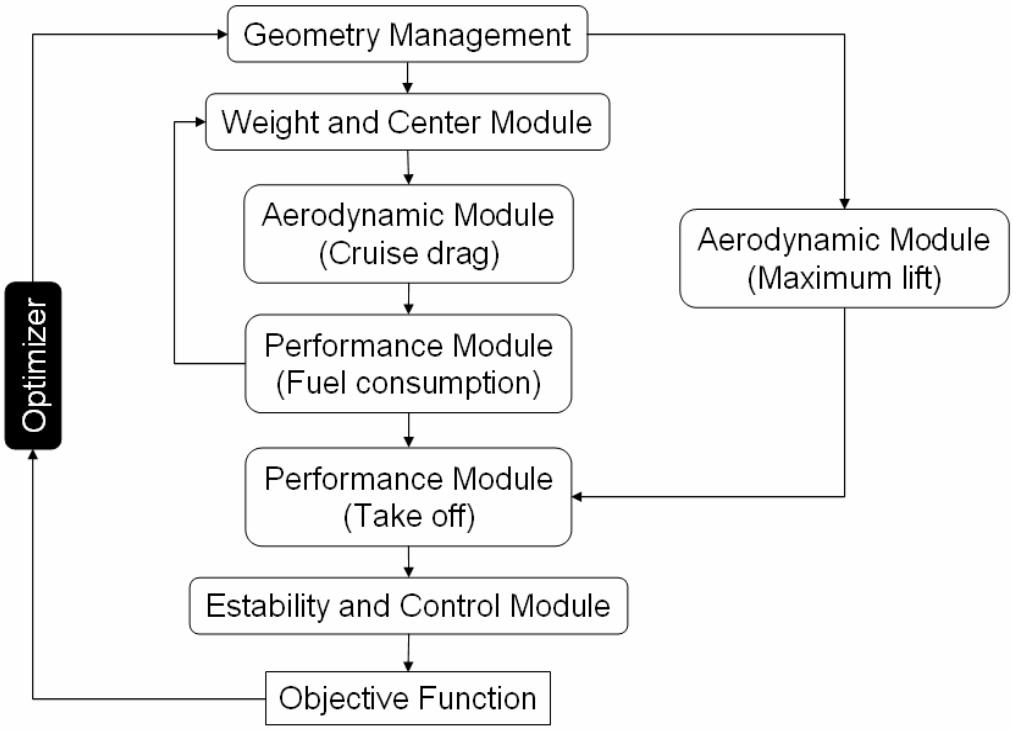

Figure 1 - MDO Workflow.

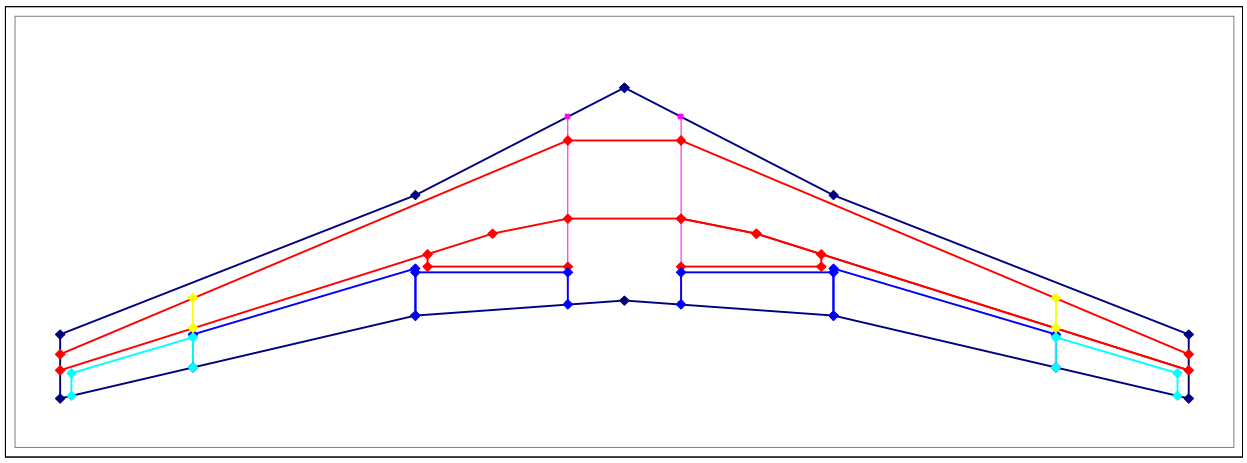

Figure 2 - Wing planform and structural layout generated by the configuration management module.

The input variables for the optimization of the wing planform are listed in **Table I** with their respective lower and upper boundaries. The variables values are allowed to change according to engineering expertise, and must be restrained in order to generate a feasible configuration. In **Figure 2**, it can be seen that the spar location must be taken as optimization variable in order to achieve a compromise among the inertia of the wingbox, volume of the fuel tank and, and areas of flaps and ailerons.

The semi-empirical method adopted in the present work does not require the spars and ribs layout for the weight estimation. For this reason, the inertia of the wingbox is not calculated. Thus, the spar layout is not considered as optimization variable and therefore it will be kept constant relative to the root and tip wing chords.

The geometry management module allows for checking the wing physical construction feasibility. This is performed by measuring the following distances at the kink spanwise station: between the front spar and the leading edge, L_{1-LE} ; form the trailing edge to the auxiliary or secondary spar, L_{23-TE} , depending on the kink station location. When these distance becomes negative, i.e, when the spars cross the leading or trailing edges of the wing, representing a non-feasible solution, the fuel tank volume is calculated as zero and the maximum fuel tank capacity constraint will penalize this experiment.

Variable	Short description	Lower boundary	Upper boundary
AR_w	Aspect ratio	6	11
λ_i	Taper ratio of inner wing	0.5	0.8
λ_o	Taper ratio of outer wing	0.1	0.5
Y_K	Location of the break station	0.3	0.4
Λ_{LE_i}	Leading-edge sweep angle of inner wing	15º	35º
Λ_{LE_o}	Leading-edge sweep angle of outer wing	15º	35º
S_w	Reference area	80 m^2	150 m^2
W_p	Wing position relative to fuselage	40 %	50 %
V_H	Volume coefficient of the horizontal tail	0.8	1.5

Table I – Geometric variables for the optimization process.

The module for the management of the aircraft configuration also calculates the so called reference – equivalent - wing. The equivalent wing is a method which attempts to transform a cranked wing into a trapezoidal one, simplifying numerous geometrical based analyses. There are several equivalent wing generation methods. Askin[1] proposed the ESDU equivalent wing method for wings with non-constant leading edge sweep. The basic principles of this method are show at **Figure 3**.

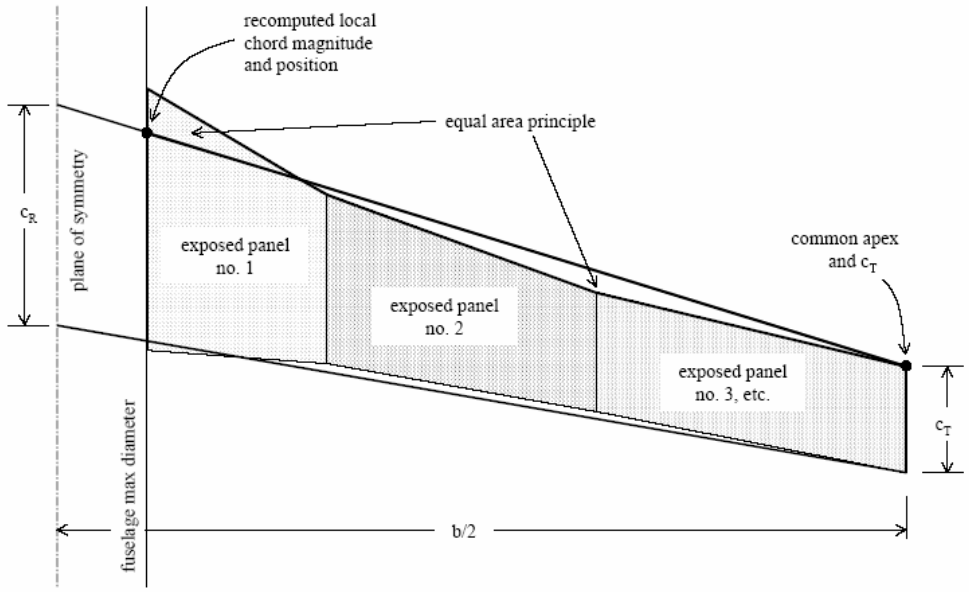

Figure 3 - ESDU definition for reference wing.

Due to CFD analisys implemented at the aerodynamic calculations, which can compute more complexes wing layout, the usefulness of equivalent wing was restricted to the weight estimation only - described in the following section.

The airfoil lofting was parameterized with polynomials[12], which provide the thickness and camber curves.

$$y_t = a_1\sqrt{x} + a_2 x + a_3 x^2 + a_4 x^3 + a_5 x^4 \tag{1}$$

$$y_c = b_1 x + b_2 x^2 + b_3 x^3 + b_4 x^4 + b_5 x^5 + b_6 x^6 \tag{2}$$

The values for the coefficients of the polynomials in **Eqs. (1)** and **(2)** are obtained from the 11 characteristics variables for three spanwise stations (root, break and tip wing locations). The parameterization method is able in providing a very concise description of supercritical airfoils. After planform and airfoils definitions, the wing surface topology is built by airfoils linear interpolations (**Figure 4).**

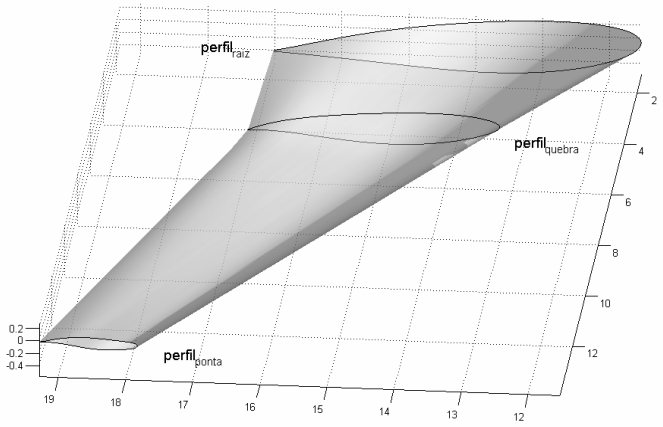

Figure 4 – Typical transport aircraft wing defined by three airfoil geometries.

3.2 Weight and Balance Module

This module performs the estimation of the wing weight and the calculation of the momentum of inertia. The wing weight estimation is based at Torenbeek[4] and Raymer[5] semi-empirical formulation described at **Eq. 1** and **2.**

$$W_{w_T} = K_T \cdot 0.0017 \cdot MZFW \cdot \left(\frac{b_w}{\cos\left(\Lambda_{1/4}\right)} \right)^{0,75} \cdot \left(1 + \left(6.3 \cdot \frac{\cos\left(\Lambda_{1/4}\right)}{b_w} \right)^{0,5} \right) \cdot \cdot n_{ult}^{\,0,55} \cdot \left(\frac{b_w \cdot S_w}{\left(t/c\right)_{avg} \cdot MZFW \cdot \cos\left(\Lambda_{1/4}\right)} \right)^{0,3} \tag{3}$$

$$W_{w_R} = K_R \cdot 0.0051 \cdot \left(MTOW \cdot n_{ult}\right)^{0.557} \cdot S_w^{\,0.649} \cdot AR_w^{\,0.5} \cdot \left(t/c\right)_r^{\,-0.4} \cdot \left(1+\lambda\right)^{0.1} \cdot \cdot \cos\left(\Lambda_{1/4}\right)^{-1} \cdot S_{ctr}^{\,0.1} \tag{4}$$

Eq. 1 and **2** are in English units, and K_T and K_R are Torenbeek and Raymer methodology calibration factors, respectively. These factors were calibrated in the present work for aircraft listed in **II**. The parameter n_{ult} is the ultimate load factor, from which was proposed by Askin a value of 3.75 for jet transport aircraft; S_{ctr} is the wing controls surface area; b_w is the span of the wing; $MZFW$ and $MTOW$ are the maximum zero-fuel and maximum take off weight, respectively; $(t/c)_{avg}$ and $(t/c)_r$ are the average airfoil thickness and the thickness of the wing section at the junction to the fuselage. $\Lambda_{1/4}$ is the symbol for the quarter-chord sweep of the reference wing; λ is the taper ratio of the reference wing.

Method	Embraer 170	Embraer 190
Raymer	1 %	-1 %
Torenbeek	-1 %	1 %

Table II – Errors of the wing weight from the method adopted in the present work.

Therefore, the wing weight calculation in the present work will be carried out according to **Eq. 3**.

$$W_W = \frac{W_{W_T} + W_{W_R}}{2} \tag{5}$$

It can be noticed from **Eq. 3** and **4** that the maximum takeoff and the maximum zero-fuel weight (MTOW and MZFW) must be known in order to estimate the wing weight. However, for MTOW calculation, the wing weight must be added to the so called fixed weight (fuselage, empennage, payload and all other aircraft parts that will be constant during optimization) and to the fuel weight. This implies that an iterative solution is in place, considering that the wing and fuel weight can not be determined until weight and performance modules finalize their calculations, respectively. **Figure 5** show schematics on how this iteration is implemented at the workflow.

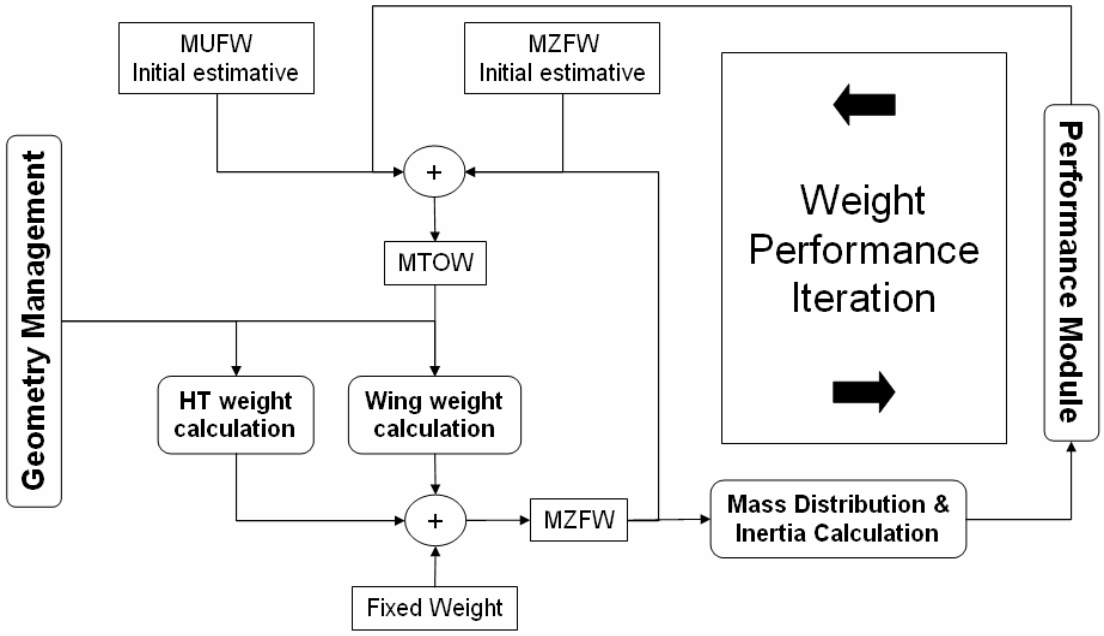

Figure 5 - MZFW and required fuel calculation.

It can be seen from **Figure 5** that the weight calculation of the HT is also needed for the MZFW prediction. However, since only horizontal tail volume will be changed, hence, only its area, no semi-empirical method will be used, and the HT weight will be considered as changing proportionally with its area. This hypothesis can be emphasized considering that no additional parameter at the HT will be changed, such as aspect ratio or sweep.

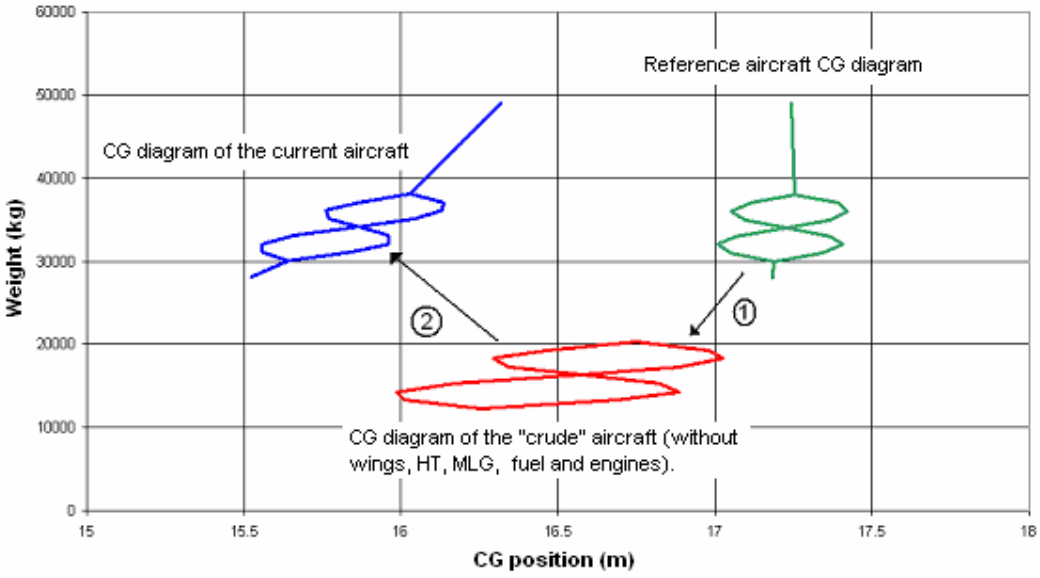

Figure 6 - CG diagram.

As can be seen from **Figure 5**, the weight and balance module also performs the mass distribution and inertia calculation of the aircraft. That is necessary for the stability and control module, which needs forward and aft CG position of the aircraft and their respective inertia. The CG position, in middle of cruise is another important calculation because it is required to calculate the aerodynamic forces acting on the wing and HT. This is performed by considering a CG diagram of a reference aircraft, then the components subjected to weight and position modification are moved out and then these new components are placed at the current aircraft with their new values of weight and position, as show in **Figure 6**.

3.3 Aerodynamic calculation at cruise

The aerodynamic modules described in **Figure 1**, performs different tasks along the optimization process. The cruise aerodynamic module computes the aircraft drag at a given lift coefficient. This lift coefficient is computed considering the medium cruise weight, calculated at the weight module. Since in the present work the block-time is considered as an objective to be minimized, the cruise Mach number is considered as an independent design variable, with upper and lower limits of 0.75 and 0.85, respectively. Considering the design variables of **Table I**, the present work takes into account 10 design variables.

In order to compute the lifting force at the wing and HT, a calculation for trimmed aircraft is performed. The drag for the wing and HT are calculated separately. The drag part due to wing is calculated by using a full-potential code with boundary layer correction for lifting surfaces. The code is only able to perform calculations for wing-body configurations. A typical multi-block mesh result can been seen in **Figure 7**. The drag from the horizontal tail is obtained using classical aerodynamic formulation for drag calculation.

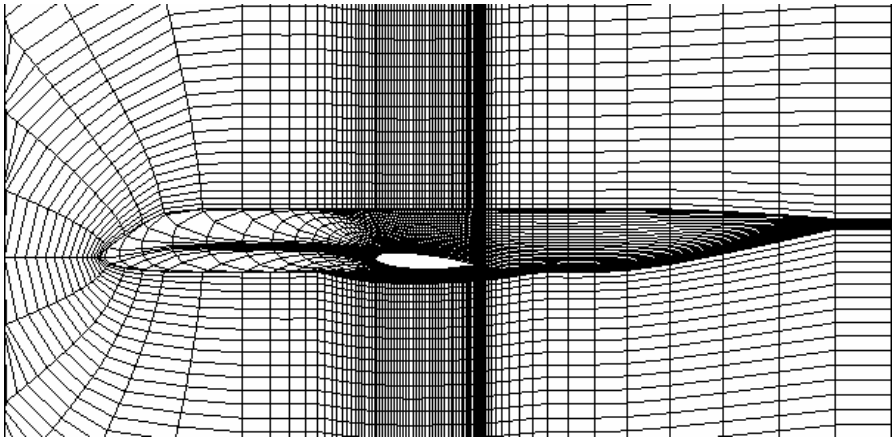

Figure 7- Cut view of a typical mesh for the full-potential code employed in the present work.

3.4 Maximum Lift Coefficient Calculation

The wing maximum lift calculations was estimated by Critical Section Method, that using a Vortex Lattice formulation for computing the spanwise lift distribution and 2-D data[13] for airfoil maximum lift coefficient. Once the maximum lift coefficient for sections is calculated, the wing maximum lift distribution can be obtained for comparison between span wise distribution and airfoils maximum lift. **Figure 8** shows a scheme for the calculation of the minimum distance between the spanwise lift distribution and the section maximum coefficient.

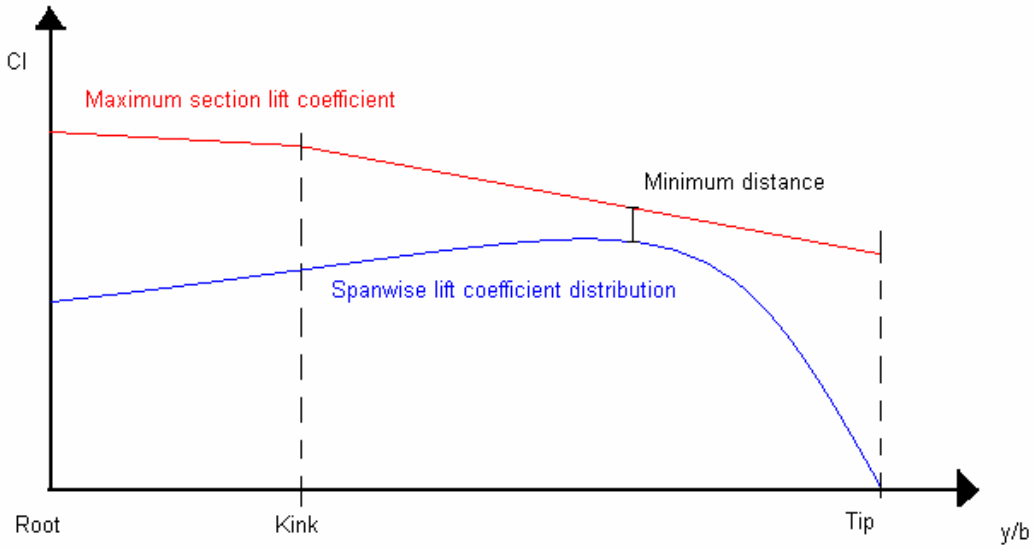

Figure 8. Critical section method for C_{Lmax} calculation.

Once the minimum distance expressed at **Figure 8** is know, a Mathworks® - MatLab script was developed, which attempts to minimize this by changing the wing AOA. So, the wing stall is considered to begin when the spanwise lift coefficient distribution intersects its respective maximum section lift coefficient. This methodology is considered a conservative one, since real wings can slightly increase its lift even if some spanwise sections are already stalled.

3.4 Stability and Control Module

The stability and control module will perform calculations in order to verify the aircraft flight quality. It will also check the controllability of the aircraft by computing the deflection of the HT at the approach flight phase. The implemented stability calculation is simplified formulation proposed by Nelson[7] and this is based on the so called dimensional derivatives. **Table III** contains a summary of the dimensional derivatives related to the longitudinal short-period dynamic mode.

$$Z_\alpha = C_{Z_\alpha}\frac{q\cdot S_w}{W} \qquad M_q = C_{m_q}\frac{\bar{c}}{2\cdot u_0}\frac{q\cdot S_w\cdot\bar{c}}{I_{yy}} \tag{6}$$

$$M_\alpha = C_{m_\alpha}\frac{q\cdot S_w\cdot\bar{c}}{I_{yy}} \qquad M_{\dot{\alpha}} = C_{m_{\dot{\alpha}}}\frac{\bar{c}}{2\cdot u_0}\frac{q\cdot S_w\cdot\bar{c}}{I_{yy}} \tag{7}$$

Table III - Longitudinal short-period dimensional derivatives.

The stability derivatives presented in **III** were calculated using the expressions presented in **Table IV** and the aerodynamics derivatives presented in **Table IV** were calculated using the full potential code when related to the wing, and the so called Vortex-Lattice, an aerodynamic code for subsonic calculation, when related to the HT.

$$C_{Z_\alpha} = -\left(C_{L_{\alpha_{wf}}} + C_{L_{\alpha_{HT}}}\frac{S_{HT}}{S_w}\left(1-d\varepsilon/d\alpha\right)\right) \tag{8}$$

$$C_{m_q} = \left(-2\cdot C_{L_{\alpha_{HT}}}\cdot\eta\cdot V_H\frac{l_{HT}}{\bar{c}}\right)\cdot 1{,}1 \tag{9}$$

$$C_{m_\alpha} = C_{L_{\alpha_{wf}}}\left(\bar{X}_{CG}-\bar{X}_{AC_{wf}}\right)+C_{L_{\alpha_{HT}}}\cdot\eta\cdot\left(1-d\varepsilon/d\alpha\right)\cdot\left(\bar{X}_{CG}-\bar{X}_{AC_{HT}}\right)\frac{S_{HT}}{S_w} \tag{10}$$

$$C_{m_{\dot{\alpha}}} = -2\cdot C_{L_{\alpha_{HT}}}\cdot\eta\cdot V_{HT}\frac{l_{HT}}{\bar{c}}\cdot\frac{d\varepsilon}{d\alpha} \tag{11}$$

Table IV - Longitudinal stability derivatives summary.

It is also necessary to compute the controls derivatives and the dimensional controls derivatives, expressed in **Tables V** and **VI**.

$$C_{Z_{\delta_e}} = -C_{L_{\alpha_{HT}}}\cdot\tau\cdot\eta\cdot S_{HT}/S_w \tag{12}$$

$$C_{m_{\delta_e}} = -C_{L_{\alpha_{HT}}}\cdot\tau\cdot\eta\cdot V_H \tag{13}$$

Table V - Control derivatives.

$$Z_{\delta_e} = C_{Z_{\delta_e}}\frac{q\cdot S_w}{W} \tag{14a}$$

$$M_{\delta_e} = C_{m_{\delta_e}}\frac{q\cdot S_w\cdot\bar{c}}{I_{yy}} \tag{14b}$$

Table VI - Control dimensional derivatives.

The parameter τ is the so called flap effectiveness parameter, and can be computed as a function of the elevator to HT ratio, as show in **Figure 9**.

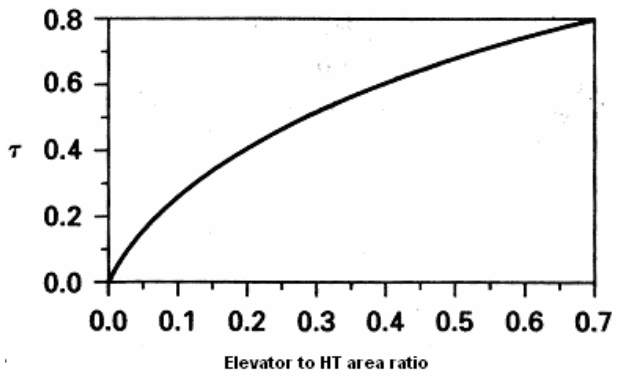

Figure 9 - Flap effectiveness parameter.

Provided all dimensional derivatives are calculated, Nelson[7] demonstrated that the state-space of the short-period system dynamics can be expressed as show in **Eq. 15**.

$$\begin{bmatrix} \dot{\alpha} \\ \dot{q} \end{bmatrix} = \underbrace{\begin{bmatrix} Z_\alpha / u & 1 \\ \left(M_\alpha + M_{\dot{\alpha}} \cdot Z_\alpha / u\right) & \left(M_q + M_{\dot{\alpha}}\right) \end{bmatrix}}_{A} \underbrace{\begin{bmatrix} \alpha \\ q \end{bmatrix}}_{X} + \underbrace{\begin{bmatrix} Z_{\delta_e} / u \\ M_{\delta_e} + M_{\dot{\alpha}} \cdot Z_{\delta_e} / u \end{bmatrix}}_{B} \cdot \left[\delta_e\right] \tag{15}$$

By obtaining the eigen values of the matrix A, it is possible to obtain the natural frequency and damping ratio of the short-period mode. Providing these two parameters are calculated, the aircraft flight quality can then be analyzed using the graph shown in **Figure 10**.

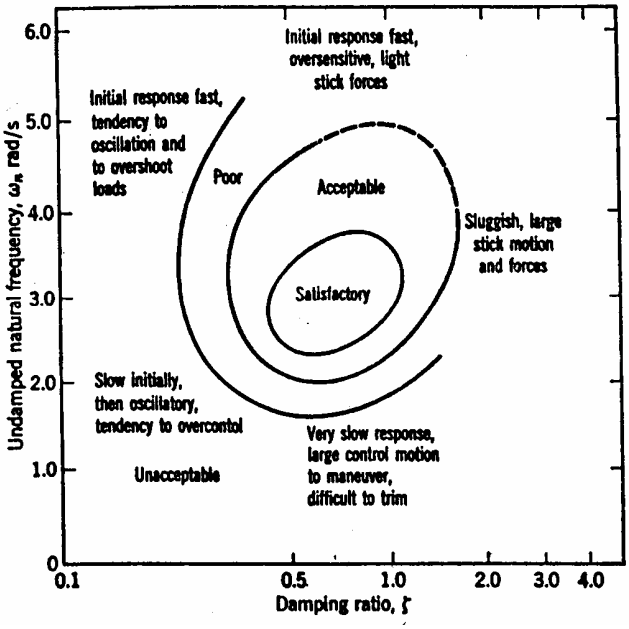

Figure 10 - flight quality diagram for the short-period behavior.

After analyzing the aircraft flight quality in the so called direct mode, i.e, without any stability augmentation system (SAS) in action, a simple SAS can be implemented to evaluation of some the benefits from its application. The implemented SAS has a simple architecture and works with the feedback of the aircraft AOA and the pitch rate, as shown in **Figure 11**.

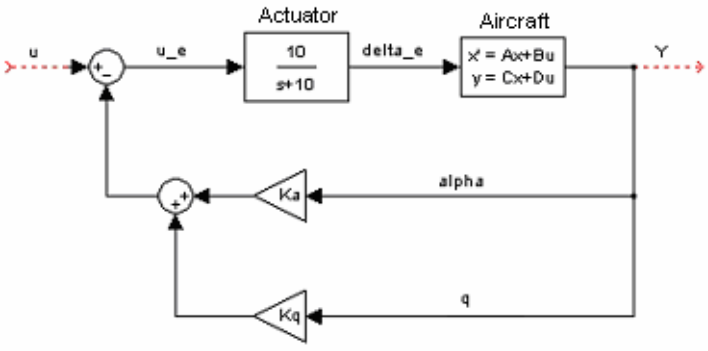

Figure 11- SAS architecture.

The SAS control logic was implemented with MatLab®, and its main task is to improve the closed loop system dynamics in order that its natural frequency and damping ratio be located in the center of the region relative to the satisfactory flight quality (**Figure 10**), by changing the values of the AOA and pitch rate gains. The desired natural frequency and damping ratio was set at the SAS to be 3 rad/s and 0.7 respectively.

The flight quality analysis were performed for two different flight phases, classified in level B and C, related to the cruise stage and the last to the approach stage, respectively.

3.5 Performance Module

The performance module uses the cruise aerodynamic module information to perform the block-fuel calculation for a mission of 2511 nm @ 37,000 ft with a payload of 6890 kg. The block-time is calculated based at the cruise Mach number, hence the climb and descent time are not being considered in the current analysis. Precisely 1600 kg fuel reserves for a 100 nm alternative and a 45 minutes holding have to be taken into account and were considered for all designs. Aircraft specific range, *SR* can be calculated as show in **Eq. 16**.

$$SR = M \cdot \frac{L}{D} \cdot \frac{1}{SFC(M)} \tag{16}$$

In **Eq. 16**, the Mach number is a design variable, the lift to drag ratio is considered at being at the mean value at the cruise flight phase, and provided by the aerodynamic module, and the *SFC(M)* is the engine specific fuel consumption. Since at the current analysis the engine is considered the same for all designs, the *SFC* will be the same. However, it is a function of the cruise Mach number and the cruise flight level. Once the cruise flight level is also considered as being constant, the engine *SFC* was predicted by a simple polynomial interpolation, as a function of the Mach number, as showed at **Eq. 16**. Once the aircraft *SR* is calculated, the block-fuel can be computed simply multiplying the *SR* by the cruise range, as seen on **Eq. 17**.

$$blkf = k_1 \cdot SR \cdot range \tag{17}$$

In **Eq. 17**, k_1 is a calibration factor which attempts to compute the take-off, climb and descent segments in the simple formulation described by **Eq. 17**.

The takeoff field length calculation is carried out according to the methodology described in reference [8], which is a variation of the *Take off Parameter* method. It is beyond the scope of this work to provide details regarding the fundaments of the ref. [8] method.

The parameters necessary for the calculation of the takeoff distance are

- Aircraft MTOW
- Aircraft maximum lift coefficient
- Wing area
- Engine settings at takeoff
- Aircraft lift and drag at V2.

4. Requirements for the optimization task

This section presents a brief summary of the optimization main requirements described at **Section 3**. The proposed optimization can not differs from any other optimization process. This indicates that three main topics must be clearly highlighted in the present work: optimization variables, objective functions, and constraints.

In order to compute de performance improvement due to optimization a generic aircraft were created in which the design variables were based on aircrafts from the same category already on the market. **Table VII** presents the chosen design planform variables and **Figure 12** shows the chosen airfoil sections for the reference aircraft, and **Table VIII** the baseline aircraft behavior according to the prescribed formulation.

Wing aspect ratio	8.5
Inner Wing taper ratio	0.65
Outer wing taper ratio	0.4
Break station location	0.35
Wing inner leading edge sweep	25º
Wing outer leading edge sweep	25º
Wing reference area	95 m^2
Cruise Mach number	0.78
Wing position (% fuselage)	45 %
HT volume coefficient	1.2

Table VII - Planform design variables for the baseline configuration.

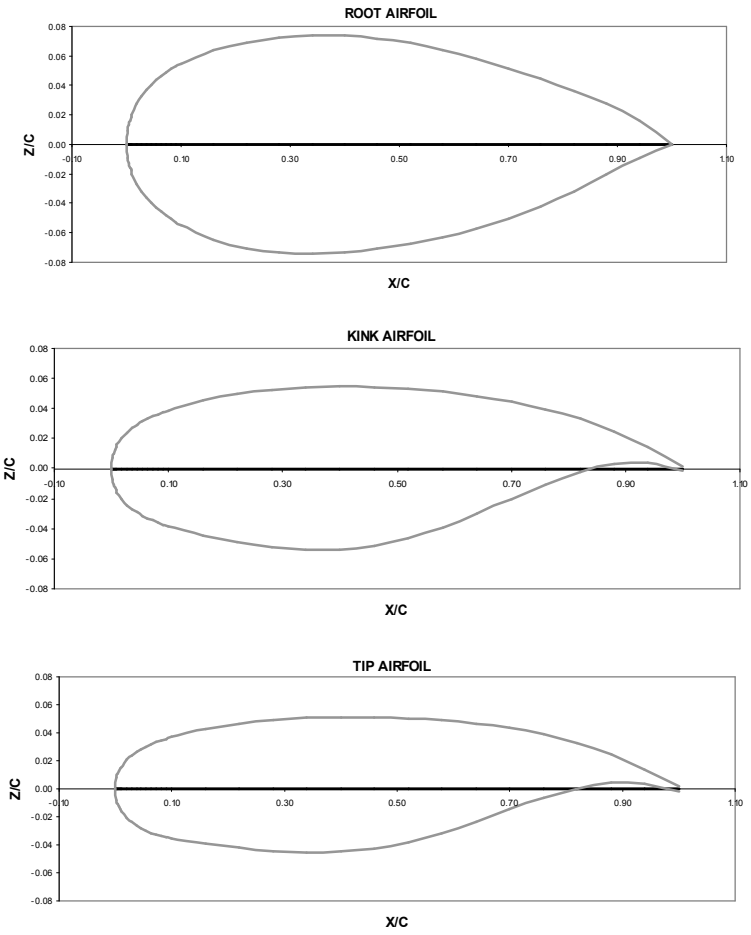

Figure 12 - Airfoil section geometries of the baseline configuration.

Block fuel			11240 kg
MTOW			47784 kg
MUFW			12905 kg
Maximum fuel tank capacity			13984 kg
TOFL			1592 m
HT deflection for trimming at approach			-6.35º
Direct mode	Flight phase B	Natural frequency	2.99 rad/s
		Damping	0.44
	Flight phase C	Natural frequency	1.93 rad/s
		Damping	0.56
SAS	Flight phase B	Natural frequency	3 rad/s
		Damping	0.7
	Flight phase C	Natural frequency	3 rad/s
		Damping:	0.7

Table VIII - Baseline aircraft behavior according to the present formulation.

From **Table VIII** it is possible to check some main performance parameters of the reference aircraft, so that in the optimization, the objective functions and constraints must be chosen in order to select a suitable aircraft relative to some parameters but keeping others at least presenting the same ones as that of the baseline configuration. **Table IX** contains a summary on the run cases objective functions and constraints.

Objective Function	Block Fuel Cruise Mach speed	
Constraints	Fuel tank capacity:	Greater than MUFW
	TOFL:	Less than 1592 m
	HT deflection for trimming at approach:	Less than -6.35º (absolute value)
	Flight quality for flight phase level B:	Greater than acceptable
	Flight quality for flight phase level C:	Greater than poor
	Flight quality with the SAS activated:	Satisfactory

Table IX - Summary on the run cases objective functions and constraints.

5. Results

This section presents the optimization the results of some simulations carried out with the described optimization framework. The workflow engine structure obtained for the all process under consideration can be seen at Figure 13.

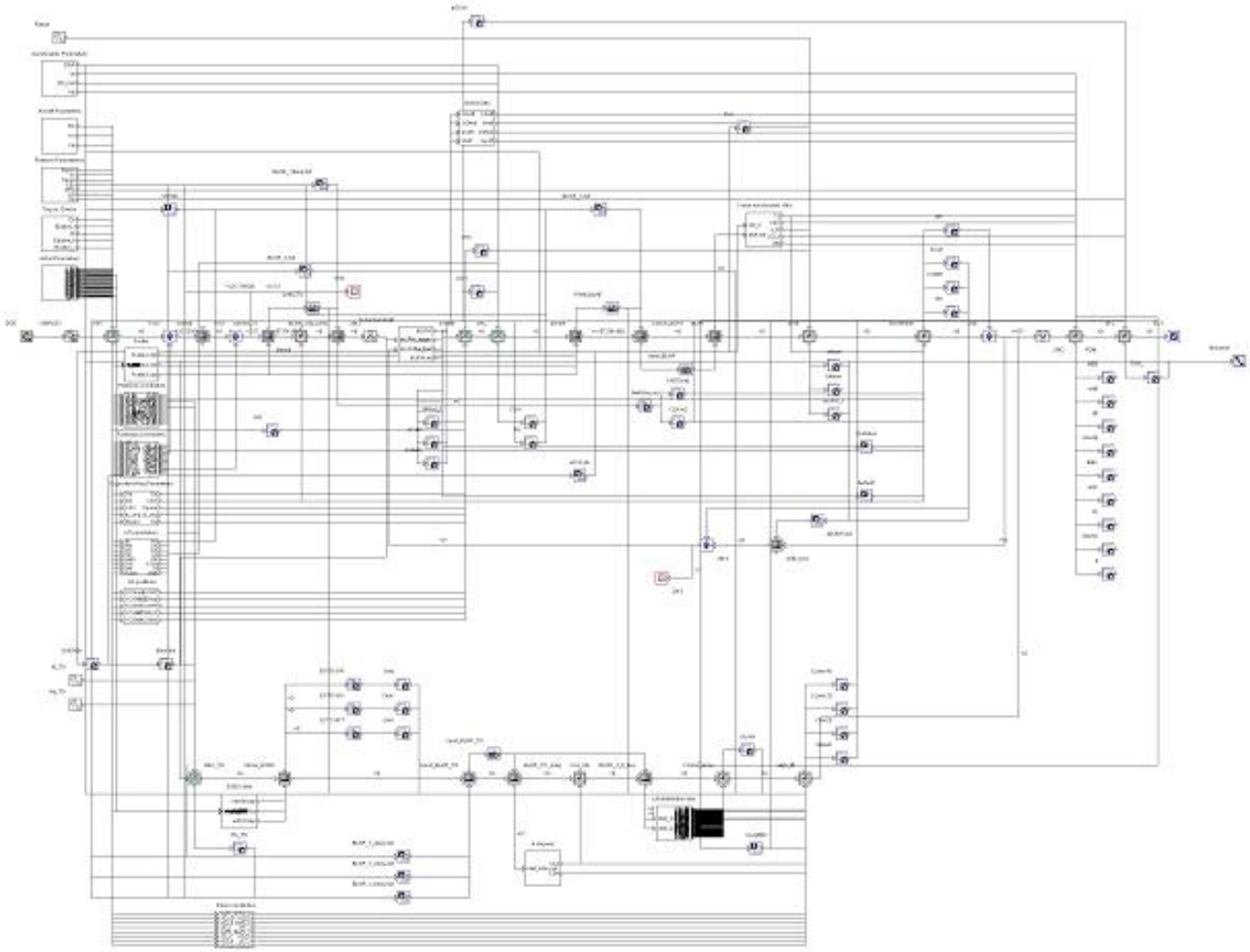

Figure 13 - Workflow engine of the present MDO methodology.

5.1 Case 1

The Test Case I is a single-objective optimization task. In this approach the objective function was composed to minimize the block fuel for a stage length with maximum payload of 2500 nm. The airfoil geometries were not allowed to change in this analysis. For this case a relaxed constrained for the flight quality was adopted. The aircraft will achieve highest flight quality level with the use of stability augmentation system. Fuel volume constraints were also in place for this test case. **Table X** provides a summary of the platform where the case was run. The simplex algorithm does not guarantee that the global maximum or minima point was achieved.

Optimization algorithm	Simplex
Design ID	268
Hardware	AMD Atlhon64 X2 4200, 2GB RAM
Computing time	17 h 59 min

Table X - Optimization performance parameters of the run case 1.

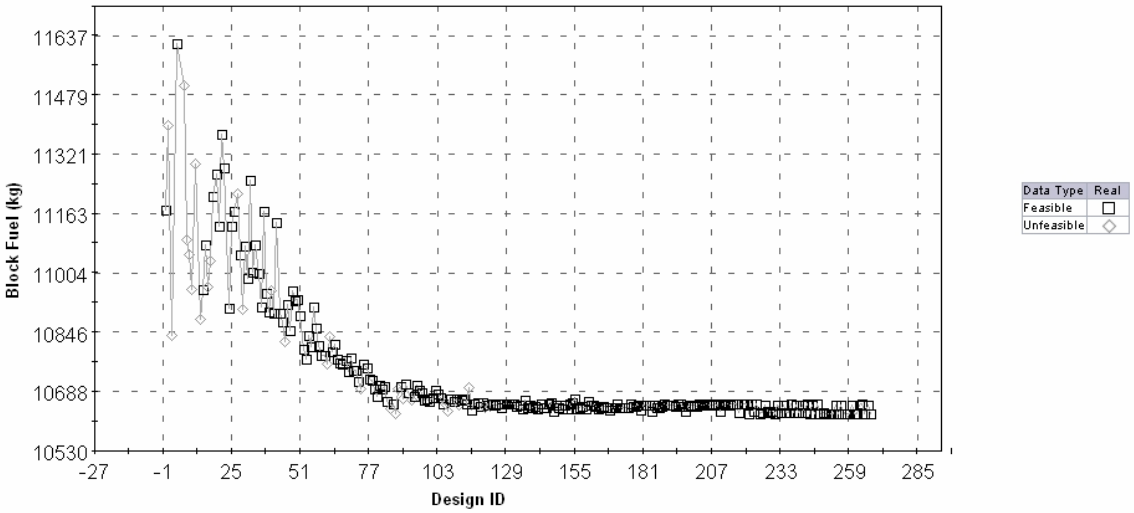

Figure 14: Block fuel history graph for Test Case I.

Leading edge sweep	24.01º
Inner wing taper ratio	0.74
Outer wing taper ratio	0.24
Break station location	31 % of the wingspan
Wing area	104.58 m^2
Wing position (referenced to fuselage length)	43 %
HT volume	1.24
Aspect ratio	10.9

Table XI - Design variables values obtained for Test Case I.

Block fuel:			10629 kg
MTOW:			48727 kg
MUFW:			12294 kg
Maximum fuel tank capacity:			12989 kg
Takeoff field length:			1380 m
HT deflection for trimming at approach:			-5.99º
Direct mode	Flight phase B	Natural frequency:	2.86 rad/s
		Damping:	0.46
	Flight phase C	Natural frequency:	1.84 rad/s
		Damping:	0.58
SAS	Flight phase B	Natural frequency a:	3.00 rad/s
		Damping:	0.7
	Flight phase C	Natural frequency:	3.00 rad/s
		Damping:	0.7

Table XII - Test Case I weights and dynamic behavior.

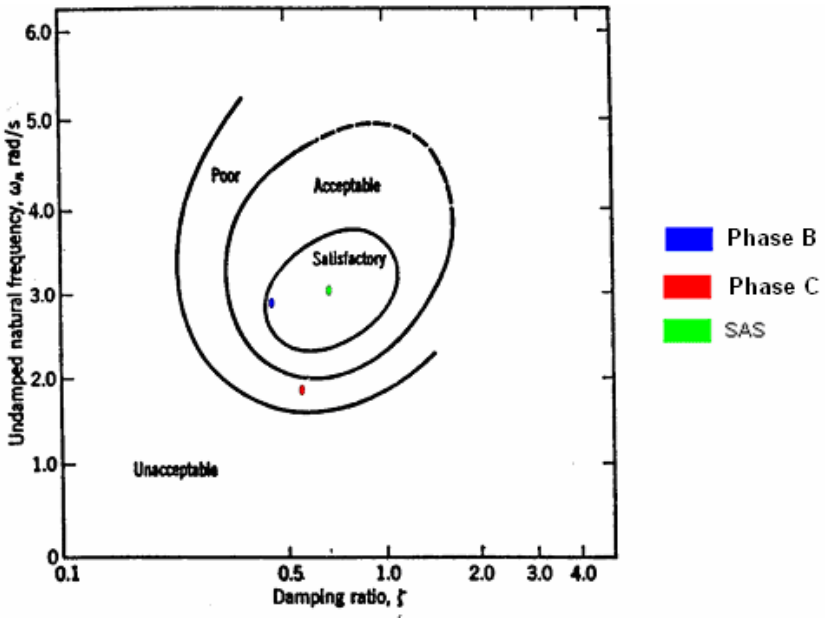

Figure 15 - Flight quality analysis for Test Case I.

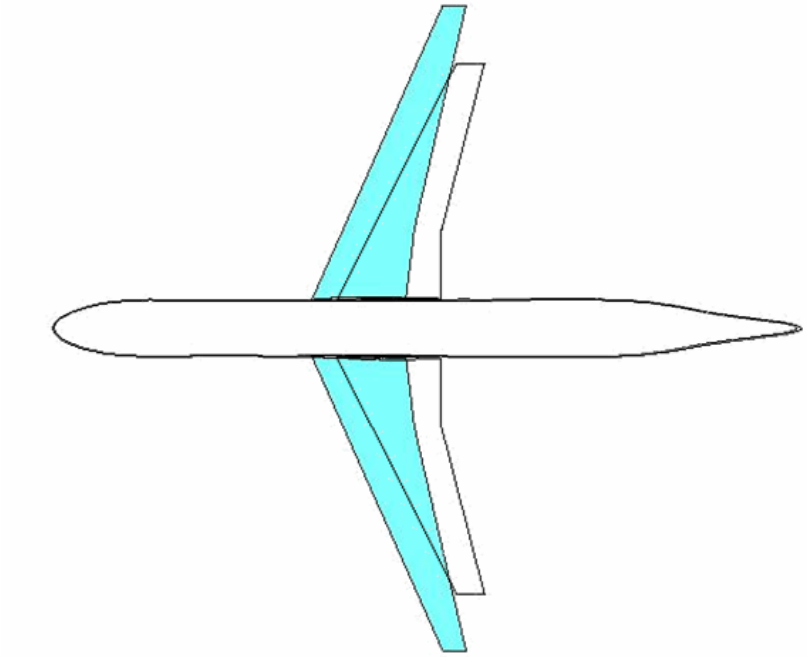

Figure 16 - Baseline aircraft compared to one obtained from Case I (filled in blue color).

5.2 Case II

For this test case II a multi-objective optimization was conducted. The objective functions are related to the block fuel necessary for a 2500-nm mission with maximum payload and the maximum lift coefficient of the configuration. The planform was not allowed to change during the simulation. All airfoils share the same trailing-edge gap. The incidence of the three basic sections – root, break, and tip stations - are optimization variables. The evolutionary algorithm MOGA was employed in the optimization task (**Tab. XIII**).

Optimization algorithm	MOGA
Design ID	2778
Hardware	Pentium 4 - 2.93 GHz - 512 MB de RAM
Computing time	365 h

Table XIII: Optimization performance parameters of the run case 2.

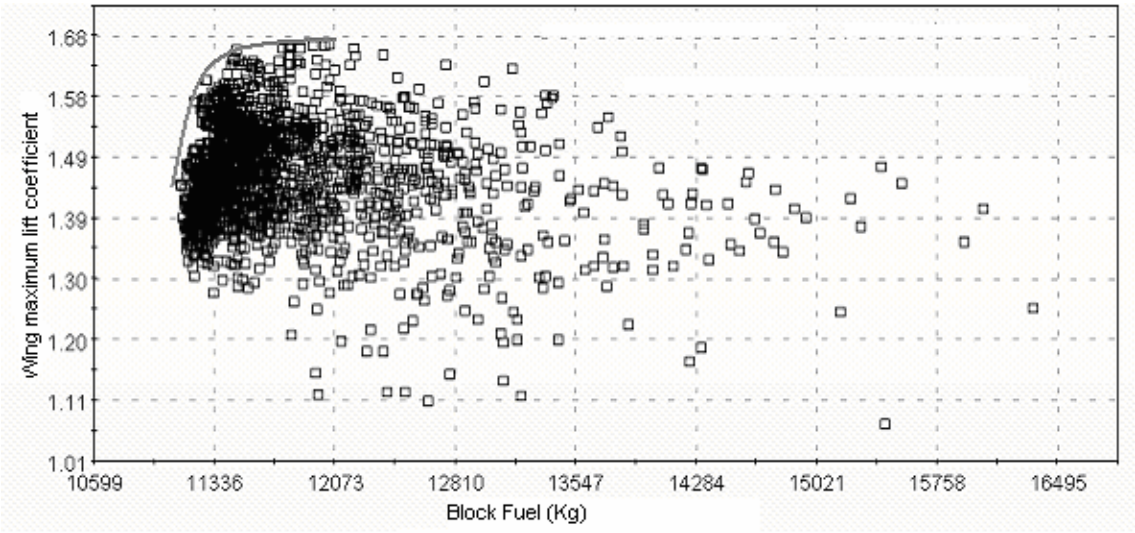

Figure 17 - Pareto Front after 18 generations.

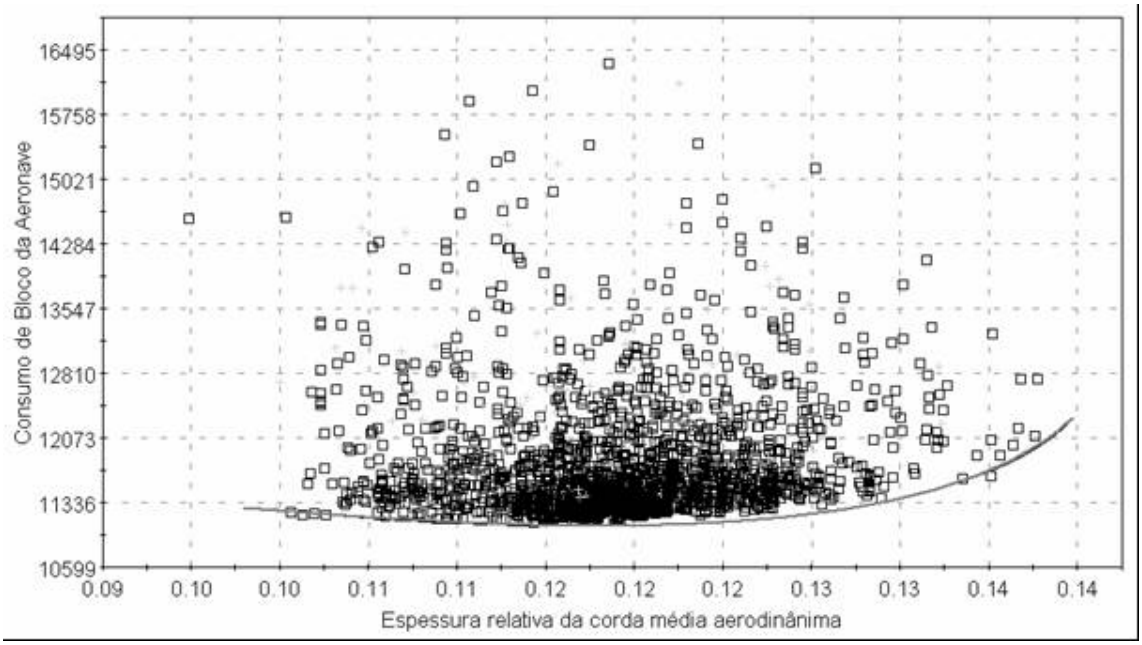

Figure 18 – Relationship between block fuel and maximum thickness of the mean aerodynamic chord.

Each population constituted of 150 individuals. The resulting Pareto Front after 18 generations for the parameters considered in the objective functions can be seen in **Fig. 17**. For the aircraft positioned in the Pareto Front the maximum lift coefficient varies from 1.45 to 1.66 and the block fuel from 11,121 to 12,038 kg. The lowest block fuel consumption occurs for the individuals in Pareto Front presenting 12% of maximum thickness for the section at the mean aerodynamic chord (**Fig. 18**). **Fig. 19** reveals a threshold value laying approximately at 11500 kg for that no increase of C_{Lmax} takes place after increasing the block fuel for the aircraft constituting the Pareto Front. The need for an increased maximum thickness of the airfoil for fuel storage and lowering the wing structural weight causes the degradation in that coefficient. For most aircraft of the Front the stall takes place at outer wing. This is highly undesirable because the loss of roll control in conditions close to stall. Aircraft presenting this kind of behavior can not be certified. In future works a routine to eliminate such configurations during the optimization task will be incorporated into the MDO workflow. **In Fig. 20** the drag divergence of two individuals (no 7 and 14) are compared. The individual presenting the higher C_{Lmax} presents a considerable lower divergence Mach number.

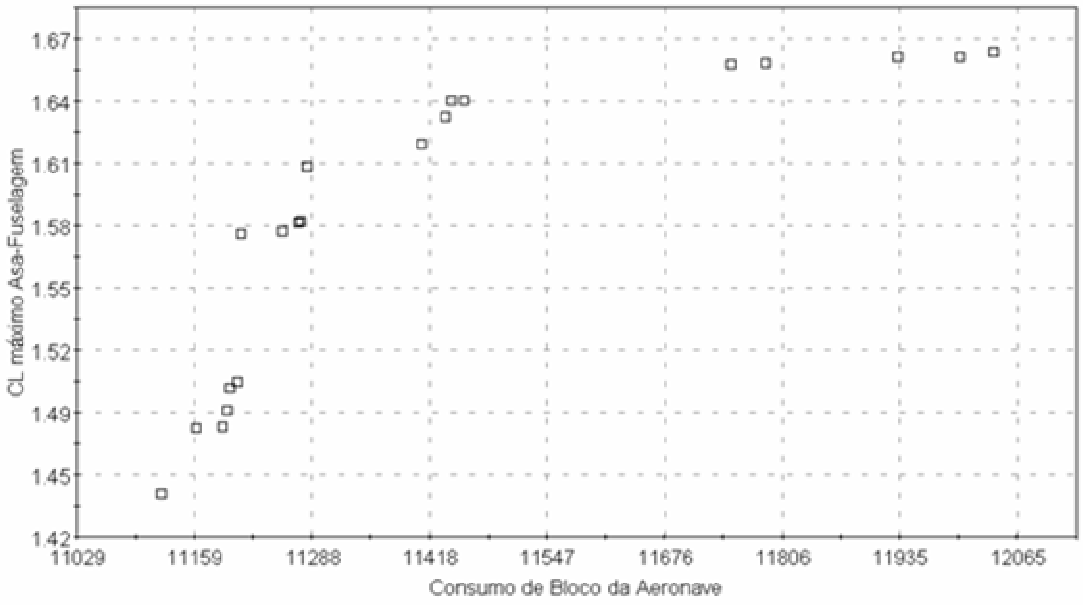

Fig. 19 – Relationship between C_{Lmax} and block fuel for the individuals belonging to Pareto Front.

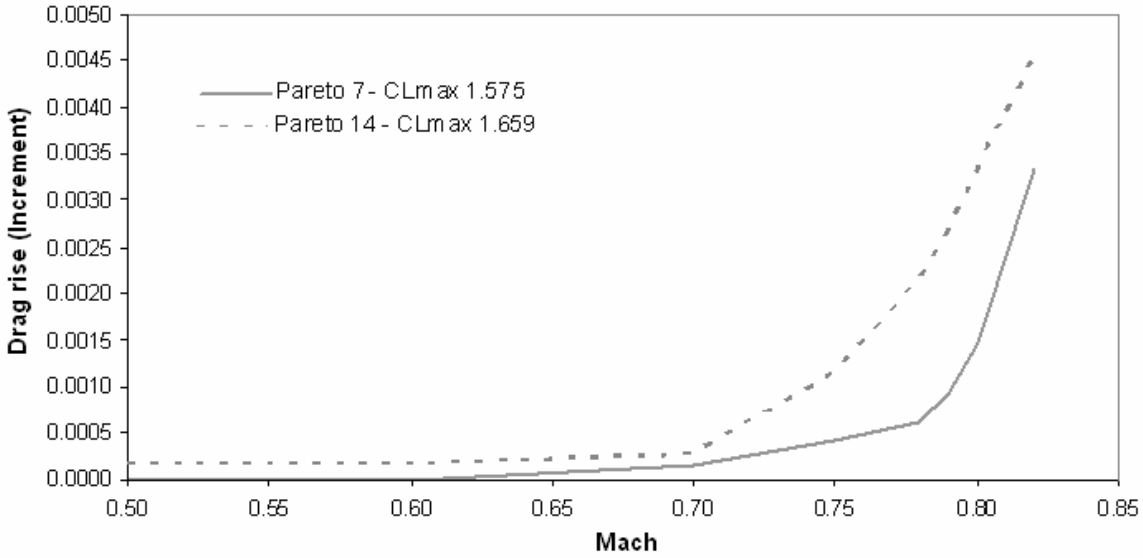

Figure 20 - Drag rise curve for two different individuals of Pareto Front.

6. Concluding Remarks

The simulation reported in the present work revealed that the optimized planform composed of fixed airfoil geometry presented an improvement of 6 % of the block fuel consumption when compared to the baseline configuration. This final configuration has an increased wing weight, which is about 20% heavier than the baseline aircraft. The simulations also indicated that the use of augmentation stability systems can improve the aircraft flight quality in such a way that the wing can be located in a forward position relative to the baseline configuration and the HT volume coefficient becomes therefore lower. This provides lower fuel consumption because the trim and friction drag are reduced for the final configuration. One highlight from the analysis of the simulation was the result concerning the variation of the wing aspect ratio. This parameter reaches the prescribed upper limit and some comments regarding this fact must be enumerated

1) The semi-empirical methods for weight prediction are based on existing aircraft of which there are not enough data for wings with aspect ratios greater than 10. Thus, such methods are not able to predict with reasonable accuracy the wing structural weight of high aspect-ratio wings. Anyway, the wing structural weight of the optimized configuration increased 1500 kg - about 20 % of that calculated for the baseline aircraft. This figure can be considered acceptable.
2) Direct Operational Cost (DOC) is of major importance when designing a transport aircraft. This parameter is composed of several factors such as crew and fuel costs and aircraft acquisition price. It is of widespread knowledge that the acquisition price of the aircraft is proportional to its weight. Therefore, a more fuel efficient aircraft with a very high MTOW might not be equivalent to the aircraft with the minimum DOC.
3) No aeroelastic analysis was performed at the present study. In order to obtain a feasible design this discipline may be part of any MDO workflow and will be taken into account in future work. Flutter and divergence pose an upper limit in the selected wing aspect ratio for a transport aircraft. Active load alleviation and other similar technologies are being employed in order to enable wings with higher aspect ratios.

The simulation for obtaining the optimal airfoil shape is very challenging because of the conflicting requirements of the two objectives, the increase in C_{Lmax} and the reduction of block fuel. Normally higher C_{Lmax} are highly desirable for enabling lower approach and landing speeds, contributing to safety operations, and reducing the wing area in order to fulfill the field performance. However, on the other hand, higher C_{Lmax} may demand more complex flap mechanisms that can lead to a more expensive aircraft and higher maintenance costs. For this reason it seems more suitable to consider the C_{Lmax} requirements as constraints rather than as an objective function.

The simulation revealed that higher incidences of the break station carry for a degradation of the C_{Lmax} of the configuration. However, the block fuel suffers some reduction when that incidence is increased. Increased camber of the tip station airfoil also provides higher C_{Lmax} figures.

The calculation of aerodynamic characteristics such as drag and lift-to-drag ratio is a major factor impacting on higher computing time for any MDO process. Thus, metamodels have to be employed in order to enable reasonable timescales for obtaining optimized configurations. Neural network techniques are the right tool in this direction[10]. Further work will reunite the planform and airfoil design into a single task.

6. Bibliography

1. Isikveren, Askin T., "Quasi-Analytical Modeling and Optimization Techniques for Transport Aircraft Design," Ph.D. Dissertation, Aeronautics Dept.,Royal Institute of Technology, Stockholm, Sweden, 2002.

2. Kroo, I. and Shevell, R., "Aircraft Design: Synthesis and Analysis," Digital Textbook, Desktop Aeronautics, Stanford, CA, 2001.

3. Versiani,, L. C., Paglione, P., and, Mattos, B. S., "Multi-Objective Design Optimization Framework for Conceptual Design of Families of Aircraft**,"** 44th AIAA Aerospace Sciences Meeting and Exhibit, Reno, Nevada, Jan, 9-12, 2006.

4. Torenbeek, E. "*Synthesis of Subsonic Airplane Design"*. S.L.: Kluwer Academic Publishers, 1982.

5. Raymer, D. P. "*Aircraft Design: A Conceptual Approach"*. S.L.: AIAA Educational Series, 2002.

6. Roskam, J. "*Airplane Design*, Part VI – Preliminary Calculation of Aerodynamic", Thrust and Power Characteristics. S.L.: DARCorporation, 2000.

7. Nelson, Robert C. "*Flight Stability and Automatic Control"*. S.L.: McGraw Hill International Editions, 1989.

8. ESDU 76011. *First Approximation to Takeoff Field Length of Multi-Engined Transport Aeroplanes*. Engineering Science Data Unit, 1999.

9. Trépanier, J.Y, Guilbault, F., Ozell, B., and Bouhemdem, D., "A Configurable Framework for Multi-disciplinary Analysis Intergration and Management," Proceedings of the International Council of Aeronautical Sciences (ICAS) 2002 Congress, Toronto, Canada, 2002.

10. Wallach, R., Mattos, B. S., and Girardi, R. M., "Aerodynamic Coefficient Prediction of Transport Aircraft Using Neural Network," 44th AIAA Aerospace Sciences Meeting and Exhibit, Reno, Nevada, Jan, 9-12, 2006.

11. Cavalcanti, J., Mattos, B. S., and Paglione, P., "Optimal Conceptual Design of Transport Aircraft," 11th AIAA Multidisciplinary Analysis and Optimization Conference, Portsmouth, Virginia, Sep, 6-8, 2006.

12. Streshinsky, J. R., Ovcharenko, V. V.. "Aerodynamic Design Transonic Wing Using CFD and Optimization Methods". ANTK "Antonov", Kiev, Ukraine, 1994.

13. ESDU 84026. Aerofoil Maximum Lift Coefficient for Mach Numbers up to 0.4. Engineering Science Data Unit, 1999.

7. Copyright notice

Proceedings of the 11th Brazilian Congress of Thermal Sciences and Engineering – ENCIT 2006
Braz. Soc. of Mechanical Sciences and Engineering – ABCM, Curitiba, Brazil, Dec. 5-8, 2006

Paper CIT06-0547

Experimental study of a T-S wave interacting with a shallow 3-D roughness element

I. B. de Paula
Universidade de São Paulo - EESC
Depto. Eng. de Materiais, Aeronáutica e Automobilística, São Carlos, Brasil
igorbra@gmail.com

W. Würz
Universität Stuttgart
Institute für Aerodynamik und Gasdynamik, Stuttgart, Germany
wuerz@iag.uni-stuttgart.de

M. T. Mendonça
Centro Técnico Aeroespacial
IAE, São José dos Campos, Brasil
marcio_tm@yahoo.com

M. A. F. Medeiros
Universidade de São Paulo - EESC
Depto. Eng. de Materiais, Aeronáutica e Automobilística, São Carlos, Brasil
marcello@sc.usp.br

Abstract. *The current paper is devoted to an experimental study of the effect of a shallow 3D roughness element on the evolution of a 2D Tollmien-Schlichting wave in a Blasius boundary layer. The experiments were carried out under controlled disturbance conditions on an airfoil section which could provide a long run with zero pressure gradient flow. A pneumatically driven slit source was used to introduce the T-S wave upstream of the lower branch of the neutral stability curve. A few wavelengths downstream, the T-S wave interacted with a cylindrical roughness element. The height of the roughness was slowly oscillating in time, which allowed a continuous measurement of the T-S wave response downstream of the roughness. The oscillation frequency was approximately 1500times lower than the frequency of the Tollmien-Schlichting wave and therefore, behaved as a steady roughness with respect to the T-S wave. Hot wire anemometry was used to measure wall normal profiles of longitudinal velocity and spanwise scans close to the maximum of the eigenfunction of the T-S wave. The oscillation of the roughness and the synchronization of all equipments permitted the use of ensemble average techniques. Two different amplitudes of T-S waves with a non dimensional frequency of F120E-06 were studied. They show a strong amplification of the disturbances in a small spanwise wave number range. The analysis of the wall normal T-S profiles suggests the growth of oblique modes.*

keywords: *Boundary layer, transition, roughness, hot-wire anemometry*

1. Introduction

Laminar to turbulent boundary layer transition caused by surface roughness elements is an important problem related to drag reduction. Since the development of the first airfoil sections with extended laminar run in the mid 40's, intensive studies, such as Tani and Hama, 1940, were performed to establish criteria for the influence of roughness elements on the boundary layer transition point. From the current viewpoint this influence can be subdivided into three categories which relate to different roughness heights: i) for very low roughness heights we have a pure receptivity problem, where the roughness elements acts as a linear transformator of disturbance of large wave length, like sound waves and freestream vorticity, into small wave length boundary layer instability waves. The boundary layer disturbances then are amplified or damped according to the stability characteristics downstream of the roughness element. ii) For medium roughness heights we have in addition to the receptivity a local mean flow distortion caused by the roughness element which leads to a receptivity process that is nonlinear with respect to the roughness height. Because of the mean flow distortion the stability characteristics downstream of the roughness are changed. iii) According with Tani and Hama, 1940 and Klebanoff *et al.*, 1954,

for high roughness elements, above a ¨ critical ¨ height, the mean flow is strongly distorted, leading to strong nonlinear effects which induces transition immediately downstream the roughness element.

In the studies performed in the 50's and 60's it was not possible to separate the different mechanism active in the problem, which typically led to a quite large scattering of data for the correlation between the local Reynolds number of transition and the roughness height. Only for the third class of problems case some degree of accuracy was obtained in the correlations which later became useful for engineering purposes. The work Tani, 1961 contains some correlations which are often used as a practical tool to help in experiment design.

Klebanoff and Tidstrom, 1972 offered a good contribution to the understanding of transition induced by two-dimensional roughness elements. They showed that the two-dimensional mean flow distortion caused by the roughness was responsible for the enhanced transition. However, for 3D roughness elements the mechanism of transition induced in the case ii) and iii) is still not well established.

Later, after Morkovin introduced the notion of receptivity Morkovin, 1968, many investigations on the roughness effect in transition concentrated in the pure receptivity problem. This increased with the development of the secondary instability theory by Craik, 1971 and Herbert, 1988, because the receptivity induced by 3D roughness elements was a good seed of oblique waves. A significant amount of the work concerning the pure receptivity study was done on the generation of instability waves by acoustic wave interacting with a three-dimensional surface roughness. Choudhari and Kerschen, 1990 obtained one of the firsts theoretical results on this problem. In that work they performed a comparison with the results of previous experiments performed by Tadjfar and Bodonyi, 1992. A good qualitative agreement with the theory. Later, quantitative agreement was found the work of Würz *et al.*, 2003. In Würz *et al.*, 2003 the roughness element was slowly oscillated. In the present work this approach was also adopted, but the roughness element used here was of a different shape and height. As one can observe, the receptivity scenario was quite well researched in recent years. However, most of this results were obtained for very shallow roughness elements. Therefore, the mean flow distortion caused by the roughness did not have a strong effect on the receptivity.

The case ii) with medium 3-D roughness height was studied by Sedney, 1973 and Tobak and Peake, 1982. Those works provided a good picture of the mean flow structure that can be generated by a 3-D roughness element immersed in the boundary layer. Later, the works of *et.al* Gaster *et al.*, 1994 and Legendre and Werlé, 2001 made this picture even clearer by using of hot-wire measurements and flow visualizations. The study of the transition induced by 3-D roughness elements was also studied by Klebanoff *et al.*, 1992. Despite the quality of the experimental results and the amount of data collected , it was not possible to reach definitive conclusions.

The generation and evolution of instability waves by the interaction of sound or T-S waves with a medium sized roughness element was numerically published by Rist and Jäger, 2004. The roughness element analysed in that work was gaussian in shape. For one single amplitude of the incoming T-S wave, they found that close to the wall there is a pattern of three-dimensional modes which they considered to be dependent of the vortices generated by the roughness. Further from the wall the evolution of the 3D pattern was similar to a propagating wave.

In general, most of the studies performed so far dealt with 2-D and 3-D T-S waves which entered in the boundary layer due to the roughness element. For practical applications, the case where a T-S wave already exists in the boundary layer and interacts with a roughness element is also important. Apparently, this case has not yet been systematically studied. The aim of the present investigation is to shed some light on the physical mechanism that lead to transition in this scenario.

2. Experimental Procedure

The experiments were carried out in the Laminar Wind Tunnel (LWT) Wortmann and Althaus, 1964 of the University of Stuttgart. The wind tunnel is of the open return type. The rectangular test section has a cross section area of 0.73 X 2.73m^2. In the range of 20-5000Hz the free stream turbulence level is lower than $0.02\%U_\infty$ for a speed of 30ms^{-1}.

The experiments were performed on an airfoil model. The XIS40MOD airfoil section was the same as that used in the controlled receptivity experiments, Würz *et al.*, 2003. This profile was chosen because by carefully adjusting the angle of attack it could provide a long stretch of zero pressure gradient boundary layer in a region of negligible surface curvature. This reduced the number of parameters involved and simplified the problem. A scheme of the experimental set-up used in the current experiment is shown in figure 1.

The controlled disturbances that produced the TS waves were introduced into the flow by a slit source Würz *et al.*, 2004, flush mounted to the airfoil surface. The velocity fluctuations used to generate TS waves were provided by 32 loudspeakers connected to the slit by plastic tubes. Care was taken that the end of the tubes flush to the wall were equally spaced. A total of 116 tubes were used to cover a spanwise range of 300mm at the airfoil surface.

The retractable roughness was mounted downstream of the TS source. The position of this element and of the TS slit source were chosen based in a detailed analysis of many parameters. The parameters considered in

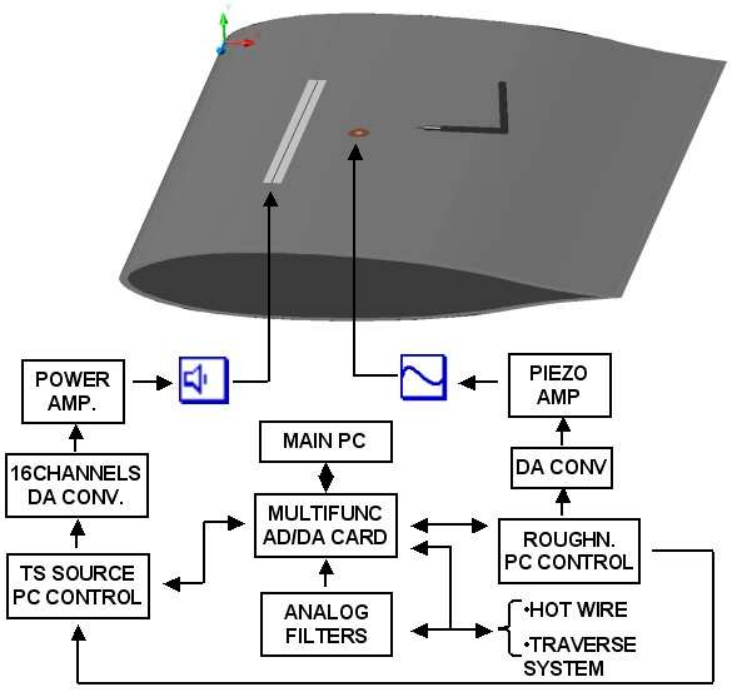

Figure 1: Experimental set-up

this analysis were the extension of zero pressure gradient region on the airfoil, the Re_{δ^*}, the non-dimensional unstable frequencies that could be observed within this range, the power of the T-S generator and a minimum distance to ensure a well developed T-S wave downstream of the source. Several configurations were evaluated in order to optimize the experiment. Eventually, the positions were fixed at 40% of the chord length for the roughness and 25% for the T-S generator. This corresponds to a distance of aproximatelly nine T-S wave lengths between the slit source and roughness, which is shown as region I in figure2, and eleven wave lengths for the region of zero pressure gradient downstream of the roughness, that is the region II in figure 2.

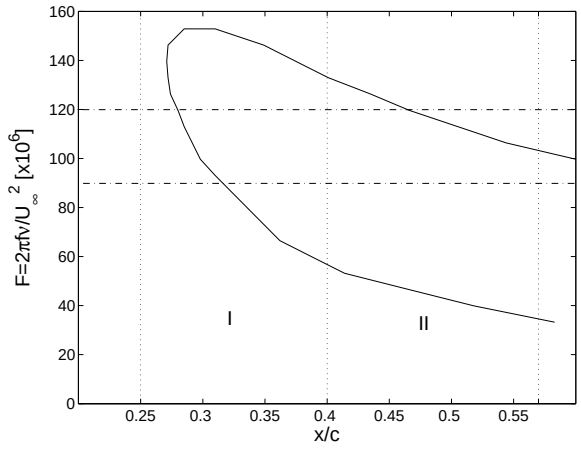

Figure 2: Stability diagram for two-dimensional TS-waves on the airfoil section with Reynolds number based on the chord length equals to 9.4E05. The wave slit source position was 20% of the chord length (C) and the roughness was positioned at 40% of C. The non-dimensional frequency used was 120E-06.

The roughness element used was of a cylindrical shape with 10mm of diameter. It was placed on airfoil at the spanwise center line at a streamwise position equal to 40% of the chord. The height of the roughness element was measured by using a Micro-Epsilon optoNCDT 1605-0,5 which is an optoelectronic micrometer device. This micrometer has a static resolution of $0.1\mu m$ and can be used with frequencies up to 10kHz.The

roughness height was controled by a piezo actuator, driven by an analog voltage input. A calibration curve of the roughness height against the voltage input is shown in the figure 3. In the figure, the standard deviation of the calibration is given as error bars. The figure also indicates the maximum roughness height used in the experiment and the height relative to the boundary layer displacement thickness (δ^*) at the roughness position. During the experiments the roughness height was slowly oscillated with a frequency approximately 1500 times lower than the T-S waves. Therefore, it could be considered as a quasi-steady roughness. The calibration curve shown in figure 3 was performed with the roughness working in this quasi-steady mode.

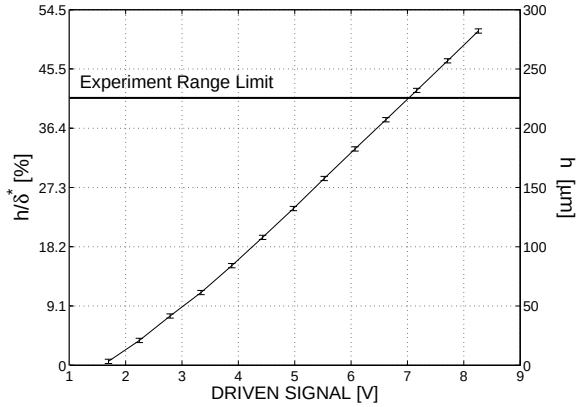

Figure 3: Roughness calibration

In figure 1 shows that all equipments worked connected to each other. This was necessary for the synchronization of the experiment. This enabled the acquisition to be triggered always at the same phase for both TS wave and the roughness element. Each equipment status along a number of acquisition cycles is shown in figure 4. The upper plot in this figure is refers to the relays status. When the status is equal to one, it means that the system was ready to start a new acquisition cycle. The second and third plots from top to bottom shows the status of the T-S generator and data acquisition system. Finally, the plot at the bottom of figure 4 shows the roughness position along the cycle. The 0 value corresponds to the lowest position and 1 to the highest one.

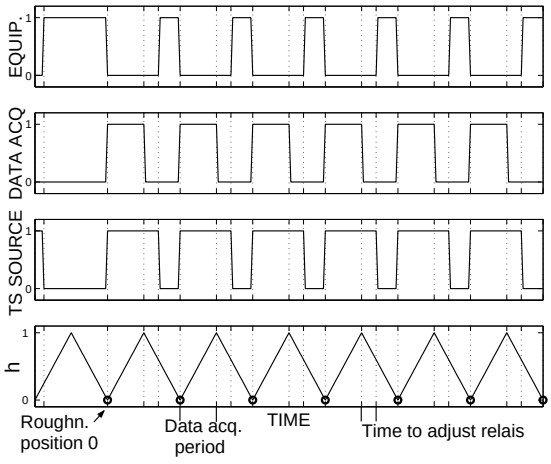

Figure 4: Scheme of equipments synchronization

This set-up enable the adjustment of the roughness initial position. Therefore it was possible to optimize the time interval of the cycle during which the data was acquired. This was important because of the time necessary for the T-S wave to reach the hot-wire probe. This transient period was also recordered because both the T-S source and the acquisition system were triggered at the same time. Hence, the first collected data points were discarded due this starting period transient.

3. Qualification of the experimental set-up

Prior to the main experiments, measurements were performed in order to adjust the airfoil angle of attack in a way to obtain a long stretch of zero pressure gradient boundary layer on the model surface. The velocity distribution was calculated from the readings of 26 pressure taps. The hot-wire traversing system was kept in place to take into account its influence on the circulation of the airfoil. From boundary layer measurements in the studied region the Falkner-Scan parameter ($\Lambda = (dU/dx)\left(\theta^2/\nu\right)$) was calculated. A close to Blasius flow was obtained with an angle of attack of -3.2^0. As can be seen in figure 5 a long zero gradient pressure region was obtained with this condition. The solid line shown in the figure corresponds to the velocity distribution predicted by simulations with the computer program Xfoil. Nevertheless, the pressure distribution was very flat, the Falkner-Scan parameter showed a comparatively larger variation inside the experimental domains. A number of measured wall normal profiles are given in figure 6. Both figures 4 and 5 indicate that a Blasius boundary layer was obtained inside of the measurement region.

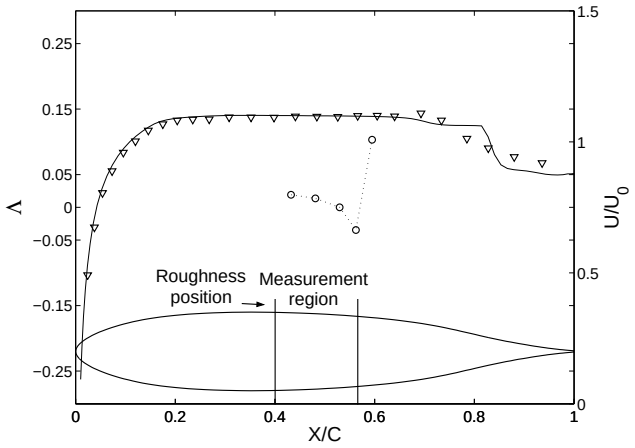

Figure 5: Velocity distribution - ∇ - and Falkner-Scan parameter (Λ) - o -

The next step was to verify the two-dimensionality of the Tollmien-Schlichting waves generated. It was important to ensure that any tri-dimensionality could arise only from the roughness. A fairly good 2D T-S wave could be produced by adjusting the power of each loudspeaker. The process adjustment was interactive. For this purpose several spanwise scans had to be performed before an appropriate level of two-dimensionality could be achieved. The resultant wave measured upstream of the roughness is shown in figure 7.

Equally important was to verify that the T-S waves generated conformed with the linear stability theory. Figure 8 shows a comparison of the experiment with theory. The data presented in this figure was obtained at 40% of the airfoil chord with the roughness element retracted. Figures 7 and 8 show that the T-S wave was virtually 2D at the roughness position. Figure 8 lends further support to the assumption of a Blasius boundary

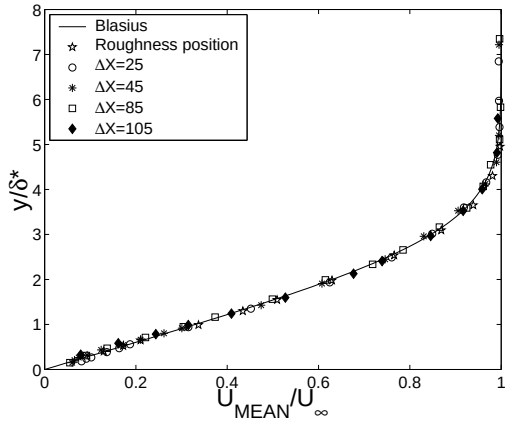

Figure 6: Measured velocity profiles in the experimental chordlength range

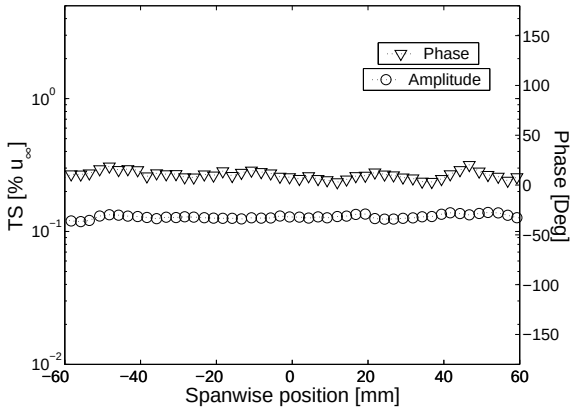

Figure 7: Characteristic of the Tollmien-Schlichting wave across the span upstream of the roughness T-S 2-dimensionality upstream of the roughness

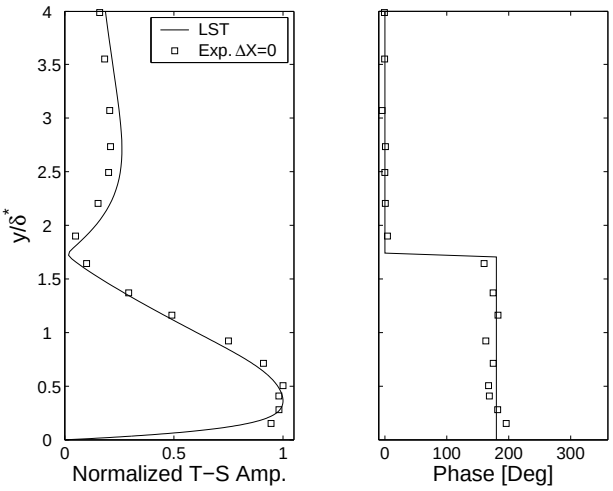

Figure 8: T-S profile and phase at the roughness position

layer.

4. Experimental results

4.1. Preliminary considerations

In this section the results of experiments on the boundary layer response to a 2D T-S wave passing over a shallow cylindrical element are presented. The measurements were done for a T-S non dimensional frequency (F=$2\pi f\nu/{U_\infty}^2$) of 120E-06. Two T-S waves with RMS amplitudes of $A_0 = 0.75\%$ and A_0 =0.45% of U_∞ at the roughness position were tested.

The equipments worked in a synchronized mode as shown in figure 4 and the roughness oscillation was quasi-steady in comparison with the T-S wave. Therefore, the effect of the roughness at a particular height could be measured by windowing the continuous time series. This continuous time series from the hot-wire signal were acquired during half of the roughness oscillation cycle. To improve the signal to noise ratio, 10 ensembles were averaged. This reduced the noise related to the variation of the roughness oscillation from cycle to cycle.

The size of the window was chosen to cover roughly a roughness variation of 5μm or 1% of the displacement thickness. The standard deviation of the hot-wire signal was associated with both the background noise and the variation of the roughness height within the windows. Larger windows increased the RMS associated with the roughness height variation and reduced that due to undeterministic background noise. The 1% window size reduced the combined standard deviation to minimum. The size of the window was further adjusted to ensure a power of 2 number of samples. This improved the efficiency of the signal processing.

The to be presented in section 4.3 were also used to estimate the experimental uncertainty. The standard

deviation (STD) was evaluated separately for each ensembled averaged data window. This was done because the T-S response to variations in the roughness height was not the same for all heights. The T-S sensitivity to the roughness height became stronger as the roughness amplitude was increased. The error of the ensembled averaged signal for each window was evaluated by the standard deviation.

$$STD = \left[\sum_{1}^{n} \sqrt{(u'(i) - u'_{ref}(i))^2} \right] \frac{1}{n}, \tag{1}$$

where n is the number of samples inside of each window, u' is the velocity fluctuation and u'_{ref} is the amplitude of the wave at the T-S driving frequency.

The error calculated for a T-S wave amplitude of $0.75\%U_\infty$ at the roughness position ($A_0 = 0.75\%$) is shown in figure 9. The error was normalized for each roughness height. They were calculated relative to the local maximum of the T-S amplitude accross the span. The error was also evaluated for the case with an $A_{TS} - 2D_{\Delta X=0}$ of $0.45\%U_\infty$ and the results are shown in figure 10. As expected, for both amplitudes the maximum error values were obtained at the last measurement station. The maximum STD achieved a level close to 10% of T-S amplitude at the center line of the airfoil section. Another pattern observed was that the maxima were concentrated at the lower and higher roughness heights. It was conjectured that the maximum at the lower end was due to the roughness position error. The positioning uncertainty was almost constant in the displacement range of the experiment. Therefore, the relative error in the positioning was higher for small roughness heights. It was conjectured that at the other end the high standard deviation was due to a strong sensitivity of the wave to the roughness height. The consequent scattering in the frequency domain could be also another source of error, because there were more energy outside T-S modes in these cases.

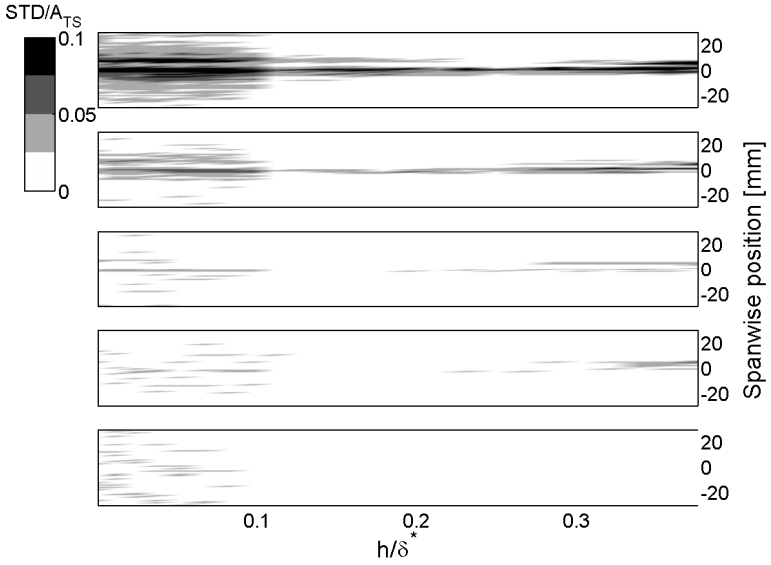

Figure 9: Standard deviation inside of each window. ΔX from bottom to top = 25, 45, 65, 85 and 105mm. A_0 $=0.75\%u_\infty$.

4.2. Measurements along the center line

The effect of the roughness on the wall-normal mean flow profiles are shown in figures 11. The measurements were carried out along the center line downstream of the roughness at different streamwise positions. According to these figures, for roughness heights of 20% of the displacement thickness and above the mean flow profiles shows a larger deviations from the Blasius one. These deviations become more evident further downstream. At $105mm$ downstream of the roughness the profile measured for $h/\delta^* = 0.3$ show a significant distortion.

The T-S wave wall-normall profiles at different streamwise stations are presented in figures 12. The profiles for the smooth surface case, presented at the bottom of figure 12, show a typical T-S wave distribution of amplitude and phase. For $h/\delta^* = 0.11$, the profiles showed a double peak structure. This structure becomes more evident further downstream. However, for this roughness height the phase distribution is not strongly affected by the roughness. In the two upper plots of figure 12 where h/δ^* is equal to 0.3 and 0.2 respectively, the

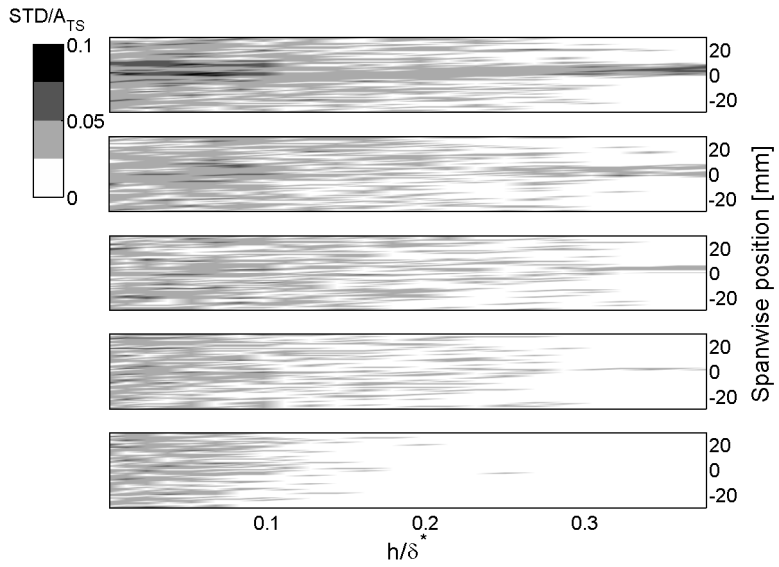

Figure 10: Standard deviation inside of each window. ΔX from bottom to top = 25, 45, 65, 85 and 105mm. A_0=0.45%u_∞.

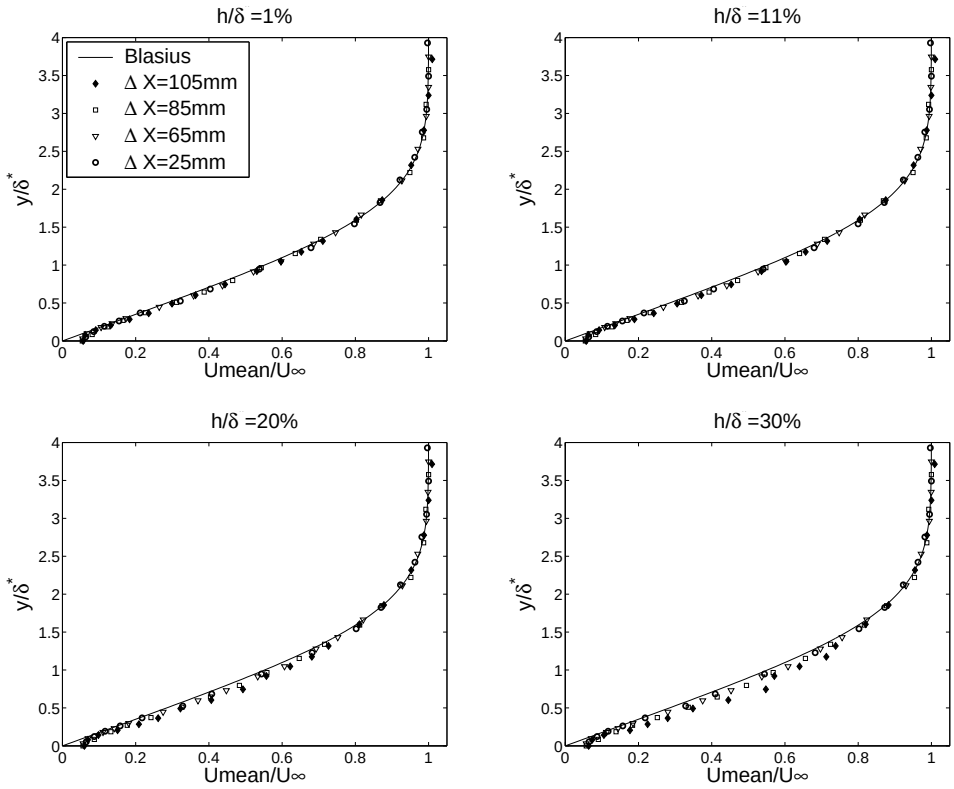

Figure 11: Mean flow profiles at different streamwise positions along the center line. A_0 =0.75% U_∞.

peak further from the wall becomes more proeminent as the T-S develops downstream. Also for this roughness heights the phase distribution was affected in the whole measurement domain. In summary, the figures show that with increasing roughness height, both amplitude and phase distribution of the T-S wave become very different from that of a 2D T-S wave.

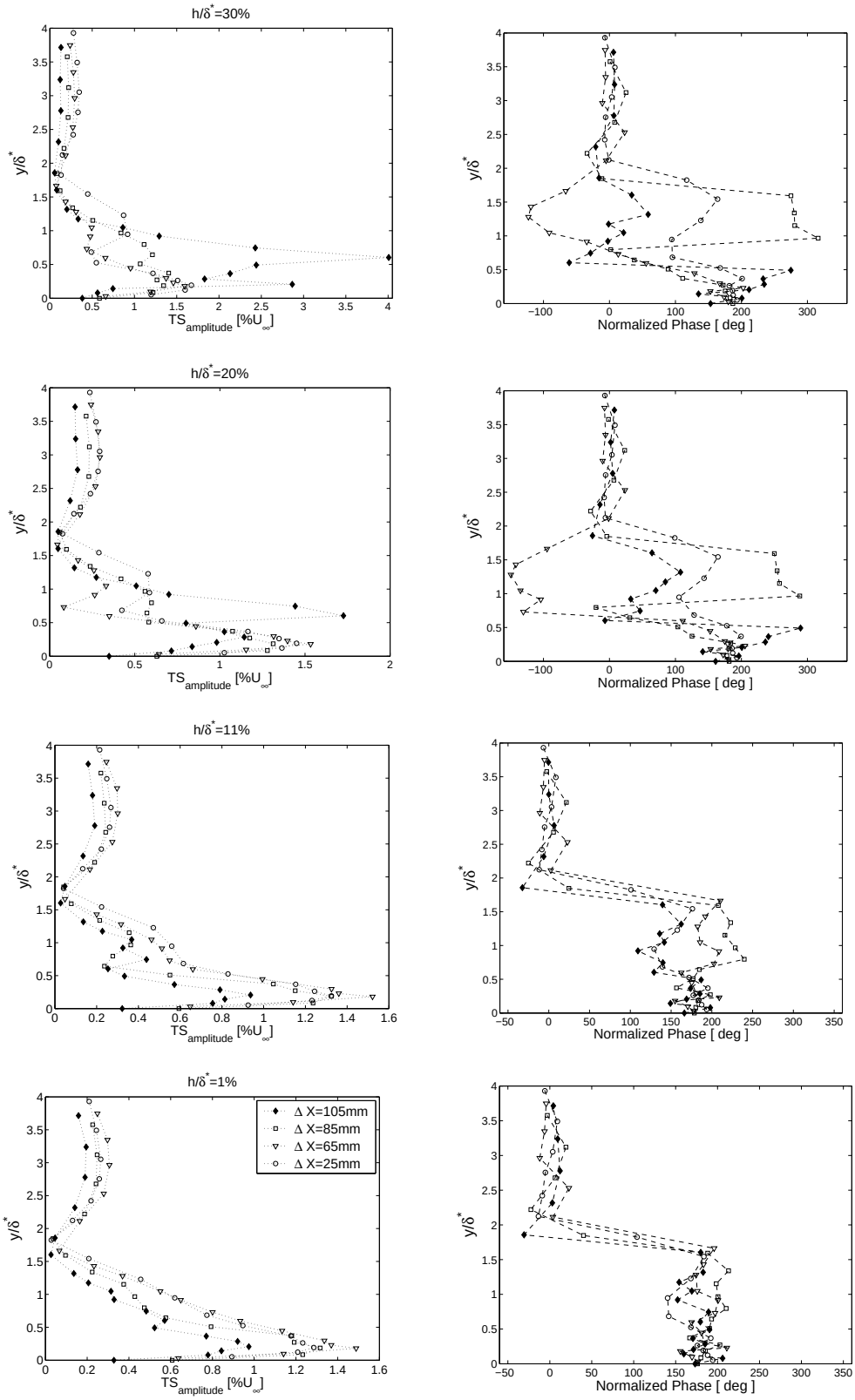

Figure 12: T-S amplitude and phase along the center line at different streamwise positions. $A_0 = 0.75\%\ U_\infty$.

4.3. Measurements out of the center line

The evolution of the T-S waves interacting with the roughness element was also measured out of the center line. These measurements were taken only at one particular non dimensional wall-normal position. The position

was close to the peak further from the wall (figure 12) namely y/δ^* equals to 0.75. In the experiments this wall normal position was obtained based on measurements of the velocity profile. By assuming a Blasius boundary layer and measuring the longitudinal velocity inside the boundary layer the selected wall-normal position could be found very accurately and kept constant during the spanwise traverses.

The amplitude and phase of the T-S waves with non dimensional frequency ($F = 120E-06$) are shown in figures 13 and 15. Results corresponding to four different roughness heights with two different initial T-S amplitudes (0.75% and 0.45% of U_∞) are given.

Figure 13 shows the results for a T-S wave amplitude of $0.75\%U_\infty$ at the roughness position ($A_0 = 0.75\%$). As the flow develops downstream a three-dimensional pattern arises. This pattern moves upstream to the roughness as the roughness height increases. For instance, the T-S amplitude and phase distribution at $\Delta X = 105mm$ for $h/\delta^* = 0.1$ resembles those at $\Delta X = 85mm$ and $\Delta X = 65mm$ for $h/\delta^* = 0.2$ and $h/\delta^* = 0.3$ respectively. Figure 13 also shows in the plots with h/δ^* equal 0.2 and 0.3 that the phase distribution was strongly affected. This influence was stronger at the last measurement station ($\Delta X = 105mm$). It is seen that for all roughness heights a significant change of the 3D pattern observed close to the roughness from the pattern observed further downstream. This behavior suggests a selection of disturbances as the wave propagates downstream.

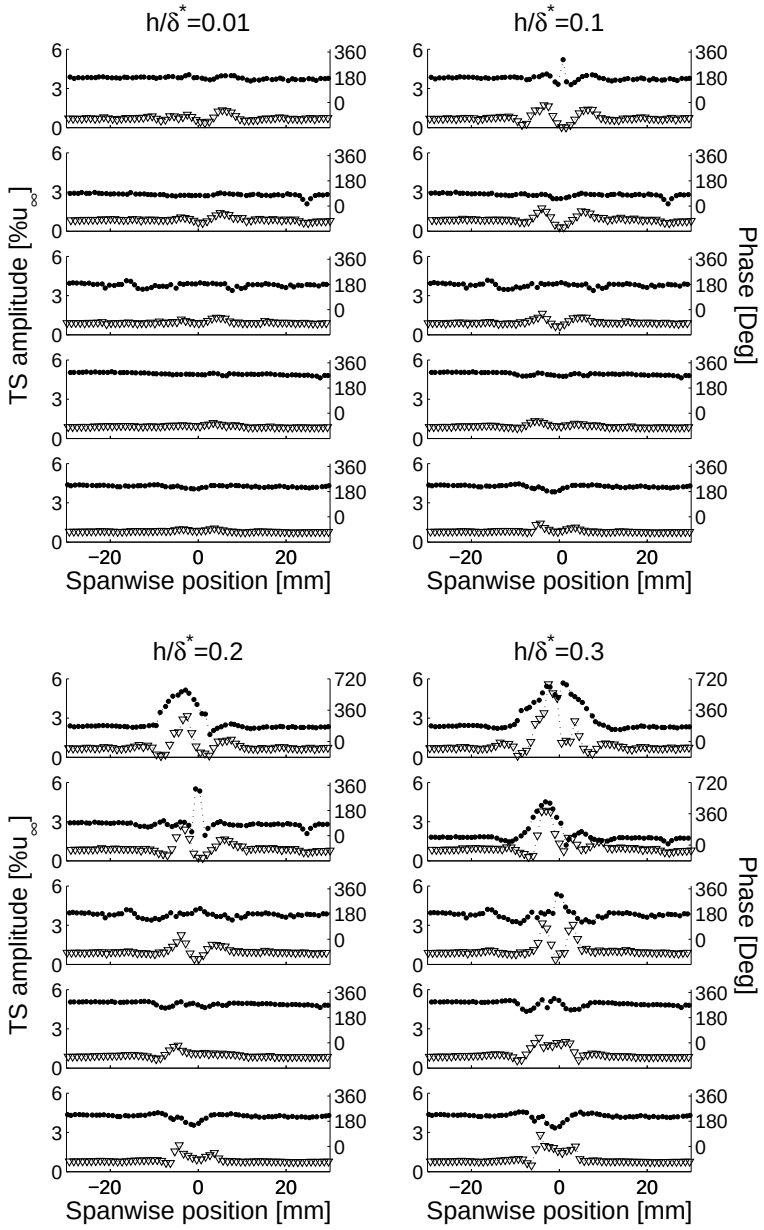

Figure 13: T-S amplitude - ∇ - and phase - $\bullet$ - distribution. ΔX from bottom to top = 25, 45, 65, 85 and 105mm. A_0=$0.75\%U_\infty$. Note the variation in the phase scale for the 2 highest roughness cases.

The downstream development of the phase of the velocity fluctuations along the center line was extracted for different roughness heights and the results are displayed in figure 14. For small roughness heights the phase development is not affected and the measured phases follow the theoretical prediction. The calculated theoretical T-S wave speed was $0.35U_\infty$. As the roughness height increases the phases increasingly deviate from the values predicted by theory. For $h/\delta^* = 0.3$ the measured development of phases indicated that the waves propagated with a wave speed lower than the speed of the non-disturbed case. The figures 13 and 14 show that when roughness was higher than $0.2\delta^*$ the influence of the roughness on the boundary layer transition was not restricted only to a pure receptivity.

The experimental results obtained with the T-S wave amplitude equal to $0.45\%U_\infty$ at the roughness position are presented in figure 15. The pattern observed for $h/\delta^* = 0.3$ is of a different nature from those of figure 13. In contrast to the high amplitude case, here the pattern is decaying downstream.

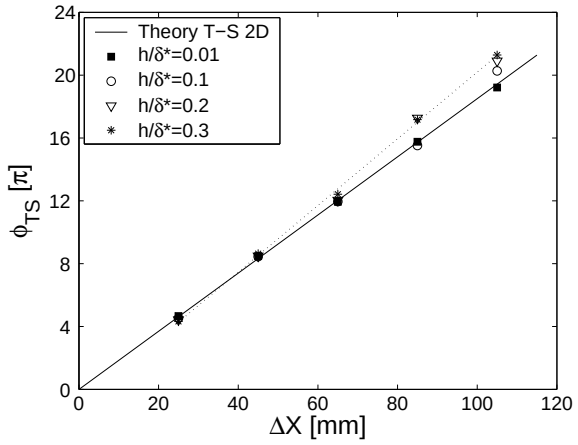

Figure 14: Downstream development of phases along the centerline for different roughness heights. Wall normal position $y/\delta^* = 0.75$. A_0 =$0.75\%U_\infty$.

In order to provide additional information on the T-S wave evolution, a spectral analysis of the spanwise T-S distribution was performed for the case of A_0 equals to 0.75% U_∞. Figure 16 present the Fourier decomposition of the spanwise T-S distribution of figure 13. A strong growth of 3-D modes occurs in a narrow bandwidth of spanwise wavenumbers.

From figure 16 is is apparent that for relatively small roughness heights (0.01 to $0.2\delta^*$) the selected modes, in general, do not depend on the roughness height. The spanwise wave number (β) of the most amplified 3D mode was around 0.1, as indicated by markers in figure 16. These results tends to suggest that a secondary instability is being responsible for the amplifications of these 3D modes. This hypothesis was further supported by the fact that a 3D structure did not arise for low T-S wave amplitudes, figure 15. It is well known from the secondary instability theory that exists a threshold in the amplitude of the T-S waves from which a self sustainable fundamental resonance arises, namely the secondary instability of the K-type. This is consistent with the experimental observation.

An additional result that reinforces the idea of a K-type instability is shown in figure 17. This figure presents a comparison between the measured wall-normal T-S profiles and combination of two T-S wave theoretical profiles. The profile was measured at the centerline of the last measurement station. The theoretical wall-normal profiles were calculated by linear stability theory. The eigenfunction of a two-dimensional T-S wave and the eigenfunction of a three-dimensional one with β equal to 0.1 were chosen to compose the theoretical profile used in the comparison. For each roughness height the amplitude and the phase of the eigenfunctions were defined according with the experiments. At the center line, where the measurements were performed, the 3-D structure had a valley. Thus, the phase of these two eigenfunctions should be shifted by 180^o from one another. The amplitude of each eigenfunction was obtained by matching their amplitude with the double peak structure of the measured profile. The peak closer to the wall was more closely related with the amplitude of the 2D profile while the peak further from the wall was related with the amplitude of the 3D eigenfunction. A single 2D T-S wave eigenfunction was also included in figure 17. This shows clearly how the measured wave profiles deviate from the corresponding 2D ones.

Figure 17 shows a good agreement between theory and experiments, in particular for lower roughness heights. Despite the differences in roughness shape, roughness height and T-S wave amplitudes a qualitative agreement was found between the measured wall-normal profiles and those obtained by Wörner, 2003. A more detailed

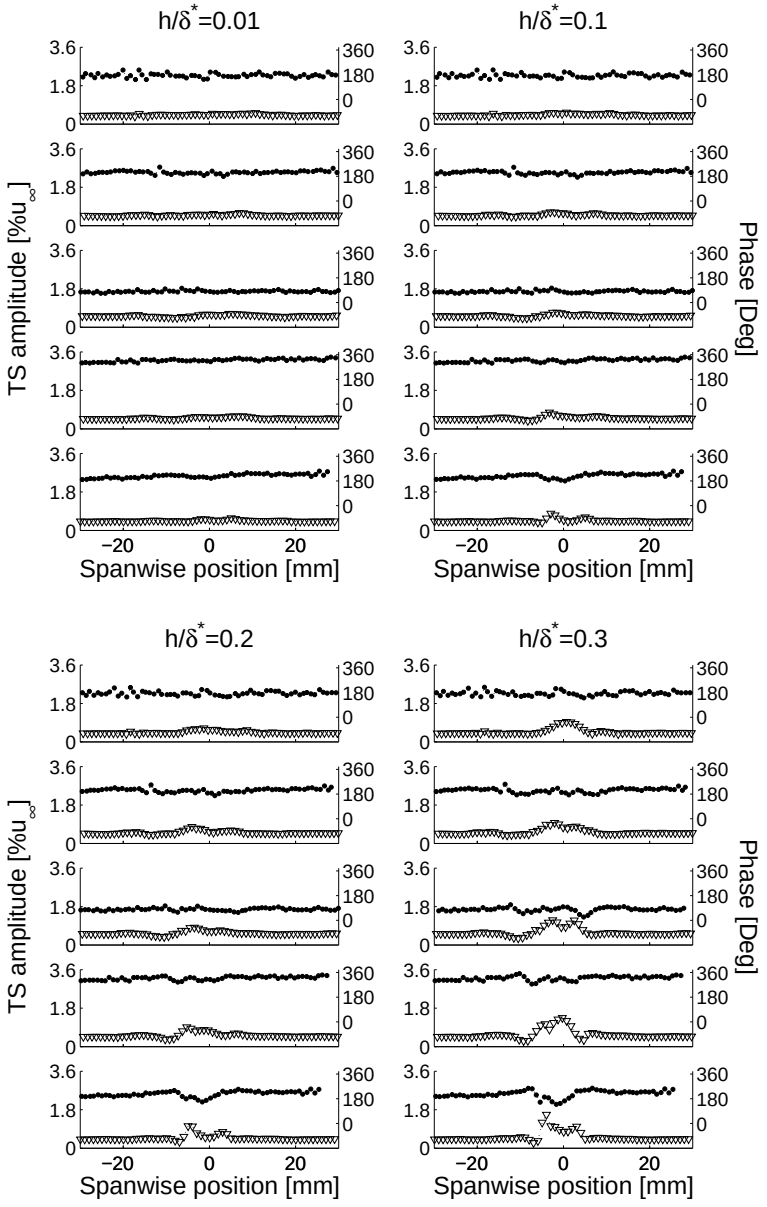

Figure 15: T-S amplitude - ∇ - and phase - $\bullet$ - distribution. ΔX from bottom to top = 25, 45, 65, 85 and 105mm. $A_0 = 0.45\%U_\infty$

comparison with that work could not be performed because Wörner presented the analysis for only one roughness height. The influence of the roughness height on the profile could be not be compared.

For the highest roughness height the agreement of the wall-normal profiles was worse than that for the small roughness. One possible reason for this might be that a significant amount of energy outside was found outside of the oblique mode ($\beta = 0.1$). In this case the 3-D structure may not be well represented by a simple oblique mode, figure 16. Another contribution to the deviation might come from the mean flow distortion. In figure 17, top frame, the theoretical peak is further from the wall than the experimental one. This might be explained by the following argument: the roughness induces a pair of steady counter rotating vortices, called horse-shoe vortex, which produce downwash right behind the roughness. This downwash would push the inner peak closer to the wall.

5. Final Remarks

The results presented concern with an experimental study of the effect of a 3D shallow roughness element on the evolution of 2D T-S waves. In the current experiments the height of the roughness was slowly oscillated. This allowed that the oscillating roughness could be treated as a quasi disturbance. Therefore data on the

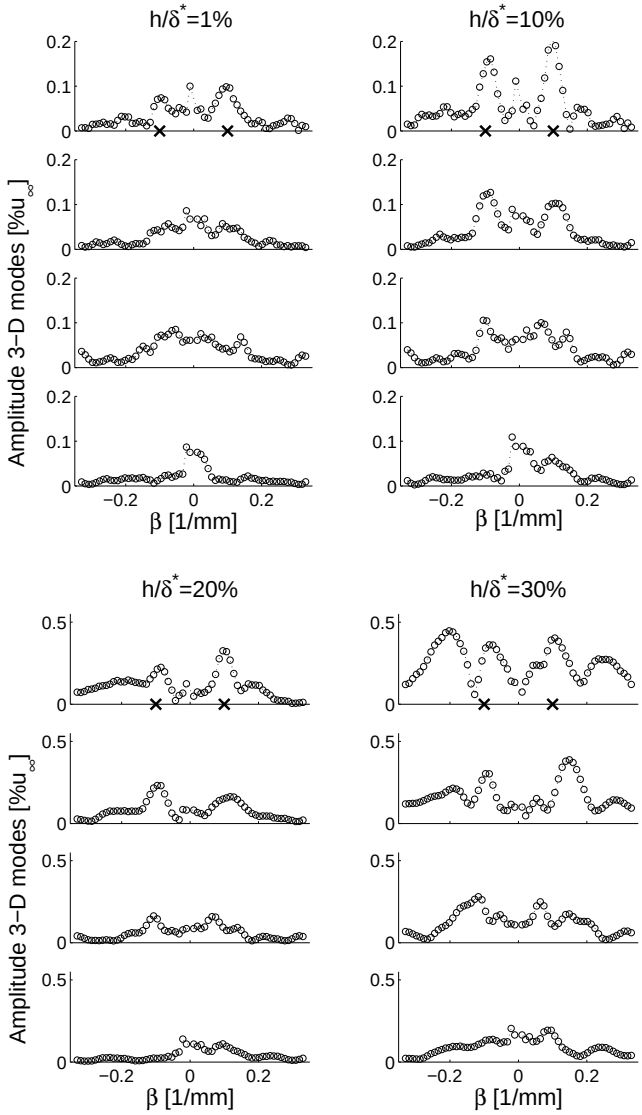

Figure 16: Disturbances evolution downstream the roughness. ΔX from bottom to top are 45, 65, 85 and 105mm. A_0=0.75%U_∞.

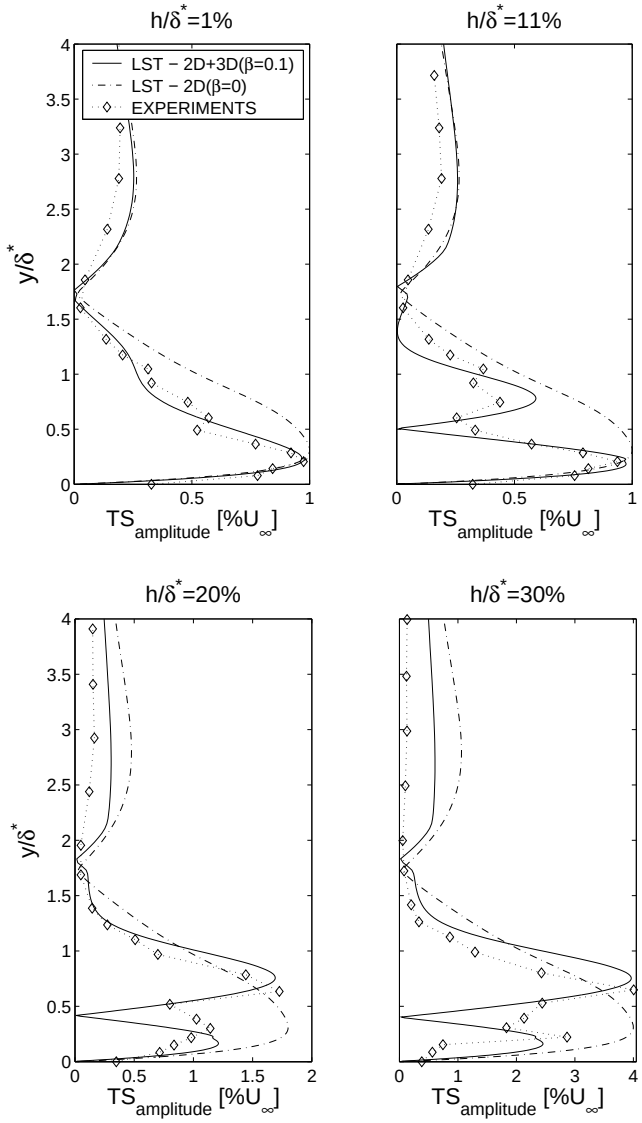

Figure 17: Wall normal T-S amplitude and phase along the center line at different streamwise positions. $A_0 = 0.75\%$ of U_∞.

phenomena could be taken for roughness heights varying from 0 to 0.3 of δ^* in a continuous way. In the paper some roughness heights were chosen for presentation. The generation of a 3D structure of a peak and valley type on the nominally 2D T-S wave was observed. The results showed that the effect of the roughness depend on the amplitude of the T-S wave. It was found that for small T-S wave the 3D structure decayed as the waves propagate downstream. For high amplitudes of the incoming two dimensional T-S wave the growth of waves in a narrow bandwidth of the spanwise spectrum was seen. In the experimental range the most amplified 3D modes did not change significantly with different roughness heights.

A comparison of wall-normal T-S wave profiles with theoretical ones was then performed. The theoretical profiles were obtained by a combination of a 3D and a 2D eigenfunction. The spanwise wave number of 3D eigenfunction chosen to compose the theoretical profile was the most amplified one according with the Fourier decomposition of the measured spanwise T-S distribution. The agreement was satisfactory.

It was conjectured that the effect of the roughness on the T-S evolution was the generation of a deterministic seed for a K-type secondary instability of the boundary layer. This seed increased with the roughness height. For roughness up to 0.2 of δ^* this conjunctures seem to be well supported by the experimental results. However, for roughness height of 0.3 of δ^* the growth of additional 3-D modes with higher spanwise wavenumbers was observed a. The reason for the growth of other modes is currently under investigation.

6. Acknowledgments

This project was financially supported by FAPESP and CAPES from Brazil.

7. References

Choudhari, M. and Kerschen, E. J., 1990, Instability wave patterns generated by interaction of sound wave with three-dimensional wall suction or roughness, "AIAA", Vol. Paper No. 90-0119.

Craik, A. A. D., 1971, Nonlinear resonant instability in a boundary layer, "Journal of Fluid Mechanics", Vol. **50**, pp. 393–413.

Gaster, M., Grosch, C. E., and Jackson, T. L., 1994, Velocity field created by a shallow bump in a boundary layer, "Physics of Fluids", Vol. **6**, No. 9, pp. 3079–3085.

Herbert, T., 1988, Secondary instability of boundary-layers, "Annual Review of Fluid Mechanics", Vol. **20**, pp. 487–526.

Klebanoff, P. S., Cleveland, W. G., and Tidstrom, K. D., 1992, On the evolution of a turbulent boundary layer induced by a trhee-dimensional roughness element, "Journal of Fluid Mechanics", Vol. **237**, pp. 101–187.

Klebanoff, P. S., Schubauer, G. B., and Tidstrom, K. D., 1954, Measurements of the effect of two-dimensional and three-dimensional roughness elements on boundary-layer transition, "Journal of Aeronautical Sciences", Vol. **21**, No. 1, pp. 62–65.

Klebanoff, P. S. and Tidstrom, K. D., 1972, Mechanism by wich a two-dimensional roughness element induces boundary-layer transition, "Physics of Fluids", Vol. **15**, No. 17, pp. 1173–1188.

Legendre, R. and Werlé, H., 2001, Toward elucidation of three-dimensional separation, "Annual Review of Fluid Mechanics", Vol. **33**, pp. 129–154.

Morkovin, M. V., 1968, Critical evaluation of transition flow laminar to turbulent shear layers with emphasis of hypersonically traveling bodies, "AFFDL TR", pp. 68–149.

Rist, U. and Jäger, A., 2004, Unsteady disturbance generation and amplification in the boundary-layer flow behind a medium sized roughness element, "IUTAM Symposium on laminar-turbulent transition".

Sedney, R., 1973, A survey of the effetcs of small protuberances on boundary-layer flows, "AIAA Journal", Vol. **11**, No. 6, pp. 782–792.

Tadjfar, M. and Bodonyi, R. J., 1992, Receptivity of a laminar boundary layer to the interaction of a three-dimensional roughness element with time-harmonic free-stream disturbances, "Journal of Fluid Mechanics", Vol. **242**, pp. 701–720.

Tani, I., 1961, Effect of two–dimensional and isolated roughness on laminar flow, "Boundary Layer and Flow Control–Pergamon Press", Vol. **2**, pp. 637–656.

Tani, I. and Hama, R., 1940, On the permissible roughness in the laminar boundary layer, "Rep. Aeronautical Research Inst. of Tokyo Imperial University", Vol. **199**, pp. 419–429.

Tobak, M. and Peake, D. J., 1982, Topology of three-dimensional separated flows, "Annual Review of Fluid Mechanics", Vol. **14**, pp. 61–85.

Wörner, A., 2003, "Numerische Untersuchung zum Entstehungsprozess von Grenzschichtstörugen durch die Interaktion von Schallwellen mit Oberflächenrauhigkeiten", PhD thesis, Universität Stuttgart, Stuttgart, Deustchland.

Wortmann, F. X. and Althaus, D., 1964, Der Laminarwindkanal des Instituts f¨ur Aerodynamik und Gasdynamik der Technischen Hochschule Stuttgart, "Z. Flugwiss", Vol. **12, No. 4.**

Würz, W., Herr, S., Wörner, A., Rist, U., Wagner, S., and Kachanov, Y. S., 2003, Three-dimensional acoustic-receptivity of a boundary layer on an airfoil: experiments and direct numerical simulations, "Journal of Fluid Mechanics", Vol. 478, pp. 135–163.

Würz, W., Sartorius, D., Wagner, S., Borodulin, V. I., and Kachanov, Y. S., 2004, Experimental study of weakly nonlinear interactions of instability waves in a non self-similar boundary layer on an airfoil - Part I: Base flow and initially tuned resonances, "12th International Conference on Methods of Aerophysical Research - ICMAR2004", Novosibirsk.

Proceedings of the 11th Brazilian Congress of Thermal Sciences and Engineering – ENCIT 2006
Braz. Soc. of Mechanical Sciences and Engineering – ABCM, Curitiba, Brazil, Dec. 5-8, 2006

Paper CIT06-0573

The Use of Genetic Algorithm for Transonic Airfoil Optimization

Rafael Gigena Cuenca
SMM – EESC – USP – Av. Trabalhador Sãocarlense, 400, CEP:13566-590 São Carlos - SP
rafaelgc@sc.usp.br

Leandro Franco de Souza
SME – ICMC – USP – Av. Trabalhador Sãocarlense, 400, CEP:13560-970 São Carlos - SP
lefraso@icmc.usp.br

Rodrigo Fernandes de Mello
SME – ICMC – USP – Av. Trabalhador Sãocarlense, 400, CEP:13560-970 São Carlos - SP
mello@icmc.usp.br

Abstract. *The improvement in aircraft performance for fuel consumption and operational cost reductions have become important in the context of modern aviation. The aeronautical projects have as challenge a high level of optimization. In the present work a novel approach was used to optimize an airfoil for high speed airplanes. A compressible formulation (Euler equations) for subsonic and transonic flows was adopted. The numerical code for flow simulation was based in Jameson's method applied in a unstructured triangular mesh. The airfoil optimization was performed by a genetic algorithm. This algorithm creates a group of generations culminating in the adoption of the airfoil with best optimization. A family of parametric shapes (PARSEC) for super-critical airfoils was used to define the individuals used in the numerical simulations. The performance parameters used in the optimization were the values of: Cl, L/D, Cm, Cl^3/Cd^2 and the gradient of pressure. The results show that the optimization by using Genetic Algorithm requires a good fitness function, which has to consider all the parameters for optimization and their relationship.*

keywords: *Compressible flow, Finite Volume, Jameson Method, Genetic algorithm, Airfoil Optimization*

1. Introduction

For the development of modern aviation, researches are required to improve the aircraft performance. One of the most important researches is related to the flight cost reduction, minimizing the power and, consequently, the fuel consumption. One of the most prominent ways to commit these needs is by using the balance of forces over an aircraft. For this, one may consider the aircraft lift (L) equal to its weight (W) and its drag (D) equal to its trust (T). These parameters are used to calculate the power:

$$P = V \cdot T \tag{1}$$

where V is the speed necessary to a steady flight. Before adopting the Eq. (1), one may calculate the lift and drag under a certain flight condition. To calculate the lift – Eq. (2), the speed (V), the planform area (S) and the lift coefficient (CL) were considered. The drag is obtained by Eq. (3) where CD is the drag coefficient.

$$L = \frac{\rho \cdot V^2 \cdot S \cdot CL}{2} \tag{2}$$

$$D = \frac{\rho \cdot V^2 \cdot S \cdot CD}{2} \tag{3}$$

By using the previously presented equation, the power (P) can be written as:

$$\begin{aligned} P &= D \cdot V = 0.5 \cdot \rho \cdot V^3 \cdot S \cdot CD \\ &= 0.5 \cdot \rho \cdot S \cdot CD \cdot \left(\frac{2 \cdot W}{\rho \cdot S \cdot CL} \right) \\ &= \sqrt{\frac{2}{\rho \cdot S}} \cdot \sqrt{\frac{W^3}{\frac{CL^3}{CD^2}}} \end{aligned} \tag{4}$$

The best improvement of the airplane is related with the cost reduction too. According to Mair and Birdsall, 1992, to transonic airplanes, the specific range of an airplane is defined by Eq. 5.

$$r_a = \frac{V}{c\beta W} \tag{5}$$

where r_a is the specific range, W is the airplane weight. Considering the air temperature constant, V is proportional to Ma, where Ma is the Mach number. So to improve r_a in a fixed Ma, is necessary to maximize $\frac{L}{D}$.

For reducing the required power, we have to consider the weight reduction, the improvement of $\frac{Cl^3}{Cd^2}$, and the enlargement of the planform area. The maximization of range is taken maximizing $\frac{L}{D}$. The weight reduction is obtained by modifications in the aircraft structure. The planform area increases the structure weight and reduces aircraft speed. The aerodynamic performance is the result of forces produced by the airflow over the aircraft geometry.

The main aerodynamic structure for an aircraft, and the one which determine its performance, is the wing. The wing is responsible to generate the lift and for a great part of the drag. The most important geometric feature, which defines the aerodynamic, is the wing profile. Many works have been done in the development of new methods to optimize airfoil shapes and wing planforms (Ray and Tsai, 2004, Holst, 2004, Song *et al.*, 2003, Oyama *et al.*, 2000b, Oyama *et al.*, 2000a, Obayashi, 1995, Oyama *et al.*, 2001) with the objective of maximization of the aerodynamic efficiency.

In the commercial aviation, the high-speed aircraft with supercritical wings are predominant and the challenge is to minimize shock wave effects which increase the drag during cruiser flight. Studies have been addressed to determine good methods to optimize airfoils during design. Two different approaches are often employed in the aerodynamic design (Song and Keane, 2004): the inverse design and the direct numerical optimization (DNO).

The first method, named inverse design, tries to find out a geometry which produces a prescribed pressure distribution. The second, named the direct numerical optimization (DNO) method, considers a set of geometries and an aerodynamic analysis code, in an iterative process, to obtain an optimum design (Yamamoto and Inoue, 1995).

Other work considers the unconstrained single-objective airfoil design. Some of them, analyze optimization problems using evolutionary algorithms (EA), genetic algorithms (GA) with real number encoding, and hybrids comprised of GA and gradient-based methods. Constrained single-objective airfoil design problems have also considered solutions based on GA such as non dominated sorting genetic algorithm (NSGA), multiobjective GA, and NSGA coupled with artificial neural networks (Ray and Tsai, 2004). According to Ray, 2004, the GA's are good options because such problems involve highly nonlinear objectives and constraints often with functional and slope discontinuity that limits the effective use of gradient based optimization methods.

A relevant question in the aircraft design is how to consider the multiobjective optimization to improve performance measures such as the lift, drag and others. GA's and EA's are addressed to commit these needs what has been motivating many researchers. These algorithms have been also successfully applied to aerodynamic shape optimization problems such as airfoil shape design (Quagliarella and Cioppa, 1994; Yamamoto and Inoue, 1995), Multi-element airfoil shape design (Cao and Blom, 1996), subsonic wing shape design (Obayashi and Oyama, 1996) and supersonic wing shape design (Oyama *et al.*, 1999). Besides, these algorithms also aims at solving non-linear problems.

Motivated by the solutions provided by genetic algorithm, this paper proposes some multiobjective function to optimize the aerodynamic performance of airfoils. A Computational Fluid Dynamics (CFD) code was used to solve the Euler equation. The multiobjective function is applied over airfoil generations until reaching a profile which satisfies the performance needs. In the present work, the Parsec parametric airfoils (Sobieczky, 1998) were adopted.

This paper is divided as follows: section 2 shows the aerodynamic formulation used to evaluate the airfoil performance; section 3 explains the numerical methods used of this work; section 4 describes the geometry family that defines the airfoil shape; section 5 shows how the numerical code works; section 6 shows the code validation and the results obtained for three different fitness functions. The last section presents the main conclusions of the present work.

2. Formulation

The Navier-Stokes (NS) equations represent the mathematical model for any kind of flow. For transonic flow simulations over airfoils, one of the most important phenomena is related with the compressibility, ie. shock wave. When using the supercritical airfoil, the interaction between boundary layer and shock wave is important to represents the shock location and to analyze moderns wings profiles. These profiles are called *Natural Laminar Flow* (NLF), were the reduction of drag is caused by an increment of laminar flow percentage

($\geq$ 30% of chord) on the foil surface (Selig *et al.*, 1995). However, the viscous effects were neglected in the current work, simplifying the NS equations. This simplification leads do the called Euler equations. These equations in conservative form and in Cartesian coordinates becomes:

$$\frac{\partial Q}{\partial t} + \frac{\partial E}{\partial x} + \frac{\partial F}{\partial y} = 0, \tag{6}$$

where

$$Q = [\rho, \rho u, \rho v, e]^t, \tag{7}$$

$$E = \left[\rho u, \rho u^2 + p, \rho uv, (e+p)u\right]^t, \tag{8}$$

$$F = \left[\rho u, \rho uv, \rho v^2 + p, (e+p)v\right]^t, \tag{9}$$

$$e = \rho(e_i + \frac{1}{2}(u^2 + v^2)), \tag{10}$$

$$p = \rho RT, \tag{11}$$

$$e_i = \frac{p}{(\gamma - 1)\rho}. \tag{12}$$

These equations were simulated in a numerical code. The details of the numerical code is presented in the next section.

3. Numerical Methods

To accomplish the present work, it was necessary the implementation of some numerical methods to simulate and optimize the wing section leaving to computer the job to calculate and evaluate the performance of airfoil and decide which one is the best. This section is divided in two parts, the first one describes the numerical method used to solve the Euler equations and the second describes the Genetic Algorithm adopted.

3.1. Euler solver

To evaluate the performance of a wing section on a compressible flow, it is necessary to simulate the flow around the airfoil, using any method of solution for the Euler equations. There are a lot of these methods, that differ about the mesh, the discretization of equation and the accuracy.

In the current work, it was adopted a finite volume (FV) method proposed by Jameson (Jameson *et al.*, 1981; Jameson, 1982; Jameson and Mavriplis, 1986) on a unstructured triangular mesh. This mesh allows an easy definition of the geometry around the airfoil. The grid generation were made automatically by a scripted commands program. A detailed description of Jameson can be found in Hirsch, 1991.

3.2. Genetic Algorithms

Genetic Algorithms (GA) are being applied as search and optimization techniques in several domains. These algorithms are based on nature select mechanisms focusing at survival of the most capable individuals. GA does not always give the best possible solution, however provides good local solutions for NP-complete problems.

The problem solution using genetic algorithms involves two different aspects: solution encoding into the form of chromosomes, where each chromosome represents a possible solution, and a fitness function applied to find the best solution.

Different encoding techniques can be used for different kind of problems, such as binary strings, bitmaps, real numbers, and so on. The fitness function is responsible for the evaluation of possible solutions. This function receives a chromosome as parameter and returns a real number, informing the quality of the obtained solution, e.g., how adequate is the solution for the currently studied problem.

The most adequate chromosomes are identified and stored during the evolution process. The weakest ones, on the other side, are eliminated. Different techniques can be applied for the identification of the best chromosomes, such as the proportional selection, ranking selection and tournament-based selection (Back *et al.*, 1999b; Back *et al.*, 1999a).

In the proportional selection, individuals are transferred to the next generation according to their fitness value probability proportion. One of the possible implementations of this technique consists in the usage of a

roulette, divided into N parts, N being the number of individuals (chromosomes) in the current population. The size of each part is proportional to the fitness value of each individual. The roulette is rotated N times afterward, and at each turn the appointed individual is selected and inserted into the new population.

Ranking-based selection can be subdivided into two steps. During the first one, the solutions are ordered according to their fitness function values. Once the list is ordered, each individual receives a new fitness function value equivalent to its position in the ranking. After that, a procedure that selects the individuals, according to their ranking position, is applied. Thus, the individuals with better ranking position have more chances to be selected.

Finally, a tournament-based selection does not automatically attribute probabilities to individuals. A tournament size (k) is defined, with $k \geq 2$ individuals. Then, k individuals are chosen randomly from the current population, and their fitness functions are compared. The individual with best fitness value is selected for reproduction. The k value is defined by the user, representing the selection pressure – e.g., the speed with the strongest individuals will dominate the population, generating the extermination of the weakest ones.

Once selected the individuals for the reproduction, it is necessary to modify their genetic characteristics using reproduction techniques known as genetic operators. The most common operators are crossover and mutation.

The crossover operator allows to exchange genetic material between two individuals, known as the parents, combining their information in a way that provides a significant chance of creation of new individuals with better characteristics than the original ones (Hinterding, 2000).

The single-point crossover operator is the most used one. In order to apply it, two individuals (parents) are selected and two new individuals are created from them (children). A single random splitting point is selected in parents chromosomes, and the new chromosomes are created from the combination of the parents, as shown in Tab. 1. In this table, label (a) shows the parent individuals and the splitting point marked by | symbol. The New individuals created from the combination of the parent chromosomes are shown in the same table with label (b), illustrating the crossover operator.

Table 1: Crossover operator

$X_1X_2\|X_3X_4X_5X_6$	$X_1X_2\|Y_3Y_4Y_5Y_6$
$Y_1Y_2\|Y_3Y_4Y_5Y_6$	$Y_1Y_2\|X_3X_4X_5X_6$
(a) Before the crossover	**(b) After the crossover**

The mutation operator, on its turn, is used for changing a single gene value for a new random one. When an individual is represented by a bitmap, this operation consists of a random choice of a chromosome gene and the swapping of its value from 1 to 0 (or from 0 to 1, correspondingly). The goal of the mutation operator is to maintain the diversity of a population, always allowing a chromosome to cover a significantly large result space (Hinterding, 2000). It is usually applied at a low rate, as at high ones the results tends to be random.

4. Parametric airfoil shape

A parametric airfoils families were adopted, with the objective of generating a big number of airfoils shapes for the use with GA. These families are very appropriated because allow the generation of different types of shapes using a limited number of parameters. These parameters are used for the GA as the chromosomes of the individuals. According to Song and Keane, 2004 and Ray and Tsai, 2004, there are many functions proposed to evaluate the shape, like: analytical functions (PARSEC, NACA, etc); splines, B-splines and Bezier curves to via interpolation methods; and others.

The objective of the present work is to evaluate a method for optimize supercritical airfoils. The Parsec family of wing sections defined by 11 geometric parameters was used. According to Sobieczky, 1998, a blend of two or more airfoils schemes can be used to improve number of shapes representations and consequently the possibilities of geometries. To make a simple analysis, only the Parsec shapes were analyzed. This family is detailed bellow.

4.1. The Parsec Family

The PARSEC representation is particularly attractive as it uses a small number of design variables, all of which are related to some properties of the shape (Ray and Tsai, 2004). It parameterizes the upper and the

lower airfoil surfaces using polynomials in coordinates X and Z as:

$$Z = \sum_{n=1}^{6} a_n X^{n-\frac{1}{2}} \tag{13}$$

where a_n are real coefficients. The parameters of a PARSEC representation include the leading-edge radius r_{le}, upper and lower crest heights Z_{UP}, Z_{LO} and location X_{UP}, X_{LO}, curvatures at the upper and lower crests Z_{XXUP}, Z_{XXLO}, trailing-edge thickness ΔZ_{TE} and ordinate Z_{TE}, and direction and wedge angle α_{TE}, β_{TE}. The parameters are schematically shown in Fig. 1.

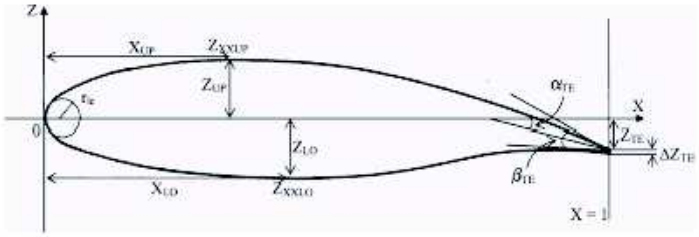

Fig. 3 Variables in the PARSEC representation scheme.

Figure 1: Variables in the Parsec representation scheme

5. A Multiobjective Function to Optimize the Aerodynamic Performance of Airfoils Using CFD

On the context of aviation design, in the conceptual project and in the detailed one, the aerodynamic analysis became very important. This importance leads to find out the optimum design, with the multiobjective optimization. The airfoil shape is one of the most optimized in the aviation design.

To perform the design optimization, many studies used several optimization methods like: GA, evolutionary algorithms, gradient-based methods and others. All show its capability to optimize on the aerodynamic design context, looking for single objective and multiobjective optimization, with or without constraints.

In the present paper, the optimization method using a GA with a Euler solver to evaluate the aerodynamic performance were carried out.

To classify the individuals on GA, it was used a fitness function defined by:

$$fitness = \begin{cases} 0, \text{ to t} > 20\% \text{ of chord} \\ 0, \text{ to camber} > 10\% \text{ of chord} \\ \text{fitness function} \end{cases} \tag{14}$$

where: t is the maximum thickness of the airfoil; *camber* are the maximum coordinate of the mean line (*camber* line) of airfoil; and three fitness functions were adopted. These functions are shown in detail the section results.

To make this optimization possible, it was necessary the integrations between the steps described above: definition of geometry; grid generation; Euler solution; post-process of the result of Euler simulation; and the genetic algorithm implementation. The methodology is illustrated on Fig. 2.

To improve the computational cost, it was made an evaluation of the geometry before the mesh generator or the Euler solution start. The thickness and the camber condition were used in this evaluation.

6. Results

This section was divided in two subsections, the first one shows the validation of the present Euler Solver code, where the numerical results are compared with numerical and experimental results. The second subsection shows the results obtained with three different fitness functions, with the fitness evolutions and the optimized airfoil shapes.

6.1. Euler Solver Validation

The aerodynamic code was validated comparing the numerical results with experimental data. It cold to see on Fig. 3 the comparison between experimental Cp distribution of RAE-2822 transonic airfoil and the numerical result obtained with the implemented code. The figure shows that the numerical code is able predict the flow,

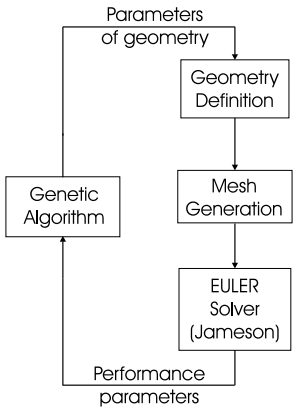

Figure 2: Methodology structure used on implementation.

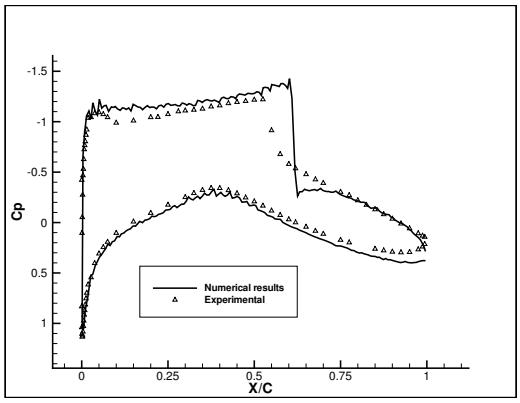

Figure 3: Numerical and experimental results for Cp distribution over RAE-2822 airfoil.

with some differences in the position and intensity of the shock wave. This differences are attributed to the viscous effects that were neglected in the present study.

The mesh used in optimization used about 11000 cell. A refinement near the airfoil were used to capture the shock wave and its effect on airfoil performance and the pressure distribution. On foil surface, the maximum length of the size of volumes were defined as 0.007 chord.

6.2. Optimization

To optimize the airfoil and to configure the Genetic algorithm, we restricted the random generation of geometry parameters. The limits of this values adopted are shown in Tab. 2.

Table 2: Parameters limits

Param.	r_{le}	X_{up}	Z_{up}	Zxx_{up}	X_{lo}	Z_{lo}	Zxx_{lo}	α_{te}	β_{te}	Z_{te}	dZ_{te}
Lower	0.001	0.3	0.05	-0.5	0.3	-0.05	0.55	8^o	10^o	0	0
top	0.007	0.5	0.12	0.1	0.45	0.1	1.35	17^o	11.5^o	0.05	0

The parameters that we want to maximize are: L/D, Cl^3/Cd^2 according to the fitness functions presented in the next sections; that are direct related to the power required, the trust required to a steady flight and range of airplane. These parameters express the size of engine needed and the consumption of airplane. To reduce the down force necessary to equilibrate the airplane, we want to minimize the Cm and to determine the flight speed, we want to restrict the Cl to 0.2.

The parameters of the genetic algorithm was: 70 individuals per generation; 70% of crossover probability; and 1% of mutation probability. The flight condition were defined as: $Ma = .75$; incidence of airfoil $\alpha = 0^o$.

6.2.1. Fitness function 1

The first fitness function adopted is given by Eq. 15.

$$F_i = \frac{\frac{L}{D} + \frac{Cl^3}{Cd^2} + P1 + P2}{(|Cl - 0.2| + 0.01) \cdot (|CM| + 0.01) \cdot (I1 + I2 + 0.01)} \tag{15}$$

where: F_i is the fitness value for the proposed solution i; $\frac{L}{D}$ is the aerodynamic efficiency; $\frac{Cl^3}{Cd^2}$ is the aerodynamic influence in the required power; $P1$ and $P2$ are defined according to the adverse gradient of pressure over the airfoil surface (upper and lower surface, respectively); Cl is the lift coefficient; CM is the pitch moment coefficient; $I1$ and $I2$ are the fraction of supersonic flow over the airfoil surface (upper and lower surface, respectively); 0.2 defines the desired restriction; and, finally, the constants 0.01 avoid the division by zero.

The fitness evolution is shown in Fig. 4 - left. The individual has adapted with forty generations. The Fig. 4 - right shows the optimized profile with the Mach isolines distribution. In this figure it can be seen big acceleration of flow on upper surface and a strong shock.

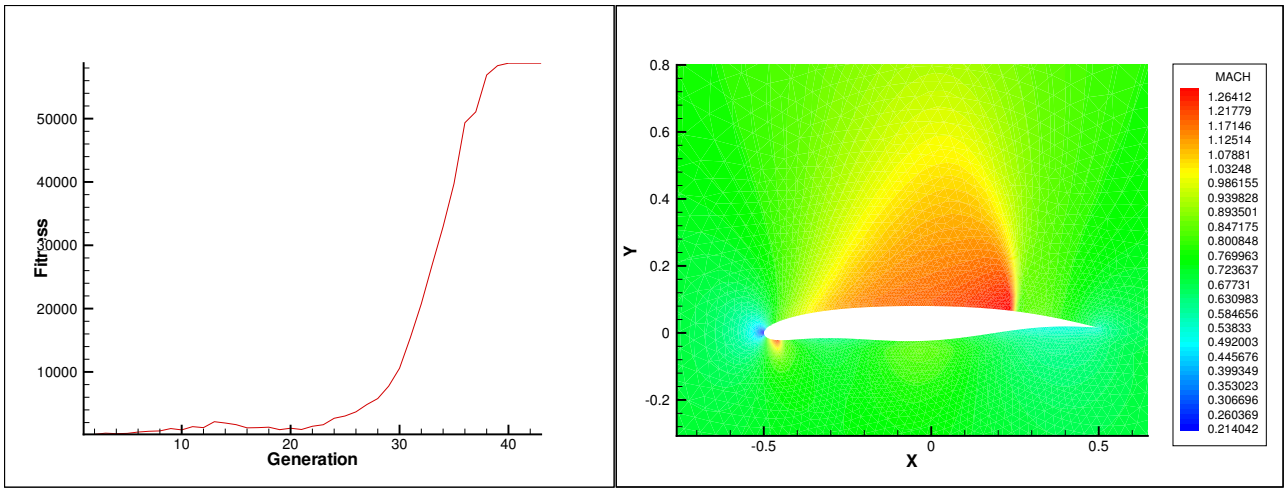

Figure 4: Fitness evolution - left and the optimized profile with Mach isolines for the first fitness function - right.

6.2.2. Fitness function 2

The second fitness function adopted was

$$F_i = \frac{\frac{L}{D} + P1 + P2}{(|Cl - 0.2| + 0.01) \cdot (|CM| + 0.01) \cdot (I1 + I2 + 0.01)} \tag{16}$$

the parameters shown here were defined in section 6.2.1. The fitness evolution is shown in Fig. 5 - left. The optimization converged with thirty generations. The Fig. 5 - left shows the evolution of optimization. This airfoil has a reduction of sonic flow over the upper surface comparing with the first result, but the shock wave are still present.

6.2.3. Fitness function 3

The third fitness function is given by Eq. 17. The parameters are defined in section 6.2.1. The optimized airfoil obtained with Mach isolines is shown in Fig. 6 - right. The Fig. 6 - left show the fitness evolution of optimization. The optimization converged with thirty five generations.

$$F_i = \frac{\frac{L}{D}}{(|Cl - 0.2| + 0.01) \cdot (|CM| + 0.01)} \tag{17}$$

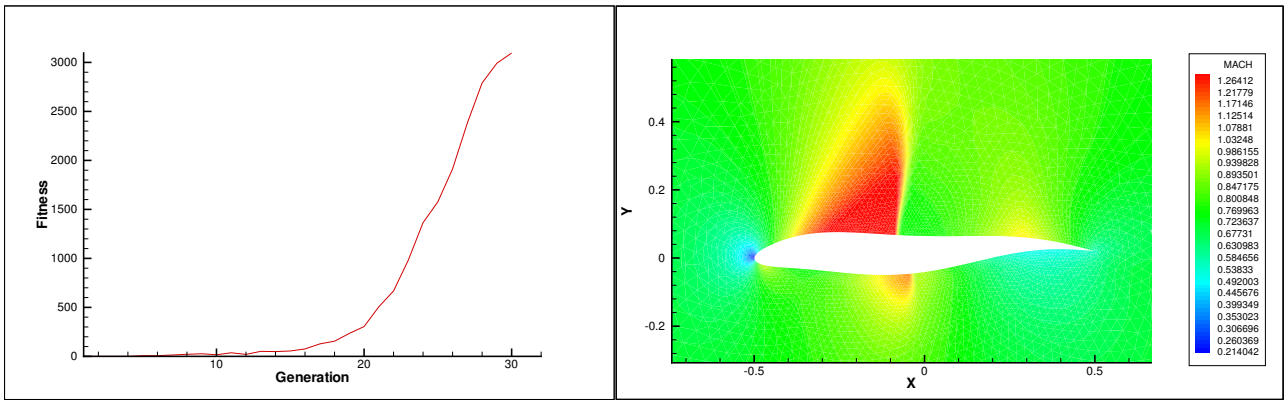

Figure 5: Fitness evolution - left and the optimized profile with Mach isolines for the second fitness function - right.

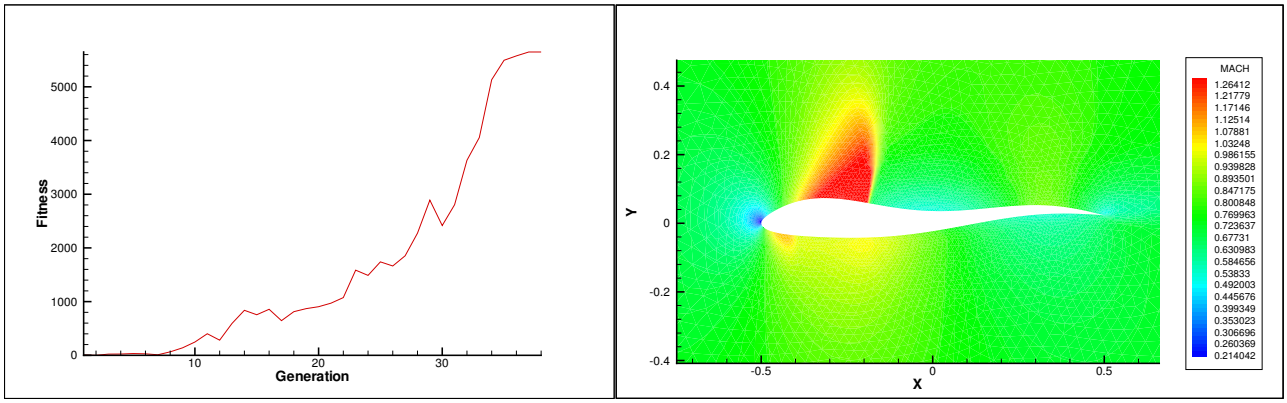

Figure 6: Fitness evolution - left and the optimized profile with Mach isolines for the third fitness function - right.

6.2.4. Comparison between results

The results of the coefficients obtained with each fitness function are shown in Tab. 3. In this table, the column **fit. RAE** show the fitness function obtained by the performance parameters of RAE-2822 airfoil for the flow condition. The column % shows the percentage comparison of the RAE fitness with our optimized airfoil solution.

Table 3: Comparison of optimization results

func.	Cl	Cm	L/D	Cl^3/Cd^2	$fitness$	$fit.RAE$	%
1	0.7066	-0.38435	102.31	7398.2	58760	4.12E+10	0.000143
2	0.4649	-0.28020	24.76	285.1	3096	6794	45.6
3	0.1937	-0.16412	6.8	8.95	5648	3096	182.42
RAE	0.4422	-0.23391	177.02	13855			

Comparing the results, is possible to see that $fitness_1$ function take a Cl greater than desired and the $fitness_2$ function take a Cl near to the RAE-2822, but the $fitness_3$ function could restrict the Cl to 0.2 as desired. The minimization of Cm was performed better by $fitness_3$ function. The maximizations of $\frac{L}{D}$ and $\frac{Cl^3}{Cd^2}$ were performed by $fitness_1$ function. The results obtained show that the Cl restriction "fights" with the maximizations. The comparison between the fitness of generated airfoils and the RAE-2822 shows that the $fitness_3$ function gives the better Cl and Cm. The $fitness_1$ function gave the better maximization terms.

The Cp distributions of the optimized airfoils obtained with each fitness function and the RAE-2822 Cp are shown in Fig. 7. The Cp curves show that every airfoils have supersonic flow over its surface and strongs shock waves, despite the maximization of aerodynamic efficiency.

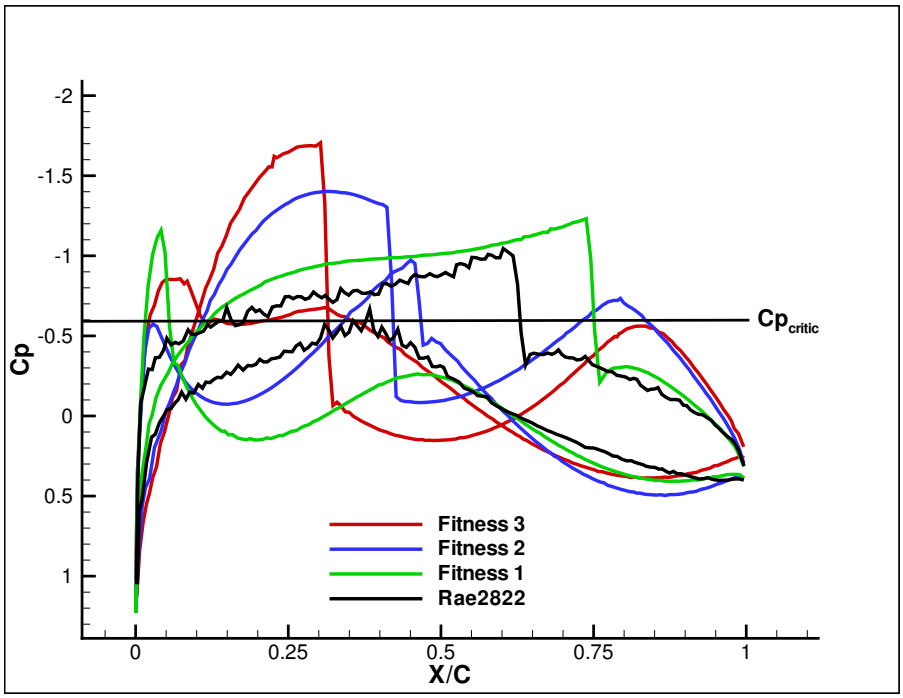

Figure 7: *Cp* distribution of foil.

7. Conclusions

In the current work a optimization study of a transonic airfoil was presented. A compressible formulation (Euler equations) was adopted. The numerical code for flow simulation was based in Jameson's method applied in a unstructured triangular mesh. The airfoil optimization was performed by a genetic algorithm. A family of parametric shapes (PARSEC) for super-critical airfoils was used to define the individuals used in the numerical simulations. The performance parameters used in the optimization depends on the fitness function adopted. The results show that the optimization by using Genetic Algorithm requires a good fitness function, which has to consider all the parameters for optimization and their relationship.

8. Acknowledgments

The authors acknowledge the financial support given by CNPQ and FAPESP under grant 04/07507-4.

9. References

Back, T., Fogel, D. B., and Michalewicz, Z., editors, 1999a, "Advanced Algorithms and Operators", IOP Publishing Ltd., Bristol, UK, UK.

Back, T., Fogel, D. B., and Michalewicz, Z., editors, 1999b, "Basic Algorithms and Operators", IOP Publishing Ltd., Bristol, UK, UK.

Cao, H. V. and Blom, G. A., 1996, Navier-Stokes/Genetic Optimization of Multi-Element Airfoils, "AIAA", Vol. , No. 96-2487.

Hinterding, R., 2000, Representation, Mutation and Crossover Issues in Evolutionary Computation, "Proc. of the 2000 Congress on Evolutionary Computation", pp. 916–923, Piscataway, NJ. IEEE Service Center.

Hirsch, C., 1991, "Numerical Computation of Internal and External Flows volume 2: Computational Methods for Inviscid and Viscous Flows", John Wiley & Sons, Chichester.

Holst, T. L., 2004, Genetic Algorithms Applied to Multi-Objective Aerospace Shape Optimisation, "AIAA", Vol. , No. 2004-6512.

Jameson, A., 1982, "Numerical Methods in aeronautical fluid dynamics", chapter Transonic airfoil calculations using the Euler equations. Academic Press, New York, USA.

Jameson, A. and Mavriplis, D., 1986, Finite Volume Solution of the two-Dimensional Euler Equations on a Regular Triangular Mesh, "AIAA Journal", Vol. 24, No. 41, pp. 611–618.

Jameson, A., Schimidt, W., and Turkel, E., 1981, Numerical Simulation of the EULER Equations by Finite Volume Methods Using Runge-Kutta TIme Stepping Schemes, "AIAA Paper", Vol. , No. 81-1259.

Mair, W. A. and Birdsall, D. L., editors, 1992, "Aircraft Performance", Cambridge University Press, Melbourne, Australia.

Obayashi, S., 1995, Genetic Algorithm for Aerodynamic Inverse Optimization, "Genetic Algorithm in Engeneering Systems: Innovations and Applications", Vol. , No. 414.

Obayashi, S. and Oyama, A., 1996, Three-Dimensional Aerodynamic Optimization with Genetic Algorithms, "Proceedings of the Third ECCOMAS Computational Fluid Dynamics Conference", Vol. , pp. 420–424.

Oyama, A., Obayashi, S., Nakahashi, K., and Hirose, N., 2000a, Aerodynamic Wing optimisation via Evolutionary Algorithms Based on Structured Coding, "CFD Journal", Vol. .

Oyama, A., Obayashi, S., Nakahashi, K., and Nakamura, T., 1999, Euler/Navier-Stokes Optimization of Supersonic Wing Design Based on Evolutionary Algorithm, "AIAA Journal", Vol. 37, No. 10, pp. 1327–1329.

Oyama, A., Obayashi, S., Nakahashi, K., and Nakamura, T., 2000b, Aerodynamic Optimization of Transonic Wing Design Based on Evolutionary Algorithm, "ICNPAA", Vol. .

Oyama, A., Obayashi, S., and Nakamura, T., 2001, Real-coded Adaptive Range Genetic Algorithm Applied to Transonic Wing Optimization, "Applied Soft Computing Journal", Vol. 3, No. 1, pp. 179–187.

Quagliarella, D. and Cioppa, A. D., 1994, Genetic Algorithms applied to the Aerodynamic Design of Transonic Airfoils, "AIAA", Vol. , No. 94-1896-CP.

Ray, T., 2004, Application of Multi-Objective Evolutionary Algorithms in Engineering design, "Applications of Multi-Objective Evolutionary Algorithms", Vol. 2, No. 3, pp. 29–52.

Ray, T. and Tsai, H. M., 2004, Genetic Algorithm for Aerodynamic Inverse Optimization, "AIAA Journal", Vol. 42, No. 2.

Selig, W. S., Maughmer, M. D., and Somers, D. M., 1995, Natural-Laminar-Flow Airfoil for General-Aviation Applications, "Aircr", Vol. 32, No. 4, pp. 710–715.

Sobieczky, H., 1998, Parametric Airfoils and wings, Vol. .

Song, W., Keane, A., Eres, H., Pound, G., and Cox, S., 2003, Two Dimensional Airfoil Optimisation Using CFD in a Grid Computing Environment, "Euro-Par", Vol. .

Song, W. and Keane, A. J., 2004, A Study of Shape parametrisation Methods for Airfoil Optimisation, "AIAA Paper", Vol. , No. 2004-4482.

Yamamoto, K. and Inoue, 1995, Application of Genetic Algorithm to Aerodynamic Shape Optimization, "AIAA Paper", Vol. , No. 95-1650-CP, pp. 43–51.

Proceedings of the 11th Brazilian Congress of Thermal Sciences and Engineering -- ENCIT 2006
Braz. Soc. of Mechanical Sciences and Engineering -- ABCM, Curitiba, Brazil,- Dec. 5-8, 2006

Paper CIT06-0594

NUMERICAL SIMULATION OF THE TRANSONIC LAMINAR FLOW IN AIRFOILS WITH HIGH AMPLITUDE PLUNGING MOTIONS

Rúdner Lauterjung Queiroz
Universidade de Brasília, ENM – FT – UnB, Campus Universitário Darcy Ribeiro, Asa Norte, 70910-900, Brasília, DF, Brasil
rudner@gmail.com

Roberto Francisco Bobenrieth Miserda
Universidade de Brasília, ENM – FT – UnB, Campus Universitário Darcy Ribeiro, Asa Norte, 70910-900, Brasília, DF, Brasil
rfbm@unb.br

Abstract. *This work is a direct numerical simulation of the transonic laminar flow in airfoils with high amplitude plunging motions. The problem is solved for a non-inertial system of reference which is moving with the airfoil, and for this reason, the associated pseudo-force is included as a source in the momentum equation and the work done is also included as a source in the energy equation. This methodology allows the solution of high amplitude plunging motions, since the problem is solved from a non-inertial frame of reference which is moving with the airfoil and, for this reason, no grid deformation is needed to account for the motion. The compressible Navier-Stokes equations are solved using the skew-symmetric form of Ducros' shock-capturing algorithm, with fourth-order accuracy in space and third-order accuracy in time. Five cases are studied: the static airfoil and the plunging motions with amplitudes of 2.5%, 13%, 22% of the airfoil chord. For all the cases, the Reynolds number is 10,000, the Mach number of the free flow is 0.8 and the plunging frequency has same value of the vortex emission frequency of the static case. The numerical results show a very complex and unsteady interaction between the boundary layer, the detached vortex wake and the transonic shock-wave system for the four cases studied. There are also some characteristic shock phenomena at the last two cases.*

Keywords. *Transonic, Laminar Flow, Plunging Motion, High Amplitude*

1. Introduction

This work is aimed at the numerical simulation of the strong vortex-shock interaction that arises in the transonic flow over BGK-1 supercritical airfoil in laminar regime, submitted to plunging motion. This kind of interaction is typical of the unsteady aerodynamics of bodies in transonic flows, directly connected to limit cycle oscillations in transonic flows and flutter phenomena. Such phenomena are of high interest in the aerospace sciences.

The complex nature of these interactions demands numerical methods with shock-capturing schemes to obtain accurate results. In the case of plunging motions, a modified set of governing equations in order to simulate the oscillations of the body is also necessary.

Using this methodology, the study of transonic flows started with the investigation of Transonic Buffet in airfoils (Bobenrieth Miserda *et al*., 2004) and the investigation of transonic flows in a near-base (Bobenrieth Miserda and Mendonça, 2005). After that, the investigation of the transonic flow with plunging and pitching motions (Lauterjung *et al*., 2005 and Bobenrieth Miserda *et al*., 2006) has begun. Meanwhile, the subsonic flow with plunging motion (Bobenrieth Miserda and Carvalho, 2006) and with pitching motion (Guimarães and Silva, 2005) were also being studied. In order to start exploring turbulent flows, the transonic cylinder (Bobenrieth Miserda and Leal, 2006) was also investigated.

2. Mathematical Model

In this work, the system of equations is written using a non-inertial frame of reference which is fixed to the plunging airfoil. The effect of this motion is accounted by a pseudo-force term in the right-hand side of the momentum equation which acts as a body force (Batchelor, 1983). In similar manner, the work done by this pseudo-force is accounted by a pseudo-work term in the right-hand side of the energy equation. With these considerations, the nondimensional form of the Navier-Stokes equations can be written as:

$$\frac{\partial \rho}{\partial t} + \frac{\partial}{\partial x_i}(\rho u_i) = 0 \tag{1}$$

$$\frac{\partial}{\partial t}(\rho u_i) + \frac{\partial}{\partial x_j}(\rho u_i u_j) = -\frac{\partial p}{\partial x_i} + \frac{\partial \tau_{ij}}{\partial x_j} + f_i \tag{2}$$

$$\frac{\partial}{\partial t}(\rho e_T)+\frac{\partial}{\partial x_i}(\rho e_T u_i)=-\frac{\partial}{\partial x_i}(p u_i)+\frac{\partial}{\partial x_i}(t_{ij}u_j)-\frac{\partial q_{x_i}}{\partial x_i}+f_i u_i \tag{3}$$

All variables are in nondimensional form and have their usual meaning, i.e., ρ is the density, t is the nondimensional time, x_i is the i-direction spatial coordinate, u_i is the i-direction component of the velocity vector, p is the pressure, t_{ij} denotes the viscous stress tensor, e_T is the total energy per unit of mass, q_{xi} is the heat-flow density in the i-direction and f_i is the pseudo-force due to the plunging motion.

The nondimensional form of the flow variables and properties are defined as

$$\begin{aligned} &x_i=\frac{x_i^*}{c^*},\quad u_i=\frac{u_i^*}{U_\infty^*},\quad t=\frac{t^*}{c^*/U_\infty^*},\quad p=\frac{p^*}{\rho_\infty^*\left(U_\infty^*\right)^2},\quad \rho=\frac{\rho^*}{\rho_\infty^*},\quad e_T=\frac{e_T^*}{\left(U_\infty^*\right)^2},\\ &m=\frac{m^*}{m_\infty^*},\quad e=\frac{e^*}{\left(U_\infty^*\right)^2},\quad e_k=\frac{e_k^*}{\left(U_\infty^*\right)^2},\quad c_v=\left[\frac{T_\infty^*}{\left(U_\infty^*\right)^2}\right]c_v^*,\quad T=\frac{T^*}{T_\infty^*}, \end{aligned} \tag{4}$$

where the asterisk denotes dimensional quantities, c^* is the chord of the airfoil, μ^* is the dynamic viscosity, T^* is the temperature. U_∞^*, T_∞^*, ρ_∞^* and μ_∞^* are, respectively, the velocity, temperature, density and dynamic viscosity of the undisturbed flow. The nondimensional viscous stress tensor is given by

$$t_{ij}=\frac{1}{\mathrm{Re}}\left(\mu S_{ij}\right)=\frac{1}{\mathrm{Re}}\left\{\mu\left[\left(\frac{\partial u_i}{\partial x_j}+\frac{\partial u_j}{\partial x_i}\right)-\frac{2}{3}\delta_{ij}\frac{\partial u_k}{\partial x_k}\right]\right\} \tag{5}$$

where δ_{ij} is the Kronecker delta. The Reynolds number is defined as

$$\mathrm{Re}=\frac{\rho_\infty^* U_\infty^* c^*}{\mu_\infty^*}. \tag{6}$$

Defining e as the nondimensional internal energy per unit of mass, e_k as the nondimensional kinetic energy per unit of mass and c_v as the nondimensional specific heat at constant volume, the total energy is given by the sum of the internal and kinetic specific energy as

$$e_T=e+e_k=c_v T+\frac{u_i u_i}{2} \tag{7}$$

and the nondimensional heat-flux density is

$$q_{x_i}=-\frac{\mu}{(\gamma-1)M^2\,\mathrm{Re}\,\mathrm{Pr}}\left(\frac{\partial T}{\partial x_i}\right) \tag{8}$$

where the M and Pr are the Mach and the Prandtl numbers, respectively, and are defined as

$$M=\frac{U_\infty^*}{\sqrt{\gamma R^* T_\infty^*}},\qquad \mathrm{Pr}=\frac{c_p^*}{k_\infty^*}\mu_\infty^* \tag{9}$$

where γ is the specific heat ratio, R^* is the specific gas constant, c_p^* is the specific heat at constant pressure and k_∞^* is thermal conductivity of the undisturbed flow.

In this work, the Prandtl number is considered a constant with the value $\mathrm{Pr}=0.72$. For a thermally and calorically perfect gas, the nondimensional equation of state can be written as

$$p=(\gamma-1)\rho e \tag{10}$$

and

$$T = \frac{g\ M^2 p}{r} \tag{11}$$

The nondimensional molecular viscosity is obtained using Sutherland's formula, where C_1 and C_2 are the nondimensional first and second gas constants,

$$m = C_1 \frac{T^{3/2}}{T + C_2}, \qquad C_1 = \left[\frac{\left(T_\infty^*\right)^{1/2}}{m_\infty^*}\right] C_1^*, \qquad C_2 = \frac{C_2^*}{T_\infty^*}. \tag{12}$$

The pseudo-force f_i, which appears in Eqs. (2) and (3), accounts for the two types of motion when the Navier-Stokes equations are written for a non-inertial frame or reference. When the plunging motion is imposed, and its linear amplitude is sinusoidal in time, the components of the pseudo-force, f_i, are given by

$$f_i = \frac{1}{2} r A_i w_i^2 \sin\left(w_i t\right) \tag{13}$$

The nondimensional maximum amplitude, A_i, and angular frequency, w_i, of the plunging motion are defined as

$$A_i = \frac{A_i^*}{c^*}, \qquad w_i = \frac{w_i^*}{U_\infty^* / c^*}. \tag{14}$$

The boundary conditions at the wall of the two-dimensional airfoil are a no-slip condition for the velocity field, an adiabatic wall for the temperature field and a null gradient in the normal direction at the wall for the pressure field.

3. Numerical Method

Since the geometry of interest is a two-dimensional airfoil and the flow around it is laminar, the two-dimensional form of the Navier-Stokes equations is used. In order to numerically solve these equations using a finite volume approach associated with a fixed grid, Eqs. (1), (2) and (3) are written in the following vector form (Anderson, 1983):

$$\frac{\partial \mathbf{U}}{\partial t} + \frac{\partial \mathbf{E}}{\partial x} + \frac{\partial \mathbf{F}}{\partial y} = \mathbf{R} \tag{15}$$

where **U** is the nondimensional conservative-variables vector, **E** and **F** are the nondimensional flux vectors. These vectors are given by

$$\mathbf{U} = \begin{bmatrix} r \\ ru \\ rv \\ re_T \end{bmatrix}, \quad \mathbf{E} = \begin{bmatrix} ru \\ ru^2 + p - t_{xx} \\ ruv - t_{xy} \\ (re_T + p)u - ut_{xx} - vt_{xy} + q_x \end{bmatrix}, \quad \mathbf{F} = \begin{bmatrix} rv \\ rvu - t_{xy} \\ rv^2 + p - t_{yy} \\ (re_T + p)v - ut_{xy} - vt_{yy} + q_y \end{bmatrix}, \tag{16}$$

where *u* and *v* are, respectively, the nondimensional component of the velocity vector in the *x*-direction and *y*-direction.

In this work, the plunging motion of the airfoil is imposed in the *y*-direction, and consequently, for this case the nondimensional **R** vector, which is associated with the plunging motion, is

$$\mathbf{R} = \begin{bmatrix} 0 \\ 0 \\ \frac{1}{2} r A_y w^2 \sin\left(w_y t\right) \\ \frac{1}{2} r A_y w^2 \sin\left(w_y t\right) v \end{bmatrix}. \tag{17}$$

Defining the flux tensor Π as

$$\Pi = \mathbf{E} \otimes \mathbf{i} + \mathbf{F} \otimes \mathbf{j} \tag{18}$$

where **i** and **j** are unit vectors in the *x*-direction and *y*-direction. Eq. (15) can be rewritten as

$$\frac{\partial \mathbf{U}}{\partial t} + \nabla \cdot \Pi = \mathbf{R} \tag{19}$$

Integrating the above equation over the control volume *V*, and applying the divergence theorem to the first term of right-hand side results

$$\frac{\partial}{\partial t}\int_V \mathbf{U}\, dV = -\int_V (\nabla \cdot \Pi)\, dV + \int_V \mathbf{R}\, dV = -\int_S (\Pi \cdot \mathbf{n})\, dS + \int_V \mathbf{R}\, dV \tag{20}$$

Defining the volumetric mean of vectors **U** and **R** in the control volume *V* as

$$\overline{\mathbf{U}} \equiv \frac{1}{V}\int_V \mathbf{U}\, dV, \qquad \overline{\mathbf{R}} \equiv \frac{1}{V}\int_V \mathbf{R}\, dV, \tag{21}$$

The upper bar means volumetric mean of the variable. Eq. (20) is written as

$$\frac{\partial \overline{\mathbf{U}}}{\partial t} = -\frac{1}{V}\int_S (\Pi \cdot \mathbf{n})\, dS + \overline{\mathbf{R}} \tag{22}$$

For the volume (i, j), the first-order approximation of the temporal derivative is given by

$$\left(\frac{\partial \overline{\mathbf{U}}}{\partial t}\right)_{i,j} = \frac{\Delta \overline{\mathbf{U}}_{i,j}}{\Delta t} + O(\Delta t) \tag{23}$$

and the temporal approximation of Eq. (22) for a quadrilateral and two -dimensional control volume is

$$\Delta \overline{\mathbf{U}}_{i,j} = -\frac{\Delta t}{V_{i,j}}\left[\int_{S_{i+1/2}} (\Pi \cdot \mathbf{n})\, dS + \int_{S_{i-1/2}} (\Pi \cdot \mathbf{n})\, dS + \int_{S_{j+1/2}} (\Pi \cdot \mathbf{n})\, dS + \int_{S_{j-1/2}} (\Pi \cdot \mathbf{n})\, dS\right] + \Delta t\, \overline{\mathbf{R}} \tag{24}$$

where $S_{i+1/2}$ is the common surface between volume (i, j) and volume $(i+1, j)$, **n** is the normal unit vector, *Dt* is the nondimensional time step. Defining

$$F\left(\overline{\mathbf{U}}\right)_{i,j} = (\Pi \cdot \mathbf{S})_{i+1/2} + (\Pi \cdot \mathbf{S})_{i-1/2} + (\Pi \cdot \mathbf{S})_{j+1/2} + (\Pi \cdot \mathbf{S})_{j-1/2} \tag{25}$$

the spatial approximation of Eq. (24) is

$$\Delta \overline{\mathbf{U}}_{i,j} = -\frac{\Delta t}{V_{i,j}}\left[F\left(\overline{\mathbf{U}}\right)_{i,j} - D\left(\overline{\mathbf{U}}\right)_{i,j}\right] + \Delta t\, \overline{\mathbf{R}} \tag{26}$$

where $D\left(\overline{\mathbf{U}}\right)_{i,j}$ is an artificial dissipation. It is important to note that Eq. (26) is a spatial approximation of Eq. (24) because tensor Π is considered constant over each of the four control surfaces that define the control volume. In order to calculate $F\left(\overline{\mathbf{U}}\right)_{i,j}$, the flux of tensor Π trough the control surfaces must be calculated. The explicit form of this calculation as well as the implementation of the artificial dissipation, $D\left(\overline{\mathbf{U}}\right)_{i,j}$, is given by Bobenrieth Miserda and Mendonça (2005).

In order to advance Eq. (26) in time, a third-order Runge-Kutta is used as proposed by Shu (Yee, 1997). This yield to

$$\overline{\mathbf{U}}^1 = \overline{\mathbf{U}}^n - \frac{\Delta t}{V_{i,j}}\left[F\left(\overline{\mathbf{U}}^n\right) - D\left(\overline{\mathbf{U}}^n\right)\right] + \Delta t\, \overline{\mathbf{R}}^n, \tag{27}$$

$$\overline{\mathbf{U}}^2 = \frac{3}{4}\overline{\mathbf{U}}^n + \frac{1}{4}\overline{\mathbf{U}}^1 - \frac{1}{4}\left\{\frac{\Delta t}{V_{i,j}}\left[F\left(\overline{\mathbf{U}}^1\right) - D\left(\overline{\mathbf{U}}^1\right)\right] + \Delta t\,\overline{\mathbf{R}}^1\right\}, \tag{28}$$

$$\overline{\mathbf{U}}^{n+1} = \frac{1}{3}\overline{\mathbf{U}}^n + \frac{2}{3}\overline{\mathbf{U}}^2 - \frac{2}{3}\left\{\frac{\Delta t}{V_{i,j}}\left[F\left(\overline{\mathbf{U}}^2\right) - D\left(\overline{\mathbf{U}}^2\right)\right] + \Delta t\,\overline{\mathbf{R}}^2\right\}. \tag{29}$$

As used in this work, the numerical method is fourth-order accurate in space and third-order accurate in time.

4. Results

For all cases studied in this work the Reynolds number is 10,000, and the characteristic length is the chord of the airfoil, c^*. The Mach number of the free flow is 0.80 and the angle of attack is 0 degrees. A c-grid is used, where 920 control volumes discretize the airfoil surface. The smallest grid size is $5.0\text{x}10^{-4}c^*$, and it is located at the leading-edge surface. The grid extends $10c^*$ in the upper and lower normal directions, and approximately $10c^*$ in the upstream and downstream directions. The total number of control volumes for this grid is 324,000, resulting in a problem with 1,296,000 degrees of freedom.

Four cases are studied. For the first case the airfoil is studied with no plunging motion. From the second to the fourth case, the reduced frequencies for the plunging motion, w_y, are the same and equal to 11.33. This value results in motions with a frequency equal to the vortex-emission frequency of the static case for this airfoil in 0° of angle of attack, obtained in the first case. The amplitudes used in the second, third and fourth cases are respectively 2.5%, 13.0% and 22% of the chord, which gives an maximum reference Mach number (resultant of the sum of the free flow velocity and the plunging velocity), M_{ref}, of 0.81, 1.0 and 1.3, respectively.

The visualizations presented on this work are the nondimensional magnitude of the density gradient, called *pseudo-Schlieren* in order to be compared with experimental gradient visualizations, called *Schlieren* visualizations. The density gradient was chosen in order to emphasize the high compressible nature of the cases. The pressure gradient and the temperature gradient are very similar, except by the intensity of some phenomena.

Figure 1 shows a region of the computational domain in conjunction with a magnified view showing the resolution of the computational grid at the trailing edge, which has the same order of resolution at the leading edge.

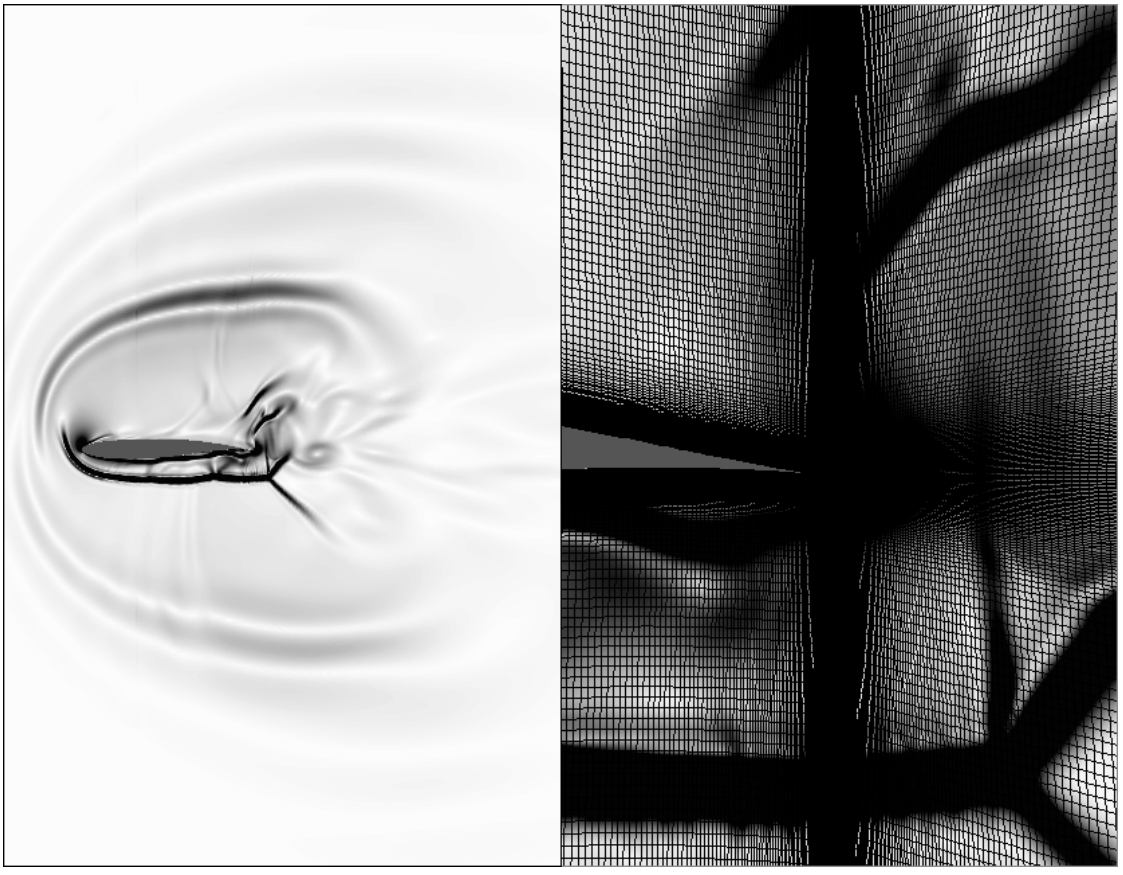

Figure 1. Flow visualization for $A_y = 0.22$. The variable plotted is the nondimensional magnitude of the density gradient. White corresponds to 0.0 and black to 10.0.

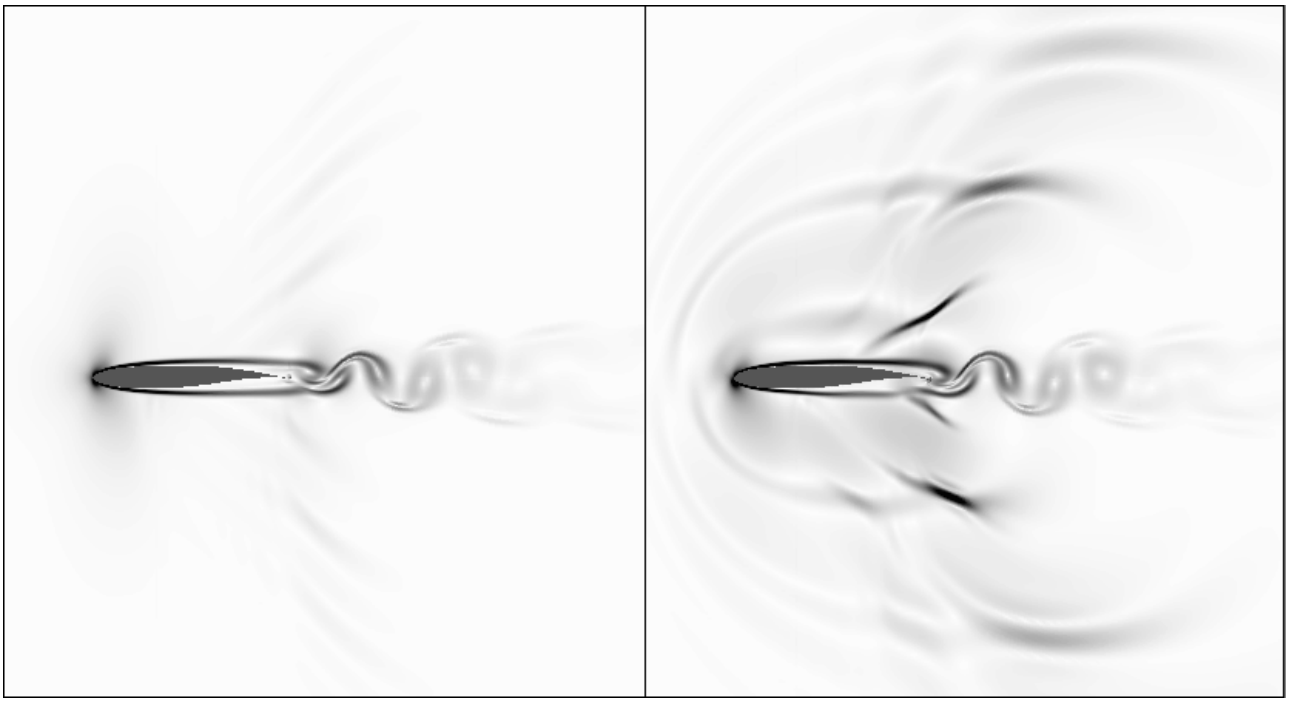

Figure 2. Flow visualization for $A_y = 0.0$ (left) and $A_y = 0.025$ (right). The variable plotted is the nondimensional magnitude of the density gradient. White corresponds to 0.0 and black to 6.0.

Figure 2 shows the visualization for an instant of the static and 2.5% plunging motion. In both cases, the visualization shows some aeroacoustic waves generated by the vortex emission at the trailing edge. In the plunging case (right), the visualization shows some acoustic waves due to the oscillation of the body and some lambda shock waves of short lifetime which appears near the trailing edge, that loose energy and becomes aeroacoustic waves propagating on the field with the plunging acoustic waves. In both cases, the skew-symmetric vortex street is very we ll defined.

Figure 3. Flow visualization for $A_y = 0.13$ (left) and $A_y = 0.22$ (right) for an instant of downward velocity. The variable plotted is the nondimensional magnitude of the density gradient. White corresponds to 0.0 and black to 10.0.

Figure 3 shows the visualization for an instant of downward velocity of the 13% and 22% plunging motions. In both cases, the visualization shows shock waves, emitted by the oscillation of the body, they loose energy and become acoustic waves propagating on the field, as well as some lambda shocks, near the trailing edge, and connecting shocks,

between the vortexes emitted at the downstream. Those very different characteristics of the flow cause some variation at the lift and drag coefficients as shown next.

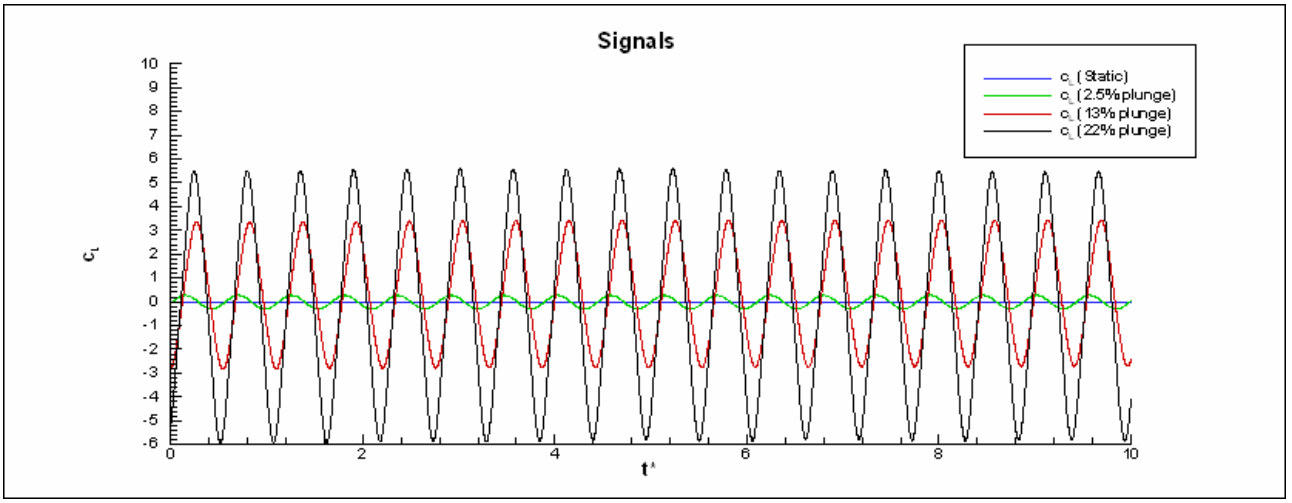

Figure 4. Unsteady lift coefficients as function of time. The blue, green, red and black colors correspond to the static, 2.5%, 13% and 22% of plunge cases, respectively.

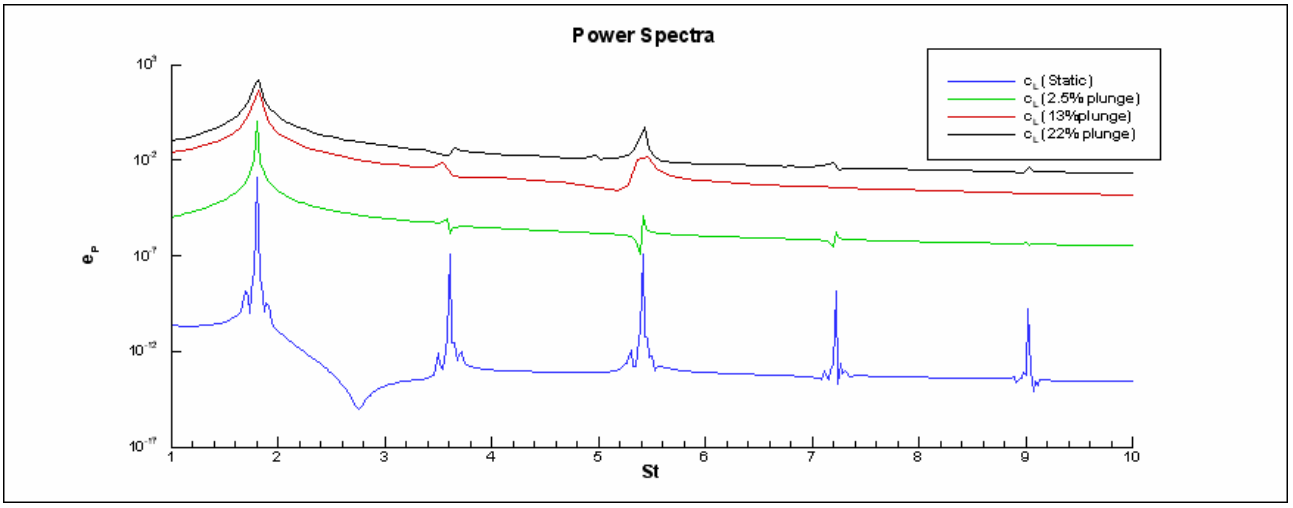

Figure 5. Power Spectra for the unsteady lift coefficients.

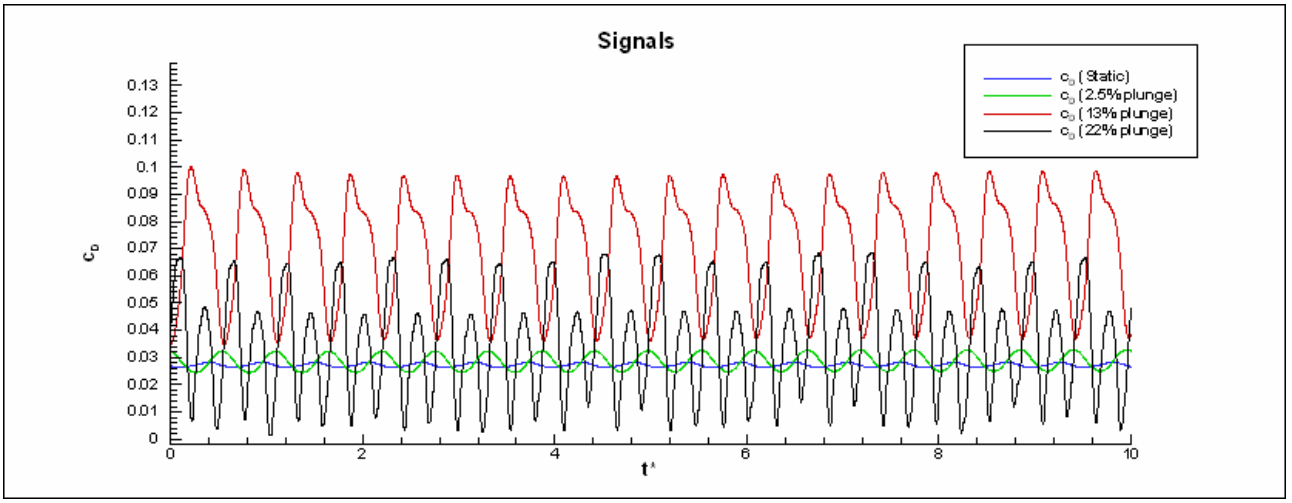

Figure 6. Unsteady drag coefficients as function of time. The blue, green, red and black colors correspond to the static, 2.5%, 13% and 22% of plunge cases, respectively.

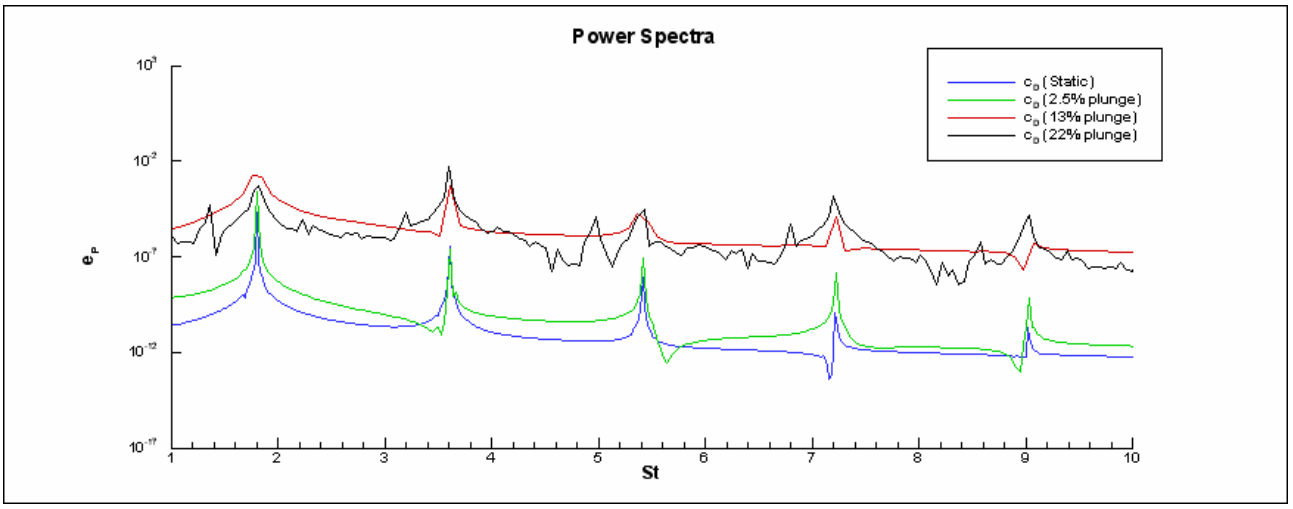

Figure 7. Power Spectra for the unsteady drag coefficients.

As the lift coefficient signals show, the variation of amplitude of the plunging motion seems to only change the amplitude of the lift coefficient fluctuation, keeping the mean value of the lift coefficient the same as its frequency of fluctuation. The power spectra show that there is one characteristic frequency and sub-harmonics of same values on the four cases studied. It shows also that all the cases are non-chaotic, in the lift coefficient point of view. But as the drag coefficient signals show, the behavior of the system changes drastically between the cases two and three.

In the first two cases, the mean value of the drag coefficient is the same, as well as the frequency of its fluctuation. The curves look like sinusoidal ones and are non-chaotic. There is one main value of frequency, with sub-harmonics, which are the same for both cases.

In the third case, the mean value of the drag coefficient rises considerably, as well as its fluctuation. There is still one main frequency, which is the same of the first two cases, and sub-harmonics. The curve is still non-chaotic, but it does not look like sinusoidal anymore.

In the fourth case, the mean value of the drag coefficient is reduced. There are two main frequencies, the power spectra show that the first one has the same value of the other cases and the second one is twice the value of the first one, but this frequency has more energy than the first one. There is also a broader distribution of the energy in the power spectrum, but with peaks on those two frequencies and their sub-harmonics, showing a pre-chaotic behavior.

5. Conclusions

A methodology is proposed in order to simulate the transonic laminar flow around the BGK-1 airfoil with imposed plunging motions, some with considerable amplitudes. It is based on the methodology proposed by Bobenrieth Miserda and Mendonça (2005), with the addition of pseudo-force and pseudo-work terms in the momentum and energy equations, respectively, in order to solve the system of governing equations from a non-inertial frame of reference which is moving with the airfoil, as proposed by Bobenrieth Miserda *et al.* (2006).

The dynamic response of the system is different when it is referenced to the lift coefficient to when it is referenced to the drag coefficient. When the lift coefficient is in sigh, there is no greater change when the amplitude is increased, causing just an increase on the fluctuation of the mean value, which was kept the same for all the cases studied. This simple change did not correspond to a very different nature of the flows, as seen on the visualizations, which gave the idea to investigate the signals of the drag coefficient.

When the drag coefficient is in sigh, the cases could be separated in two groups. In the first group of cases (the first and second cases), the increase of amplitude did only increase the fluctuation of the mean value of the drag coefficient, which was the same response seen at the lift coefficient study. But in the second group of cases (the third and fourth cases), the dynamic response became very different. In the third case, the mean value has increased and the curve was not sinusoidal anymore. In the fourth case, the mean value has decreased and other frequencies appeared in the response.

These differences may be related to the fact that in the third case, the reference Mach number is sonic, increasing the supersonic regions, as well as the number of shock waves, in many directions of the flow-field, such as connecting shocks, lambda shocks and other shock waves and phenomena. The appearance of those new shock waves in other directions and the level of energy associated to those flows may be also some reasons of these differences, which caused those differences on the drag coefficient dynamic response.

6. References

Anderson, D.A., Tannehill, J.C. and Pletcher, R.H., 1983, "Computational Fluid Mechanics and Heat Transfer", Hemisphe Publishing Corporation, New York.

Batchelor, C.K., 1983, "An introduction to Fluid Dynamics", University Press, Cambridge.

Bobenrieth Miserda, R.F., Jalowitzki, J.R., Lauterjung Q., R., and Mendonça, A.F. de, 2004, "Numerical Simulation of the Laminar Transonic Buffet in Airfoils", 10th Brazilian Congress of Thermal Sciences and Engineering – ENCIT 2004, CIT04-0609, Rio de Janeiro, Rio de Janeiro.

Bobenrieth Miserda, R.F., and Mendonça, A.F. de, 2005, "Numerical Simulation of the Vortex-Shock Interactions in a Near-Base Laminar Flow", AIAA 43rd Aerospace Sciences Meeting and Exhibit, AIAA 2005-0316, Reno, Nevada.

Bobenrieth Miserda, R.F., and Carvalho, A.R., 2006, "On the Effect of the Plunging Velocity over the Aerodynamic Forces for an Airfoil in Subsonic Laminar Flow", AIAA 44th Aerospace Sciences Meeting and Exhibit, AIAA 2006-0453, Reno, Nevada.

Bobenrieth Miserda, R.F., and Leal, R.G., 2006, "Numerical Simulation of the Unsteady Aerodynamic Forces over a Circular Cylinder in Transonic Flow", AIAA 44th Aerospace Sciences Meeting and Exhibit, AIAA 2006-1408, Reno, Nevada.

Bobenrieth Miserda, R.F., Lauterjung Q., R., and Jalowitzki, J.R., 2006, "On the Effect of the Plunging and Pitching Motions over the Dynamic Response of an Airfoil in Transonic Laminar Flow", AIAA 44th Aerospace Sciences Meeting and Exhibit, AIAA 2006-0452, Reno, Nevada.

Guimarães, R., and Silva, T., 2005, "Simulação Numérica do Escoamento Transônico Laminar em Aerofólios com Oscilação Angular", Relatório de Projeto de Graduação, Departamento de Engenharia Mecânica, Universidade de Brasília, Brasília, Distrito Federal.

Lauterjung Q., R., Jalowitzki, J.R., and Bobenrieth Miserda, R.F., 2005, "Numerical Simulation of the Transonic Laminar Flows in Airfoils with Pitching and Plunging Motion", 18th International Congress of Mechanical Engineering – COBEM 2005, COBEM2005-2431, Ouro Preto, Minas Gerais.

Yee, H.C., 1997, "Explicit and Implicit Multidimensional Compact High-Resolution Shock-Capturing Methods: Formulation", Journal of Computational Physics, Vol. 131, pp. 216-232.

7. Copyright Notice

Proceedings of the 11th Brazilian Congress of Thermal Sciences and Engineering -- ENCIT 2006
Braz. Soc. of Mechanical Sciences and Engineering -- ABCM, Curitiba, Brazil,- Dec. 5-8, 2006

Paper CIT06-0740

ASPECTS OF ISOLATED NACELLES NEAR THE GROUND DURING CROSSWIND OPERATION

Luís Gustavo Trapp
Empresa Brasileira de Aeronáutica S.A. – EMBRAER
Av. Brigadeiro Faria Lima, 2170
12227-901 São José dos Campos - SP
email: Gustavo.Trapp@embraer.com.br

Henrique Gustavo Argentieri
Empresa Brasileira de Aeronáutica S.A. – EMBRAER
Av. Brigadeiro Faria Lima, 2170
12227-901 São José dos Campos - SP
email: Henrique.Argentieri@embraer.com.br

Francisco José de Souza
Empresa Brasileira de Aeronáutica S.A. – EMBRAER
Av. Brigadeiro Faria Lima, 2170
12227-901 São José dos Campos - SP
email: Francisco.Souza@embraer.com.br

Roberto da Motta Girardi
Instituto Tecnológico da Aeronáutica - ITA
Praça Marechal Eduardo Gomes, 50
2228-900 – São José dos Campos – SP
email: Girardi@ita.br

Jet aircraft operation on the ground is affected by wind and the aircraft engines are particularly affected by crosswinds and tailwinds. Some aspects of the crosswind operation are the inlet sepation and the vortex that forms between the engine inlet and ground at very low to zero aircraft speeds. This ground vortex is created by the interaction between the inlet flow and the crosswind, can suck foreign objects into the engine and damage it and also affect engine operability. Ground vortices have been widely studied since the 1950s, more recently CFD tools have been applied to their understanding with relative success. The present study analyze some aspects of the nacelle operation with crosswinds near the ground, involving the inlet ground vortex and its visualization and some factors that influence vortex strength and inlet lip separation.

Keywords: propulsion, CFD, crosswind, operability, engine, nacelle, visualization techniques, post-processing

1. Introduction

Aircraft operation on the ground can be adversely impacted by wind, particularly when the wind is not frontal. Crosswind impacts all aspects of an aircraft ground operation: start, taxiing, takeoff and landing. Aircraft start is mainly affected by tailwind because it may drive the engine rotors to rotate opposite to its normal direction, however if the winds are too great it is always possible to reorient the aircraft with its nose into the wind before starting the engines. Crosswind affects taxiing in a lesser way: aircraft lift and speed are not great, engine speed is also low therefore the aircraft is usually controllable by the nose steering; engine behavior is normally not much affected by crosswinds at low engine speeds. Crosswind landings can affect the aircraft during approaches by wandering it off to the runway side, by leading it to asymmetric touchdowns and by the weather vaning effect after touch down and thrust reverser operation.

During crosswind takeoffs the aircraft has a weather vaning tendency and controllability may be difficult during initial phases of takeoff due to low vertical tail efficiency at low speed. It is during takeoffs that crosswind has a greater effect on the engine, mainly when the aircraft is static at the runway threshold at high power, just before brake release and the takeoff roll.

A high power static engine is affected by crosswind in at least three different ways: fuselage vortex shedding, inlet separation and ground vortex. These phenomena generate a non-uniform flow for the inlet that affects the engine operation and may even affect its physical integrity. This non-uniform flow ingested by the inlet is generally referred to as “inlet distortion” or more simply “distortion”.

Effects of distortion on the engine have been studied extensively and aircraft and engine manufacturers are able to assess its effects on fan blade vibratory stresses through standard procedures (SAE, 1999). However most of the research has been made to correctly simulate flight conditions distortion on test benches and isolated inlets (Beale et alii, 2002).

Engine operation on the ground induces inlet flow far below sonic values, however if crosswind exists the flow speed on the inlet internal surface can become locally supersonic (Boles and Stockmann, 1979) and induce inlet separation, which is a major source of inlet distortion.

Another issue raised on crosswind operation is the vortex that forms between the engine inlet and ground at very low to zero aircraft speeds. This ground vortex, created by the interaction between the inlet flow and the crosswind, can suck foreign objects into the engine and damage it, also affecting engine operability.

According to Yadlin and Shmilovich, 2006, the angular momentum due to the turning of the flow into the engine inlet in combination with the stagnation streamline off the ground plane leads to the creation of the ground vortex, in a mechanism that can be usually considered as an inviscid phenomenon.

CFD tools have been applied recently to the understanding of the ground vortex with relative success. Nakayama and Jones, 1999, used panel methods to simulate the inlet and ground interaction, noting that the wind speed needed to blow the vortex away was lower than the measured experimentally; Navier-Stokes calculations, on the other hand, were beyond the available computational capability at the time due to the refined grid needed to capture the vortex. Tourette, 2002, performed N-S analysis of an isolated nacelle near the ground with different turbulence models and was able to get a good comparison of static pressure over the nacelle lip with experimental results, however fan face inlet distortion, vortex intensity and location were less accurate. Yadlin and Shmilovich, 2006, performed CFD N-S analysis of installed nacelles on a high wing aircraft, also taking into account the effect of the thrust-reverser.

The present study analyze some aspects of the nacelle operation with crosswinds near the ground, involving the inlet ground vortex and its visualization and some factors that influence vortex strength and inlet lip separation.

2. Test case

In order to study the inlet vortex interaction with the ground it was chosen to use the DLR F6 nacelle (DLR, 2003), a wind tunnel model long duct nacelle from the wing-body-pylon-nacelle configuration used on the AIAA Drag Prediction Workshops. This nacelle has a publicly available lofting and is originally a through-flow nacelle (TFN), it was modified to better represent a real engine, incorporating outlet and inlet boundary conditions (Figure 1).

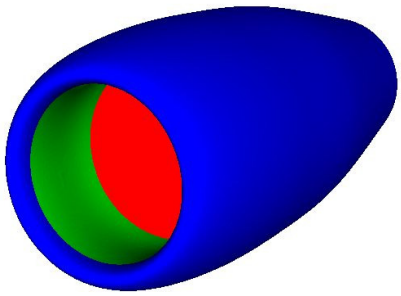

Figure 1 – DLR F6 long duct nacelle

Geometrical parameters of the DLR-F6 nacelle are given on Table 1

Table 1 – DLR-F6 nacelle dimensions

	Dimension (mm)
Length	180.0
Hilite Diameter	55.1
Inlet Throat Diameter	49.4
Fan Diameter	54.8
Max Diameter	76.2
Exhaust Diameter	50.0

Major inlet parameters that impact engine operation are the inlet diffuser ratio and the inlet contraction ratio. The inlet diffusion ratio is the ratio between the fan diameter and the inlet throat; it influences the flow speed that the fan will operate. The diffusion ratio will also impact the inlet length because the expansion shall be smooth enough to avoid separation. The inlet contraction ratio is defined as the ratio between the inlet hilite and the inlet throat areas and dictates the nacelle flexibility to ingest flows that are not aligned with its inlet (i.e. flight at high angles of attack, sideslips, crosswind operation on the ground, etc.). This DLR-F6 nacelle design parameters are given on Table 2.

Table 2 – DLR-F6 nacelle design parameters

Diffusion ratio	1.1
Contraction ratio	1.24

Boles and Stockmann, 1979, have determined that inlet peak Mach numbers between 1.4 and 1.6 induce separation and these are a direct function of the inlet contraction ratio, the lower the contraction ratio the greater the chance of separation when the flow is misaligned with the inlet. However a high contraction ratio inlet, despite its benign crosswind characteristics, has, at cruise operation, higher spillage, which increases external drag – therefore the contraction ratio has to be balanced to fulfill both ground and cruise requirements.

Other factors that influence the inlet lip Mach number during aircraft ground operation are the inlet mass flow (function of engine thrust setting), wind speed and wind direction relative to the inlet.

In order to assess the behavior of the nacelle near the ground a typical condition was set: sea level, aircraft static, ISA day, 90° crosswind and fan face with 90 000 Pa absolute static pressure. Crosswind effects were evaluated between 5 and 30 knots speeds (between 2.6 and 15.4 m/s). The nacelle was positioned at a distance between hilite (i.e. the leading edge of the nacelle) and the ground equal to the hilite radius.

It is important for the engine that the nacelle operates in crosswind conditions without flow separation. The DLR F6 nacelle was designed for cruise analysis and does not have a contraction ratio compatible with high crosswinds. In order to proceed with the study its contraction ratio was modified to a 1.34 ratio to make it more resistant to high crosswind levels, keeping all other geometrical parameters the same. The new nacelle was designated DLR F6 MOD1.

3. Numerical setup

The compressible, three-dimensional Navier-Stokes equations were solved by the commercial code CFD++ 5.2. For the turbulence modeling, a RANS (Reynolds-Averaged Navier-Stokes) approach was adopted, and the realizable k-epsilon model was employed. Advanced wall functions available in CFD++ were used at all wall surfaces. A hybrid tetrahedra-prism mesh was generated with the commercial code ICEM 10.0 for the viscous runs, while a simpler tetrahedral mesh was used on the Euler initial runs. The grids for the isolated nacelle contained nearly 5 million elements in the hybrid case and 3 million in the tetrahedral case. The parameter y+, which is important in evaluating the ability of the grid to capture near-wall effects, was below 10 in all viscous cases.

4. CFD Results

4.1. Vortex visualization

The inlet vortex is a low pressure, high vorticity, high speed flow that is ingested by the engine inlet. However the physical phenomenon around a static inlet near ground is more complex than only a vortex: high levels of vorticity are generated by the wind on all walls, vortex shedding is triggered leeward of the nacelle and low pressure is generated inside the engine inlet by the engine. Therefore it is difficult to isolate the ground vortex from the other phenomena.

A major issue during the CFD results post-processing was to define a methodology to correctly capture and isolate the ground vortex. Different post-processing criteria were evaluated and are presented in this section. Some criteria simply deal with the basic scalar results; other methods involve operations with the vectors, while some work also with the geometrical cell characteristics.

On the vortex core there is a low pressure region and an obvious post-processing choice is to detect the vortex with a static pressure isosurface. Figure 2 shows CFD results of a 20 knots crosswind upon the nacelle through a pressure isosurface of 99 500 Pa. The vortex boundaries near the ground can be seen, however as the vortex approaches the inlet the negative pressure is increased due to engine suction and hid the vortex, making this kind of post processing unsuitable for vortex tracking. Also in figure 2 the ground is colored by static pressure intensity, the center of the vortex can then be seen on the ground.

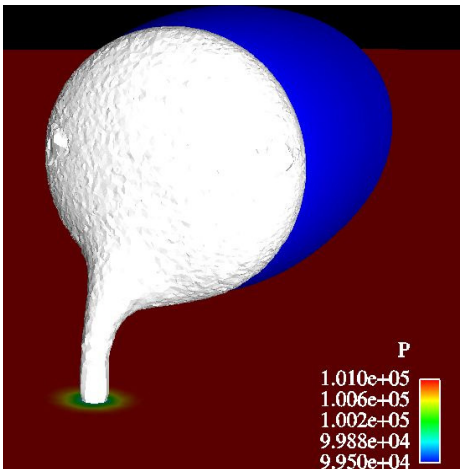

Figure 2 – Isosurface of low pressure near the nacelle inlet

Figure 3 shows the same case and a high vorticity isosurface. Near the walls, as expected, the speeds are higher and therefore more vorticity is created, rough contours of the vortex can be seen in the same location where the pressure isosurface showed it. The inlet region is visible; however the vorticity isosurface does not get far into it, not reaching the fan.

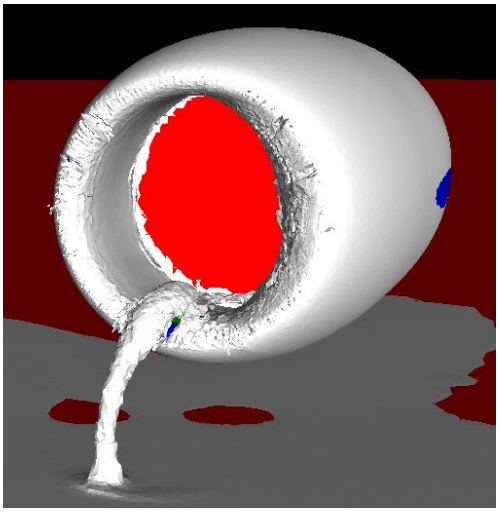

Figure 3 – Isosurface of vorticity near the nacelle inlet

Another choice is to use relative helicity (Ensight, 2005) or normalized helicity (Sadarjoen et alii, 1998) - h_n, which is the defined as:

$$h_n = \frac{\vec{v} \cdot \vec{\omega}}{|\vec{v}| \cdot |\vec{\omega}|}$$

Where $\vec{v}$ is the velocity vector and $\vec{\omega}$ the vorticity vector. Relative helicity represents the cosine of the angle between flow velocity and vorticity. Isosurfaces of highest (yellow) and lowest (white) helicity are depicted on figure 4, but do not capture the ground vortex. It seems that while the ground vortex vorticity is high, the resulting flow velocity in the suction direction is not. Therefore, when comparing the ground vortex region to other areas on the domain the vortex is not easily distinguishable.

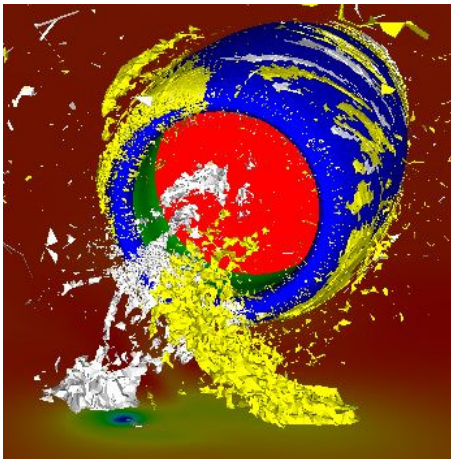

Figure 4 – Isosurfaces of helicity near the nacelle inlet, h_n=0.995 (yellow) and h_n=-0.995 (white)

The function λ_2 (Jeong and Hussain, 1995) is defined as the second largest eigenvalue of the tensor $S^2 + \Omega^2$, where $S = \frac{1}{2}(\vec{\nabla}\vec{v} + (\vec{\nabla}\vec{v})^T)$ and $\Omega = \frac{1}{2}(\vec{\nabla}\vec{v} - (\vec{\nabla}\vec{v})^T)$.

Negative results of λ_2 indicate vortical regions and are shown on Figure 5. They show a approximate location for the vortex, but discontinuous, with spurious regions also selected together with most of the nacelle inlet wall.

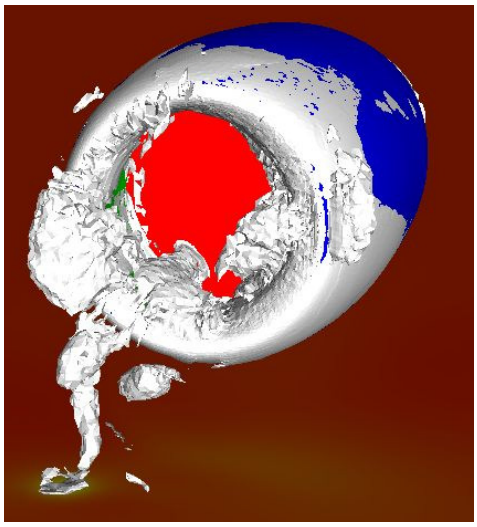

Figure 5. – isosurface of λ_2 equal -8.10^5

The function Q (Jeong and Hussain, 1995) is the second invariant of the velocity gradient tensor $\nabla\vec{v}$:

$$Q = \tfrac{1}{2}\left(|S|^2 - |\Omega|^2 \right)$$

If the velocity is taken in index notation ($v_{i,j}$) then the function becomes:

$$Q = -\frac{1}{2}\left(v_{i,j}v_{j,i}\right)$$

Regions of Q function positive indicate vortical regions, which are shown on fig. 6. This method shows lots of improvement when compared with the λ_2 method, showing an almost continuous vortex, but still including the inlet wall region.

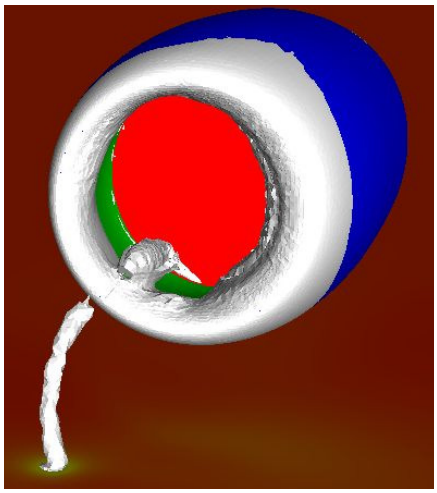

Figure 6 – isosurface of Q equal 10^7

The vortex cores function from Ensight was then tested (Ensight, 2005). It helps visualize the centers of swirling flow by creating vortex core segments from the velocity gradient tensor of the flow field. Results for vortex core visualization are shown on fig. 7 together with the ground static pressure isosurface.

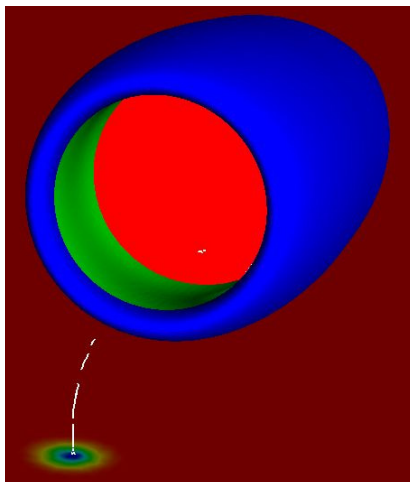

Figure 7 - vortex cores on the engine inlet

The vortex cores showed to be much better on vortex characterization – the ground vortex being much more intense than other vertical phenomena like vortex shedding and wall vorticity. However the vortex core visualization involves some operations that need to be performed within the mesh grid, which is difficult to implementate on a commercial post-processing code, if it does not includes this feature.

The vortex core algorithm also has problems finding cores of curved vortices and usually fails to predict vortex core segments in regions of weak vortices (Ensight, 2005). The latter problem does not impact the ground vortex identification because it is supposed to be the stronger vortex on the system. The curved vortices un-identification seems to be affecting the visualization because the vortex is not captured approximately on the region where it is turning more steeply into the engine. However a turn around to this problem is to release particle traces from the vortex core which will approximately show the vortex path.

4.2. Influence of viscosity

Once a approximate method of vortex visualization was defined another aspects of the nacelle operation with crosswinds could be studied, initially with an inviscid fluid.

Initial CFD runs were performed with 30 kts crosswind and showed separation. Also this wind intensity blew the inlet vortex away and avoided it from attaching to the ground. Similar results occurred with a 15 knots crosswind and can be seen on Fig 8, where the nacelle wall and pressure outlet are colored by Mach intensity and vortex cores are depicted on the left of the nacelle. Wall separation is seen in the low Mach number contours on the pressure outlet. The maximum Mach number on the nacelle lip was of the order of 0.80.

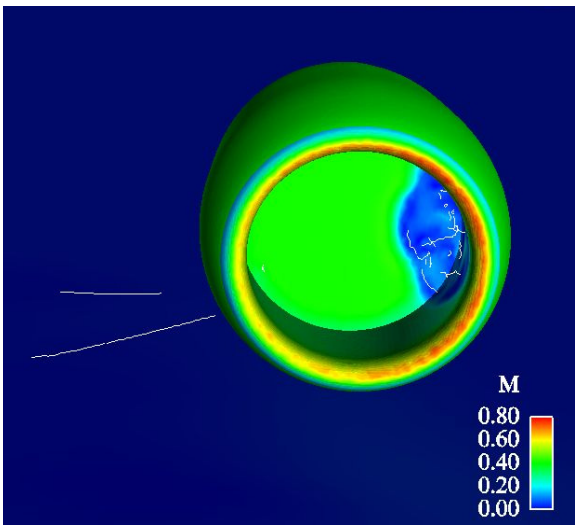

Figure 8 – Mach number isocontours on the nacelle and fan surfaces and vortex cores at 30kts crosswind

The crosswind was subsequently reduced to 5kts and the results are depicted on figure 9: there is no inlet separation and the ground vortex is visible. Mach number on the inlet is close to sonic. The ground is colored by pressure isocountours, where a low pressure region can be seen where the vortex hits it.

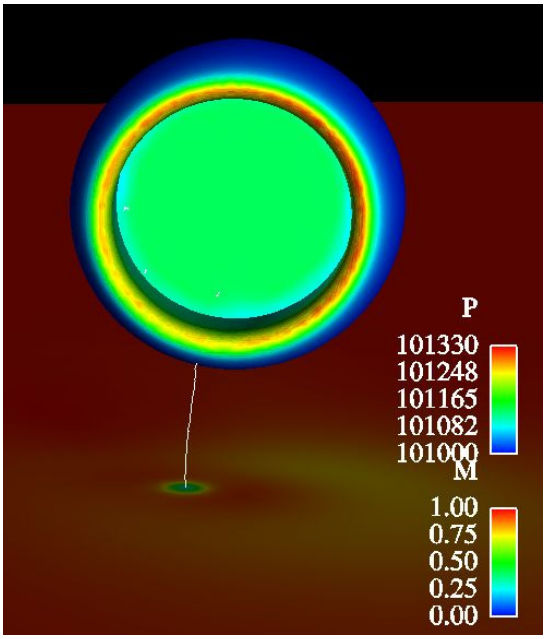

Figure 9 – Mach number isocontours on the nacelle and fan surfaces, vortex cores and static pressure isocountours on the ground at 5 kts crosswind

The vortex detachment from the ground with 15kts cross was unexpected. It was then decided to compare the effects of viscosity on the vortex behavior more directly and cases were run viscous and inviscid at 20kts crosswind, Results for these cases can be seen on fig.10 without and with viscosity respectively. Although both cases exhibit inlet separation the Euler case shows a vortex that does not attach to the ground, the viscous case has a vortex attached to the ground.

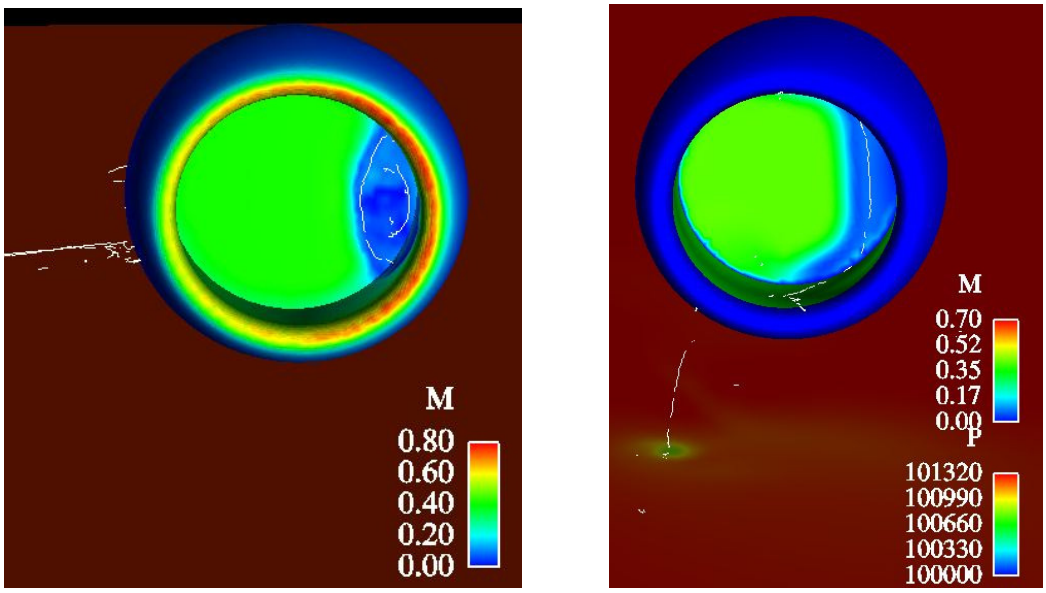

Figure 10 – Mach number isocontours on the nacelle and fan surfaces, vortex cores and static pressure isocontours on the ground at 20 kts crosswind, Euler and Navier-Stokes calculations respectively.

Besides the marked difference on the ground vortex behavior, the separation region has a different shape which can be seen through the lower pressure region on the fan face. It is clear that the viscosity plays an important role on both vortex and separation phenomenon and can not be disregarded.

4.3. Lip cross-section

Results of the DLR F6 MOD1 nacelle were compared with results from other applications with similar contraction ratios. At equivalent winds and engine thrust the DLR F6 MOD1 nacelle had inlet separation, while other nacelles did not. It was then clear that other factors influenced separation. Other geometrical parameters where then analyzed, among them the inlet lip leading edge shape: it was modified from a circular leading edge to an elliptical cross section. Results for a 30 kts crosswind for this MOD2 nacelle are shown on Figure 11.

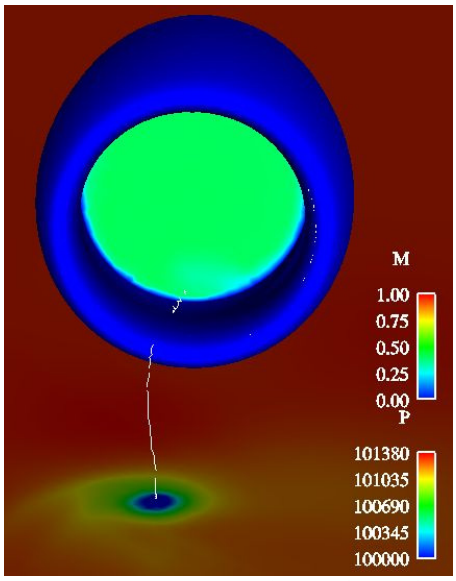

Figure 11 – Mach number isocontours on the MOD2 nacelle and fan surfaces; vortex cores and static pressure isocontours on the ground at 20 kts crosswind.

The fan surface Mach number, on figure 11, indicates that the inlet is not separating anymore; showing that, besides the contraction ratio, the inlet lip geometry also influences inlet separation. Another interesting results, comparing the static pressure on the ground of figures 10 and 11 is that the separated nacelle vortex is less strong than the attached nacelle. This indicates that the highest probability of foreign objects ingestion by the engine is not necessarily with the highest wind intensity if the nacelle inlet lip flow separates at some point.

5. Conclusions

Ground vortex visualization still do not have appropriate tools available, none of the methods used was capable of fully detect the vortex. Among the methods tested the vortex core presented the best results.

Comparison between viscous and inviscid calculations showed different results, with the vortex in the inviscid calculation detaching from the ground at a lower crosswind speed and the inlet separation pattern different than the viscous analysis. The vortex phenomena is usually considered to be inviscid, however the interaction of the vortex with the ground shear layer has a viscous effect that needs to be taken into account, when simulating a ground vortex, to represent correctly the phenomena.

In regards to inlet separation, other geometrical parameters than the contract ratio are of influence, the lip cross-section among them. An elliptical lip cross section is less prone to separation than a circular one. Inlet separation also influences on ground vortex strength, a separated inlet vortex is less strong than an attached inlet one. Therefore its possible for a nacelle separated at high crosswinds to be less susceptible to foreign object ingestion than the same nacelle at lower crosswinds with the inlet flow attached.

6. References

Beale, D.K., Cramer K.B, King P.S., 2002, "Development of Improved Methods for Simulating Aircraft Inlet Distortion in Turbine Engine Ground Tests", Proceedings of the 22nd AIAA Aerodynamic Measurement Technology and Ground Testing Conference, 24-26 June 2002, Saint Louis, USA. AIAA 2002-3045.

Boles, M. A., Stockmann, N. O., 1979, "Use of Experimental Separation Limits in the Theoretical Design of V/STOL Inlets", Journal of Aircraft, Vol.1, No. 1, pp. 29-34.

Colehour, J.L. , Farquhar, B.W., 1971, "Inlet Vortex", Journal of Aircraft, Vol. 8, No. 1, pp. 39-43.

De Souza, F.J, De Jesus, A.B., 2006, "CFD Study of the Influence of Geometrical Parameters on Nacelle Design", Proceedings of ENCIT 2006, ABCM, Curitiba, Brazil.

DLR F6 Geommetry. 2nd AIAA Drag Prediction Workshop, 2003, http://aaac.larc.nasa.gov/tsab/cfdlarc/aiaa-dpw/Workshop2/DLR-F6-geom.html

Ensight User's Manual for Version 8.0, 2005, Computational Engineering International, Inc., Apex, EUA

Haimes, H., Jordan, K., "A Tractable Approach to Understanding the Results from Large-Scale 3D Transient Simulations", AIAA-2000-0918, Jan. 2001.

Jeong, J., Hussain, F., 1995, "On the identification of a vortex". Journal of Fluid Mechanics, 285, pp. 69-94

Johns , C. J., 2002, "The Aircraft Engine Inlet Vortex Problem", AIAA-2002-5894, 2002.

Nakayama , A., Jones , J.R., Correlation for Formation of Inlet Vortex, AIAA Journal, Vol. 37, No.4, 508-510, 1999.

SAE Aerospace Information Report, Inlet Total-Pressure-Distortion Considerations for Gas-Turbine Engines, AIR1419 Rev. A (1999).

Strawn, R., Kenwright, D., 1999, "Computer Visualization of Vortex Wake Systems", AIAA Journal, Vol. 37, No.4, pp. 511-512.

Sajardoen, A., Post, F.H., Ma, B., Banks, D.C., Pagendarm, H.G., 1998, "Selective Visualization of Vortices in Hydrodynamic Flows", IEEE Visualization, pp: 419-422.

Tourrette, L., 2002, "Navier-Stokes simulations of air-intakes in crosswind using local preconditioning", Proceedings of the 32nd AIAA Fluid Dynamics Conference and Exhibit, 24-26 June 2002, Saint Louis, USA. AIAA 2002-2739.

Yadlin, Y., Shmilovich, A., 2006, "Simulation of Vortex Flows for Airplanes in Ground Operations", Proceedings of the 44th Aerospace Sciences Meeting & Exhibit, 9-12 January, 2006, Reno, NV, USA. AIAA-2006-0056.

7. Copyright Notice

Proceedings of the 11th Brazilian Congress of Thermal Sciences and Engineering -- ENCIT 2006
Braz. Soc. of Mechanical Sciences and Engineering -- ABCM, Curitiba, Brazil,- Dec. 5-8, 2006

Paper CIT06-0781

Toward the validation of a newly developed CFD code: the case of a jet in cross flow

Luís Fernando Figueira da Silva, Fernando Oliveira de Andrade
Pontifícia Universidade Católica do Rio de Janeiro, Mechanical Engineering Department, Rua Marquês de São Vicente, 225
22453-900 Rio de Janeiro/RJ Brazil
{luisfer, fandrade}@mec.puc-rio.br

Sandro Barros Ferreira
Pontifícia Universidade Católica do Rio de Janeiro, Institute of Energy, Rua Marquês de São Vicente, 225
22453-900 Rio de Janeiro/RJ Brazil
sandro@ituc.puc-rio.br

Abstract. *During the past few years a computational fluid dynamics computer code specifically taylored for compressible aerodynamical application has been developed by a group of brazilian enterprises and universities. This code solves the transport equations of mass momentum and energy for both laminar or turbulent flows on general unstructured meshes. Several turbulence models are avaliable. The governing equations are discretized by a finite volume technique, and different central and upwind schemes may be used for computing the fluxes. Temporal discretization may be performed either by explicit or implicit schemes, multigrid convergence acceleration is available. This work describes part of the code validation effort performed. A high speed jet in cross flow configuration, for which experimental data is available, is considered. The results obtained with the different turbulence models, spatial discretization schemes are compared to the experimental data and to computational results obtained with a commercial computer code. These comparisons show that the choices of the turbulence model and of the spatial discretization scheme exert a strong influence on the computed results.*

Keywords*. Jets, computational fluid dynamics, numerical study, code validation.*

1. Introduction

Computational Fluid Dynamics (CFD) is a technique now integrated on the design phase of new aircraft. Besides the airframe itself, several subsystems of the aircraft rely on the flow of gases or liquids to perform according to the desired specifications. Among such subsystems lie the anti-icing, air conditioning and the engine. As a consequence, before it can be considered apt to using throughout the design process of the whole aircraft, any CFD tool should be thoroughly verified, and validated in circumstances representative of the functioning of these different systems. In particular, among the situations in which CFD tools are beginning to provide for innovative insights, is the operation of the thrust reversers during aircraft landing (Gatlin and Quinto, 1988, Strash, 1997, Trapp and Oliveira, 2003) and auxiliary air inlets (Pérez et al, 2006).

The present paper is related to the development of new computational tool specifically aimed at the prediction of flowfields characteristic of the aeronautical industry. This tool, which is the outcome of a partnership developed between Brazilian universities, research centers and enterprises, is tailored for the solution of compressible, turbulent, flowfields. The jets which are issued from the thrust reverser during landing are one of such flowfields of interest, and its prediction is the main motivation behind the computational results which will be presented here. However, the sheer complexity involved, where compressibility, turbulence, unsteady effects and tridimensional effects are interwoven (Andrade et al., 2006), precludes the direct use of such a configuration in code validation. Therefore, a representative situation of the thrust reverser configuration should be used in which the main physical characteristics are retained at the expense of pure geometrical complexity. In this work we have chosen the circular jet in a cross flow to represent the main flow characteristics found during thrust reverser operation.

This configuration has been calculated using the newly developed CFDk and Fluent CFD codes. The former code was under still under development, having few operational time and spatial discretization methods and turbulence models. The numerical results obtained using different turbulence models and spatial discretization options are compared to experimental data available (Margason, 1968, Schetz, 1980). A good agreement is shown to exist between the results obtained with both computer codes and the mean jet path. However, the overall jet shape and the jet breakdown patterns present some discrepancies. Before analyzing these results, a brief presentation is made of the models and the boundary conditions used.

2. Mathematical Modeling

The evolution of flowfields of interest is governed by the transport equations of mass, momentum and energy, i.e., the Navier-Stokes equations. Since the direct numerical simulation of the configuration studied is still beyond limits of

the available computational power, Reynolds averaging is used upon these transport equations. As these flow configurations involve variable density, the value of this property and of the pressure are decomposed as Reynolds (time) averages plus a fluctuation, whereas the remaining properties are treated by density-weighted (Favre) averaging. As a consequence, unclosed Reynolds stresses appear, representing correlations between the velocity fluctuations, which should be modeled. In this work four different models are used to express these unclosed terms: the Spalart-Allmaras (1992), the Shear Stress Transport (Menter, 1993), the realizable k-ε (Shih et al., 1995) and the Reynolds Stress Model (Hanjalic and Launder, 1972). It is not the purpose of this paper to detail the models employed, which are supposed to have been implemented in their classical form by the code developers. Note that the source code was not open to us at the time this work was developed. The interested reader should consult the corresponding references if the aim is to gain insight on these models. However, one should note that the Spalart-Allmaras is a one-equation modified eddy viscosity transport model which was specifically developed for aerodynamic applications. The realizable k-ε model is a recent extension on the classical k-ε model, which uses the Boussinesq hypothesis to link the unclosed Reynolds stresses to the deformation tensor through an eddy viscosity. Lastly, the Reynolds Stress Model (RSM) solves six model equations for the Reynolds stresses, supplemented by an equation for the turbulence dissipation rate, ε, and thus is not an eddy viscosity model. This model is, in principle, able to account for the production of turbulence by vorticity. It is, thus, expected that the RSM model presents the best results among the models used.

The computer codes used in this study employ different schemes to discretize the governing equations. On the one hand this is detrimental to the validation effort, since algorithm-specific issues could prevent useful conclusions to be drawn. On the other hand, if a good agreement is observed between the computed results, it could be likely that both codes correctly implement the equations.

The newly developed code, CFDk, is an edge-based, unstructured, finite volume code. Among several spatial discretization schemes available, this works uses Jameson's second order central differences and Roe's first order flux difference splitting schemes. These models were chosen since, at the time this work was performed, those were the models for which the multi-grid convergence acceleration technique was functional. The time integration technique used is a five-step Runge-Kutta scheme with second order accuracy, which was the only functional time-stepping scheme, although several others were under development. Cell based agglomeration multigrid convergence acceleration technique is used. The results obtained in this work considered three grid levels, with three interactions on the coarsest level. This code is based on previously tested algorithms (Bigarella et al., 2004, 2005), and further details can be obtained on these references.

Fluent is a general purpose commercial CFD code (Anon., 2006), which uses a pressure-based algorithm to solve the governing equations. In this work a steady state, implicit coupled solver was used. The interpolation scheme used for the convection term is the First-Order Upwind Scheme. The algorithm applied for the pressure-velocity coupling is SIMPLE.

3. Jet in Cross Flow Model

3.1 Geometrical Configuration and Computational Mesh

The configuration analyzed is based on an experimental study, which consists of a 25.4 mm diameter jet situated next to the leading edge of a flat plate, directing the flow at a perpendicular angle into a subsonic freestream (Margason, 1968). Figure 1 shows the side and top view of the model configuration. The computed geometry consists of a rectangle, with a length of 30.5 times the jet diameter; a width of 24 times the jet diameter and a height of 20 times the jet diameter. These dimensions were chosen based on the actual wind tunnel cross section.

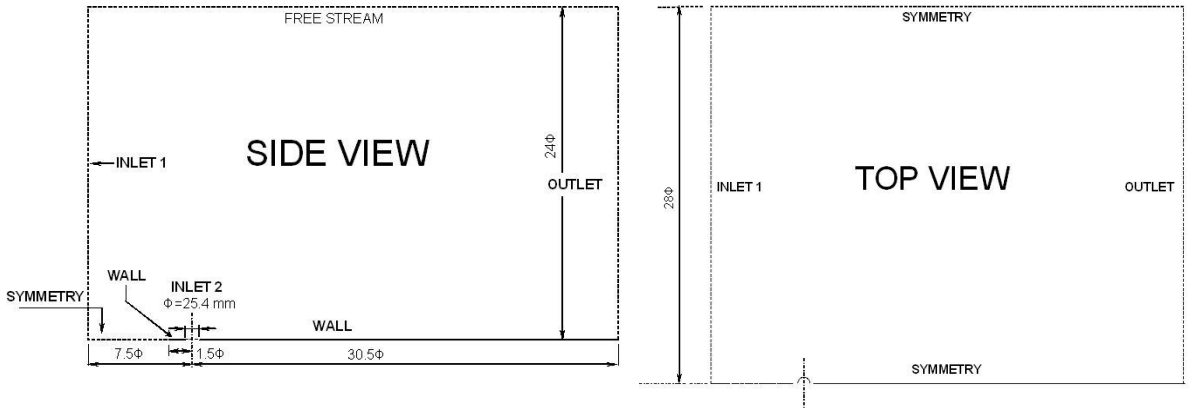

Figure 1. Side and top views of the CFDk jet in cross flow model configuration.

Figure 2 shows a perspective view of the computational mesh, which possesses approximately 400,000 elements. Results obtained with a mesh containing roughly 800,000 elements did not present significant discrepancies with respect to the coarse mesh results. Even if a detailed assessment of mesh convergence has not been attempted yet, the present mesh is considered sufficient for validation purposes. In figure 2 it can also be seen that the flow enters the INLET 1 face along the x-direction. The jet flow enters the domain at the INLET 2 and interacts with the freestream flow. The flow leaves the domain through the OUTLET face. Since no attempt was made to resolve the boundary layer which develops along the tunnel walls, symmetry is imposed on the lateral sides and on the top side of the computational domain. The bottom side is considered to be a smooth adiabatic wall. The use of symmetry conditions imply that only half of the circular jet is actually computed.

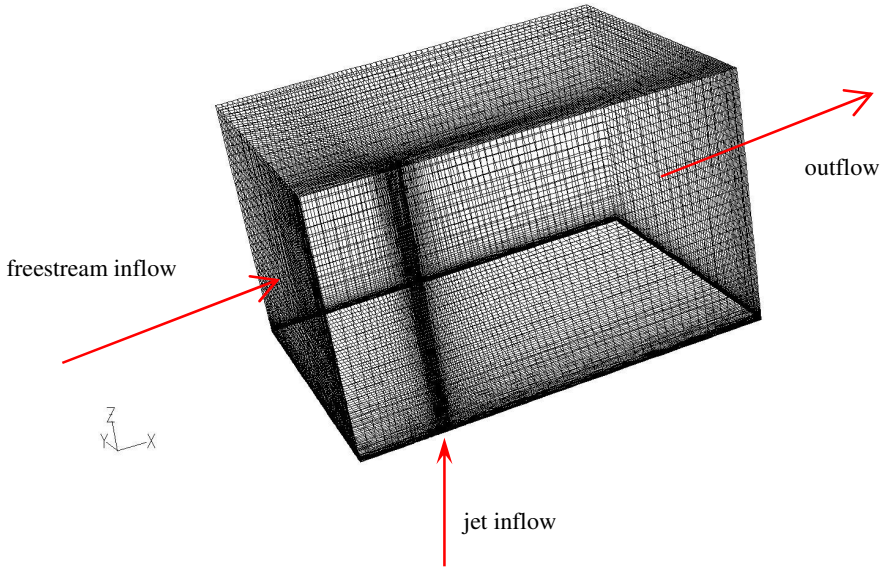

Figure 2. Perspective view of the mesh generated for the jet in cross flow application.

3.2 Boundary and Initial Conditions

The top, the sides and the symmetry plane upstream of the flat plate were assumed, for the sake of simplicity, as symmetry boundaries. The wind tunnel wall is an adiabatic no-slip stationary surface. The outflow was considered as a pressure outlet with a prescribed value of 101325 Pa. The wind tunnel inlet was considered to be a pressure inlet and corresponds to the x-axis oriented freestream entrance, where a total pressure of 103159 Pa, a static pressure of 101325 Pa, and a total temperature of 300 K were prescribed, resulting in a velocity of 67.5 m/s. The jet inlet is a z-axis oriented pressure inlet, and correspond to the jet entrance. A total pressure of 161005 Pa, a static pressure of 101325 Pa, and a total temperature of 300 K were prescribed, resulting in a jet velocity of 277.7 m/s.

The computations were initialized with the wind tunnel farfield conditions, using the data from the main air inlet.

4. Results and Discussion

This section presents the results of the jet in cross flow simulations obtained with Fluent for four different turbulence models: Spalart-Allmaras, Realizable k-ε, SST and Reynolds Stress Model. The results of CFDk using the Spalart-Allmaras model, with First Order Roe and Jameson discretization methods are also shown. Table 1 summarizes the parameters of the simulations performed with the Fluent and CFDk packages.

The numerical results are compared with experimental data available (Margason, 1968, Schetz, 1980). The comparisons are performed in terms of the path of the jet into the subsonic freestream, and in terms of the cross sectional pressure contours for five planes normal to the jet.

Table 1. Configuration of the simulations with Fluent and CFDk.

CASE	Turbulence Model	Spatial Discretization	CFD Package
JSAR	Spalart Allmaras	1 order Roe	CFDk
JSAJ	Spalart Allmaras	Jameson	CFDk
JSAF	Spalart Allmaras	1 order upwind	Fluent
JKER	k-ε realizable	1 order upwind	Fluent
JSST	SST	1 order upwind	Fluent
JRSM	Reynolds Stress Model	1 order upwind	Fluent

4.1 Jet Path Considerations

The experiment adopted for the CFDk validation used a water vapor injection flow visualization technique in order to provide for visible jet paths. In the experiments, the path of the jet perpendicular to the freestream was photographed through a range of effective velocity ratios from 0.10 to 0.83. Effective velocity V_e is defined as the square root of freestream dynamic pressure to the jet dynamic pressure

$$V_e = \sqrt{\frac{\rho_\infty V_\infty^{\,2}}{\rho_j V_j^{\,2}}}. \tag{1}$$

An empirical equation of the center line of the jet was developed, compared and validated with previous investigations. The form of this equation describes the locus of maximum pressures in the jet wake,

$$\frac{x}{D} = k\left(\frac{z}{D}\right)^a V_e^{\,b}, \tag{2}$$

where k, a and b are -0.25, 3, and 2 respectively, and D is the jet diameter. This equation is applicable up to a region of 10 to 12 diameters downstream from the jet exit.

Figure 3 shows a photograph superimposed with the empirical correlation of the jet path for a value of effective velocity V_e of 0.21, and a ratio of the jet dynamic pressure to the atmospheric pressure of 0.589. This particular experimental result is used here for validation purposes.

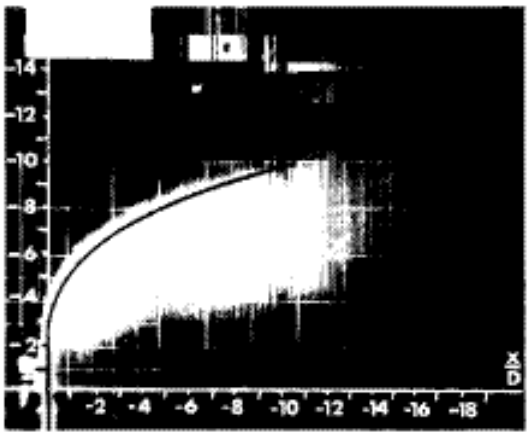

(a) V_e = 0.210; q_j/p_a = 0.589.

Figure 3. Water vapor visualization of the jet in cross flow.

4.2 Convergence of the Solutions

Figure 4 shows the residuals for the jet in cross flow simulation using Fluent with the Spalart-Allmaras (JSAF case), *k-ε* Realizable (JKER case), SST (JSST case) and Reynolds Stress (JRSM case) turbulence models, and using CFDk with the Spalart-Allmaras model, first order Roe (JSAR case) and Jameson (JSAJ case) spatial discretization methods, respectively.

The case JSAF, which used the Spalart-Allmaras turbulence model, achieved stabilization of the residuals after 10,000 iterations, however with an important oscillation. The residuals ranged between 10^{-3} for the y-velocity component to 10^{-7} for the modified turbulent viscosity. The case using the *k-ε* Realizable model achieved convergence after 5,000 iterations. The residuals ranged between 10^{-5} for the y-velocity component to around 10^{-7} for the turbulent kinetic energy. The case using the SST model achieved convergence after 6,000 iterations. The residuals ranged between 10^{-3} for the y-velocity component to around 10^{-5} for the turbulence dissipation rate. Note that the case using the Reynolds Stress model achieved convergence after 6,000 iterations, but only after the coupled solver was replaced by the segregated one at the iteration 3,000. This led all the residuals to the range of 10^{-7}, achieving a stall of convergence.

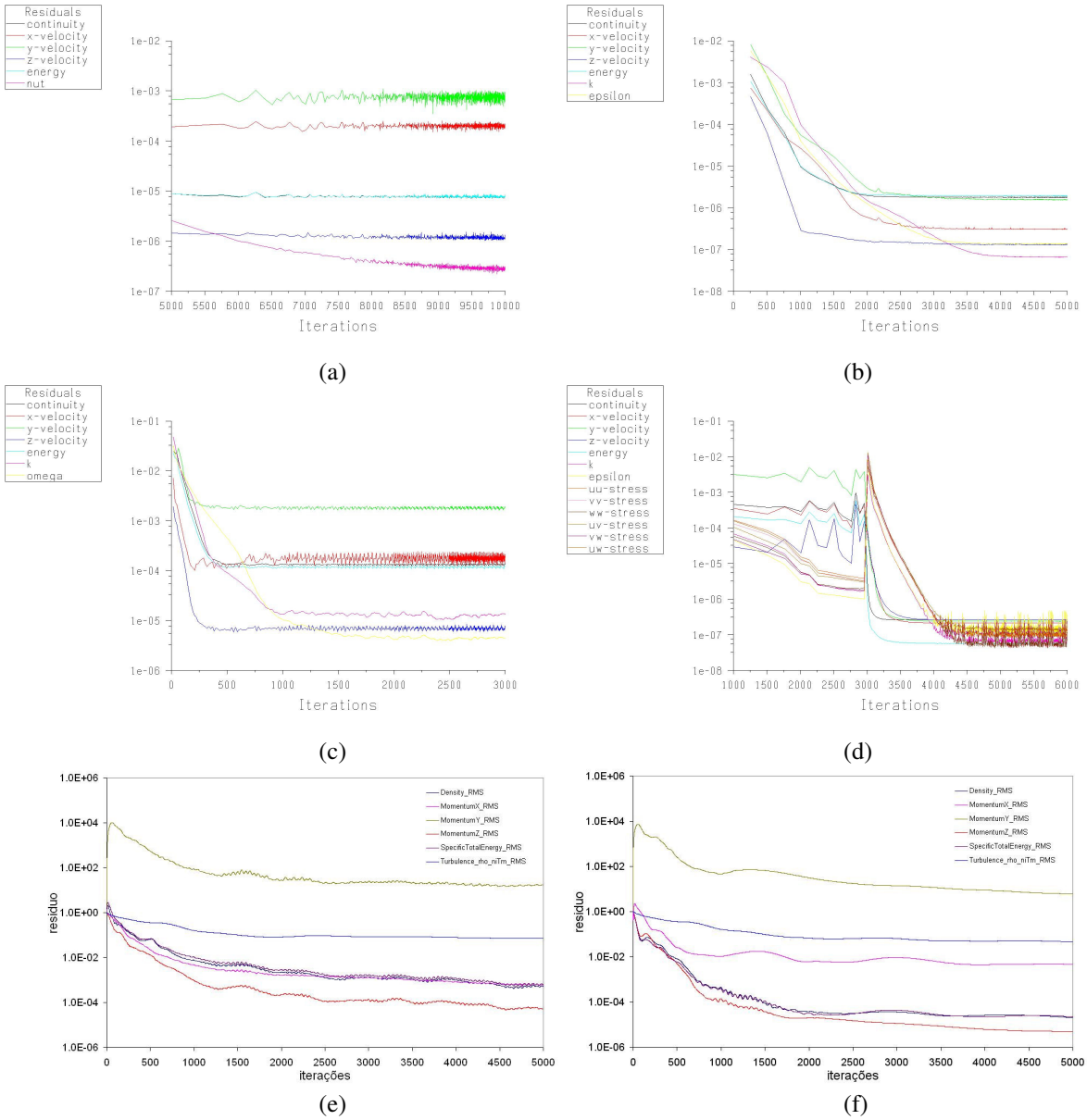

Figure 4. Evolution of the RMS values of the residuals, cases:
(a) JSAF, (b) JKER, (c) JSST, (d) JRSM, (e) JSAJ, and (f) JSAR.

For the CFDk case JSAJ, the normalized residuals became stable after 5,000 iterations. The normalized residuals for the x and z components of momentum, energy, and continuity stabilized around a value of 10^{-4}. The normalized residuals for the y component of momentum became stable at 10^{2} and the modified turbulent viscosity achieved a

steady state around 10^1. Note that, despite these high values, which are due to the normalization, there is at least a two order of magnitude decrease in the residuals for each property, with the exception of the modified turbulent viscosity.

For the JSAR case, the normalized residuals also became stable after 5,000 iterations. The normalized residuals for the x component of momentum, energy, and continuity stabilized around a value of 10^{-5}. The normalized residuals for the z component of momentum stabilized around 10^{-2}. The normalized residuals for the y component of momentum became stable at 10^2 and the modified turbulent viscosity achieved a steady state around 10^1.

4.3 Jet Path Comparisons

The jet comparisons are performed based on a high momentum experimental configuration (Margason, 1968), which corresponds to the greater ratio of the jet velocity to the freestream velocity. The calculated effective velocity is equal to 0.21 and the ratio of the jet dynamic pressure to the atmospheric pressure is 0.589.

Figures 5 and 6 show the distributions of modulus and of the x-component of momentum, respectively. The results are shown at the jet longitudinal symmetry plane for the cases using Fluent with the Spalart Allmaras, k-ε Realizable, SST and Reynolds Stress turbulence model, and using CFDk with Spalart Allmaras model with first order Roe and Jameson discretization methods. The obtained numerical results are compared to the experimental jet path available (Margason, 1968). Figure 7 shows the velocity vector distribution at the jet longitudinal symmetry plane for these cases.

Initially, it is important to note that all simulation results exhibited a good agreement with the experimental jet path, with small discrepancies related to the choice of turbulence model. Analyzing the results obtained with Fluent using the four different turbulence models, it can be noted that the Spalart-Allmaras and the k-ε Realizable models produced quite similar results. The results of the SST model differed from the former two, presenting a larger spreading around the jet centerline and a small discrepancy concentrated on the region of the jet exit. The most important differences were presented by the Reynolds Stress model, which led to a considerably different momentum distribution from the three other cases, mainly on the region downstream from the jet, where a reverse flow region is more evident. Note that the shape of the reverse flow region is more elongated in this case. According to Ibrahim and Gutmark (2006) the reverse flow region is formed as the cross flow travels around the periphery of the jet column and gets pulled back into the origin region of the jet. This occurs due to the influence of the adverse pressure gradient which results, leeward of the jet, from the blockage effect of the jet to the oncoming cross flow. The reverse flow acts to support the jet on the leeward side by inducing local upward lifting force to lift-off the jet from the wall. The strength of the reverse flow region is dependent on the extent of blockage the jet poses to the freestream. This translates into the rate of deceleration of the freestream as it travels around the jet as well as the magnitude of the adverse pressure gradient developed. In such a flow configuration, where vorticity may lead to turbulence generation, the RSM is presumably the most accurate model.

Concerning the CFDk results, it can be seen that the results of the JSAJ case are similar to those of the JRSM case, which is rather surprising and could not be expected. An explanation for the presence of a secondary plume in the JSAJ case is lacking. The use of Roe first order spatial discretization together with the Spalart-Allmaras model led to results which are quite similar to those obtained with Fluent (JSAF). However, the jet plumes computed with CFDk seem to diffuse less than those obtained with Fluent.

The development of the boundary layer along the wall is similar for the Fluent computations using the Spalart-Allmaras, realizable k-ε and SST models, whereas the CFDk computed boundary layer closely resembles the one computed with the RSM, which presents a smaller thickness. This may be attributed to lower levels of artificial dissipation added to the spatial discretization algorithms present at the CFDk, but require further analysis for confirmation. Since no measurements of the boundary layer are available, it is impossible to determine which result better corresponds to the experiments in such a tri-dimensional flowfield.

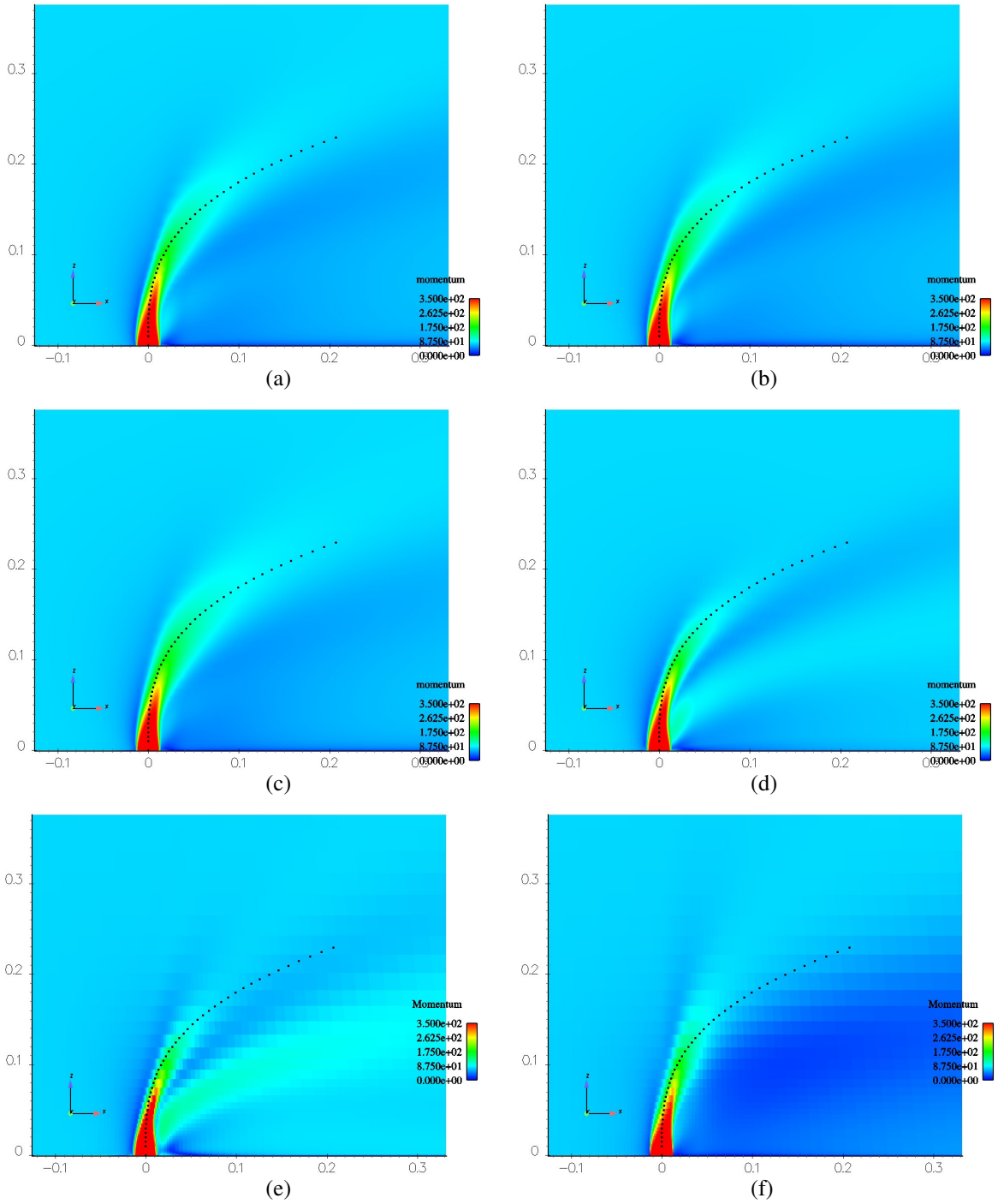

Figure 5. Comparison of the jet momentum distribution to the empirical jet path (dimensions in m); cases: (a) JSAF, (b) JKER, (c) JSST, (d) JRSM, (e) JSAJ, and (f) JSAR.

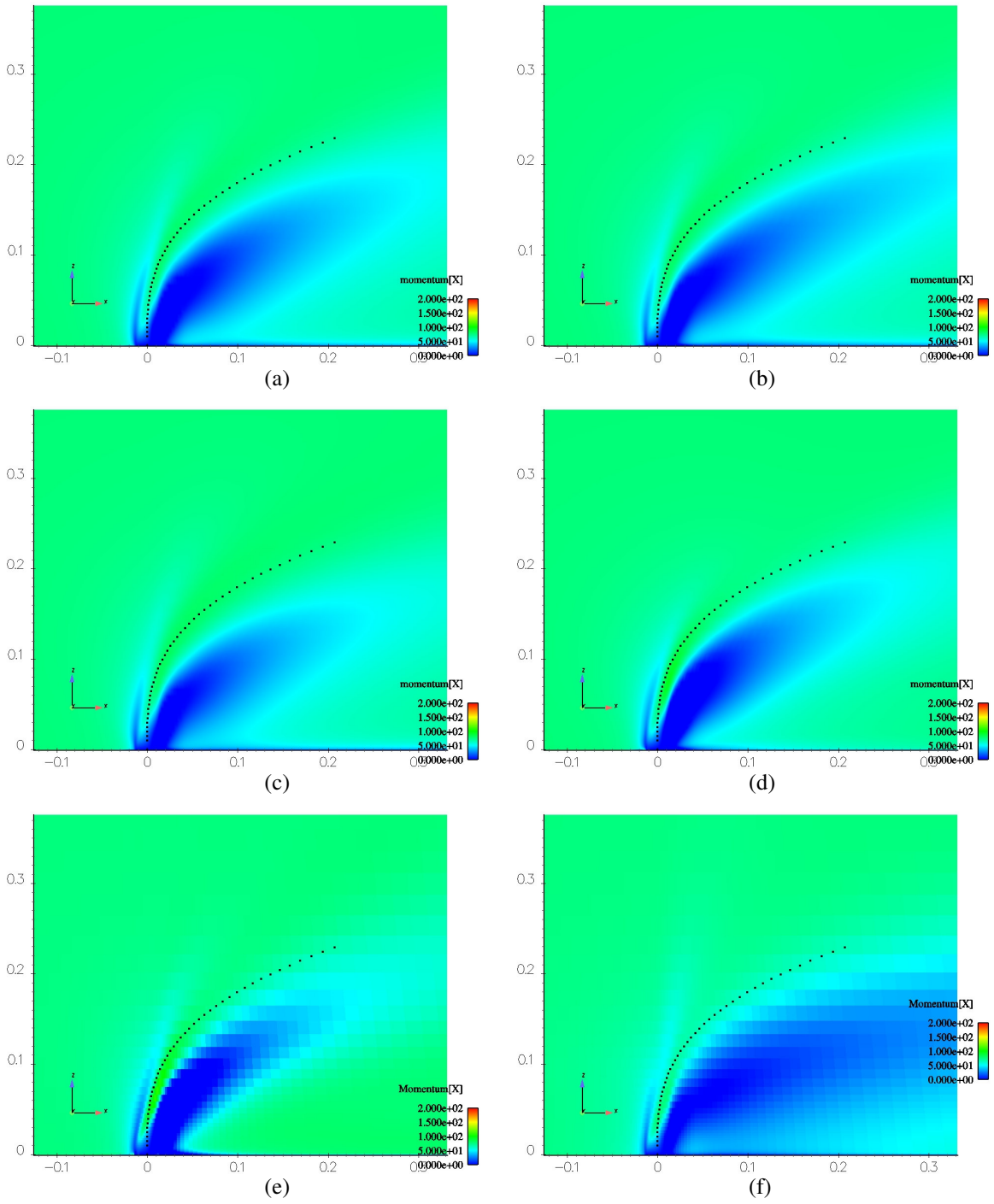

Figure 6. Comparison of the jet x-momentum distribution to the empirical jet path (dimensions in m); (a) JSAF case, (b) JKER case, (c) JSST case, (d) JRSM case, (e) JSAJ case, and (f) JSAR case.

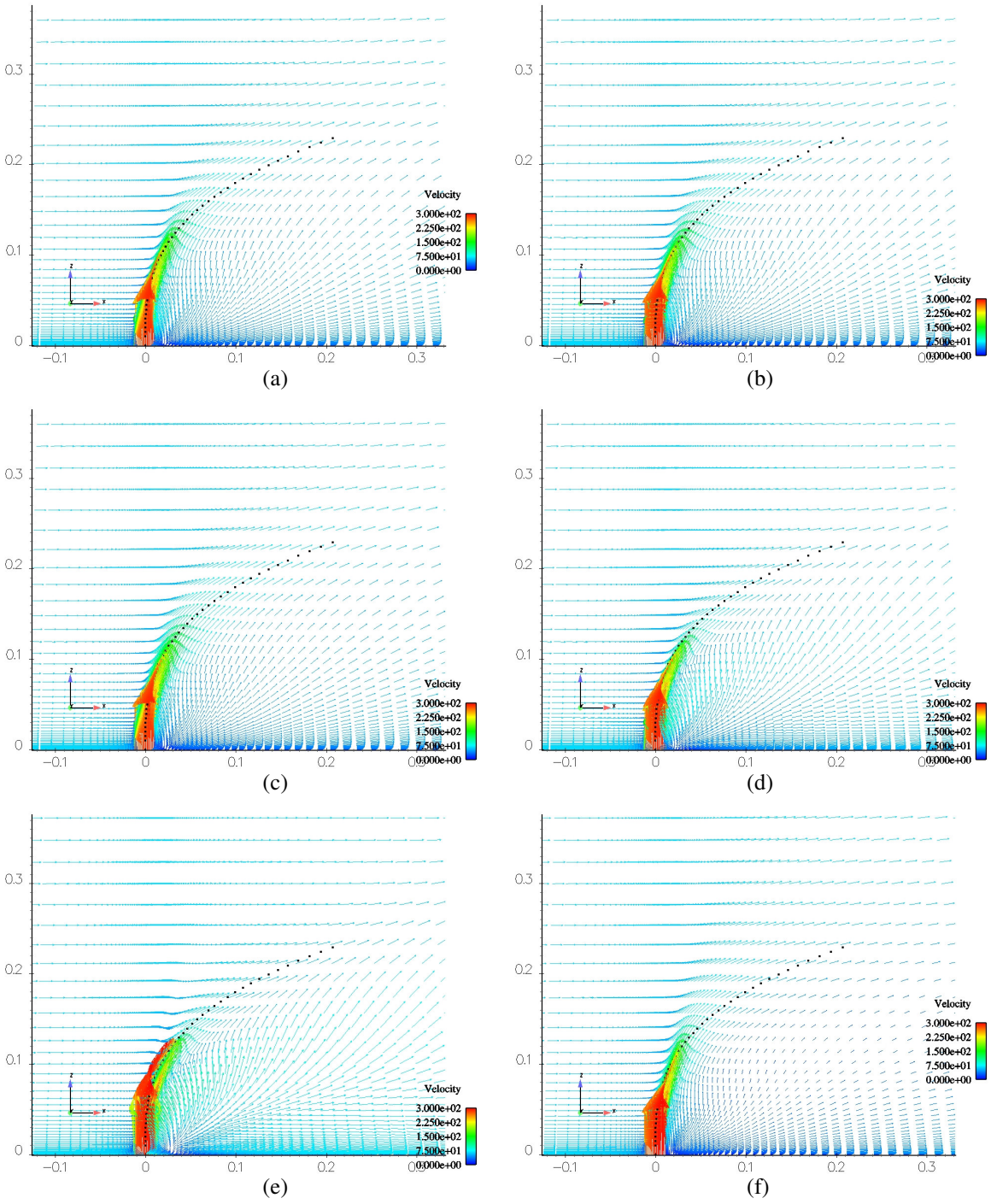

Figure 7. Comparison of the velocity vector distribution to the empirical jet path (dimensions in m); cases: (a) JSAF, (b) JKER, (c) JSST, (d) JRSM, (e) JSAJ, and (f) JSAR.

4.4 Pressure Contours Comparisons

The comparisons are performed based on the pressure distribution for five planes normal to the jet at different heights from the wall (Schetz, 1980). The overall structure of the flow for a case with 90 degree injection can be seen in Figure 8, where are shown the pressure contours in cross sections which are perpendicular to the initial orientation of the jet. The "bean-shaped" nature of the jet as it is deflected and distorted by the cross stream is particularly visible. Another characteristic is a stretch of the shape as the jet develops along the cross-sections. It is expected that the calculated momentum of the jets at the five normal planes follow the same bean-shaped behavior observed in the experiments for the static pressure evolution.

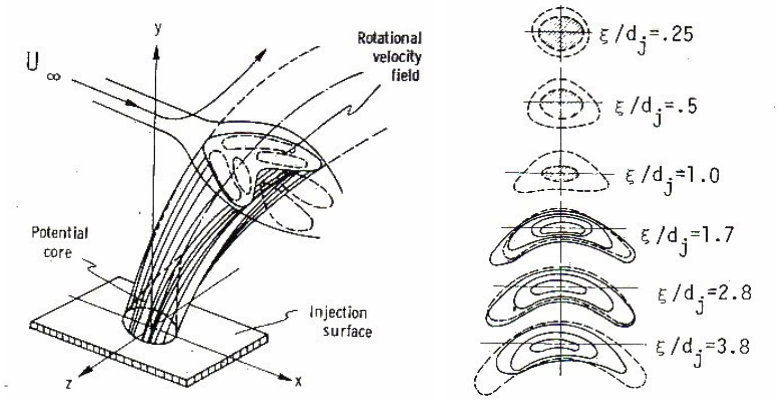

Figure 8. Cross-section pressure contours in a transverse jet; solid and dashed lines are constant of static pressure, and the shaded areas denote the potential core (Schetz, 1980).

Figure 9 shows the contours of z-momentum for planes parallel to the wall located at 0.25, 0.50, 1.00, 1.70 and 2.80 diameters above the jet exit. In this figure, results obtained with Fluent using both the RSM and Spalart-Allmaras models and CFDk with the Spalart-Allmaras model and the two spatial discretizations considered. The results obtained with the RSM are clearly in good qualitative agreement when compared with the pressure contours of Fig. 8. The progressive distortion and breakdown of the calculated jet closely follows the experimental behavior, and the computed aspect ratio of the bean-shaped jet resembles that of the experiments.

The secondary jet plume is evident in the results obtained with the RSM. This plume cans also be observed in the results obtained with the CFDk code using the Spalart-Allmaras model together with the Jameson spatial discretization method. The results of this case, JSAJ, also exhibit a much larger jet breakdown, which is evident by the large aspect ratio of the momentum contours. The results obtained with the Spalart-Allmaras model using Fluent and the CFDk with first order Roe spatial discretization are quite similar. The development and breakdown of the jet are practically identical, and the final aspect ratio of the bean-shaped jet smaller than those observed in the cases JRSM and JSAJ. The fact that both Fluent and CFDk fisrt order schemes yield similar results indicates that the Spalart-Allmaras implementation of the CFDk is correct at least when the Roe scheme is used.

Furthermore, the results shown in Fig. 9 can be understood by recalling that the Jameson spatial discretization is a centered second order scheme, and thus *a priori* less dissipative than either the Fluent first order upwind scheme or the first order Roe scheme implemented in the CFDk. Thus the more elongated distortion of the jet in the JSAJ case when compared to the JSAR one, and also the ability of the computation with the Jameson method to capture the secondary plume predicted in the second-order RSM. This plume is practically absent from the first order computations, possibly due to the dissipative nature of the discretization. Thus, it is expected that the Jameson second-order discretization is correctly implemented in the CFDk.

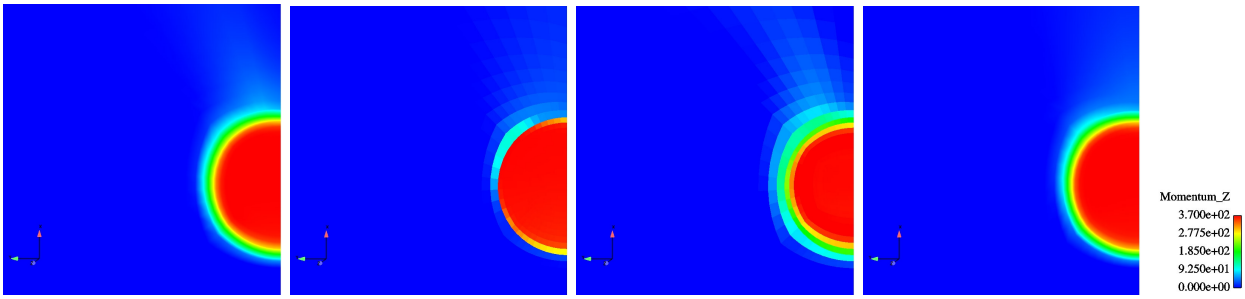

(a) horizontal plane located 0.25 diameters above the jet exit,

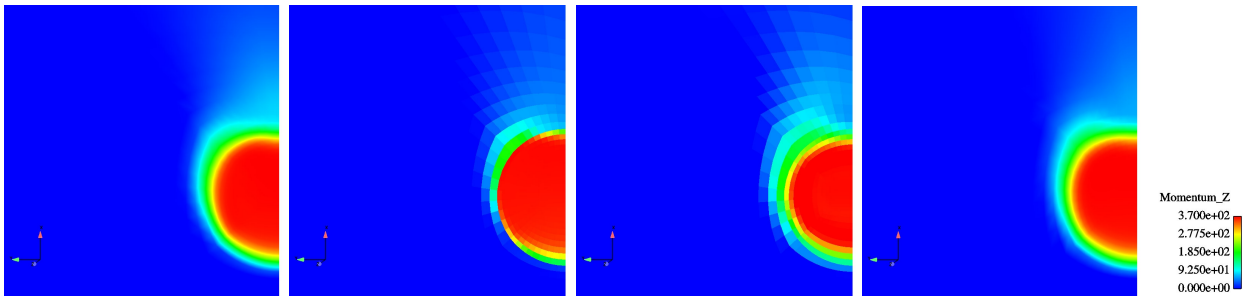

(b) horizontal plane located 0.50 diameters above the jet exit,

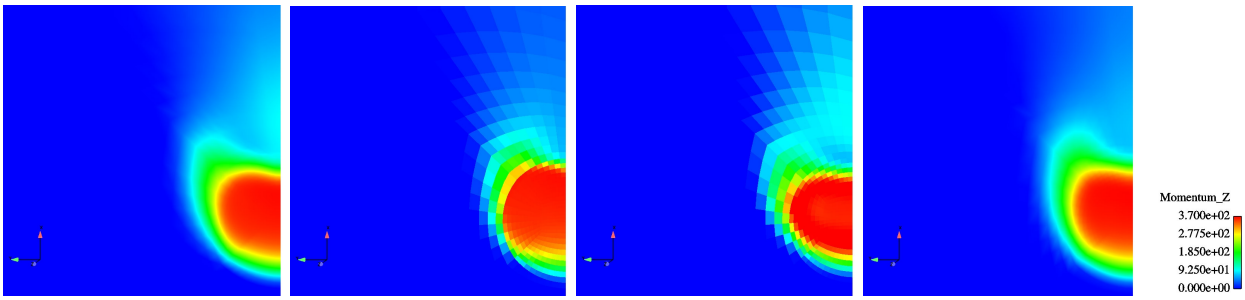

(c) horizontal plane located 1.00 diameters above the jet exit,

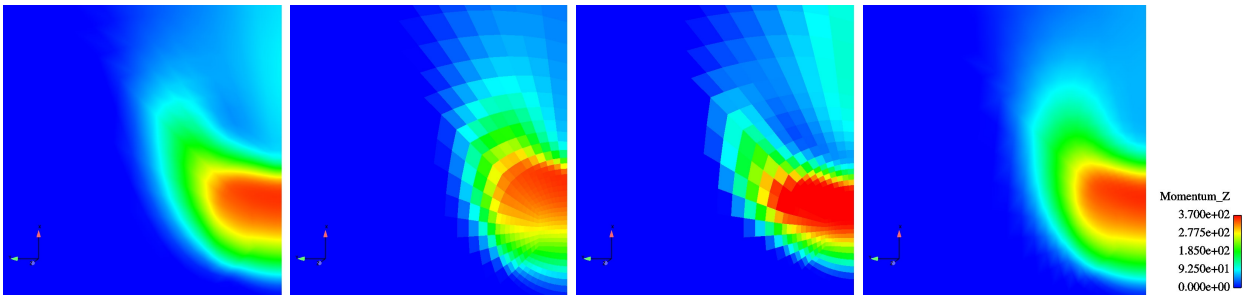

(d) horizontal plane located 1.70 diameters above the jet exit,

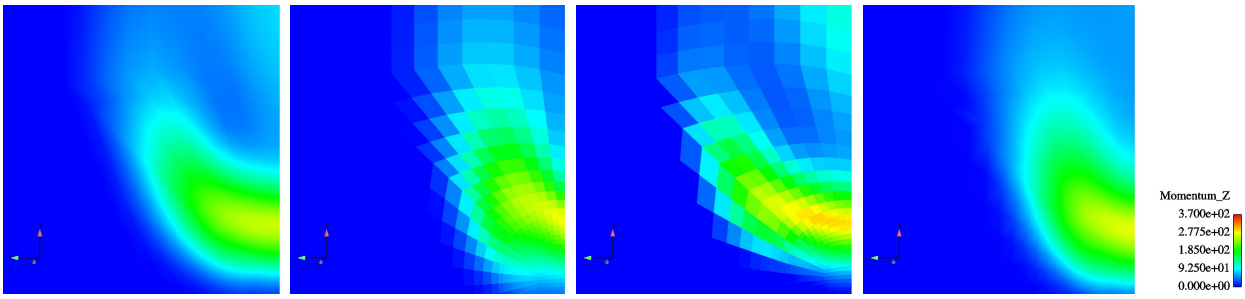

(e) horizontal plane located 2.8 diameters above the jet exit,

Figure 9. Contours of z-momentum for planes parallel to the wall, located at different heights above the jet exit: from left to right, cases JRSM, JSAR, JSAJ and JSAF. The dimensions of all figures correspond to 60 mm in the longitudinal direction and 57 mm in the transversal direction of the jet.

5. Conclusions

The CFDk validation study was performed through the comparison of the CFDk results with Fluent results. Both numerical results were compared to the experimental data available in terms of the path of the jet into the subsonic freestream, and in terms of the cross sectional pressure contours for five planes normal to the jet. The CFDk results used for the comparisons were obtained using the Spalart-Allmaras turbulence models with first order Roe, and second order Jameson spatial discretization methods, respectively. The Fluent computations considered four different turbulence models, including a second-order Reynolds Stress Model.

The CFDk results showed good agreement with the experimental data in terms of the jet path, even though the overall strucutre of the flowfield was not entirely coincident with the Fluent results. The analysis of the jet breakdown in terms of the evolution of the momentum in planes perpendicular to the jet allowed confirming that the results obtained with Fluent and CFDk with the Spalart-Allmaras model using first order spatial discretizations are in very good agreement. Finally, the results obtained with the second order Jameson's spatial discretization method were shown to be less dissipative than those computed with the first order methods. The jet breakdown is more developed than in the first order computations and seem to closely follow the experimental results. However, validation can only be proven once the computed results are compared to detailed experimental data.

6. Acknowledgements

This work was performed with financial support from Embraer and Fapesp while the first author was on leave from *Laboratoire de Combustion et de Détonique, Centre National de la Recherche Scientifique*, France. Mr. Rodrigo Ferraz, from Engineering Simulation and Scientific Software, Ltda., was responsible for the mesh generation.

7. References

Andrade, F. O., Ferreira, S. B., Figueira da Silva, L.F., Jesus, A. B. and Oliveira, G. L., 2006, "Study of the influence of aircraft geometry on the computed flowfield during thrust reverser operation," 24th AIAA Applied Aerodynamics Conference, AIAA Paper 2006-3673, San Francisco.

Anonimous, 2006, "Fluent 6.0 User´s Guide," Fluent 6.0 Documentation, Fluent Inc.

Bigarella, E. D. V., Basso, E. and Azevedo, J. L. F., 2004, "Centered and Upwind Multigrid Turbulent Flow Simulations with Applications to Launch Vehicles," 22nd AIAA Applied Aerodynamics Conference and Exhibit, AIAA Paper 2004-5384, Providence.

Bigarella, E. D. V., Basso, E. and Azevedo, J. L. F., 2005, "A Study of Convective Flux Computation Schemes for Aerodynamic Flows," 43rd AIAA Aerospace Sciences Meeting and Exhibit, AIAA Paper 2005-0633, Reno.

Gatlin, G. M. and Quinto, P. F., 1988, "Thrust-reverser flow investigation on a twin-engine transport", NASA-TP-2856; L-16426; NAS 1.60:2856 , 19881201

Hanjalic, K. and Launder, B. E., 1972, "A Reynolds stress model of turbulence and its application to thin shear flows", Journal of Fluid Mechanics, Vol. 52, pp. 609-638.

Ibrahim, I. M. and Gutmark, E. J., 2006, "Dynamics of single and twin circular jets in cross flow", 44th AIAA Aerospace Science Meeting and Exhibit, AIAA Paper 2006-1281, Reno, USA.

Margason, J. R., 1968, "The Path of a Jet Directed at Large Angles to a Subsonic Free Stream", NASA Technical Note TN D-4919

Menter, F. R., 1993, "Zonal two-equation k-w turbulence model for aerodynamic flows", AIAA Paper 1993-2906.

Pérez, C. C., Figueira da Silva, L. F., Ferreira, S. B., Jesus, A. B. and Oliveira, G. L., 2006, "Numerical Study of the Perfomance Improvement of Submerged Air Intakes Using Vortex Generators," 25th Congress of International Council of Aeronautical Sciences, Hamburg, Germany.

Schetz, J. A., 1980, "Injection and Mixing in Turbulent Flow", Progress in Astronautics and Aeronautics, Vol. 68. American Institute of Aeronautics and Astronautics.

Shih, T.-H, Liou, W.W., Shabbir, A., Yang, A. and Zhu, J., 1995, "A new k-ε eddy viscosity model for high Reynolds number turbulent flows", Computers and Fluids, Vol. 24, No. 3, pp. 227-238.

Spalart, P. R. and Allmaras, S. R., 1994, "A one-equation turbulence model for aerodynamic flows," La Recherche Aérospatiale, No. 1, pp. 5–21.

Strash, D. J., Summa, J. M., Frank, J. H. and Standish, R., 2000, "Aerodynamic Analysis of an Installed Thrust Reverser", Journal of Propulsion and Power, Vol.16 No. 1, pp. 10-15.

Trapp, L. G. and Oliveira G. L., 2003, "Aircraft Thrust Reverser Cascade Configuration: Evaluation Through CFD", 41st Aerospace Science Meeting & Exhibit, American Institute of Aeronautics and Astronautics.

Proceedings of the 11th Brazilian Congress of Thermal Sciences and Engineering -- ENCIT 2006
Braz. Soc. of Mechanical Sciences and Engineering -- ABCM, Curitiba, Brazil,- Dec. 5-8, 2006

Paper CIT06-0815

DIRECT NUMERCIAL COMPUTATION OF THE SOUND GENERATED BY TRANSONIC FLOW OVER A DEEP CAVITY

Alexandre Gonçalves Feijó de Carvalho
Universidade de Brasília, ENM – FT – UnB, Campus Universitário, Asa Norte, Brasília, DF, 70910-900, Brasília, DF, Brasil
alepfl@terra.com.br

Roberto Francisco Bobenrieth Miserda
Universidade de Brasília, ENM – FT – UnB, Campus Universitário, Asa Norte, Brasília, DF, 70910-900, Brasília, DF, Brasil
rfbm@unb.br

Abstract. *The objective of this work is the direct numerical computation of the aeroacoustic far-field and near-field generated by a transonic flow over a deep cavity. The compressible Navier-Stokes equations (with no turbulence model) are numerically solved using a finite volume discretization where the fluxes are computed using the skew-symmetric form of Ducros' fourth-order numerical scheme while the time marching process is achieved using a third-order Runge-Kutta scheme proposed by Shu. Pressure coefficient data and respective phase-diagram and power spectra are obtained from the center of the cavity front wall and an analysis is made concerning the trends observed. The Reynolds number is 66,000 and the Mach number is 0.9. For this case, it is observed that the sound wave system seems to originate by the flapping motion of the shear layer interacting with the trailing edge wall, which is the possible main sound generation mechanism.*

Keywords*. sound generation, pressure coefficient, deep cavity, transonic flow*

1. Introduction

Impinging shear layer are known to exhibit strong coherent oscillation associated with intense noise radiation in a wide range of applications (Rockwell, 1983). In this study, the noise radiated by a transonic flow past a two-dimensional cavity is investigated. A severe acoustic environment within and outside the cavity arises from a feedback loop, locked in by the geometry and the flow itself, as shown in many similar experimental observations (Rockwell *et al.*, 1978).

For low Mach number, the flapping shear layer crosses the cavity mouth, impinges on the back edge of the cavity, and causes an oscillating mass flow rate in the region of the cavity mouth. Sound is produced by the interaction of the shear layer with the back edge wall or by the oscillating mass flow rate in the cavity mouth region (Henderson, 2000). In this paper, it is investigated if the same mechanism is responsible for the aeroacoustic field generated in transonic flows.

The oscillations occurring in cavity flows can be categorized as fluid-dynamic, fluid-resonant, or fluid-elastic (Rockwell *et al.*, 1978). Fluid-dynamic oscillations arise from the instability of the shear layer in the cavity mouth. Fluid-resonant oscillations are the result of, or are enhanced by, resonant waves within the cavity. For shallow cavities, with depth to length ratio less than one ($D^*/L^* < 1$), transverse waves (waves traveling between the cavity floor and mouth) can be excited. Deep cavities, cavities with a depth to length ratio greater than one ($D^*/L^* > 1$), produce longitudinal waves (waves traveling between the front edge and back edge walls) (Roshko, 1954; Morse, 1999 and Rossiter, 1966). Fluid elastic resonance occurs when fluid resonance is enhanced by oscillations of the cavity surface.

The great interest in cavity flows and the large number of papers devoted to this subject stem from the wide number of applications subject to this type of flow field. These include, but are not limited to, automobile components, gas transport systems, aircraft wheel and weapon bays, and aircraft research telescope/radar cavities. In all of these applications, the designer would like to eliminate the occurrence of high pressure amplitude oscillations because they lead to unsteady loadings on components within or near the cavity or because they lead to unwanted sound.

The general noise spectrum of cavity noise contains both broadband components, introduced by the three-dimensional effects of turbulence across the shear layer, and tonal components introduced by the quasi two-dimensional flapping motion of the shear layer. In order to reduce the computational effort associated to a very well resolved computational grid, in this paper is carried out a two-dimensional simulation, although it is known that the turbulence is a three-dimensional phenomenon, and doing so, the fluctuations in the third direction are not taken into account. However, the large scale flapping motion of the shear layer, which is responsible for the low frequency tonal components can be well predicted. Broadband components on the other hand, are generated by the three-dimensional effects of turbulence and will not be predicted in a precise way with a two-dimensional unsteady flow calculation (Rubio *et al.*, 2005). On the other hand, the boundary layer prior to the separation in the cavity lip is laminar, so the transition from a laminar two-dimensional shear layer to a three-dimensional one must happen in some point over the

cavity mouth, further restricting the onset of the three-dimensional effects in the cavity, resulting in a highly transitional flow. An upstream laminar boundary layer (just ahead of the cavity) is imposed in this work since it was observed experimentally (Krishnamurty, 1956) that an initially laminar shear layer tends to produce a more intense sound field when compared to the sound field associated to an initially turbulent shear layer because in the former case the resulting flapping motion of the shear layer is quasi two-dimensional. The classical work of Rossiter (1966) pointed out that even for three-dimensional subsonic and transonic cavities the fundamental behavior, particularly along the cavity centerline, appears to be predominantly two-dimensional. Rizzetta (1988) carried out numerical studies over a three-dimensional cavity at a Mach number of 1.5 and also came with the same conclusion, i.e., the fundamental behavior of the unsteady phenomena is two-dimensional. The overview paper of Grace (2001) points out various works where a two-dimensional simulation is performed in order to predict the aeroacoustic field in subsonic, transonic and supersonic cavities at high Reynolds number.

The geometrical parameters of the cavity are based on the benchmark problem for category 6 of the Third Computational Aeroacoustics (CAA) Workshop on Benchmark Problems, organized by the National Aeronautics and Space Administration (NASA), held in 2000. This benchmark is intended for automotive door gap problems, associated to low Mach numbers. In this paper, the geometry of this benchmark is used to analyze aeronautic door gap problems in the transonic range. The Mach number is 0.9 and the Reynolds number is 66,000. The numerical code implemented by Bobenrieth Miserda and Mendonça (2005), used in the present simulation, solves the compressible Navier-Stokes equations (with no turbulence model) through a finite volume discretization, where the fluxes are computed using the skew-symmetric form of Ducros' fourth-order numerical scheme (Ducros *et al.*, 2000) while the time marching process is achieved using a third-order Runge-Kutta scheme proposed by Shu (Yee, 1997).

2. Methodology

In this work, a Direct Noise Computation (DNC), based on the solution of the two-dimensional compressible Navier-Stokes equations, with no turbulence model, is performed. The nondimensional form of the Navier-Stokes equations can be written as:

$$\frac{\partial \rho}{\partial t} + \frac{\partial}{\partial x_i}(\rho u_i) = 0\,, \tag{1}$$

$$\frac{\partial}{\partial t}(\rho u_i) + \frac{\partial}{\partial x_j}(\rho u_i u_j) = -\frac{\partial p}{\partial x_i} + \frac{\partial \tau_{ij}}{\partial x_j}\,, \tag{2}$$

$$\frac{\partial}{\partial t}(\rho e_T) + \frac{\partial}{\partial x_i}(\rho e_T u_i) = -\frac{\partial}{\partial x_i}(p u_i) + \frac{\partial}{\partial x_i}(\tau_{ij} u_j) - \frac{\partial q_{x_i}}{\partial x_i}\,. \tag{3}$$

All the variables are in nondimensional form and have their usual meaning, i.e., ρ is the density, t is the temporal coordinate, x_i is the i-direction spatial coordinate, u_i is the i-direction component of the velocity vector, p is the pressure, τ_{ij} denotes the viscous stress tensor, e_T is the total energy per unit of mass and q_{xi} is the heat-flow density in the i-direction.

The nondimensional form of the flow variables and properties are defined as

$$x_i = \frac{x_i^*}{b^*},\quad u_i = \frac{u_i^*}{U_\infty^*},\quad t = \frac{t^*}{b^*/U_\infty^*},\quad p = \frac{p^*}{\rho_\infty^*\left(U_\infty^*\right)^2},\quad \rho = \frac{\rho^*}{\rho_\infty^*},\quad e_T = \frac{e_T^*}{\left(U_\infty^*\right)^2} \tag{4}$$

$$\mu = \frac{\mu^*}{\mu_\infty^*},\quad e = \frac{e^*}{\left(U_\infty^*\right)^2},\quad e_k = \frac{e_k^*}{\left(U_\infty^*\right)^2},\quad c_v = \left[\frac{T_\infty^*}{\left(U_\infty^*\right)^2}\right] c_v^*,\quad T = \frac{T^*}{T_\infty^*}, \tag{5}$$

where the asterisk denotes dimensional quantities, b^* is the width of the overhang at the cavity entrance Fig. (1), μ^* is the dynamic viscosity and T^* is the temperature. U^*_∞, T^*_∞, ρ^*_∞ and μ^*_∞ are, respectively, the velocity, temperature, density and dynamic viscosity of the undisturbed flow.

The nondimensional viscous stress tensor is given by

$$\tau_{ij} = \frac{1}{\mathrm{Re}}\left(\mu S_{ij}\right) = \frac{1}{\mathrm{Re}}\left\{\mu\left[\left(\frac{\partial u_i}{\partial x_j} + \frac{\partial u_j}{\partial x_i}\right) - \frac{2}{3}\delta_{ij}\frac{\partial u_k}{\partial x_k}\right]\right\}, \tag{6}$$

where δ_{ij} is the Kronecker delta. The Reynolds number is defined as

$$\mathrm{Re} = \frac{\rho_\infty^* U_\infty^* b^*}{\mu_\infty^*}. \tag{7}$$

Defining e as the nondimensional internal energy per unit of mass, e_k as the nondimensional kinetic energy per unit of mass and c_v as the nondimensional specific heat at constant volume, the total energy is given by the sum of the internal and kinetic specific energy as

$$e_T = e + e_k = c_v T + \frac{u_i u_i}{2} \tag{8}$$

and the nondimensional heat-flux density is

$$q_{x_i} = -\frac{\mu}{(\gamma-1)M^2\,\mathrm{Re}\,\mathrm{Pr}}\left(\frac{\partial T}{\partial x_i}\right), \tag{9}$$

where the M and Pr are the Mach and the Prandtl numbers, respectively, and are defined as

$$M = \frac{U_\infty^*}{\sqrt{\gamma R^* T_\infty^*}}, \qquad \mathrm{Pr} = \frac{c_p^*}{k_\infty^*}\mu_\infty^*, \tag{10}$$

where γ is the specific heat ratio, R^* is the specific gas constant, $c_p{}^*$ is the specific heat at constant pressure and $k_\infty{}^*$ is the thermal conductivity of the undisturbed flow.

In this work, the Prandtl number is considered a constant with the value $\mathrm{Pr} = 0.72$. For a thermally and calorically perfect gas, the nondimensional equation of state can be written as

$$p = (\gamma-1)\rho e \tag{11}$$

and

$$T = \frac{\gamma M^2 p}{\rho}. \tag{12}$$

The nondimensional molecular viscosity is obtained using the Sutherland's formula, where C_1 and C_2 are the nondimensional first and second gas constants,

$$\mu = C_1\frac{T^{3/2}}{T + C_2}, \qquad C_1 = \left[\frac{\left(T_\infty^*\right)^{1/2}}{\mu_\infty^*}\right]C_1^*, \qquad C_2 = \frac{C_2^*}{T_\infty^*}. \tag{13}$$

The boundary conditions at the walls of the two-dimensional cavity and at the downstream surface are a no-slip condition for the velocity field, an adiabatic wall for the temperature field and a null gradient in the normal direction at the wall for the pressure field. The boundary condition for the upstream surface is a slip condition till the beginning of the cavity overhang in order to develop an appropriate boundary layer thickness for the present case. The adiabatic wall and null pressure gradient in the normal wall direction are also applied for the latter surface.

Since the geometry of interest is a two-dimensional cavity, the two-dimensional form of the Navier-Stokes equations is used. In order to numerically solve this equations using a finite volume approach, Eqs. (1), (2) and (3) are written in the following vector form (Anderson, 1983):

$$\frac{\partial \mathbf{U}}{\partial t} + \frac{\partial \mathbf{E}}{\partial x} + \frac{\partial \mathbf{F}}{\partial y} = 0, \tag{14}$$

where **U** is the nondimensional conservative-variables vector, **E** and **F** are the nondimensional flux vectors. These vectors are given by

$$\mathbf{U}=\begin{bmatrix}\rho\\ \rho u\\ \rho v\\ \rho e_T\end{bmatrix},\quad \mathbf{E}=\begin{bmatrix}\rho u\\ \rho u^2+p-\tau_{xx}\\ \rho uv-\tau_{xy}\\ (\rho e_T+p)u-u\tau_{xx}-v\tau_{xy}+q_x\end{bmatrix},\quad \mathbf{F}=\begin{bmatrix}\rho v\\ \rho vu-\tau_{xy}\\ \rho v^2+p-\tau_{yy}\\ (\rho e_T+p)v-u\tau_{xy}-v\tau_{yy}+q_y\end{bmatrix}, \tag{15}$$

where *u* and *v* are, respectively, the nondimensional component of the velocity vector in the *x*-direction and *y*-direction.

Defining the flux tensor Π as

$$\Pi=\mathbf{E}\otimes\mathbf{i}+\mathbf{F}\otimes\mathbf{j}, \tag{16}$$

where **i** and **j** are unit vectors in the *x*-direction and *y*-direction. Eq. (14) can be rewritten as

$$\frac{\partial\mathbf{U}}{\partial t}+\nabla\cdot\Pi=0, \tag{17}$$

Integrating the above equation over the control volume *V*, and applying the divergence theorem to the first term of right-hand side results

$$\frac{\partial}{\partial t}\int_V\mathbf{U}\,dV=-\int_V(\nabla\cdot\Pi)\,dV=-\int_S(\Pi\cdot\mathbf{n})\,dS\cdot \tag{18}$$

The volumetric mean of vectors **U** in the control volume *V* is defined as

$$\bar{\mathbf{U}}\equiv\frac{1}{V}\int_V\mathbf{U}\,dV, \tag{19}$$

where the upper bar means volumetric mean of the variable. Eq. (18) is written as

$$\frac{\partial\bar{\mathbf{U}}}{\partial t}=-\frac{1}{V}\int_S(\Pi\cdot\mathbf{n})\,dS\cdot \tag{20}$$

For the volume (i,j), the first-order approximation of the temporal derivative is given by

$$\left(\frac{\partial\overline{\mathbf{U}}}{\partial t}\right)_{i,j}=\frac{\Delta\overline{\mathbf{U}}_{i,j}}{\Delta t}+O(\Delta t), \tag{21}$$

and the temporal approximation of Eq. (20) for a quadrilateral and two-dimensional control volume is

$$\Delta\,\bar{\mathbf{U}}_{i,j}=-\frac{\Delta t}{V_{i,j}}\left[\int_{S_{i+1/2}}(\Pi\cdot\mathbf{n})\,dS+\int_{S_{i-1/2}}(\Pi\cdot\mathbf{n})\,dS+\int_{S_{j+1/2}}(\Pi\cdot\mathbf{n})\,dS+\int_{S_{j-1/2}}(\Pi\cdot\mathbf{n})\,dS\right], \tag{22}$$

where $S_{i+1/2}$ is the common surface between volume (i,j) and volume $(i+1,j)$, **n** is the normal unit vector and Δt is the nondimensional time step. Defining

$$\mathcal{F}\left(\overline{\mathbf{U}}\right)_{i,j}=(\Pi\cdot\mathbf{S})_{i+1/2}+(\Pi\cdot\mathbf{S})_{i-1/2}+(\Pi\cdot\mathbf{S})_{j+1/2}+(\Pi\cdot\mathbf{S})_{j-1/2}, \tag{23}$$

the spatial approximation of Eq. (22) is

$$\Delta\overline{\mathbf{U}}_{i,j}=-\frac{\Delta t}{V_{i,j}}\left[\mathcal{F}\left(\overline{\mathbf{U}}\right)_{i,j}-\mathcal{D}\left(\overline{\mathbf{U}}\right)_{i,j}\right], \tag{24}$$

where $\mathcal{D}\left(\overline{\mathbf{U}}\right)_{i,j}$ is an artificial dissipation. It is important to note that Eq. (24) is a spatial approximation of Eq. (22) because the tensor Π is considered constant over each of the four control surfaces that define the control volume.

In order to calculate $\mathcal{F}\left(\overline{\mathbf{U}}\right)_{i,j}$, the flux of tensor Π trough the control surfaces must be calculated. The explicit form of this calculation as well as the implementation of the artificial dissipation, $\mathcal{D}\left(\overline{\mathbf{U}}\right)_{i,j}$, is given by Bobenrieth Miserda and Mendonça (2005).

In order to advance Eq. (24) in time, a third-order Runge-Kutta is used as proposed by Shu (Yee, 1997). This yield to

$$\overline{\mathbf{U}}^{1} = \overline{\mathbf{U}}^{n} - \frac{\Delta t}{V_{i,j}}\left[\boldsymbol{\mathcal{F}}\left(\overline{\mathbf{U}}^{n}\right) - \boldsymbol{\mathcal{D}}\left(\overline{\mathbf{U}}^{n}\right)\right], \tag{25}$$

$$\overline{\mathbf{U}}^{2} = \frac{3}{4}\overline{\mathbf{U}}^{n} + \frac{1}{4}\overline{\mathbf{U}}^{1} - \frac{1}{4}\left\{\frac{\Delta t}{V_{i,j}}\left[\boldsymbol{\mathcal{F}}\left(\overline{\mathbf{U}}^{1}\right) - \boldsymbol{\mathcal{D}}\left(\overline{\mathbf{U}}^{1}\right)\right]\right\}, \tag{26}$$

$$\overline{\mathbf{U}}^{n+1} = \frac{1}{3}\overline{\mathbf{U}}^{n} + \frac{2}{3}\overline{\mathbf{U}}^{2} - \frac{2}{3}\left\{\frac{\Delta t}{V_{i,j}}\left[\boldsymbol{\mathcal{F}}\left(\overline{\mathbf{U}}^{2}\right) - \boldsymbol{\mathcal{D}}\left(\overline{\mathbf{U}}^{2}\right)\right]\right\}. \tag{27}$$

As used in this work, the numerical method is fourth-order accurate in space and third-order accurate in time.

3. Numerical Specifications

3.1. Cavity Geometry

The geometry used from the category 6 problem (Henderson, 2000) is showed in Fig. (1).

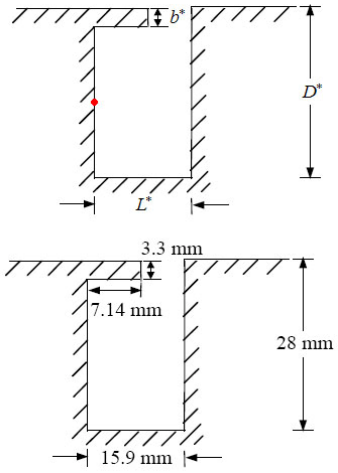

Figure 1. Cavity geometry.

The red point at the center of the left cavity wall indicates the location where c_p data as a function of time is obtained.

3.2. Computational Grid

A portion of the computational mesh is displayed in Fig. (2). The total mesh is compounded by one non-uniform Cartesian grid outside the cavity and two uniform Cartesian grid inside the cavity in order to provide the cavity overhang, as required from the category 6 problem (Henderson, 2000).

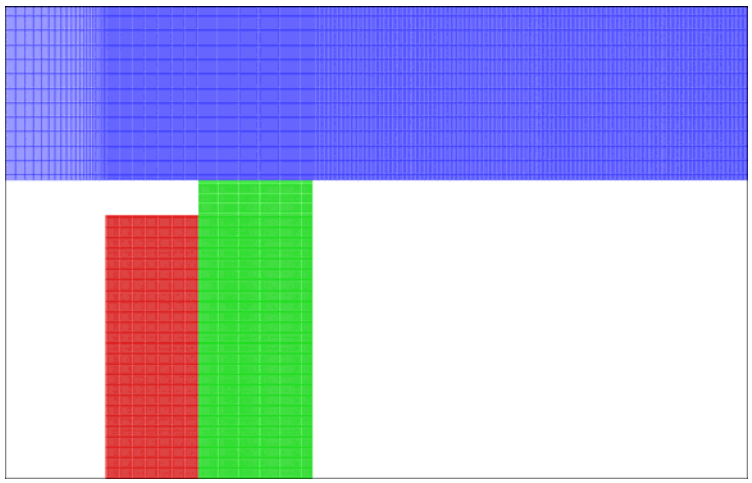

Figure 2. Portion of the cavity Mesh. The outside cavity grid (blue) has 1050 × 975 volumes; the grid below the cavity overhang (red) has 72 ×228 volumes and the last one (green) has 90 ×255 volumes.

The computational domain extends $343\,b^*$ downstream and $228\,b^*$ in the normal direction.

4. Results

4.1. Far-Field Results

Figure (3) displays a visualization based on the magnitude of the gradients of nondimensional temperature showing the structures of the radiated field. This type of visualization is used since the aeroacoustic phenomenon studied involves the interaction of boundary and shear layers, vortex structures, pressure and shock waves. The gradients of the nondimensional temperature field are very sensitive to all the aforementioned flow features, facilitating their joint presentation. It is possible to observe two types of pressure wave patterns, being the first one originated from the interaction of the flapping shear layer with the cavity lip (at the separation point) and the second one resulting from the interaction of the flapping shear layer with the back edge of the cavity (at the reattachment point).

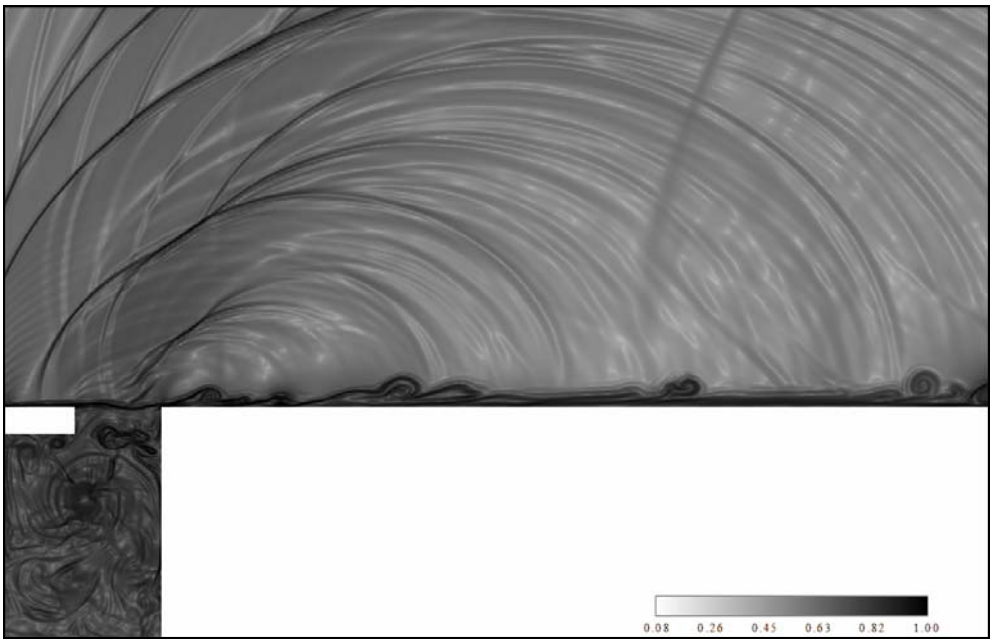

Figure 3. Far-field visualization of the two wave patterns based on gradients of nondimensional temperature.

Also it is noted from Fig. (3) the sound waves production from the collision between vortices along the downstream boundary layer.

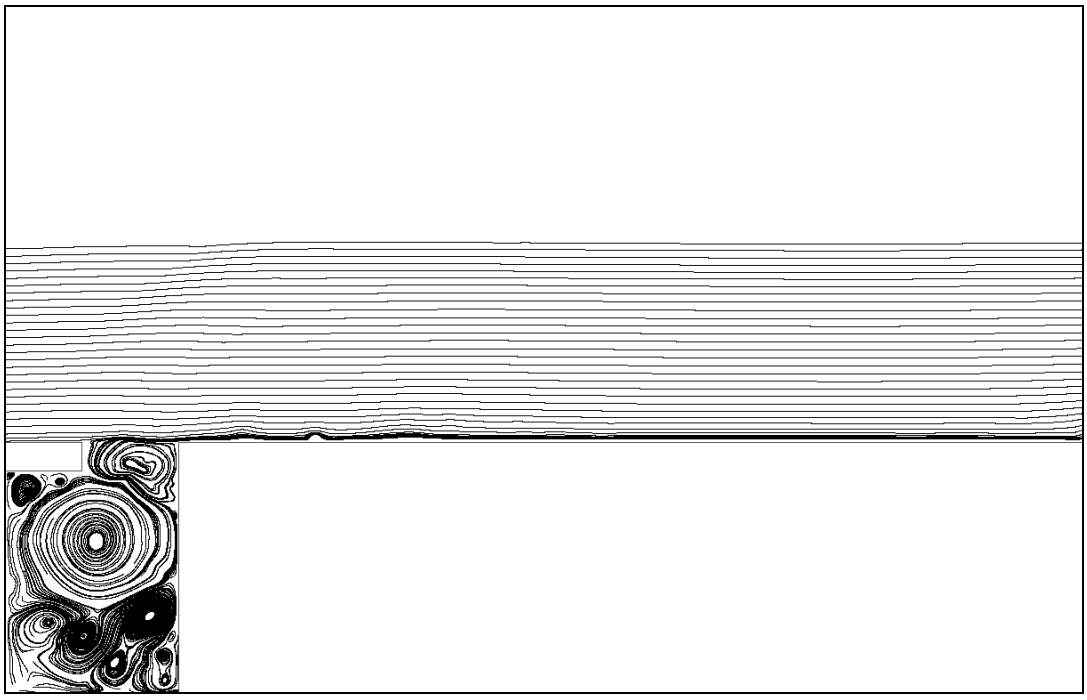

Figure 4. Far-field visualization of the two wave patterns based on mean streamlines.

Figure (4) shows the mean streamlines from the same visualization of Fig. (3). It is noted that the streamlines along the cavity mouth are nearly horizontal and a main vortex dominates half the cavity region. Figure (5) displays a low pressure region just in the centre of the main vortex and this region appears to be the result of the vortical swirling motion in the cavity. At the impingement region (rear edge of the cavity), C_p reaches its higher value about 0.6. These qualitative flow features is very similar to those presented by Rowley *et al.* (2002) concerning the shear-layer mode of oscillation which is characterized by a feedback process: the roll-up of vorticity in the shear layer, impingement and scattering of acoustics waves at the downstream cavity edge, upstream acoustic wave propagation, and receptivity of the shear layer to acoustic disturbances.

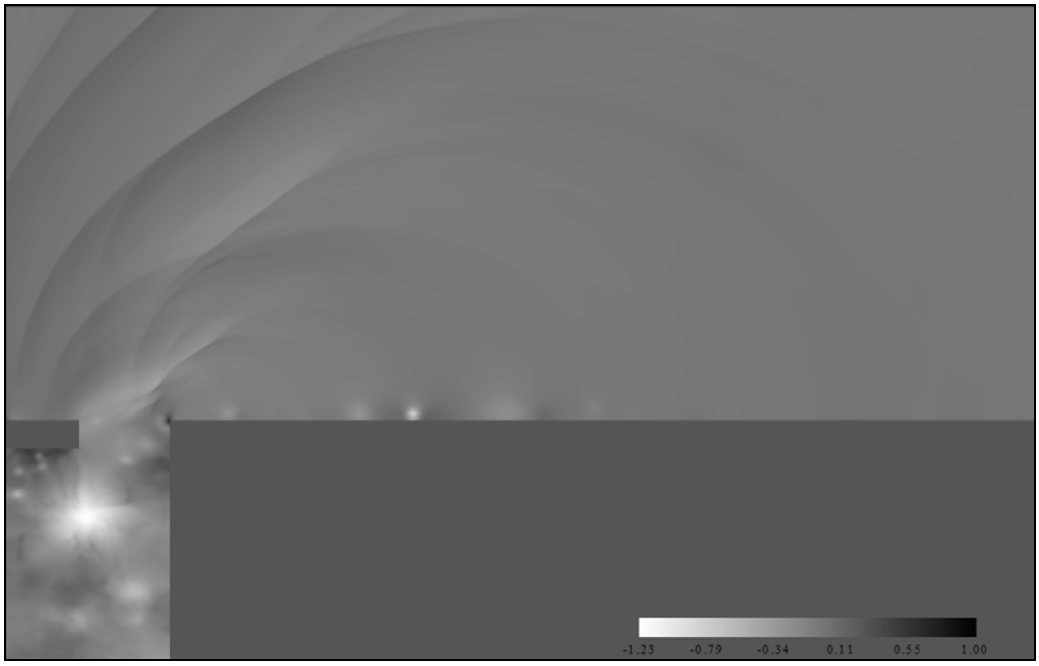

Figure 5. Far-field visualization based on contours of C_p.

4.2. Near-Field Results

The near field is now investigated to identify the noise generation mechanism, and in particular to determine the origin of the two wave patterns observed previously in Fig (3). Figure (6) presents the cycling mechanism of the flapping shear layer crossing the cavity mouth and a vortex structure inside it. It is observed a dominant vortex structure inside the cavity that presents a circular movement around the cavity centre and generates radial waves that are reflected longitudinally between the cavity walls. The vortex inside the shear layer is shed from its front edge separation and travels downstream, growing with convection (Fig. (6), (a) and (b)). As it impinges on the back edge, the shear layer vortex centre is clipped on this edge (Fig. (6), (c)). Part of the vortex spills over the cavity and is convected downstream, increasing the thickness of the reattached boundary layer. The other component is swept downward into the cavity creating recirculating regions. Figure (6), (d) shows the restart of the shear layer vortex formation. As the vortex shedding at the front edge wall and the clipping of its centre on the back edge wall occur, the two far-field wave patterns seem in Fig. (3) are formed by consequence.

A portion of the signal of the unsteady pressure coefficient is shown is Fig. (7) as well as its mean. It is worth noting that this mean has a cumulative nature, resulting in a value that stabilizes with time. The flow inside the cavity has a self-sustained oscillatory nature but is still irregular. This unsteady flow behavior inside the cavity appears to be driven by the main vortex structure generating the radial waves which may be the main responsible for the pressure oscillations. However, the mean value of c_p stabilizes after a time of about $858 b^* / U_\infty$.

From the phase-diagram displayed in Fig. (8) there is a non-periodic behavior of the pressure field within the cavity possibly due to the random formation of small vortex structures and the dynamics of generation of radial waves from the main vortex structure, that are reflected longitudinally between the cavity walls. The overall power spectra indicates two major peaks at $St = 0.125$ and $St = 0.130$, which the former seems to correspond to the impingement frequency of the radial waves on the cavity left wall and the latter seems to be related to the frequency of the circular movement of the main vortex inside the cavity, approaching and distancing from the cavity left wall.

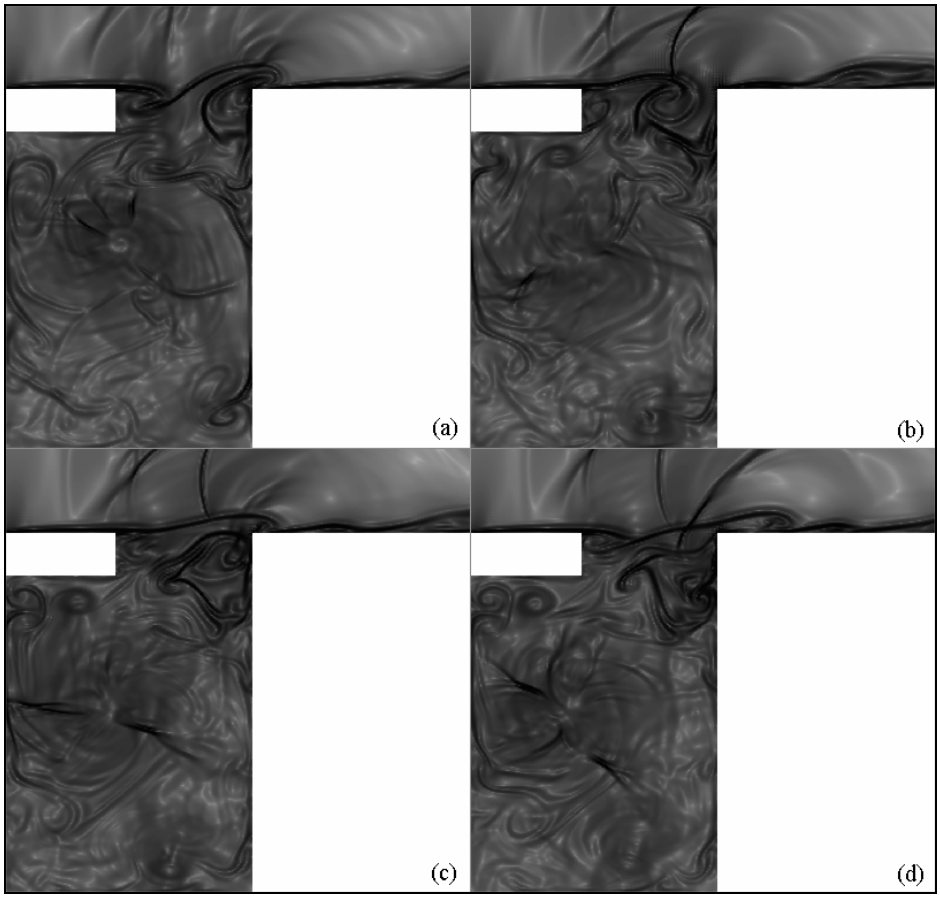

Figure 6. Near-field visualizations based on gradients of nondimensional temperature displaying the main vortex and its generated radial waves inside the cavity and the interaction between the shear layer and the leading edge and trailing edge cavity walls. White corresponds to 0 and black corresponds to 1.

Several secondary peaks are observed at $St = 0.146$, $St = 0.158$ and $St = 0.180$ which could be related to several types of wave frequency propagation caused by small vortex structures formed inside the cavity.

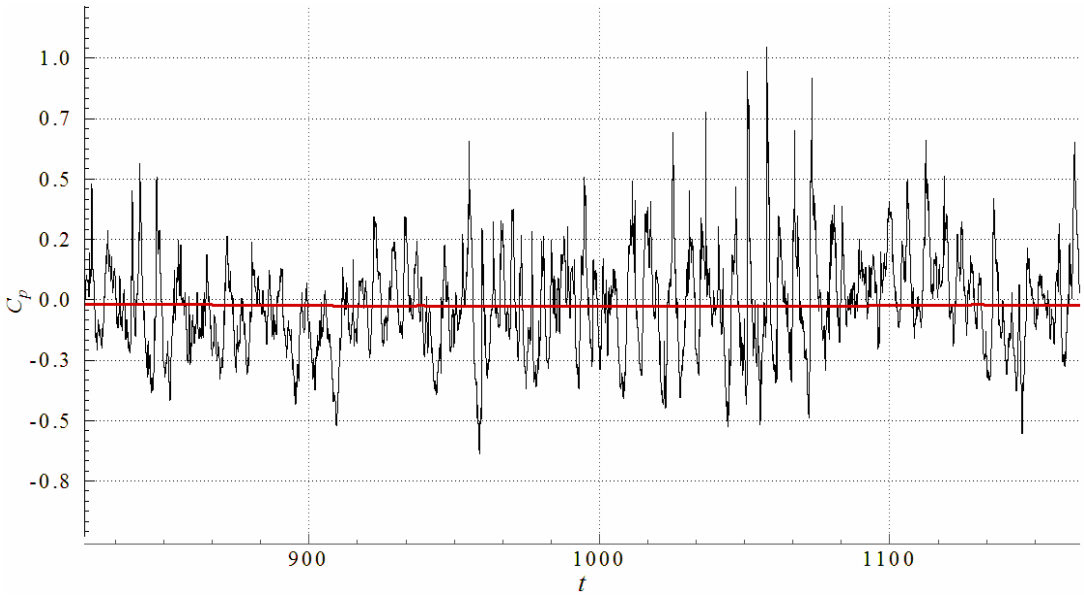

Figure 7. Unsteady (black) and mean (red) pressure coefficient as a function of nondimensional time extracted from the point located at the center of the cavity left wall.

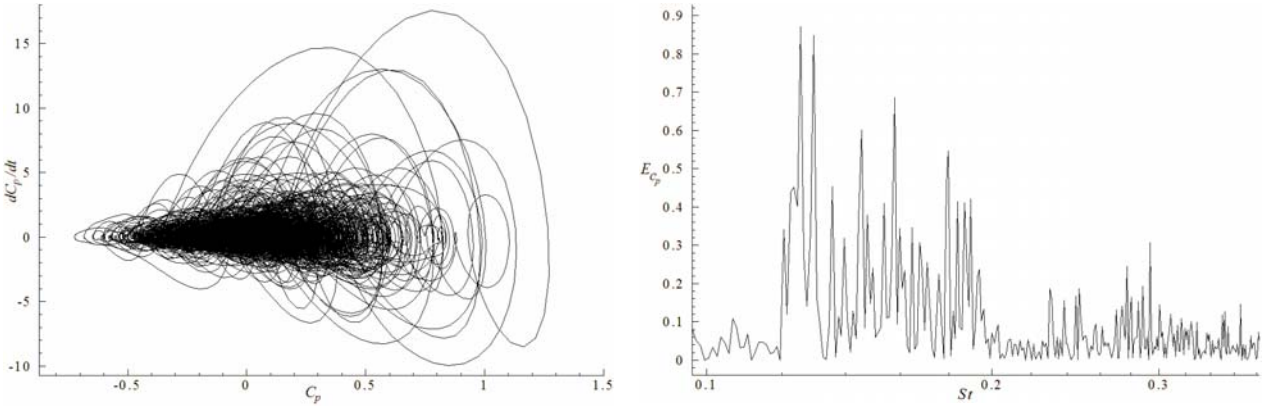

Figure 8. Phase-diagram and power spectra as a function of the Strouhal number, $St = f^* L^* / U_\infty^*$, derived from the c_p data as a function of time.

5. Conclusion

A direct calculation of the sound radiated by a flow over a 2-D deep cavity is carried out. This methodology was implemented in order to asset the effects of the shear layer impingement on the back edge wall of the cavity as the possible main responsible for the noise generation mechanism concerning the aeroacoustic far-field. Although it was carried out a 2D simulation, this approach is capable to provide all the necessary interactions between the flow and acoustics, proving to be a powerful tool to determine the noise generation mechanism. The far field dynamics of the wave sound formation are very similar to those observed by Rowley *et al.* (2002) concerning the shear-layer mode of oscillation which is characterized by a feedback process. It was observed inside the cavity a formation of small vortex structures and a main one that generates radial waves which are reflected longitudinally between the cavity walls. These waves' reflections confirm their longitudinal pattern inherent from cavities with a depth to length ratio greater than one ($D^* / L^* > 1$) (Roshko, 1954; Morse, 1999 and Rossiter, 1966). The phase-diagram presented in Fig. (8) indicates an non-periodic pressure field behavior inside the cavity and the correspondent power spectra shows that the greatest part of the energy is concentrated in two peaks that seems to be related to the impingement frequency of the radial waves on

the cavity front wall and to the frequency of the circular movement of the main vortex inside the cavity, approaching and distancing from the cavity front wall.

6. References

Anderson, D. A., Tannehill, J. C. and Pletcher, R. H., 1983, "Computational Fluid Mechanics and Heat Transfer", Hemisphe Publishing Corporation, New York.

Bobenrieth Miserda, R. F., Mendonça, A. F. de, 2005, "Numerical Simulation of the Vortex-Shock Interactions in a Near-Base Laminar Flow", AIAA 43rd Aerospace Sciences Meeting and Exhibit, AIAA 2005-0316, Reno, Nevada.

Ducros, F., Laporte, F., Soulères, T., Guinot, V., Moinat, P. and Caruelle, B., 2000, "High-Order Fluxes for Conservative Skew-Symmetric-like Schemes in Structured Meshes: Application to Compressible Flows", Journal of Computational Physics, Vol. 161, pp. 114-139.

Grace, S. M., 2001, "An Overview of Computational Aeroacoustic Techniques Applied to Cavity Noise Prediction", 39th AIAA Aerospace Sciences Meeting and Exhibit, Reno, NV.

Henderson, B., 2000, "Automobile Noise Involving Feedback Sound Generation by Low Speed Cavity Flows", Third Computational Aeroacoustics (CAA) Workshop on Benchmark Problems, NASA, pp. 95-100.

Kryshnamurty, K., 1956, "Sound Radiation from Surface Cutouts in High Speed Flow", California Institute of Technology, Pasadena, California.

Morse, P., and Shieh, C., 1999, "Parallel Numerical Simulation of Subsonic Cavity Noise", AIAA paper 99-1891.

Rizzetta, D. P., 1988, "Numerical Simulation of Supersonic Flow over a Three-Dimensional Cavity", AIAA Journal, Vol 26, No 7.

Rockwell, D., and Naudasher, E., 1978, "Review – Self-sustaining Oscillation of Flow Past Cavities", Transactions of ASME, pp. 152-165.

Rockwell, D, 1983, "Oscillations of Impinging Shear Layers", AIAA Journal 21, pp. 152-165.

Roshko, A., 1954, "Some Measurements of the Flow in a Rectangular Cutout", NACA NAW-6296.

Rossiter, J.E., 1966 "Wind Tunnel Experiments on the Flow Over Rectangular Cavities at Subsonic and Transonic Speeds", Aeronautical Research Council Reports and Memorandum No. 3438.

Rowley, C.W., Colonius, T., Basu, A. J. 2002 "On Self-Sustained Oscillation in Two-Dimensional Compressible Flow Over Rectangular Cavities", Journal of Fluid Mechanics, vol. 455, pp. 315-346.

Rubio, G., Roeck, W., Baelmans, M., Desmet, W., 2005 "Numerical Study of Noise Generation Mechanism in Rectangular Cavities", Euromech Colloquium 467: Turbulent and Noise Generation, July 18-20, Marseille, France.

Yee, H. C., 1997, "Explicit and Implicit Multidimensional Compact High-Resolution Shock-Capturing Methods: Formulation," Journal of Computational Physics, Vol. 131, pp. 216, 232

Proceedings of the 11th Brazilian Congress of Thermal Sciences and Engineering -- ENCIT 2006
Braz. Soc. of Mechanical Sciences and Engineering -- ABCM, Curitiba, Brazil,- Dec. 5-8, 2006

Paper CIT06-864

NUMERICAL SIMULATION OF THE LAMINAR FLOW AROUND A CIRCULAR CYLINDER WITH STREAM-WISE HARMONIC OSCILLATION

Daniel Martins da Silva
Departamento de Engenharia Mecânica, Faculdade de Tecnologia, Universidade de Brasília, Campus Universitário Darcy Ribeiro, 70910-900, Brasília, DF, Brasil
danielunb@pop.com.br

Roberto Francisco Boberieth Miserda
Departamento de Engenharia Mecânica, Faculdade de Tecnologia, Universidade de Brasília, Campus Universitário Darcy Ribeiro, 70910-900, Brasília, DF, Brasil
rfbm@unb.br

Abstract. *The objective of the present study is the numerical simulation of the two-dimensional laminar flow around a circular cylinder that oscillates harmonically in the stream-wise direction. The problem is solved for a non-inertial frame of reference that is moving with the cylinder and, for this reason, the associated pseudo-force and pseudo-work terms are included as sources in the compressible Navier-Stokes equations. These equations are solved using a finite volume formulation, where the fluxes are calculated using the fourth-order skew-symmetric form of Ducros' algorithm, while the time marching is achieved using the third-order Runge- Kutta scheme proposed by Shu. For all cases studied, the Reynolds number is 100 and the Mach number is 0,20. In the present work, the impact over the flow topology of two parameters is analyzed. The first one is the maximum linear velocity of the oscillating cylinder and the second one is the frequency of the harmonic oscillation. Depending on the combinations of these parameters the structure of the wake presents three distinct forms: (i) periodic and symmetric, where a symmetric vortex pair is emitted in each cycle of oscillation resulting in a null normal force; (ii) periodic and anti-symmetrical, resulting in a superposition of the previous mode over the von Kármán vortex street and (iii) chaotic, where the vortex systems are emitted with no regularity in each cycle of oscillation.*

Keywords: *Numerical simulation, stream-wise oscillation, wake topology, laminar flow, dynamic systems.*

1. Introduction

Usually, when vortices inducing oscillations on rigid bodies are mentioned the primordial thought is of a cylinder oscillating in the normal direction of the flow, since the emission of vortices for a compressible flow produces periodic forces that act primordially in the transversal direction of the flow. The component in the parallel direction of the flow has frequency next to two times the frequency of emission of vortices, number of Strouhal (*St*), and typically its magnitude is less than the component in the normal direction and incapable to excite the structure. The Strouhal number is a dimensionless parameter that represents the frequency with which consecutive vortices of same signal are emitted and is defined as $St = f\ D/U_\infty$, where f represents the characteristic frequency of emission of vortices, D represents the characteristic length of the system and U_∞ indicates the velocity of the non-disturbed region. In this context, one of the pioneers in the experimental analysis for this configuration of the flow was Griffin and Ramberg (1976), it was evidenced that the flow submitted to harmonic oscillations depends strongly on the Keulegan-Carpenter, KC, nondimensional number that represents the relation between the frequencies of oscillation by the convective time scale. Was noticed that to the measure that KC increases, remaining constant the Reynolds number, the format of the emitted vortices was modified. Tastsuno & Bearman (1990), in an experimental work and based in visualization, describe the several regimes.

Under purpose of the present research project, Öngoren & Rockwell (1988), had carried through extensive experiments on the forced oscillation of an in-line circular cylinder with the incident flow, two basic modes of emission of vortices had been observed, the symmetrical form and the anti-symmetrical form, this last one with four possible configurations as shown in Fig. 01, in which modes A-III and A-IV only occur when the cylinder describes a harmonic oscillation, they had evidenced that the dominant model of emission of vortices is the symmetrical case, observed in Fig. 1(a). Öngoren & Rockwell (1988), had noticed that initially when the cylinder describes a sine movement, have a transient emission of vortices that is characterized by the symmetrical mode, which decay gradual for the anti-symmetrical mode, however, it's possible for certain configuration of the parameters to have the steady symmetrical form. In general lines, they had concluded that the excitement of the cylinder in the direction of the flow generates symmetrical disturbances, while the natural and predominant occurrence in the normal direction generates anti-symmetrical disturbances. Consequently, it will have competitions between the phenomena, symmetrical and anti-symmetrical mode, consequently under certain conditions one in the modes it will prevail, producing the synchronization it enters the structure of the flow near to the cylinder and its movement.

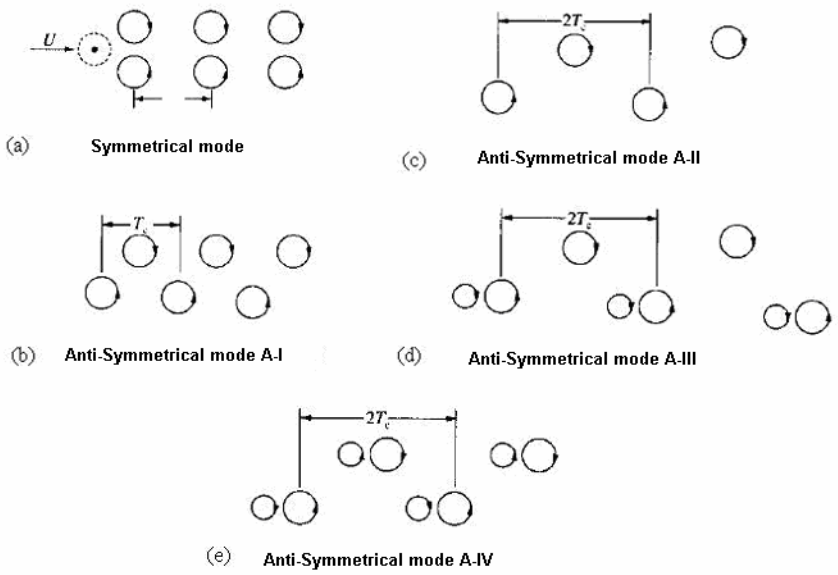

Figure 1:Modes of emission of vortices, removed from Öngoren & Rockwell (1988). (a) Symmetrical mode; (b) Anti-Symmetrical mode A-I; (c) Anti-Symmetrical mode A-II; (d) Anti-Symmetrical mode A-III; (e) Anti-Symmetrical mode A-IV; Forms of topology of wake observed by Öngoren & Rockwell (1988).

Later, Cetiner & Rockwell (2001) had carried through focused experimental study in the *Lock-on* state, or synchronization, in the formation of the vortices. This phenomenon occurs when the frequency of emission of vortices is determined primordially by the frequency of oscillation of the cylinder. They had noticed that this phenomenon occurs for the harmonic ones of the basic frequency of emission of vortices, in the case where the cylinder remains static. Additionally, some analyses of numerical simulations has been proposals for the cylinder oscillating in the direction of an incident flow, carried through for Justesen (1991) that confirms some regimes described for Tatsuno & Bearman (1990) for a static fluid; Guilmineal et. al (2002) simulating oscillations in the direction of the flow for Re=100 and KC=5, however for static flow; Song et. al (2002) that they argue a flow in the limit of the laminar flow, Re=200; beyond Dütsch et. al (1998), had confirmed numerically all regimes of flow argued by Öngoren & Rockwell (1988). Two new concepts are added to the introduction; the reduced velocity, and the reduced frequency, of the cylinder. The reduced velocity represents the rate between the maximum velocity of displacement of the cylinder by the velocity of the flow not disturbed. Therefore, if the displacement of the cylinder is a harmonic function of the type presented in Eq. 1.1:

$$x_c(t) = \frac{\mathrm{A}}{2} sin(2\pi f\ t). \tag{1.1}$$

The velocity of the cylinder is given by the first derivative of Eq. 1.1, in the form that follows:

$$\mathrm{U}_c(t) = \pi f\ \mathrm{A}\ cos(\underbrace{2\pi f\ t}_{\phi}). \tag{1.2}$$

The point of maximum of the function represented by the Eq. 1.2 occurs when $\phi = 0$, where $cos(2\pi f\ t) = cos(0) = 1$. Therefore, the reduced velocity is given by:

$$\mathrm{U}_r = \pi f\ \mathrm{A}\ . \tag{1.3}$$

The reduced frequency is defined as the rate between the oscillation frequency of the cylinder by the vortex-emission frequency in the static case, where f_c represents the oscillation frequency of the cylinder.

$$f_r = \frac{f_c}{f_0}. \tag{1.4}$$

2. Methodology

The physical formulation of the problem considers a compressible and two dimensional Newtonian fluid over a non-inertial frame. This aspect of the flow is added to the mathematical formulation as a pseudo-force in momentum equation and as a pseudo-work in the energy equation, Batchelor (2000). Therefore, the governing equations of the problem are presented in Einstein notation and non-dimensional form of its propertys as: the conservation mass, momentum and energy equations, respectively:

$$\frac{\partial \rho}{\partial t} + \frac{\partial}{\partial x_i}\left(\rho u_i\right) = 0 \,; \tag{2.1}$$

$$\frac{\partial}{\partial t}\left(\rho u_i\right) + \frac{\partial}{\partial x_j}\left(\rho u_i u_j\right) = -\frac{\partial p}{\partial x_i} + \frac{\partial \tau_{ij}}{\partial x_j} + \rho f_i \,; \tag{2.2}$$

$$\frac{\partial}{\partial t}\left(\rho e_T\right) + \frac{\partial}{\partial x_i}\left(\rho e_T u_i\right) = -\frac{\partial}{\partial x_i}\left(p u_i\right) + \frac{\partial}{\partial x_i}\left(\tau_{ij} u_j\right) - \frac{\partial q_i}{\partial x_i} + \rho f_i u_i \,; \tag{2.3}$$

$$x_c(t) = \frac{\mathrm{A}}{2}\mathbf{sin}\left(2\pi f\, t\right); \tag{2.4}$$

where x_i represents the spatial cartesian coordinate in *i*-direction; ρ, the specific mass; t, temporal coordinate; *p*, the thermodynamic pressure; τ_{ij}, the viscous tensor for a Newtonian fluid; e_T, is the total energy by mass unit; u_i and u_j represents the velocity component in *i* and *j*-direction; q_i is the density heat transfer in *i*-direction; and ρf_i represents the pseudo-force in *i*-direction. This collection of equations is named as Navier-Stokes equations and is normalized as suggested by Anderson (2001). Additionally, the hypothesis of a gas caloric and thermally perfect is accepted; moreover the perfect gas state equation is used to connect the pressure and the temperature.

The pseudo-force is attached to the oscillatory movement of the circular cylinder represented by $x_c(t)$; resulting in the above equation,

$$\rho f_i = \rho \frac{\partial^2}{\partial t^2}\left[x(t)\right] = \rho 2\mathrm{A}\,\left(\pi f\right)^2 \mathbf{sin}\left(2\pi f\, t\right). \tag{2.5}$$

where, *f* and A represents, respectively, the non-dimensional frequency of oscillation and amplitude of displacement of the cylinder.

The boundary conditions consist of imposing the non-slip condition in the solid wall of the cylinder, condition of adiabatic wall and null gradient of pressure in the normal direction to the wall, approximation of boundary layer, which implies at, respectively;

$$u_i = u_{is} \quad , \quad \frac{\partial T}{\partial n} = 0 \quad , \quad \frac{\partial p}{\partial n} = 0 \,, \tag{2.6}$$

where the subscript *is* corresponds to the component of the velocity vector in the *i*-direction on the solid surface and *n* represents the normal direction to the surface.

The Eq. 2.2, 2.3, 2.4 can be written in vectorial notation as follows:

$$\frac{\partial \mathbf{U}}{\partial t} + \frac{\partial \mathbf{E}}{\partial x} + \frac{\partial \mathbf{F}}{\partial y} = \mathbf{R} \,, \tag{2.7}$$

where, **U**, represents the conservative variable vector in a non-dimensional form; **E** and **F** represents the flux vectors of the properties in a non-dimensional form; and **R** represents the source term, Anderson et al (2000), which is responsible for the pseudo-force, originated by the oscillatory displacement of the cylinder. However, the movement of the cylinder occurs only in the *x*-direction, therefore, the vector **R** results in:

$$\mathbf{R} = \begin{bmatrix} 0 \\ \rho f_x \\ 0 \\ \rho u f_x \end{bmatrix}, \tag{2.8}$$

To numerically solve the described system the explicit method of Ducros is used, the formulation uses a finite volumes approach which was demonstrated in Mendonça (2004). Then, to make the spatial discretization a flux tensor $\mathbf{\Pi}$ was defined, with the following property:

$$\nabla \cdot \mathbf{\Pi} = \frac{\partial \mathbf{E}}{\partial x} + \frac{\partial \mathbf{F}}{\partial y}. \tag{2.9}$$

Therefore, the Eq. 2.9 can be rewritten in the form that follows:

$$\frac{\partial \mathbf{U}}{\partial t} + \nabla \cdot \mathbf{\Pi} = \mathbf{R}. \tag{2.10}$$

The equation above is integrated for an arbitrary control volume $\forall$, resulting in the following equation:

$$\frac{\partial}{\partial t}\int_{\forall} \mathbf{U}\, d\forall - \int_{\forall} \nabla \cdot \mathbf{\Pi}\, d\forall + \int_{\forall} \mathbf{R}\, d\forall. \tag{2.11}$$

Thus, under the hypothesis of that the control volume is invariant with the time the divergent theorem is applied to the flux terms, transforming the integral of volume into an integral of surface, resulting in:

$$\frac{\partial}{\partial t}\int_{\forall} \mathbf{U}\, d\forall = -\int_{S} \mathbf{\Pi} \cdot \mathbf{n}\, dS + \int_{\forall} \mathbf{R}\, d\forall, \tag{2.12}$$

where $\mathbf{n}$ represents the normal vector to the surface of the control volume .

If the volumetric averages of the vectors $\mathbf{U}$ and $\mathbf{R}$ can be defined for arbitrary control volume $\forall$, the following equations are obtained:

$$\overline{\mathbf{U}} \equiv \frac{1}{\forall}\int_{\forall} \mathbf{U}\, d\forall \quad \text{e} \quad \overline{\mathbf{R}} \equiv \frac{1}{\forall}\int_{\forall} \mathbf{R}\, d\forall, \tag{2.13}$$

which, if replaced in the Eq. 2.12, results in:

$$\frac{\partial \overline{\mathbf{U}}}{\partial t} - \frac{1}{\forall}\int_{S} \mathbf{\Pi} \cdot \mathbf{n}\, dS + \overline{\mathbf{R}}. \tag{2.14}$$

For a two dimensional control volume a first order approach is realized, inducing a temporal variation of the vector U , shown in the Eq. 2.15.

$$\left(\frac{\partial \overline{\mathbf{U}}}{\partial t}\right)_{i,j} = \frac{\Delta \overline{\mathbf{U}}_{i,j}}{\Delta t} + (O)\Delta t, \tag{2.15}$$

where, $\Delta\overline{\mathbf{U}}$ represents the variation of the vector $\overline{\mathbf{U}}$ in the time step, Δt. Resulting in a temporal approach of the Eq. 2.14, which for a quadrilateral bidimensional control volume, results in:

$$\Delta\overline{\mathbf{U}} = -\frac{\Delta t}{\forall_{i,j}}\left[\int_{s_{i+1/2}} \mathbf{\Pi} \cdot \mathbf{n} dS + \int_{s_{i-1/2}} \mathbf{\Pi} \cdot \mathbf{n} dS + \int_{s_{j+1/2}} \Pi \cdot \mathbf{n} dS + \int_{s_{j-1/2}} \mathbf{\Pi} \cdot \mathbf{n} dS\right] + \Delta t\, \overline{\mathbf{R}}_{i,j}, \tag{2.16}$$

where $S_{i+1/2}, S_{i-1/2}, S_{j+1/2}, S_{i-1/2}$, represents the surfaces that define the faces of the quadrilateral, shown in Fig. 2. The sub-index represent the adjacent control volumes with which the control surfaces are shared, it means, the surface $S_{i+1/2}$ are shared by the volume (i, j) with the volume $(i+1, j)$.

However, to numerically solve the Eq. 2.16, it is necessary to approach the integrals of surface. Therefore, the consideration of the flux tensor Π is a constant in the surface S are used, as follows;

$$\int_{S} \mathbf{\Pi} \cdot \mathbf{n}\, dS \cong \mathbf{\Pi} \cdot \int_{S} \mathbf{n}\, dS = \mathbf{\Pi} \cdot \mathbf{S}, \tag{2.17}$$

where, $\mathbf{S}$ represents the surface vector associated to the surface S. The approximation is necessary because, in a finite volume formulation, only the volumetric averages of the properties are known.

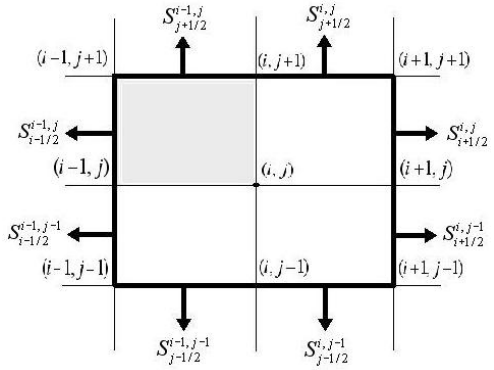

Figure 2: Control volume contend a point of the mesh for the bidimensional case with fourth order of spatial precision. The solid line of bigger thickness involves the volume around of the mesh point; the volume shading represents the discretization in finite volumes.

It is defined, then, the function of liquid flux, $F\left(\overline{\mathrm{U}}\right)_{i,j}$, of the tensor $\mathbf{\Pi}$ on the control surface, in the form;

$$F\left(\overline{\mathrm{U}}\right)_{i,j} = \frac{\Delta t}{\overline{\mathrm{V}}_{i,j}}\left[\left(\mathbf{\Pi}\cdot\mathbf{S}\right)_{i+1/2} + \left(\mathbf{\Pi}\cdot\mathbf{S}\right)_{i-1/2} + \left(\mathbf{\Pi}\cdot\mathbf{S}\right)_{j+1/2} + \left(\mathbf{\Pi}\cdot\mathbf{S}\right)_{j-1/2}\right]. \tag{2.18}$$

Then, the Eq. 2.16 can be rewritten as follows:

$$\Delta\overline{\mathrm{U}}_{i,j} = -\left[F\left(\overline{\mathrm{U}}\right)_{i,j} + D\left(\overline{\mathrm{U}}\right)_{i,j}\right] + \Delta t\,\overline{\mathrm{R}}_{i,j}, \tag{2.19}$$

where, $D\left(\overline{\mathrm{U}}\right)_{i,j}$ represents an artificial dissipation in the volume (i,j). This dissipation is explicitly imposed to stabilize the numerical method.

To carry out the temporal evolution of the Eq. 2.19, a variation of the Runge-Kutta method with a third order precision is used, proposal by Shu and described by Yee (1997), as follows:

$$\overline{\mathbf{U}}^{1} = \left[F\left(\overline{\mathbf{U}}^{n}\right) + D\left(\overline{\mathbf{U}}^{n}\right) + \Delta t\,\overline{\mathbf{R}}^{n}\right]; \tag{2.20}$$

$$\overline{\mathbf{U}}^{2} = \frac{3}{4}\overline{\mathbf{U}}^{n} + \frac{1}{4}\overline{\mathbf{U}}^{1} - \frac{1}{4}\left[F\left(\overline{\mathbf{U}}^{1}\right) + D\left(\overline{\mathbf{U}}^{1}\right) + \Delta t\,\overline{\mathbf{R}}^{1}\right]; \tag{2.21}$$

$$\overline{\mathbf{U}}^{n+1} = \frac{1}{3}\overline{\mathbf{U}}^{n} + \frac{2}{3}\overline{\mathbf{U}}^{1} - \frac{2}{3}\left[F\left(\overline{\mathbf{U}}^{2}\right) + D\left(\overline{\mathbf{U}}^{2}\right) + \Delta t\,\overline{\mathbf{R}}^{2}\right]. \tag{2.22}$$

In the previous equations, $\overline{\mathrm{U}}^{1}$ and $\overline{\mathrm{U}}^{2}$ are intermediate vectors used to the accomplishment of the calculation of $\overline{\mathrm{U}}^{n+1}$ and the respective fluxes, $F\left(\overline{\mathrm{U}}^{n}\right)$, and dissipations, $D\left(\overline{\mathrm{U}}^{n}\right)$.

The numerical simulation uses a structuralized grid with O format and resolution of 360 points in the angular direction and 315 points in the radial direction, totalizing 113400 volumes. The time-step, Δt, are determined using the criterion of entrance of Courant-Friedrichs-Lewis (CFL), Anderson et al (2000), considering the velocity of propagation of the sound. Moreover, the boundary conditions of the computational domain considers the hypothesis of that the flux of any property, ϕ, of the fluid is invariant on the surface, η_f, of the border. It means;

$$\frac{\partial\phi}{\partial\eta_f} = 0\,. \tag{2.22}$$

These conditions are used in the border of the domain because the imposition of non-disturbed properties of the flow in the computational border would cause the reflection of the waves of pressure generated by the oscillation movement of the cylinder and it would cause interference in the near region to the cylinder.

3. Results

3.1 Static Cylinder

The numerical simulation of the laminar flow around of a fixed circular cylinder, $\mathrm{Re} = 100$, was executed in order to use the output parameters, as the number of Strouhal, f_0. The following figure, Fig. 3, represents the power spectrum of the lift coefficient, where the peak indicates the dominant frequency that the alternating emission of vortices occurs and defines the number of Strouhal, $f_0 \approx 0.15$.

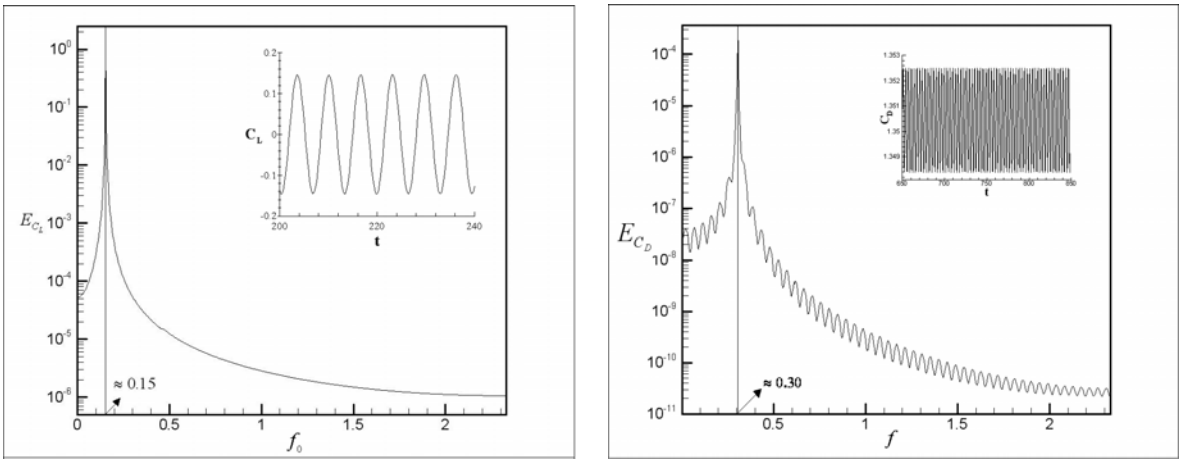

Figure 3: Power Spectrum of the lift coefficient on the left side and the drag coefficient on the right side, component that acts in the normal direction to the flow on the cylinder, Re=100. In the upper right corner the signal of the lift coefficient in function of the nondimensional time.

Can be observed from the figures that the dominant frequency of the drag coefficient it's about two times the frequency of the lift coefficient, as expected from the literature. The flow around a static cylinder presented itself steady, has emission of alternating and symmetrical vortices, characterizing the wake of the type presented by von Kármán, the Fig. 4 shows the temperature gradient visualization.

Figure 4: Temperature gradient visualization for the static cylinder at Re=100.

This type of configuration of wake is a typically defined as von Kármán wake and in this case the temporal average of the lift coefficient is null, but the r.m.s *(root mean square)* average have the value of $C_{L\,r.m.s} = 0.1033$ and in the other hand the temporal average of the drag coefficient is $C_D = 0.1033$. The power spectra of the output were obtained applying to the output a FFT *(Fast Fourier Transform)*.

3.2 Oscillatory Cylinder

In the hypothesis of the cylinder oscillating in-line with the flow, some simulations with different configurations of reduced velocity, reduced frequency and non-dimensional amplitude are proposals. The purpose of these simulations is topologically group the possible types of wake, inside of the executed simulations, using as analysis tool the generated graphs, from the output signals of the lift and the drag coefficient, and the visualization of the temperature gradient. Leaving of this premise, are presented the data of the simulations executed for the different configurations of the considered flow, varying the reduced velocity and the reduced frequency.

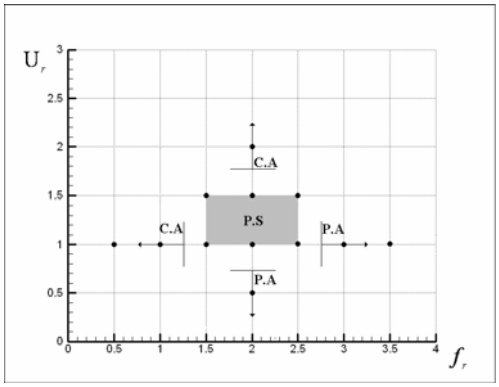

Figure 5: Demonstrative of executed simulation.

The graphic of the Fig. 5 shows the executed simulations on this work, the shading part of the graphic means the periodic symmetrical region, P.S; C.A means chaotic anti-symmetrical; and P.A means periodic anti-symmetrical. These symbols represent the topology of wake found in this present work and shows its tendency to become.

3.2.1 Periodic Symmetrical

In this configuration of the flow, pairs of vortices are emitted to each cycle of oscillation of the cylinder, having become the flow completely symmetrical. The consequence of this symmetry reflects in the extinguishing of the component of normal force on the cylinder, lift force, only acting the in-line component with the flow. This characteristic of the flow is the greater point and importance of the present study, once to certain parameters a component of force that normally would act on the system is annulled.

The emission dynamics of vortices can be described in the following way: In accordance with the movement of the cylinder in the negative direction of the oscillation axle, a zone of recirculation in the boundary layers in the upper and lower side of the cylinder is formed, which separates in the same place above and in a low position of the surface of the cylinder, Fig. 6(a); it forms then two zones of recirculation of same intensity and size, resulting in a same format downstream of the cylinder, Fig. 6(b); however, with appositive rotation. The increase of this zone of recirculation arrives to the end when the cylinder reaches the position $_{-A/2}$, position in which is initiated the contrary movement of displacement, positive direction in relation to the oscillation axle, Fig. 6(c); as the cylinder covers the positive direction, a new boundary layer is generated, must be noticed that if it didn't have an incident flow the formation of the vortices would be that described by Tatsuno & Bearman (1990), however, the incident flow functions as a barrier to the formation of these "opposite vortices" in relation to the vortices of bigger intensity, confining them as seemed in the Fig. 6(d); additionally, the emission of the pairs of vortices occurs when it has the inversion of the movement from the point of maximum of the displacement of the cylinder, Fig. 6(e).

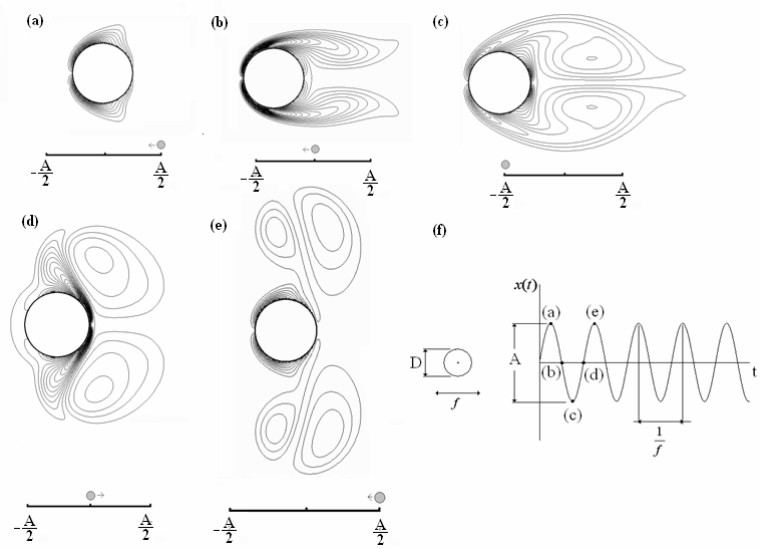

Figure 6 : Visualization of vorticity iso-lines, for: $\theta = 2\pi f_c \cdot t$; (a) $\theta \approx 90°$, (b) $\theta \approx 180°$, (c) $\theta \approx 270°$, (d) $\theta \approx 360°$, (e) $\theta \approx 450°$.

The following figures show the temperature gradient visualization for the shading region of the graphic of Fig. 5.

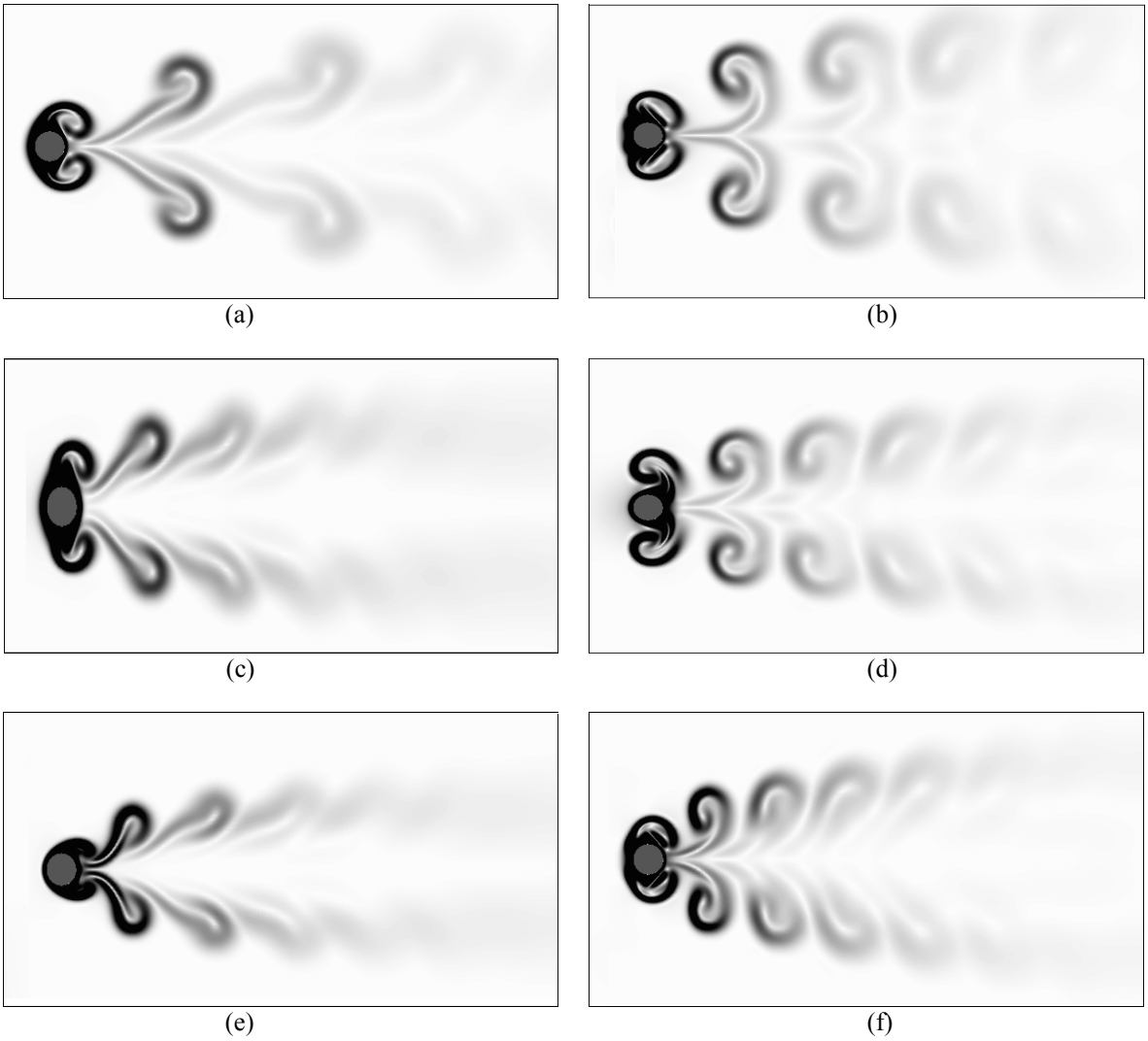

(a) (b) (c) (d) (e) (f)

Figure 7: Temperature gradient visualization, (a) U_r=1.0 and f_r=1.5; (b) U_r=1.5 and f_r=1.5; (c) U_r=1.0 and f_r=2.0; (d)U_r=1.5 and f_r=2.0; (e) U_r=1.0 and f_r=2.5; (f) U_r=1.5 and f_r=2.5.

The following figures illustrate the power spectrum of the drag coefficient;

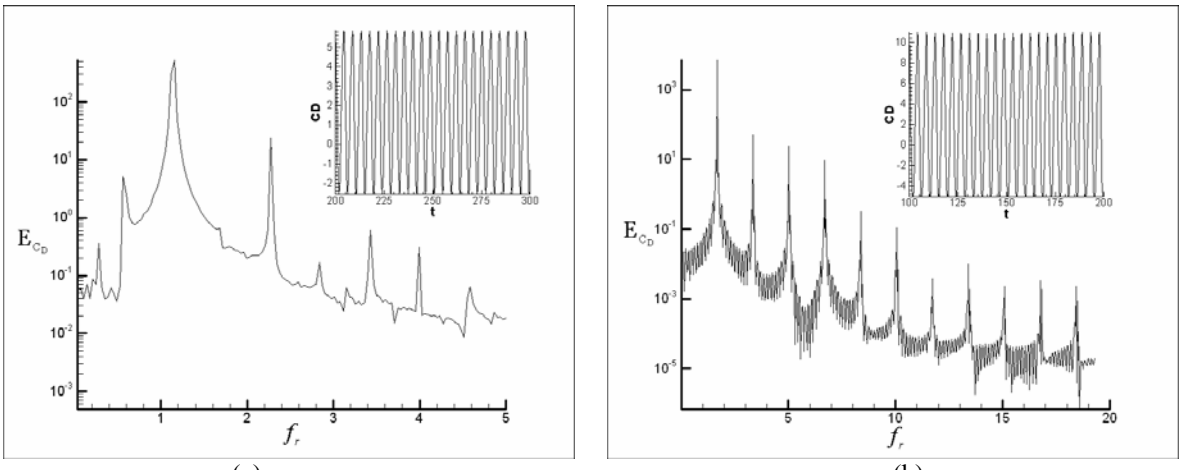

(a) (b)

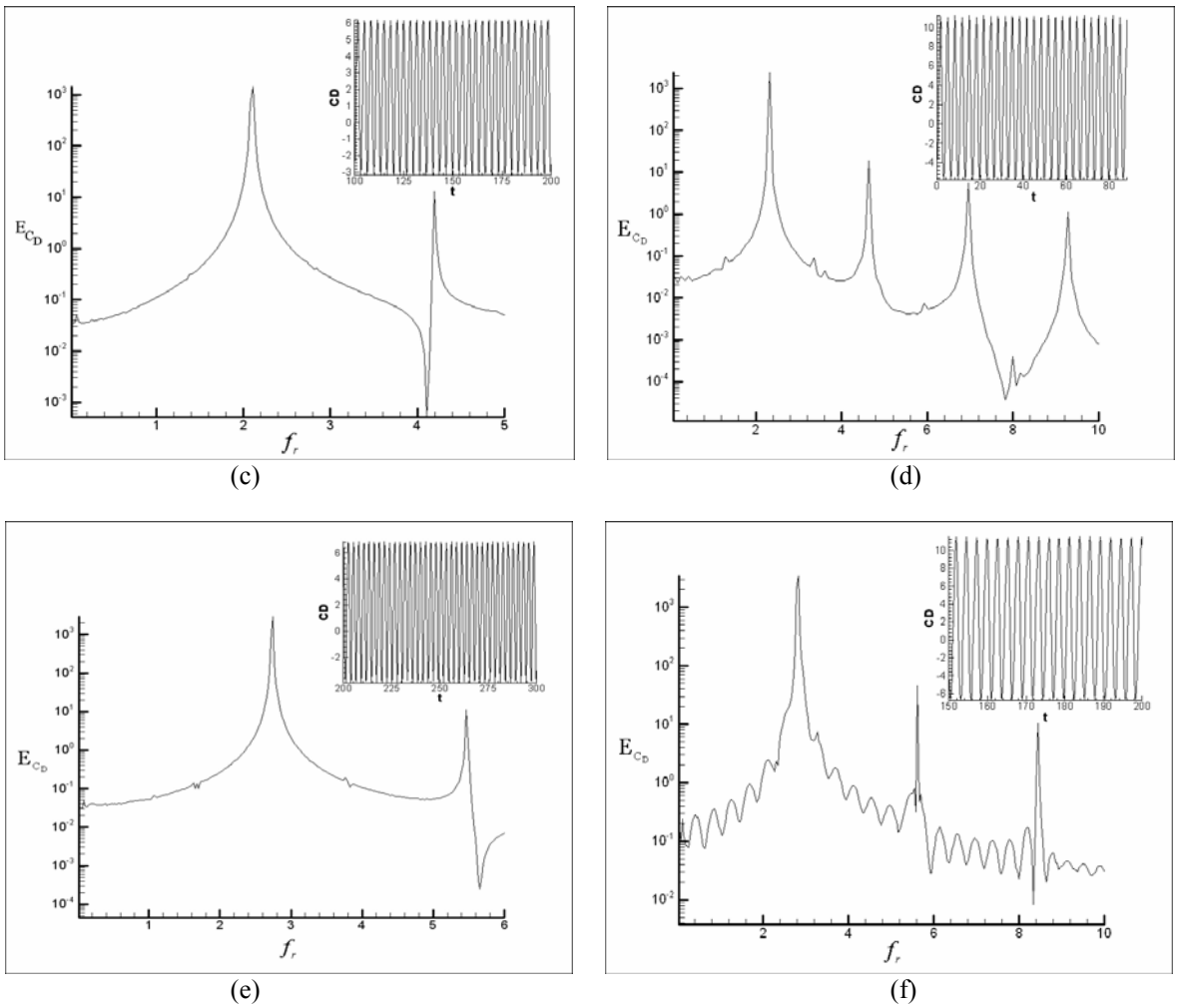

Figure 10: Power spectrum of the drag coefficient, (a) U_r=1.0 and f_r=1.5; (b) U_r=1.5 and f_r=1.5; (c) U_r=1.0 and f_r=2.0; (d) U_r=1.5 and f_r=2.0; (e) U_r=1.0 and f_r=2.5; (f) U_r=1.5 and f_r=2.5.

In this case all the dominant frequencies showed by power spectrum are harmonics of the frequency of excitation of the system. The analysis of the signal of lift coefficient was omitted because

3.2.2 Periodic Anti-Symmetrical

This configuration of the flow presents an interesting characteristic, in the near region of the cylinder the wake has similar topology to P.S mode, periodic symmetrical. However, the vortices generated by the displacement of the cylinder combine themselves for form a vortex of bigger intensity and that will give beginning to a wake with typical characteristic of the von Kármán wake. Composing itself by two distinct regions: the first one near to the cylinder that shares characteristics with P.S mode; and the other region away from the cylinder that has the characteristic of the von Kármán vortices, however the disturbance that provokes the decline for P.A mode, has origin in a region away from the cylinder, dislocating itself from the downstream of the wake until the near region to the cylinder inducing, then, the coalescence of the vortices and forming the described topology, as exposed in the following graphics of Fig. 9.

The disturbance that support the decline to P.A mode evolve temporarily in the downstream direction of the flow, from a distant point of the cylinder, $L >> D$. The vorticity field grows with the time and that increase of magnitude that initially forms a great steady region of vorticity with opposite rotational direction, although for some reason the whole structure comes down because the disturbance travels in the downstream direction and when it approaches to the region of influence of the cylinder, near wake region, occurs the rupture of this zone of recirculation and consequence of that is the emission of vortices.

By the power spectrum can be seem that the output signals of the system with the excitation of the cylinder has many frequencies as response for principal excitation of the cylinder, producing a highly modulated signal.

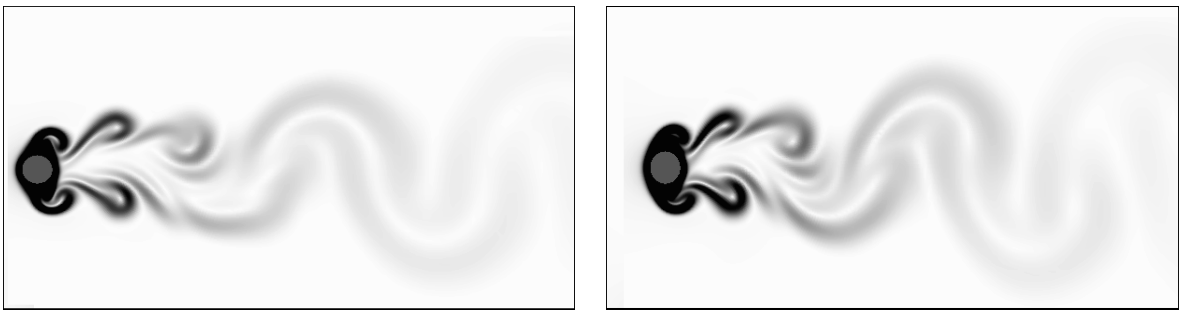

(a) (b)

Figure 9: Temperature gradient visualization, (a) U_r=1.0 and f_r=3.0; (b) U_r=1.0 and f_r=3.5

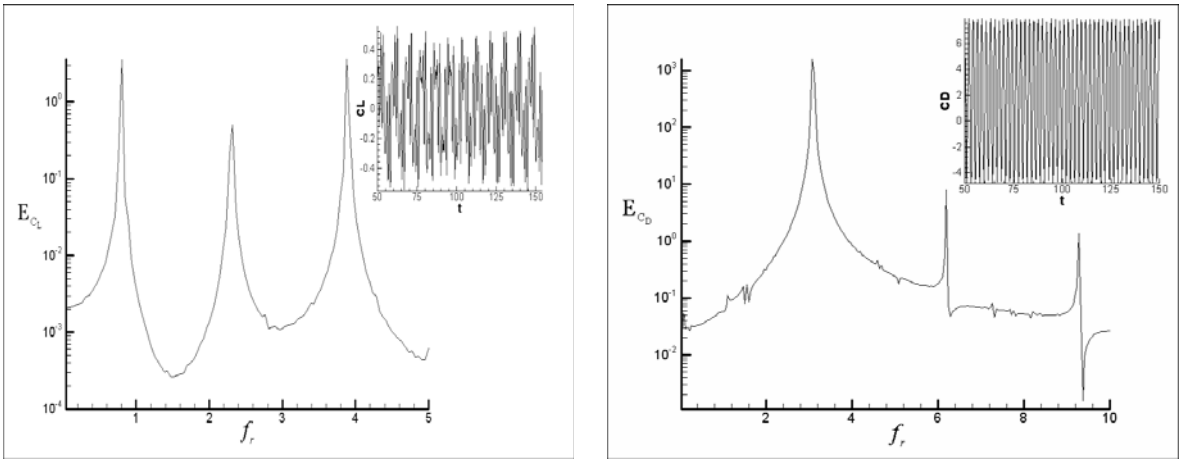

(a) (b)

Figure 10: Power spectrum of the output signals for U_r=1.0 and f_r=3.0.

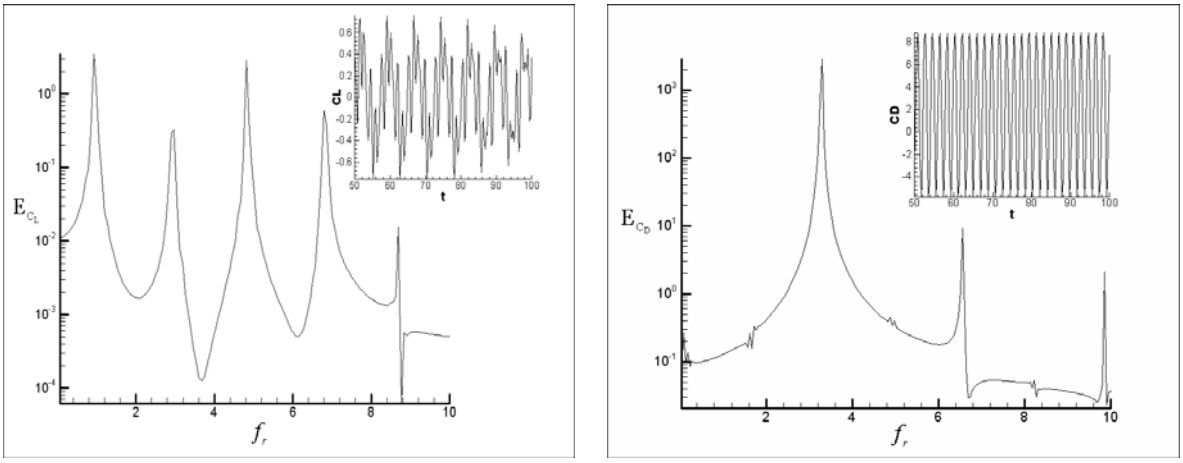

(a) (b)

Figure 11: Power spectrum of the output signals for U_r=1.0 and f_r=3.5; (a) lift and (b) drag coefficient.

3.2.3 Chaotic Anti-Symmetrical

In this flow configuration the vortices are generated and emitted aleatorily without any synchrony or regularity, and in which the interaction mechanism between the vortices, cylinder and flow is extremely complex and a non linear configuration, the disturbance that induces the decline for C.A mode has origin in the near wake region to the cylinder, the Fig. 12, as show below that illustrate two visualizations of this chaotic regime;

The Fig. 15 explains the time average values of the lift and drag coefficient for comparison.

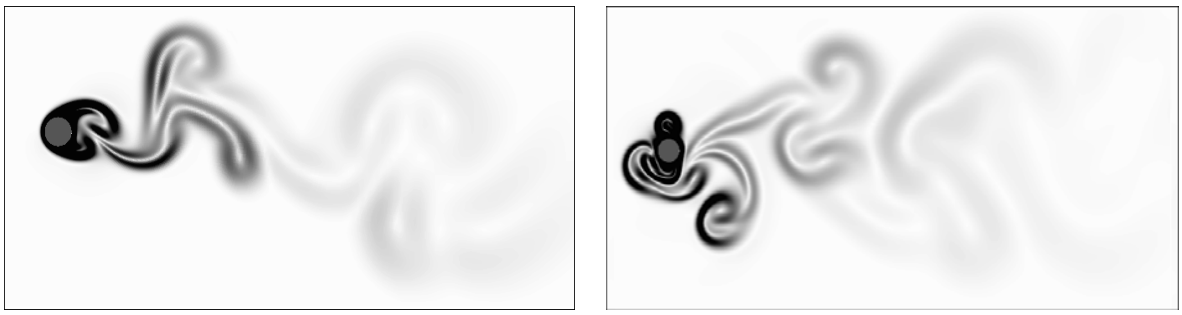

(a) (b)

Figure 12: Temperature gradient visualization, (a) U_r=1.0 and f_r=0.5; (b) U_r=2.0 and f_r=2.0

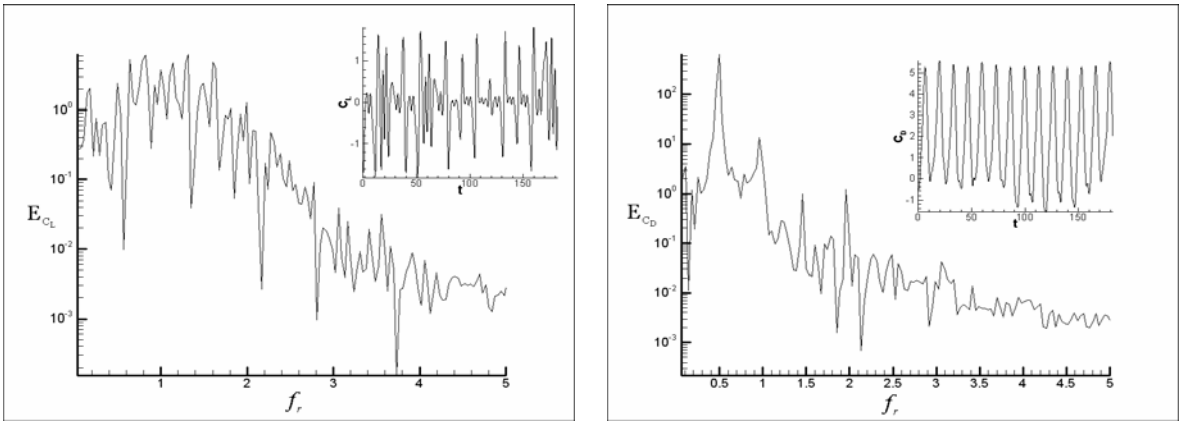

(a) (b)

Figure 13: Power spectrum of the output signals for U_r=1.0 and f_r=0.5; (a) lift and (b) drag coefficient.

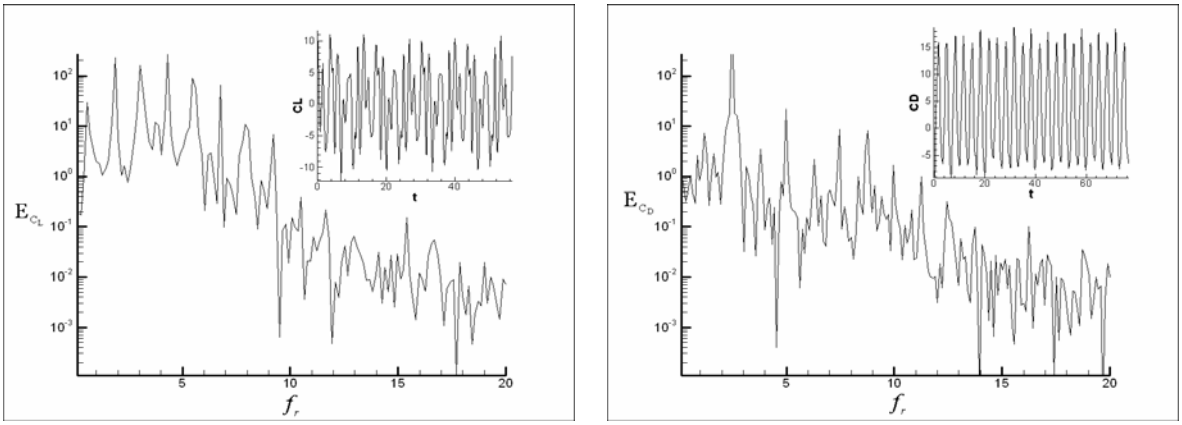

(a) (b)

Figure 14: Power spectrum of the output signals for U_r=2.0 and f_r=2.0; (a) lift and (b) drag coefficient.

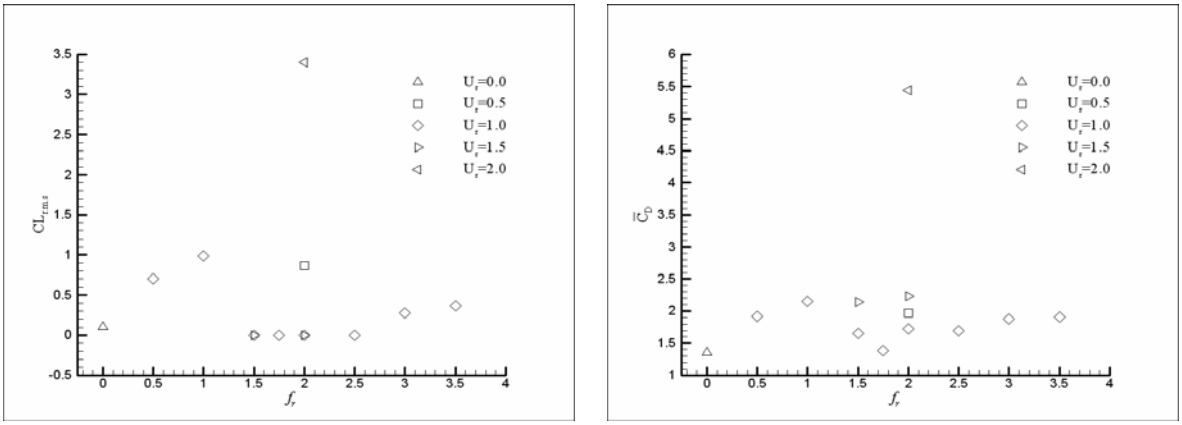

(a) (b)

Figure 15: The temporal averages of the output coefficient; (a) lift (r.m.s) and (b) drag coefficient.

4. Conclusions

The present study had as main proposal, the topological analysis of a laminar flow around a circular cylinder with streamwise oscillation, through the analysis of the data of the numerical simulations. Ahead on this, it was observed the existence of three main and distinct ways of topology: the main way is called periodic symmetrical, P.S, where the symmetry in relation to the x-axle promotes the extinguishing of the normal component of operating force on the cylinder, without affect or increases the magnitude of in-line component acting on the cylinder, its main characteristic, in P.S mode, is the emission of pairs of vortices in each cycle of oscillation of the cylinder. The secondary ways are characterized by the decline of P.S mode to: chaotic anti-symmetrical, C.A; and periodic anti-symmetrical, P.A, modes.

In the secondary mode, C.A, the characteristics of the flow are chaotic anti-symmetrical, this means that the topology of the wake doesn't present a permanent configuration, throughout the time, additionally in this mode the component of normal force to the flow, doesn't present a null temporal average. in the secondary mode, P.A, the wake are divided in two regions, the first one near to the cylinder which has similar characteristics with the mode P.S, and other region away from the cylinder, in the wake, and that have topology of the type von Kármán.

On this work was found some possible topology wake, becoming it successful in its initial proposal. However, could be possible that other configurations of the parameters reduced velocity and reduced frequency may promote the sprouting of other types of wake topology, once that the literature on the subject mentions endless configurations for the wake topology.

5. References

ANAGNOSTOPOULOS, P. & ILIADIS, G., "Numerical study of the flow pattern an the in-line respose of a flexible cyrcular cylinder in an oscillating stream", J. Fluid and Structures (1998), vol. 12, pp. 225-258.

ANDERSON, D. A., TANNEHILL, J. C. & PLETCHER, R., "Computational Fluid Mechanics and Heat Transfer", Hemisphere Publishing Company, New York, 2000.

ANDERSON, J. D., Jr., "Fundamentals of Aerodynamics", McGraw-Hill Higher, Education, 2001, p.p. 15-21.

BATCHELOR, C. K, "An Introdution to Fluid Dynamics", University Press, Cambridge (2000).

BLACKBURN, H. M. & HENDERSON R. D., "A study of two-dimensional flow past an oscillating cylinder", J. Fluid and Structures (1999), vol. 385, pp. 255-286.

CENTINER, O. & ROCKWELL, D., "Streamwise oscillations of a circular cylinder in a steady current. Part 1. Loked-on states of vortex formation and loading.", L. Fluid Mech (2001), vol, 427, pp. 1-28.

GOVARDHAN, R. & WILLIAMSON C. H. K, "Modes of vortex formation and frequency response os a freely vibrating cylinder", J. Flui Mech. (2000), vol. 420, pp. 85-130.

GRIFFIN, O. M. & RAMBERG, S. E., "Vortex shedding from a cylinder vibrating in line with an incident uniform flow", J. Fluid Mech. (1976), Vol. 75, pp. 257-271.

GUIMINEAU, E. & QUEUTEY, P, "A numerical simulation of vortex shedding from na oscillaing circular cylinder", J. Fluid and Structures (2002), vol. 16(6), pp. 773-794.

H. DÜTSCH, F. DURST, S. BECKER & H. LIENHART, "Low-Reynolds-number flow around an oscillating circular cylinder at low Keulegan-Carpeter number", J. Fluid Mech (1998), vol. 360, pp. 249-271.

JUSTESEN, P., "A numerical study of oscillating flow around a circular cylinder", J. Fluid Mech (1991), vol. 222, pp. 157-196.

MENDONÇA, A. F. "Simulação Numérica do Escoamento Laminar em uma Base Bidimensional. Dissertação de Mestrado em Engenharia Mecânica, Publicação ENM.DM-081A-04, Departamento de Engenharia Mecânica, Universidade de Brasília, Brasília, DF, 143p. ano (2004).

NOBARI, M. R. H & NADERAN, H., "A numerical study of flow past a cylinder with cross and inline oscillation", Computers & Fluids (2005), pp. 1-14.

ÖNGOREN, A. & ROCKWELL, D., "Flow structure from an oscillating cylinder. Part 2. Mode competition in the near wake", J. Fluid Mech (1988), vol. 191, pp. 225-245.

TATSUNO, M & BEARMAN, "A visual study of the flow around na oscillating circular cylinder at low Keulegan-Carpenter number and low Stokes number",

ZDRAVKOVICH, M. M., " Diferent modes of vorex shedding: an overview", J. Fluid and Structrures (1996), vol. 10, pp. 427-437.

Proceedings of the 11th Brazilian Congress of Thermal Sciences and Engineering -- ENCIT 2006
Braz. Soc. of Mechanical Sciences and Engineering -- ABCM, Curitiba, Brazil, Dec. 5-8, 2006

Paper CIT06-0913

H_2O_2/Paraffin Hybrid Rockets for Launching Nanosats into LEO

Leonardo Henrique Gouvêa
leo@lcp.inpe.br

Ricardo Vieira
rvieira@lcp.inpe.br

Fernando de Souza Costa
Instituto Nacional de Pesquisas Espaciais
Rodovia Presidente Dutra, km 40, Cachoeira Paulista/SP, Brasil
fernando@lcp.inpe.br

Abstract. *The launching of small payloads or nanosats into low Earth orbit (LEO) by hybrid rockets has been considered in the last years. In the present work it is determined the mass distribution of hybrid propulsion systems using H_2O_2 and solid paraffin as propellants, to place a 20 kg payload into a 300 km circular equatorial orbit. Two cases are considered: a three-stage hybrid rocket with a total characteristic velocity of 9300 m/s, and three stage air-launched rockets with a total characteristic velocity of 8700 m/s. The effects of the O/F ratio, H_2O_2 concentration and paraffin composition on specific impulse, thrust coefficient and mass distribution are studied.*

Keywords: Paraffin, H_2O_2, nanosats, low Earth orbit (LEO), specific impulse, mass distribution

1. Introduction

Hybrid rocket technology is known for more than 50 years, however only in the 1960's its safety characteristics motivated a significant research. Nowadays, the need for green propellants (propellants with low toxicity and low pollutant characteristics), the requirements of safe operation and storability, low cost missions, and the interest for launching small payloads and nanosats into LEO made hybrid rockets more attractive.

Hybrid propulsion systems employ propellants in different phases, being the most usual hybrid systems with a solid fuel and a liquid oxidizer.

The main disadvantage of hybrid rockets is the low thrust level attainable, due to the relatively low regression rates of the solid fuel grain, making necessary the use of a large number of ports. According to Karabeyoglu et al. (2003a) multi-port grains have characteristics such as:

- Large fractions of the fuel remain unburned and are not used for propulsion;
- Problems of grain integrity at the end of burning when the web thickness is too small and makes the grain susceptible to structural failure (To solve the problem, supports can be used, however they increase the mass and the complexity of the system);
- Manufacturing of multi-port grains is more difficult and expensive than of a single port grain;
- Need of multiple injectors or a pre-combustion chamber;
- Potential non-uniform burning among the ports.

Some methods to increase the fuel regression rate are known but, in general, they have undesirable characteristics, for example:

- Insert screens or mechanical devices in the ports to increase the turbulence level and, therefore, increase the heat transfer rates: this method increases the complexity of design and the failure possibilities;
- Use of metallic addictives: this method increases slightly the regression rate, however it increases the vulnerability to instabilities due to the pressure-dependence of the regression rates, and it increases the environmental impact.
- Use of oxidizers mixed within the solid fuel: this method converts the hybrid system in almost a solid system, eliminating the safety characteristics of the hybrid system;
- Increase the surface rugosity adding small solid particles, which would burn at a different rate from the main fuel: this method has a small effect on regression rates but large solid particles in the exhaust gases reduce the system efficiency, and it causes an increase in costs of fuel production.

The safe operation of hybrid propulsion systems is related to the separation of fuel and oxidizer, differently from solid systems which mix fuel and oxidizer in the grain. Another important safety characteristic is the independence of the regression rate with respect to the chamber pressure, making hybrid systems safer than solid systems if pressure peaks do occur.

The control of the oxidizer flow rate in hybrid systems allows several starts and an accurate control of the thrust level.

Hybrid systems have only one liquid propelllant, thus they require only one liquid line and a relatively simple injection system, as compared to liquid bipropellant systems which require two separate liquid lines and a complex injection plate in order to collide and mix the fuel and oxidizer jets.

The hydrogen peroxide (H_2O_2) is a well-known oxidizer or monopropellant and has been used for decades in propulsion systems, as described by Walter (1954), who related his experiences with the German Navy during the II World War, when hydrogen peroxide was used in ATO (Assisted Take Off) engines. He describes the decomposition and detonation characteristics of peroxide and mentions that peroxide at concentrations lower than 82 % is not detonable and that pressure does not affect the peroxide decomposition velocity. Williams et al. (2004) states that HTP (High Teste Peroxide) is similar to nitroglicerin in terms of shock sensitivity and explodes with the same strength than the same quantity of TNT (Trinitrotoluen).

The paraffin used as fuel, specially in candles, is part of human culture for hundreds of years, but only in the last 5-10 years, has beeen considered as a rocket fuel.

Recently, it was developed in the Stanford University and in the Ames-NASA Research Center, both in the USA, a new paraffin-based fuel whose regression rate is approximately three times higher than conventional hybrid fuels (Karabeyoglu et al., 2003a,b, 2004). Promising results were obtained by several researchers (Brown and Lydon, 2005; Karabeyoglu et al., 2004; Santos et al., 2005; McCormick et al., 2005) using paraffin with different oxidizers – liquid oxygen (LOX), gaseous oxygen (GOX), nitrous oxide (N_2O) and hydrogen peroxide (H_2O_2).

Figure 1 shows the regression rates of paraffin with different oxidizers, for various oxidizer flow rates.

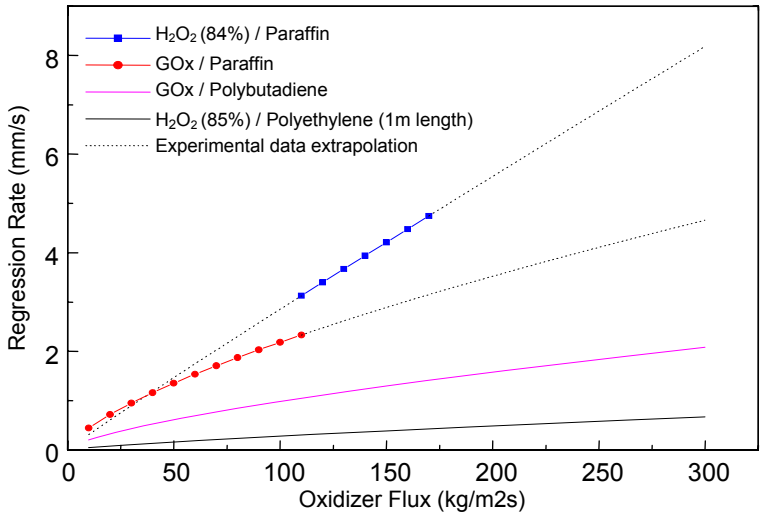

Figure 1. Regression rate of paraffin burning with different oxidizers versus oxidizer flow rates.

The mass of the propulsion systems can be significantly reduced by using air launching rockets, since there is lower drag, lower gravitational losses, and there is a gain in the system initial velocity.

The objective of this work is to describe hybrid propulsion systems using paraffin/H_2O_2 to launch a 20 kg nanosat into a low Earth equatorial circular orbit of 300 km. Two cases are considered: i) a three stage rocket with a total characteristic velocity of 9300 m/s; and ii) a three stage air-launched rocket with a total characteristic velocity of 8700 m/s.

2. Propulsion Performance Parameters

The efficiency parameters of a propulsion system depend on the combustion characteristics. The reaction between paraffin and hydrogen peroxide in the rocket combustion chamber is described by the chemical equation:

$$C_nH_{2n+2} + \left(\frac{3n+1}{\phi x}\right)\left(xH_2O_2 + (1-x)H_2O\right) \rightarrow \eta_{H_2O}H_2O + \eta_{CO_2}CO_2 + \eta_{CO}CO + \eta_{H_2}H_2 + \eta_{O_2}O_2 + \eta_{OH}OH + \eta_O O + \eta_H H \quad (1)$$

where x is the molar fraction of peroxide in the solution, ϕ is the fuel/oxidizer equivalence ratio and η_i is the stoichiometric coefficients of product i. A chemical equilibrium code was written in MATLAB language, using the equilibrium constant method, to calculate the stoichiometric coefficients in Eq. (1) and the adiabatic flame temperature, T_c. From these data, obtained with a given chamber pressure, P_c, the following variables are calculated:

$$X_j = \eta_j / \eta_{total} \tag{2}$$

$$M_{prod} = \sum_{j=1}^{N} \eta_j X_j \tag{3}$$

$$\bar{C}_p = \sum_{j=1}^{N} X_j \bar{C}_{p,j} \tag{4}$$

$$\gamma = \bar{C}_p / \left(\bar{C}_p - \bar{R} \right) \tag{5}$$

where X_j is the molar fraction of each product species, M_{prod} is the molar mass of products, $\bar{C}_p$ is the molar specific heat at constant pressure, γ is the ratio of specific heats, $\bar{R} = R_o/M_{prod}$ is the gas constant, and R_o = 8314 kJ/kmolK is the universal gas constant. The specific heats are temperature functions obtained from NIST (www.nist.gov).

After calculation of the chamber conditions, i.e., M_{prod}, γ and T_c, at a given chamber pressure, P_c, several propulsion performance parameters can be calculated: specific impulse, *Isp*; exhaustion characteristic velocity, C*; thrust coefficient, C_F; the mass flow rate, $\dot{m}$; and thrust, F, for a given ambient pressure, P_a, and nozzle expansion rate, ε.

The propulsion parameters are calculated with the following simplifying assumptions:

- Isentropic flow in the chamber and nozzle;
- Frozen flow along the nozzle;
- Constant pressure in the chamber;
- Perfect gases and perfect mixture;.
- Average γ in the nozzle.

The specific impulse, for a constant thrust rocket, is defined as the ratio between thrust and weight consumption rate of propellants:

$$I_{sp} = C_F C^* / g_0 \tag{6}$$

where g_0 is the gravity acceleration at sea-level.

The characteristic exhaustion velocity C^* is given by

$$C^* = \sqrt{\gamma R T_c} / \Gamma \tag{7}$$

where $\Gamma = \gamma \left[2/(\gamma+1) \right]^{\frac{\gamma+1}{2(\gamma-1)}}$.

The thrust coefficient, C_F, is given by:

$$C_F = \sqrt{\left(\frac{2\gamma^2}{\gamma-1} \right) \left(\frac{2}{\gamma+1} \right)^{(\gamma+1)/(\gamma-1)} \left[1 - \left(\frac{P_e}{P_c} \right)^{(\gamma-1)/\gamma} \right]} + \frac{P_e - P_a}{P_c} \frac{A_e}{A_t} \tag{8}$$

where A_e is the nozzle exit area, A_t is the nozzle throat area and P_e is the nozzle exit pressure. The thrust F generated by the exhaustion of gases through the nozzle is calculated by

$$F = \dot{m} v_e + \left(P_e - P_a \right) A_e \tag{9}$$

where $\dot{m}$ is the propellants mass flow rate, given by

$$\dot{m} = \Gamma \frac{A_t P_c}{\sqrt{\gamma R T_c}} \tag{10}$$

and v_e is the products exhaustion velocity, given by

$$v_e = \sqrt{\frac{2\gamma RT_c}{\gamma - 1}\left[1 - \left(\frac{P_e}{P_c}\right)^{\frac{(\gamma-1)}{\gamma}}\right]} \tag{11}$$

Equation (8) shows that the thrust coefficient is function of γ that depends on temperature and products composition. Figure 2 shows the effects of the H_2O_2 mass fraction and O/F (oxidizer/fuel) mass ratio on thrust coefficient, assuming γ frozen at chamber conditions and assuming an average γ along the nozzle. As can be seen in Fig. 2 there is a small difference of about 0.7 % in C_F values for the two cases.

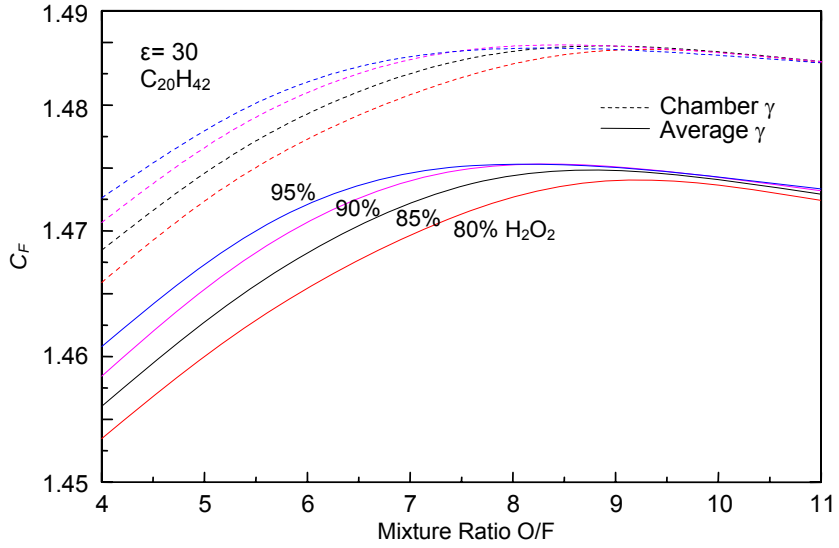

Figure 2. Effects of O/F mass mixture ratio and hydrogen peroxide mass fraction on thrust coefficient, C_F.

Figures 3 and 4 show the effects of hydrogen peroxide mass fraction and O/F mass ratio on specific impulse and on adiabatic flame temperature, respectively, for different paraffin fuels. It can be verified in Figs. 3 and 4 that both specific impulse and combustion temperature increase with increasing hydrogen peroxide mass fractions, since the reduction in water content increases the products temperature.

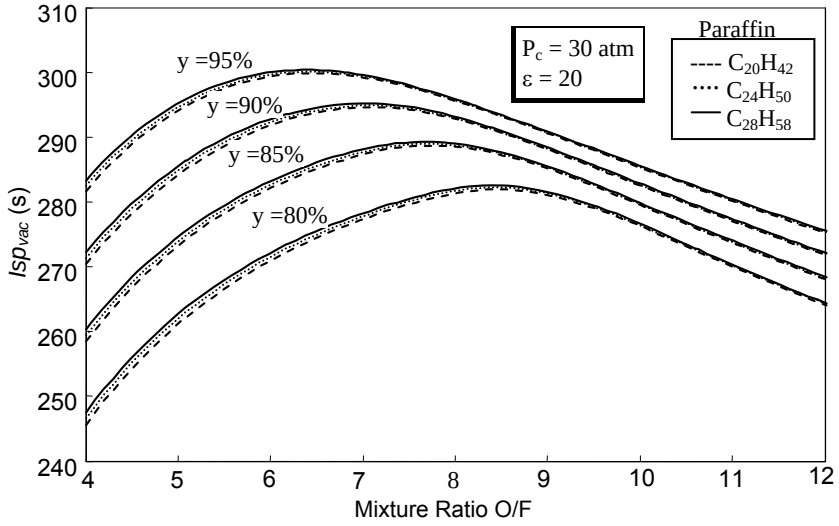

Figure 3. Effects of O/F mass mixture ratio and hydrogen peroxide mass fraction on specific impulse, for different paraffin fuels.

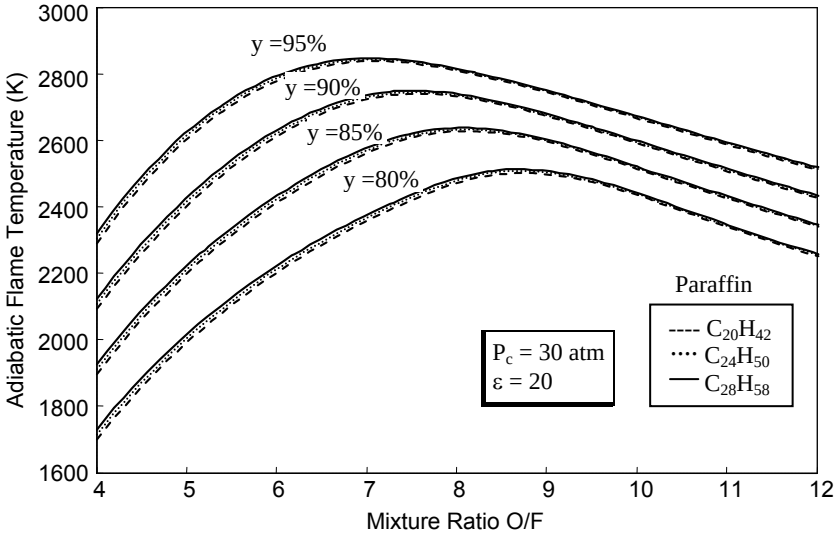

Figure 4. Effects of O/F mass mixture ratio and hydrogen peroxide mass fraction on combustion temperatures, for different paraffin fuels.

It can be verified on Fig. 3 that there is a reduction on the ideal O/F mass ratio, which yields the largest specific impulses, from 8.5 to 6.4 when the peroxide mass fraction increases from 80 to 95 %. The required mass of oxidizer per unit mass of paraffin decreases with increasing peroxide concentrations.

The paraffin molecular size has negligible effect on specific impulses and adiabatic flame temperatures, as shown in Figs. 3 and 4.

Karabeyoglu et al. (2003) studied the effects of adding aluminum particles to solid paraffin. They found that an aluminum content of 40% in mass can increase up to 25% the regression rate of paraffin burning with N_2O.

Therefore, the NASA CEA-2004 equilibrium code was used to study the influence of Al mass fraction of paraffin burning with H_2O_2 on specific impulses and adiabatic flame temperatures, as shown by Figs. 5 and 6, respectively.

It was observed a significant increase of maximum specific impulses assuming equilibrium flow along the nozzle, but no significant effects on maximum specific impulses assuming frozen flow along the nozzle. The most important effect in both cases – with equilibrium or frozen nozzle flows - was a continuous reduction of the ideal O/F mixture ratios with Al content, thus allowing a potential reduction on oxidizer mass. As seen in Fig. 6, the maximum flame temperature increases and its corresponding O/F ratio diminishes with Al mass fraction.

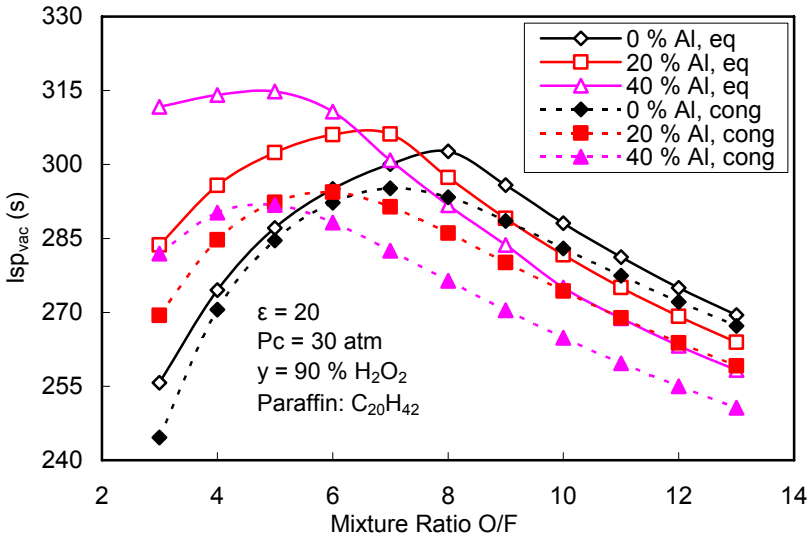

Figure 5. Effects of O/F mass mixture ratio and Al mass fraction in paraffin on vacuum *Isp*, considering equilibrium and frozen nozzle flows.

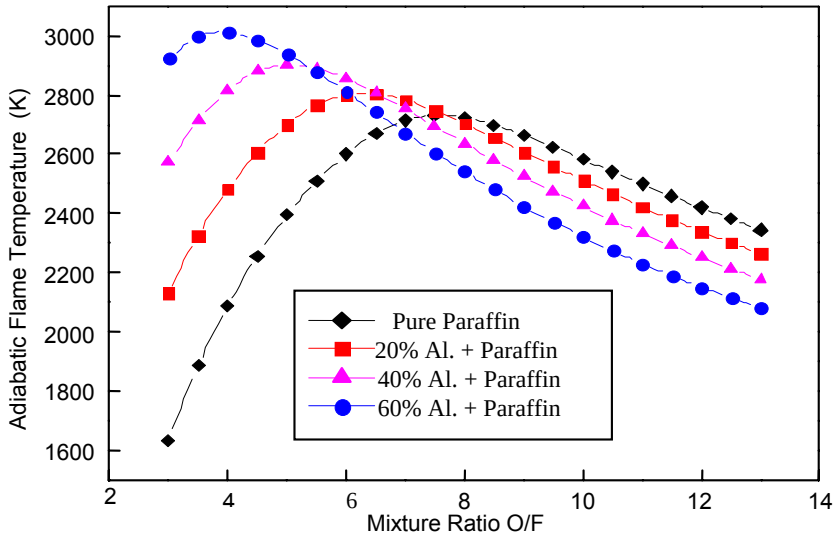

Figure 6. Effects of O/F mass mixture ratio and Al mass fraction in paraffin on adiabatic flame temperature, T_c, considering a frozen nozzle flow. Propellants: $C_{20}H_{42}$ burning with 90% H_2O_2.

In order to compare the performance of paraffin with other common hybrid fuels (PE and HTPB) and a common liquid fuel (RP-1 querosene), their specific impulses were calculated using 90% H_2O_2 as oxidizer, as depicted in Fig. 7. It can be seen in Fig. 7 that all fuels present similar specific impulses. However, since paraffin presents higher regression rates than HTPB and PE, it can yield a larger thrust for a given propulsion system configuration, and the bipropellant system RP-1/H_2O_2 is more complex and expensive.

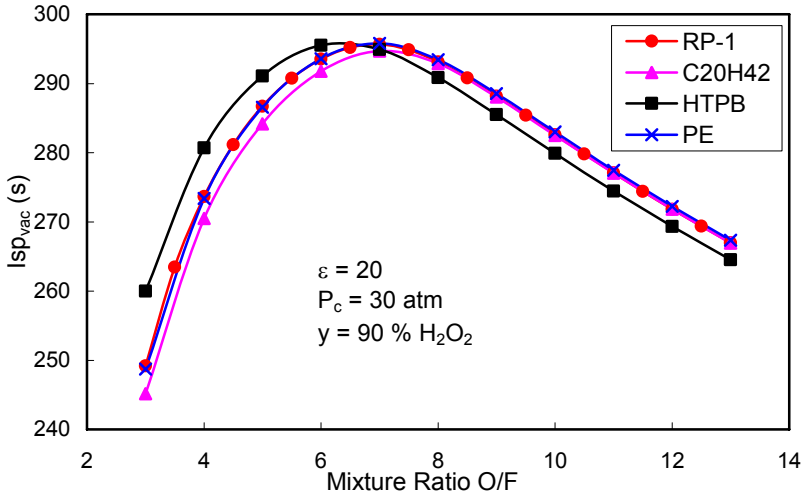

Figure 7. Effects of O/F mass mixture ratio on specific impulses of several propellants burning with 90% H_2O_2.

3. Rocket Mass Distribution

In this section it is presented a preliminary analysis of the mass distribution of rockets to place a nanosat of 20 kg into a circular equatorial LEO of 300 km, using paraffin and H_2O_2 as propellants. Two configurations are analysed and compared: a three stage rocket launched from ground and a three stage air-launched rocket. The characteristic velocities for these two rockets are given next.

A circular low Earth orbit velocity, v_{LEO}, of a rocket can be calculated by integration of the 2nd Newton law applied to the rocket, which can be written as:

$$v_{LEO} = \int_{t_0}^{t_f} \frac{F}{m} dt - \int_{t_0}^{t_f} \frac{F}{m}(1-\cos\alpha)\, dt - \int_{t_0}^{t_f} \frac{D}{m} dt - \int_{t_0}^{t_f} g \sin\gamma dt \qquad (12)$$

where D is drag, F is thrust, m is the instantaneous rocket mass, α is the steering angle or angle between the thrust vector and the velocity vector, γ is the local flight path angle or angle from local horizontal to velocity vector, t is time, t_o is the ignition time and t_f is the burnout time. Defining:

Mission characteristic velocity: $\Delta V = \int_{t_0}^{t_f} \frac{F}{m} dt$ (13a)

Steering characteristic velocity: $\Delta V_{steering} = \int_{t_0}^{t_f} \frac{F}{m}\left(1-\cos\alpha\right) dt$ (13b)

Drag characteristic velocity: $\Delta V_{drag} = \int_{t_0}^{t_f} \frac{D}{m} dt$ (13c)

Gravitational characteristic velocity: $\Delta V_{gravitational} = \int_{t_0}^{t_f} g \sin\gamma dt$ (13d)

The mission characteristic velocity can be calculated by

$$\Delta V = v_{LEO} + \Delta V_{steering} + \Delta V_{drag} + \Delta V_{gravitational} \tag{14}$$

The LEO circular velocity at 300 km height is obtained from:

$$v_{LEO} = \sqrt{\frac{M_{Earth} G}{R_{Earth} + h}} = \sqrt{\frac{5.9742\times10^{24} \times 6.6742\times10^{-11}}{6378+300}} = 7714 m/s \tag{15}$$

Humble et al. (1995) presents historical data of steering, drag and gravitational characteristic velocities for LEO missions, yielding mission characteristic velocities from 8800 to 9300 m/s. In this work it is considered ΔV = 9300 m/s for a ground-launched rocket and ΔV = 8700 m/s for air-launched rockets. For comparison, the well-known Pegasus rocket is launched by an airplane with M = 0.8 at 10 km height, yielding an initial velocity of 243 m/s, and lower drag, steering and gravitational losses than ground launched rockets.

The inert mass fraction, f_{inert}, and the propellant mass fraction, f_{prop}, of a stage are defined, respectively, by:

$$f_{inert} = \frac{m_{inert}}{m_{prop} + m_{inert}} \tag{16}$$

$$f_{prop} = 1 - f_{inert} \tag{17}$$

where m_{inert} is the stage mass excluding the payload mass and m_{prop} is the stage propellant mass. It should be noted that the payload mass of a given stage is the added mass of all upper stages.

Tables 1 and 2 show the inert mass fractions and the propellant mass fractions of several solid and liquid propellant rocket engines. The inert mass fractions depicted on Tables 1 and 2 vary from 0.07 to 0.19 for liquid rocket motors, and from 0.061 to 0.141 for solid rocket motors.

Tables 3 and 4 show the initial conditions assumed for the preliminary design of a 20 kg nanosat hybrid launcher, considering a three stage ground launched rocket and a three stage air launched rocket.

The parameter F/W_0 on Tables 3 and 4 is the ratio between stage thrust, F, and the initial stage weight, W_0, expressed in terms of g number. The F/W_0 and nozzle expansion rates were obtained from historical data (Isakowitz et al., 1999).

For the rocket systems analysed in this paper, it was adopted a conservative value f_{inert} = 0.15, based on data from Tables 1 and 2, F/W_0 = 2.5 and a chamber pressure P_c = 3 MPa for each stage.

Thrust and specific impulses of each stage were considered constants for the preliminary design and the O/F ratios were chosen to yield the maximum Isp's for pure paraffin reacting with 90 % H_2O_2.

Table 1. Mass distributions and fractions of Solid Rocket Motors (adapted from Humble et al., 1995)

Motor Designation	**Propellant**	**Insulation**	**Case**	**Nozzle**	**Igniter**	**Misc.**	**Inert**	f_{prop}	f_{inert}
Castor IVA	10,101	234	749	225	10	276	1494	0.871	0.129
GEM	11,767	312	372	242	7.9	291	1224.9	0.906	0.094
ORBUS 21	9707	145	354	143	16	7	665	0.936	0.064
OBUS 6E	2721	64.1	90.9	105.2	9.5	5.3	275	0.908	0.092
Star 48B	2010	27.1	58.3	43.8	0.0	2.2	131.4	0.939	0.061
Star 37XFP	884	12.7	26.3	31.7	0.0	1.3	72	0.915	0.085
Star 63D	3250	71.4	106.3	60.8	1.0	11.6	251.1	0.928	0.072
Orion 50SAL	12,160	265.2	547.9	235.4	9.1	21.0	1078.6	0.918	0.082
Orion 50	3024	75.6	133.4	118.7	5.3	9.9	342.9	0.898	0.102
Orion 38	770.7	21.9	39.4	52.8	1.3	10.6	126	0.859	0.141

Table 2. Mass distributions and fractions of Liquid Rocket Motors (adapted from Isakowitz et al., 1999)

Motor Designation	**Propellant**	**Inert**	f_{prop}	f_{inert}
YF-40	14,200	1,000	0.93	0.07
YF-73	8,500	2,000	0.81	0.19
11D49	18,700	1,435	0.93	0.07
LE5-A	14,000	2,700	0.84	0.16
LE-5B	16,600	3,000	0.85	0.15
RL10B-2	16,820	2,457	0.87	0.13
AJ10-118K	6,004	950	0.86	0.14
RS27A	95,500	6,820	0.93	0.07
11D58M	14,600	2,720	0.84	0.16
RD-171	325,700	28,600	0.92	0.08

Table 3. Initial conditions for preliminary design of a three stage ground-launched hybrid rocket.

ΔV_{total} (m/s)	9300		
STAGES	**1**	**2**	**3**
ΔV_j, j = 1, 2, 3 (m/s)	3100	3100	3100
Expansion rate, ε (-)	10	40	60
Isp (s)	262	291	297

Table 4. Initial conditions for preliminary design of a three stage air-launched hybrid rocket.

ΔV_{total} (m/s)	8700		
STAGES	**1**	**2**	**3**
ΔV_j, j = 1, 2, 3 (m/s)	2900	2900	2900
Expansion rate, ε (-)	10	40	60
Isp (s)	262	291	297

3.1 Masses, Consumption Rates and Burning Times

The j-stage propellant mass is given by

$$m_{prop,j} = \frac{m_{pay,j}\left[e^{\left(\Delta V_j / Isp_j g_0\right)} - 1\right]}{1 - f_{inert} e^{\left(\Delta V_j / Isp_j g_0\right)}} \tag{18}$$

where $m_{pay,j}$ is the j-stage payload, which is the initial mass of the j+1-stage.

The j-stage inert mass is calculated from

$$m_{inert,j} = \frac{f_{inert,j}}{1 - f_{inert,j}} \tag{19}$$

The *j*-stage initial mass is given by

$$m_{0,j} = m_{prop,j} + m_{inert,j} + m_{pay,j} \tag{20}$$

The *j*-stage average thrust (assumed as constant) is obtained from

$$F_j = \left(F/W_0\right)_j m_{0,j} g_0 \tag{21}$$

The *j*-stage propellant consumption rate, $\dot{m}_{prop,j}$, is obtained from

$$\dot{m}_{prop,j} = F_j \Big/ \left(Isp_j g_0\right) \tag{22}$$

The *j*-stage fuel consumption rate, $\dot{m}_{fuel,j}$, is

$$\dot{m}_{fuel,j} = \frac{\dot{m}_{prop,j}}{1 + \left(O/F\right)_j} \tag{23}$$

The *j*-stage oxidizer consumption rate, $\dot{m}_{oxid,j}$, is

$$\dot{m}_{oxid,j} = \dot{m}_{prop,j} \frac{\left(O/F\right)_j}{1 + \left(O/F\right)_j} = \dot{m}_{prop,j} - \dot{m}_{fuel,j} \tag{24}$$

The burning time, t_b, is obtained from

$$t_{b,j} = \frac{m_{prop,j}}{\dot{m}_{prop,j}} \tag{25}$$

Tables 5 and 6 show the masses and burn times using Eqs. (18-25) with the initial conditions presented on Tables 3 and 4, for three stage ground-launched rockets and three stage air-launched rockets, respectively.

Table 5. Results for a three stage ground launched rocket.

STAGE		**1**	**2**	**3**
m_{prop}	(kg)	1574.5	261.6	57
m_{fuel}	(kg)	196.8	32.7	7.1
m_{oxid}	(kg)	1377.7	228.9	49.9
m_{pay}	(kg)	394.9	87.14	**20**
m_{inert}	(kg)	277.9	46.16	10
$\dot{m}_{prop}$	(kg/s)	21.4	3.39	0.73
$\dot{m}_{fuel}$	(kg/s)	2.6	0.42	0.09
$\dot{m}_{oxi}$	(kg/s)	18.8	2.97	0.64
t_b	(s)	73.4	77.1	77.8
m_0	(kg)	**2247**	394.9	87.14

Table 6. Results for a three stage air launched rocket.

STAGE		**1**	**2**	**3**
m_{prop}	(kg)	1027.7	197.9	48.8
m_{fuel}	(kg)	128.5	24.7	6.1
m_{oxid}	(kg)	899.2	173.2	42.7
m_{pay}	(kg)	310.3	77.4	**20**
m_{inert}	(kg)	181.3	34.9	8.61
$\dot{m}_{prop}$	(kg/s)	14.5	2.6	0.65
$\dot{m}_{fuel}$	(kg/s)	1.82	0.3	0.08
$\dot{m}_{oxi}$	(kg/s)	12.68	2.3	0.57
t_b	(s)	70.9	74.3	74.9
m_0	(kg)	**1519**	310.3	77.4

Figure 8 shows the variation of the stage total mass versus f_{inert} for the two cases considered. It can be noted that the stage total mass grows exponentially with f_{inert}, i.e., a small variation on f_{inert} causes significant changes on the total vehicle mass.

If the payload mass - with upper stages' masses - is included as inert mass of a given stage, the inert mass fractions of all stages become about 0.3 and higher.

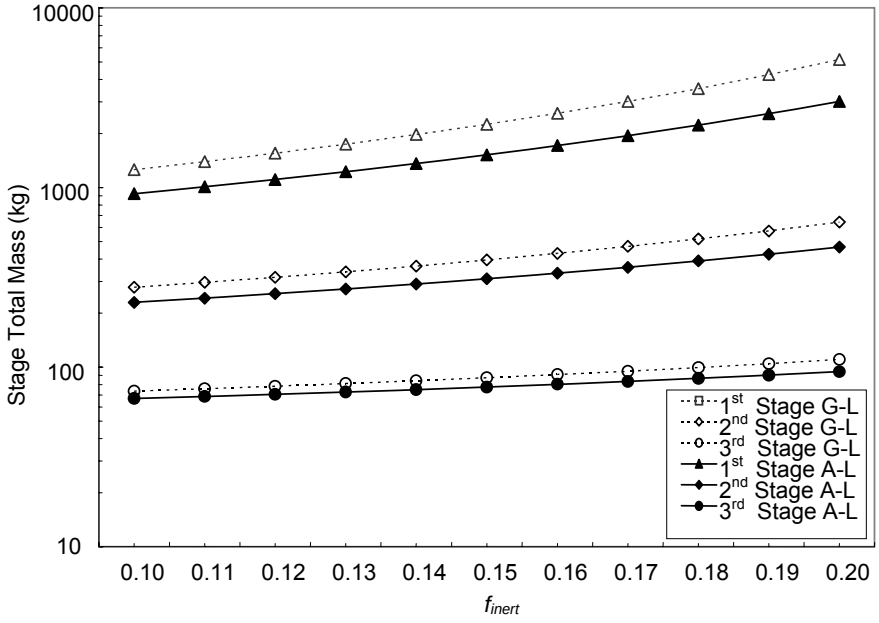

Figure 8. Effects of inert mass fraction on the stages' total mass for three stage ground-launched rockets (G-L) and three stage air-launched rockets (A-L)

5. Comparison of Results and Conclusions

This paper presented a preliminary analysis of the mass distribution of rockets to place a nanosat of 20 kg into a circular equatorial LEO of 300 km, using paraffin and H_2O_2 as propellants.

It was verified that paraffin has a good potential as a hybrid fuel when compared to other polymers and RP-1, using hydrogen peroxide as oxidizer. Hydrogen peroxide can be decomposed catalytically and generates O_2 and H_2O at high temperatures. Thus it is not required an ignition system to burn the fuel. It has a relatively high density (~1.4 g/cm^3) (Schumb, 1995) which reduces the tank weight and size. It can be also used as a pressurizer.

The preliminary design indicated that an air-launched three stage hybrid rocket would have a total initial mass of about 1520 kg, yielding a payload fraction of 1.316 %, while a ground-launched three stage hybrid rocket would have a total initial mass of about 2250 kg, in order to launch a 20 kg nanosat into LEO, with a payload fraction of 0.889 %.

In the analysis, an inert mass fraction of 0.15 was adopted, exclusive of the payload mass.

For comparison, Rothman and Siegenthaler (2003) designed a three-stage air launched rocket using off the shelf engines, and calculated an initial gross mass of 4550 kg for launching a 100 kg microsatellite into LEO, with a payload fraction of 2.198 %. The Brazilian VLS-1 launcher (www.aeb.gov.br) is designed for launching 300 kg into LEO with an initial mass of 50000 kg, and presents a payload fraction of 0.6 %.

It is seen that a three-stage air-launched rocket presents the lower initial mass, therefore the higher payload ratio. Air launched rockets can be launched almost anywhere, anytime and do not require a ground launching base, however they require the adaptation of an airplane for proper rocket release.

6. References

Brown, T. R., Lydon, M.C., 2005, "Testing of Paraffin-Based Hybrid Rocket Fuel Using Hydrogen Peroxide Oxidizer", AIAA Region 5 Student Conference, Wichita, USA.

CEA 2004 – "Chemical Equilibrium with Applications", Cleveland, OH: Glenn Research Center-NASA.

Humble, R. W., Altman, D., 1995, "Hybrid Rockets Propulsion Systems". Ed. Hollander, M.A, Space propulsion analysis and design., cap.7, pp. 365-370 .

Huzel, D. K., Huang, D. H., 1992, "Introduction To Liquid-Propellant Rock Engines", Washington, D. C., AIAA. cap. 1, pp. 4-17.

Isakowitz, S. J., Hopkins Jr, J. P., Hopkins, J. B., 1999, " International Reference Guide to Space Lauch Systems" Washington, D.C., American Institute of Aeronautics and Astronautics, 549 p.

Karabeyoglu, A., Zilliac, G., Cantwell, B.J., Dezilwa, S., Castellucci, P., 2003, "Scale-up Tests of High Regression Rate Liquefying Hybrid Rocket Fuels", 41st Aerospace Sciences Meeting and Exhibit. Nevada, USA.

Karabeyoglu, A., Zilliac, G., Cantwell, B.J., Dezilwa, S., Castellucci, P., 2004, "Scale-up Tests of High Regression Rate Paraffin-Based Hybrid Rocket Fuels", Journal of Propulsion and Power, v.20, n.6, pp. 1037-1045, November-December.

Karabeyoglu, A., Zilliac, G., Castellucci, P, Urbanczyk, P., Stevens, J., Inalhan, G., Cantwell, B,J., 2003, "Development of High-Burning-Rate Hybrid-Rocket-Fuel Flight Demonstrators", 39th AIAA/ASME/SAE/ASEE Joint Propulsion Conference, Huntsville, Alabama, USA.

McCormick, A., HultgreN, E., Lichtman, M., Smith, J., Sneed, R., Azimi, S. 2005, "Design, Optimization, and Launch of a 3" Diameter N_2O/Aluminized Rocket", AIAA/ASME/SAE/ASEE Joint Propulsion Conference and Exhibit, 41, Tucson, Arizona, USA.

Rothman, J., Siegenthaler, E., 2003, "The F-15 Microsatellite Launch Vehicle", 1st Responsive Space Conference, AIAA-LA Section/SSTC, April 1–3, Redondo Beach, CA, USA.

Santos, L. M. C., Almeida, L.A.R, Veras, C.A.G., 2005, "Design and Flight Test of a Paraffin Based Hybrid Rocket", 18th International Congress of Mechanical Engineering, Ouro Preto, Brasil.

Schumb, W. C.; Satterfield, C. N.; Wentworth, R. L., 1955, "Hydrogen Peroxide", New York: Reinhold Publishing Corporation, 759 p.

Sutton, G. P., 1992, "Rocket Propulsion Elements, An Introduction to the Engineering of Rockets", New York: Wiley, 636 p.

Williams, G., Macklin, F., Sarigul-Klijn, M., Sarigul-Klijn, N., Bendon, J., 2004, "Almost There: Responsive Space", 2nd Responsive Space Conference , Los Angeles, CA, USA.

Proceedings of the 11th Brazilian Congress of Thermal Sciences and Engineering -- ENCIT 2006
Braz. Soc. of Mechanical Sciences and Engineering -- ABCM, Curitiba, Brazil,- Dec. 5-8, 2006

Paper CIT06-0921

CONTROL OF HIGH SPEED WIND TUNNEL STAGNATION PRESSURE

Silva, Maurício Guimarães da
Comando Geral de Tecnologia Aeroespacial (CTA)/
Instituto de Aeronáutica e Espaço (IAE)/ Divisão de Sistemas de Defesa(ASD)
maugsilva@iae.cta.br

Falcão, João Batista Pessoa Filho
Comando Geral de Tecnologia Aeroespacial (CTA)/
Instituto de Aeronáutica e Espaço (IAE)/ Divisão de Sistemas de Aeronáuticos(ASA)
falcao@iae.cta.br

Mello, Ollympio Achilles de Faria
Comando Geral de Tecnologia Aeroespacial (CTA)/
Instituto de Aeronáutica e Espaço (IAE)/ Divisão de Sistemas de Aeronáuticos(ASA)
oamello@iae.cta.br

Abstract. *A simulink block diagram code was used to solve a mathematical model consisted of a set of ordinary differential and algebraic equations, which simulated a supersonic blow-down wind tunnel operation, by controlling its stagnation pressure in the settling chamber. A non-linear mathematical model was used for analyzing the open-loop system characteristics and a linearized mathematical model was obtained for the controller design. A great difficulty in supersonic blow-down wind tunnels is the undesirable variation of the Reynolds number in the test section during a tunnel run, as a consequence of the decrease in the stagnation temperature due to the adiabatic expansion in the vessel. Heat regenerators inside the storage tank, which were also modeled, were used to limit this variation. Performance of the supersonic wind tunnel using a PI (proportional-plus-integral) controller was found to be satisfactory, as confirmed by the results.*

Keywords. *Blow-down wind tunnel, Pressure Control, Temperature Control, PI controller, Simulink*

1. Introduction

This paper deals with the solution of the Reynolds number control problem in a Supersonic Wind Tunnel facility (SWT). A typical blow-down wind tunnel consists basically of a storage tank filled with high-pressure air, a convergent-divergent nozzle (CD nozzle), a test section and a diffuser. Blow-down wind tunnels require increasingly higher pressure as the Mach number increases. The pressure required to start the tunnel is experimentally found to be about twice the normal shock pressure loss, for a referenced test section Mach number. The tunnel starts with the openning of an automatic pressure regulator valve, located just after the storage tank outlet. The high-pressure air in the storage tank expands and settles down in the settling chamber, where the air is kept at a constant pressure. Downstream of the settling chamber, a CD nozzle accelerates the flow to supersonic condition up to the end ot the test section. Into the diffuser, the flow is then decelerated to near sonic condition by means of a second throat section and, finally, decelerated to atmospheric conditions by the increase ot the cross section area. A sketch of the facility is shown in Fig.1. This wind tunnel has an asymmetric sliding-block nozzle which yields a variable Mach number capability over the range of Mach number 1.5 to 4.0. Dry air is stored in a 56.6 m^3 tank at up to 2.07 MPa. Testing requirements call for regulated stagnation pressures in the range of 0.34 MPa to 1.72 MPa for typical test duration of 15 to 45 seconds. This facility is similar to the Penn State Supersonic Wind Tunnel (Fung, 1987).

At a given Mach number, it is sometimes required to maximize the test duration by running the tunnel at the lowest possible stagnation pressure – but still sufficient to maintain supersonic flow condition. Similarly, it is often necessary to obtain different Reynolds numbers at a given Mach number, by means of adjusting levels of stagnation pressure and temperature. However, a great difficulty of supersonic blow-down wind tunnels is the undesirable variation of Reynolds number in the test section during a tunnel run. This is a consequence of the stagnation temperature decrease, due to the adiabatic expansion in the vessel – heat regenerators are used to limit this variation. In all cases, a stable level of stagnation pressure and temperature during the test is the basic requirement.

The main purpose of the present work is to design and implement a controller that can sense the stagnation pressure at the settling chamber and adjust a control valve automatically in order to reach a desirable pressure level. The stagnation pressure in the settling chamber is usually controlled by one or more pressure regulator valves. The valve is opened progressively wider during a run as the storage tank pressure decreases continuously. When SWTs were first developed, they were manually operated. Since that time, many SWTs have been modified to provide better

performance. Advances in microcomputers and measurement technologies have enabled operators to obtain pressures and temperatures that are more accurate, allowing SWT's control to use simpler operating system. Controller's type varies among wind tunnels depending on their size and budget. They vary from a purely mechanical controller using a set of needle valves of different diameters to a pneumatic valve with PID control (proportional-plus-integral-plus-derivative control action), Matsumoto and Wilson (2001). One of the most advances in wind tunnel operating system uses a real time neural net controller with a parallel processing workstation (Buggele and Decker, 1994). This SWT can be operated with as few as three people and has a Mach number deviation of 0.005 and total pressure deviation of 0.7 kPa (0.1 psi).

The control procedure maintains the stagnation pressure constant regardless of test section Mach number. The regulator valve is opened progressively wider during a tunnel run as the storage tank pressure continuously decreases. A satisfactory solution to this control problem has been achieved through a single-loop Proportional-plus-Integral (PI) controller with constant parameter settings.

The second purpose of this work is to present a tool to design heat regenerators in which the heat source consists of flat steel plates displaced at equal distances, Spiegel (1956). Expansion of the air from the storage tank through heat exchanger matrix (metallic flat plates) limits air temperature decay, which avoids the variation of the Reynolds number in the test section during a tunnel run.

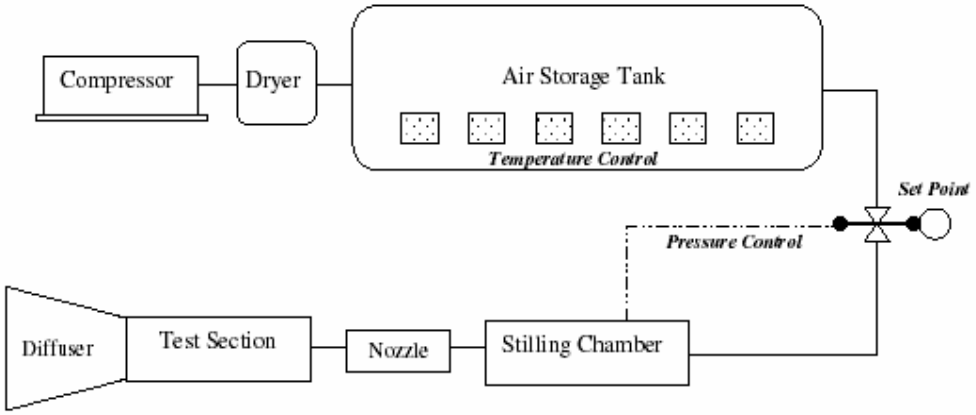

Figure 1. Schematic of supersonic wind tunnel

2. Mathematical Model

The dynamic analysis of the system SWT is divided into three modules, which are: Storage Tank, Settling Chamber and Nozzle. These modules are mathematically represented by control volumes. It is assumed that pressure, temperature and density distribution are uniform over the whole control volume during the test. Should be noted that it is assumed that all the thermodynamic processes are isentropic during the test time (no shock waves, neglect friction and heat transfer), except in the heat regenerators/tank module. The change of potential energy of the gas is small and can be neglected.

2.1. Storage tank

During a test, it is assumed that the mass influx from the compressor is negligible. Hence, the rate of decrease of mass in air tank is equal to the rate of mass efflux through the valve:

$$\frac{d\rho_t}{dt} = -\frac{1}{V_t}\dot{m}_v, \tag{1}$$

where ρ_t is the storage tank air density, $\dot{m}_v$ is the mass efflux through the valve and V_t is the storage tank volume. The subscript "*t*" refers to storage tank. By assuming the energy loss through the valve is negligible small, the internal energy change in the storage tank is equal to the enthalpy plus the kinetic energy through the valve. Therefore:

$$\frac{dU_t}{dt} = -\dot{m}_v h_v - \frac{1}{2}\dot{m}_v v_v^2, \tag{2}$$

where U_t is the storage tank air internal energy, h_v is the specific enthalpy of the air through the valve and v_v is the velocity of the air through the valve. In terms of the pressure, the Eq. (2) can be written (Fung, 1987):

$$\frac{dP_t}{dt} = -\left(\frac{c_p}{c_v}\frac{R}{V_t}\right)\dot{m}_v T_t \cdot \tag{3}$$

The quotient $\gamma = c_p / c_v$ is the specific heat ratio and *R* is the gas constant.

The valve characteristics are described in Fisher Controls Company (1984), from the manufacturer. The mass flow at different valve positions is given by:

$$\dot{m}_v = \frac{2.2958x10^{-8}}{\sqrt{T_t}} C_g P_t \sin\left(2.71\sqrt{\frac{\Delta P}{P_t}}\right) \cdot \tag{4}$$

where C_g is the "gas sizing coefficient" of the valve. Table 1 shows some characteristic values in the valve operating range. The variables T_t and P_t are the thermodynamics properties (temperature and pressure) of the air into storage tank. ΔP is the pressure difference across the valve. It is assumed that $\Delta P = P_t - P_0$, where P_0 is the stagnation pressure at the settling chamber.

Table 1 – The gas sizing coefficient of the valve

θ	0	10	20	30	40	50	60	70	80	90
C_g	0	194	1680	3767	6230	9288	12835	16351	18942	23120

2.2. Settling Chamber

The second control volume is the settling chamber as shown in Fig. 1. Air flows into the settling chamber from the control valve and goes through the CD nozzle to the test section. Therefore, the mass flow difference rate from inlet and outlet section of the control volume yields the net rate of mass buildup inside the control volume. In other words, the relation of mass conservation in the settling chamber is given by:

$$\frac{d\rho_0}{dt} = \frac{1}{V_0}\left(\dot{m}_v - \dot{m}_*\right) \cdot \tag{5}$$

Subscript "0" refers to the settling chamber and subscript "*" refers to mass flow rate through the nozzle. The energy entering the settling chamber volume with mass flow $\dot{m}_v$ minus the energy exiting through the nozzle with mass flow $\dot{m}_*$ is equal to the internal energy rate in the settling chamber. Therefore, the relation of conservation of energy for the settling chamber is:

$$\frac{dU_0}{dt} = \dot{m}_v h_v + \frac{1}{2}\dot{m}_v v_v^2 - \dot{m}_* h_* + \frac{1}{2}\dot{m}_* v_*^2 \ . \tag{6}$$

Rewriting the Eq.(6) in terms of pressure, results (Fung, 1987):

$$\frac{dP_0}{dt} = \left(\frac{c_p}{c_v}\frac{R}{V_0}\right)\left(\dot{m}_v T_t - \dot{m}_* T_0\right) \cdot \tag{7}$$

2.3. Nozzle

The nozzle of the supersonic wind tunnel is asymmetric, variable-geometry with converging-diverging geometry. Sliding the lower block changes the test section Mach number. It is assumed that the flow from the settling chamber to the test section runs an isentropic process. Considering the air as a perfect gas and the stagnation state as the reference state, it can be written $\dot{m}_*$ as function of stagnation pressure and the nozzle throat area A_*, which are:

$$\dot{m}_* = \frac{0.6847 P_0 A_*}{\sqrt{RT_0}}, \tag{8}$$

where

$$\frac{A}{A_*} = \frac{1}{Mach}\left\{\frac{1+\left[\gamma-1/2\right]Mach^2}{\left[\gamma+1/2\right]}\right\}^{\frac{\gamma+1}{[2(\gamma-1)]}}. \tag{9}$$

3. Control Problem

The primary reason for installing a good controller to a wind tunnel is to significantly improve flow quality in the test section. The required flow steadiness may vary with the type of tunnel. For a typical airplane test, criteria such as less than 1.0 percent of error in *Cd* and *Cp* are usually sufficient. To meet those criteria, the Mach number steadiness in the test section must stay about ± 0.3 percent at *M* = 3.0 (Marvin, 1987). Unlike Mach number, it is hard to maintain Reynolds number at a constant value since the temperature of the storage tank drops during a test.

The present pressure control problem is relatively simple once only accuracy and stability are matters of prime concern. Then it was judged that the complexities of optimal control, neural networks and so on, are neither needed nor desired for present purposes. Besides that, the variation of the air temperature into the test section can be satisfactorily reduced with the aid of heat regenerators.

3.1. Stagnation pressure in storage tank

The objective in setting up the controller parameters for the valve is to minimize the initial transient duration to obtain as long steady run time as possible. The control process needs a model of the pressure transmitter, the digital valve controller and the automatic ball valve to perform the SWT's control. The stagnation pressure in the settling chamber is converted to current signal by a pressure transmitter located upstream the nozzle. Then this signal feeds the digital valve controller. The controller has two parameters that can be changed to maintain a steady settling pressure, a proportional gain (K_p) and an integral time (K_i). The digital valve controller compares the stagnation pressure with a set pressure and derives a corrective output signal according to the setting of its two parameters. These parameters may be modified to increase the process performance. The transfer function of the PI controller is:

$$G(s) = \frac{\Theta(s)}{E(s)} = K_p\left(1+\frac{1}{K_i s}\right), \tag{10}$$

where $\Theta(s)$ is the valve opening position and $E(s) = P_d - P_0(s)$ is the error signal between the reference input P_d (desired stagnation pressure), and the system output $P_0(s)$ (the actual pressure measured into the settling chamber). Applying the inverse Laplace transform, the differential relationship between the input $E(t) = P_d - P_0(t)$ and output $\Theta(t)$ of the PI controller is:

$$\frac{d\Theta(t)}{dt} = -K_p\frac{dP_o(t)}{dt} + \frac{K_p}{K_i}\left(P_d - P_0(t)\right). \tag{11}$$

3.2. Stagnation temperature in storage tank

The stagnation temperature control problem was solved using heat regenerators. The heat source consists of a beam of flat steel plates equally displaced. The working air flows through the space between these plates. In order to reduce the number of independent variables that must be considered in the analysis, an assumption was made that the heat conduction along the plates can be neglected. Furthermore it will be assumed that changes in density and thermal constants with the temperature may be neglected. Denoting the air temperature by T_t and the steel temperature by T_s the amount of heat transferred per unit time and per unit area of the plates can be expressed by the formula (Spiegel, 1956):

$$q = h(T_s - T_t), \tag{12}$$

where h is the heat transfer coefficient between the plates and the air. Therefore, the relation of conservation of energy for the heat regenerators is given as:

where *h* is the heat transfer coefficient between the plates and the air. Therefore, the relation of conservation of energy for the heat regenerators is given by:

$$\begin{cases} Sq = -Mc_s \dfrac{dT_s}{dt} \\ Sq = Nc_p \dfrac{dT_t}{dt} \end{cases}. \tag{13}$$

In these expressions *M* represents the mass of the steel plates in the regenerator, *N* is the mass of the air in the regenerator at the time *t*, *S* the total plate area (for every plate both sides are taken), c_s and c_p are the specific heats of steel and air, respectively. The term $\dfrac{d(\ )}{dt} = \dfrac{\partial(\ )}{\partial t} + u\dfrac{\partial(\ )}{\partial x}$ represent the substantive derivative, where u is the velocity in axial direction.

Consider the time that an air particle passed in the regenerator. With moderate air velocity, this time will be very short compared with the tunnel running time. During this short time, the air temperature at a fixed position *x* in the regenerator changes very little as a consequence of the slow variation in the air temperature entering in each station of the regenerator. On ground of these considerations, the term $\dfrac{\partial T_t}{\partial t}$ can be neglected. As it has been said previously, the heat conduction along the plates can be neglected, and this results that $\dfrac{\partial T_s}{\partial x} = 0$. The system of differential equation can now be approximated to:

$$\begin{cases} -Mc_s \dfrac{\partial T_s}{\partial t} = Sh(T_s - T_t) \\ Nc_p \dfrac{\partial T_t}{\partial x} = Sh(T_s - T_t) \end{cases}. \tag{14}$$

For the determination of the heat transfer coefficient use will be made of Reynolds formulation of the analogy between heat transfer and skin friction, which can ultimately be expressed by the formula (Spiegel, 1956):

$$h = \frac{1}{2}\rho_t c_a w C_f . \tag{15}$$

where C_f is the coefficient of skin friction, C_a is the specific heat of the air and $\rho_t w$ is the product of air density by air velocity in heat regenerator.

In order to solve this system of partial differential equations certain boundary conditions must be given. Initially the steel temperature T_s has the same value as the air temperature in the storage tank, thus, at *t* = 0 s holds:

$$T_t = T_s = T_{amb} \qquad in \qquad t = 0. \tag{16}$$

The second boundary condition can be found by considering the air temperature at the inlet of the regenerator during the tunnel operation (Spiegel, 1956). Since the pressure and temperature variation in the test section is small during a test, it may be assumed, that the air used during the test is removed from the air tank at a constant rate ($\dot{r}$). The relation between the initial mass of air in the tank (G_0) and the mass (G) at any time *t* during the test can thus be written:

$$G = G_0\left(1 - \frac{\dot{r}\ t}{G_0}\right). \tag{17}$$

In terms of the air density (ρ), this relation can be given in the form:

$$\rho_t = \rho_{init}\left(1-\frac{\dot{r}\ t}{G_0}\right). \tag{18}$$

As the air is flowing out of the tank at constant rate, it is clear that the ratio $\frac{G_0}{\dot{r}}$ can be interpreted as the time (t_m) in which the tank would be empty. Assuming that the air in the tank is expanded isentropically during operation of the tunnel, it can be easily deduced that the air temperature in the tank is related to the parameter $\tau = \frac{t}{t_m}$ by the formula:

$$T_{inlet\_t} = T_{init}(1-\tau)^{\gamma-1}, \tag{19}$$

where T_{inlet_t} is the air temperature into the tank, before the heat regenerators, at a given time *t*.

4. Numerical Implementation

From the preceding discussion, expressions were obtained which describe the behavior of the SWT and the control systems. These are summarized here:

- Supersonic Wind Tunnel:

Storage Tank:

$$\frac{d\rho_t}{dt} = -\frac{1}{V_t}\dot{m}_v, \tag{1}$$

$$\frac{dP_t}{dt} = -\left(\frac{c_p}{c_v}\frac{R}{V_t}\right)\dot{m}_v T_t. \tag{3}$$

Settling Chamber:

$$\frac{d\rho_0}{dt} = \frac{1}{V_0}\left(\dot{m}_v - \dot{m}_*\right). \tag{5}$$

$$\frac{dP_0}{dt} = \left(\frac{c_p}{c_v}\frac{R}{V_0}\right)\left(\dot{m}_v T_t - \dot{m}_* T_0\right). \tag{7}$$

Valve:

$$\dot{m}_v = \frac{2.2958x10^{-8}}{\sqrt{T_t}} C_g P_t \sin\left(2.71\sqrt{\frac{\Delta P}{P_t}}\right). \tag{4}$$

Control Valve:

$$\dot{m}_v = \frac{2.2958x10^{-8}}{\sqrt{T_t}} C_g P_t \sin\left(2.71\sqrt{\frac{\Delta P}{P_t}}\right). \tag{4}$$

Nozzle:

$$\dot{m}_* = \frac{0.6847 P_0 A_*}{\sqrt{RT_0}}. \tag{8}$$

- Control devices:

Valve Angle:

$$\frac{d\Theta(t)}{dt} = -K_p\frac{dP_o(t)}{dt} + \frac{K_p}{K_i}\left(P_d - P_0(t)\right), \tag{11}$$

Heat Regenerator:

$$\begin{cases} -Mc_s\dfrac{\partial T_s}{\partial t} = Sh\left(T_s - T_t\right) \\ Nc_p\dfrac{\partial T_t}{\partial x} = Sh\left(T_s - T_t\right) \end{cases}. \tag{14}$$

The above equations become a system of five first-order nonlinear differential equations, in the time, with five state variables: P_t, ρ_t, P_0, ρ_0, T_s. The inputs of this system are: test section Mach number, which results in a determined nozzle geometry; the valve position $\Theta(C_g)$, which determines the control valve behavior, according to changes in C_g; the air temperature into the storage tank before the heat regenerators T_{inlet_t}, which give us the boundary conditions for determination of storage tank temperature (T_t). The output of this system are the stagnation pressure (P_0) and temperature (T_0) in the settling chamber.

Figures 2 and 3 show schematic blocks diagrams regarding the SWT model (control pressure and controller), making use of a graphical editor of the MATLAB-Simulink package (The Mathworks, 2002). Figure 4 presents a general block diagram (for the whole wind tunnel) that includes the former ones. It illustrates the data loading, input signals and taking out the results.

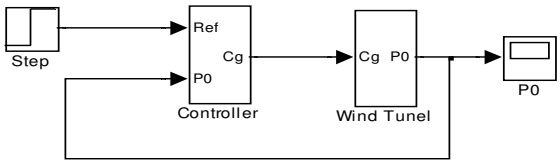

Figure 2. Block diagram: Control Pressure

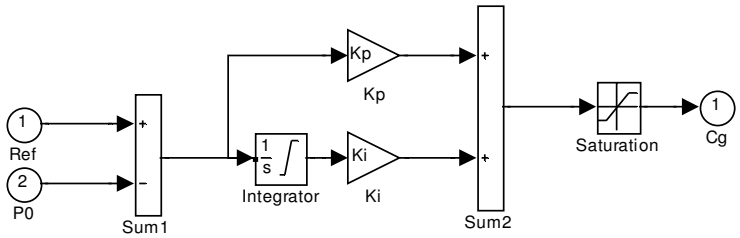

Figure 3. Block diagram: Controller

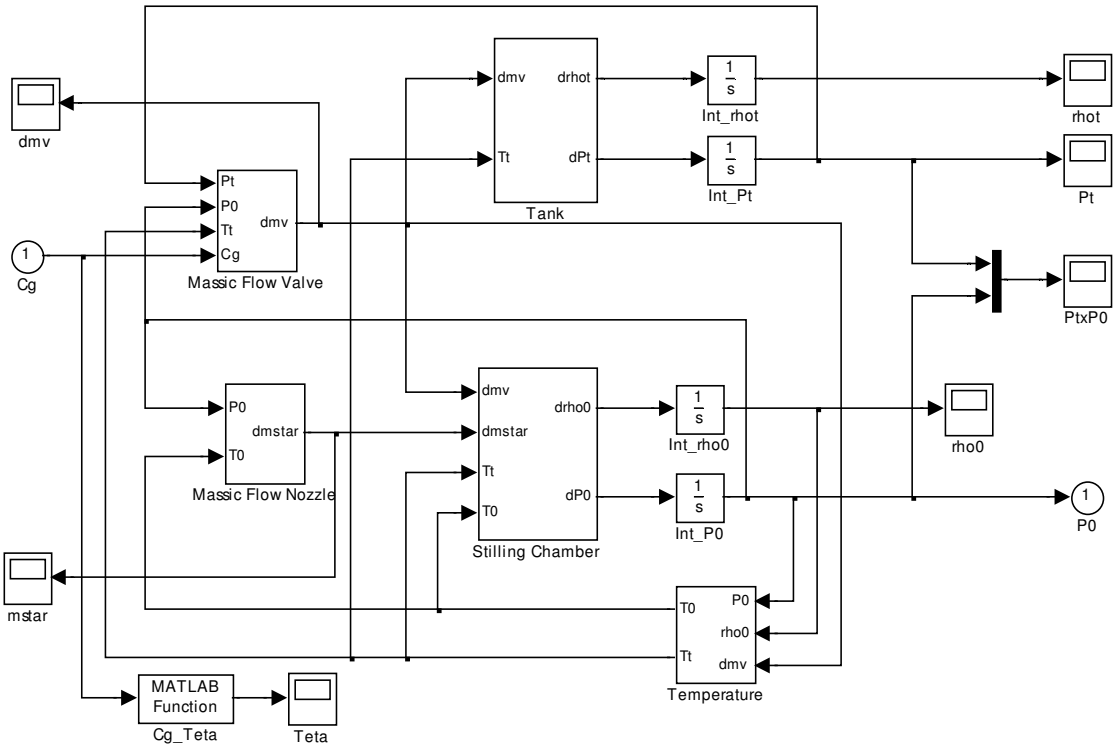

Figure 4. Block diagram: Wind Tunnel

Consider once more the system of differential equations (14). If one substitutes the derivatives by their linear differences, the system becomes:

$$\begin{cases} T_s(x,t+\Delta t) = T_s(x,t)+\beta\,\Delta t\,[T_s(x,t)-T_t(x,t)] \\ T_t(x+\Delta x,t) = T_t(x,t)+\alpha\,\Delta x\,[T_s(x,t)-T_t(x,t)] \end{cases}. \tag{20}$$

The parameters of heat transfer α and β are defined by:

$$\alpha = \frac{C_f L}{\delta}, \tag{21}$$

$$\beta = \frac{-(\rho_t w) C_a C_f t_m}{C_m\, \varepsilon e}, \tag{22}$$

where C_m and ε area the specific heat and specific weight of the steel, respectively. The geometric parameter δ is the distance between the flat plates, L is the length of the regenerator, the parameter *e* is the plate thickness. The quantity t_m, as previously defined, is the ratio between the initial air mass in the tank and the mass flow (the quantity being transported) ($\dot{r}$). In this approximation, the variable t_m was defined constant during all the simulation, i. e., $\dot{r} = const$.

5. Results

5. 1. Configuration of the Simulation

Tunnel run time depends on the kind of tests are to be made and also on their particularities. In pressure tests, for example, several pressure orifices are normally installed at various locations in the surface of the wind tunnel model. Connections are made to these orifices with flexible tubes that go outside of the tunnel. Then, the tubes are connected to pressure-measuring devices from which the pressures are recorded. In this type of test, a significant amount of time is usually required in order to stabilize the pressure at the measuring device, particularly if the passage orifice diameters are of small size. The tubes are normally quite small and causes high resistance to air flow. As the pressure at the orifice and at the measuring device approach each other, the pressure differential decreases, with the result that the measured pressure approaches the orifice pressure asymptotically. In a blow-down wind tunnel it would be unwise to depend on pressure stabilization in less than 15 or 20 seconds with a system of the type described. This is an important factor in specifying run-time requirements. Of course, with large model, and pressure transducers located very near the orifices, within the model, a much faster response can be obtained (Pope, 1965). Because of the data recording times required for force and pressure tests, and the time for the pressure control valve to provide a stable operating pressure, blow-down wind tunnels are usually designed for **minimum run** times of **20 to 40 seconds** (Pope, 1965). In order to satisfy this requirement for the present facility, adequate initial conditions were stablished, as shown in Tab.2.

By adding a controller in a feedback loop to the wind tunnel plant (Figure 2), the mathematical model for the closed-loop system is established. The result settings for the control parameters K_p and K_i are presented in Tab. 3. The wind tunnel geometrical design parameters considered herein are shown in Table 4. Table 5 shows the heat transfer parameters used in the heat regenerator design. Here the parameters α and β had been chosen based on other similar cases, just for academic reasons. It does not objective in this work to design a heat regenerator for this tunnel, in particular. The primary reason here is to offer a mathematical tool for the stagnation temperature control in the settling chamber.

Table 2 – Initial and **desired** conditions

T_t [K]	P_t [Pa]	T_0 [K]	P_0 [Pa]	**Pressure (Set Point) [Pa]**	**Mach (Test Section)**
298	$1.8\ 10^6$	298	$1.01\ 10^5$	**$5.\ 10^5$**	**2.5**

Table 3 – Parameters of the pressure controller

K_p	K_i
0.5	1.5

Table 4 – Geometric configuration of SWT

V_t [m^3]	V_0 [m^3]	A (Test Section) [cm^2]	A* (Nozzle) [cm^2]
56.61	V_t/20	15x18	0.0102

Table 5 – Parameters of the heat regenerator

α	β
3.	-3.

5. 2. SWT without Control

In order to judge the accuracy and efficacy of the mathematical model, experimental (Fung, 1987) and simulation results for the stagnation pressure, when the tunnel is running at Mach number 4.0, were compared with the valve fully opened condition. The initial pressure of the storage tank is 1.8 MPa. It is important to note that blow-down wind tunnels, invariably, must essentially operate at a constant pressure level during each run. However, in accordance with the Figs. 5 and 6, the pressure did not remain constant in the settling chamber. Additionally it is also observed that there was a significant fall in the temperature. Therefore, it can be concluded that control systems for pressure and temperature are both essential for this facility.

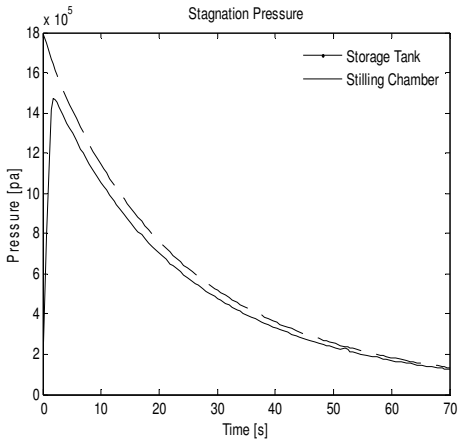

Figure 5. Variation in stagnation pressure (valve fully open)

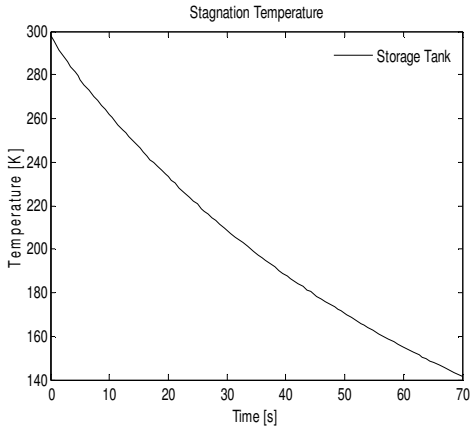

Figure 6. Variation in stagnation temperature (valve fully open)

5. 3. SWT with Pressure Control

At a given test section Mach number it is desirable to maintain steady-state condition for the stagnation pressure in the settling chamber, as long as possible, to obtain the maximum span of test time. Since the pressure in the tank continuously decreases during the test, the valve opening should be gradually increased for maintaining constant stagnation pressure. In this particular case, only the pressure control was operational – no heat regenerator into the tank was considered. Figures 7 and 8 show that the mathematical model used in the simulation could successfully capture this behavior. Although the pressure has been controlled, the temperature in the settling chamber has fallen significantly (see Fig. 9). This temperature decay caused a significant variation in test section Reynolds number during the tunnel run. Thus, considering the geometric and thermodynamic parameters adopted for the tunnel, one can conclude that it is very convenient the use of heat regenerators in the storage tank.

For a determined Mach number, each stagnation pressure value gives a different Reynolds number in the test section. To obtain a response with a minimum steady-state error and overshoot, as well as fastest settling time, the controller parameters K_p and K_i must be adjusted. One aim of this work is, basically, to provide a range of controller parameters that could reasonably be implemented – avoiding too many experimental runs to determine these parameters on a trial-and-error basis. It can be observed in Fig. 8 that, with exception of the initial transient period, the derivative changes of the opening angle valve are very smooth. Therefore, for this test configuration (size of storage tank, test section Mach number and so on), the pressure regulator valve can be manually adjusted. It was worth noting here that numerical simulations are essential for the decision on project parameter such as, for example, the size of the air storage tanks.

It is also observed that the pressure control system allowed a longer high temperature level in the storage tank. This behavior is evidenced when compared the derivatives of stagnation temperature in Figs. 6 and 9.

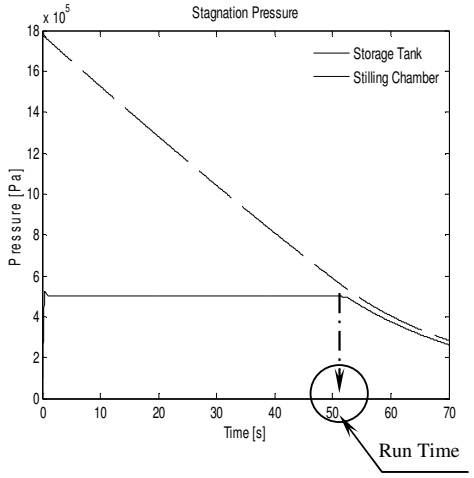

Figure 7. Variation in stagnation pressure (Pressure Control)

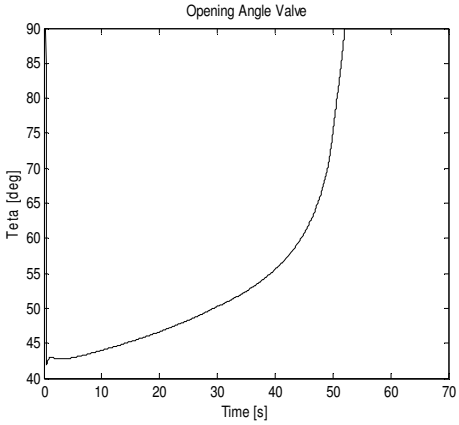

Figure 8. Variation in valve opening angle (Pressure Control)

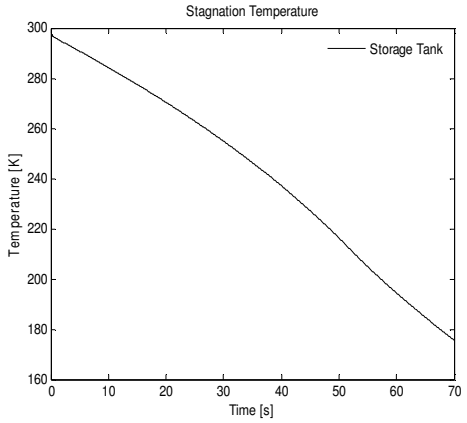

Figure 9. Variation in stagnation temperature (Pressure Control)

5. 4. SWT with Pressure and Temperature Control

Achieving constant stagnation pressure is a critical concern for SWT testing. However, it is not sufficient to comply with the requirements of flow accuracy in test section. It is also necessary a stagnation temperature control. The previously noted decrease in air stagnation temperature during a test run is due to the expansion of the remaining air in the tank, to a lower pressure, once part of the air in the tanks was removed to run the tunnel. The expansion of the air in the tank does not follow an adiabatic process, because while the air temperature in the tank drops, heat is transferred from the tank walls to the air. This result in a polytropic expansion process with a polytropic exponent of expansion process *n* between 1.0 (isothermal process) and 1.4 (adiabatic process) in the equation (Pope, 1965):

$$\frac{T_t^i}{T_t^f} = \left(\frac{P_t^i}{P_t^f} \right)^{\frac{n-1}{n}}, \tag{23}$$

where the subscript "*i*" refers to initial condition and "*f*" to final condition in the storage tank. This drop in stagnation temperature inside of the storage tank can become a real trouble. It affects the test section Mach number and Reynolds number during a test run. Some effort is therefore justified to reduce this temperature drop or perhaps completely nullify it. In Figs. 10 to 12 are depicted the stagnation pressure variation, valve opening angle and stagnation temperature with the time, respectively. During these tests the controller parameters K_p and K_i had not been modified. On the basis of Fig. 11, it can be concluded that it is necessary a light adjust in controller parameters K_p and K_i, in view of the oscillatory character observed. In certain cases, this implementation is of basic importance since it influences directly in the mass flow through the valve and, as a consequence, in run time of SWT (Figures 7 and 10).

It can be observed that the linearized mathematical model used to control the stagnation pressure was also found to be satisfactory (see Fig.10). In this particular simulation, with pressure and temperature controls, the polytropic exponent (n_{TP}) was 1.0002 – the physically possible expected range is $1. < n_{TP} < 1.4$. As the polytropic exponent is very near to isothermal process, it can be concluded that the heat regenerators are too large for this facility.

In the other hand, the polytropic coefficient calculated from the simulation with only the pressure control (n_P) (last case) was 1.39. The physical expected value would be 1.40 once no heat transfer was considered during the simulation. However, it is worth noting that the Eq. (23) is applied to a quasi-static process, derived from a steady-state approximation of Bernoulli equation and, of course, some approximation errors may be expected. In this context, the value n_P = 1.39 is consistent with the formulation adopted and a good physical approximation.

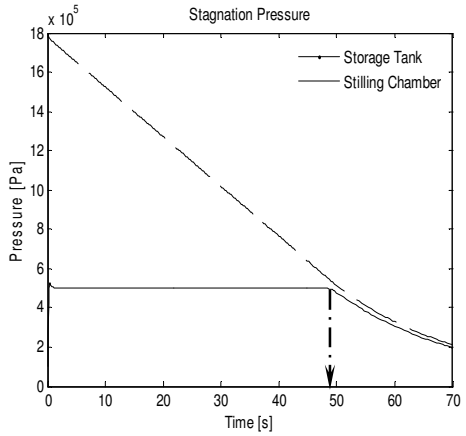

Figure 10. Variation in stagnation pressure (Pressure and Temperature Control)

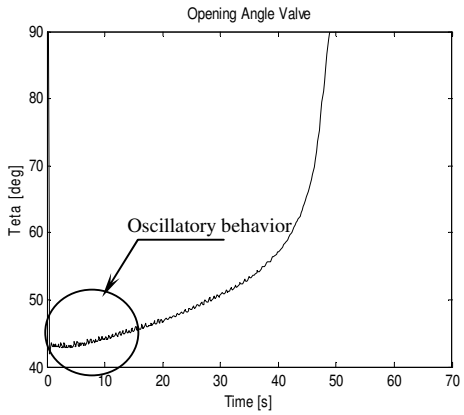

Figure 11. Variation in valve opening angle (Pressure and Temperature Control)

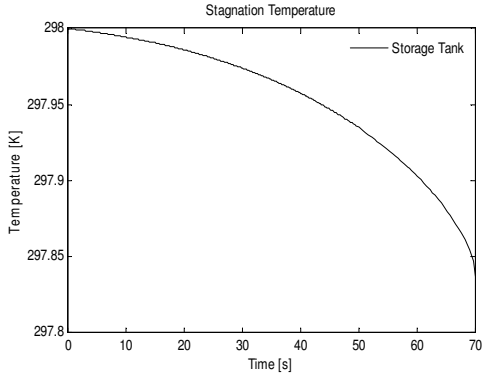

Figure 12. Variation in stagnation temperature (Pressure and Temperature Control)

6. Conclusions

This research deals with the solution of the stagnation pressure control problem using a PI controller in a supersonic wind tunnel. The objective is to provide a controlled airstream, in terms of temperature and pressure, so that, items of interest to aeronautical engineers can be tested. The simulink block diagram code was used to solve a model consisted of a set of ordinary differential and algebraic equations to control the stagnation pressure inside a supersonic blow-down wind tunnel. A great difficulty in supersonic blow-down tunnels is the undesirable variation of the Reynolds number in the test section during a test run as a consequence of the decrease in stagnation temperature due to the adiabatic expansion into the vessel. In order to limit this variation, it was used heat regenerators. Performance of the supersonic wind tunnel using a PI controller together with heat regenerator models was found to be satisfactory.

The required flow accuracy may vary with the type of tunnel. Most of recent systems developed are based on real-time controllers. Generally, a real-time feedback loop such as a proportional-plus-integral-plus-derivative (PID) controller works very well with long-duration wind tunnels. For this case, the storage air pressure decreases slowly enough to allow devices with slow time response to have sufficient time to respond to the pressure change. However, when the storage volume is limited, a real-time loop may fail to keep up with the fast pressure decay. In addition, very small time delays due to the motion of the mechanical elements of a valve become critical. Under such circumstances, alternative approaches, such as neural networks may be needed. A pre-programmed controller is proposed as a simple alternative to a neural net controller to achieve a fast responding system. It offers the capability of starting the wind tunnel very quickly and providing a stable flow, overcoming the slow response of a PID controller. Therefore, just after investigating different control algorithms it will be possible to estimate performance parameters for different classes of SWT.

8. References

Buggele, A. E. and Decker, A. J. , 1994, “Control of Wind Tunnel Operations Using Neural Net Interpolation of Flow Visualization Records”, NASA Technical Memorandum 106683.

Ficher Control Company, 1984, ”Rotary Shaft Control Valve Specifications.”, Marshalltown, Iowa.

Fung, Y.T., Settles, G.S. and Ray, A., 1987, “Microprocessor Control of High-Speed Wind Tunnel Stagnation Pressure”, The Pensylvania State University, Master of Science, 59 p.

Marvin, J. G., 1987, “Wind Tunnel Requirements for Computational Fluid Dynamics Code Verification”, NASA Technical Memorandum 100001.

Matsumoto J., Lu, F. K. and Wilson, D. R., 2001, “Pre-Programmed Controller For A Supersonic Blowdown Tunnel”, 95th Meeting of the Supersonic Tunnel Association International April 29 – May 2, 2001, Hampton, VA

Pope, A., and Goin, K. L., 1965, “High Speed Wind Tunnel Testing,” Wiley, New York.

Van Spiegel, E., 1956, “Method of Calculation for Heat-Regenerators of Blowdown Wind tunnels”, Nationaal Luchtvaartlaboratorium, NLL-TM, F.190.

The MathWorks, Inc., 2002, Using Simulink (Version 5).

9. Copyright Notice